



Tveitnes, Trym (2001) *Application of added mass theory in planing*. PhD thesis.

<http://theses.gla.ac.uk/2890/>

Copyright and moral rights for this thesis are retained by the author

A copy can be downloaded for personal non-commercial research or study, without prior permission or charge

This thesis cannot be reproduced or quoted extensively from without first obtaining permission in writing from the Author

The content must not be changed in any way or sold commercially in any format or medium without the formal permission of the Author

When referring to this work, full bibliographic details including the author, title, awarding institution and date of the thesis must be given

# **Application of Added Mass Theory in Planing**

by

**Trym Tveitnes**

*BEng, University of Glasgow*

**Thesis Submitted for the Degree of Doctor of Philosophy**

**Department of Naval Architecture and Ocean Engineering  
&  
Department of Mechanical Engineering**

**University of Glasgow**

**July 2001**

To my Parents,  
*Sidsel and Johannes*

## DECLARATION

Except where reference is made to the work of others,  
this thesis is believed to be original.



---

## ACKNOWLEDGEMENTS

---

This thesis is the result of the work carried out by the author for the degree of Doctor of Philosophy at the University of Glasgow. Thanks are due to those who directly or indirectly contributed to the completion of this thesis.

First of all, sincerely thanks to my two supervisors: Dr. A.C. Fairlie-Clarke, for guidance, discussions and consistent supervision throughout these studies. Dr. K.S. Varyani for his advice, for fighting my case for required equipment and for his ever prompt response to any enquiries.

Thanks to the heads of the two departments, under which this work has been carried out, for providing the necessary financial support: Professor N. Barltrop, Naval Architecture and Ocean Engineering and Professor J. Hancock, Mechanical Engineering.

A very special thanks to my favourite ladies in Glasgow, Thelma Will and Maureen McGrady, secretary staff at NAOE. I can not express enough gratitude for what you have meant to me during my stay with the department. Also, thanks to David James Percival at NAOE and Yassamine Mather at ME for providing computer support.

Thanks are due to George Falconer, Brian Robb, George Silvie, Alexander Torry at the Mechanical Engineering Workshop for their excellent manufacture of components for the test rig and, equally important, for the nice conversations we had.

I would like to thank Chief Technician David Sinclair and his staff at the Hydrodynamics Laboratory, not only for their involvement in the experimental work, but also for the joyful and friendly atmosphere at the “tank”. Thanks to Bernie Reiley for assistance with manufacture of the test rig, Bill Wright for his skilful model making, Frank Sweeney for guidance with the electronics and Donald Nicholson and Grant Dunning for their assistance with conducting the experiments.

Thanks to my friend Frode Sætren who helped manufacture models for the experiments.

A special thanks to the janitor at James Watt Building, Michael, for always having a humorous comment to spare, and for brightening up many grey days. Thanks also to the nice cleaner at James Watt Building, Florence, for the early morning conversations and her smiles.

To my research colleges during my years in Glasgow, Ioannis Tsarouchas and Robert Olsen, I wish to express gratitude for getting to know you, for your honest friendship and the many good moments we have shared. All the best for the future.

Finally, most indebted am I to my parents, Sidsel and Johannes Tveitnes. Thanks for your continuous support and encouragement, for your trust, and most of all for your love. I owe you everything....

---

## LIST OF CONTENT

---

DECLARATION	1
ACKNOWLEDGEMENTS	2
LIST OF CONTENT	4
SUMMARY	10
NOTATION	11
<b>CHAPTER 1,INTRODUCTION</b>	<b>17</b>
1.1.    Planing Concept	18
1.2.    Planing Lift Prediction	20
1.3.    Research Motivation	21
1.4.    Aims and Objectives	23
1.5.    Layout of Thesis	23
<b>CHAPTER 2,RESEARCH APROACH</b>	<b>25</b>
<b>CHAPTER 3,PLANING THEORY AND LITERATURE REVIEW</b>	<b>29</b>
3.1.    Planing and Impact Theory	30
3.2.    Experimental Investigations of Planing And Impact	55
<b>CHAPTER 4,CFD SIMULATION OF TWO-DIMENSIONAL WATER ENTRY</b>	<b>57</b>
4.1.    Finite Volume Method	58
4.1.1.    Governing Equations	58
4.1.2.    Solution of The Differential Equations	61

4.1.3.	Free-Surface Model	63
4.2.	Simulation Issues	63
4.2.1.	Grid Generation	64
4.2.2.	Pre-Processing	68
4.2.3.	Solving	71
4.2.4.	Post-Processing	72
4.3.	Simulation Program	72
4.4.	Results	72
4.4.1.	Force Data	72
4.4.2.	Pressure Data	76
4.4.3.	Free-Surface Elevation	80
4.4.4.	Gravity Effect Analysis	101
<b>CHAPTER 5, EXPERIMENTAL WORK</b>		<b>107</b>
5.1.	Design Requirements	112
5.1.1.	Vertical Loads and Accuracy	112
5.1.2.	Side Loads	113
5.1.3.	Model Carrier	113
5.1.4.	Sensors and Data Acquisition	114
5.2.	Description of Test Equipment	115
5.2.1.	Drive System	115
5.2.2.	Guide and Support Structure	119
5.2.3.	Test Sections	124
5.2.4.	Model Carrier	125
5.2.5.	Sensors and Data Acquisition	126
5.3.	Design Evaluation	128
5.3.1.	Drive System	128
5.3.2.	Guide System and Support Structure	130



5.3.3.	Model Carrier	131
5.3.4.	Sensors and Data Acquisition	131
5.4.	Manufacture and Assembly	133
5.4.1.	Parts	133
5.4.2.	Rig Assembly	134
5.5.	Operation of Test Rig	142
5.5.1.	Commissioning and Drive Optimisation	143
5.5.2.	Motion Tasks	144
5.5.3.	Limit Switches	144
5.5.4.	Data Acquisition	146
5.5.5.	Video Recording	147
5.6.	Test Program	147
5.6.1.	Constant Velocity Water Entry	147
5.6.2.	Constant Velocity Water Exit	149
5.6.3.	Accelerated/Decelerated Water Entry	150
5.6.4.	Oscillation Tests	150
5.7.	Test Rig Performance	152
5.8.	Test Results	153
5.8.1.	Vertical Position of Test Section	153
5.8.2.	Viscous Force	154
5.8.3.	Force Data	157
5.8.4.	Water Surface Shape	178
<b>CHAPTER 6, COMPARISON AND DISCUSSION OF RESULTS</b>		<b>186</b>
6.1.	Comparison Between CFD and Experiment	187
6.1.1.	Forces	187
6.1.2.	Wetting Factor	193
6.1.3.	Free Surface Elevation	195

6.2.	Comparison with the Work of Others	197
6.2.1.	Slamming Force Coefficient	197
6.2.2.	Maximum Pressures	198
6.2.3.	Wetting Factor	199
6.3.	Validation of Buoyancy Ratio Function using CFD Data	200
6.4.	Most Reliable Source of Data for Development of Theory	202

## **CHAPTER 7, ADDED MASS THEORY FOR WATER ENTRY AND**

	<b>EXIT</b>	<b>204</b>
7.1.	Water Entry Theory	205
7.1.1.	Hypothesis for Separation of Water Entry Forces	206
7.1.2.	Analysis of Constant Velocity Water Entry Data	208
7.1.3.	Comparison of Water Entry Theory with Experimental Results	214
7.1.4.	Comparison of Water Entry Theory with Results from Constant Velocity Simulations by Others	219
7.2.	Water Exit Theory	220
7.2.1.	Analysis of Constant Velocity Water Exit Data	221
7.3.	Verification of Theory by Analysis of Remaining Test Data	225
7.3.1.	Max Added Mass - Analysis of Wet Chines Oscillation Test Data	226
7.3.2.	Dry Chines Added Mass - Analysis of Accelerated Water Entry Data	230

7.3.3.	Evidence of Flow Momentum Force	234
7.4.	Comparison of Added Mass Coefficients	235
7.4.1.	Dry Chines	236
7.4.2.	Wet Chines	237
7.5.	Prediction of Dry Chines Oscillation Forces – Comparison with Dry Chines Oscillation Experiment	238

## **CHAPTER 8, APPLICATION OF WATER ENTRY THEORY IN**

	<b>PLANING</b>	<b>245</b>
8.1.	Hydrodynamic Lift on Slender Planing Surfaces	246
8.2.	Hydrostatic Lift on Planing Surfaces	250
8.2.1.	Flat Plates	250
8.2.2.	Prismatic Surfaces	252
8.3.	Comparison of Present Slender Theory with Planing Data	253
8.3.1.	Flat Plates	253
8.3.2.	Wet Chines Prismatic Surfaces	255
8.3.3.	Dry Chines Prismatic Surfaces	257
8.4.	Hydrodynamic Lift on Non-Slender Planing Surfaces	259
8.4.1.	Flat Plate Theory	261
8.4.2.	Two-Dimensional Planing Plate	262
8.4.3.	Prismatic Theory, Wet Chines	266
8.4.4.	Prismatic Theory, Dry Chines	270
8.5.	Validation of The Applied Hydrostatic Lift	

Component	271
8.6. Comparison of Non-Slender Body Equations with Experiments	274
<b>CHAPTER 9, CONCLUSIONS AND RECOMMENDATIONS</b>	<b>278</b>
9.1. Conclusions	279
9.2. Recommendations for Future Work	282
9.3. Closure	283
<b>APPENDIX A - EARLIER WATER ENTRY EXPERIMENTS</b>	<b>285</b>
<b>APPENDIX B - TEST RIG MANUFACTURE DRAWINGS</b>	<b>293</b>
<b>APPENDIX C - TEST RIG EQUIPMENT SHEETS</b>	<b>313</b>
C.1. DDE1000 Load Cell – Datasheet	314
C.2. Load Cell 1 – Calibration Sheet	315
C.3. Load Cell 2 – Calibration Sheet	316
C.4. Load Cell 3 – Calibration Sheet	317
C.5. Load Cell 4 – Calibration Sheet	318
C.6. Ball Screw – Drawing	319
C.7. Timing Belt Drive – Calculation	320
C.8. Servomotor – Datasheet	321
C.9. Digital Servo Amplifier – Datasheet	322
<b>LIST OF FIGURES</b>	<b>323</b>
<b>LIST OF TABLES</b>	<b>335</b>
<b>REFERENCES</b>	<b>336</b>



---

## SUMMARY

---

Prediction of the hydrodynamic forces on planing craft by strip method requires the force acting on two-dimensional sections in vertical motion on the free surface to be known. The motion of a transverse section of a prismatic hull in steady planing corresponds to a constant velocity water entry of a wedge shaped section. The force acting on the wedge section before the chines get wetted is found from a consideration of the rate of change of the section added mass. The current added mass impact theory does not give a satisfying definition of the change in added mass after chines wetting, and hence predictions of non-constant velocity water entry can not be made accurately. As a consequence, the theory is not applicable for use in prediction of the lifting force on hulls in unsteady planing or on hulls in steady planing with non-straight keel line, i.e. phenomena corresponding to non-constant water entry. Also, in unsteady planing, sections experience exit motion due to the pitch and heave response of the craft. If applying the added mass theory in exit predictions, the resulting force acts in the direction of motion, something in contradiction with intuition and common sense.

The work described in this thesis has resulted in a new added mass theory for water entry and exit of transverse sections of typical planing craft. A program of numerical simulations and experiments with wedge shaped sections have been carried out, providing force data for water entry and exit of such bodies to and from the water. Analysis of these data have led to separation of the added mass and damping forces and to the development of quasi-empirical expressions applicable for both constant and non-constant velocity force predictions. Thus the new theory provides a basis for strip method for prediction of the unsteady motion forces of planing craft.

Further, the new added mass theory for water entry has been applied to predict the steady planing lift force on slender body hulls, and consistency with published planing data has been found. Also, an empirical aspect ratio correction has been derived, allowing application to large aspect ratio (non-slender) planing hulls.

---

## NOTATION

---

$A$	-	aspect ratio of planing surface
$b$	-	beam of planing surface or hull section
$c$	-	width of a submerged body
$C_f$	-	frictional coefficient
$C_{fm}$	-	two-dimensional flow momentum coefficient
$C_F$	-	two-dimensional slamming force coefficient on immersion depth
$C_{F,b}$	-	two-dimensional force coefficient on beam
$C_{F,b-f}$	-	two-dimensional frictional force coefficient on beam
$C_{m'}$	-	two-dimensional added mass coefficient
$C_p$	-	pressure coefficient
$C_v$	-	speed coefficient
$C_{L_{S_w}}$	-	lift coefficient on $S_w$
$C_{L,CD_{S_w}}$	-	cross flow lift coefficient on $S_w$
$C_{L_b,0}$	-	flat plate lift coefficient on beam squared
$C_{L_b,\beta}$	-	deadrise angle surface lift coefficient on beam squared
$C_{m'_\infty}$	-	two-dimensional infinite immersion depth added mass coefficient on half-beam squared

$C_{L_l}$	-	lift coefficient on length squared
$C_{L_b}$	-	lift coefficient on beam squared
$C_{AB_b}$	-	Archimedes' buoyancy force on beam squared
$C_{AB_l}$	-	Archimedes' buoyancy force on length squared
$C_{HS_b}$	-	hydrostatic lift force on beam squared
$C_{HS_l}$	-	hydrostatic lift force on length squared
$C_{L,m'_b}$	-	added mass lift on beam squared
$C_{L,fm_b}$	-	flow momentum lift on beam squared
$C_{L,m'_l}$	-	added mass lift on length squared
$C_{L,fm_l}$	-	flow momentum lift on length squared
$d$	-	vertical keel to chine distance
$D_f$	-	frictional resistance
$e$	-	angle between downwash and horizontal at centre of pressure
$f(A)$	-	aspect ratio correction
$F'$	-	force per unit length
$F'_{fm}$	-	flow momentum force per unit length
$F'_{m'}$	-	added mass force per unit length
$F_{4LC}$	-	sum of forces measured by four load cells
$f_n$	-	natural frequency

$G$	-	weight
$g$	-	gravitational acceleration
$k$	-	immersed chines added mass factor
$l$	-	length of planing surface defined by intersection with calm water
$l_w$	-	wetted length of planing surface
$l_{ws}$	-	length along wedge surface of two-dimensional wedge
$L$	-	lift force, vertical component of normal force $N$
$L_{AB}$	-	Archimedes' buoyancy lift force
$m'$	-	added mass per unit length
$m'_0$	-	added mass per unit length at the point the chines become wetted
$m'_w$	-	added mass per unit length of chines immersed wedge section
$m'_\infty$	-	added mass per unit length of chines immersed wedge section at infinite immersion depth
$m'_x$	-	added mass per unit length at transom section of planing hull
$m_0$	-	two-dimensional lift curve slope
$M_M$	-	mass of test section
$m_w$	-	sum of sectional added mass along the length of a planing hull
$N$	-	normal pressure force acting on hull
$R_n$	-	Reynold's number
$S_w$	-	wetted surface area
$T$	-	thrust from propulsion



$u$	-	velocity in x-direction
$U_0$	-	steady planing velocity
$v$	-	velocity in y-direction
$V_n$	-	normal velocity
$V_p$	-	parallel velocity
$V_{ws}$	-	velocity along wedge surface
$w$	-	velocity in z-direction
$WF$	-	wetting factor
$WL$	-	calm water level
$x$	-	dimension along the keel-line
$y$	-	half-distance between intersections of hull section and calm water level
$z$	-	immersion depth taken normal to the keel-line
$Z$	-	vertical distance from keel along the wedge surface
$z_c$	-	chines immersion, measured as the further immersion from chines become wetted
$z_{ce}$	-	nominal immersion depth at the instant the chines emerge during a water exit
$z_{pf}$	-	immersion depth at which the peak force occur during wedge water entry
$Z_{p-max}$	-	vertical distance from keel to peak pressure on the wedge surface

$Z_{pt}$	-	vertical distance from keel to pressure termination point on the wedge surface
$\Delta C_m$	-	added mass coefficient increment from chines immersion
$\Delta m'$	-	added mass increase from chines immersion
$\Phi$	-	ratio of predicted to measured lift force
$\alpha$	-	angle of incidence
$\beta$	-	angle of deadrise
$\beta_e$	-	angle of deadrise of a trimmed hull taken in the vertical plane
$\phi$	-	velocity potential
$\phi_0$	-	buoyancy ratio, true hydrostatic force/Archimedes' buoyancy
$\rho$	-	density of water
$\tau$	-	trim angle

---

**CHAPTER 1**

**INTRODUCTION**

---

The work described in this thesis concerns the hydrodynamic performance of planing craft. In particular, the thesis describes a program of numerical simulation and experiments with wedge sections, the results of which are used to formulate an improved theoretical basis for the prediction of lift forces under both steady and also unsteady planing conditions, involving both entry and exit of the planing surface to and from the water.

Numerical methods, based on fluid flow equations, already exist, which are capable of solving the flow around and the hydrodynamic forces acting on planing craft in unsteady motion. However, the knowledge, equipment, time and cost of carrying out such analysis makes it an impractical tool for e.g. preliminary design. Empirical equations exist that are suitable for preliminary design, but limitations in their theoretical basis restrict the range of parameters and conditions to which they can be applied, and in particular they cannot handle the exit of sections from the water, which is a requirement for seakeeping studies. The aim of this thesis is to provide an improved basis for preliminary design and seakeeping studies of planing craft.

## 1.1. Planing Concept

The planing concept provided the earliest form of high-speed marine vehicle and has been applied since the beginning of the 20<sup>th</sup> century. Early research on hydrodynamics of planing surfaces was motivated mainly by the design requirements of water based aircraft rather than by the development of planing craft. Developments of lightweight marine engines gave increased prospects for use of the planing concept with marine vehicles, and thus stimulated further planing research. Today the planing concept is used in a variety of applications such as patrol boats, lifeboats, powerboats and pleasure craft, as well as its continuing use in water based aircraft.

In common with other forms of high-speed marine vehicles, the principle of the planing concept is to lift the craft out of the water to obtain reduced frictional and wave making resistance. While other concepts deploy hydrofoils or air cushioning



to lift the craft, the planing hull is lifted out of the water by dynamically developed pressure forces acting directly on the hull itself. A planing craft moves with the planing surface at an angle to the horizontal, referred to as the trim angle. This causes a deflection of the water that passes underneath the hull. Deflection of the water particles requires a force and the reaction to this force is experienced as pressure acting on the planing surface. The main advantage of this concept is its simplicity both in construction and operation.

Planing is only achieved when the craft is travelling above a certain speed. At low speed the buoyancy supports the majority of the weight. As the speed increases, the dynamic pressures increase and support more and more of the craft's weight. When the dynamically developed pressure supports the majority of the weight force, the craft is said to be in its planing region. The speed at which planing occurs is dependent of the relationship between the weight, the hull geometry and the longitudinal location of the centre of gravity.

A vast number of planing hull designs have been developed since the concept was initially applied. The most commonly used is the single hard chine mono hull, which is also the type under consideration herein. Other designs comprise multiple chines, round bilge and transverse step. Various basic cross section shapes are deployed. Among these are the inverted bell sections, the convex and concave sections and the simplest but yet widely used straight line or v-section.

Being able to predict how a marine craft is going to perform is of great importance regardless of its concept. The performance is divided into calm water and seakeeping characteristics. Calm water performance characteristics include the running trim, draft and resistance. Seakeeping characteristics include dynamic responses to the encounter of a seastate in form of heave, pitch and roll attitude. The characteristics given most attention depend on the intended operation of a craft. Typically there is a trade-off between the various performance characteristics. An example of this is the deep-v planing hull that gives a softer ride in head seas than the low deadrise hull. But this is at the cost of a higher steady planing resistance because the lower dynamic lift acting on the deep-v planing hull causes it to run deeper and with greater wetted surface.

## 1.2. Planing Lift Prediction

The forces that act on a planing craft are shown in Figure 1-1. Of primary interest is the normal pressure force  $N$ , the vertical component of which is the lifting force.

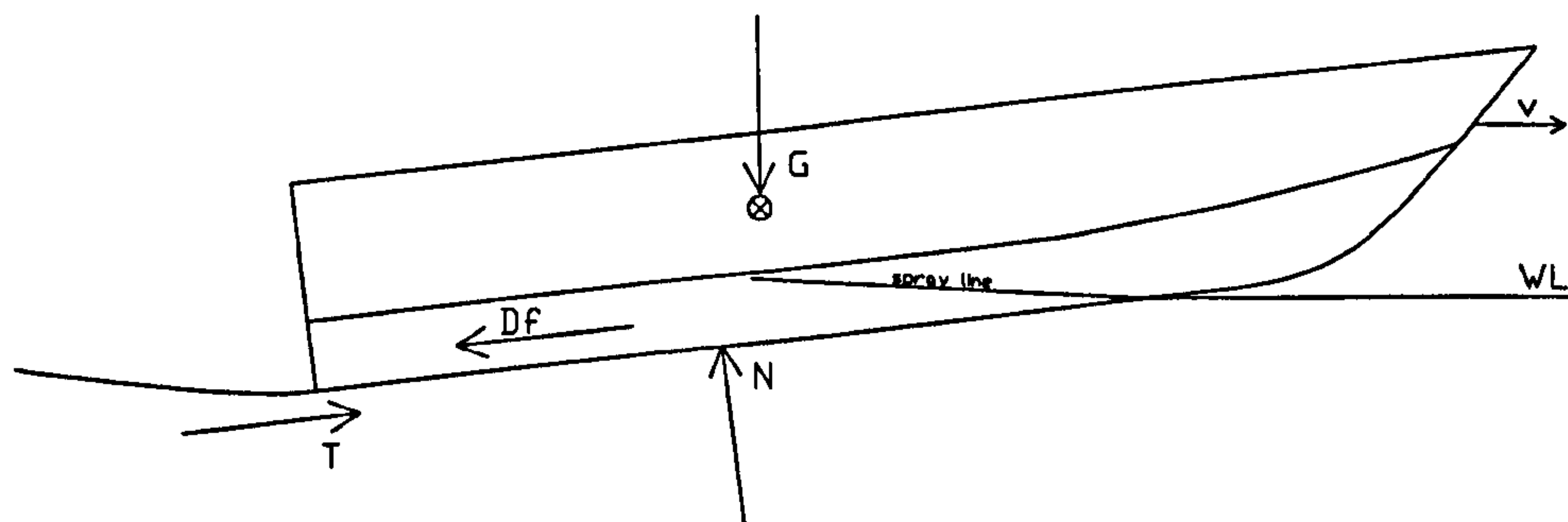


*Figure 1-1. Forces acting on a planing craft.*

The predictions of both steady and unsteady planing characteristics depend on determining the hydrodynamic lifting force that acts on the hull. The theoretical methods that have been developed for prediction of the planing lift force have followed two main approaches: lifting line methods, adopted from airfoil theory, and added mass methods, which are related to slender body theory. The lifting line methods are only applicable for prediction of the steady planing lift force, while some of the added mass methods also include prediction of the unsteady planing lift forces that act on a hull during impact with the water.

When travelling on a disturbed water surface, planing craft sections experience periodic exit from the water due to the pitching and heaving motion. Therefore, to allow estimates in such cases, the added mass method has been subject to an investigation to extend its applicability to include the estimate of forces on transverse sections of planing hulls during water exits as well as impacts.



### 1.3. Research Motivation

A study of the current added mass theory for calculation of planing lift and water impact loads revealed anomalies when applied to certain cases. These were initially pointed out in unpublished studies by Farlie-Clarke (1997).

Farlie-Clarke questions the approach used in added mass theory whereby the entire water entry force is explained in terms of changes to the added mass. He explains: "The current theory has the advantage that it is simple, but the application of the theory is limited since it is not an accurate representation of the hydrodynamic events. In ship motion theory, the hydrodynamic forces are explained by dividing them into two parts, one part proportional to the acceleration with the constant of proportionality given by the added mass, and a second part proportional to velocity with the constant of proportionality described as the damping coefficient. The same division needs to be made when looking at the water entry problem. During water entry, the total vertical momentum of all the water that is set in motion is equal to the vertical impulse applied to the hull. However, if the hull is then decelerated, not all of the water that has been set in motion will react in the same way. Some will behave as if attached to the hull and will decelerate, giving up its momentum as a force acting upwards on the hull, but some of the fluid will be far from the hull and its velocity will be largely unaffected by later changes in motion of the hull. One way to view this is that part of the process of setting the water in motion is reversible and part is not reversible. The term 'added mass' should be reserved exclusively for the reversible part, while the forces associated with the irreversible part can be described in terms of flow momentum. A consequence of the present practice of explaining the total water entry force as a change in added mass is that the theory cannot be applied if there is a reversal of the velocity (i.e. water exit) as will occur on a planing hull moving in waves or during porpoising. The theory would then predict an upward force acting on the hull, equal but opposite to the entry force, as the momentum was recovered from the added mass. The flow momentum also provides a better explanation than cross flow drag, or additional added mass, of the force acting during water entry after chine immersion. It is unlikely that the

added mass will change much in these circumstances, but the water displaced by the hull entry must flow away from the hull and this gives rise to a flow momentum force. Constant velocity entry and exit force data is needed for planing simulation”

The most recent added mass planing theory, Payne (1992, 1994, 1995), assumes a linear increase in the added mass with depth after chine immersion. It follows from this relation that the sectional force in the entire chines wetted portion of a planing hull is regarded as constant. Based on the assumption that the hydrodynamic lift is entirely added mass related, the wet chines added mass gradient is determined by Payne by fitting to experimentally obtained lift forces on prismatic planing surfaces. This has resulted in reasonably accurate equations for planing lift in cases when the vertical velocity component is constant throughout the length of the surface. However, this approach assumes that the entire force impulse exerted by the hull on the water is contributing to an increase in the added mass, the momentum of which is recoverable in full. If this assumption does not hold, it follows that the added mass values that are derived are overestimated, and the approach will be invalid for calculation of non-constant velocity water entry forces and calculation of lift force on non-prismatic planing surfaces. In other words, if added mass is wrong, any acceleration effect will be poorly estimated.

Also, to the best of the author’s knowledge, there is no data from constant velocity water entry experiments available to verify the constant velocity water entry theory. Many experiments have been conducted to explore the water entry and impact problem, but these have all been so-called drop tests. During a free-fall drop test, the gravitational driving force is constant and therefore the impacting body is subject to deceleration and acceleration during the course of the water entry as the impact force varies. Nor are there currently any experimental data available from constant velocity water exits, and only very limited experimental data on vertical oscillation of wedge sections partially submerged. Thus, there is a need for producing force data for velocity controlled water entries and exits.



## 1.4. Aims and Objectives

The main objective of the investigation described herein is to investigate planing behaviour and to develop the added mass theory for planing so that it can handle unsteady motions and water exit. The aims are summarised as follows:

1. To find a basis to divide the forces acting on two-dimensional wedge sections during water entry between those caused by change in added mass momentum and those due to flow momentum.
2. To evaluate the change of added mass, if any, after chine wetting.
3. To produce a revised added mass theory for water entry forces that is consistent for accelerated entry as well as constant velocity entry for dry and wet chine conditions.
4. To explore the validity of the revised added mass theory for prediction of water exit forces on wedge sections.
5. To apply the two-dimensional water entry added mass theory directly in a procedure to predict the steady planing lift force on slender body planing surfaces.
6. To study the three-dimensional flow effects on the slender body hydrodynamic lift force for finite length to beam ratio planing surfaces, and to merge this with the theory for the two-dimensional plate.

## 1.5. Layout of Thesis

The research approach adopted to achieve the above aims and objectives is described in Chapter 2. The research issues are discussed together with justifications of the approach taken. In Chapter 3, the planing theories are discussed and a review of the relevant published work in the field is given. Then the numerical simulations and the experiments that have been carried out to provide a basis for the development of the present theory are described in

Chapters 4 and 5. Further on, in Chapter 6, the results from this work are compared with published data and the results that provide the basis for the new are discussed. Chapter 7 deals with the analysis of the data that leads to development of the present added mass theory. In Chapter 8 this theory is applied to predict the lift force on prismatic planing hulls, and comparisons are made with published experimental prismatic planing data. Finally, in Chapter 9, conclusions are given on the work carried out and the findings made in the present investigation, along with recommendations for future work in this field.

---

**CHAPTER 2**

**RESEARCH APPROACH**

---



This section describes the research approach applied to achieve the objectives with the present investigation.

The first step was to carry out a study of the past theoretical and experimental work that has been carried out in the field of water entry and planing. Using the slender body assumption, the planing of a prismatic hull can be modelled as a constant velocity water entry of a transverse section of the hull. Thus, the water entry, or impact, problem has an important bearing on planing. An investigation into the separation of the dynamic lift components on planing surfaces therefore required knowledge of the total force acting on wedge shaped sections (typical planing craft cross sections) during constant velocity water entry. Surprisingly, it was found that no experimental results for constant velocity water entry of hull sections are available in the literature. Many experiments have been conducted to explore the water entry and impact problem, but these have all been so-called drop tests, in which the body is subject to deceleration and acceleration as the impact force varies. Since the water exit problem was also under investigation, results for such were also required. No experimental data could be found for constant velocity water exits. Nevertheless, due to the requirements for force data from constant velocity water entry and exits of a series of wedges, such data had to be produced as part of the present research. Lift data from planing experiments with prismatic hulls were widely available from the literature.

It was decided that both CFD simulations and experimental work should be carried out to obtain the required constant velocity water entry and exit data. Data from only CFD work would not provide a reliable source of information, as the quality of the results from such simulations currently cannot be guaranteed. Therefore analogous experimental work had to be carried out both to generate direct data and for verification of the CFD results. One might think that since performing experiments anyway, results from the CFD simulations would be redundant. However, before conducting experiments there are always uncertainties whether the experimental set-up is going to be successful, and hence it is not guaranteed that useful results will be obtained. Therefore it was deemed important also to carry on with the CFD work. Another reason for carrying out



analogous CFD and experimental work was that it would give an opportunity to evaluate the quality of the CFD simulations, so that the CFD method might also provide a basis for extrapolating from the experimental results. Also, the CFD method makes it possible to do simulations in a zero gravity environment and thus exclusively study the hydrodynamic force acting on wedge sections.

The water exit CFD simulations were abandoned at an early stage because it was realised that it would be difficult to relate data from such simulations to experimental data, as the force acting during the stages when the chines emerges was found highly sensitive to initial depth and acceleration to constant velocity. Consequently, the CFD work was limited to water entries with wedge shaped sections. Instead, effort was concentrated on performing both gravity and zero-gravity simulations for the purpose of isolating the effect of gravity on the total force so as to obtain the true hydrodynamic and hydrostatic force contributions during water entry.

Experiments with water entry and exit of wedge sections were conducted. Both constant and non-constant velocity tests were carried out. Non-constant velocity tests were conducted so that the true acceleration dependent forces, and thus the added mass, could be extracted. Oscillation tests with the wedge sections fully immersed (wet chines throughout the cycles) were also carried out so that the added mass of sections at deep immersion could be found. Dry chines oscillation tests were included in the test series for use in the revised added mass theory for prediction of the forces acting on wedges in cyclic motion in a free surface.

Comparison between the results by others and those obtained from the present work were necessary as part of evaluating the reliability of the data. Through this evaluation it was decided which data sets were the most reasonable basis for development of the revised added mass theory for planing.

A hypothesis, based on the momentum theorem, for separation of the hydrodynamic force into velocity dependent and acceleration dependent forces was established. The CFD data were used to aid in extracting the hydrodynamic contribution from the experimental measurements. The extracted hydrodynamic

data were analysed on the basis of the hypothesis to derive the hydrodynamic coefficients defining the two different components, thus providing a basis for prediction of the forces on planing craft in unsteady motion.

Further, the new added mass theory for water entry and exit was applied to estimate the lift force on slender body prismatic planing surfaces. An aspect ratio correction was derived to enable the theory to be applied also to craft with low length to beam ratios where the slender body assumption does not hold true.

The work makes new information available to the field of study in the form of systematic data for constant velocity water entry and exit of wedge shaped sections, and by providing a theoretical basis for separating the force components during water entry into acceleration and velocity dependent parts.

---

**CHAPTER 3**

**PLANING THEORY AND LITERATURE REVIEW**

---



This section contains an introduction to planing theories along with a review of the past theoretical and experimental work in the field of planing and impact that is relevant for the present investigation. Research into the planing and the impact phenomena and advances in these theories have to a large extent followed each other, and are therefore discussed jointly in this section. Only a few of the theories are free from empirical corrections for improved comparison with experimental data, while the majority have larger corrections to improve the correlation with experimental data. Purely empirical equations have also been derived from the experimental data. Fitting of such equations to the data has to an extent been based on mathematical forms adopted from theoretical approaches, e.g. the separation into linear and non-linear terms. Apart from one widely used procedure, the purely empirical methods are not included in the following review. In addition to covering planing and impact phenomena, a section is included that reviews work on hydrodynamics of heaving sections.

### **3.1. Planing and Impact Theory**

Planing theory has developed along two main streams; the added mass theories, and the lifting line theories. The added mass theories relate to slender body theory in that they use the flow around a two dimensional section during a vertical water impact as an analogy for the steady flow in transverse planes across a planing hull in order to predict the normal force on the hull. This analogy is demonstrated by considering a thin transverse slice of water as the hull passes over it. It is shown in Figure 3-1 that what the slice of water experiences is similar to a transverse section moving vertically into the water with a velocity equal to the vertical velocity component of the hull at that point. (The notations in this figure differs from the notations of the thesis in that  $T$  denotes trim angle and  $v$  denotes forward speed).

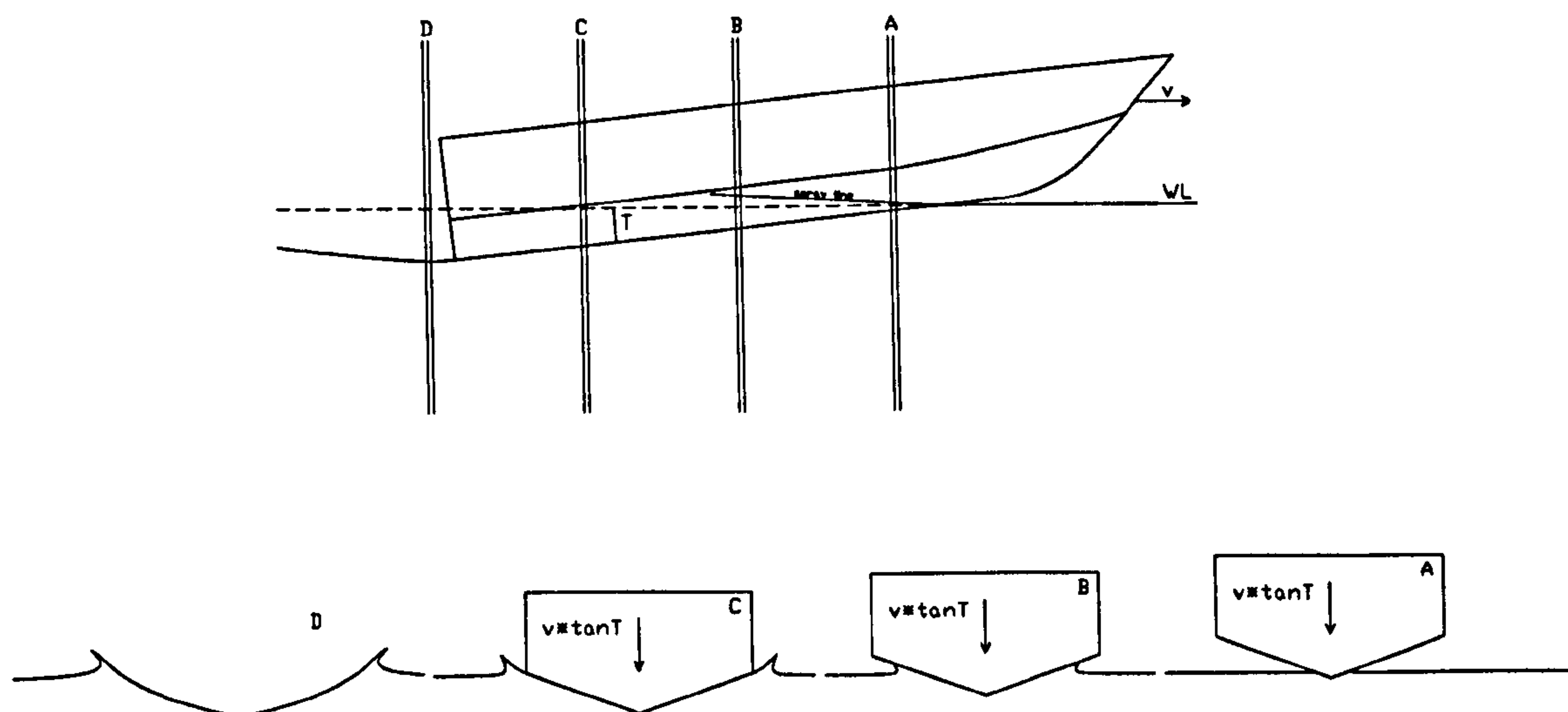


Figure 3-1. The analogy of the impact/water entry and the planing phenomena.

There is a cross sectional added mass momentum due to the vertical velocity component. The added mass theory relates the sectional lifting force to the rate of change of momentum of the cross sectional added mass as the planing surface passes a section of water. For prismatic hulls, the integral of the sectional force over the length of the planing surface, which gives the lifting force, is given by the product of the vertical momentum of the added mass at the transom and the forward velocity of the hull. Thus, knowing the added mass of the stern hull section during a vertical impact, the momentum of the downwash from the planing hull is evaluated and the lifting force found. Many researchers have derived added mass values directly for a range of cross sectional shapes by studying the two-dimensional water entry problem, and these have been applied in planing lift prediction. Another approach taken is to obtain values indirectly by fitting the transom cross sectional added mass data to experimental planing lift data. The slender body assumption is only reasonable for large length to beam ratios and moderate trim angles. At low length to beam ratios, the longitudinal flow has a significant effect on the lifting force. The added mass theory uses empirical aspect ratio corrections to account for this lift reduction. For the forward portion of a planing hull where the chines are dry, the lift force is accounted for by an increase in the added mass due to increase in cross sectional wetted width as



the hull passes over the considered slice of fluid. Once the chines become immersed, the added mass does not increase, or increases only slowly. While early added mass planing theories accounted for the lift on the wet chine portions of the hull as cross-flow drag, more recent studies have accounted for this lift by claiming a further increase in the added mass after chine immersion.

The other main stream that planing theory has developed along is descended from the lifting line theory. The lifting line theory originates from aerodynamics where it is a useful tool in computing lift and induced drag on wings. It consists of modelling the wing by a set of vortices bound from tip to tip along the wingspan, and computing the reduction of vorticity due to vortices bent backward (shedding) from the wing. A theorem states that vortices shed from the wing in flight reduce the strength of the vortices along the wingspan. The local lift force along the span of the wing is found to be proportional to the component of the vortices at right angles to the local flow direction. The mathematical solution of the lifting line theory results in a relation between the lifting force on a wing of finite aspect ratio and that of the two-dimensional case, i.e. infinite aspect ratio. A wing or airfoil has flow on both its lower and upper side, while a planing hull has flow only on the lower side. The theory has therefore been adapted for use in computations of planing lift by correcting for the fact that there is flow only on the pressure side of the planing hull.

The earliest studies of the water impact of planing hull shapes were motivated by requirements to predict the hydrodynamic load acting on seaplane floats during landing. Initially the vertical impact of a slender float at zero trim was considered. Von Karman (1929) presented a pioneering impact theory for calculation of the vertical force on wedge shaped floats, which was based on conservation of the sum of the momentum of the seaplane mass and an added mass. The product of the added mass times the impact velocity represented the vertical momentum imparted to the water under the float. Von Karman approximated the flow around the wedge shaped float as the flow around an expanding flat plate of a half-width

that was related to the immersion depth  $z$  of the immersing wedge by  $y = \frac{z}{\tan \beta}$ .

The sectional added mass was taken as half of that which was known for a fully submerged flat plate of infinite length, which gives

$$m' = \frac{1}{2} \rho \pi \cdot y^2 \quad (3-1)$$

where the dash denotes that the added mass is sectional.

As the wedge immerses, the half-width  $y$  increases and from Equation (3-1) it follows that there is an increase in the added mass. From Newton's 2<sup>nd</sup> law, it follows that the force acting on the wedge equals the time rate of change of momentum of the added mass. For a unit length of wedge with entry velocity  $w$

$$F' = \frac{d(m'w)}{dt} = m' \cdot \frac{dw}{dt} + w \cdot \frac{dm'}{dt} = m' \cdot \frac{dw}{dt} + w^2 \cdot \frac{dm'}{dz} \quad (3-2)$$

Substituting Equation (3-1) in Equation (3-2) and noting that  $y = \frac{z}{\tan \beta}$  gives

$$F' = \frac{1}{2} \rho \pi \frac{z^2}{\tan^2 \beta} \cdot \frac{dw}{dt} + w^2 \cdot \rho \pi \frac{z}{\tan^2 \beta} \quad (3-3)$$

For constant velocity this reduces to

$$F' = w^2 \cdot \rho \pi \frac{z}{\tan^2 \beta} \quad (3-4)$$

It is shown later in this thesis that Von Karman's theory is in reasonably good agreement with present experimental work for 45 degree deadrise angle wedges, while the discrepancy increases to about a 50 percent under-estimate of the forces during water entry of a 5 degree deadrise angle wedge. Von Karman's theory assumes that the float is of infinite length, so that only transverse flow occurs. This is a reasonable assumption for the general slender float impact at zero trim.



However, most landings are performed at a trim angle and hence initially the wetted length to width ratio of the impacting body is much lower.

Pabst (1930) followed up on Von Karman's added mass impact theory, but considered the velocity component normal to the keel, rather than the vertical impact velocity, to make the theory applicable for the cases where the impact trim is not zero. This modification also ensured that the additional impact velocity resulting from the forward speed of the seaplane during landing was accounted for. Pabst also introduced an empirical aspect ratio correction to the added mass of the float that was based on results from vibration tests of submerged flat plates, yielding the added mass of a wedge shaped float expressed as

$$m' = \frac{1}{2} \rho \pi \cdot y^2 \cdot \left(1 - \frac{y}{l}\right) \quad (3-5)$$

where  $l$  is the length of the float. It is seen that for large  $l$ , the added mass given by Equation (3-5) approaches the two-dimensional added mass given by Von Karman in Equation (3-1).

Without reference to Von Karman's work, Wagner (1931) applied the same added mass momentum consideration to calculate the impact force on wedges. He also solved the potential flow about a submerged flat plate and used the vertical velocity components in the fluid to compute the shape of the free surface adjacent to the impacting wedge. The wetted width due to pile-up of water was thereby calculated to be increased by a wetting factor of  $WF = \frac{\pi}{2}$  times greater than the nominal width. Using this finding, Wagner postulated that the added mass should be associated with the wetted half-width rather than nominal half-width, and thus obtained the force on a wedge during constant velocity water entry as

$$F' = w^2 \cdot \rho \pi \cdot \left(\frac{\pi}{2}\right)^2 \cdot \frac{z}{\tan^2 \beta} \quad (3-6)$$



that is,  $\left(\frac{\pi}{2}\right)^2$  times greater than that by Von Karman (1929).

Later Wagner (1932) computed a solution of the potential flow beneath an immersing triangular prism with deadrise angle of 18 degree to find the force during constant velocity water entry of this wedge. He then derived an equation that passes through the calculated point at 18 degree and which approaches zero force at 90 degree deadrise and infinite force at 0 degree deadrise, given by

$$F' = \pi \left( \frac{\pi}{2\beta} - 1 \right)^2 \cdot \rho \cdot w^2 \cdot z \quad (3-7)$$

As will be shown later in this thesis, Equation (3-7) proves to be in reasonably good agreement with present experimental results from constant velocity water entry tests.

Sydow (1938) equated the constant velocity term of Equation (3-2) to Wagner's (1932) force equation (3-7) to derive an expression for added mass as a function of deadrise angle.

$$m' = \rho \frac{\pi}{2} \left( \frac{\pi}{2\beta} - 1 \right)^2 \cdot z^2 \quad (3-8)$$

which is referred to as the Wagner-Sydow equation.

Kreps (1943) combined the added mass treatment by Wagner with the aspect ratio correction of Pabst. In addition, Kreps advanced an idea not previously included in impact theory. In addition to the forces associated with rate of change of flow pattern (or changes in added mass momentum), he included a force term representing the instantaneous flow pattern. The familiar flat plate drag coefficient of 1.28 was adopted as the basis for the additional force term. Kreps performed

drop-tests with floats of deadrise angle less than 30 degree and used the data to evaluate the proposed equations by means of comparing the deceleration during the impact. Approximate agreement of the theory with test data was indicated. It is not raised as a point in Kreps' paper, but the inclusion of the instantaneous flow pattern drag resulted in a theory that gave non-zero force for chines immersed water entry. Although the soundness of the force term is questionable, this was something previously not achieved with added mass impact theories.

Mayo (1945) presented an added mass impact theory for wedge shaped seaplane floats where the effect of the velocity components, normal to ( $V_n$ ) and parallel to ( $V_p$ ) the keel, are treated in separate terms. The total normal force on the float during oblique impact is given as the sum of changes in added mass momentum in planes normal to the keel plus the rate at which momentum is imparted to the downwash

$$N = \frac{d}{dt}(m_w V_n) + m'_x V_n V_p \quad (3-9)$$

where  $m_w$  denotes the sum of the added mass in planes normal to the keel and  $m'_x$  denotes the two-dimensional added mass at the transom. For a constant trim angle and zero vertical velocity, the wetted length and thus the total added mass is constant. If the horizontal velocity is also constant, Equation (3-9) is reduced to the second term only, yielding an expression for calculation of the total steady planing normal force, which is given by

$$N = m'_x U_0^2 \sin \tau \cos \tau \quad (3-10)$$

noting that  $U_0 \sin \tau = V_n$  and  $U_0 \cos \tau = V_p$ . In his steady planing normal force equation, Mayo used the two-dimensional added mass given by Sydow in Equation (3-8) and the aspect ratio correction given by Pabst to account for the longitudinal flow that occurs at low length to beam ratios, yielding



$$m'_x = \frac{1}{2} \rho \pi z^2 \cdot \left( \frac{\pi}{2\beta} - 1 \right)^2 \cdot \left( 1 - \frac{y}{l} \right) \quad (3-11)$$

where  $z$  is immersion depth taken normal to the keel-line at the transom, and  $y$  is defined as the nominal width of the transom section (distance between intersections of float and calm water line). Since Pabst obtained his aspect ratio correction factor from analysis of vibrating submerged flat plates, its use in planing was somewhat questionable. Therefore, Mayo used a large amount of prismatic planing data to determine the adequacy of Equation (3-11). The normal force, given by Equation (3-10), was solved for  $m'_x$  by substituting experimental values of  $V$  and  $\tau$ . After comparison with theoretical values for  $m'_x$ , Mayo inserted a correction factor of 0.82 into Equation (3-11).

Bisplinghof and Doherty (1950) presented a computation of the added mass for wedges. Solving the potential flow about an expanding prism, the free surface was modelled as a line of zero potential parallel to the undisturbed water surface and at an elevation given by the point of intersection of the body and the piled-up water surface. Following Wagner's (1931) assumption, the contour of free surface was computed by integrating over time the vertical velocity of the water particles at the line of zero potential. The added mass was obtained by equating the total kinetic energy in the fluid domain to the kinetic energy of the added mass moving at the entry velocity of the body as follows

$$-\frac{\rho}{2} \int \phi \frac{\partial \phi}{\partial n} ds = \frac{1}{2} m' w^2 \quad (3-12)$$

This gave added mass estimates close to those obtained by the Wagner-Sydow equation. Further, Bisplinghof and Doherty applied the computed added mass values to a differential equation of motion for two-dimensional wedge impacts that was based on conservation of the sum of body and added mass momentum, as was Von Karman's (1929) equation. Bisplinghof and Doherty also performed

free-fall drop tests with wedges, where the acceleration/deceleration during the drop/impact was measured. The measured accelerations are presented together with accelerations obtained by solution of the differential equation of motion. The theory and experiments agree well for cases with 20, 30, 40 and 50 degree deadrise angles, while significant discrepancy is seen for the 10 degree case. Disregarding the lowest deadrise angle case, Bisplinghof and Doherty's comparison between theory and experiment demonstrates the usefulness of the simple added mass theory for impact prediction if proper consideration is given to the value of the added mass.

Korvin-Kroukovsky (1950) developed a finite width, flat plate planing theory. Unlike Mayo, Korvin-Kroukovsky did not adopt the aspect ratio correction from Pabst. Instead, an expression for the lift coefficient as a function of aspect ratio was advanced from a merging of the known theories for the two limits, i.e. for a truly slender plate (infinite length) and for a two-dimensional planing plate (infinite width). Pierson and Leshnover (1950) presented the analytical solution to the two-dimensional planing plate potential flow problem, originally examined by Wagner (1932), which resulted in the lift-curve slope of

$$\frac{dC_{L_{S_w}}}{d\alpha} \approx \pi \quad (3-13)$$

where  $C_{L_{S_w}}$  is the lift coefficient based on wetted area  $S_w$  (which, for two-dimensional planing, is given by wetted length and unit width) and  $\alpha$  is the angle of incidence. Korvin-Kroukovsky proposed that Equation (3-13) could also be considered valid for planing plates of finite width, provided that the angle  $\alpha$  was taken as that between the planing surface and the velocity vector at its centre of pressure, i.e. the angle between the downwash and the planing plate. Thus the trim angle of the plate is defined by

$$\tau = e + \alpha \quad (3-14)$$



where  $e$  is the angle between the downwash and the horizontal at the centre of pressure. The downwash angle at the centre of pressure for plates of finite width was derived by comparison with the flat plate slender body planing lift equation. In the slender body approach, the lift force is found as the reaction to the rate at which vertical momentum is imparted to the water, and is given by

$$L = \frac{1}{2} \rho \cdot U_0 \cdot w \cdot \pi \left( \frac{b}{2} \right)^2 \quad (3-15)$$

where  $w$  is the vertical velocity imparted to the water. By energy consideration, the vertical velocity of the downwash at the centre of pressure was taken by Korvin-Kroukovsky to be half of the vertical velocity imparted at the transom. Thus the downwash angle  $e$  was found as

$$e = \frac{w}{2 \cdot U_0} \quad (3-16)$$

Taking  $w$  from Equation (3-15) and substituting in Equation (3-16) gave

$$e = \frac{4L}{\rho \pi b^2 U_0^2} \quad (3-17)$$

Expressing  $L$  in Equation (3-17) in terms of the lift coefficient based on water plane area  $C_{L_{sw}}$  gave

$$e = \frac{2C_{L_{sw}}}{\pi A} \quad (3-18)$$

where the aspect ratio is beam over wetted length,  $A = b/l_w$ . It can be easily shown that substituting Equation (3-18) in Equation (3-14), differentiating with respect to  $C_{L_{sw}}$ , and then substituting the inverse of Equation (3-13) yields

$$\frac{dC_{L_{sw}}}{d\tau} = \frac{\pi A}{A+2} \quad (3-19)$$

A correction factor of 0.73 was introduced by Korvin-Kroukovsky to obtain better correlation with experimental data obtained by himself and others at the Stevens Institute of Technology. The lift curve slope for finite width flat plates was then given by

$$\frac{dC_{L_{sw}}}{d\tau} = 0.73 \cdot \frac{\pi A}{A+2} \quad (3-20)$$

Korvin-Kroukovsky recognised that at large aspect ratios the linear Equation (3-20) was inadequate due to additional lift force caused by the flow in the transverse plane. Siler (1949) had already demonstrated that this cross flow effect could simply be added to the lift component derived from consideration of the momentum imparted to the downwash. The cross flow component had been given by Lamb (1932) as

$$\Delta C_{L_{sw}} = \frac{2\pi}{4+\pi} \cdot \sin^2 \tau \approx 0.88 \cdot \tau^2 \quad (3-21)$$

(which is the same as that given by Bobyleff (1881)). Korvin-Kroukovsky added this cross flow component to his own linear lift term and thus obtained

$$C_{L_{sw}} = 0.73 \cdot \frac{\pi A}{A+2} \tau + 0.88 \cdot \tau^2 \quad (3-22)$$

The theory developed by Korvin-Kroukovsky was an elegant merging of the theories acknowledged at that time for the two extreme cases of the slender body planing plate and the two-dimensional planing plate. However, in advancing his theory, assumptions were made that are not fully explained or justified, e.g. the energy consideration yielding the downwash angle at the centre of pressure is only partially justified. Also, adopting the cross-flow term from Lamb is doubtful since this is based on flow in infinite fluid and does not include the effect of a free surface.

Schnitzer (1953) presented a theoretical method for determination of motions and loads of prismatic bodies during immersed chines water impact. The impact force equation was derived by consideration of the added mass momentum as initially proposed by Von Karman in Equation (3-2). The impact velocity  $w$  in Equation (3-2) was taken by Schnitzer as the velocity component normal to the keel, defined as the sum of the normal components of horizontal and vertical velocity of a trimmed hull. Like Mayo, Schnitzer adopted Pabst's correction for the added mass of bodies of finite length. However, instead of using the original aspect ratio correction from Pabst (1930), Schnitzer used an empirically revised equation given in a later publication by Pabst (1931) as

$$f(A) = \sqrt{\frac{1}{1+A^2}} \cdot \left( 1 - \frac{0.425}{\frac{1}{A} + A} \right) \quad (3-23)$$

The added mass for wedges prior to chine immersion was taken from Wagner (1932), and thus Schnitzer's theory yields results identical to Wagner's for dry chines impact. Schnitzer advanced the impact theory by postulating that the presence of a force after chine immersion is due to a further increase in the added mass and not due to cross-flow drag. However, the rate of increase of added mass in Schnitzer's theory was derived using the magnitude of the known cross-flow force per unit length on a submerged flat plate, which had been computed by Bobyleff (1881) to be  $0.88 \cdot \frac{1}{2} \rho \cdot V_p^2 \cdot b$ , where  $V_p$  is velocity component normal to the plate. Schnitzer equated Bobyleff's force to the rate of change of added mass momentum after chine immersion for an infinite length plate expressed by  $w^2 \cdot \frac{dm'}{dz}$ , and solved for  $m'$ . This resulted in the added mass due to chines immersion given by  $\Delta m' = 0.88 \cdot \frac{1}{2} \rho \cdot b \cdot z_c$  where  $z_c$  is the chine immersion (which for a flat plate equals immersion depth  $z$ ). This gives the total sectional added mass as



$$m' = \frac{1}{2} \rho \pi \cdot \left( \frac{b}{2} \right)^2 \cdot \left( 1 + 1.12 \cdot \frac{z_c}{b} \right) \quad (3-24)$$

When calculating the transom sectional added mass of a planing hull by Equation (3-24), the chine immersion is proportional to trim angle. Also, the normal component of the forward velocity of a planing hull is proportional to the trim angle for small angles of trim. Thus, when multiplying the transom added mass by the normal velocity for calculation of the lift force, the second term becomes non-linear. Although the non-linear force acting on the chines immersed part of a planing hull is explained as a different phenomena than by Korvin-Kroukovsky, its derivation is based on a force term that is of the same magnitude (Bobyreff's and Lamb's cross-flow forces are identical). Thus, the non-linear terms of Schnitzer's and Korvin-Kroukovsky's equations give the same lift for identical cases. However, while Korvin-Kroukovsky's non-linear term is explained as cross-flow associated, Schnitzer's is explained as added mass related.

Mayo's equation and the linear terms of Korvin-Kroukovsky's and Schnitzer's equations can all be described as added mass theory. Shuford (1954) however, presented a theory for flat planing plates that was based on Prandtl's (1905) lifting line theory. From the lifting line theory the lift on an airfoil, non-dimensionalised on wetted surface area, is given by

$$C_{L_{sw}} = \frac{\frac{\pi A}{m_0} \cdot \tau}{\frac{\pi A}{m_0} + 1} \quad (3-25)$$

where  $m_0$  is the two-dimensional lift curve slope for the lifting surface. Shuford assumed that the lift coefficient for a planing surface is half of that given by Equation (3-25) because of flow on one side only. By also taking the lift curve



slope  $m_0$  for a two-dimensional flat planing plate as half of the known value for the corresponding airfoil, the lift coefficient for a planing surface was given as

$$C_{L_{sw}} = \frac{\pi A}{2A + 2} \cdot \tau \quad (3-26)$$

On an airfoil, there is a suction effect on the lee side near the leading edge that contributes to the lifting force. Shuford recognised that this component is not present on a planing surface since this area is above the water surface on a planing plate. He corrected for this by deducting the airfoil leading edge suction component which had already been derived by Wagner (1948) as  $C_{L_{sw}} \cdot \sin^2 \tau$ .

Deducting this component from Equation (3-26) yields

$$C_{L_{sw}} = \frac{\pi A}{2A + 2} \cdot \tau \cdot (1 - \sin^2 \tau) \quad (3-27)$$

Shuford also included a nonlinear term to account for the additional lift that acts on small aspect ratio plates due to the cross flow. The cross flow force component was also adopted from airfoil theory, where the non-dimensional cross flow drag of a two-dimensional flat plate is given as 2.0. The cross flow component was modified for planing by assuming one-half of this value, yielding the flat planing plate cross flow force coefficient as 1.0. Thus, the cross flow term is given by

$C_{L,CD_{sw}} = \sin^2 \tau \cdot \cos \tau$ , where  $\sin^2 \tau$  accounts for the normal component of the forward velocity and  $\cos \tau$  for the vertical component of the normal force, i.e. the lift component. Adding the cross flow term to Equation (3-27) yields Shuford's equation for total lift on a pure-planing flat plate as

$$C_{L_{sw}} = \frac{\pi A}{2A + 2} \cdot \tau \cdot (1 - \sin^2 \tau) + \sin^2 \tau \cdot \cos \tau \quad (3-28)$$

Shuford also reviews the significant planing theories and empirical equations available at the time, and compares some of these to his own theory (given by Equation (3-28)), to experimental data available from Shoemaker (1934),

Weinstein and Kapryan (1953), Locke (1948), Sottorf (1932) and to various unpublished NACA data. The comparison shows that Shuford's equations provide the best agreement with the experimental data, for most ranges of trim angle and length to beam ratio.

Later, Shuford (1958) presented a revision of his previous theory and advanced it to include deadrise surfaces. On the basis of analysis of deadrise hull planing data, Shuford introduced a function  $(1 - \sin \beta_e)$ , where  $\beta_e$  is the deadrise angle of a trimmed hull measured in the vertical plane to account for the effect of deadrise on the linear lift component. This resulted in a linear lift term for deadrise surfaces given by  $\frac{\pi A}{2A + 2} \cdot \tau \cdot (1 - \sin \beta_e)$ . Bobyleff's (1881) theoretical account of deadrise effect, approximated by  $\cos \beta_e$ , was applied to the cross flow force term. In addition to this, the flat plate cross flow force coefficient was adjusted from 1.0 to  $4/3$ , yielding the term  $\frac{4}{3} \cdot \sin^2 \tau \cdot \cos \tau \cdot \cos \beta_e$ . The correction accounting for loss of leading edge suction was applied by Shuford (1958) to both the linear and the cross flow terms. Thus, the total lift on a pure-planing deadrise surface was given by

$$C_{L_{sw}} = \left( \frac{\pi A}{2A + 2} \cdot \tau \cdot (1 - \sin \beta_e) + \frac{4}{3} \cdot \sin^2 \tau \cdot \cos \tau \cdot \cos \beta_e \right) \cdot (1 - \sin^2 \tau) \quad (3-29)$$

Equation (3-29) was validated by comparison with deadrise hull planing data from a number of experiments and proven to be of reasonable accuracy for all deadrises, trim angles and length to beam ratios apart from flat plate cases at low length to beam ratios.

Various researchers have presented empirically derived equations for the planing lift. The most commonly used planing equations for engineering application are those presented by Savitsky (1964). Using the experimental data from investigations by Sottorf (1932), Shoemaker (1934), Sambrus (1936), Sedov



(1947) and Locke (1948), Savitsky established empirical equations that expressed the relations between the many planing variables and the hydrodynamic lift, drag, pitching moment and wetted area. The flat plate lift coefficient on beam squared is expressed by

$$C_{L_b,0} = \tau^{1.1} \cdot \left( \frac{0.012}{\sqrt{A}} + \frac{0.0055}{C_v \cdot A^{2.5}} \right) \quad (3-30)$$

and is applicable for  $0.6 \leq C_v \leq 13$ ,  $2^\circ \leq \tau \leq 15^\circ$  and  $A \geq 0.25$ .

The lift on a deadrise surface is expressed as a function of the lift of a flat plate with identical values of  $\tau$ ,  $A$  and  $C_v$  as

$$C_{L_b,\beta} = C_{L_b,0} - 0.0065\beta \cdot C_{L_b,0}^{0.6} \quad (3-31)$$

Savitsky also presents a complete computational procedure for the prediction of running trim, draft and power requirements using Equations (3-30) and (3-31). He also reviews previous work done on porpoising stability of planing surfaces, and presents a relation between the lift coefficient, the running trim and the porpoising limit.

Vugts (1968) performed heaving experiments by forced oscillations of various transverse ship sections. The force data were analysed to extract added mass and damping coefficients, which were compared with theoretical approaches reviewed in the same publication. Added mass and damping coefficients were presented for a range of heaving frequencies. The results show that the coefficients are frequency dependent, something resulting from the waves induced by the motion. Although the research by Vugts is intended to provide a basis for solution of the dynamic equilibrium of forces and moments acting on displacement ships in motion at sea, the data are useful for comparison with the added mass coefficients applied in planing.

Payne (1981a) developed an added mass theory for calculation of the normal force acting on rectangular flat planing plates. The normal force was taken as the reaction force to the vertical momentum impacted to the downwash per second, given by

$$N = U_0^2 \cdot m'_x \cdot \tan \tau \quad (3-32)$$

where  $m'_x$  is the sectional added mass of the transom section and  $U_0 \tan \tau$  is the vertical velocity component. Following Schnitzer (1953), the theory differed from previous added mass approaches to planing by including an increase in added mass with chine immersion. Schnitzer derived the added mass increment due to chines immersion using the cross flow force given by Bobyleff. Instead, Payne determined the transom added mass  $m'_x$  of a slender flat plate, as a function of chine immersion depth to plate width  $z/b$ , by adopting Taylor's (1930) variation of added mass of rectangles with varying height to width ratio in finite fluid. The added mass was found as

$$m'_x = \frac{1}{2} \rho \pi \left( \frac{b}{2} \right)^2 \cdot (1 + \Delta C_{m'}) \quad (3-33)$$

where

$$\Delta C_{m'} = \sqrt{\frac{l \cdot \sin \tau}{2b}} \quad (3-34)$$

Payne realised that at high aspect ratios longitudinal flow reduced the added mass. By equating the two-dimensional planing plate normal force coefficient presented by Pierson and Leshnover (1948),  $N \approx \frac{1}{2} \rho U_0^2 b l \cdot \pi \cdot \tau$  (for small  $\tau$ ), to Equation (3-32), Payne obtained an expression for added mass as infinite aspect ratio, given by

$$m'_x = \frac{1}{2} \rho \pi \cdot b \cdot l \quad (3-35)$$



The transition between Equation (3-33) and Equation (3-35) was tackled by the introduction of a bridging function, derived by neglecting  $\Delta C_m$  in Equation (3-33)

$$\frac{m'}{m'_{A=0}} = \frac{1}{1 + \frac{A}{4}} \quad (3-36)$$

Thus yielding the general expression for added mass as

$$m'_x = \frac{\frac{1}{2} \rho \pi \left(\frac{b}{2}\right)^2 \cdot \left(1 + \sqrt{\frac{l \cdot \sin \tau}{2b}}\right)}{1 + \frac{A}{4}} \quad (3-37)$$

Payne included a cross-flow term by adopting a force coefficient of  $0.88 \sin^2 \tau$ , which was attributed the Raleigh-Kirchoff free streamline solution. The total normal force coefficient was therefore given by

$$C_{N_s} = \frac{N}{\frac{1}{2} \rho U_0^2 \cdot b \cdot l} = \frac{\pi \cdot \left(1 + \sqrt{\frac{l \cdot \sin \tau}{2b}}\right) \cdot \tan \tau}{1 + \frac{4}{A}} + 0.88 \cdot \sin^2 \tau \quad (3-38)$$

where  $l$  is the nominal length, i.e. distance from the transom to the intersection of plate and calm water level, and thus the normal force is made non-dimensional on nominal surface area. While the non-linearity with trim angle  $\tau$  in Schnitzer's equation was assigned to the added mass term and in Korvin-Kroukovsky's and Shuford's equations to the cross-flow term, both the added mass and cross-flow terms are non-linear in Equation (3-38).

In Payne (1982) the added mass bridging function was modified on the basis of an analysis of the added mass data from Kennard (1967). The revised bridging function was given by

$$\frac{m'}{m'_{A=0}} = f(A) = \frac{1}{\sqrt{1 + \left(\frac{A}{4}\right)^2}} \quad (3-39)$$

Payne (1988) suggested that the non-dimensional added mass increment of a flat plate due to chine immersion in Equation (3-33) should be taken as

$$\Delta C_{m'} = k \cdot \frac{l \cdot \tau}{b} = \frac{4}{3} \frac{l \cdot \tau}{b} \quad (3-40)$$

rather than that given by Equation (3-34).

Payne (1988) makes a comparison with Vugts' (1968) added mass coefficients. He states that the coefficients that apply in planing are the limiting values approached when the oscillation frequency tends toward infinity. He extrapolated the added mass coefficients given by Vugts to estimate the infinite frequency added mass values of various sections at different immersion depths, and compared these estimates to the added mass coefficients applied in his theory. This comparison showed agreement. However, Payne does not justify the claimed relation between infinite frequency oscillations and the water entry phenomenon. The soundness of this comparison is questionable. At infinite frequency, the oscillating section is constantly moving in disturbed water, while during a water entry it encounters undisturbed fluid as it penetrates further into the water. Thus, it seems to be more correct to compare the zero frequency oscillations with the water entry problem. The results given by Vugts for low frequency oscillations show that for large amplitudes the added mass coefficients tend to large values, while for small amplitudes, where there will be less encounter with disturbed water, they tend toward zero. It is therefore difficult to relate the added mass coefficients from oscillation tests with those applicable in water entry and planing, but the two sets of data are not inconsistent.

Payne (1992) recognised that the flat plate planing theory developed through Payne (1981, 1982 and 1988) overestimates the lift when applied to planing surfaces of low aspect ratio, i.e. large length to beam ratio. Based on large trim



and high length to beam ratio plate measurements of Shuford (1958), it is shown that the added mass planing theory had been adding the same lift component twice under different names, incremental added mass and cross-flow drag. Payne argued that the force acting upon the chines-immersed portion of the hull is merely a manifestation of the added mass increase with chine immersion, and the original cross-flow component was removed from the planing equation.

Ng and Kot (1992) made computations of water impact on a two-dimensional flat-bottomed body. The computations were carried out using a finite volume approach for discretisation of the conservation of mass and momentum equations, and by application of a volume of fluid method to capture the free surface. Ng and Kot presented the slamming force (non-dimensionalised on width) that acts on the body during the impact, as obtained using three different interpolation schemes for the computations. The force plots presented show that during a flat-bottomed impact the body experiences an advanced impact force, i.e. before the body reaches the calm water level. When a flat-bottomed body approaches the water surface, air beneath it is compressed and escapes to the sides. This causes a lowering of the water surface under the centre line of the impacting body, while there is a rise in water level beneath the chines. The body then impacts the water above the calm water level so that an advanced impact occur.

Zhao and Faltinsen (1993) present a nonlinear boundary element method for solving two-dimensional impact problems. A problem faced when applying boundary element approaches to impact problems is the modelling of the jet. Zhao and Flatinsen tackled this problem by treating the jet as a one-dimensional flow that is introduced between the free surface and the body when the angle between these boundaries is less than a certain threshold. Results in terms of pressure and force coefficients obtained with the method are presented for wedges of varying deadrise angles. This paper is often referred to as the “state of the art” solution to impact problems and is widely used as a benchmark for comparison of results.

As described in a later paragraph, an appendix of Payne (1994) makes use of the results presented in Zhao and Faltinsen for verification of his added mass impact theory. In the same publication, Payne modifies the added mass aspect ratio correction in Equation (3-39) to account for the effect of deadrise angle  $\beta$  on non-flat planing plates. The new aspect ratio correction is obtained by analysis of the experimental dry chines measurements of Shoemaker (1934) and Pierson et al. (1954), and is given by

$$f(A) = \frac{1}{\sqrt{1 + \left( \frac{A}{4} + A \cdot \sqrt{\frac{2\beta}{\pi}} \right)^2}} \quad (3-41)$$

Payne also argues that the velocity parallel to the keel line of the planing hull is less than  $U_0 \cdot \cos \tau$  as applied in previous added mass planing theories. The added mass theory originates from Munk's (1924) slender body theory, which used an added mass consideration to calculate the lift on dirigibles moving at an angle to the direction of flight. Bodies inclined to the flow in an infinite fluid have increased velocity on the lee side, while the velocity is reduced on the pressure side, so that the average velocity can be treated as close to  $U_0 \cdot \cos \tau$ . However, in planing, there is flow only on the pressure side of the body. Therefore, Payne argues that the velocity is less than that given by Munk, and suggests a one-sided flow correction factor to the planing equation, which was derived from a consideration of the average pressure coefficient under the planing surface and

$$\text{Bernoulli's equation and is given by } C_{N_{sw}}(\text{corrected}) = -\frac{1}{2}C_{N_{sw}} + \sqrt{1 + \frac{1}{4}(C_{N_{sw}})^2}.$$

Payne (1994), gives the non-dimensional added mass increment in terms of chine immersion for deadrise planing surfaces as

$$\Delta C_m = k \cdot \frac{z_c}{b} \quad (3-42)$$



rather than as function of length as in Equation (3-40). The modified aspect ratio correction and the new one-sided flow correction are used with the flat plate and prismatic planing data of Shuford (1958) to refine the  $k$ -factor in Equation (3-42). The results show that a  $k$ -factor of 2.0 rather than  $4/3$  as originally suggested in Equation (3-40) gives better fit to the data.

In an appendix of Payne (1994), the impact force on a wedge is calculated by combining the work of Von Karman, Lewis (1929), Taylor (1930), Wagner (1931) and Pierson (1950). The force on a wedge during constant velocity impact was given by Von Karman as the last term of Equation (3-2). Lewis and Taylor separately calculated the added mass of half a prism in an infinite fluid and both obtained

$$m' = \left(1 - \frac{\beta}{2\pi}\right)^2 \cdot \frac{1}{2} \rho \pi \cdot c^2 \quad (3-43)$$

where  $c$  is the half-width of the half-prism. Made non-dimensional on the weight of water within a half-cylinder of radius equal to  $c$ , the added mass is expressed as

$$C_{m'} = \left(1 - \frac{\beta}{2\pi}\right)^2 \quad (3-44)$$

As already mentioned, Wagner proposed that the added mass of a wedge is associated with the wetted rather than the nominal width, and that the splash up ratio is  $\pi/2$ . Payne remarked that using the wetted width of the impacting wedge as the dimension  $c$  in Equation (3-43) results in too high impact forces at large angles of deadrise, when compared with the results by Zhao and Faltinsen. He concluded that the added mass was overestimated, and Payne applied Pierson's (1950) splash up hypothesis, which gives the ratio between wetted and nominal width, i.e. the wetting factor ( $WF$ ), as

$$WF = (1 + \psi) = \frac{\pi}{2} - \beta \left(1 - \frac{2}{\pi}\right) \quad (3-45)$$

It can easily be shown that applying the product of  $WF$  and the nominal half-width  $y$  as the dimension  $c$  in Equation (3-43), and substituting in the last term of Equation (3-2), yields Payne's equation for constant velocity impact force on a wedge section as

$$F' = \left(1 - \frac{\beta}{2\pi}\right)^2 \cdot w^2 \cdot \rho\pi \cdot \frac{z}{\tan^2 \beta} \cdot WF^2 \quad (3-46)$$

Payne presents a comparison of Equation (3-46) and the results of Zhao and Faltinsen (1992) that shows good agreement for the angles of deadrise included in the comparison (5 to 40 degree).

Payne (1995) claims that studies subsequent to Payne (1994) show no evidence of the aspect ratio correction  $f(A)$  departing substantially from Equation (3-39) in the range  $0^\circ < \beta < 40^\circ$ , and therefore rejects Equation (3-41). For higher deadrise angles, a correction is derived based on analysis of Springston and Sayre's (1955) 50 degree deadrise angle planing data and Pope's (1958) 70 degree data. The analysis resulted in an empirical relationship for the aspect ratio correction at higher deadrise angles expressed by

$$f(A) = \frac{1 - \frac{\beta^\circ - 40}{65}}{\sqrt{1 + \left(\frac{A}{4}\right)^2}} \quad , \quad \beta^\circ > 40 \quad (3-47)$$

On the basis of the modified aspect ratio function, the data used in Payne (1994) to evaluate  $k$  in Equation (3-42) was reanalysed and an empirical fairing obtained

$$k = 2.05 \cdot \left(1 - \left(\frac{2\beta}{\pi}\right)^{4.5}\right) \quad (3-48)$$

Payne (1995) also presents experimental data for the loss of buoyancy on a planing hull in motion, and gives empirical equations that correlates this data. At



high speeds, when the transom is dry, Payne shows that the buoyancy ratio is well represented by

$$\varphi_0 = \frac{\text{Actual buoyancy}}{\text{Archimedes' buoyancy}} = 1 - \frac{b}{l} \quad (3-49)$$

where Archimedes buoyancy is the vertical component of the hydrostatic pressure force acting on the hull, calculated from the calm water level. At lower speeds, when the transom is wet, the buoyancy ratio is velocity dependent and given by Payne as

$$\varphi_0 = 1 - \frac{C_{DS} \cdot C_v^2}{2 \sin \tau} \cdot \left( \frac{b}{l} \right)^2 \quad (3-50)$$

where  $C_{DS}$  is a transom drag coefficient used by Payne (1988) to compute the depression of the water behind the transom. In Payne (1988),  $C_{DS}$  values are estimated from experimental observations of the speed at which the transom clears and found to be in the range 0.08-0.22 for planing hulls. Payne (1995) states that the value needed to adequately explain the loss of buoyancy during low speed model testing is about unity, which is several times higher. Although it can be argued that the depression of the water surface behind the transom and the loss of buoyancy are related events, it seems questionable that the parameter derived for prediction of the former event is adopted to explain the second, particularly when considering the great difference in the experimentally obtained  $C_{DS}$  values for the two events.

Payne (1995) includes a substantial comparison of his theory with the equations of Savitsky (1964) and with the planing data of various researchers. The comparison shows that his theory is in good agreement with an average of the highly scattered experimental data presented for both flat plate and deadrise planing surfaces with length to beam ratios above one. For ratios lower than one, Payne's theory overestimates the lift significantly. The comparison shows that Payne's theory provides better agreement with experimental data than that of Savitsky.



Vorus (1996) presents a flat cylinder theory for computations of pressures and thus forces during impacts. His theory is presented as a compromise between direct numerical inversion of the governing equations and the simple asymptotic theories evolved from the work of Wagner (1932). Vorus gives the slamming force coefficients ( $C_F$ ), maximum pressure coefficients ( $C_{P,max}$ ) and the wetting factors ( $WF$ ) obtained from his solutions to the constant velocity impact of two-dimensional wedges with deadrise angles from 5 to 30 degrees. The slamming force coefficients are compared with those obtained by other theories, showing that Vorus's results are slightly higher than those given by Mayo (1945), while slightly lower than those given by Sydow (1938).

Zhao et al. (1997a) present a boundary element method for fully non-linear numerical simulation of the water entry of two-dimensional bodies that includes the flow separation that occurs after chines wetting. This method is validated by comparison with experimental results from drop tests with a wedge shaped section and a bow flare section. These tests were carried out with a finite length to beam test sections and two-dimensional flow was not provided by end plates. Three-dimensional flow effects were therefore theoretically estimated and the numerical results corrected accordingly, yielding good agreement between the measurements and the numerically obtained data.

Zhao et al. (1997b) present a simplified theory for the steady behaviour of a high-speed planing craft. It is a slender body theory and uses the two-dimensional water entry approach to calculate the hydrodynamic forces that act on a planing craft. The water entry simulation is performed by a simplification of the fully non-linear solution presented in Zhao et al. (1997a). The slender body steady planing lift forces obtained with their approach are compared with the empirical equations given by Savitsky (1994). The comparison shows that their approach gives lift forces that exceed the lift estimated by Savitsky's method by 15 percent at length to beam ratios of about 4 and by 40 percent at length to beam ratios of about 1. The discrepancy is explained by Zhao et al. as three-dimensional flow effects in the bow region. The slender body theory gives non-zero sectional lift force at the transom section, while the dynamic free surface boundary condition implies zero

transom sectional lift. This indicates that the discrepancy is at least partially due to three-dimensional flow effects in the aft region. Thus explaining the discrepancy purely as flow effects in the bow region seems rather incomplete.

### 3.2. Experimental Investigations of Planing and Impact

The following is a list of published experimental data available for planing hulls, and results of impact tests of wedge sections. A large number of impact tests are described in the literature. However, only a few of these are of interest in the present investigation, as the majority have been carried out to investigate the peak pressures that occur during slamming, and do not report total forces or accelerations during the impact.

Sottorf (1932) tested flat plates with trim angles varying between 2 and 10 degree, and aspect ratios from 0.2 to 10.

Shoemaker (1934) carried out tests on both flat plate and deadrise surfaces in both dry and wet chines condition. The flat plates were tested at 2 and 4 degree trim angle. The 10, 20, 30 and 40 degree deadrise surfaces were tested at trim angles from 4 to 12 degree.

Samraus (1936) tested flat plates at constant lift coefficient on beam values at trim angles varying from 2 to 5 degree and aspect ratios from 0.3 to 2.

Bisplinghof and Doherty (1950) performed drop tests with wedges of deadrise angle varying from 10 to 50 degree. Acceleration/deceleration were measured and recorded during the drop.

Chambliss and Boyd (1953) tested surfaces of 20 and 40 degree deadrise angles in both dry and wet chines conditions at trim angles from 2 to 30 degrees.

Pierson et al. (1954) tested surfaces of 10, 20 and 30 degree deadrise angles in the dry chines condition at trim angles from 2 to 12 degrees.



Shuford (1954) tested flat plates at trim angles from 2 to 30 degrees and aspect ratios between 0.13 and 10.

Savitsky and Neidinger (1954) tested 10, 20 and 30 degree deadrise surfaces in the wet chines condition at trim angles up to 15 degrees.

Springston and Sayre (1955) tested a 50 degree deadrise surface at trim angles ranging from 4 to 18 degrees.

Pope (1958) tested a 70 degree deadrise surface at trim angles from 9 to 30 degrees.

Shuford (1958) tested flat plates at trim angles from 8 to 34 degrees and at aspect ratios varying from 0.12 to 1.2, and 20 and 40 degree deadrise angle surfaces at trim angles from 12 to 34 degrees.

Chuang (1966) performed slamming tests of wedge shaped bodies of various deadrise angles. The pressures along the wedge surface were recorded during the impact.

Zhao et. al (1997) reports force, velocity and pressure measurements from drop tests with a 30 degree deadrise angle wedge section and a bow flare section. These did not provide two-dimensional data, as the test sections were of relatively low length to beam ratio ( $<2$  for the wedge section and  $<3$  for the bow flare section), and the experimental set-up did not include means of providing two-dimensional flow.



---

CHAPTER 4

CFD SIMULATION OF TWO-DIMENSIONAL  
WATER ENTRY

---

Simulations of two-dimensional constant velocity water entry of wedge sections and of a flat bottomed section have been carried out by use of computational fluid dynamics. This has been done to obtain the immersion dependent forces acting on such sections during the water entry, and also to get a description of the surrounding flow field in terms of free-surface shape, pressures and velocity vectors. A parametric study with varying deadrise angle and velocity, with and without gravity effect was undertaken using the commercial “Fluent4” CFD code.

## **4.1. Finite Volume Method**

CFD (Computational Fluid Dynamics) is a common term for all the computational procedures that solve numerically any equations describing fluid flow. These may describe the velocity potential  $\phi$  that satisfies the Laplace equation, or they may be the continuity equation combined with the Navier-Stokes (conservation of momentum) equations. The code applied in the present study uses the finite volume method to solve the conservation of mass and the conservation of momentum equations to obtain the simulated flow field. These equations provide a full description of unsteady flow, including viscous effects and gravity effects. However, preliminary investigations indicated that viscous effects were very small and could be neglected.

### **4.1.1. Governing Equations**

The continuity equation states that any amount of fluid flowing into a control volume also flows out of the control volume at the same time. For the two-dimensional case a small control volume is considered, as shown in Figure 4-1.

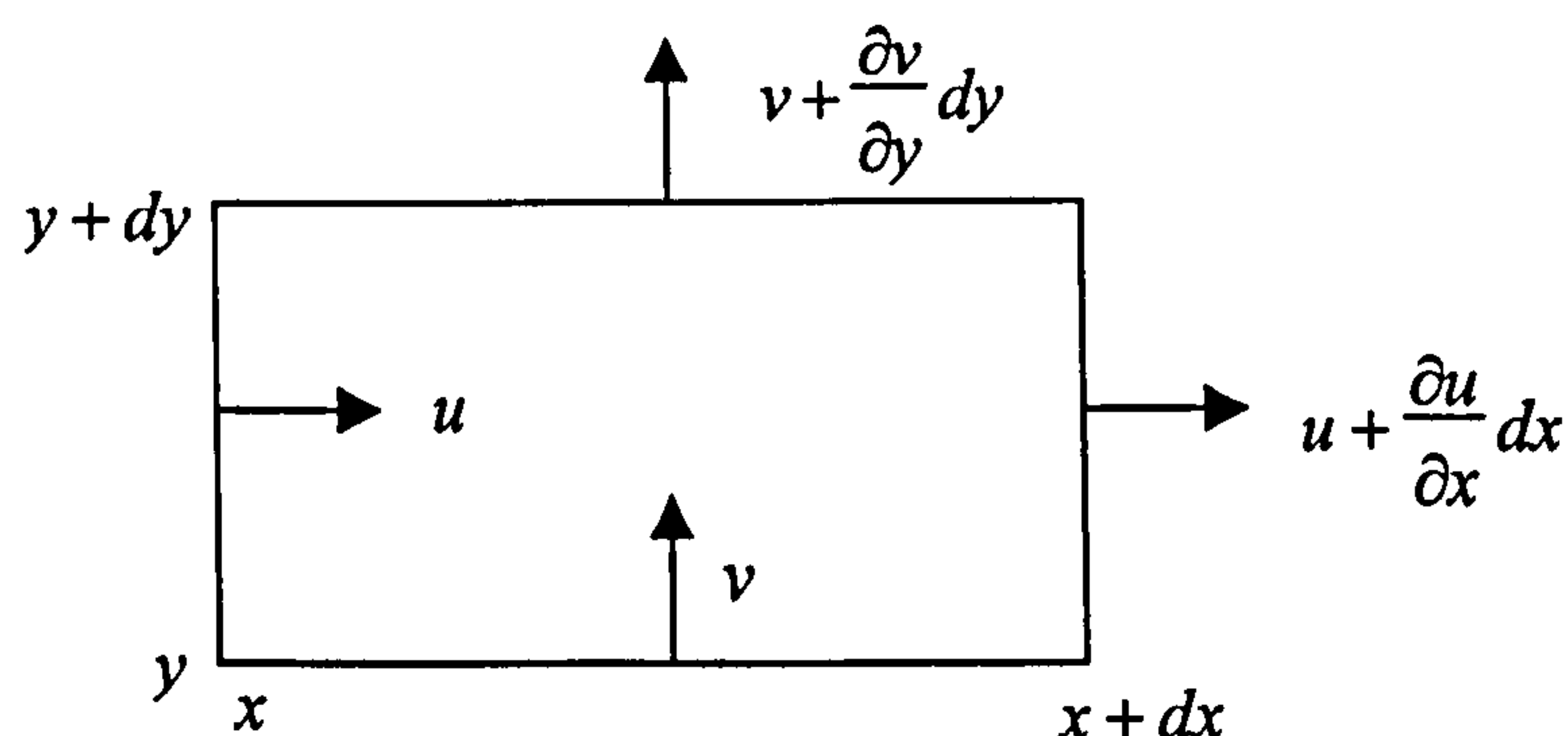


Figure 4-1. Control volume for conservation of mass.

The letters  $u$  and  $v$  denote the velocity components in the  $x$ - and  $y$ -directions. Positive mass flux means mass leave the control volume while negative mass flux means mass enters the control volume. The total mass flux satisfies the equation

$$-\rho dy u + \rho dy (u + u_x dx) - \rho dx v + \rho dx (v + v_y dy) = 0$$

which can be expressed by

$$\frac{du}{dx} + \frac{dv}{dy} = 0$$

The Navier-Stokes equations describe the conservation of momentum in the flow. Consider the external forces acting on a small control volume as shown in Figure 4-2.

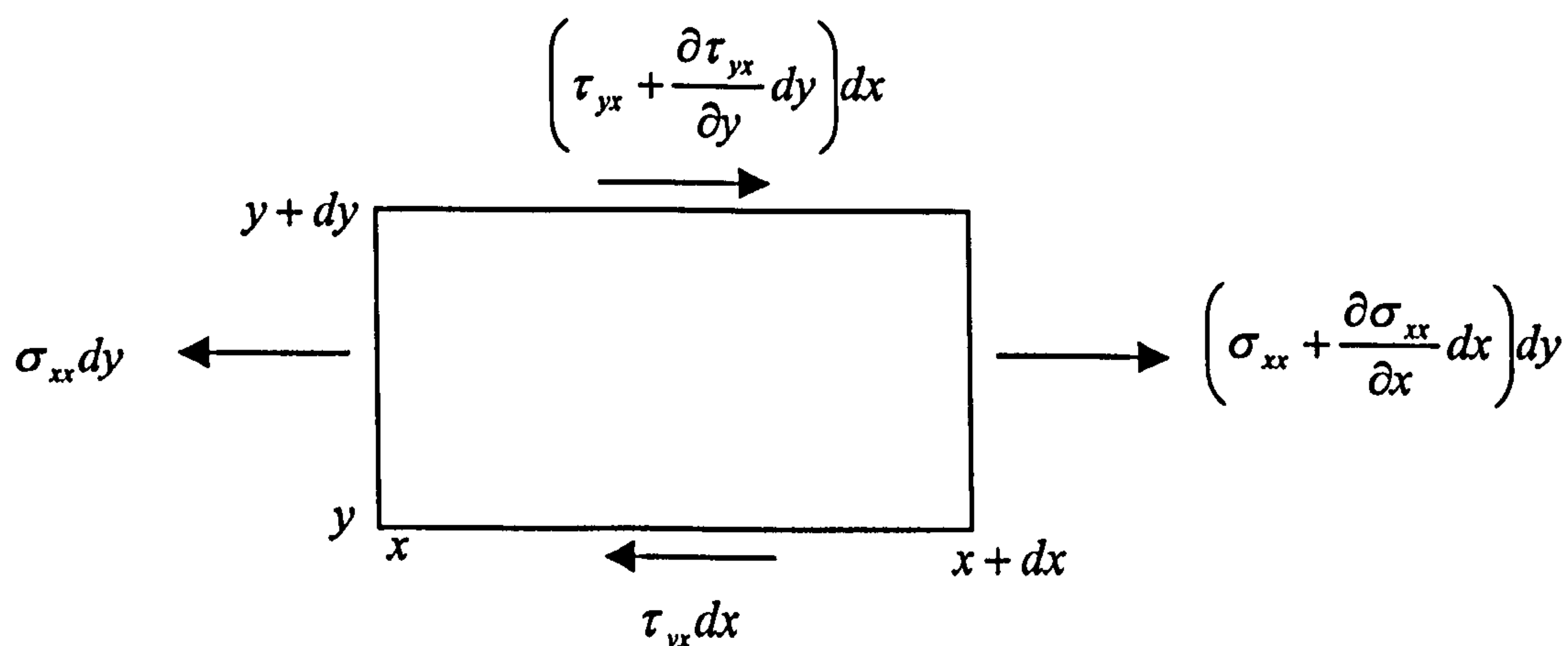


Figure 4-2. Control volume for conservation of momentum.



The surface forces on the control volume in the x and y directions are

$$F_{surface,x} = \left[ -\sigma_{xx} dy + \left( \sigma_{xx} + \frac{\partial \sigma_{xx}}{\partial x} dx \right) dy \right] + \left[ -\tau_{yx} dx + \left( \tau_{yx} + \frac{\partial \tau_{yx}}{\partial y} dy \right) dx \right]$$

$$F_{surface,x} = \left( \frac{\partial \sigma_{xx}}{\partial x} + \frac{\partial \tau_{yx}}{\partial y} \right) dx dy$$

$$F_{surface,y} = \left[ -\sigma_{yy} dx + \left( \sigma_{yy} + \frac{\partial \sigma_{yy}}{\partial y} dy \right) dx \right] + \left[ -\tau_{xy} dy + \left( \tau_{xy} + \frac{\partial \tau_{xy}}{\partial x} dx \right) dy \right]$$

$$F_{surface,y} = \left( \frac{\partial \sigma_{yy}}{\partial y} + \frac{\partial \tau_{xy}}{\partial x} \right) dx dy$$

Let  $f_x$  and  $f_y$  be the components of the body force (e.g. gravity) per unit mass, then the body forces on the control volume in the x- and y-directions are

$$F_{body,x} = \rho f_x dx dy$$

$$F_{body,y} = \rho f_y dx dy$$

By Newton's law of motion we get the equations

$$\text{x-direction: } \rho dx dy \frac{Du}{Dt} = \left( \frac{\partial \sigma_{xx}}{\partial x} + \frac{\partial \tau_{yx}}{\partial y} \right) dx dy + \rho f_x dx dy$$

$$\rho \frac{Du}{Dt} = \rho f_x + \frac{\partial \sigma_{xx}}{\partial x} + \frac{\partial \tau_{yx}}{\partial y}$$

$$\text{y-direction: } \rho dx dy \frac{Dv}{Dt} = \left( \frac{\partial \sigma_{yy}}{\partial y} + \frac{\partial \tau_{xy}}{\partial x} \right) dx dy + \rho f_y dx dy$$

$$\rho \frac{Dv}{Dt} = \rho f_y + \frac{\partial \sigma_{yy}}{\partial y} + \frac{\partial \tau_{xy}}{\partial x}$$

where  $Du/Dt$  and  $Dv/Dt$  are substantial derivatives of the velocity in the x- and y-directions, and hence denote the rate of change of velocities of the control volume.

The substantial derivatives of  $u$  and  $v$  may be expressed in terms of the field derivatives using Euler acceleration formula:

$$\text{x-direction: } \rho \left( \frac{du}{dt} + u \frac{du}{dx} + v \frac{du}{dy} \right) = \rho f_x + \frac{\partial \sigma_{xx}}{\partial x} + \frac{\partial \tau_{yx}}{\partial y}$$

$$\text{y-direction: } \rho \left( \frac{dv}{dt} + u \frac{dv}{dx} + v \frac{dv}{dy} \right) = \rho f_y + \frac{\partial \sigma_{yy}}{\partial y} + \frac{\partial \tau_{xy}}{\partial x}$$

For inviscid flow the equations are reduced to

$$\text{x-direction: } \rho \left( \frac{du}{dt} + u \frac{du}{dx} + v \frac{du}{dy} \right) = \rho f_x + \frac{\partial p}{\partial x}$$

$$\text{y-direction: } \rho \left( \frac{dv}{dt} + u \frac{dv}{dx} + v \frac{dv}{dy} \right) = \rho f_y + \frac{\partial p}{\partial y}$$

The reduced forms of the Navier-Stokes equations are known as the Euler equations and are applicable to non-viscous flows.

If the only body force is gravity, the components of the body force per unit mass become

$$f_x = 0$$

$$f_y = g$$

#### 4.1.2. Solution of the Differential Equations

The Euler equations and the continuity equation form a system of coupled, non-linear partial differential equations. An analytical solution to this system is impossible. Various codes within CFD provide methods that solve these basic field equations and the boundary conditions numerically by approaches involving

a large number of elements. These approaches lead to a large number of algebraic equations by use of various discretization techniques. The different techniques are finite element methods (FEM), finite difference methods (FDM) and finite volume methods (FVM). As mentioned earlier, Fluent 4 solves the governing equations by the finite volume method.

#### 4.1.2.1. Integration and Discretisation

The FVM involves division of the domain into a number of small cells or control volumes (grid generation). The differential equations are then integrated about each control volume, yielding finite-difference equations that conserve each quantity on a control volume basis. In the discrete form of the equations, values of the dependent variables appear at the cell faces. Fluent4 uses a non-staggered grid storage scheme where all the variables are stored at the cell center. A quadratic differencing scheme (QUICK) has been used to express the values at the cell faces in terms of values at the nearby cell centres, and this gives a set of linear equations that can be solved numerically.

#### 4.1.2.2. Solution of the Set of Linear Equations

A simultaneous solution to the set of linear equations would provide a solution in which all three unknowns (horizontal and vertical velocity components and pressure) satisfy each of the mass and momentum equations. Because a simultaneous solution is computationally intensive, the equations are solved sequentially. In the sequential solution process, an equation describing the update of pressure is required which is not explicitly available via the mass or momentum balances. Fluent4 uses the SIMPLE (Semi-Implicit Method for Pressure-Linked Equations) algorithm, which is based on a relationship between velocity and pressure corrections that is used to recast the continuity equation in terms of a pressure correction calculation. The solution process is accomplished via a line by line solver, the Line Gauss-Seidel procedure.



### 4.1.3. Free Surface Model

In addition to the conservation of momentum and continuity equations, an equation is required for modelling the interface between water and air. The specific method applied by Fluent4 is known as the Volume of Fluid (VOF) method. Unlike surface-tracking methods, surface-capturing methods, such as the VOF, are capable of solving flows with breaking waves and jet break-up. In the VOF method a variable is introduced for each fluid present in the domain. This variable specifies the amount of the particular fluid within the cell in terms of fraction of total cell volume. The volume fraction of each fluid is tracked throughout the domain and the sum of the volume fractions for all fluids sum up to unity in every cell. The fluids share a single set of momentum equations, and the fluid properties in a cell are dependent on the volume fractions of the fluids within it. The property values are taken as a volume fraction average of the properties of the fluids contained in the cell. The free surface occurs at cells that have volume fractions equal to 0.5 for each of the two adjacent fluids.

## 4.2. Simulation Issues

In the simulation domain the wedge section was held stationary while the water was flowing upward. At the bottom of the domain, an inlet was set for water to flow at the desired water entry simulation velocity, and at the top a pressure boundary allowed outflow of excess air. A sketch of the simulation domain is shown in Figure 4-3. Using the geometrical symmetry, only the flow in half of the domain was simulated.

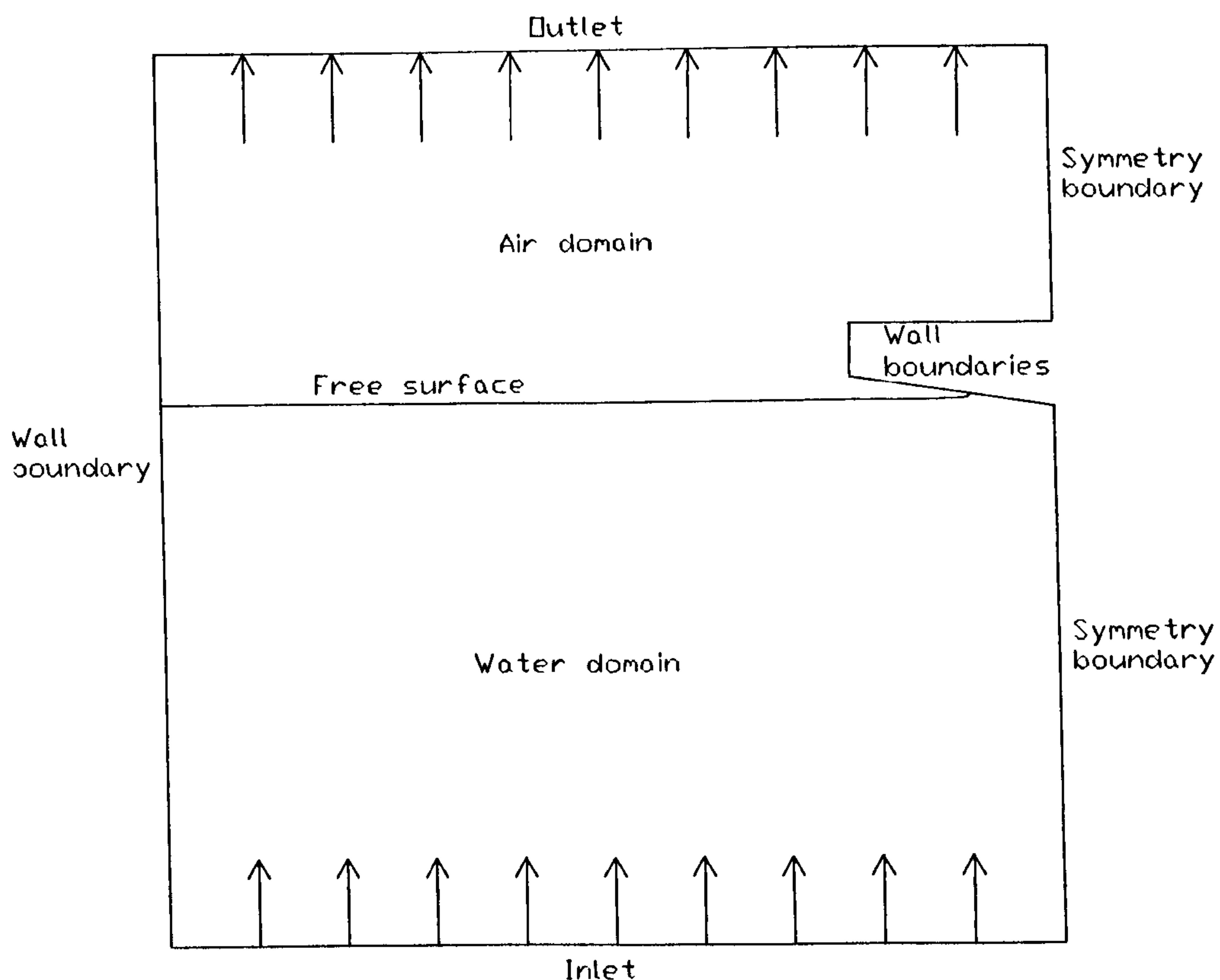


Figure 4-3. Simulation domain.

#### 4.2.1. Grid Generation

##### 4.2.1.1. Grid Topology

Two different solvers are available in Fluent4. A coupled solver for high-speed compressible applications and a segregated solver for incompressible lower speed flows. For problems involving two-phase flow with free-surface effects, only the segregated solver is available. The segregated solver only accepts structured grids. A structured grid consists of quadrilateral cells, and two cells must only share one cell face. The accuracy and numerical stability of the simulation is highly dependent on the quality of the grid. In other words, the density and distribution of the grid lines determines the accuracy with which the model represents the actual physical phenomena. In addition to the cell density, other grid parameters affecting the result are cell aspect ratio and cell skewness. A course grid results in poor computational representation, and hence inaccurate simulation. However, a

too dense grid will be unnecessarily computationally intensive. The approach used to find a suitable grid density involved simulations of the same case several times with increasing density. This was continued until further increase in density had little effect on the force results and a grid density independent solution had been achieved. Because this is a time consuming procedure and software access was time limited, it was only carried out for one of the geometries and the same number of cells was then applied for all of the simulations. A division of the computational fluid domain into about 25000 cells was found adequate for the present simulations (about 130 horizontally by 195 vertically with only small variations for the various geometries). The grid was generated using body-fitted co-ordinates. With body-fitted co-ordinates, the cell faces at the boundaries follow the same curvature as the boundary.

Before a run is started, an initial flow field must be set. The water level has to be set just below the body and given the free-stream velocity. A set of cells is chosen having a volume fraction of water equal one. The procedure for defining these cells in the Fluent4 pre-processor restricts the grid topology such that there must be a horizontal line where the initial free surface is to be set, with which all the cell faces across the domain at this level must coincide. The reason is that the free surface initially can only be set to occur along cell faces. Figure 4-4 shows the grid topology for the simulations involving deadrise angles of 15 degrees and above. All the sub-rectangles seen in Figure 4-4 are subdivisions (or blocks) into which the simulation domain is divided. The nodal distribution from which the grid is generated is defined along each of the edges of these blocks. In addition to being an edge for defining nodal distribution, the horizontal line coinciding with the keel of the section defines the initial position of the free surface faces for the simulation.



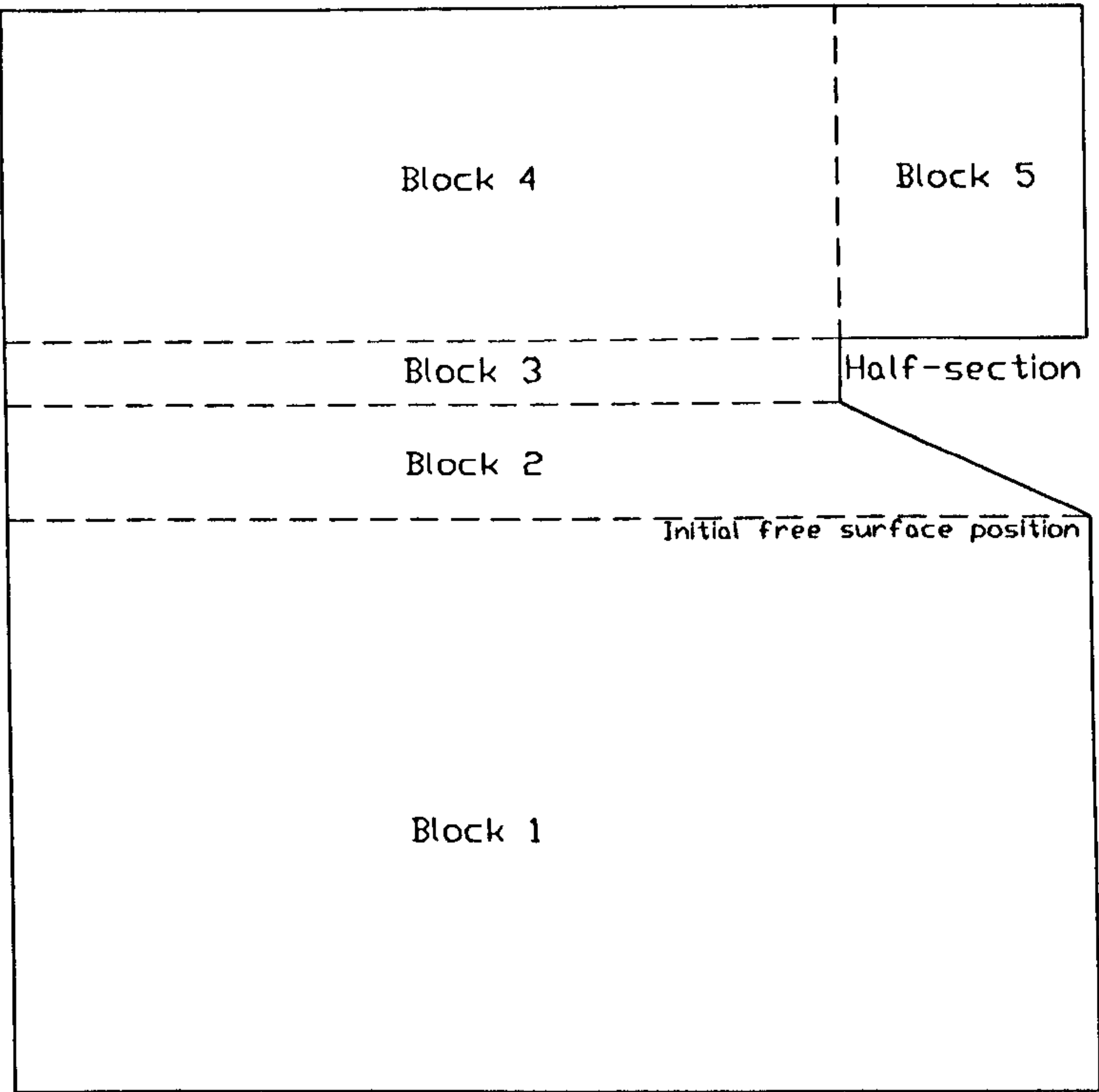


Figure 4-4. Grid topology for 15 to 60 degrees deadrise simulations.

The nodal distribution was set so that there was a clustering of cells near the wedge section. This is shown in Figure 4-5 where a part of the grid close to the wedge body is shown. Note that also the mirror image of the grid is shown in the figure.

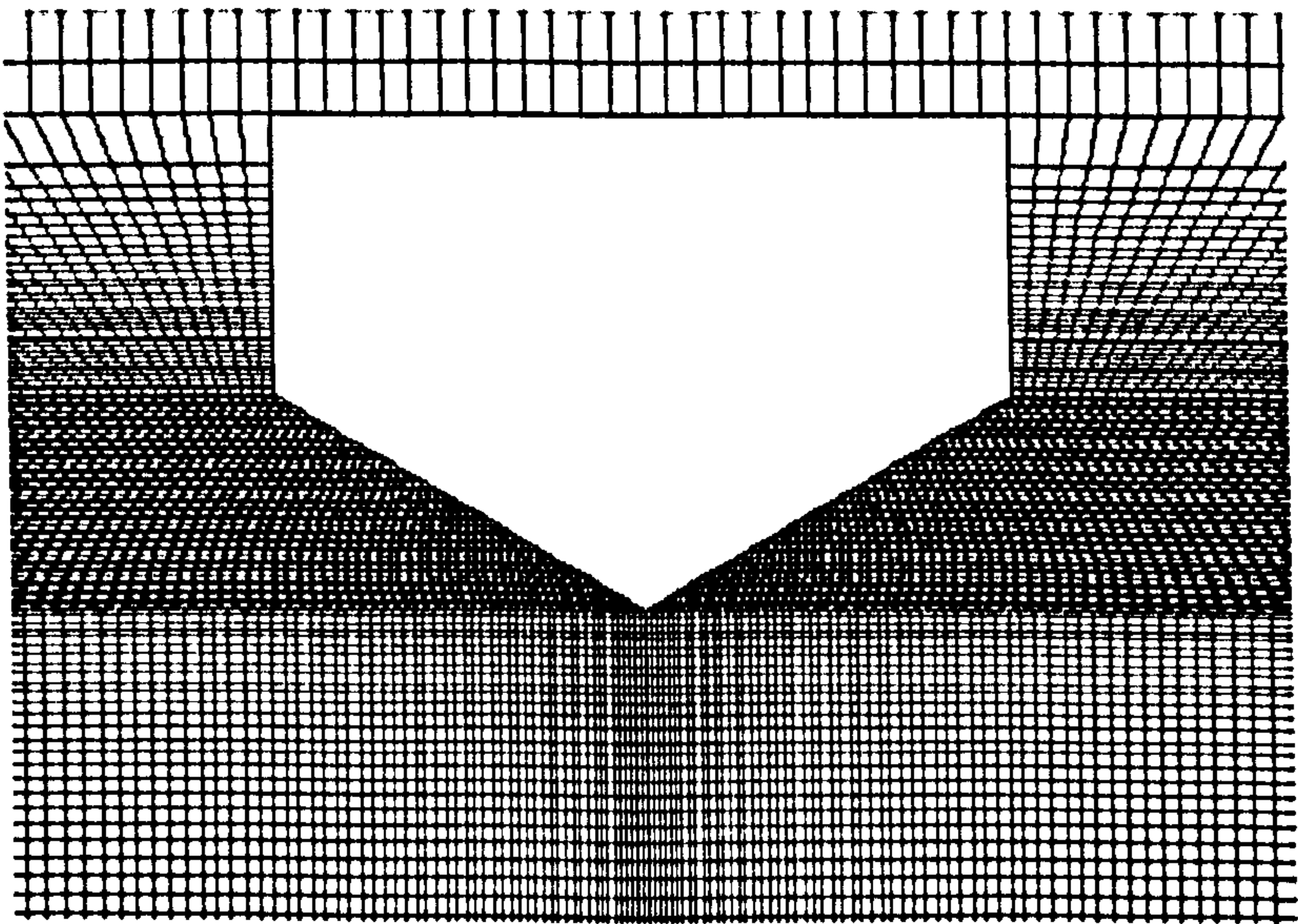
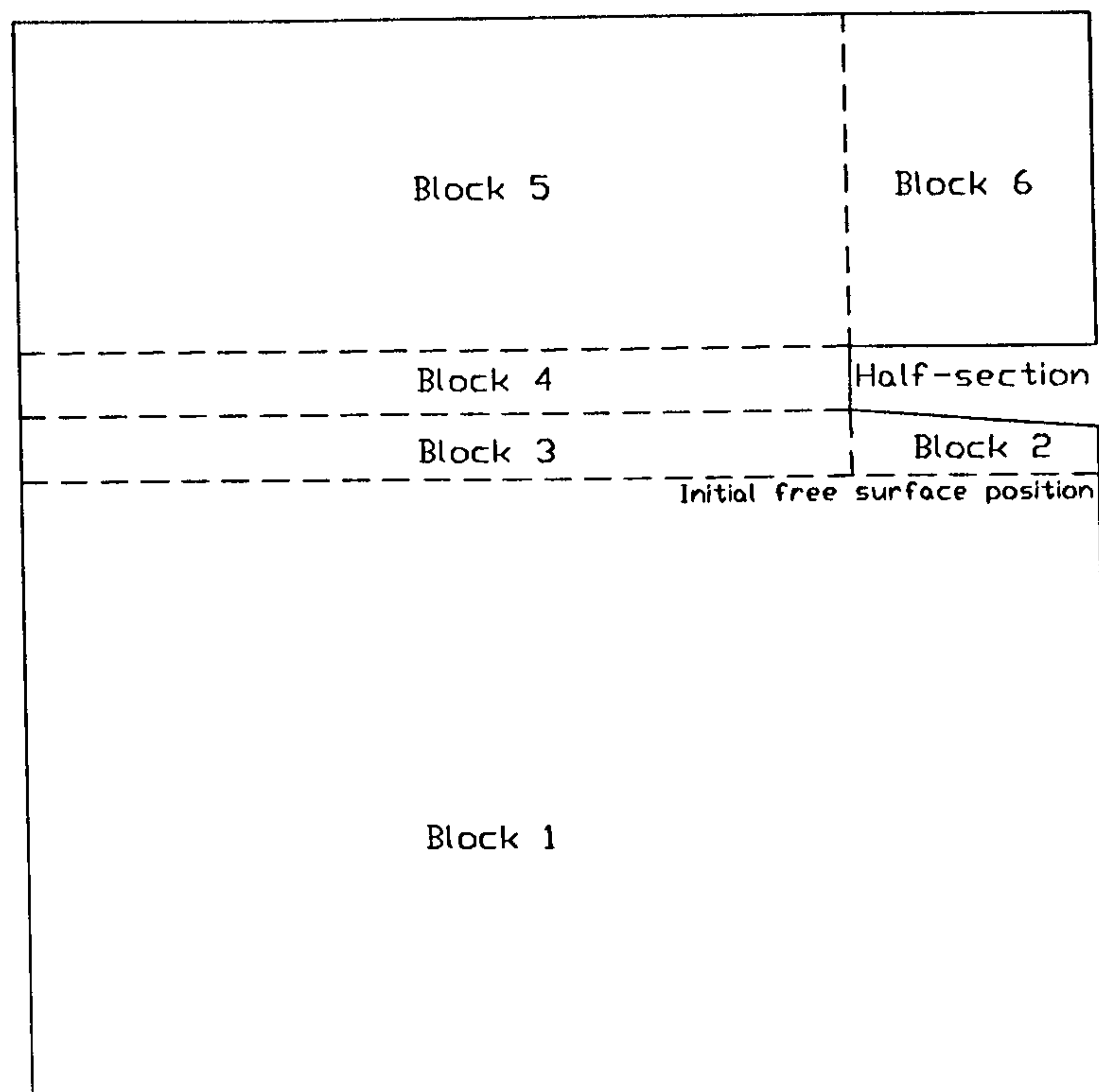


Figure 4-5. Grid close to a wedge of 30 degrees deadrise.

The clustering of cells close to the wedge body combined with the domain topology being dictated by requirement for definition of the initial free surface position, resulted in high aspect ratio cells in an area at the opposite side of the domain from the half-section. Aspect ratios of up to two thousand occurred in this area. A way of avoiding this problem is to have uniform horizontal nodal distribution throughout the domain. This would require a vast number of cells and thus greatly increase the computational effort. However, the pressure and velocity gradients in the horizontal direction of this particular area are close to zero, allowing such ratios to be acceptable without causing the solution to be numerically unstable.

A different grid topology had to be chosen for the simulations involving the lowest deadrise angles ( $< 10$  degrees). This was to avoid high skewness values in the area close to the wedge section. Instead of the edge along the wedge defining the vertical nodal distribution, the topology was chosen so that the horizontal distribution was set along this edge. To avoid large aspect ratio cells near the keel point of the wedge body, the horizontal edge going across the domain for definition of the initial free surface was defined some distance below the wedge body. The grid topology for the lower deadrise angle simulations is shown in Figure 4-6.



*Figure 4-6. Grid topology for 0 to 10 degrees deadrise simulations.*

#### 4.2.1.2. Boundary Conditions

A velocity inlet was defined at the bottom of the domain. This is a boundary condition allowing a constant flow velocity to be set. At the top of the domain a pressure boundary was defined. This boundary type defines the static pressure at flow exits, which in this simulation was set to zero. Both the body and the far end of the domain were defined as wall boundary conditions with free slip. Using free slip walls implies simulation of inviscid flow.

#### 4.2.2. Pre-Processing

##### 4.2.2.1. Discretization Scheme

Fluent stores the velocity components and scalar variables at the geometric centres of the control volumes defined by the grid. During the solution process the values of these variables at the control volume boundaries (cell faces) are required. These



face values are obtained via interpolation. Fluent4 provides a choice of three different interpolation schemes:

- 1) Power-Law Interpolation
- 2) Quadratic Upwind Interpolation (QUICK)
- 3) Blended Second Order/Central Difference

The power law interpolation scheme gives accuracy between first and second order, while the two other schemes are of higher order accuracy. Higher order accuracy is of special importance when resolving gradients in a flow that is directed at large angles to the grid. For the problems solved in the present study, the flow is at large angles to the grid, especially for the low deadrise angle simulations. This excluded application of the power-law scheme. The choice between the two other schemes was made on the basis that the formal accuracy of the QUICK scheme is higher than the second-order upwind. It was reported from the supplier of Fluent that in practice the accuracy of both schemes is often equivalent and the choice usually falls on the one proven more stable. The QUICK scheme proved stable during the present simulations and was used for the entire simulation series.

#### 4.2.2.2. VOF Formulation

Fluent4 provides three different schemes for interpolation near the free surface:

- 1) Time-dependent with the donor-acceptor interpolation scheme
- 2) Time-dependent with the implicit interpolation scheme
- 3) Steady-state with the implicit interpolation scheme

The time-dependent formulation with the donor-acceptor scheme should be used when the time-accurate transient behaviour of the VOF solution is of interest. The time-dependent formulation with the implicit interpolation scheme can be used for a steady-state solution when the intermediate transient flow behaviour is

insignificant, and the final steady-state solution depends on the initial flow conditions. The steady-state scheme can be used for the steady-state solution when intermediate transient flow behaviour is not of interest, and the final steady-state solution is not affected by the initial flow conditions. In the present simulations the time-dependent behaviour is of high interest, and therefore the appropriate VOF formulation for this problem is the time-dependent with the donor-acceptor interpolation scheme.

#### 4.2.2.3. Time Stepping

Implicit schemes are unconditionally stable and are used to allow for large time-stepping. The donor-acceptor interpolation scheme, which has been used in the present simulations, is an explicit scheme and thus extra considerations are required when defining time-step size for the simulation. The Courant number is a dimensionless number that compares the time step in a calculation to the characteristic time of transit of a fluid element across a control volume. In other words, it is a measure of how far inside a cell a fluid element travels per time step.

For explicit formulations the maximum value of the Courant number for a solution to be stable is one. This is referred to as the Courant Friedrichs Lewy criterion. However, in most cases the Courant number required to achieve numerical stability is below 0.25. When setting the time-step before a run it is difficult to judge the local Courant numbers as the flow field obviously is not known prior to the solution. Therefore Fluent4 offers an automatic time-step refinement function based on a pre-set maximum Courant number. For the present analysis this function was not used because output of data was required at certain time intervals and this was not easily controlled with the auto time step option enabled. Using free-stream velocity and the minimum vertical distance between horizontal grid lines to calculate the Courant number, it was found that this number had to be less than 0.15 for all the cases to be stable.

A number of iterations are performed at each time step. The volume fraction equation can be solved for every iteration if this is required. When using an explicit interpolation scheme, the time-stepping is low (to satisfy the Courant



Friedrichs Lewy criterion) and it is therefore unnecessary to perform the additional computations of solving for the volume fraction every iteration.

#### 4.2.2.4. Fluid Properties

The default values of fluid properties for fresh water and air at room-temperature were used, with density of  $998.2\text{kg/m}^3$  for water and  $1.293\text{kg/m}^3$  for air.

#### 4.2.3. Solving

##### 4.2.3.1. Initialisation

Before starting the iteration towards a solution to the simulated flow, the flow field must be initialised. In this process pressures, velocities and the value of volume fractions are given starting values. The closer to the solution the starting values are, the fewer iterations required for the solution to converge. Pressures were set to zero (also for the gravity simulations), while the velocity was set equal to the simulation velocity throughout the domain. The volume fractions were set so that initially the free surface was level with the apex of the wedge for deadrisers of 15 degrees and above, and a short distance below this for lower angles.

##### 4.2.3.2. Convergence

The process of obtaining a converged solution is of great importance in the simulations. For monitoring this process Fluent 4 provides a running report of the residuals for each equation at each iteration. The residuals are a measure of how closely each finite difference equation is balanced, given the current state of the solution. During the solving process, a level is set to which the sum of the normalised residuals must drop to before going on to the next time step. For the present analysis, this level was set to  $10\text{E}-3$ . To ensure that this level was adequate for these simulations, the total pressure force on the body was also plotted against the number of iterations.



#### 4.2.4. Post-Processing

The flow field variables are stored at numerous time-steps during the solution process, and this data is accessible subsequent to the simulation by use of a post-processor integrated into the Fluent software. The information that was extracted from the stored data for analysis in the present study was pressures, velocity vectors and volume fractions on the wedge body and in the surrounding field.

### 4.3. Simulation Program

The water entry of wedges with deadrise angles of 5, 10, 15, 30, 45 and 60 degrees were each simulated at three different constant entry velocities: 0.5, 1.0 and 1.5m/s. These simulations were carried out with gravitational body forces included in the momentum equations. Another simulation was carried out with each geometry with the body forces excluded. This was done to obtain data for infinite velocity, or pure dynamic effect, water entry so as to isolate the dynamic force contribution acting on the sections from hydrostatic effects. In addition to these simulations, a simulation was carried out of the water entry of a flat-bottomed section with zero gravity.

### 4.4. Results

#### 4.4.1. Force Data

The variation of total entry force with immersion depth is obtained by integration of the vertical component of pressure along the bottom of the section for a number of time-steps. The sectional entry forces are made non-dimensional on maximum beam and are presented for non-dimensional immersion depth in Figures 4-7 to 4-12. For the flat-bottomed section, the immersion depth is non-dimensionalised on the beam  $b$ , while the deadrise sections are non-dimensionalised on the vertical distance from keel to chine  $d$ .

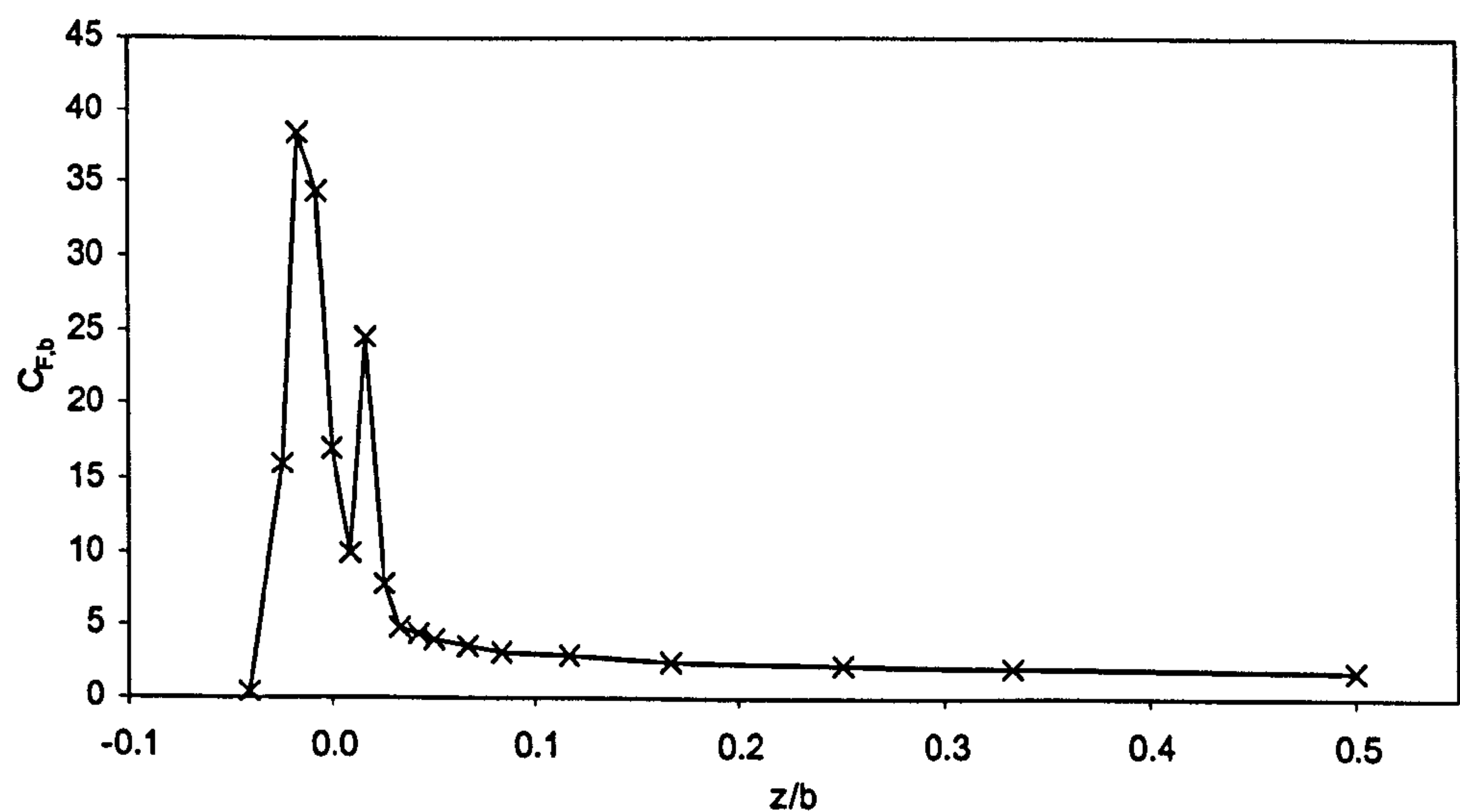


Figure 4-7. Non-dimensional water entry force, flat-bottomed section, zero gravity.

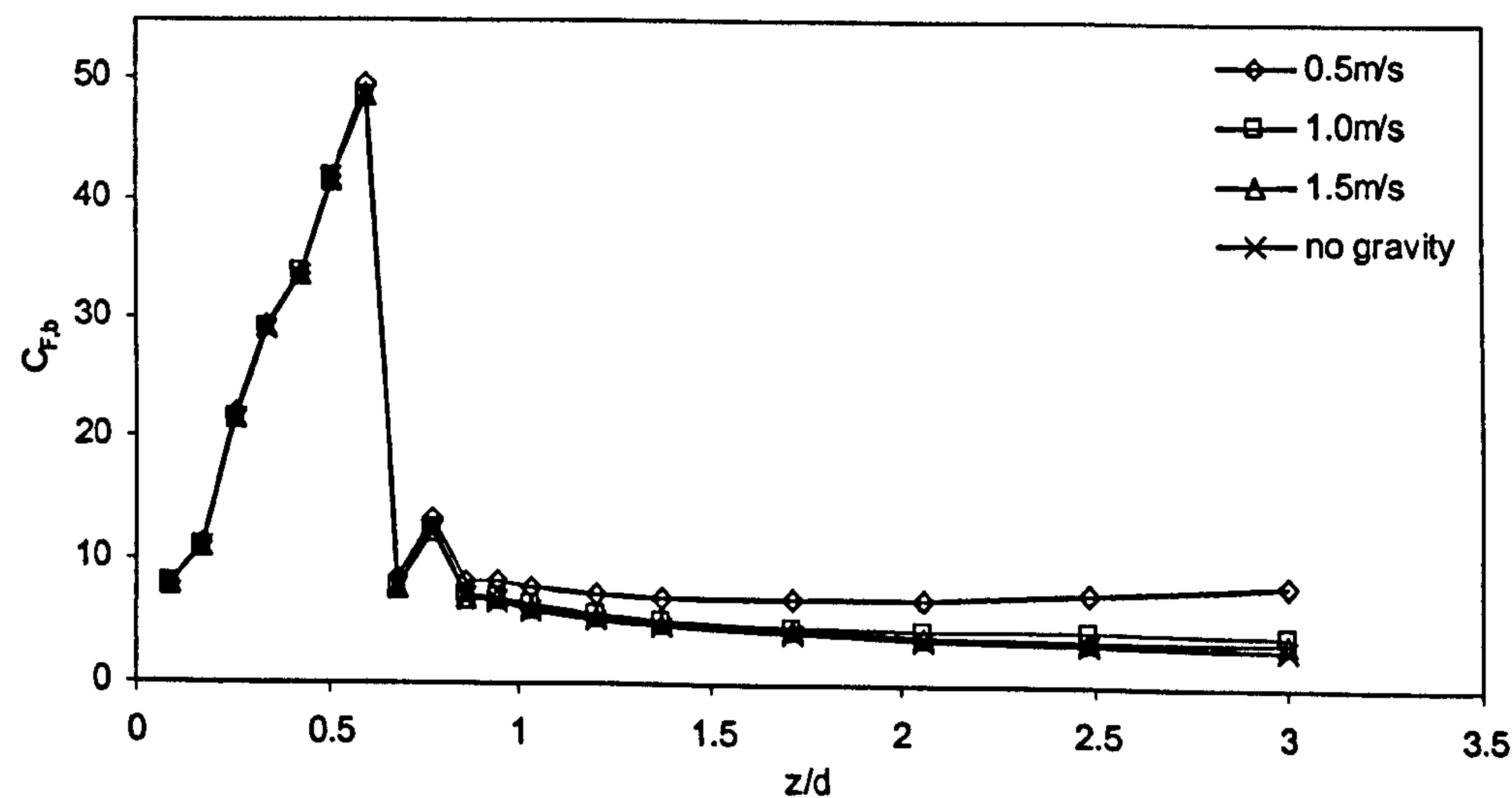


Figure 4-8. Non-dimensional water entry force, 5 degree wedge section.

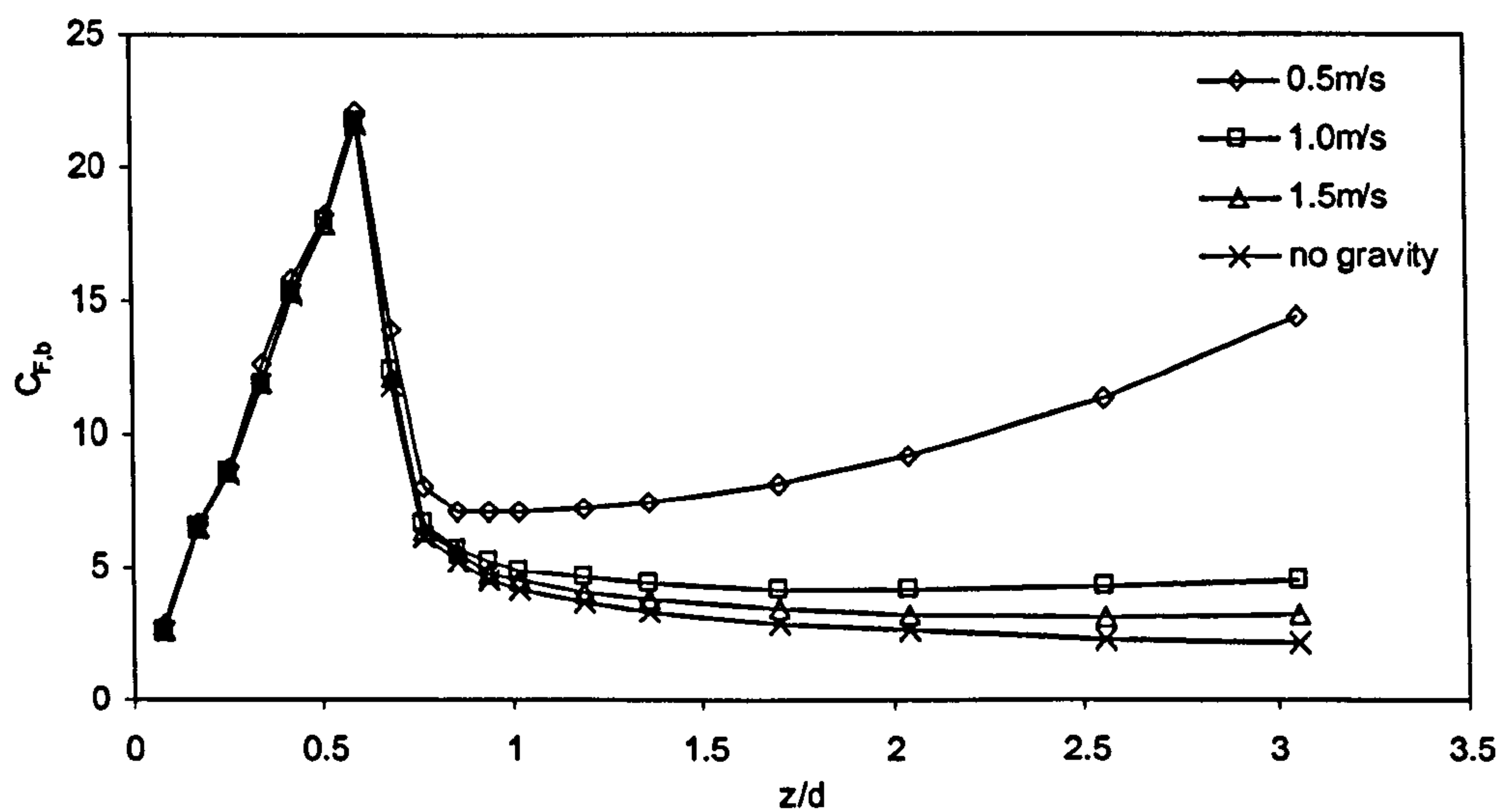


Figure 4-9. Non-dimensional water entry force, 10 degree wedge section.

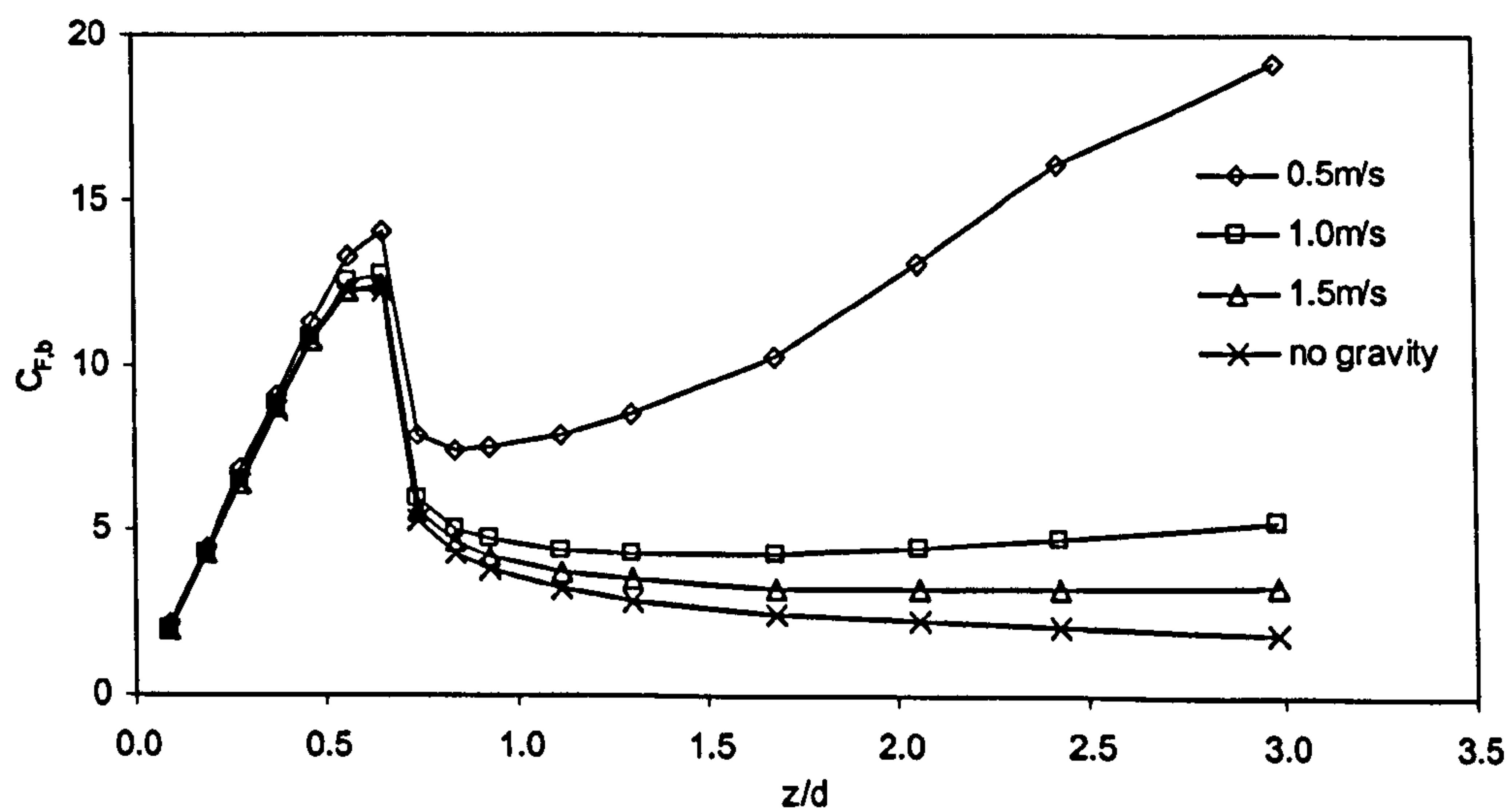


Figure 4-10. Non-dimensional water entry force, 15 degree wedge section.



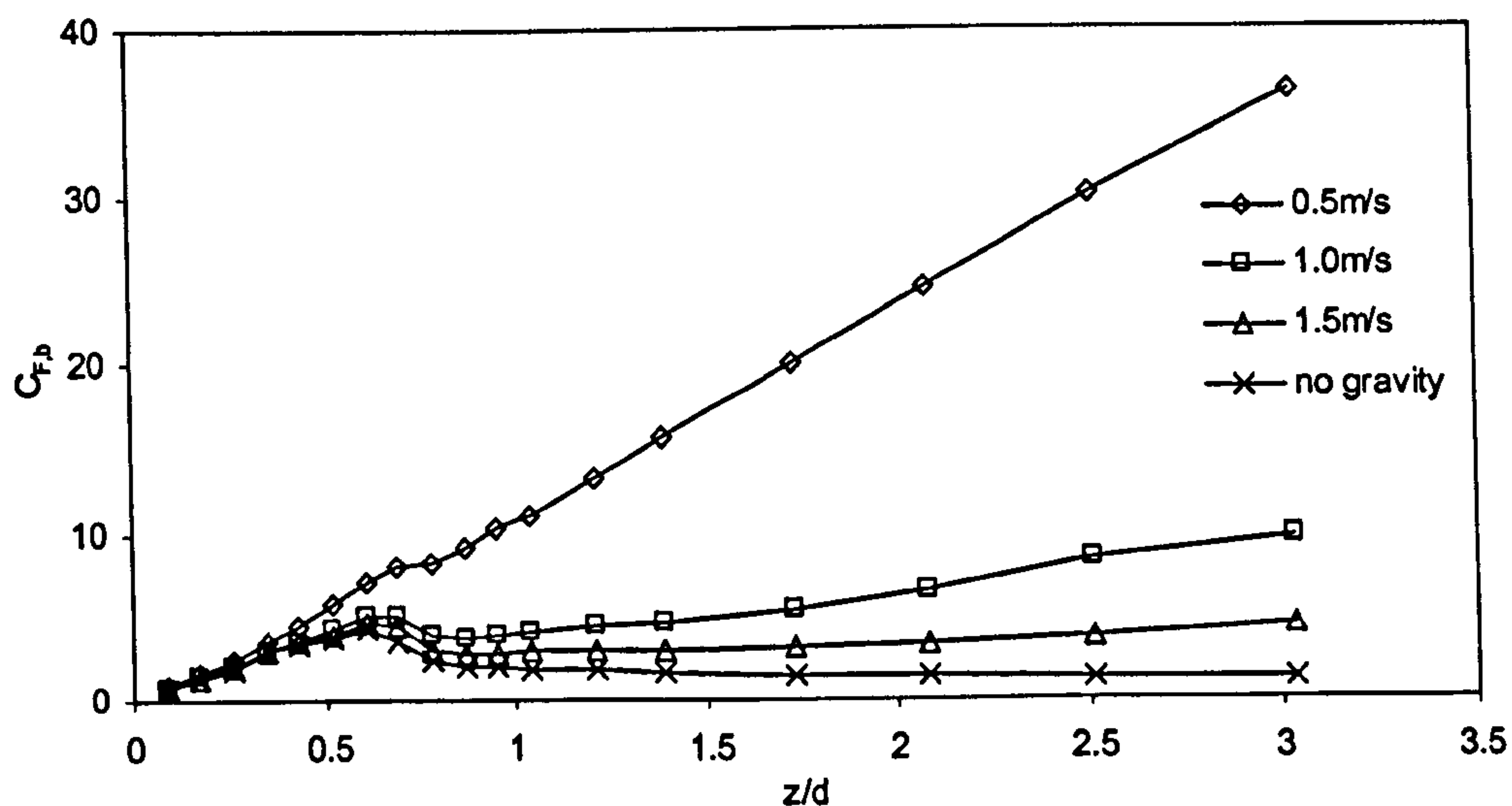


Figure 4-11. Non-dimensional water entry force, 30 degree wedge section.

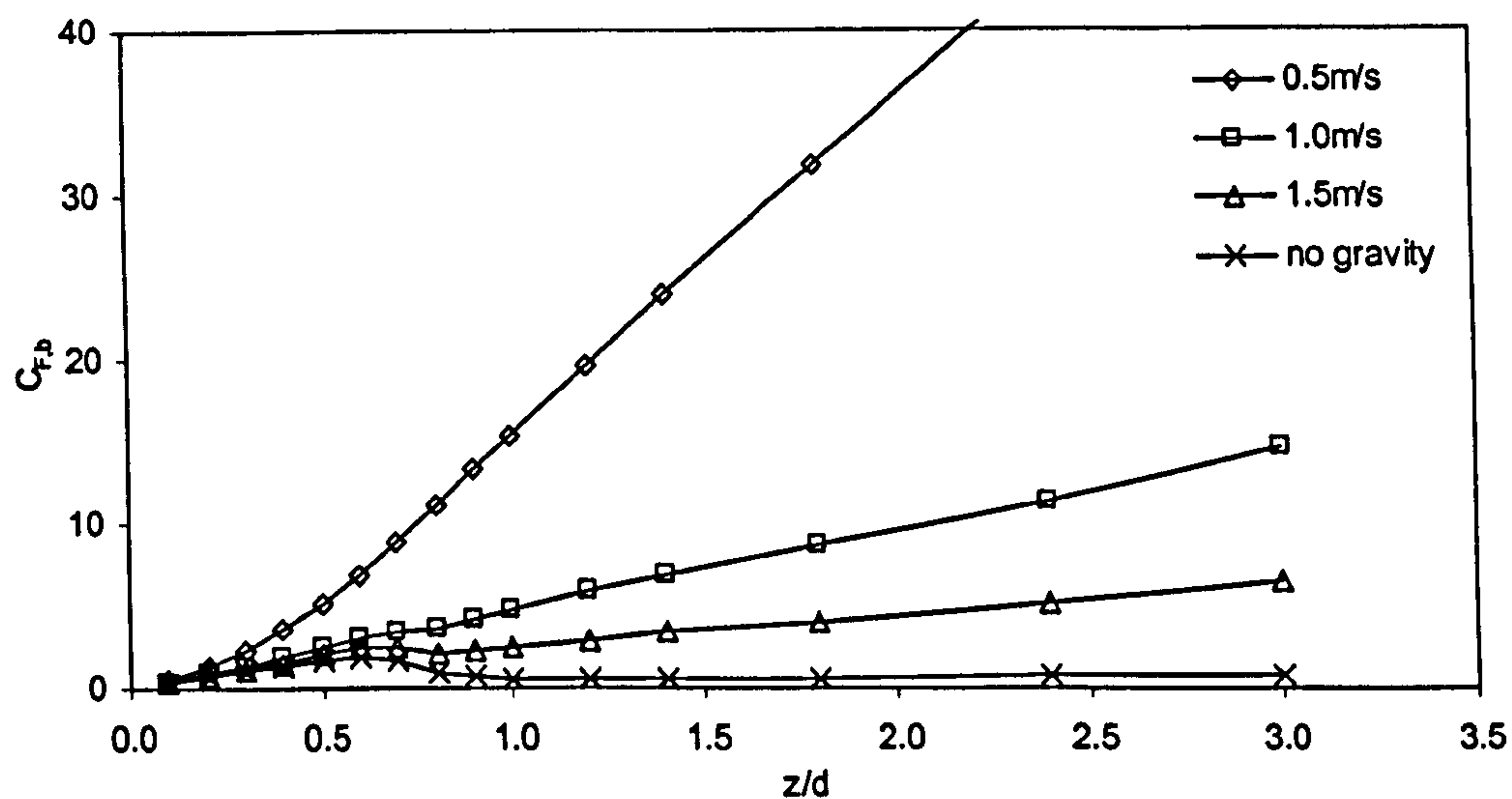


Figure 4-12. Non-dimensional water entry force, 45 degree wedge section.

It is seen that the non-dimensional gravity effects, relative to the dynamic force contribution, are greater at high deadrise angles. This is because the dynamic impact force is lower for high deadrise angles than for low ones, and also because the gravity effect (hydrostatic force) at a given non-dimensional immersion depth  $z/d$  is greater for a large deadrise section than for a low one (more immersed volume).

#### 4.4.2. Pressure Data

Pressure data is obtained for a number of time steps during the water entry simulations and has been used to produce Figures 4-7 to 4-12. In Figure 4-13, the non-dimensional pressure  $C_p$  obtained with the zero-gravity simulations at an instant before the chines are wetted are plotted against non-dimensional vertical position on the wedge surface. The pressures  $p$  are made non-dimensional on  $\frac{1}{2}\rho w^2$ , and vertical position along the wedge surface  $Z$  is made non-dimensional on immersion depth  $z$ . The pressure coefficient  $C_p$  is multiplied by  $\tan\beta$  to allow the results from all deadrise angles to be plotted on the same chart for better presentation.

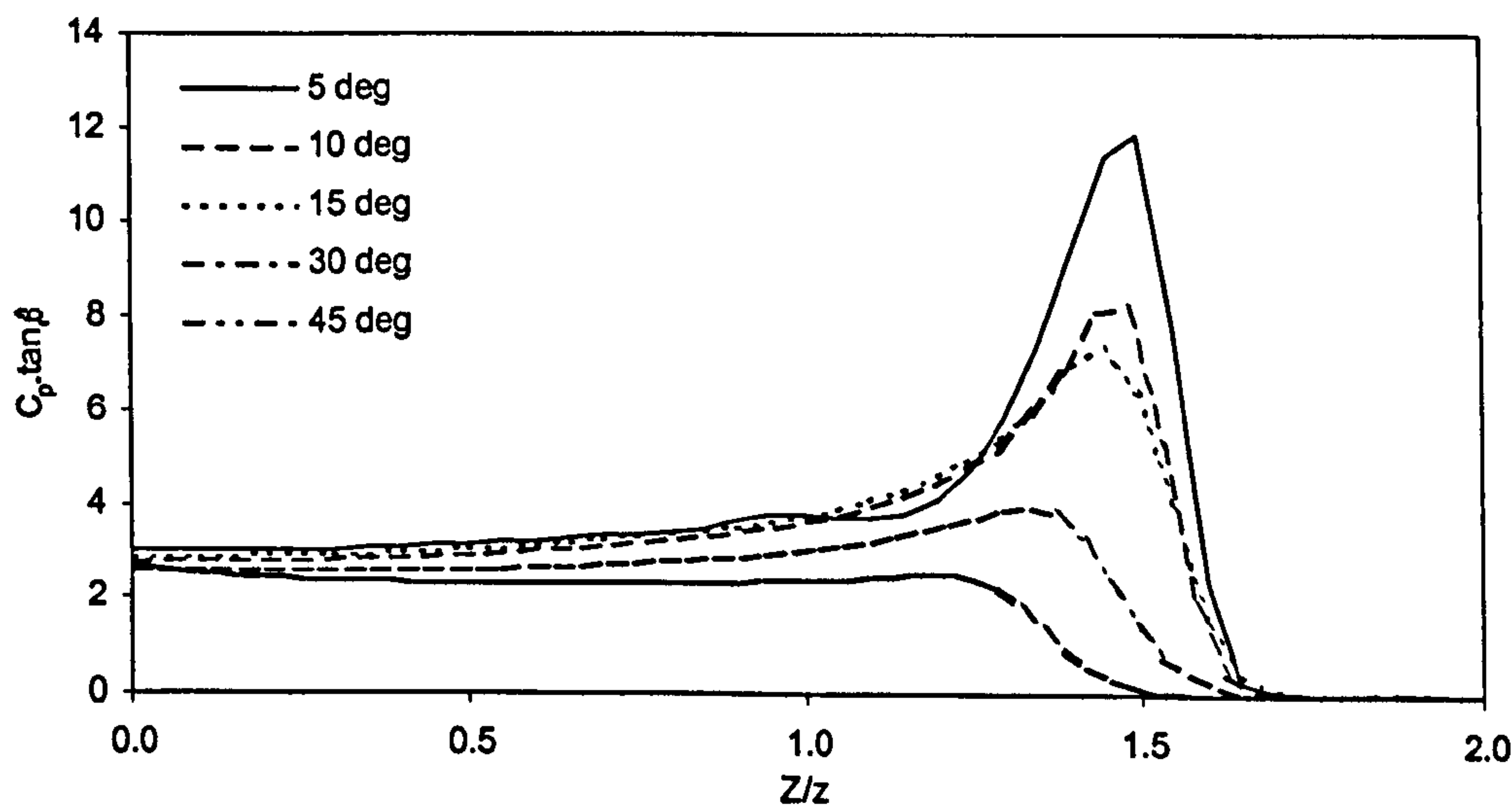


Figure 4-13. Non-dimensional pressure along wedge surface.

The pressure coefficient is more or less constant on the part of the wedge that is below the undisturbed water surface ( $Z/z < 1$ ), while the wetted wedge surface above this level experiences a pressure peak. Figures 4-8 to 4-12 show that the force after the peak at about  $z/d=2/\pi$  drops more quickly for the lower deadrise angles than for the higher ones. In Figure 4-13 it is seen that the pressure peak is greater for the lower deadrise angles than for the higher ones. It follows from this that a larger part of the total pressure force is acting in the region close to the free

surface for the lower deadrise angle sections than for the higher. Thus the impacting wedge experiences a more rapid drop in force for low deadrise sections than for higher ones when the chines get wetted.

In Figure 4-13 it is also seen that the apex of the peak has not been captured in the lower deadrise angle cases. The pressure output file from the CFD simulation contains only the values at the nodes that have been defined in the grid generation procedure. Therefore the pressure peak has been obtained by interpolation where the maximum pressure is taken at the intersection between two lines extended from the data points adjacent to the apex. The gradients of the lines are taken as the gradient at the two points adjacent to the apparent apex. The maximum pressure coefficients that were found are given in Table 4-1 together with the non-dimensional elevation, at which they occur.

$\beta$ [degrees]	$\frac{z_{p-max}}{z}$	$C_{p-max}$
5	1.48	145
10	1.47	50.5
15	1.44	29.3
30	1.33	6.93
45	1.20	2.73

Table 4-1.     Maximum pressure coefficients.

Figures 4-14 to 4-19 shows contours of non-dimensional pressure in the nearby field of the wedge sections during dry chines entry.



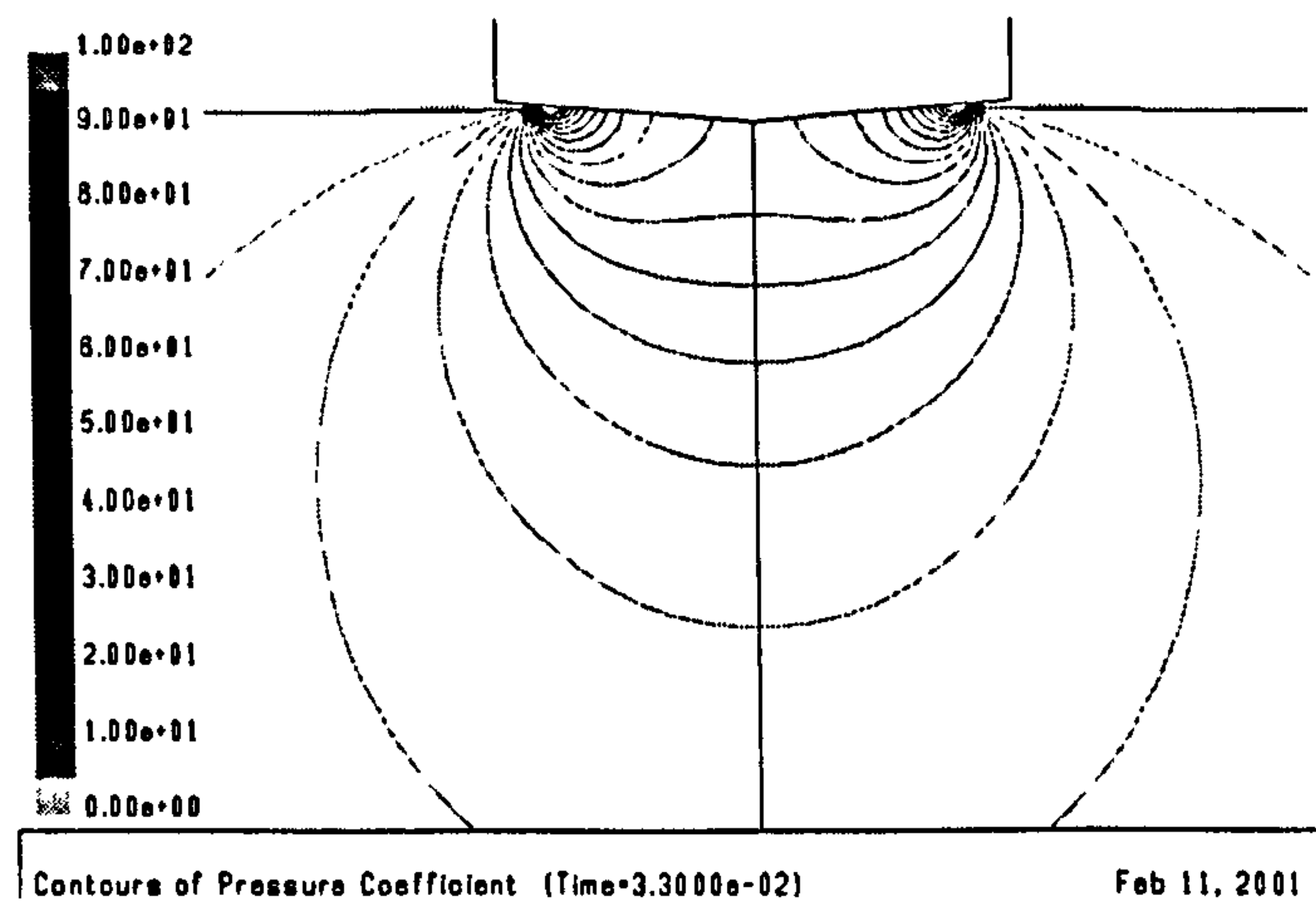


Figure 4-14. 5 degree wedge.

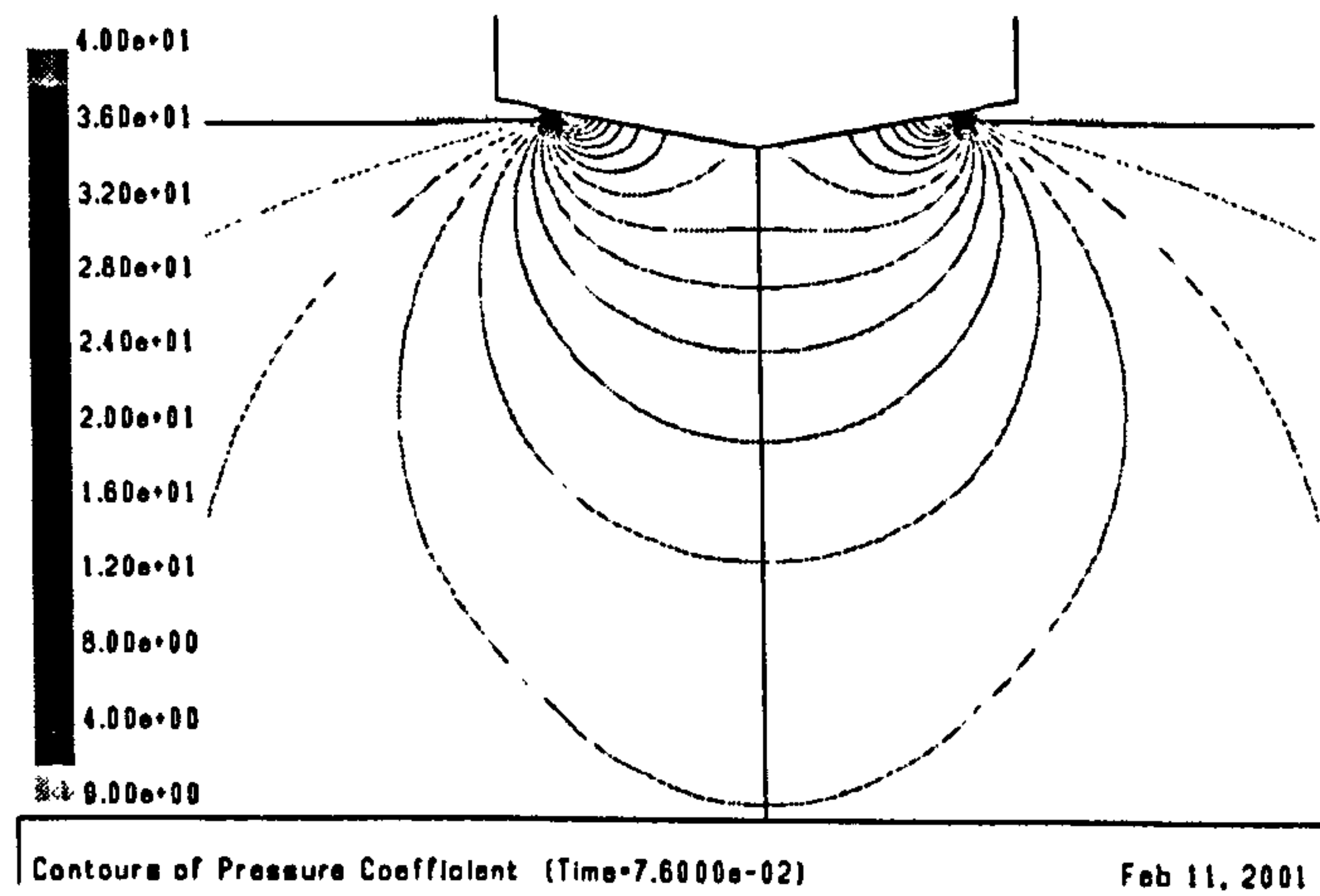


Figure 4-15. 10 degree wedge.

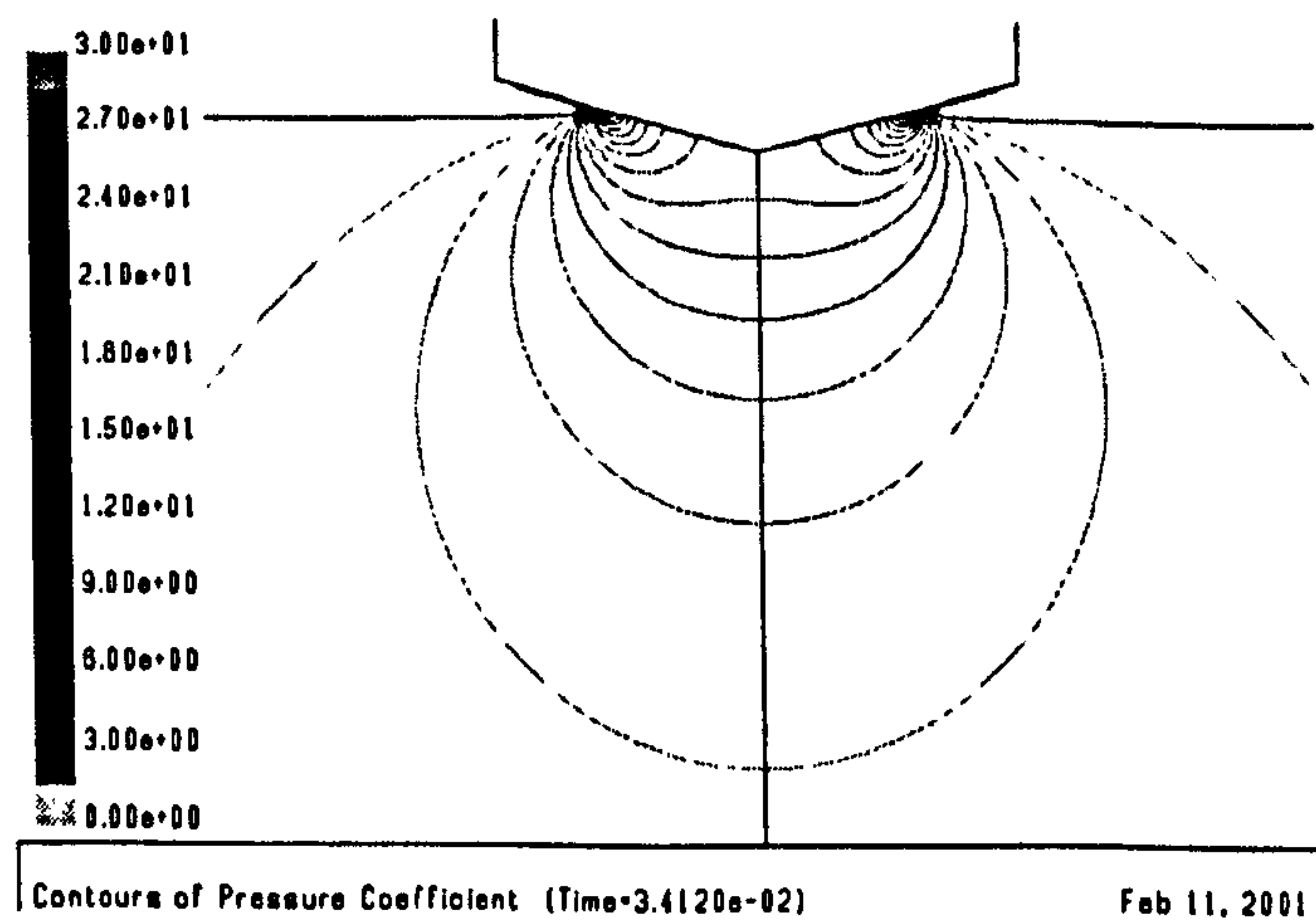


Figure 4-16. 15 degree wedge.

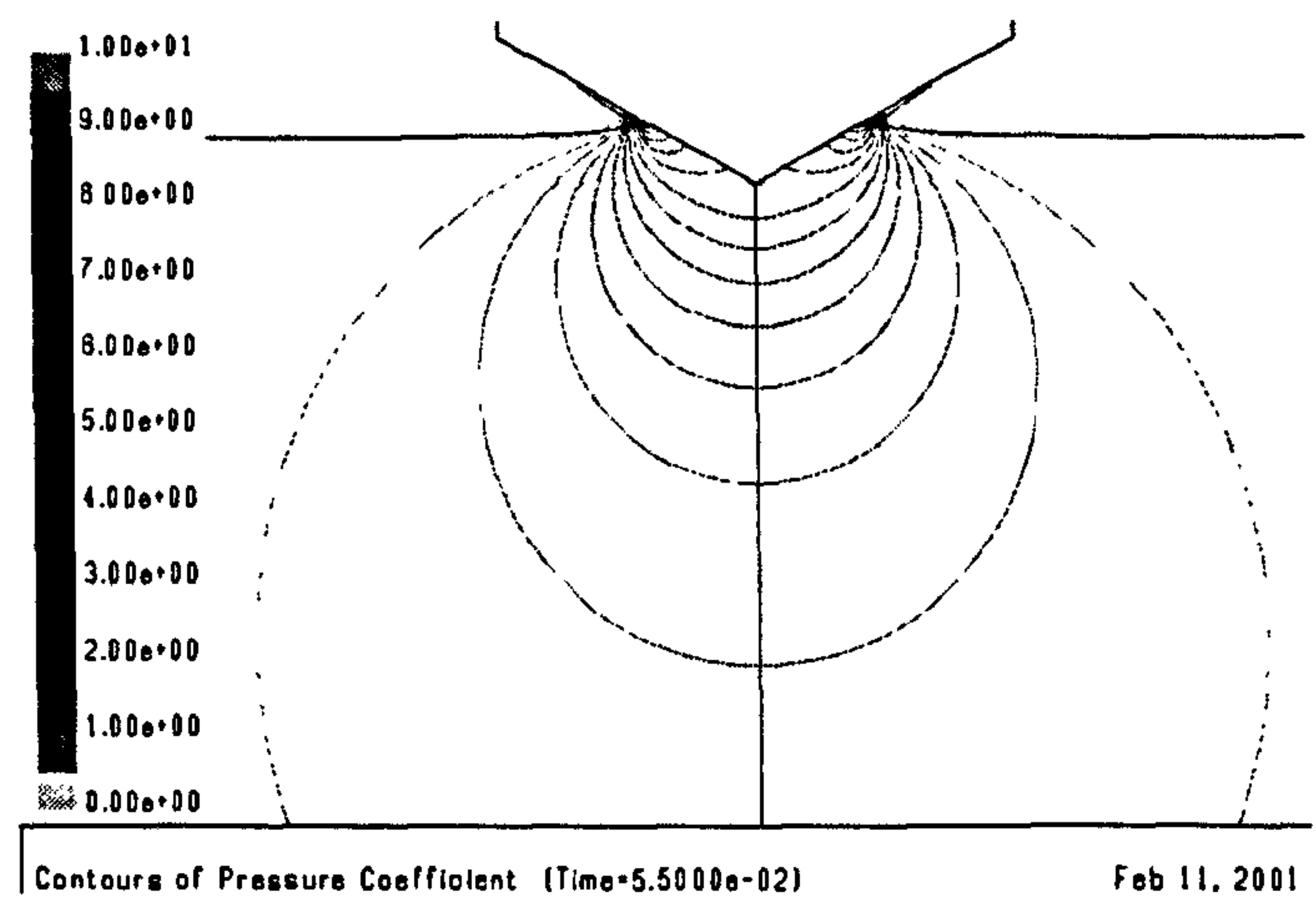


Figure 4-17. 30 degree wedge.

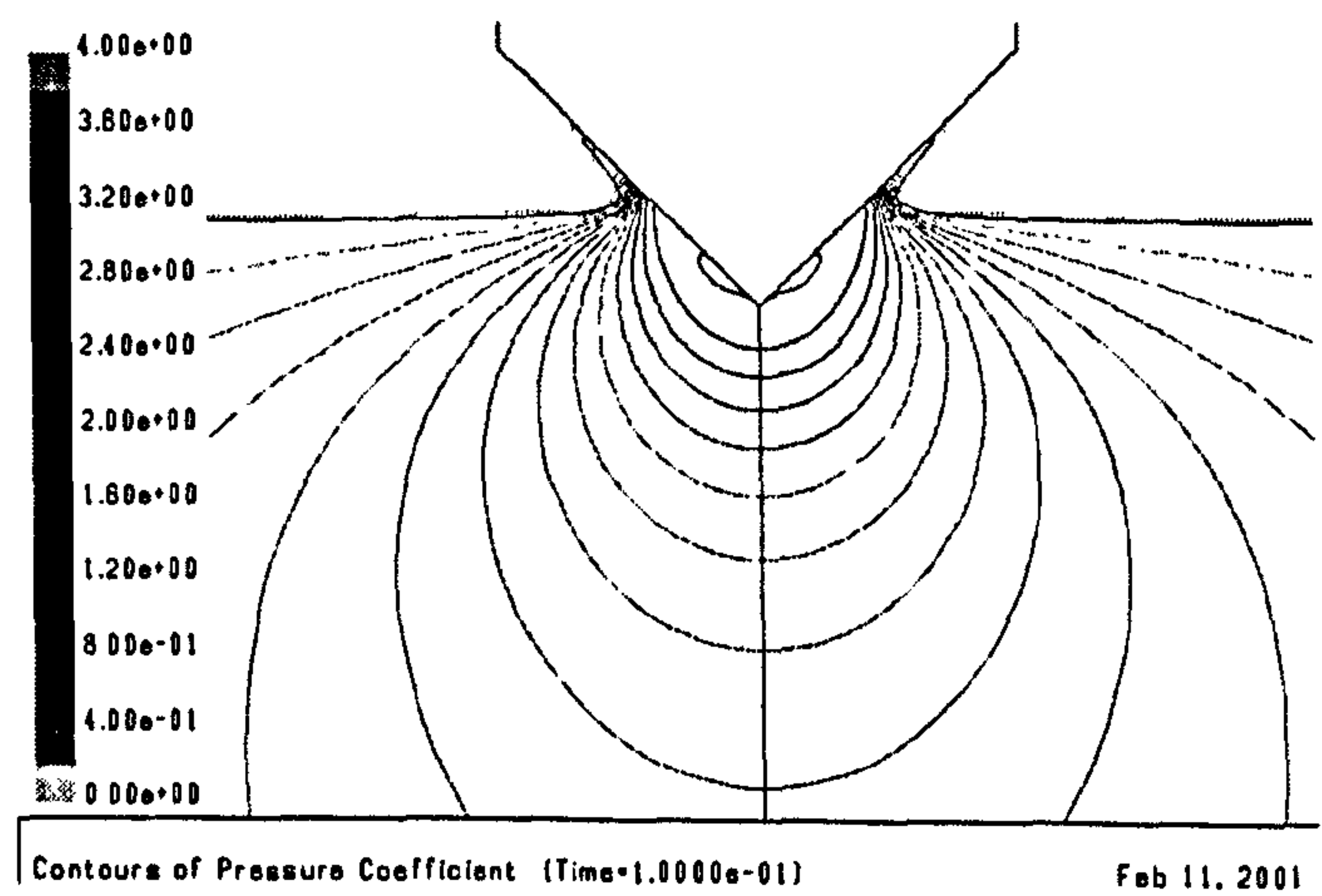


Figure 4-18. 45 degree wedge.

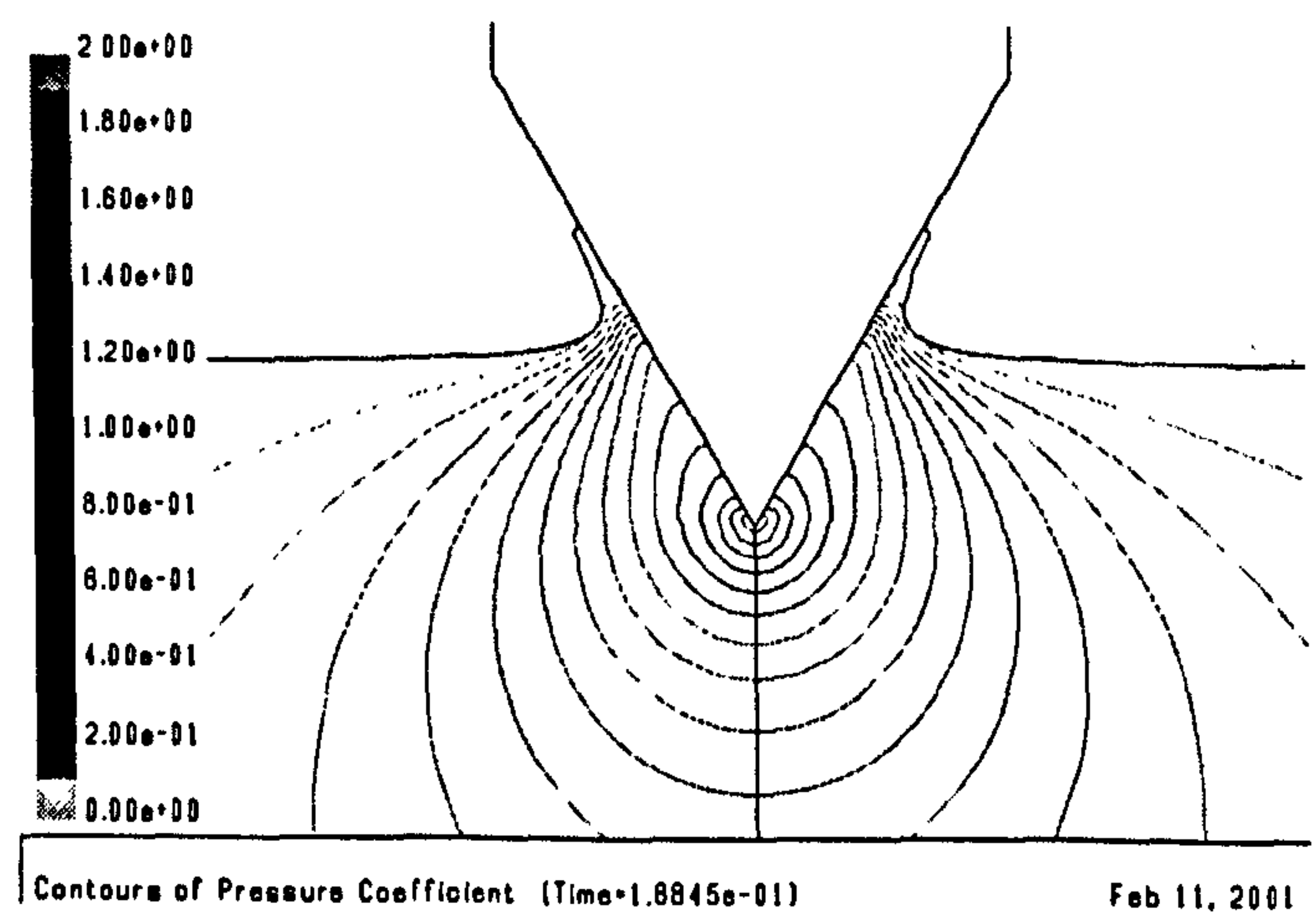


Figure 4-19. 60 degree wedge.

#### **4.4.3. Free Surface Elevation**

The contours of volume fractions throughout the domain are extracted for the same time steps during simulation as the pressures. The free surface occurs where the volume fraction value is 0.5. In Figures 4-20 to 4-39 the contour of water volume fraction of one half is plotted for six different immersions from all the deadrise angle simulations at each entry velocity.



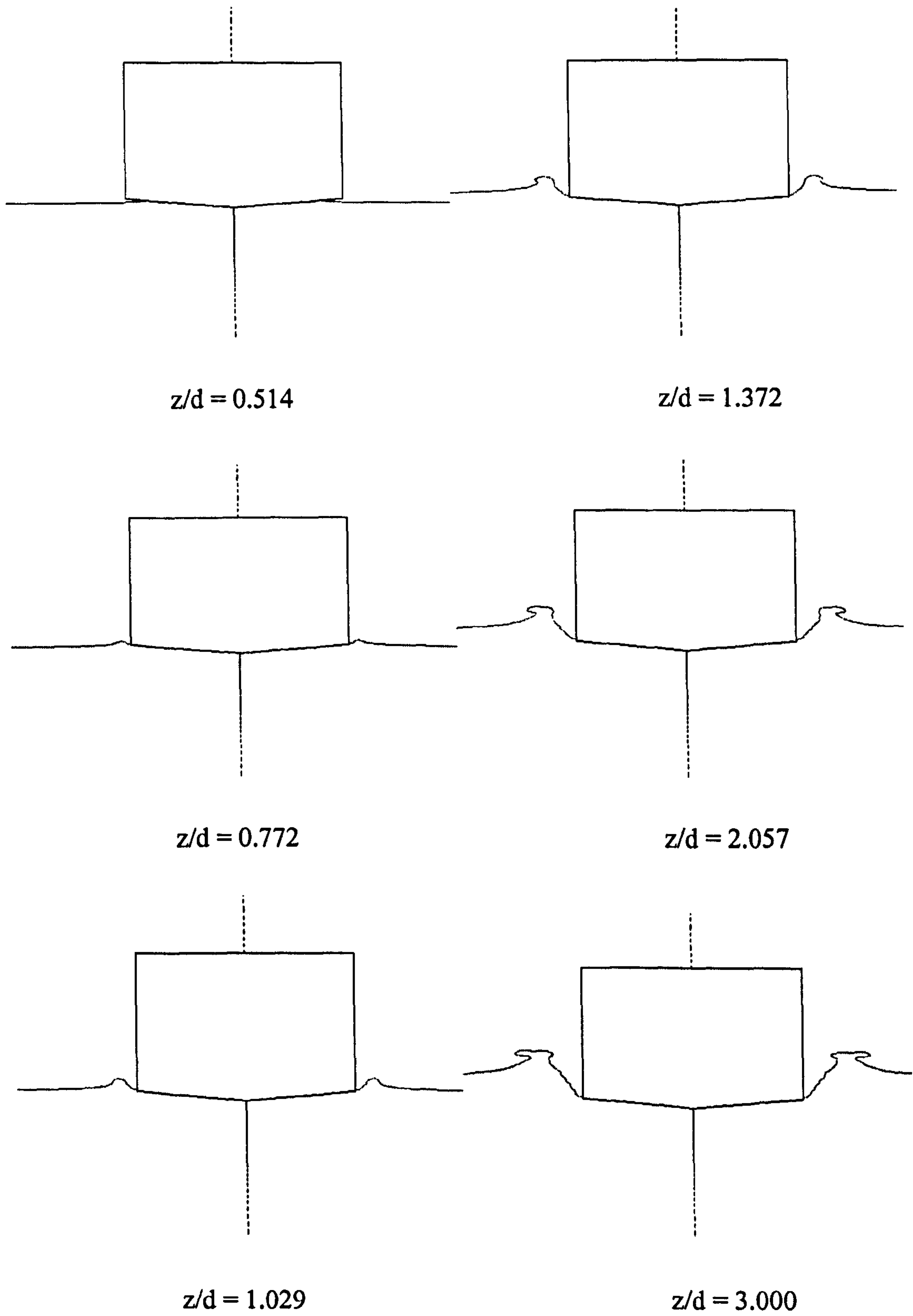


Figure 4-20. 5 degree wedge section at 0.5m/s.

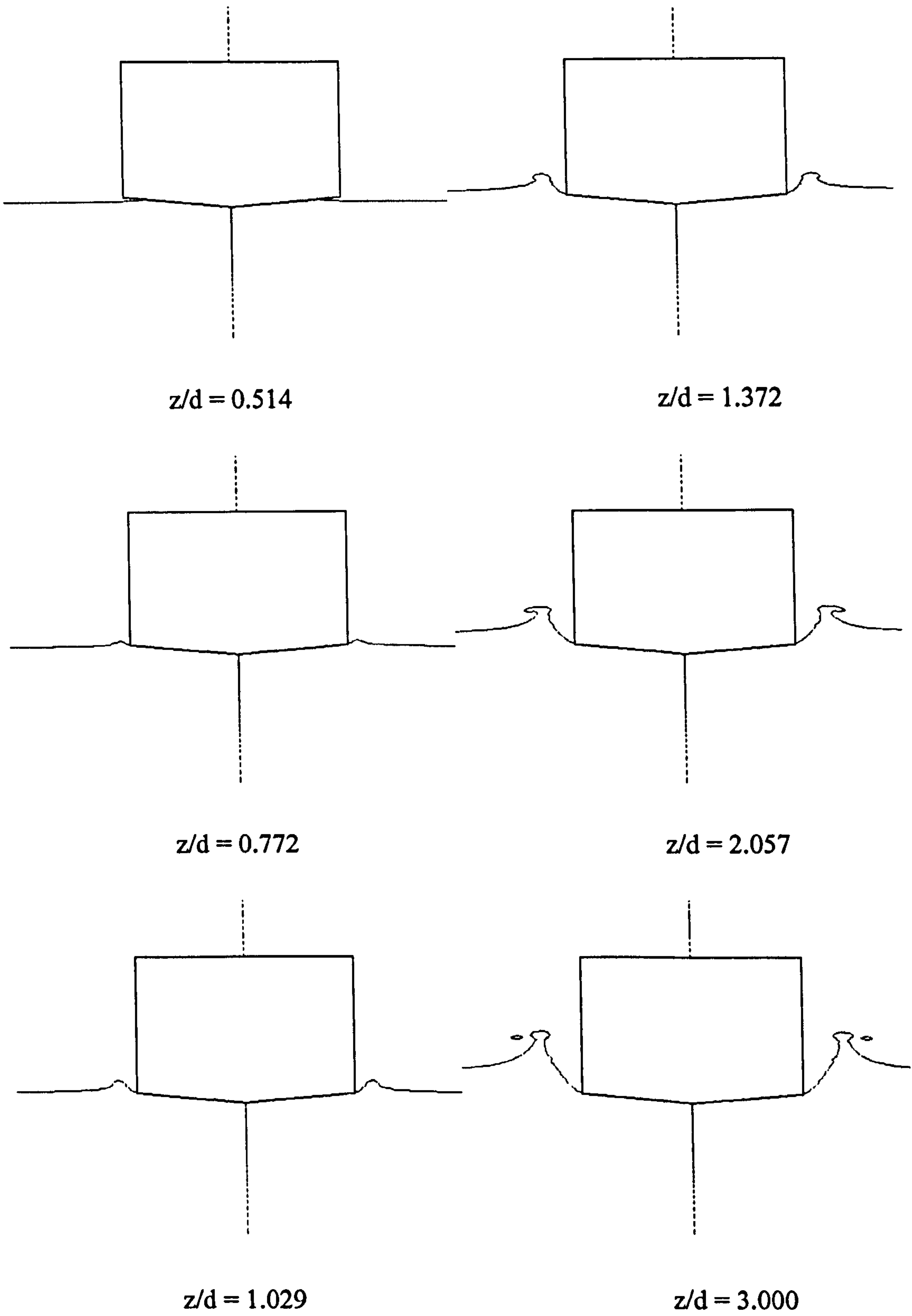


Figure 4-21. 5 degree wedge section at 1.0m/s.

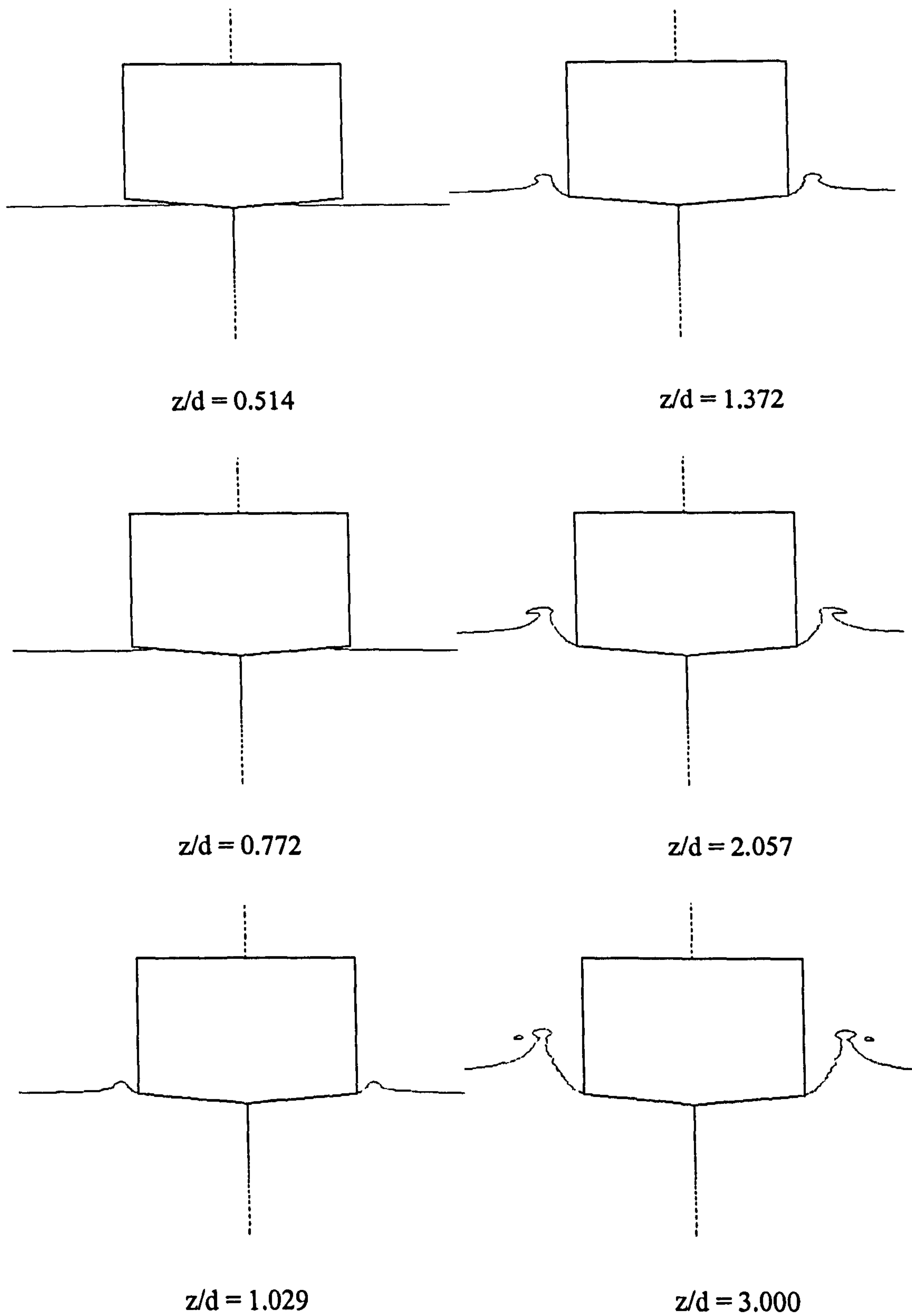


Figure 4-22. 5 degree wedge section at 1.5m/s.



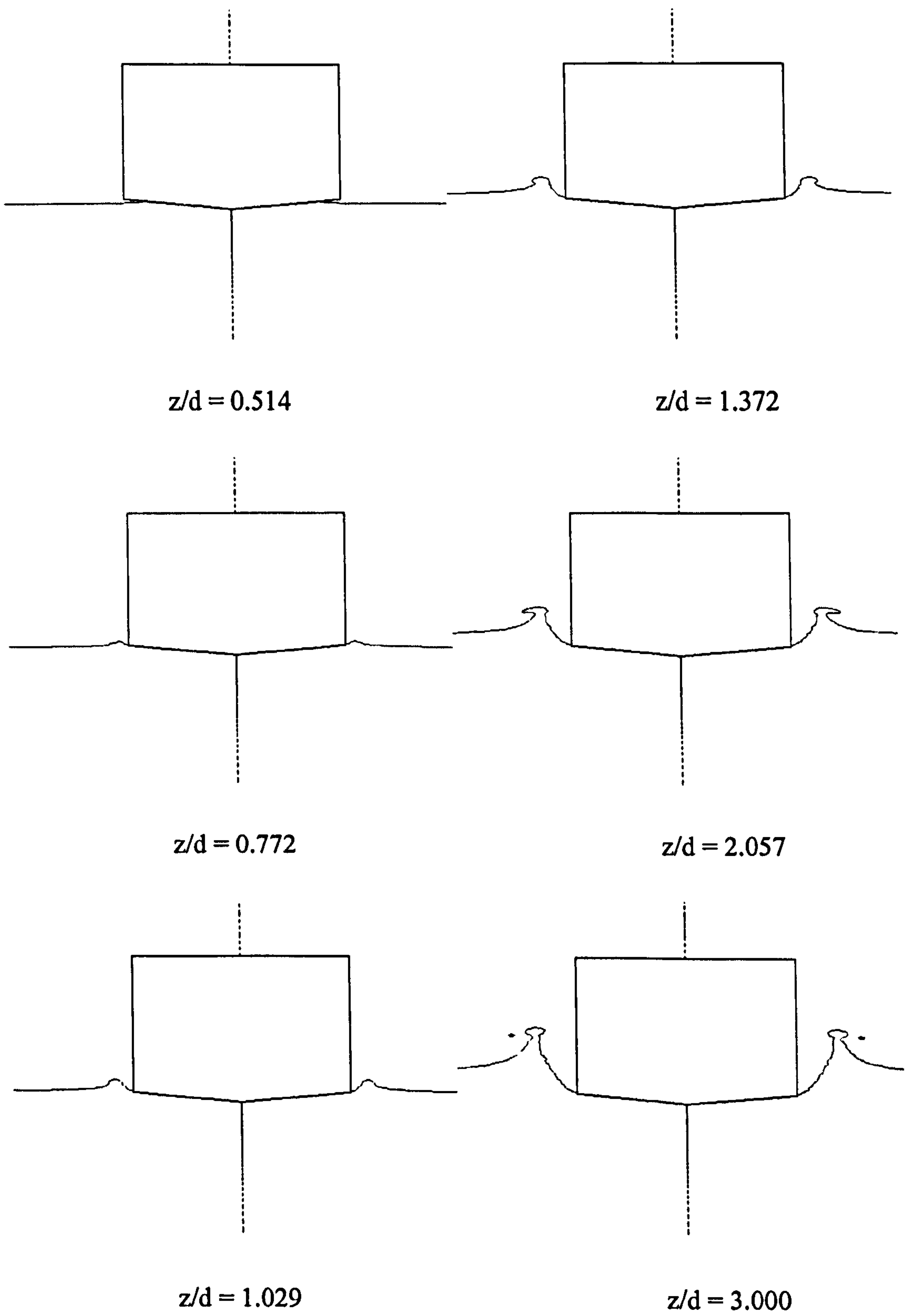


Figure 4-23. 5 degree wedge section at zero gravity.

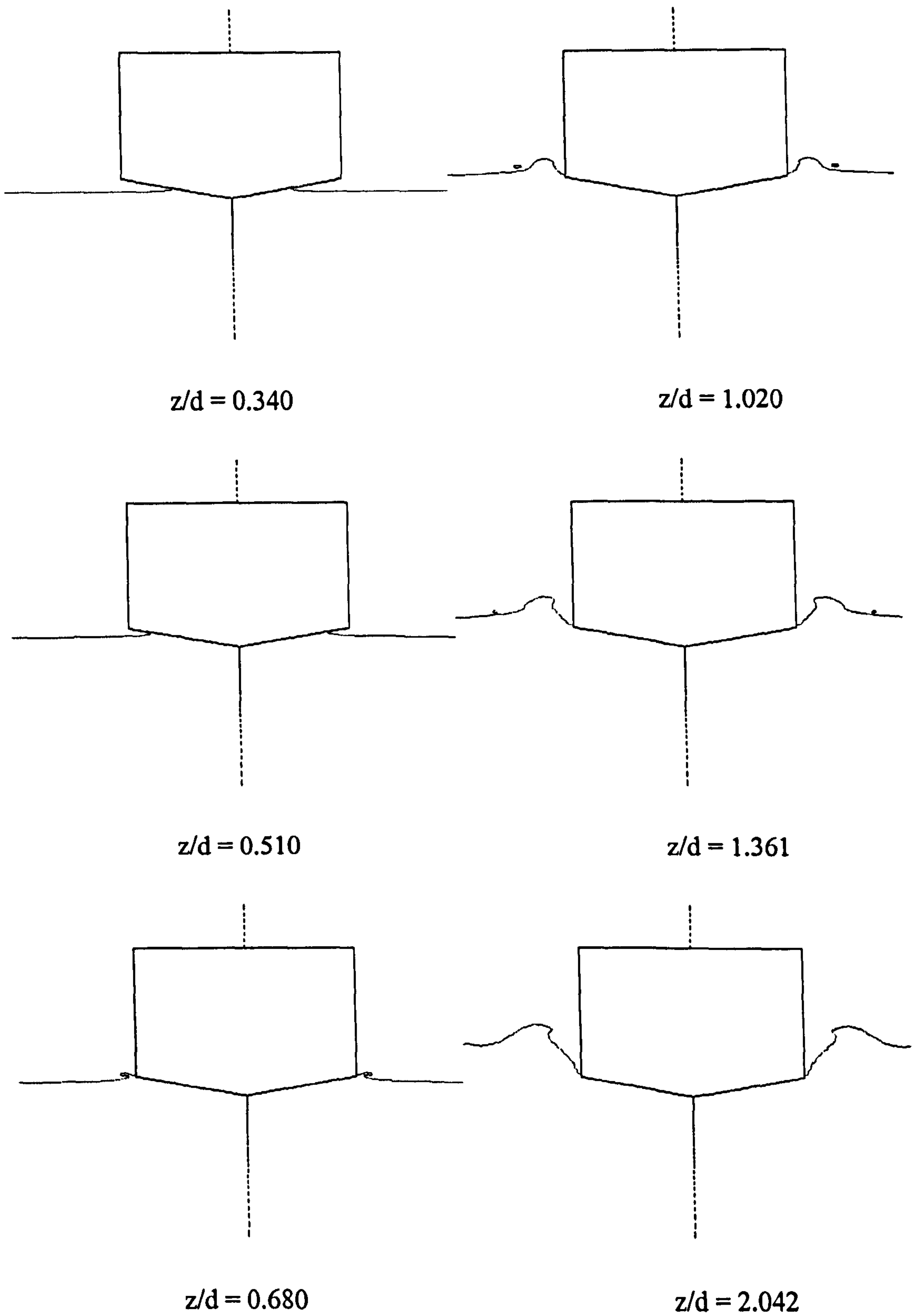


Figure 4-24. 10 degree wedge section at 0.5m/s.

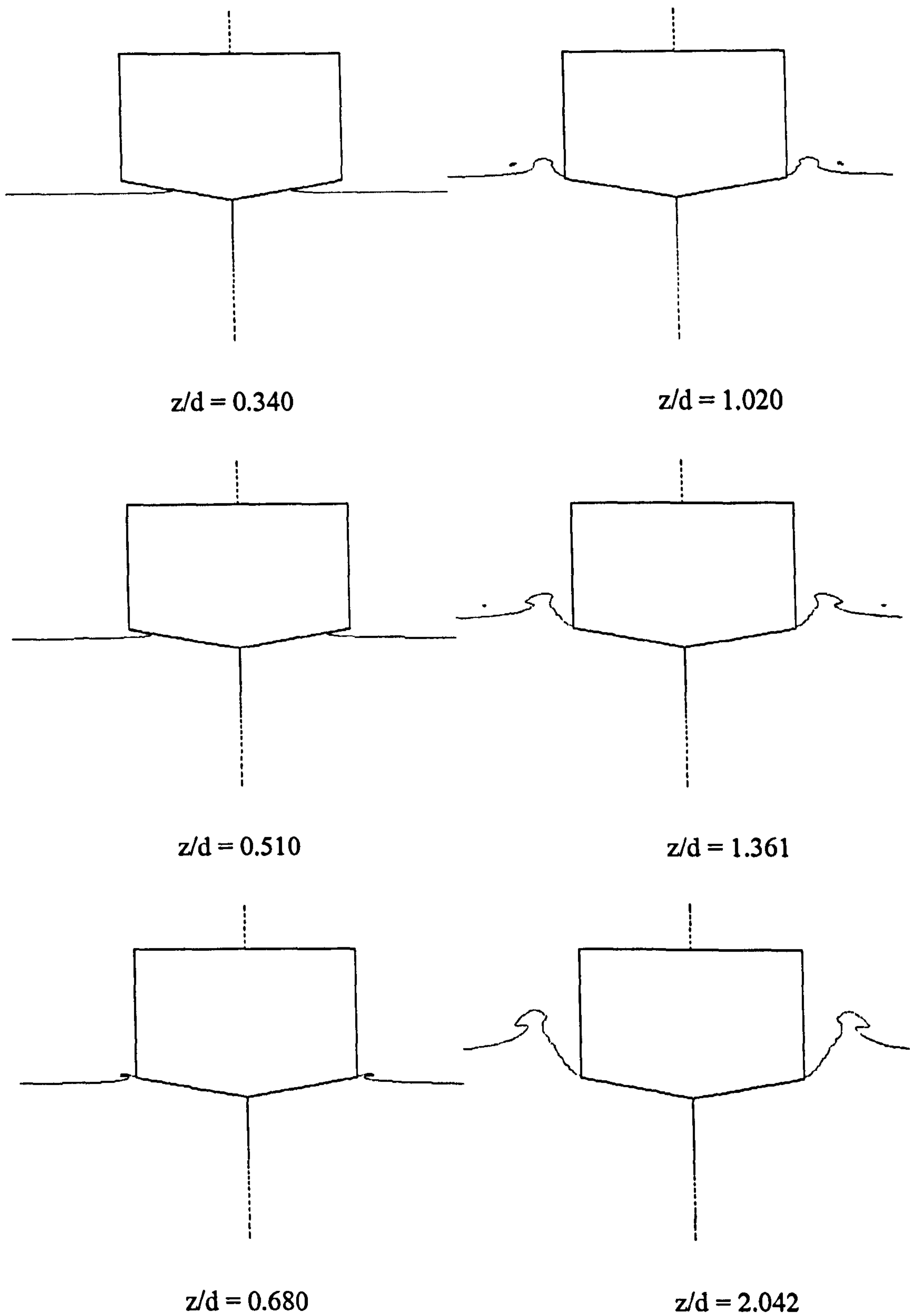


Figure 4-25. 10 degree wedge section at 1.0m/s.



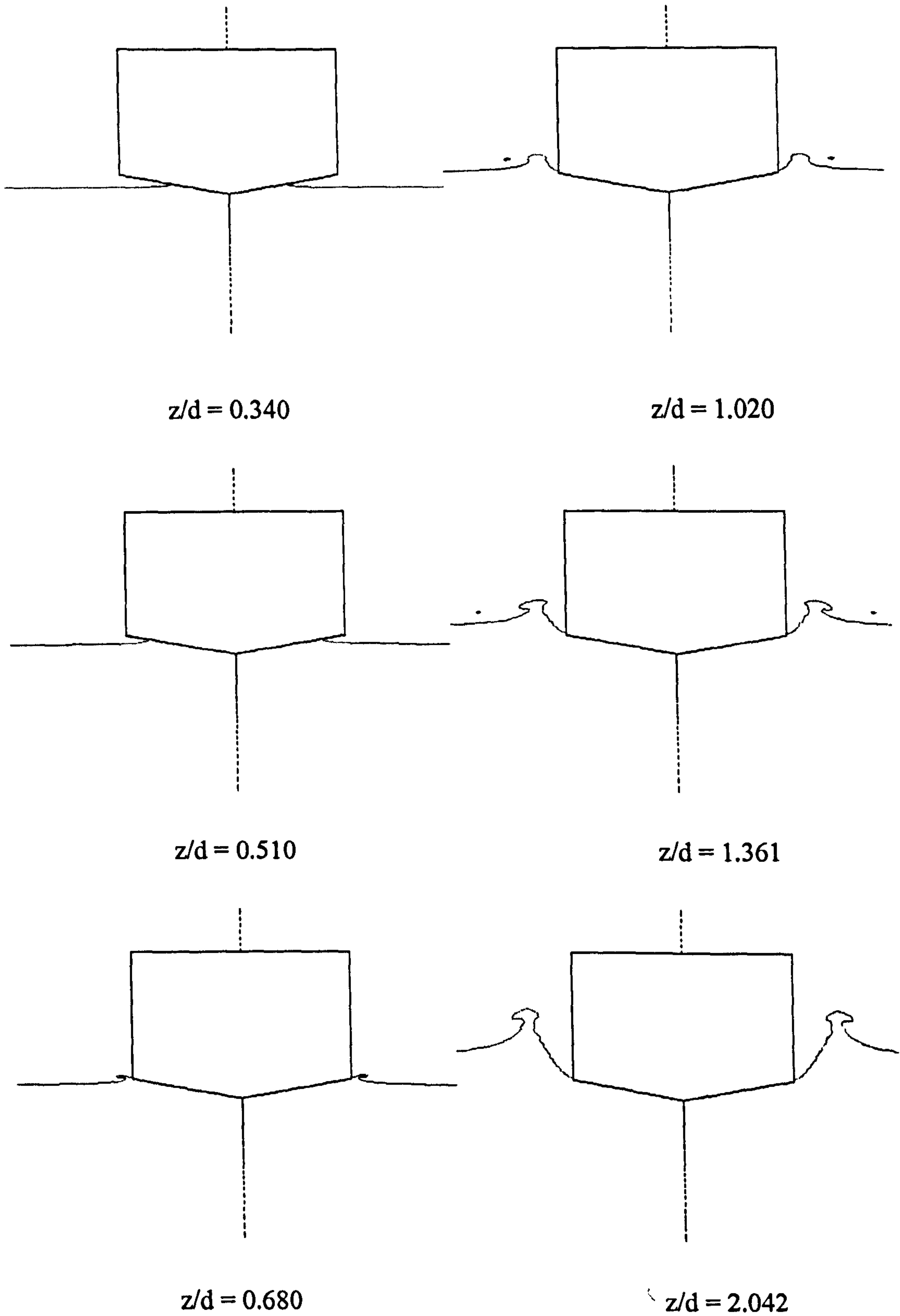


Figure 4-26. 10 degree wedge section at 1.5m/s.

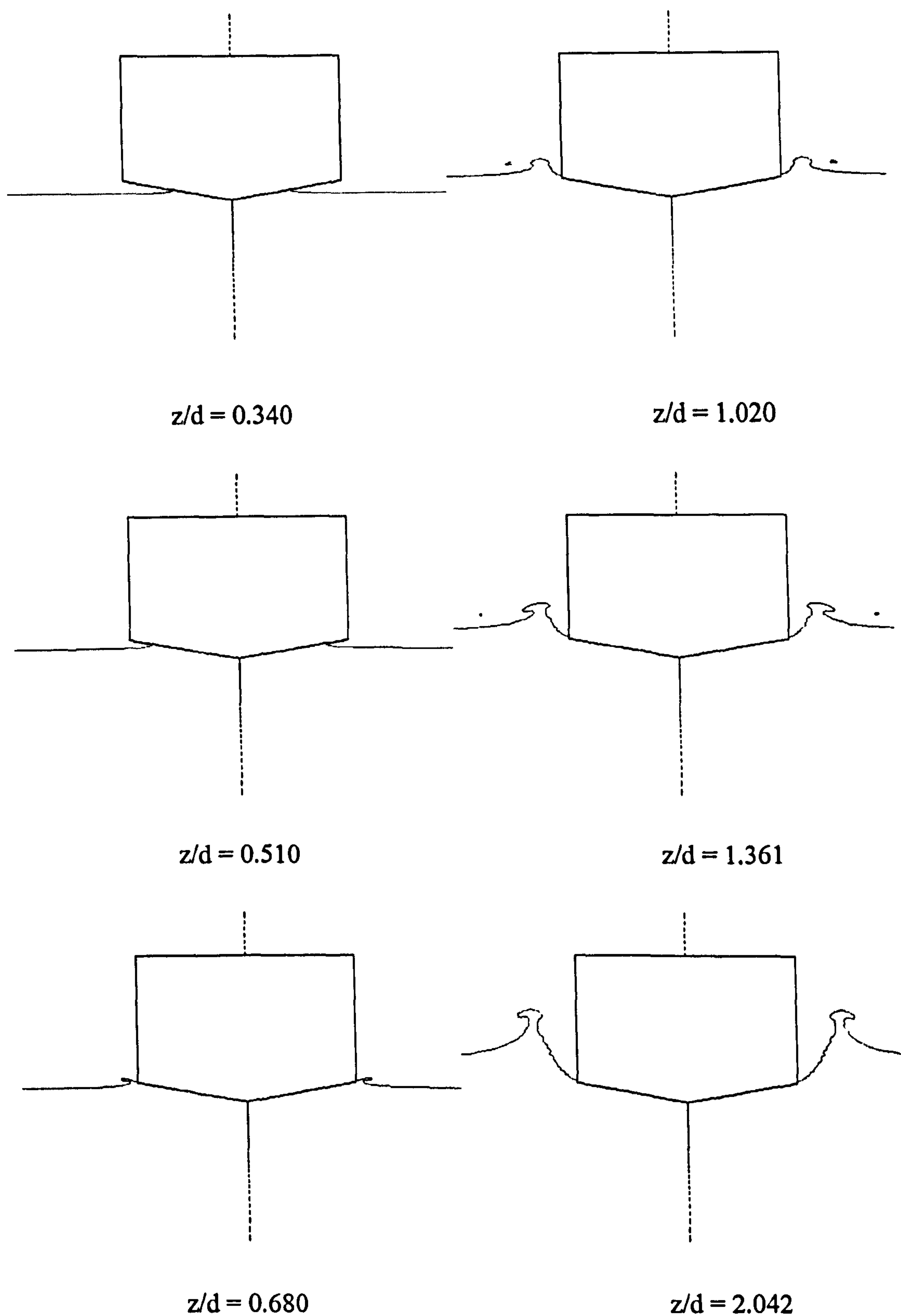


Figure 4-27. 10 degree wedge section at zero gravity.

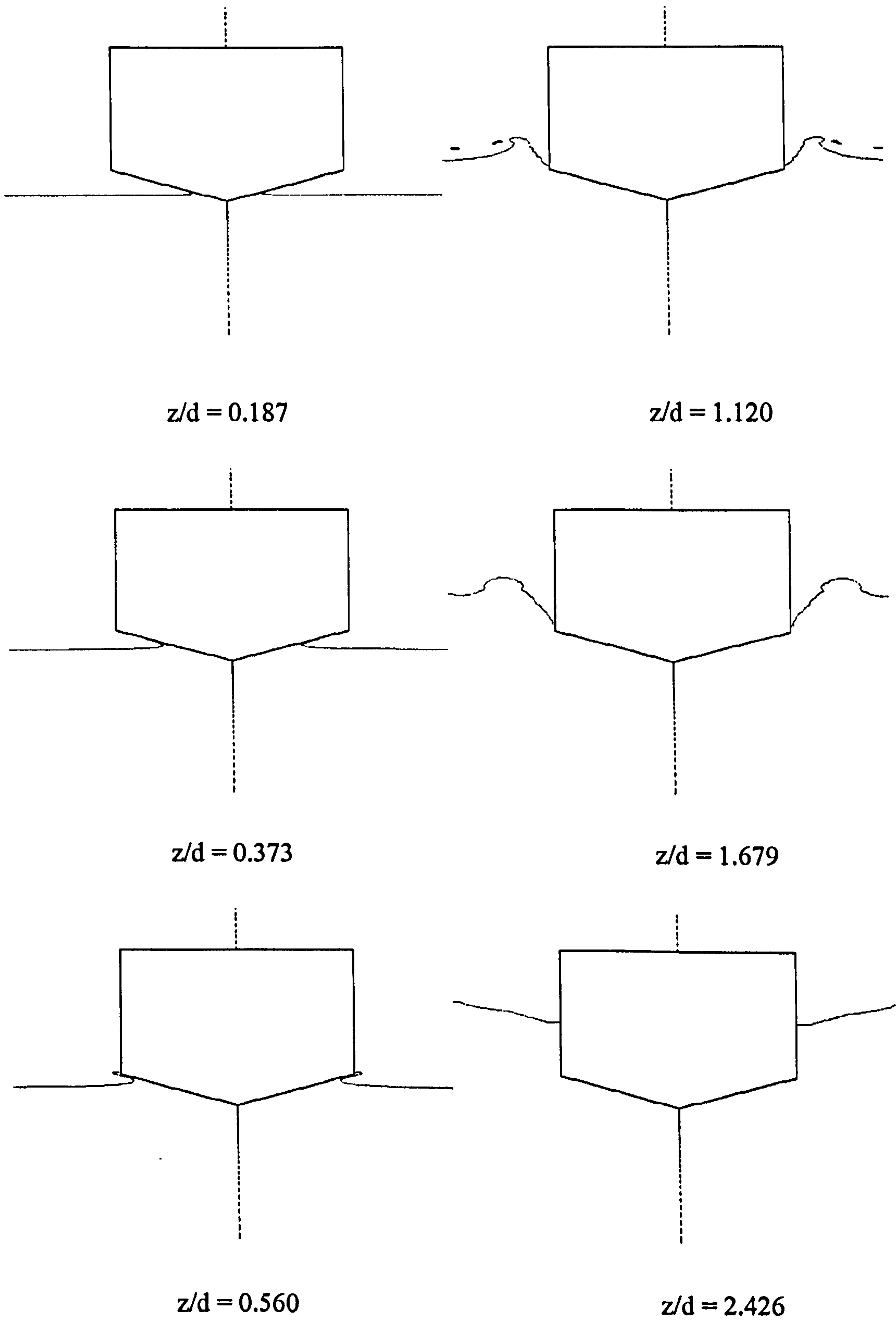


Figure 4-28. 15 degree wedge section at 0.5m/s.



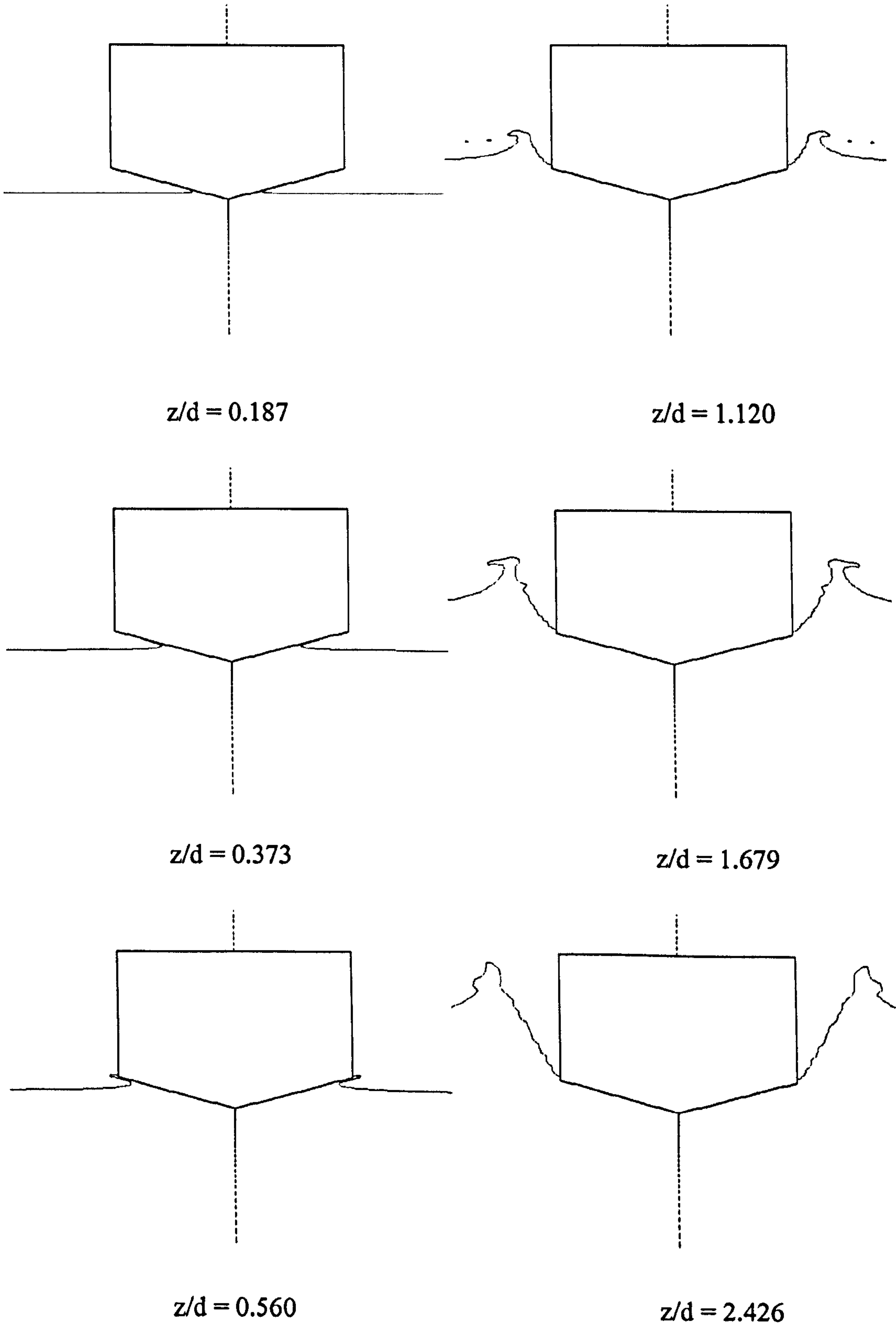


Figure 4-29. 15 degree wedge section at 1.0m/s.

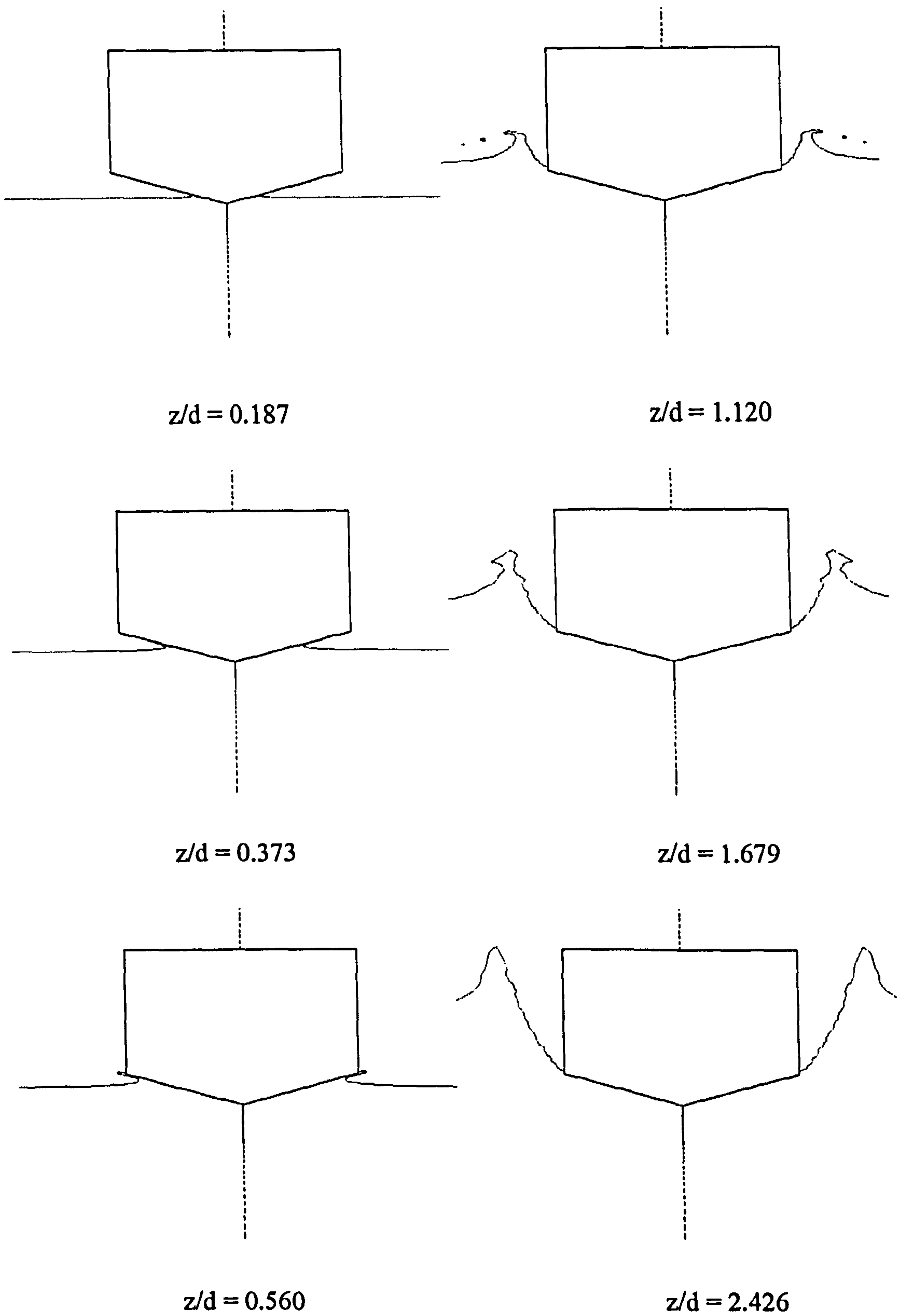


Figure 4-30. 15 degree wedge section at 1.5m/s.

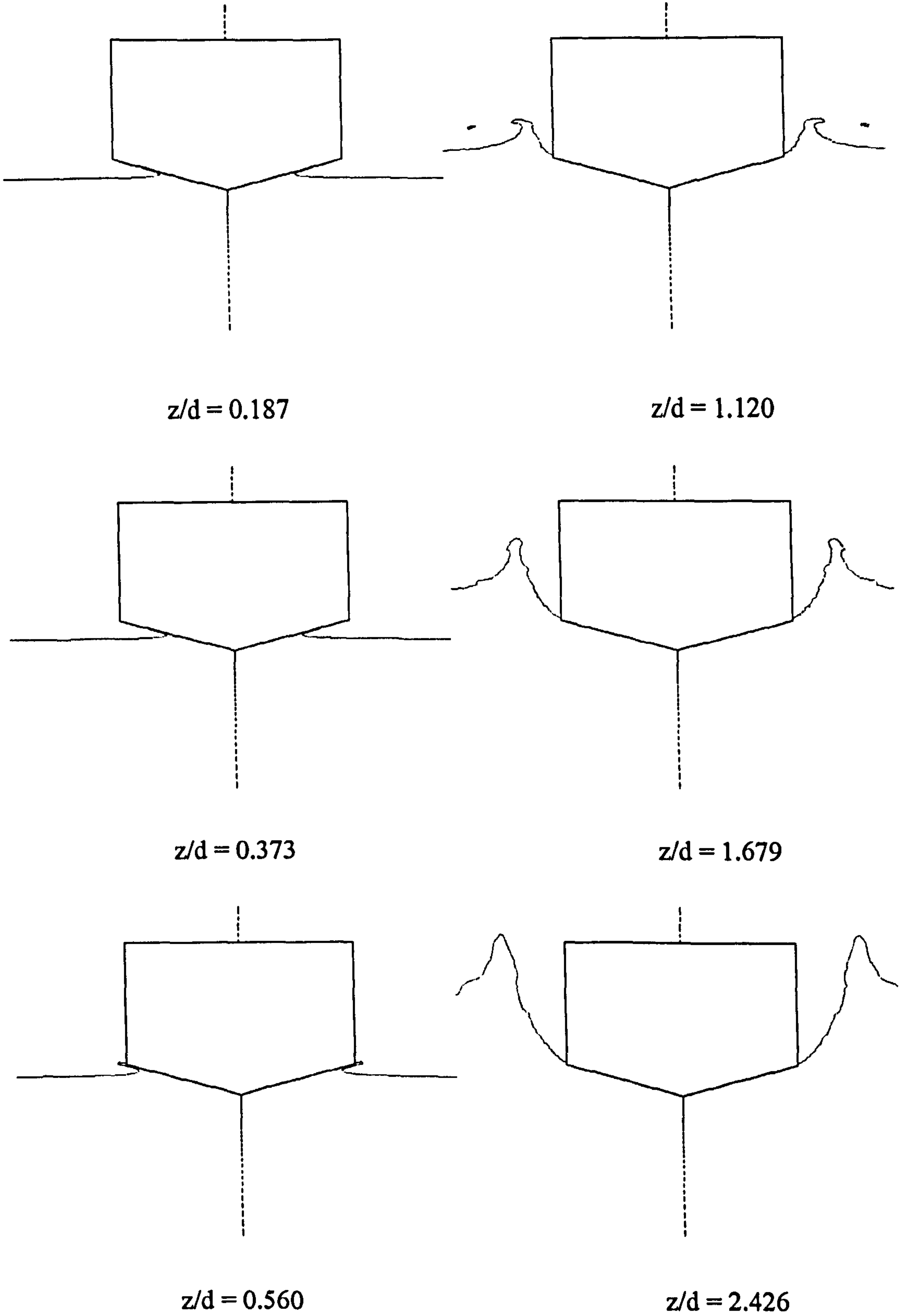


Figure 4-31. 15 degree wedge section at zero gravity.



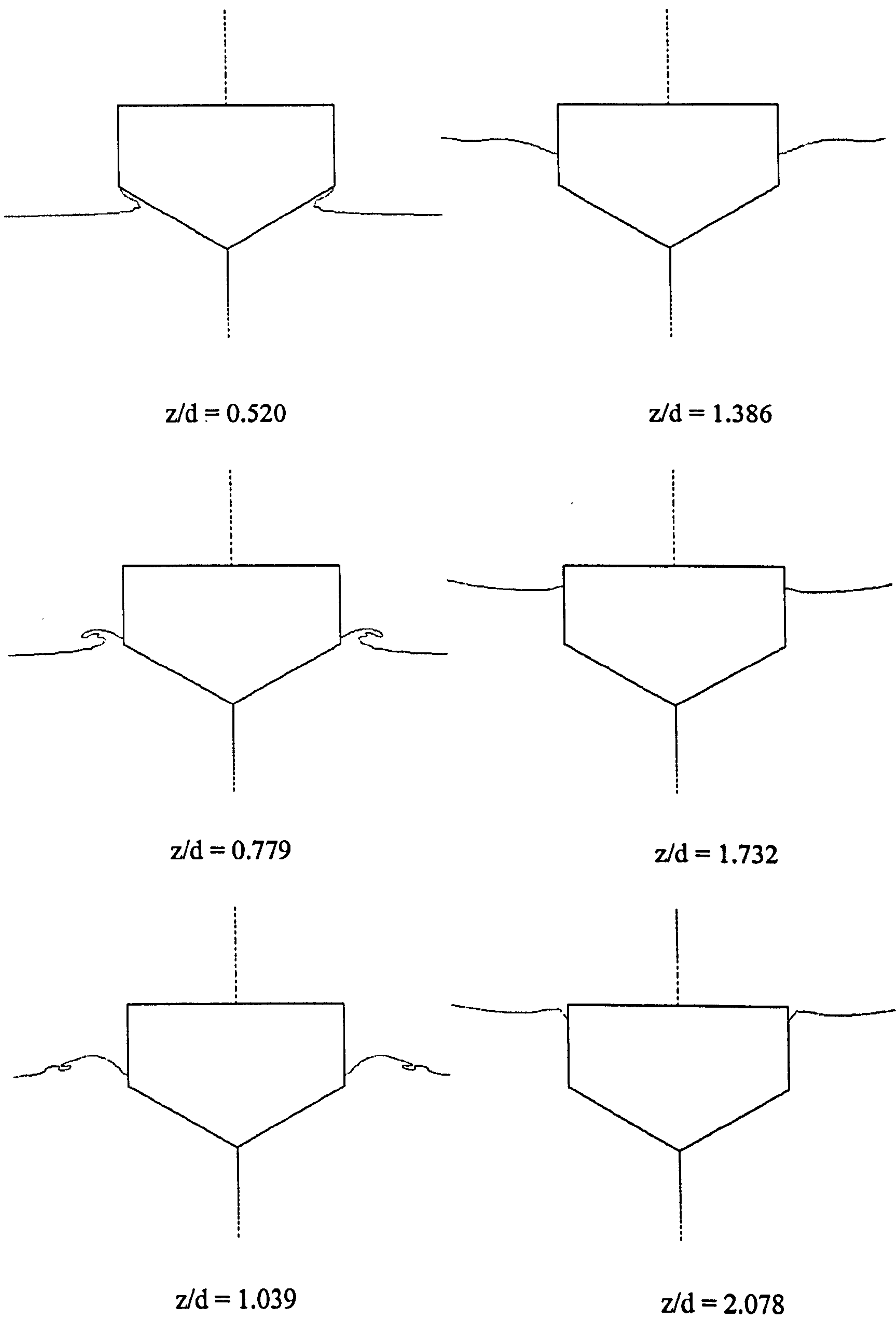


Figure 4-32. 30 degree wedge section at 0.5m/s.

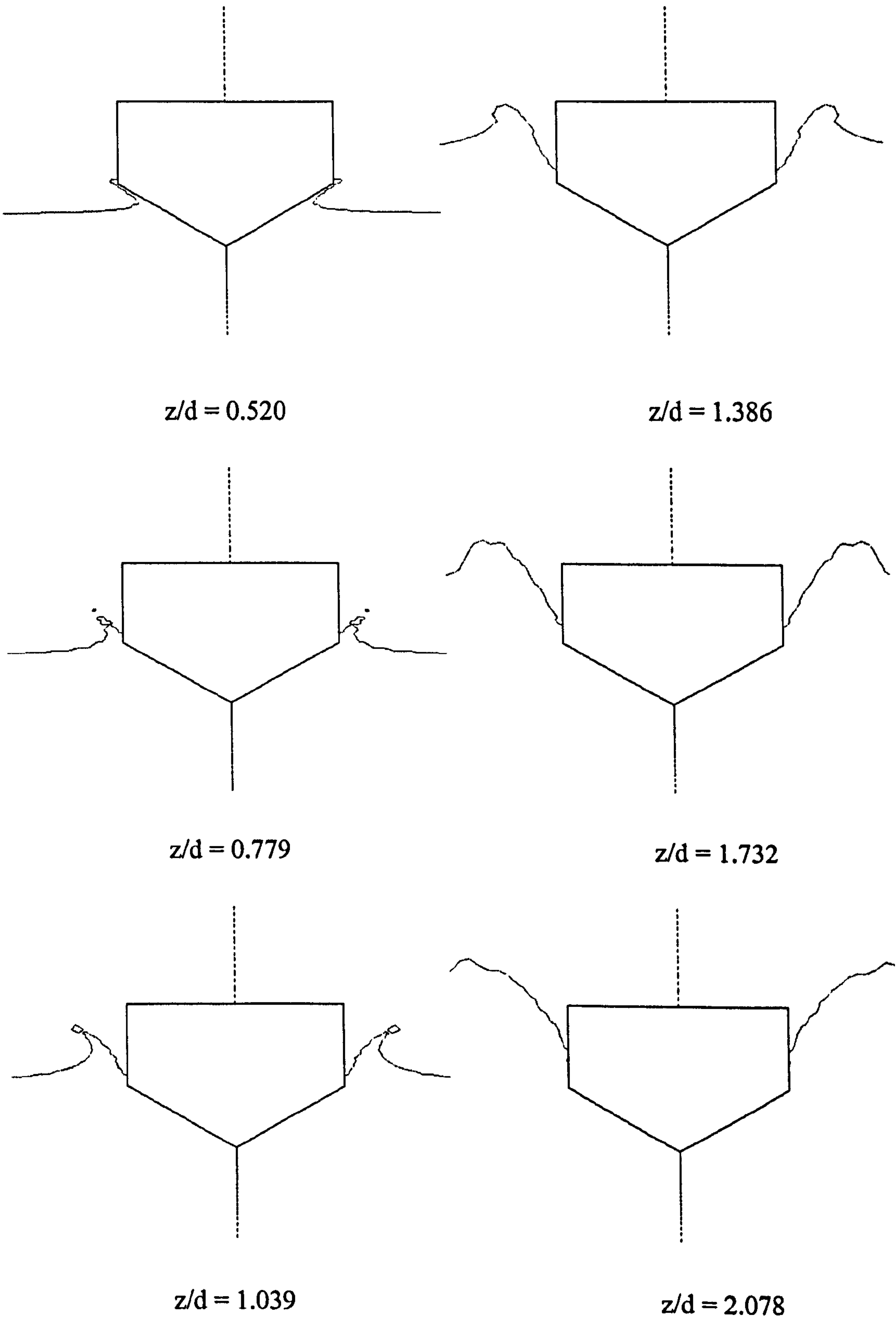


Figure 4-33. 30 degree wedge section at 1.0m/s.

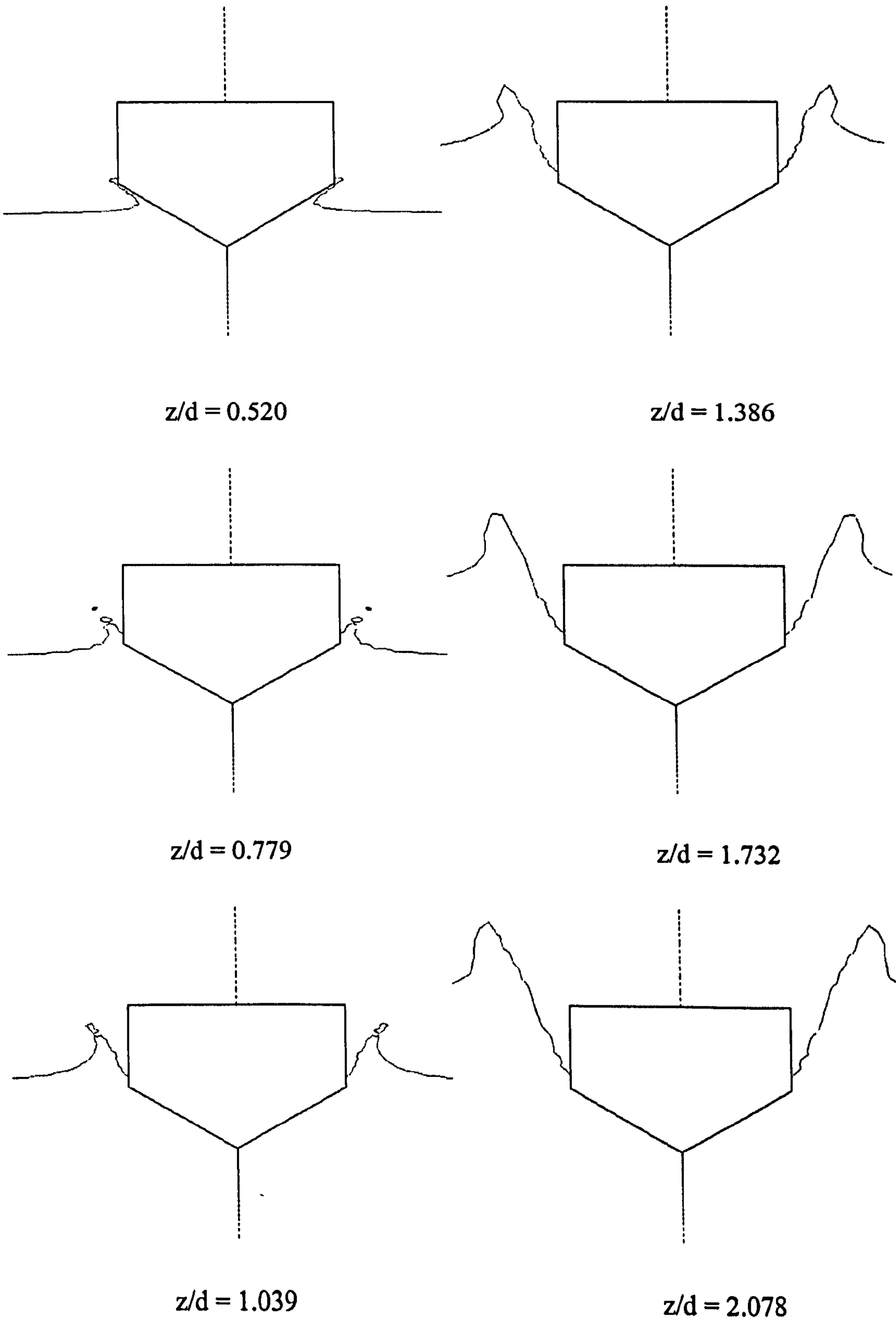


Figure 4-34. 30 degree wedge section at 1.5m/s.



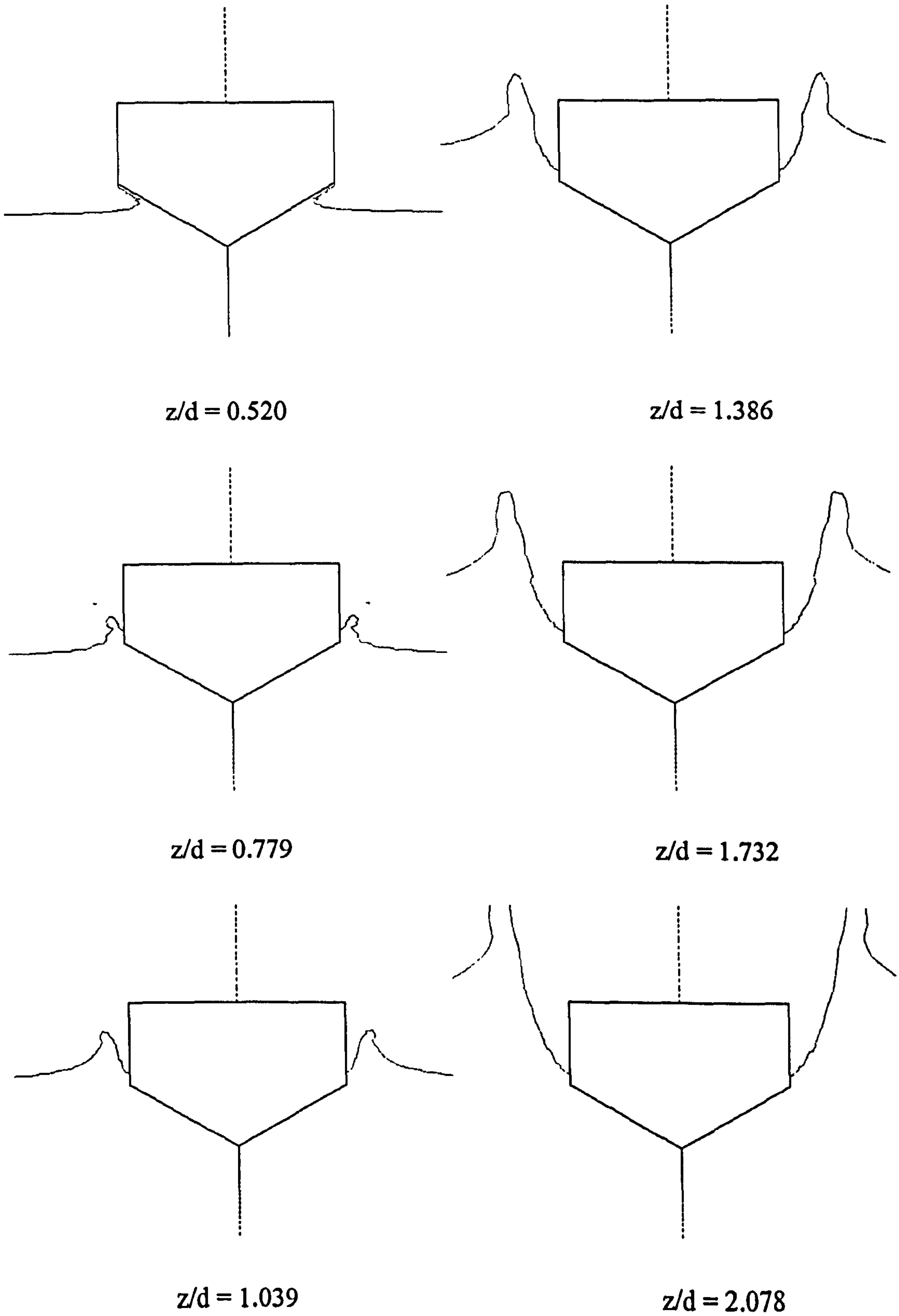


Figure 4-35. 30 degree wedge section at zero gravity.

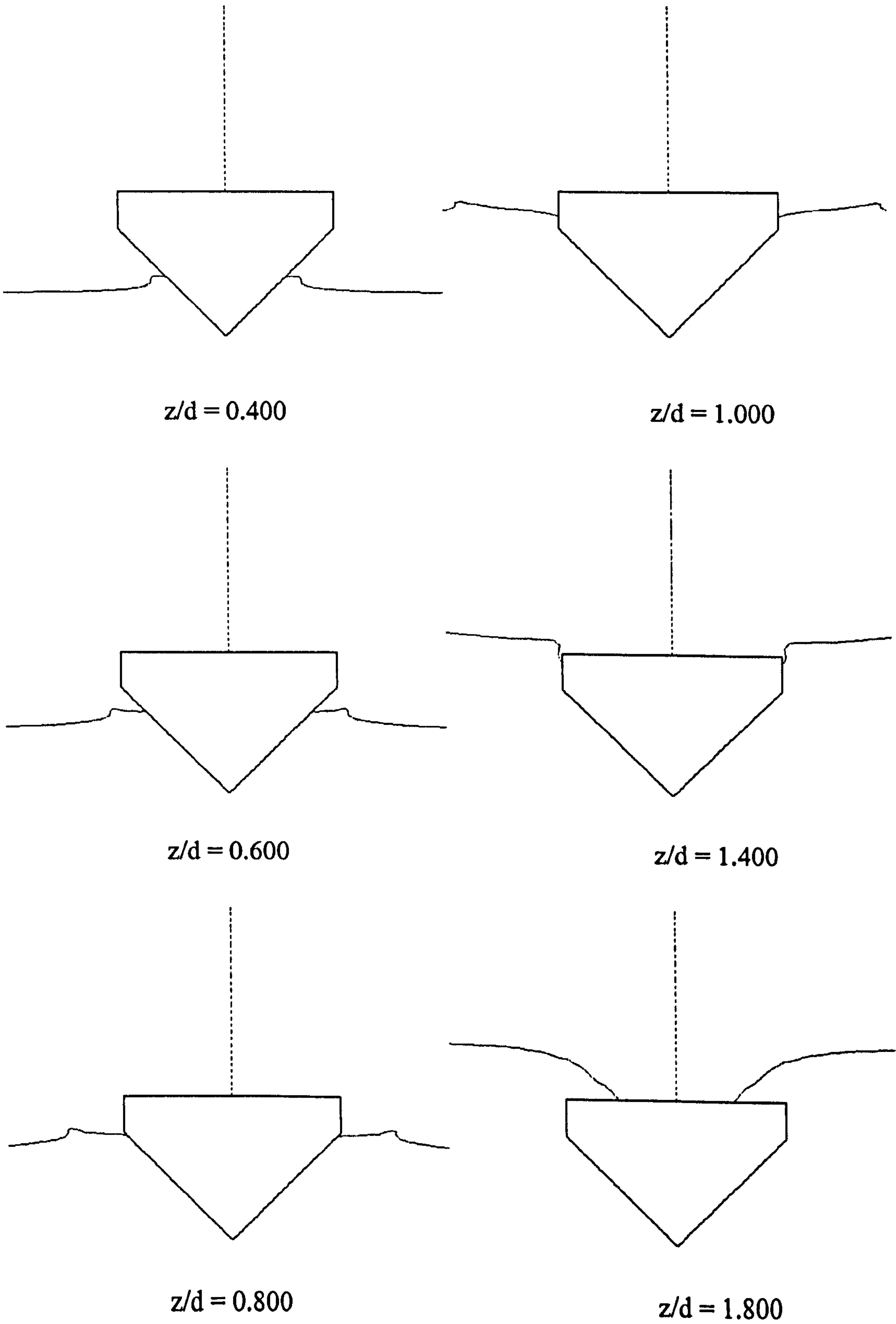


Figure 4-36. 45 degree wedge section at 0.5m/s.

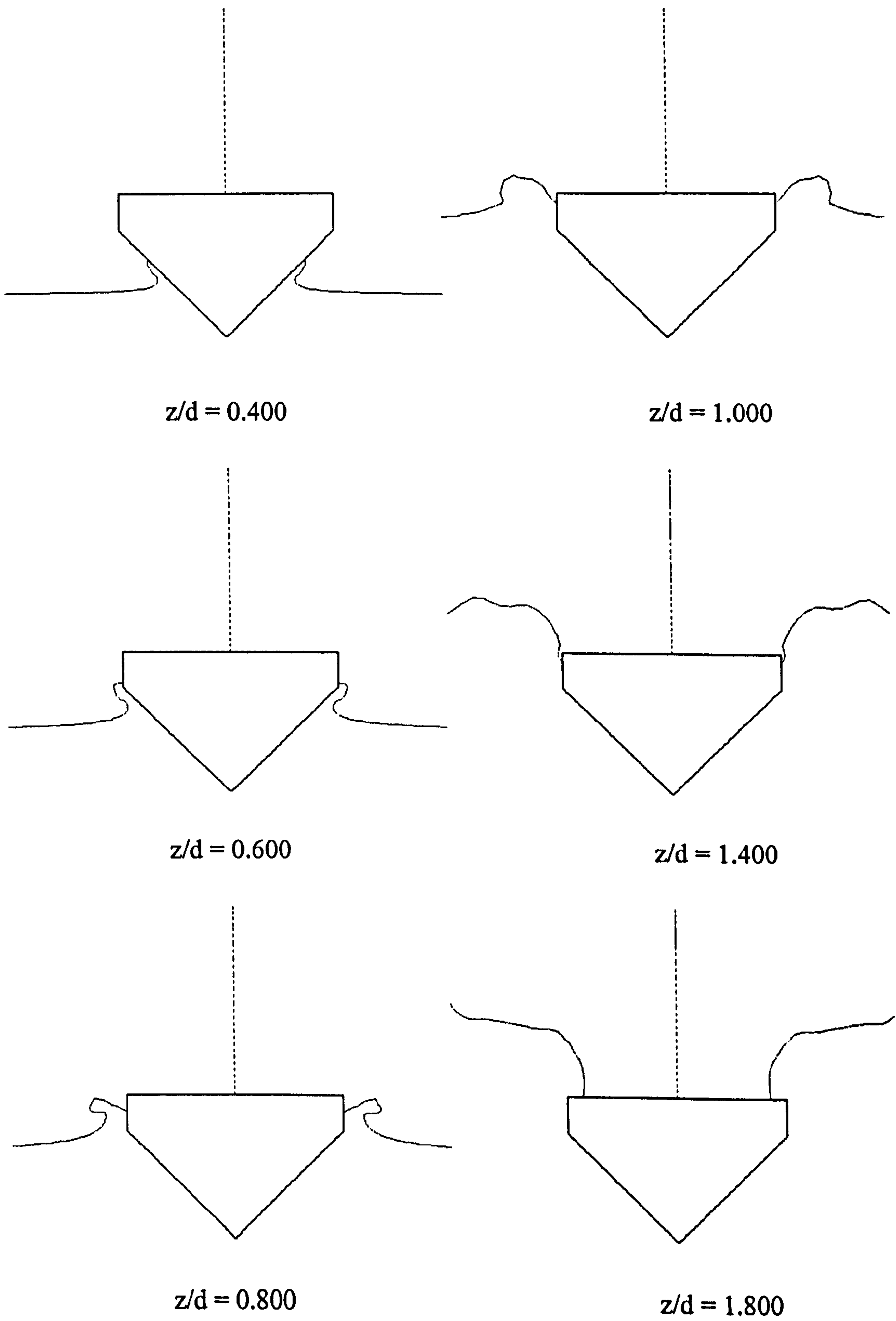


Figure 4-37. 45 degree wedge section at 1.0m/s.



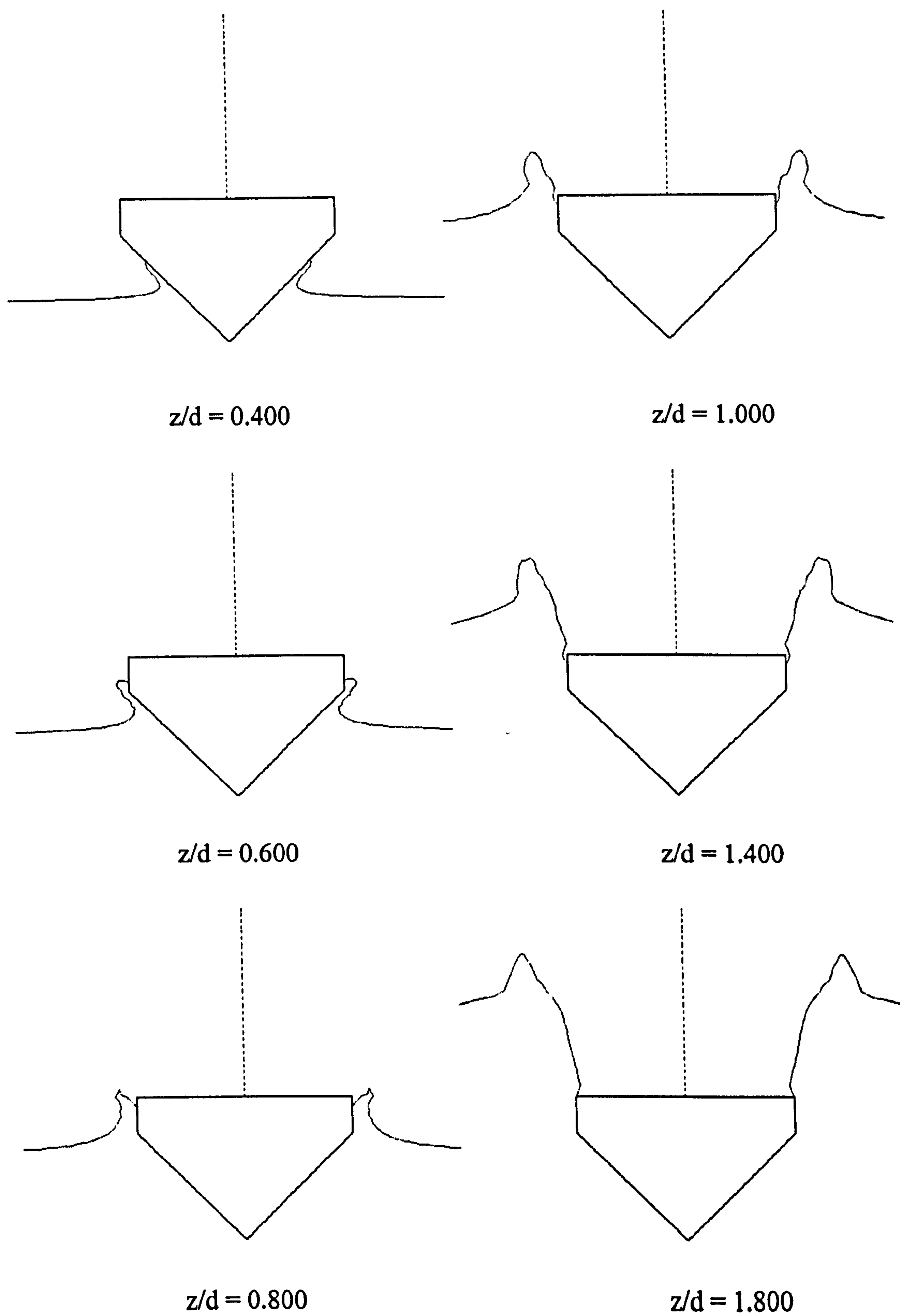


Figure 4-38. 45 degree wedge section at 1.5m/s.

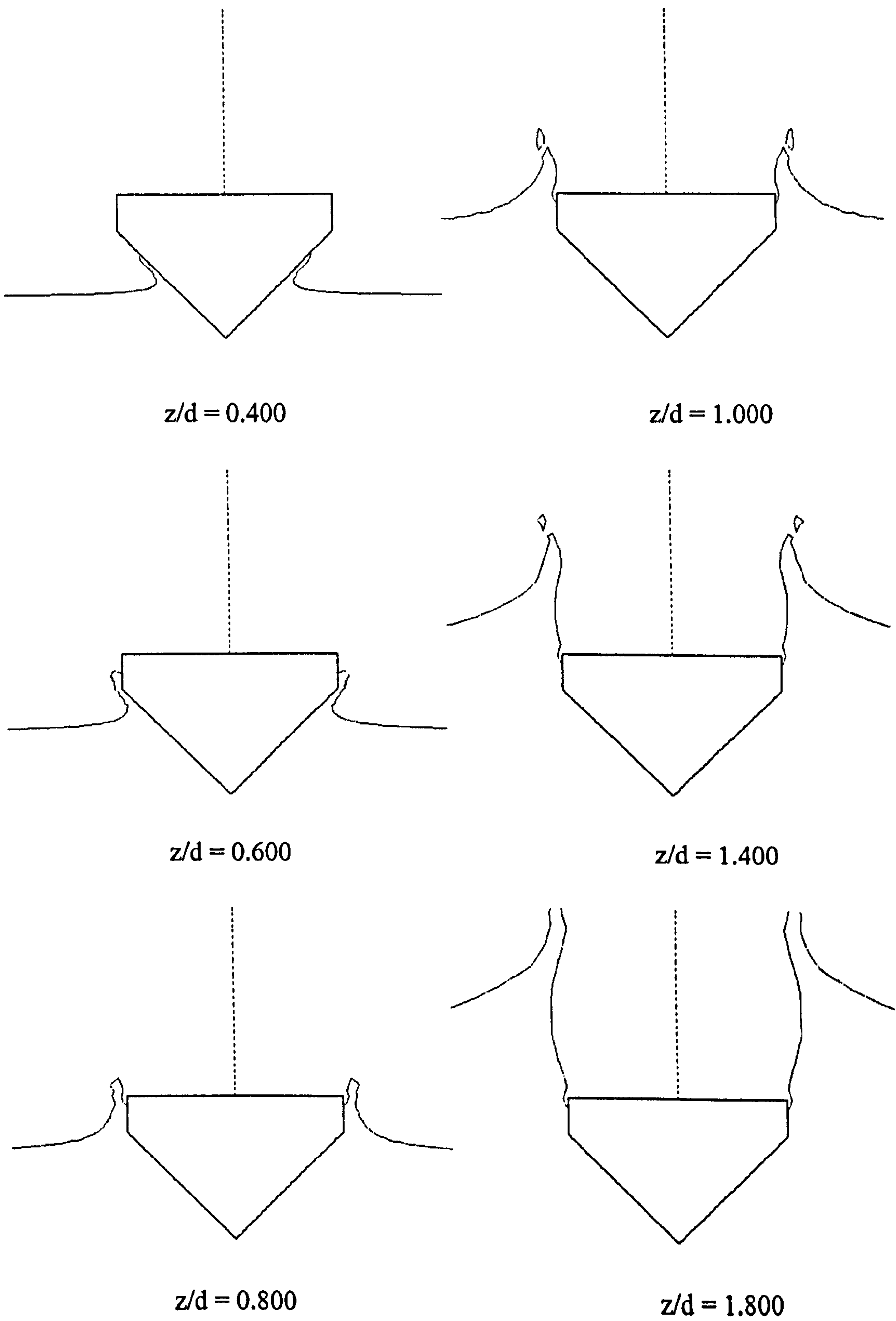


Figure 4-39. 45 degree wedge section at zero gravity.

#### 4.4.4. Gravity Effect Analysis

The data from the CFD simulations have been used to establish the effect of gravity on the entry force. In addition to causing a hydrostatic force, gravity also affects the flow and causes the hydrodynamic force contribution in a gravity environment to differ from that in a non-gravity environment, and this effect is referred to as the dynamic gravity effect. Although the influence of gravity is identified above as two separate effects, these are investigated in the present study as a coupled effect. This is justified by considering the objective of the gravity effect analysis, which is to obtain criteria for extracting the pure hydrodynamic (or infinite velocity) entry force from the experimentally measured data. Hence, only the magnitude of the total gravity effect on the force is of interest.

The full effect of gravity on entry force, referred to as gravity force component, has for each case been obtained by subtracting the corresponding zero gravity simulation force from the gravity simulation force. Dividing the full gravity force contribution by the Archimedes buoyancy to the undisturbed water level, gives a ratio referred to as the buoyancy ratio. The buoyancy ratio values calculated from the simulation results are plotted against non-dimensional immersion depth in Figure 4-40.

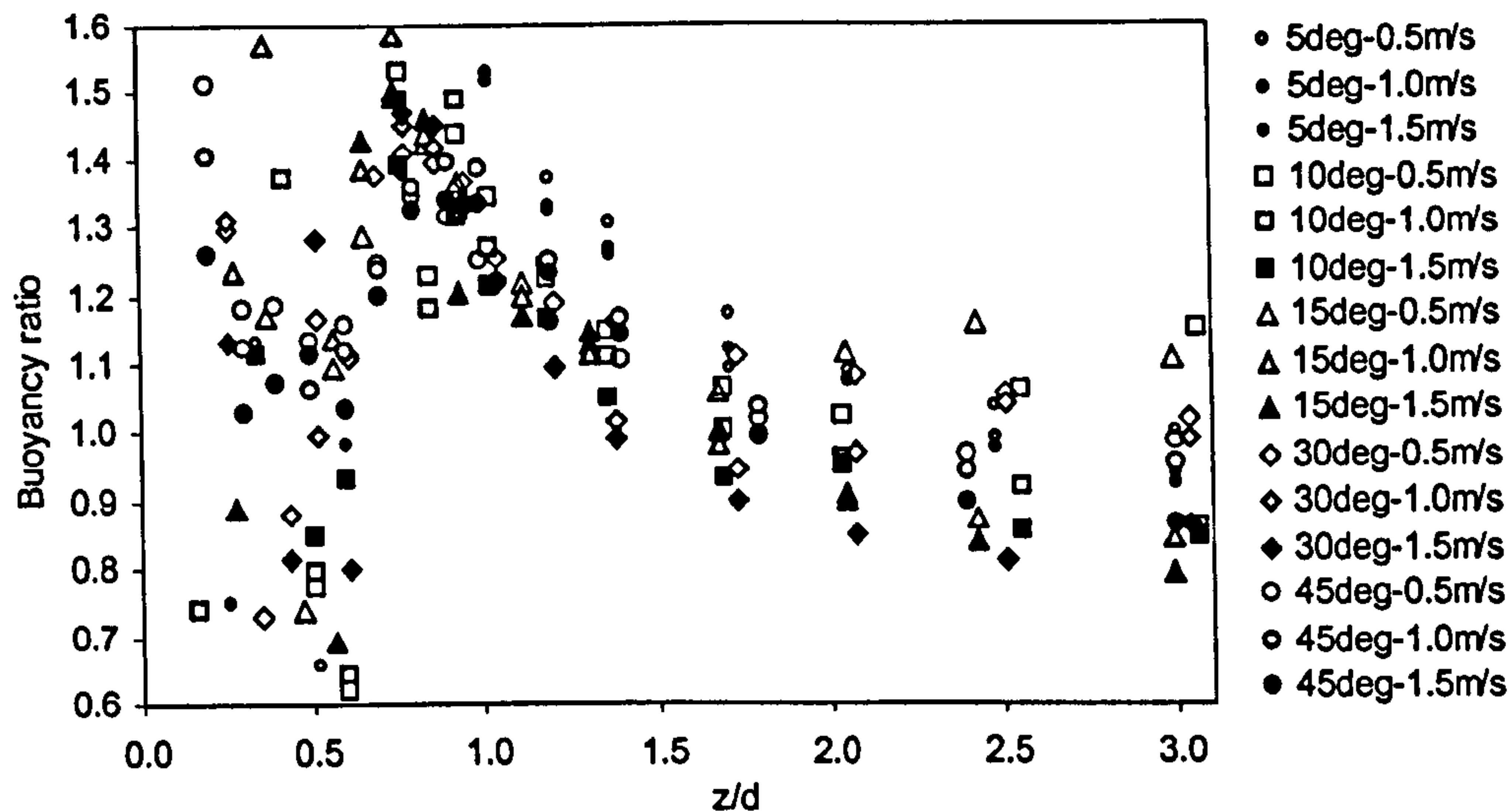


Figure 4-40. Buoyancy ratios extracted from the CFD results.

The differences between gravity and non-gravity values in Figures 4-8 to 4-12 represent the full gravity force contributions. For all but the lowest velocity 30 and 45 degree deadrise cases, the gravity data converge with the non-gravity data at non-dimensional immersion depths of less than about  $z/d=0.5$ . The small differences between gravity and zero-gravity values in this depth range result in highly scattered buoyancy ratio values in Figure 4-40, although based on the low-scattered force data from Figures 4-8 to 4-12.

At non-dimensional immersion depths from about  $z/d=0.75$  to about 1.5, the data in Figure 4-40 show that the gravity-associated force is greater than Archimedes' buoyancy and the trend is that buoyancy ratio decreases with increasing immersion. At large immersions the high velocity data are below unity while low velocity data are above. The data for immersions less than  $z/d=0.75$  reveal no obvious trend in buoyancy ratio. However, there seems to be an indication of the buoyancy ratios in this range being closer to unity.

The buoyancy ratio variation with velocity and immersion are not accounted for theoretically. However, a discussion is given that tries to explain the nature of the trends that are observed. It is suggested that the pile-up of water that occurs during a water entry causes the hydrostatic pressure head to be greater than in



corresponding static condition, and that the increased pressure head gives a gravity force that is greater than the Archimedes' buoyancy. The water pile-up becomes constant after chines immersion, and therefore the gravity-associated force relative to Archimedes' buoyancy reduces with further increase in immersion depth.

During water entry with gravity flow above a certain threshold velocity, depending on wedge angle and immersion depth, the water flows off the chines leaving the wedge section sides dry above the chine. The free surface boundary condition implies that when this occurs the pressure at the chines is equal to atmospheric pressure. There is a dynamic effect that reduces the chine pressure from that given by the hydrostatic pressure head down to the atmospheric pressure. It is suggested that this causes a reduction in the total water entry force. This chines suction effect is proportional to the hydrostatic pressure head and therefore the ratio of chines suction to Archimedes' buoyancy tends toward a constant at large immersion depths. When adding these two effects together, it follows that at large immersion depths the buoyancy ratio will tend toward a constant value of less than one as long as the velocity is greater than some threshold value above which the wedge section sides remain dry.

For a constant velocity water entry, the immersion depth at which the wedge sides become wetted above the chine is referred to as the threshold depth. Data for 30 and 45 degree wedges, and for low velocity cases of 10 and 15 degrees wedges, show that the trend of diminishing buoyancy ratio with immersion is reversed at larger depths. The point at which the inflection occurs indicates the threshold depth for the particular combination of deadrise angle and entry velocity. An example of this is the 0.5m/s, 15 degree case, which is extracted from Figure 4-40 and plotted in Figure 4-41, and shows a reversal of the buoyancy ratio trend between  $z/d=1.7$  and 2.0. In the plots of the free surface shape for this case in Figure 4-28, it is seen by studying the shape of the free surface that at  $z/d=1.679$  the wedge side is dry while at 2.426 it is entirely wetted up to the corresponding undisturbed water line. A similar correlation between the buoyancy ratio data and free surface shape is also found for the other cases.

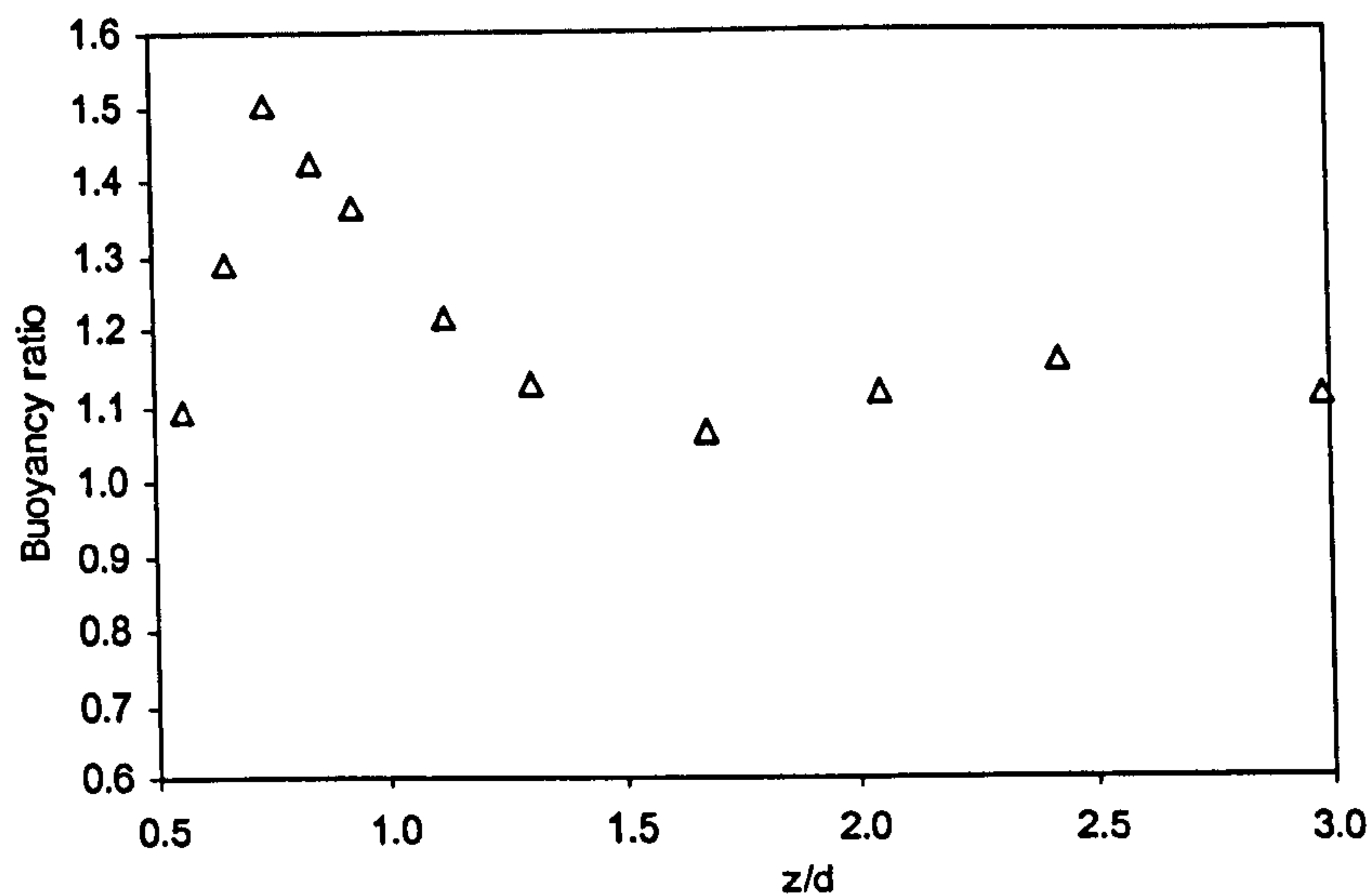


Figure 4-41 Buoyancy ratio for 15 degree, 0.5m/s case.

Equations to describe the relationship between buoyancy ratio, deadrise angle and immersion depth have been developed from the data in Figure 4-40. The poor data for low immersion depths do not make for an accurate evaluation of buoyancy ratio in this range. However, at low  $z/d$  the data are scattered about 1.0 and hence do not suggest that the full gravity differs substantially from Archimedes' buoyancy. Thus the buoyancy ratio is taken as 1.0 from  $z/d=0$  to  $2/\pi$ . The upper limiting depth for this range is the non-dimensional depth at which the chines get wetted according to a wetting factor of  $WF=\pi/2$  (which is discussed later). This crude estimate of dry chines buoyancy ratio is justified by the fact that for dry chines conditions the gravity force contribution is small relative to the hydrodynamic component, and hence an approximate estimate is going to have little impact on the total force. A linear function links the dry chines buoyancy ratio from the instant of chines wetting at  $z/d=2/\pi$  and the maximum buoyancy ratio value, which is found to occur at  $z/d=0.75$ . For immersion depths greater than  $z/d=0.75$  a function is fitted to the data that estimates the variation of buoyancy ratio with immersion depth and is asymptotic to unity. Figure 4-40 shows buoyancy ratios of less than unity for high velocity and large immersion. However, the value of unity is defined on the basis that a threshold depth exists



for any combination of angle and velocity, after which buoyancy ratio will tend toward unity.

The data from the CFD simulations show no apparent velocity effect on the buoyancy ratios at depths less than the threshold depth. The experimental velocity range is within that of the CFD simulation, and hence velocity independent buoyancy ratio equations are justified. The data at different velocities are averaged and equations fitted for each deadrise angle separately. The functions that are fitted have two discontinuities. One discontinuity is defined at the immersion depth at which the chines are considered to become wetted, i.e.  $z/d=2/\pi$ . The other discontinuity is at the depth of which maximum buoyancy ratio occurs, i.e.  $z/d=0.75$ . The buoyancy ratio functions are given in Equations (4-1) to (4-3).

Buoyancy Ratio,

$$BR = 1.0 \quad , \frac{z}{d} < \frac{2}{\pi} \quad (4-1)$$

$$BR = \frac{\left(\frac{z}{d} - \frac{2}{\pi}\right) \cdot (1.5 - 1)}{0.75 - \frac{2}{\pi}} + 1 \quad , \frac{2}{\pi} < \frac{z}{d} < 0.75 \quad (4-2)$$

$$BR = \left( \frac{1}{1 + \left(\frac{z}{d} - 0.75\right)^A} \right)^B \cdot (C - 1) + 1 \quad , 0.75 < \frac{z}{d} \quad (4-3)$$

where A, B and C are parameters that vary with the deadrise angle to give the best fit to the data. These parameters are presented in Table 4-2.

$\beta$ [deg]	A	B	C
5	1.8	2.5	1.70
10	1.5	4.0	1.50
15	1.4	4.2	1.50
30	1.4	4.2	1.50
45	2.5	4.0	1.38

Table 4-2. Buoyancy ratio curve fitting parameters

The averaged data and the fitted functions for immersion depths greater than  $z/d=0.75$  are plotted in Figure 4-42.

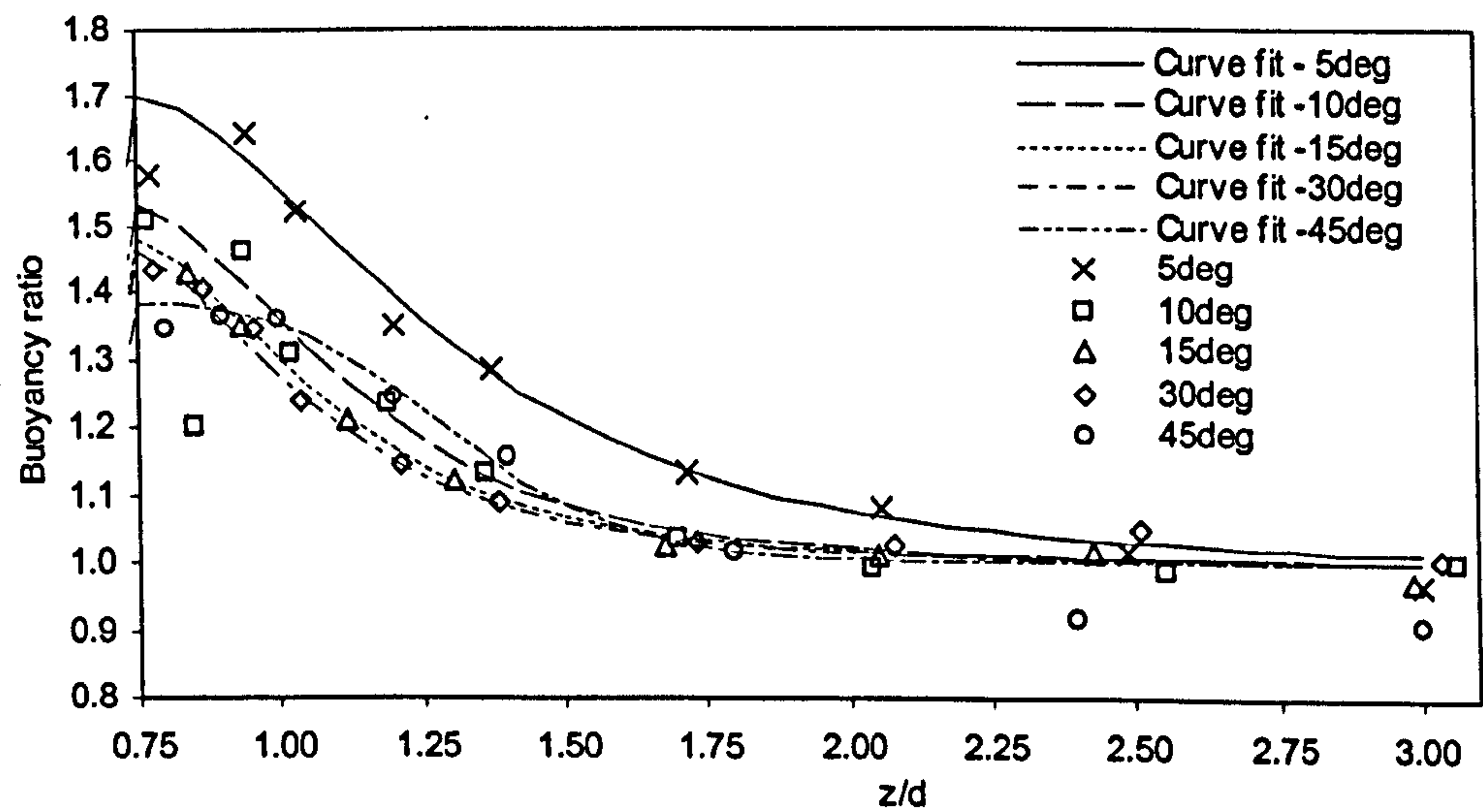


Figure 4-42. Curve fitting to the average buoyancy ratio data.



---

**CHAPTER 5**

**EXPERIMENTAL WORK**

---

The main objective of the experimental work was to measure forces acting on wedge sections during constant velocity water entry. In addition, forces during accelerating/decelerating water entry, oscillations and constant velocity water exit tests were required. To obtain the required data, a test rig for velocity controlled water entry and exit experiments was designed and manufactured. In this chapter, the experimental set-up, test program, and the data obtained are presented. The test rig design considerations, manufacture, operation and performance are also described and discussed.

Tests sections were available in the form of a series of wedges and a box section that had been used in the earlier experimental work that is described in Appendix A. The test rig was designed so that these tests sections could be attached via load sensors to a model carrier, which is connected to a combined guide and drive system, which in turn is connected to a drive frame via guide bearings. A pair of vertical guide shafts that ensure linear motion are interconnected at the upper and lower ends via assembly bars, with the model carrier attached below the lower bar. Each shaft runs through two guide bearings that are attached to a support frame. A rotating nut ball screw unit is located between the two shafts and is also connected to the upper and lower assembly bars. The nut is mounted via a thrust bearing on to a base plate on the drive frame, so that it is free to rotate, but cannot move axially. A servomotor rotates the nut via a timing belt drive. As the nut rotates, it drives the threaded shaft and thus the whole system including guide shafts and model carrier moves up or down according to motor rotational direction. The drive frame, onto which the nut and the shaft bearings are mounted, is bolted to a support structure above the test tank. To record the water surface shape during the tests, a video camera was installed next to the test rig.

Figure 5-1 shows a sketch of the entire experimental set-up, while up Figures 5-2 and 5-3 show sketches of the tests rig from various views.

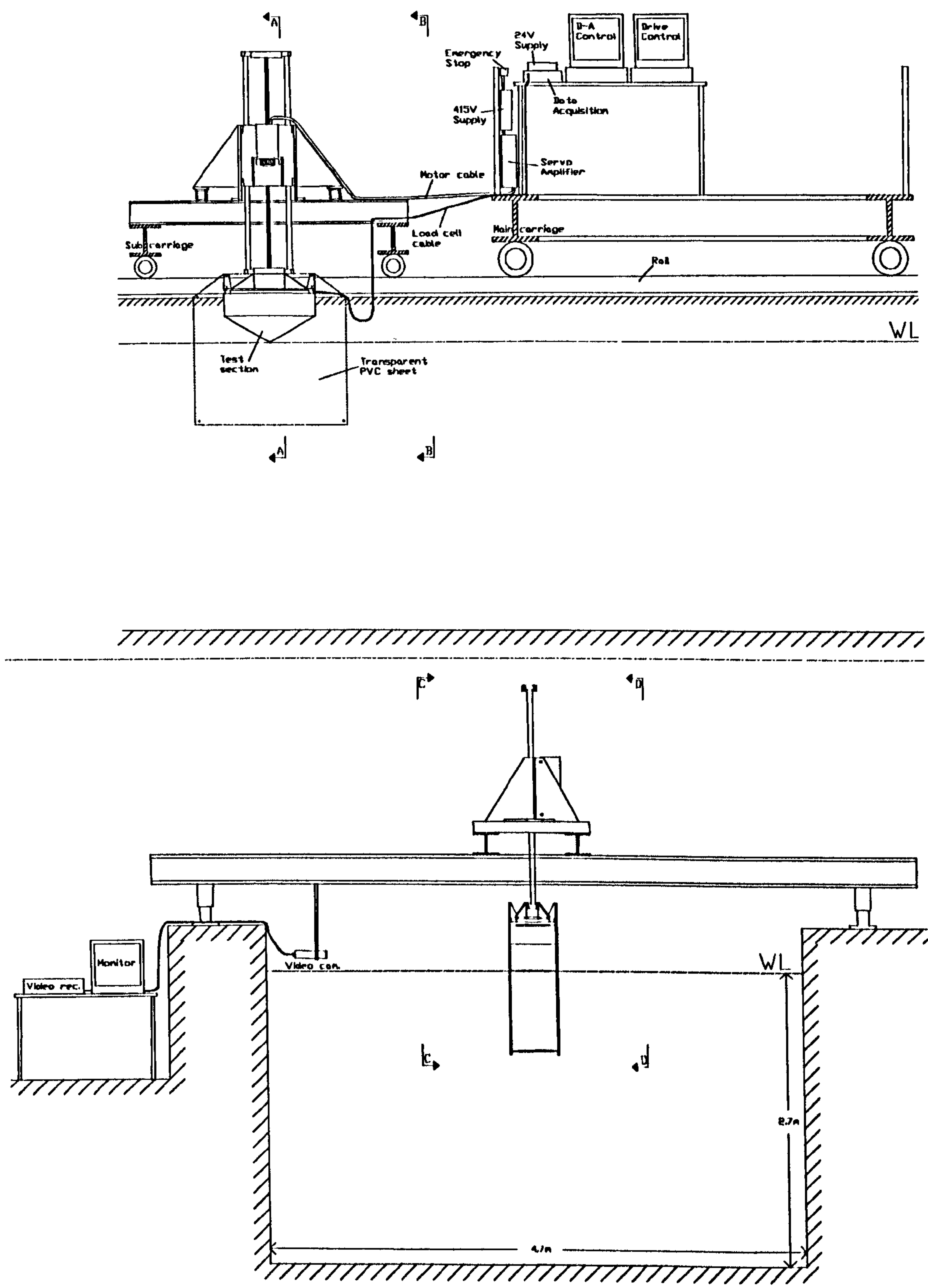


Figure 5-1. Experimental set-up.



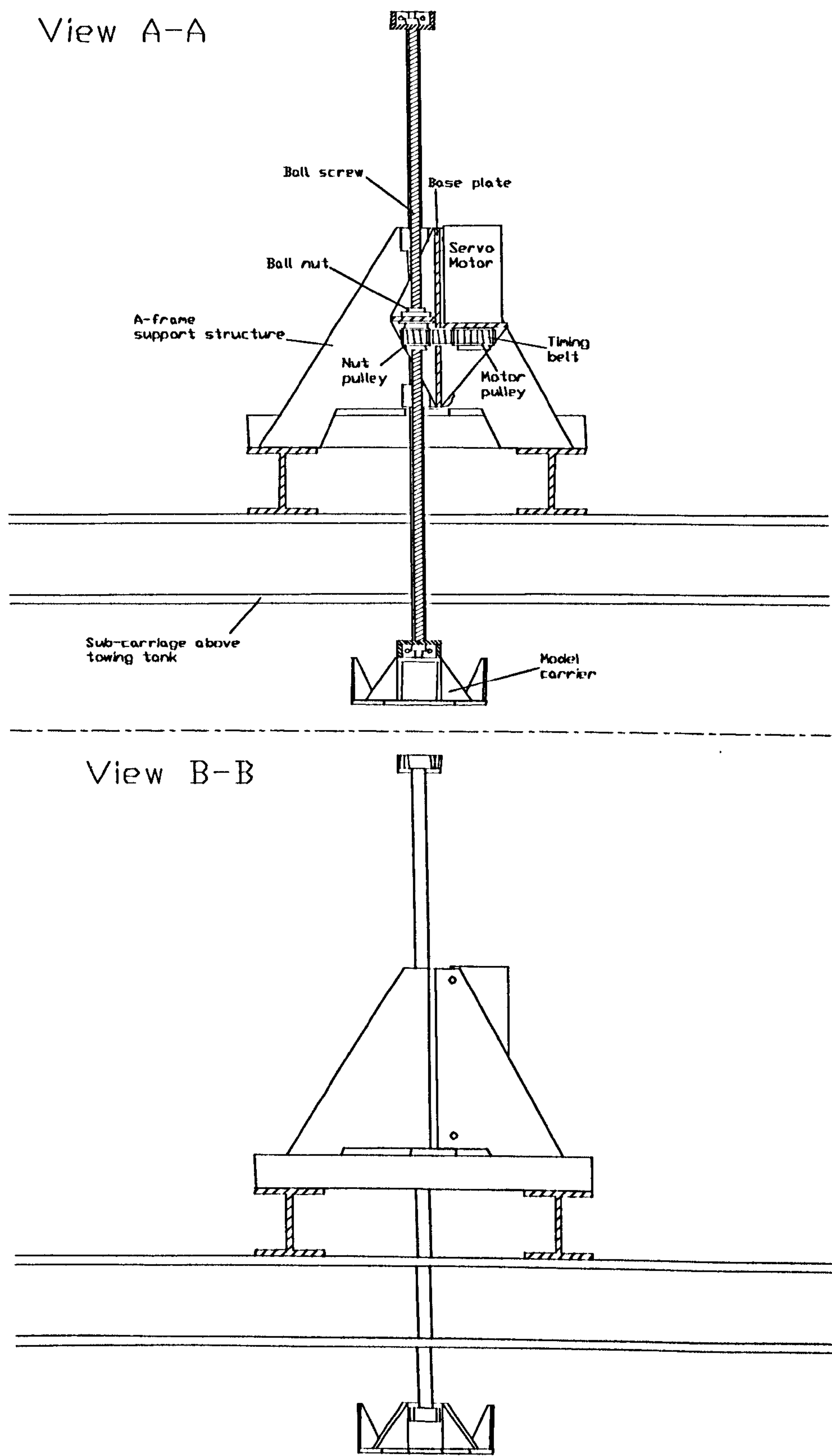


Figure 5-2. Side views of the test rig.

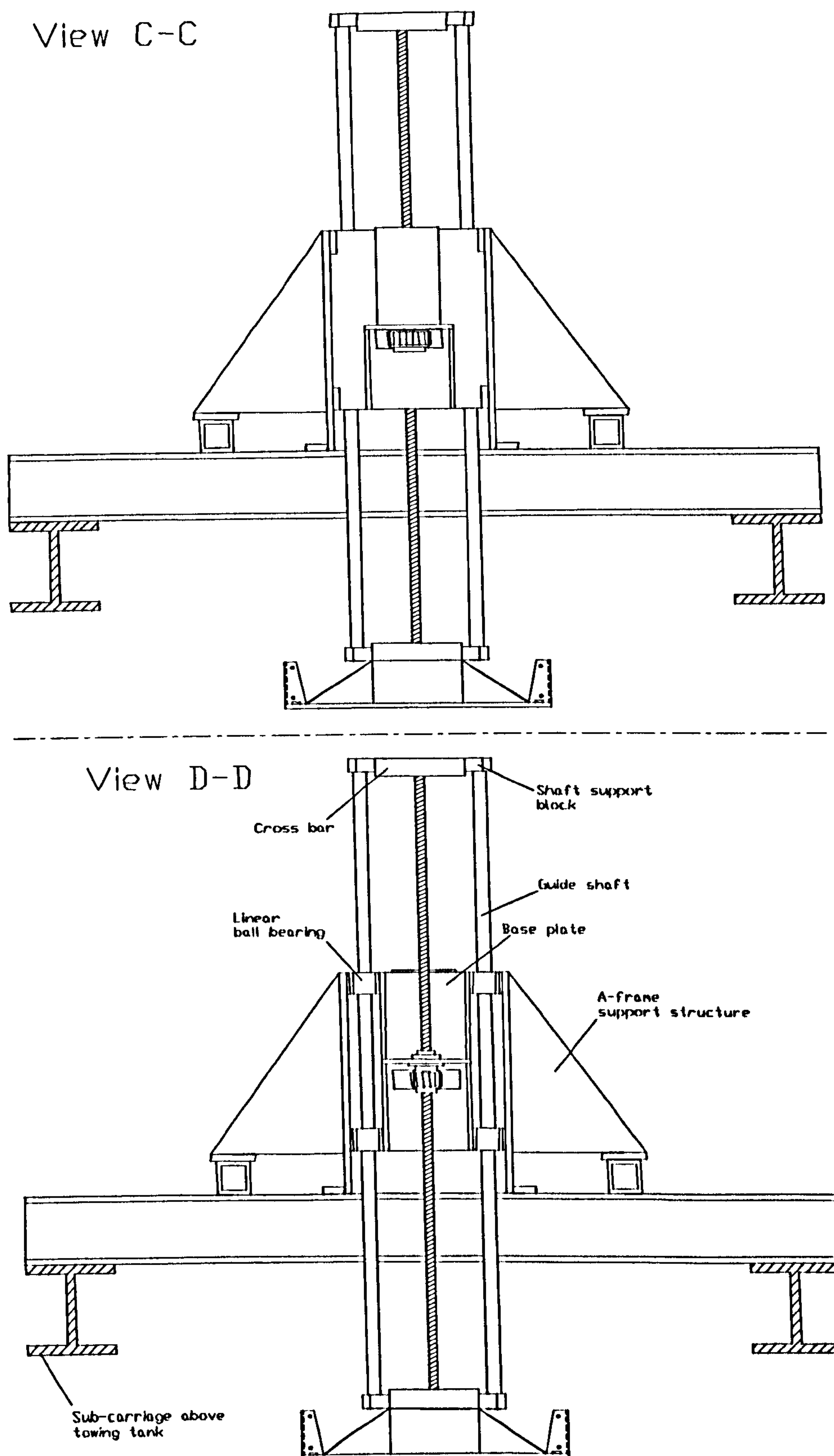


Figure 5-3. Front and back views of test rig.

## 5.1. Design Requirements

### 5.1.1. Vertical Loads and Accuracy

Some early experiments, which are described in Appendix A, showed that for some of the sections a velocity of more than 1.0m/s was required for the dynamic force component to be pronounced compared to the buoyancy. Such high velocities were not necessary for the lower deadrise angles. However, to ensure adequate capacity of the new test rig, it was decided that the water entry of a 10-degree section at 1.5m/s should be the basis for the design of the rig. In addition to this water entry case, it was also required that models could be driven in the opposite direction, i.e. out of the water. This would allow exit tests and also oscillation experiments.

A CFD simulation of the design case was carried out. The results from this are given in Figure 5-4, where it is seen that the maximum force would be approximately 4.5kN. It is also seen that the peak force occurs at immersion depth of 0.034m. The peak power required to maintain a constant velocity of 1.5m/s during water entry when subjected to this load is 6.8kW.

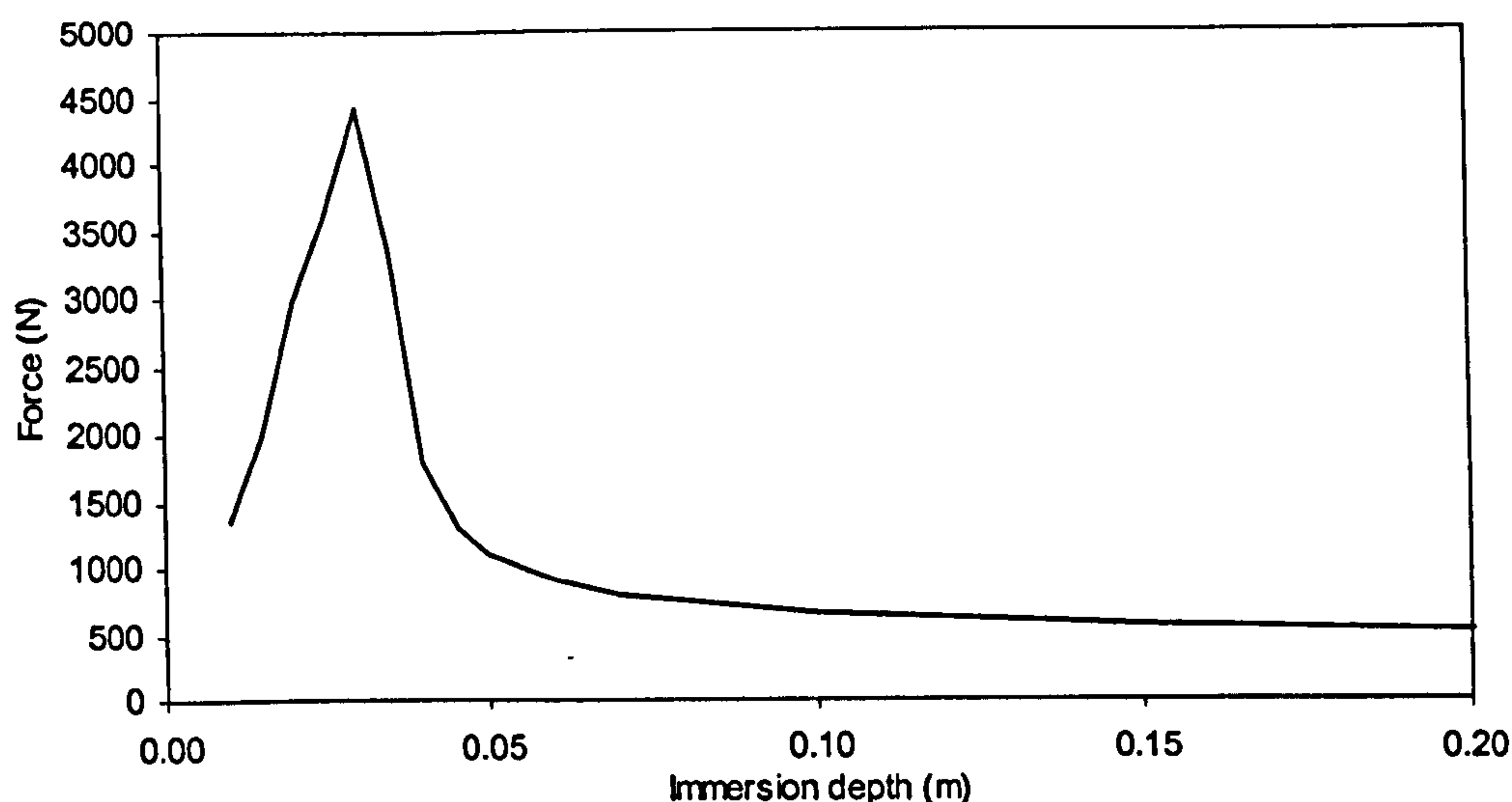


*Figure 5-4. Design case - load against immersion.*

The accuracy requirement for the motor/controller system's ability to maintain a constant velocity was specified as a velocity deviation of less than 1 percent.

### **5.1.2. Side Loads**

The drive unit and supporting structure obviously had to be designed to withstand the maximum design load. The maximum design load of 4.5kN acts in line with the vertical motion of the test section. To improve the versatility of the test equipment, possible future applications were kept in mind during the design process. A potential area for future work was to carry out slamming tests on ship models moving at forward speed in waves. This would require the test rig to be able to withstand a horizontal force component at its lower end. An additional horizontal force component could also appear due to slamming pressures acting on surfaces oriented at an angle to the horizontal plane. When designing the structure of the rig, these load conditions were considered in addition to the vertical load requirement for the present study.

### **5.1.3. Model Carrier**

A model carrier was required for attachment of the various test sections. The carrier had to provide an interface for the load sensors and to accommodate side



plates to ensure two-dimensional flow past the model sections. The latter were required because of the low aspect ratio of the test sections.

#### **5.1.4. Sensors and Data Acquisition**

The estimated time for the load to increase from 0 to 4.5kN was 23ms, according to the CFD simulation. To be able to record such a rapid increase in force a measuring device of fast dynamic response was required. One of the conclusions drawn from the preliminary experimental work described in Appendix A was that the load cells applied did not have dynamic response suitable for capturing the expected peak force that occur during the initial stages of a water entry. For the present experiment sensors capable of measuring and transferring the predicted design case force were needed. Also required was equipment for recording of measured data at a substantial sample rate. The required sample rate for the test case was decided to be no less than 500Hz, which would give about 10 samples from initial impact to peak force for the design case test.

## 5.2. Description of test equipment

The test equipment comprises five main systems:

1. Drive system to apply the force required to achieve the desired motion, comprising a motor with controller and a system for transmission of force.
2. Guide system to ensure a linear motion of the test section.
3. Test sections comprising wedges and a box.
4. Model carrier for attachment of the test sections.
5. Sensors and a data acquisition system for measurement and recording of forces during tests.
6. Video equipment for recording of experiments.

### 5.2.1. Drive system

#### 5.2.1.1. Motor and Controller

A servo motor and controller system produced by Kollmorgen Ltd. was selected for the present application. This system comprises a brushless synchronous servomotor 6SM77K and a digital servo amplifier Servostar 610, which give a PID regulated motion. The motor has a torque of 8.5Nm at 3000rpm. The servomotor and digital servo amplifier are shown in Figures 5-5 and 5-6. The details on these components are given in datasheets shown in Appendix C.



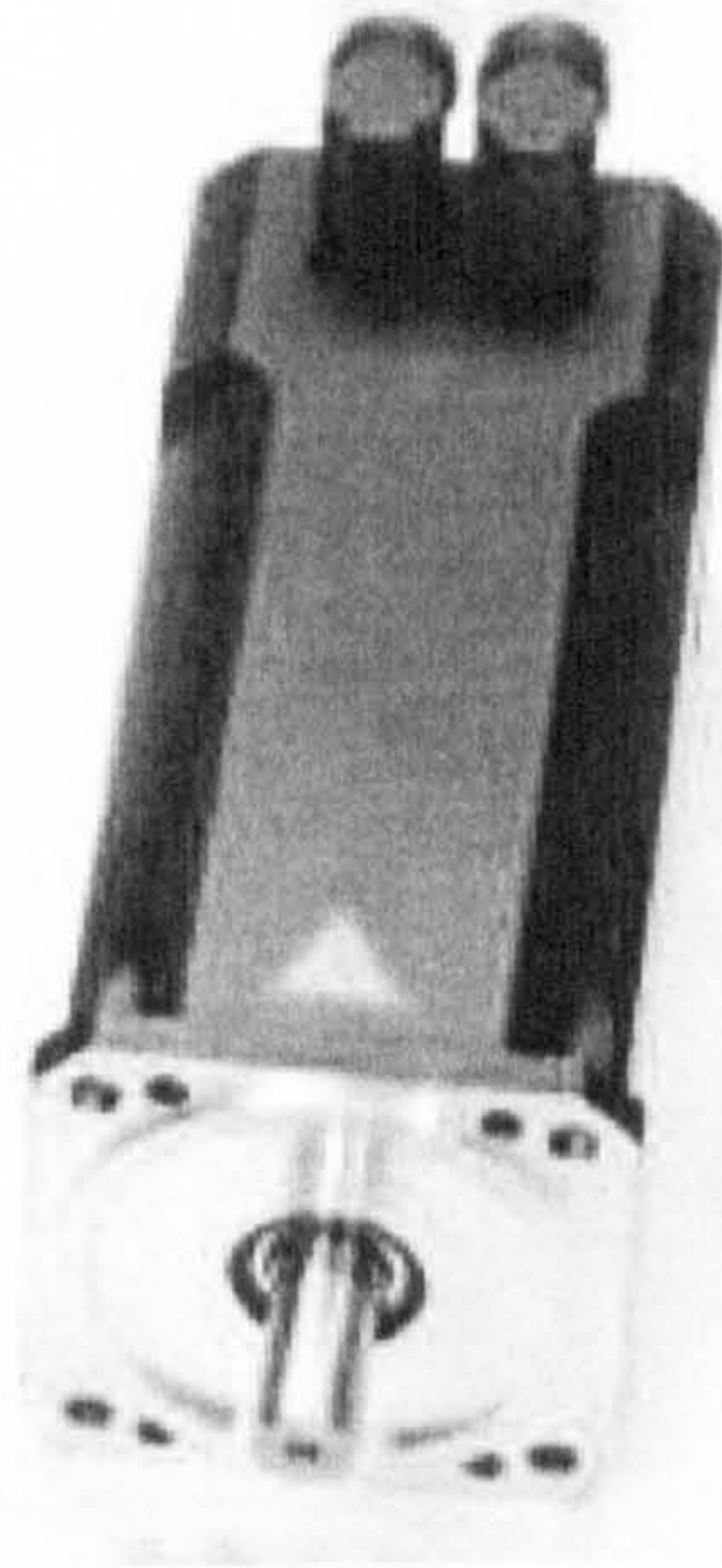


*Figure 5-5. Servomotor.*

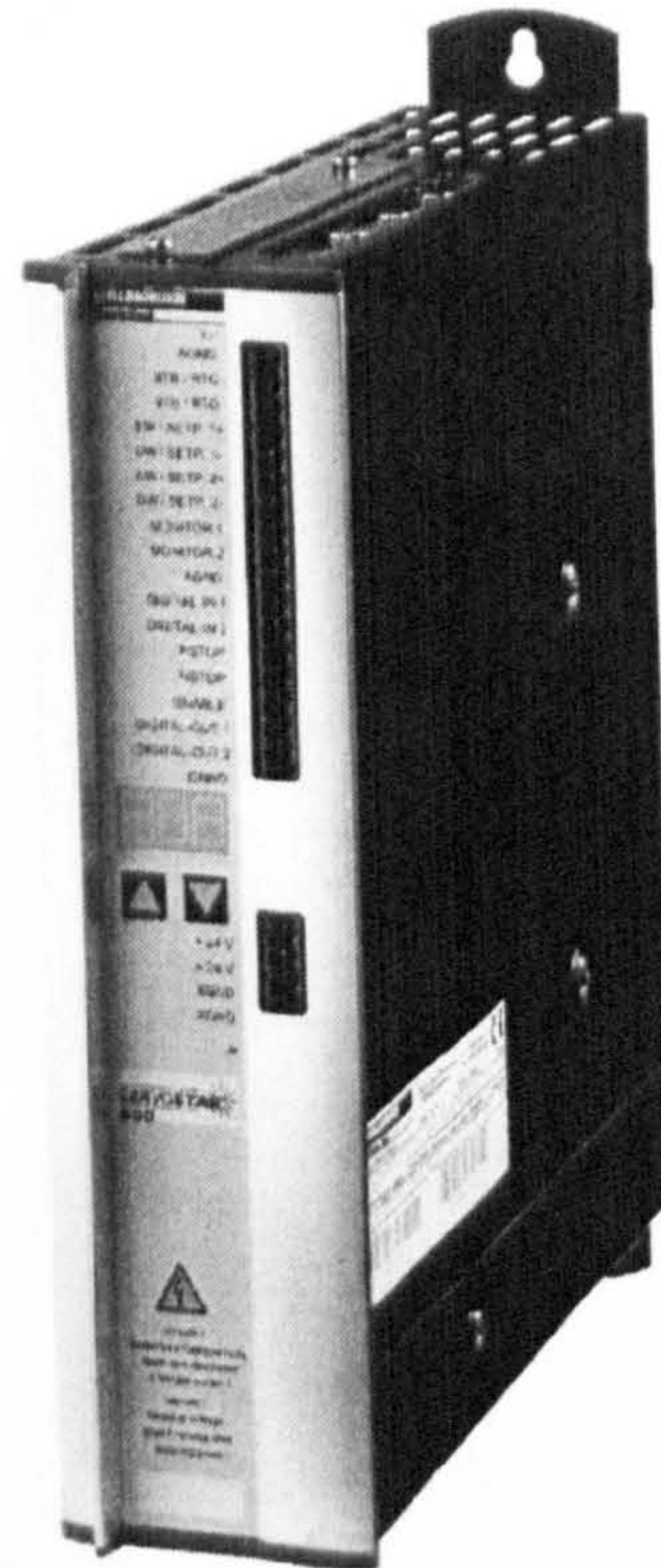


*Figure 5-6. Digital servo amplifier.*

#### 5.2.1.2. Rotary to Linear Motion

Transmission from rotational motion of the servomotor to linear motion was accomplished by use of a ball screw unit. A ball-screw operates such that a relative angular motion between a threaded shaft and a ball nut results in a relative linear motion. For the present application the ball-screw was installed with the shaft prevented from rotating but free to move in the axial direction, while the ball nut was installed such that it was prevented from translation but free to rotate. Hence, a forced nut rotation causes a linear translation of the shaft. Such ball-screw applications are made possible by incorporating a thrust bearing with the ball nut. Keyways are machined in both ends of the ball screw shaft, which is keyed to the assembly bars to prevent rotation. A rotating nut ball-screw unit manufactured by THK Japan, BLR2020-3.6UUG0 is used in the test rig application. This unit, which is shown in Figure 5-7, has a large lead screw with 20mm diameter and 20mm lead. The construction of the ball nut and the



incorporation of the thrust bearing are shown in Figure 5-8. . A detailed drawing of the end machining is shown in Appendix C.

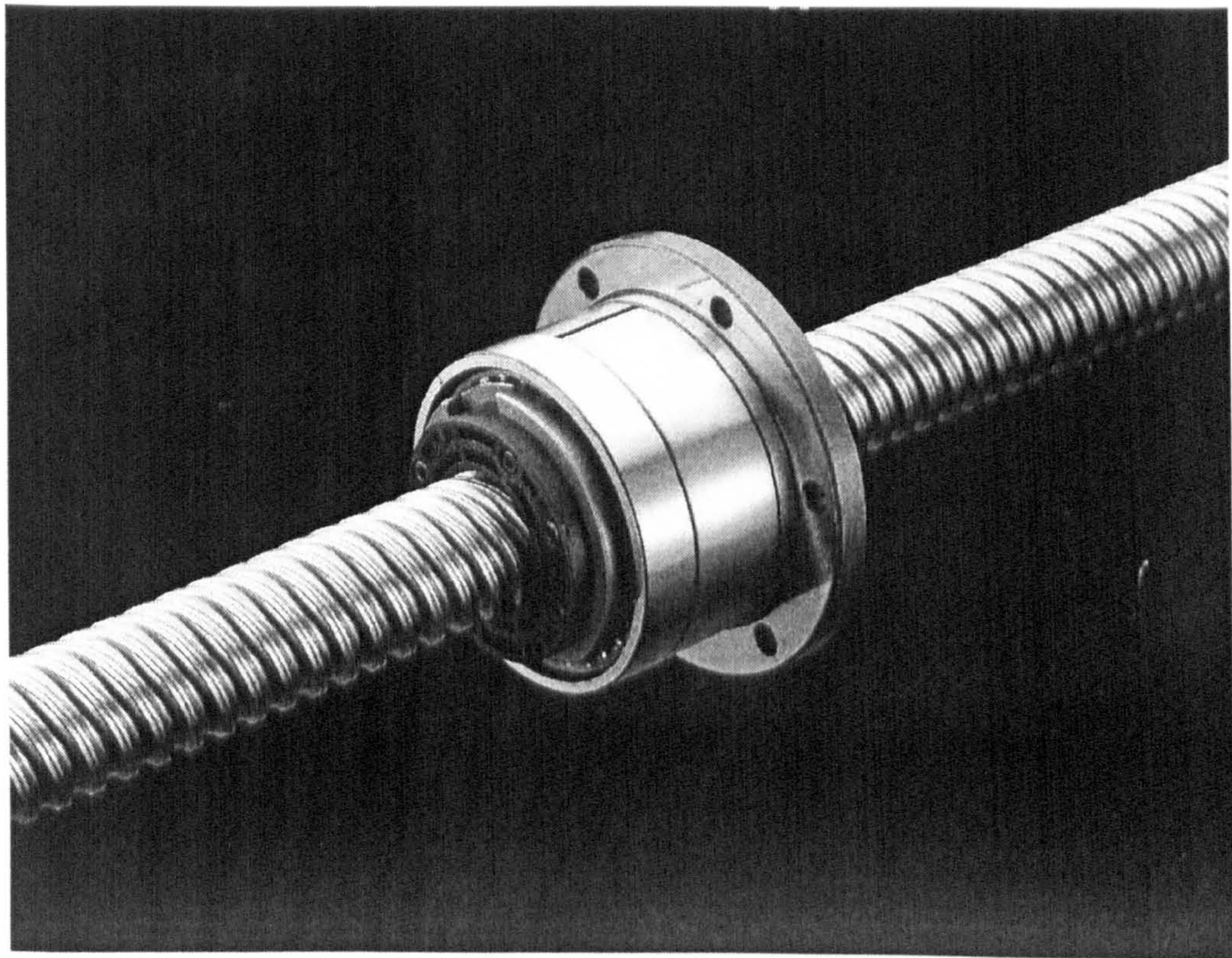


*Figure 5-7. Nut rotating ball screw unit.*



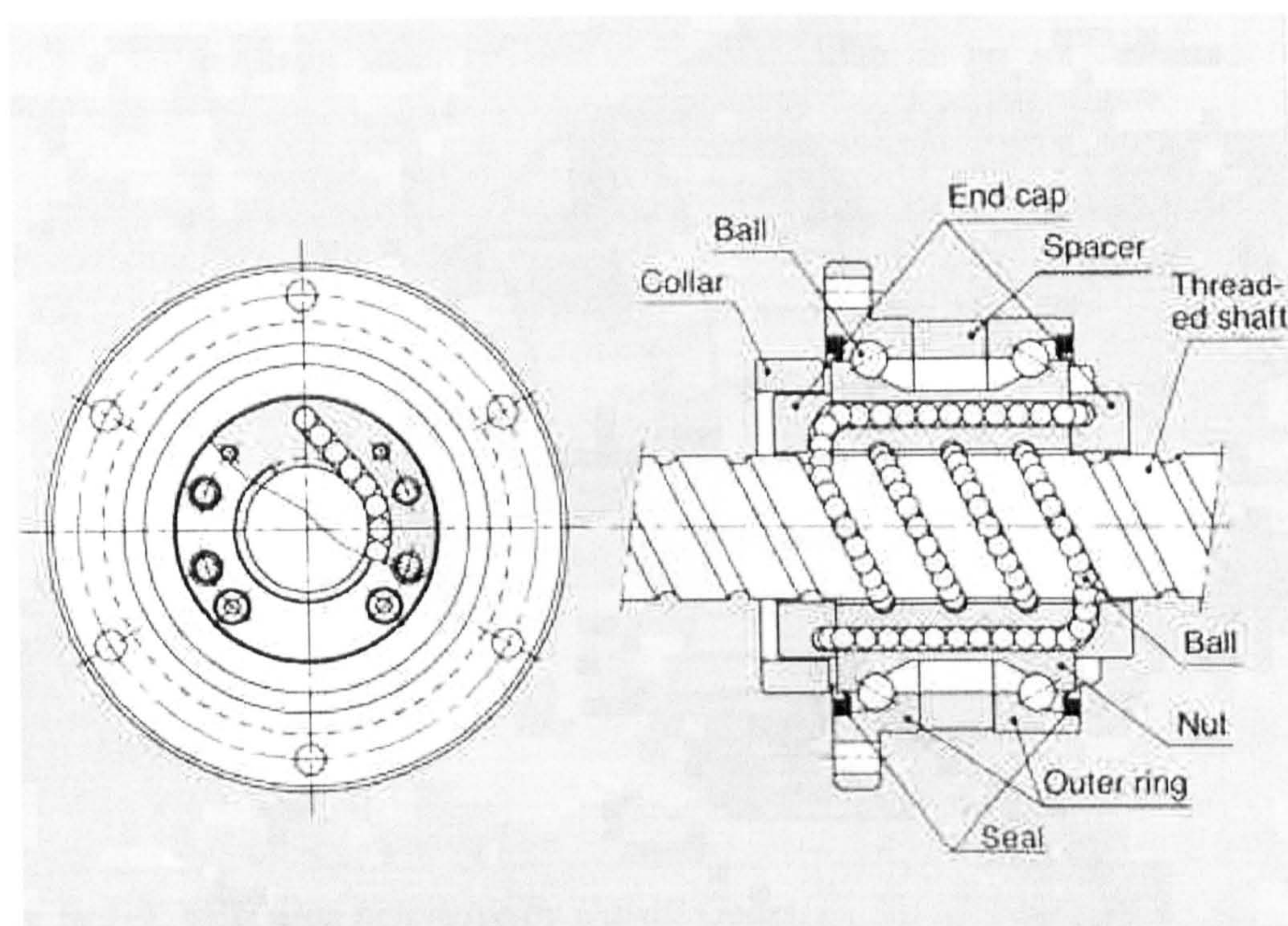
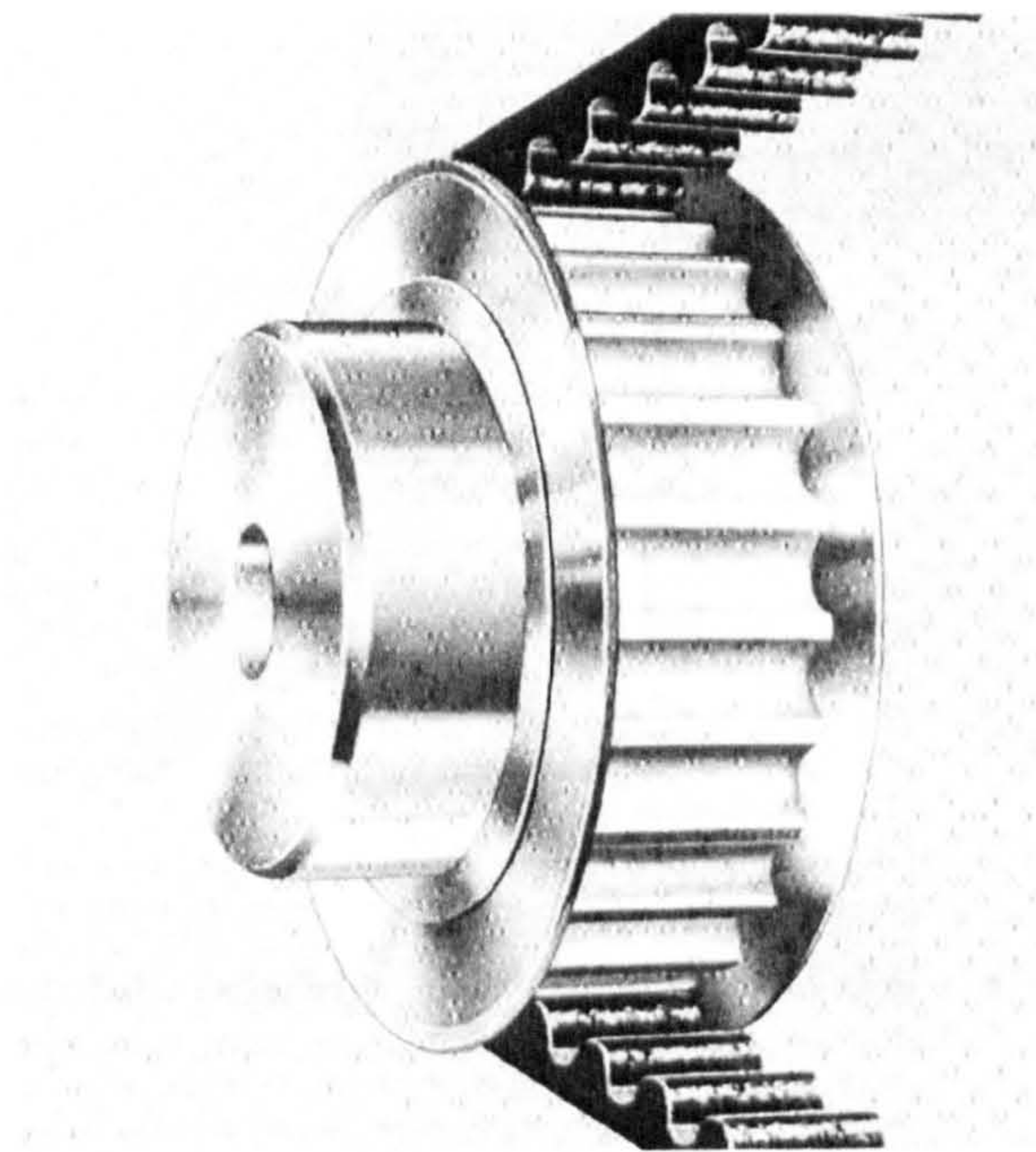


Figure 5-8. Ball nut / ball bearing construction.

#### 5.2.1.3. Transmission of Torque

The torque is transmitted from the motor shaft to the ball nut by a timing belt drive system supplied by Davall Gears. This system comprises a timing belt (560-8M-30), which is 560mm long, 30mm wide and has 8mm pitch; a pulley on the motor shaft (PL-36-8M-30), with 36 teeth and pitch diameter 91.7mm; and a pulley on the ball nut (25-8M-30), with 24 teeth and pitch diameter 61.1mm. This combination of pulleys and belt yields a pulley centre distance of 159mm. A similar belt and pulley to those applied are shown in Figure 5-9. The timing belt drive calculation is given in Appendix C.





*Figure 5-9. Timing belt drive by Davall Gears.*

### **5.2.2. Guide System and Support Structure**

The linear guide system consists of a frame made up of two 1.5m steel shafts of 30mm diameter. These are interconnected at the top and bottom via horizontal assembly bars and shaft support blocks. Each shaft slides through two linear ball bearings that are mounted 0.4m apart in the vertical direction on to a drive frame fixed to the support structure, and thereby allow movement in the vertical direction only. Deducting the length of the shafts clamped in the support blocks and the length between the outer edges of the linear ball bearings, the remaining length of frame travel was 1 metre. Shafts, bearings and support blocks were supplied by INA. The steel shafts are of type W30, the linear ball bearings of type KGHK30BPPAS and the support blocks of type GWH30B. The shaft support blocks and the housing of the linear ball bearing are made of high strength aluminium, and these are shown in Figures 5-10 and 5-11.



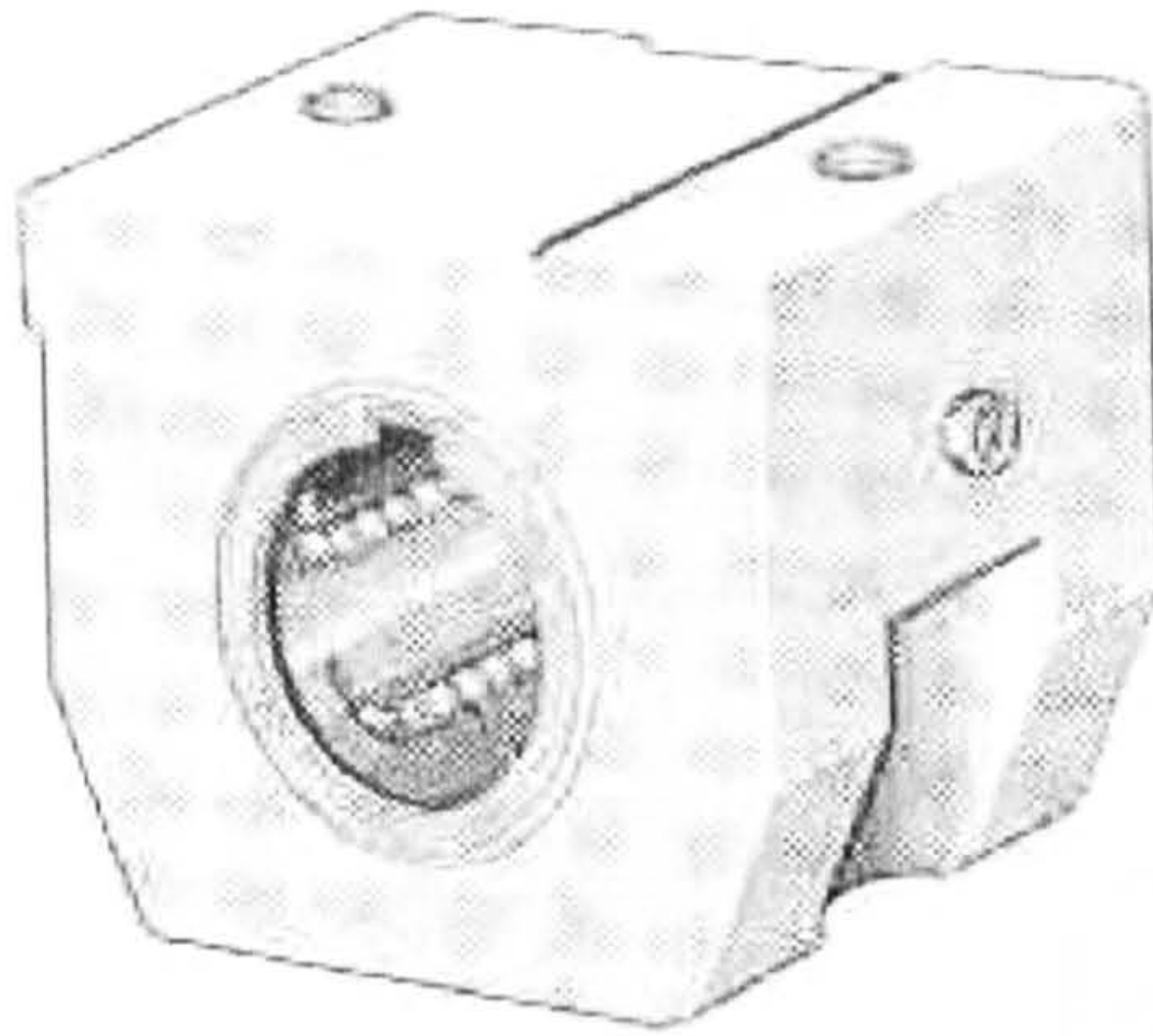


*Figure 5-10. Linear ball bearing*

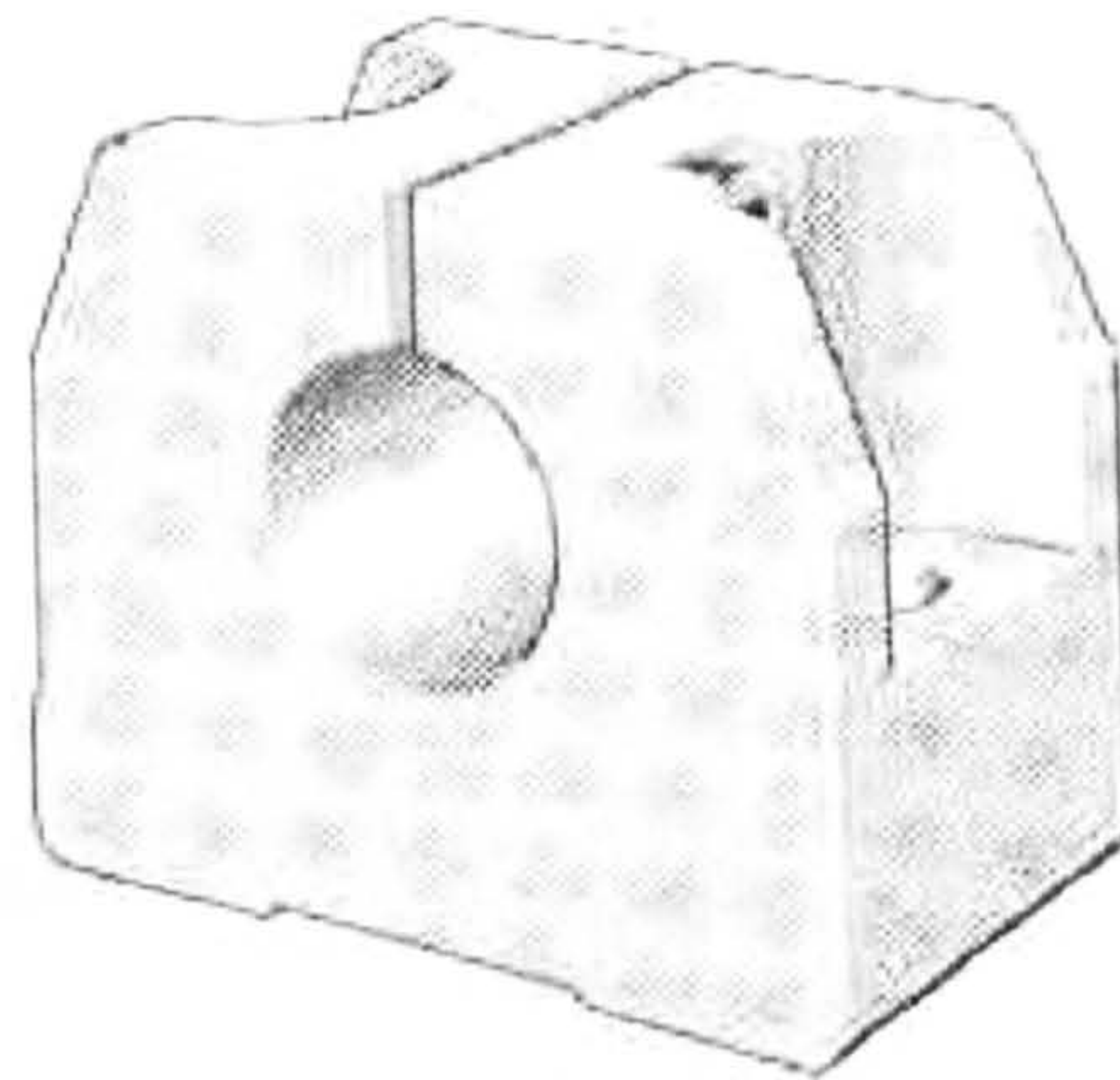


*Figure 5-11. Shaft support block.*

The drive assembly frame provides a rigid base for mounting the linear ball bearings, the servomotor and the ball nut thrust bearing. Two support brackets were designed to connect the drive frame to a large existing sub-carriage that spans the test tank. The entire drive frame, apart from the ball nut interface, is manufactured from 10mm steel plate, and the support brackets from 15mm steel plate. The ball nut interface is made of 30mm plate so that it can provide support for the outer casing of the thrust bearing throughout its depth. Top and bottom assembly bars are made of 10mm steel plate. Special interfaces for fixing the ball screw ends to the assembly bars were designed. These were machined with a keyway to prevent the ball screw from rotating. The drawings of the manufactured steel components are shown in Figures 5-12 to 5-17. The complete plate dimensions, fabrication and machining drawings are shown in Appendix B.



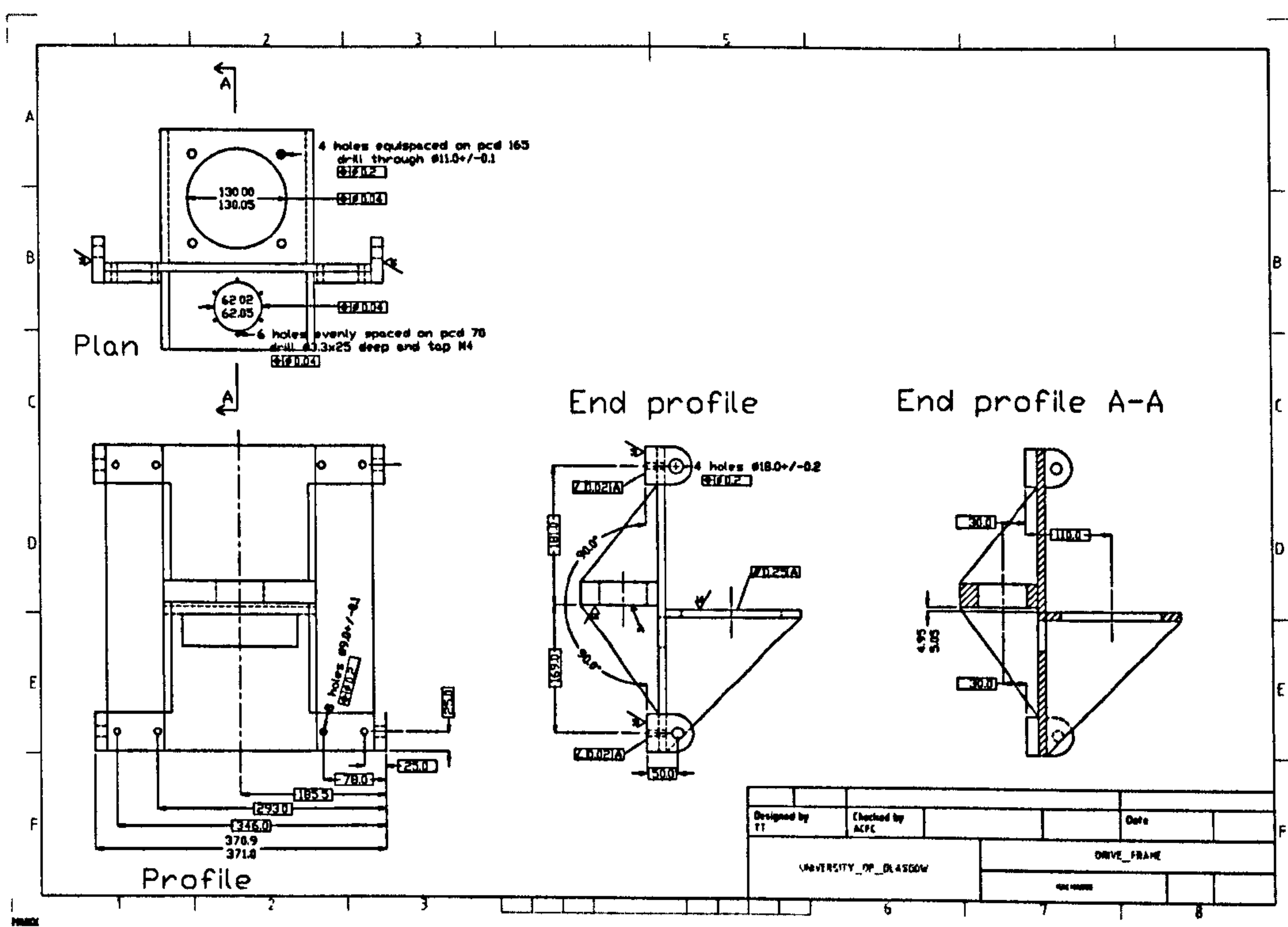


*Figure 5-12. Drive assembly frame.*

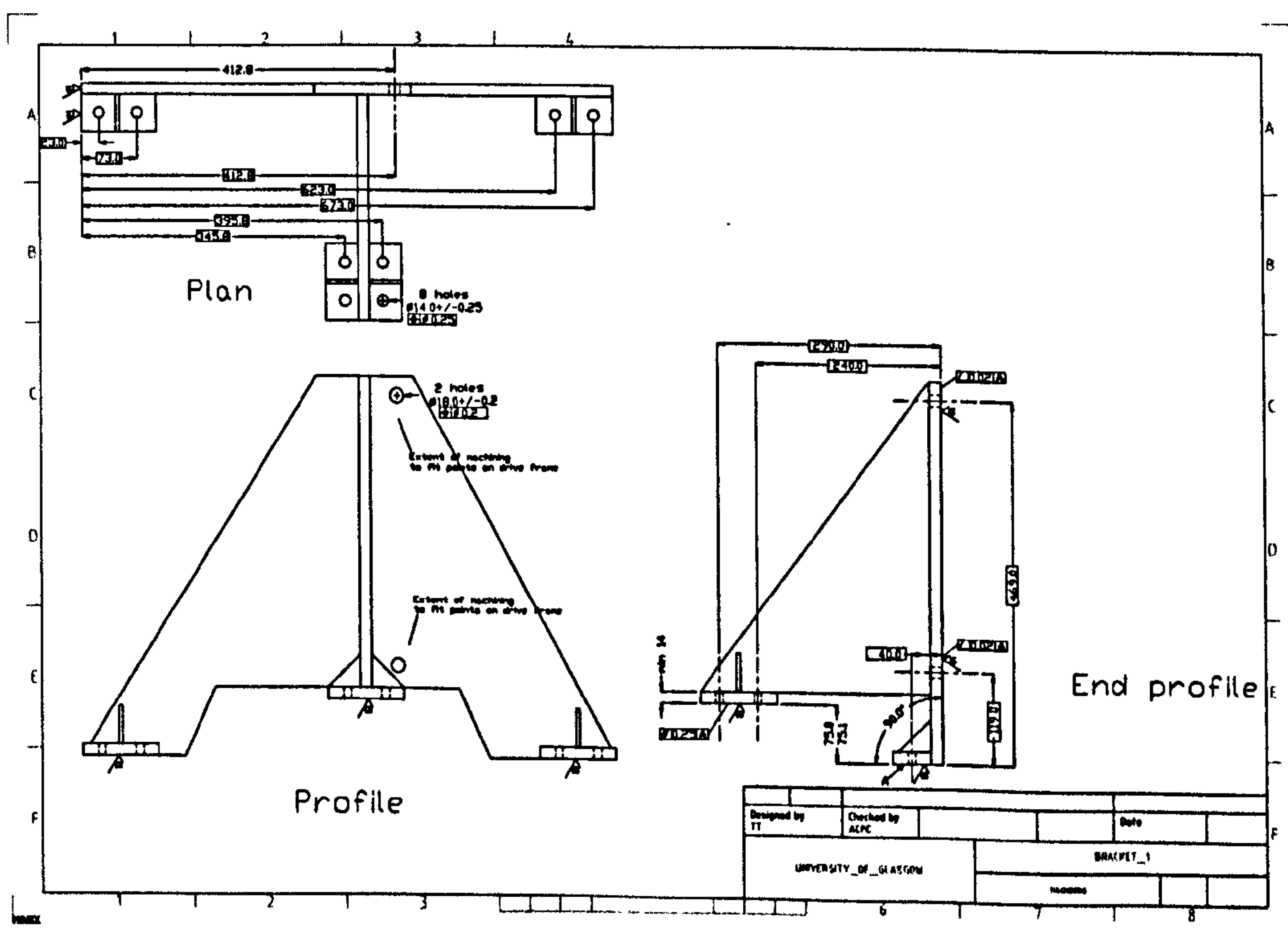


*Figure 5-13. Support bracket.*

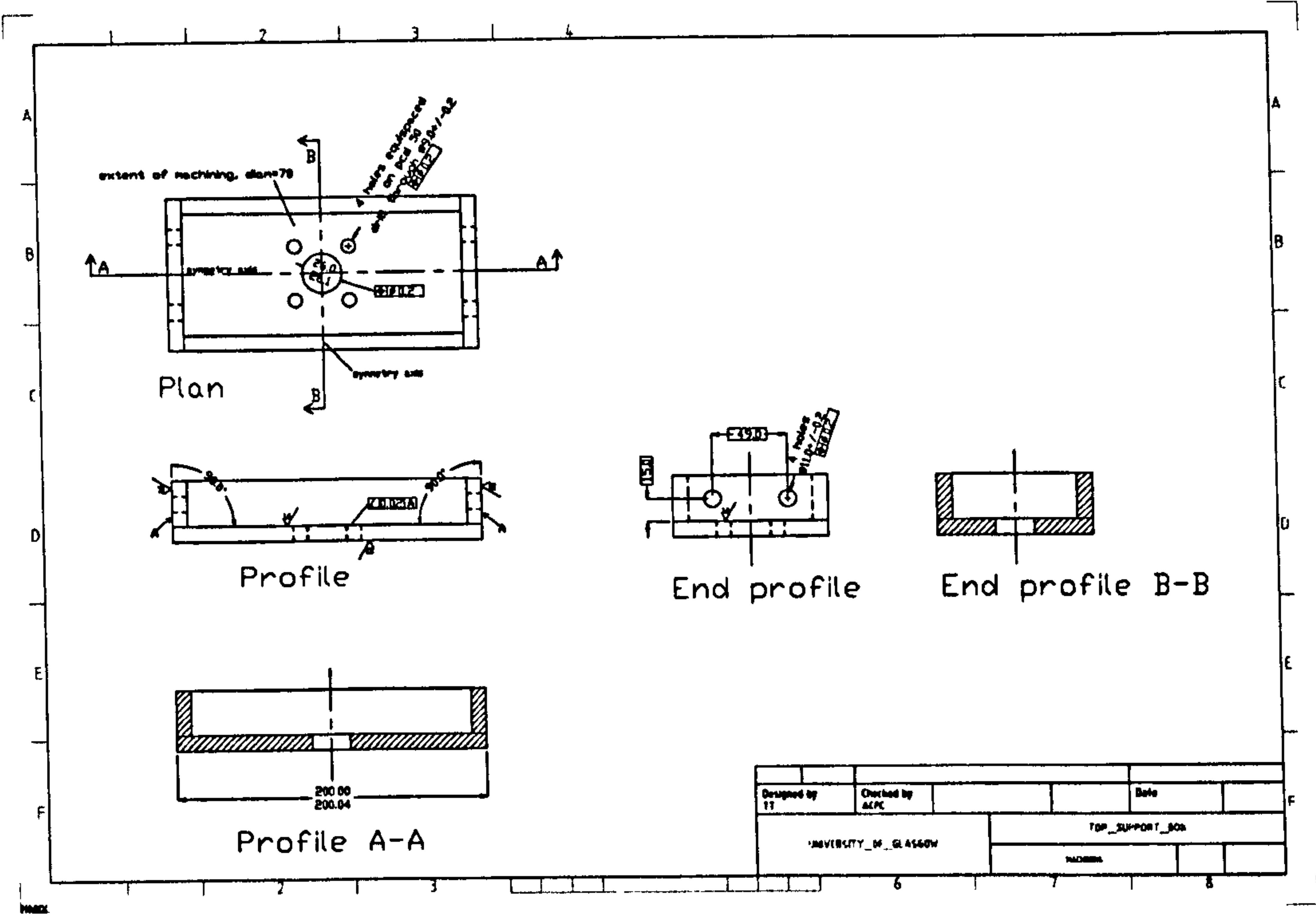


Figure 5-14. Upper assembly bar.

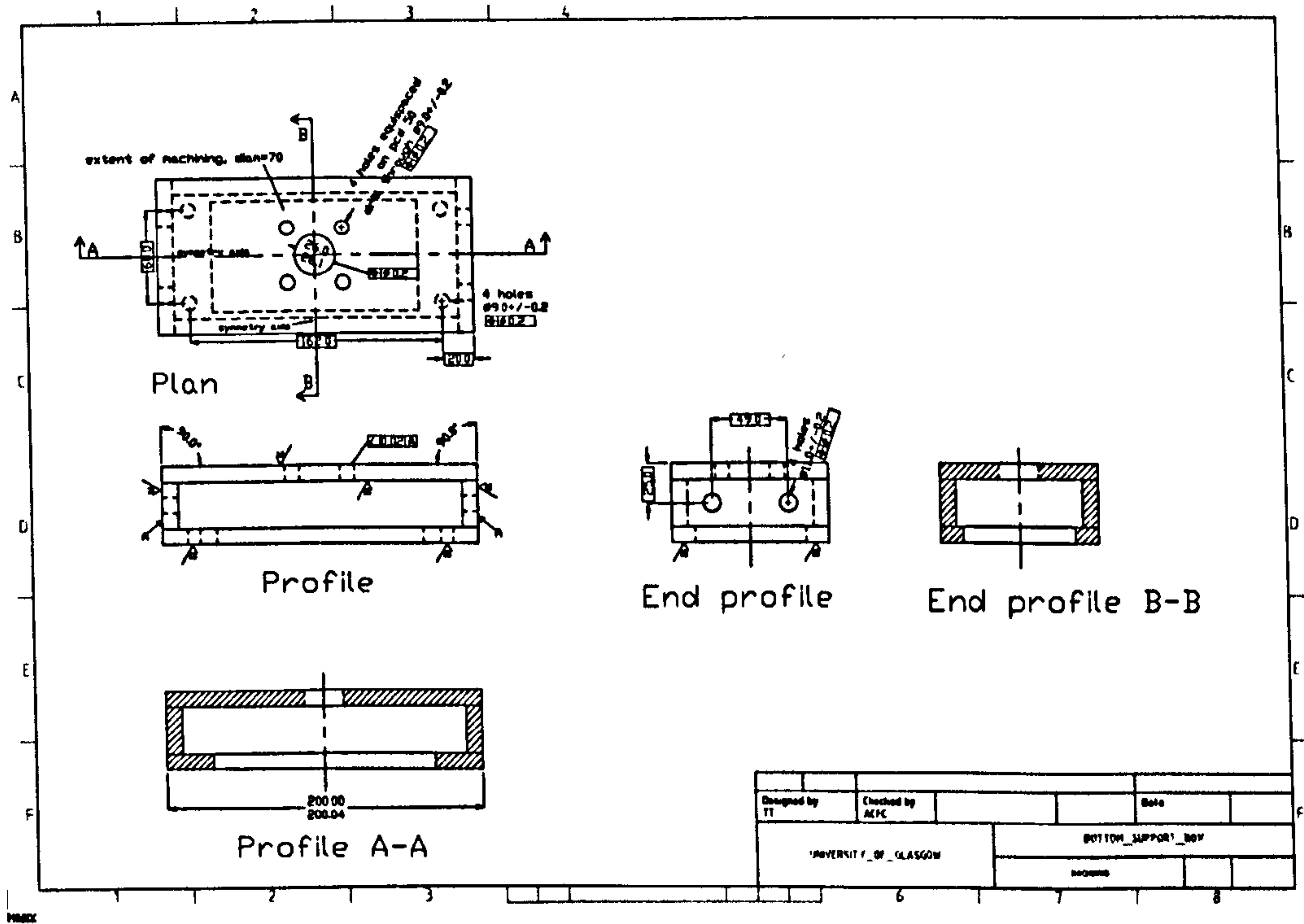


Figure 5-15. Lower assembly bar.

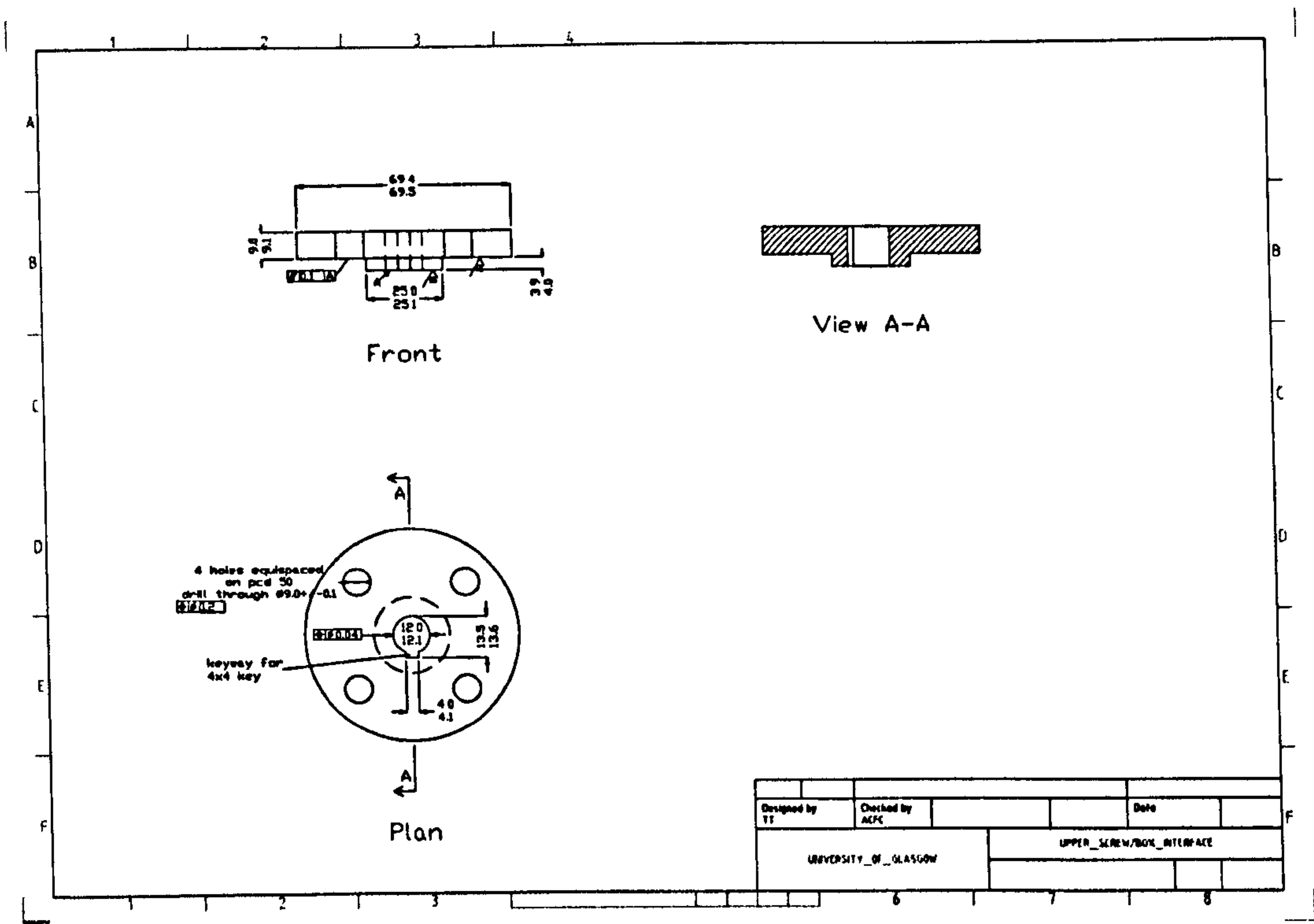


Figure 5-16. Upper assembly bar/ball screw interface.

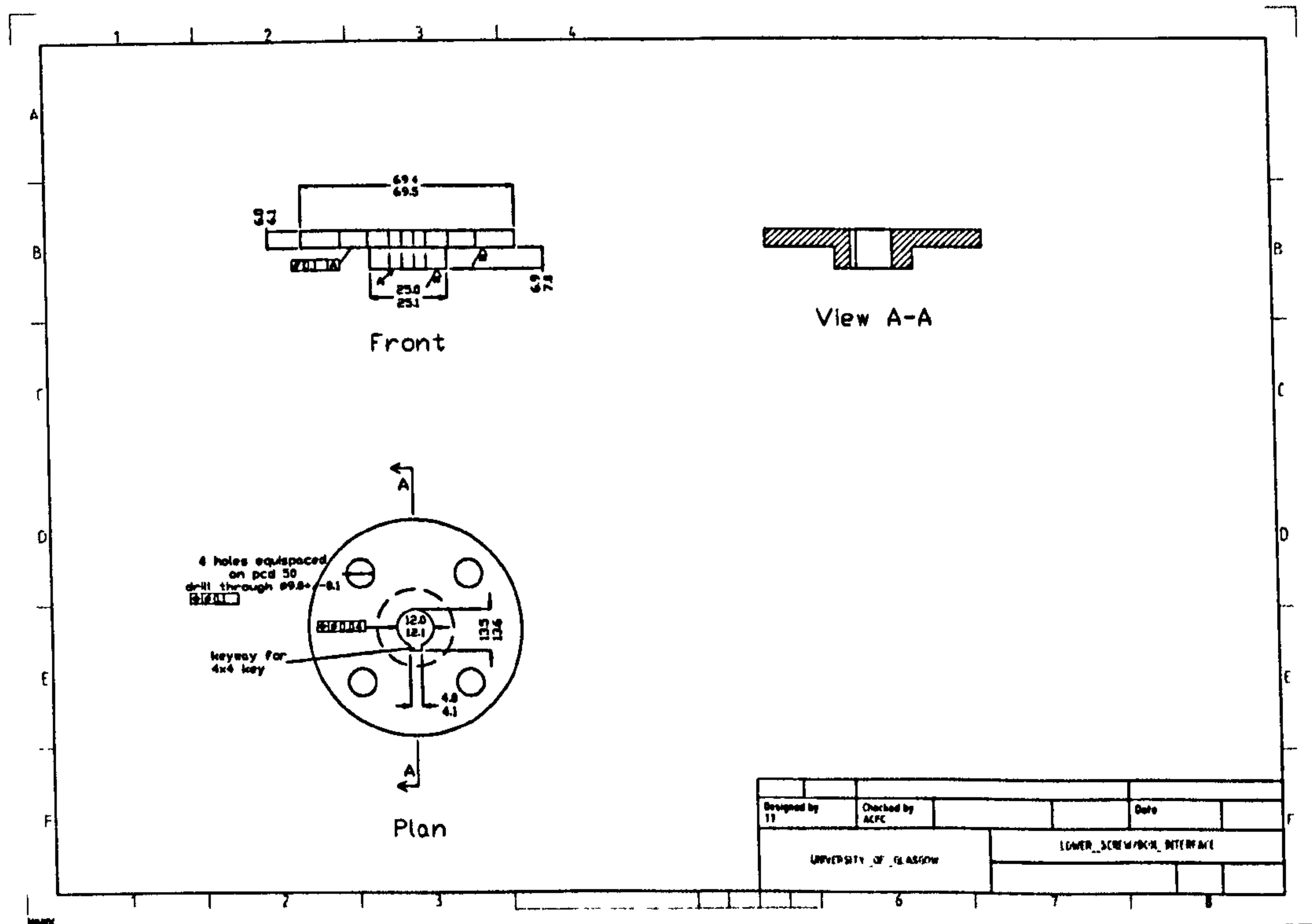
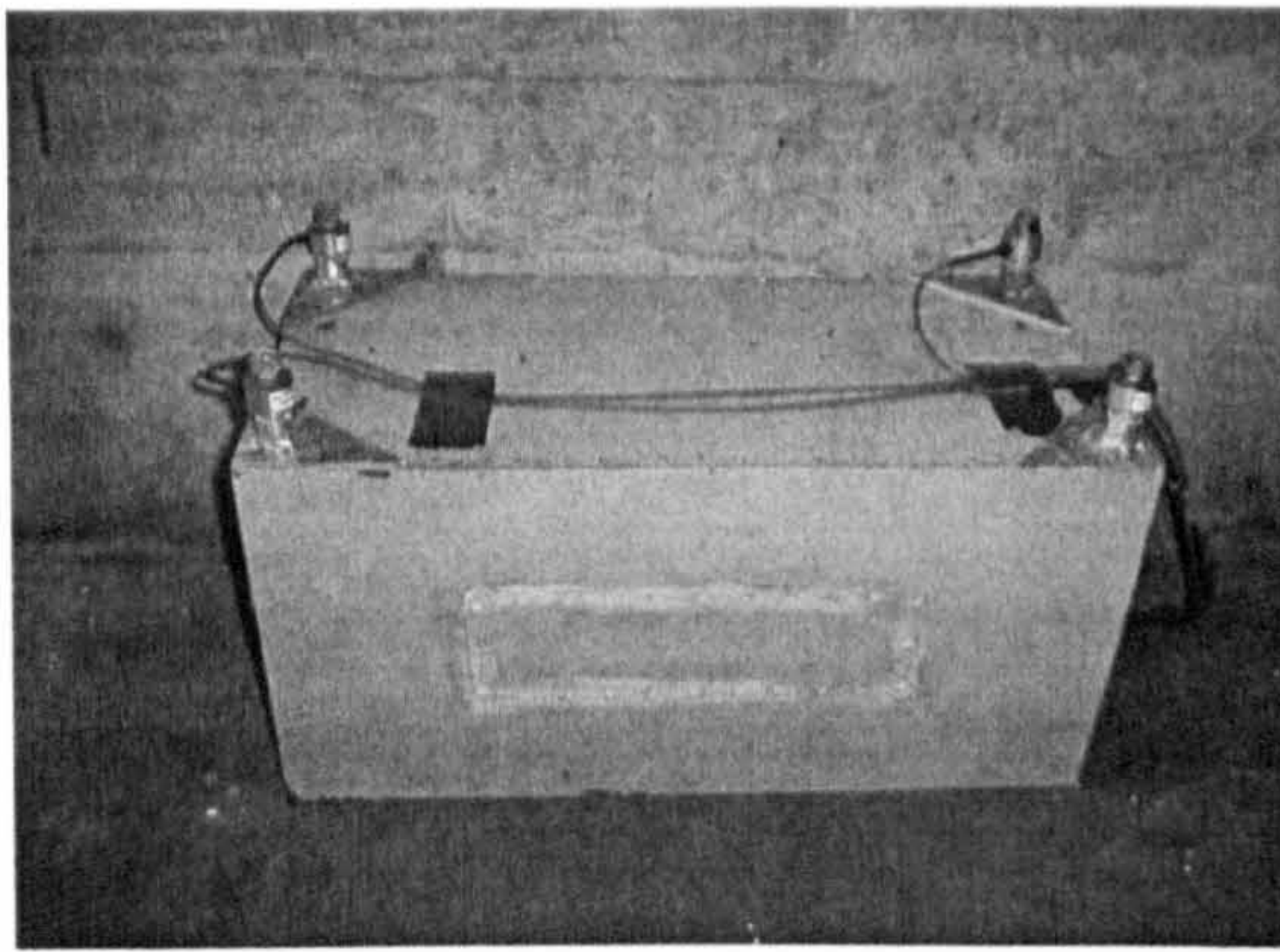


Figure 5-17. Lower assembly bar/ball screw interface.



**5.2.3. Test Sections**

The test sections consist of 5, 10, 15, 30 and 45 degree deadrise angle wedges and a box section for attachment of these. Both the box section and the wedges are of length 0.3m and width 0.6m. The height of the box section is 0.3m. The box and the 15 and 45 degree wedges were constructed of PVC sheets, while the remaining models were made of aluminium. The box section is shown in Figure 5-18 and the wedges are shown in Figure 5-19. It can be seen that there are load cells mounted on the top of the box sections. These are the sensors for force measurements during the tests and also provide the attachment to the model carrier. These issues are discussed more detailed in the next sections.



*Figure 5-18. Box section.*

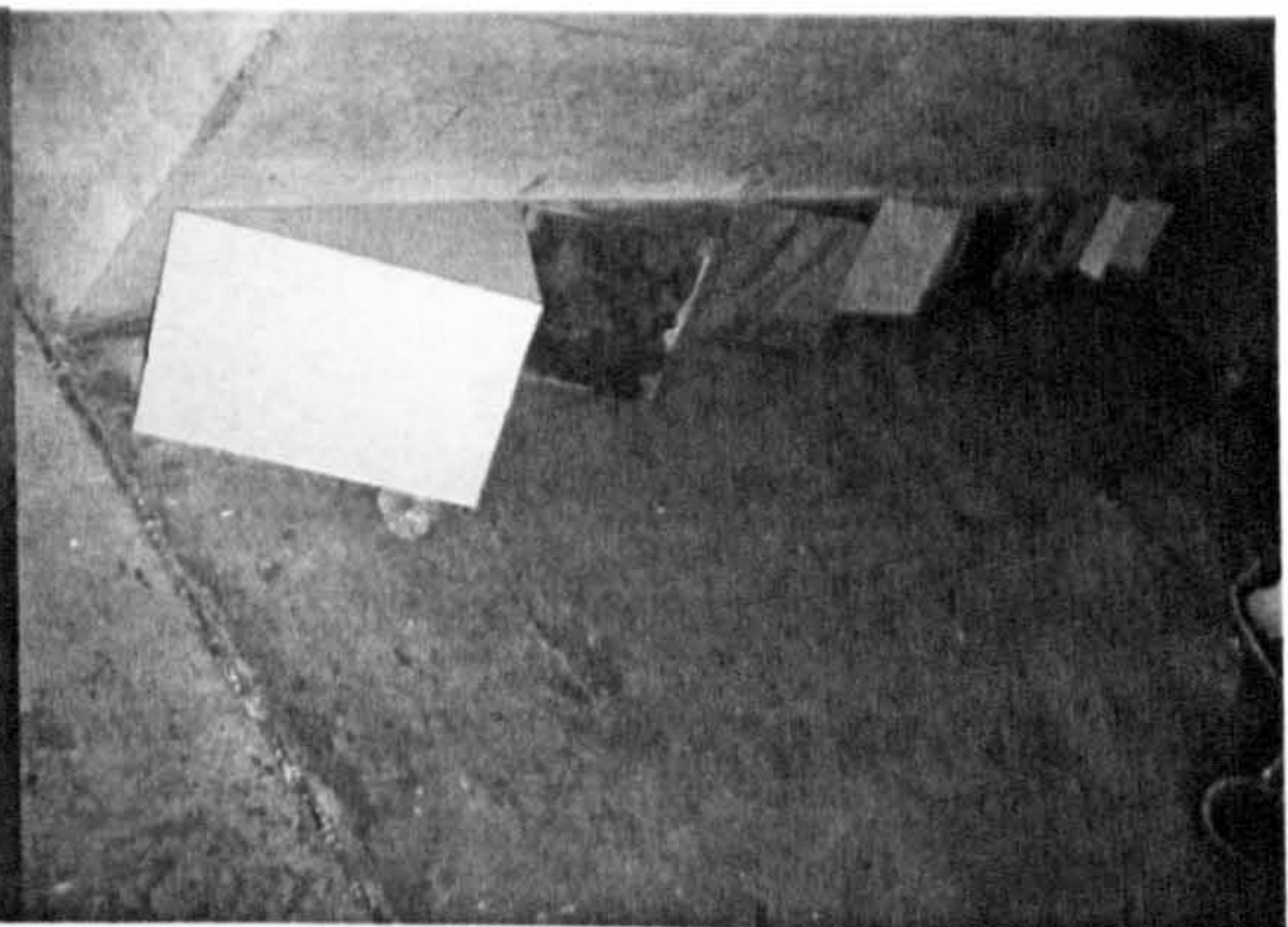


*Figure 5-19. Wedge sections.*



The mass of the wedges and the box are given in Table 5-1.

Section	Mass
Box	7.1 kg
Wedge, 5 degree	4.0 kg
Wedge, 10 degree	4.1 kg
Wedge, 15 degree	2.8 kg
Wedge, 30 degree	5.2 kg
Wedge, 45 degree	4.7 kg

Table 5-1.     *Mass of test sections.*

**5.2.4.   Model Carrier**

The model carrier is manufactured from 10mm steel plate, and has the same outer dimensions as the test piece box section. A machined surface in each corner provides an interface for mounting the load cells that interconnect the model carrier and the test piece box section. The model carrier incorporates a bracket at each corner to provide mountings for transparent PVC sheets that travel with the test section and ensure two-dimensional flow. Dimensions of the PVC sheets are 1 metre by 1 metre, and thickness is 10mm. The manufacture drawing of the model carrier drawing is shown in Figure 5-20.

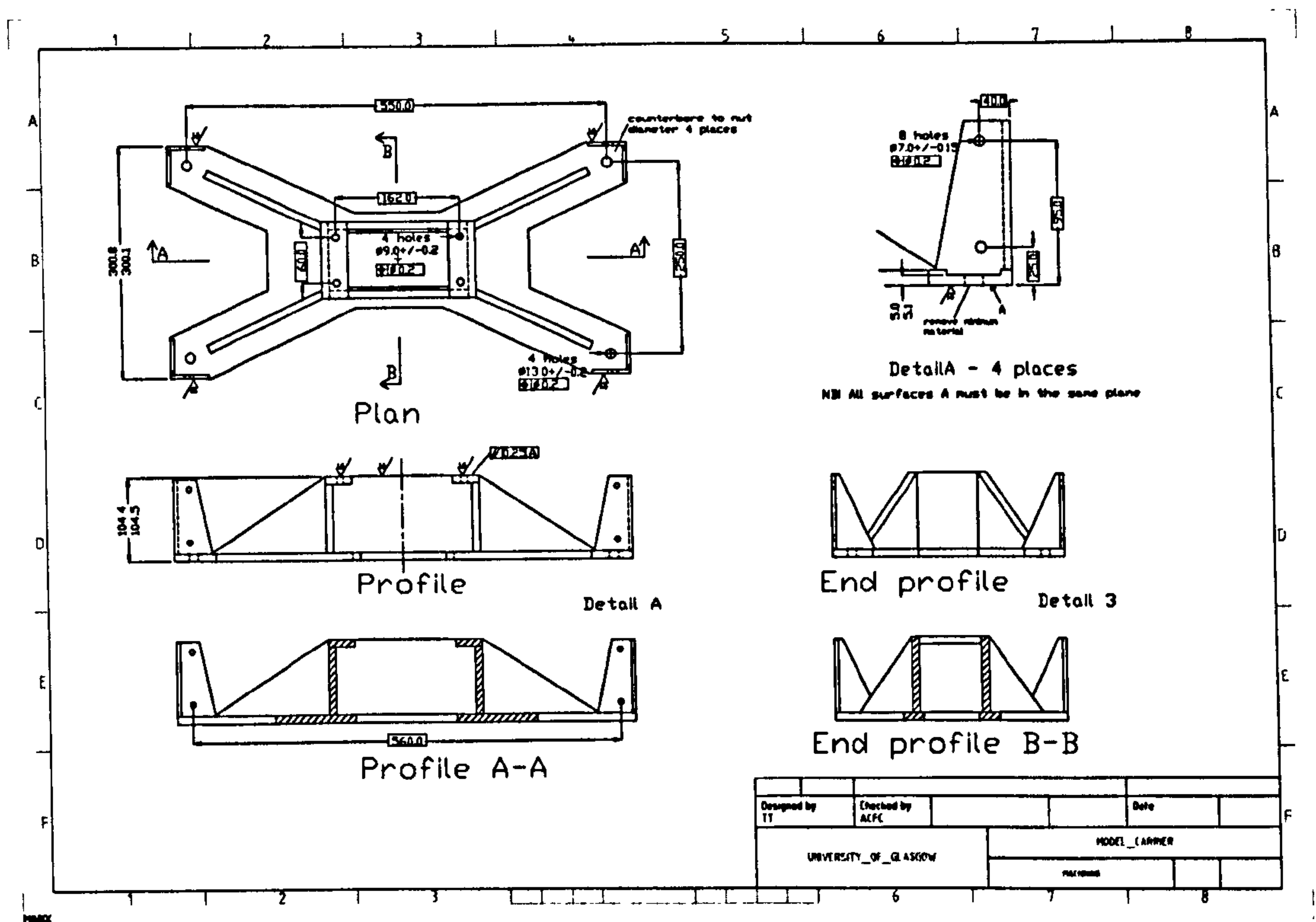


Figure 5-20. Model carrier.

5.2.5. Sensors and Data Acquisition

Graham and White supplied four high dynamic response tension/compression load cells of model DDE1000. The capacity of the DDE1000 is +/- 1000N each, and it has 50% safe overload. These particular load cells are not water submersible as originally specified. However, they were guaranteed to withstand substantial spray, and an improved sealing arrangement was provided to allow short periods of submersion. Figure 5-21 shows one of the load cells mounted on the test piece section box. The datasheet for these load cells is given together with the calibration sheets in Appendix C.



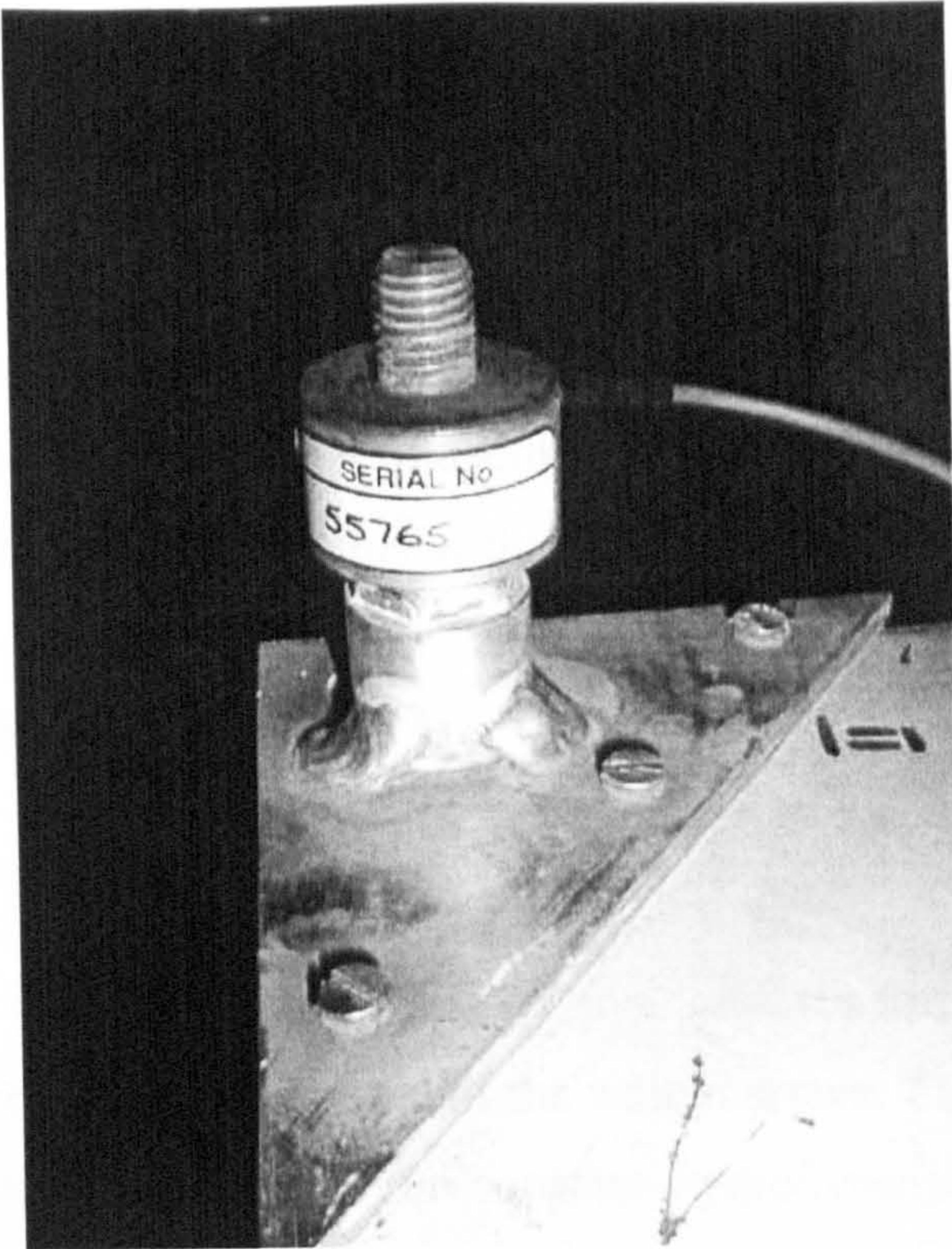


Figure 5-21. Tension/compression load cell, DDE1000.

The Strawberry Tree from DATashuttle Express was used for data logging during the tests. This system also incorporates amplifiers and filters. The Strawberry Tree hardware is shown in Figure 5-22.

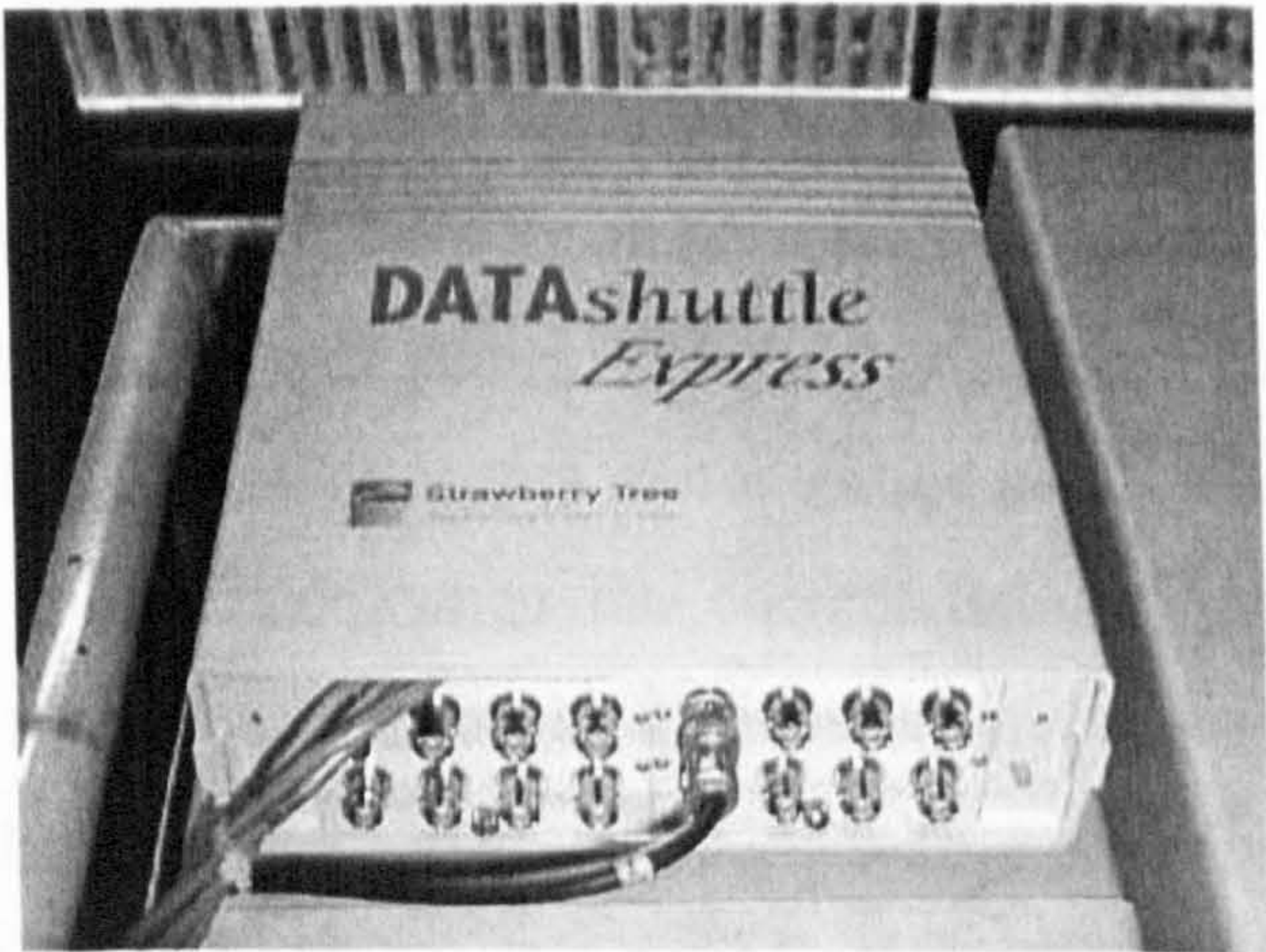


Figure 5-22. Data acquisition by Strawberry Tree.



### 5.3. Design Evaluation

Prior to the design of the main test rig, some earlier experiments were conducted using a cable attached to the frame of the towing carriage to control the entry velocity. These experiments are described in Appendix A, but did not produce reliable results. However, a number of useful lessons were learned, some of which are mentioned in this section, together with some other design issues.

#### 5.3.1. Drive System

##### 5.3.1.1. Motor and Controller

Constant velocity water entry of the test sections requires force equilibrium to be maintained throughout the penetration of the water surface. The entry force varies with immersion depth due to the non-constant hydrodynamic impact force and increasing buoyancy. It follows that the drive motor must be controlled such that the torque delivered corresponds to the constant velocity load at every moment. To achieve this, the current to the motor is adjusted to minimise any deviation between actual speed and desired speed. For the design case of the 10 degree wedge section at 1.5m/s, the time from the initial impact to the peak force occurrence is 23ms. An accurate servo system is required to keep the change in velocity at less than 1 percent in the presence of such a rapid increase in force.

The rated speed of the 6SM77K servomotor is 3000rpm. A suitable transmission from rotary to linear vertical motion was chosen so that a motor speed of 3000rpm gives the linear vertical design velocity of 1.5m/s. The design force at this velocity is 4.5kN, and from a power consideration it is found that at the chosen transmission ratio this corresponds to a motor torque of 21.5Nm. The rated motor torque of 8.5Nm is produced when the current delivery is 5A. This can be increased to 24A for a short period of 4 seconds, giving peak motor torque of 40.8Nm. The amplifier's rated capacity is 10A, with a peak delivery of 20A peak for periods up to 2 seconds. Hence, the combination of the motor and amplifier is capable of producing a torque of 34Nm for up to 2 seconds. This provides plenty of capacity to meet the torque requirements for the design case.

A smaller servomotor could have been chosen that would be able to deliver the required design torque of 21.5Nm. However, the larger option was preferred after consideration of the inertia ratio. The performance of a controlled servo system is highly dependent on the ratio between the motor inertia and the inertia of the system the motor is putting into movement. The minimum preferred ratio is 1 to 5, and by using the larger motor the system came just within this range.

The motor/amplifier system's feedback loop is 60 $\mu$ s, which means that the actual speed is checked and the current delivery updated 16667 times per second. With the expected rate of increase in the load that would occur for the design case, the suppliers estimated a speed deviation of less than a half percent.

The motor/controller system required two different power supplies, one three phase 415V supply for motor power and one 24V supply for operating the digital servo amplifier. In addition, the 24V supply doubled as emergency brake power in the event of a 415V supply cut off.

#### 5.3.1.2. Rotary to Linear Motion

An advantageous feature of nut rotating ball screw systems compared to the standard shaft rotating version is that the threaded shaft has no influence on the balance and thus higher speed operation is possible. Precision ground type ball screws such as the BLR have very high lead accuracy. The nut has been preloaded with oversized balls and this results in zero axial play. Speeds of up to 5000rpm are made possible with the BLR type rotating nut ball screw. With a 20mm lead this corresponds to a linear screw velocity of 1.67m/s.

The ball nut thrust bearing has a dynamic load rating of 26.8kN, but the maximum axial force that could be allowed was much less due to the buckling strength of the threaded shaft. The total length of the threaded shaft, including the machined ends, was 1.47m. With the frame fully extended, i.e. model carrier at lowest position, the unsupported length of the threaded shaft was 1.2m. The maximum allowed axial load at this position was calculated by the supplier to be 7.4kN. This load is more than 60 percent higher than the predicted design case peak force, and



thus gives plenty of capacity for the design load, even at maximum extension of the guide frame. At lesser extensions, the reduced unsupported length of the threaded shaft gives buckling load capacity in excess of 7.4kN.

#### 5.3.1.3. Transmission of Torque

The screw with 20mm lead achieves a linear velocity of 1.5m/s when the nut is rotated at 4500rpm. A transmission ratio between motor shaft and ball nut of 1.5:1 is required to obtain this nut speed when the servomotor is rotating at its rated speed of 3000rpm. This ratio can be achieved with any two pulleys provided the motor pulley diameter is 1.5 times the ball nut pulley diameter. However, the maximum allowed radial force on the motor shaft imposed a limit on the minimum pulley size.

When exerting a torque on a shaft, a timing belt also exerts a radial force on the shaft. For a given torque, the force that acts on the perimeter of the pulley from the belt varies as the inverse of the pulley diameter. Thus a larger pulley results in less radial force on the shaft. The motor pulley pitch diameter of 91.67mm and the design torque of 21.5N yield a radial force of 469N on the shaft, which is within the rated capacity of 730N. Belt calculations showed that a 20mm wide belt would provide sufficient strength for the application. However, to reduce stretch and thus achieve better positional accuracy, a 30mm belt was used.

#### 5.3.2. Guide System and Support Structure

Although the main purpose of the guide is to provide linear movement, it was also designed with possible future use in mind. If used for carrying out forward speed slamming tests there would be lateral loading on the lower end of the guide frame. The magnitude of the lateral loading depends on forward speed, impact speed and the angle of the model relative to the guide frame. Shafts of 30mm diameter were used to obtain a rigid guide structure that could withstand substantial lateral loading at maximum frame extension. The maximum allowed working load of each ball bearing separately is 2700N. The lateral load at the full extension that would give this load on each bearing is 1400N. At the maximum extension, the

lateral load that would cause a bending moment stress equal to the yield stress of the shaft material is 1085N. Thus the shafts would yield before exceeding the rated bearing load. A shaft bending moment safety factor of 5 gives a maximum working lateral force of 217N when the frame is fully extended. This is greater than the resistance of the ship models towed in the test tank and thus gives substantial capacity for forward speed slamming tests. To reduce the induced lateral force due to the slamming forces on a model towed with a trim angle, the whole guide frame could be tilted instead of fixing the model to the guide frame at a non-square angle. Although this reduces the lateral force it does not prevent the bending moment caused by the centre of slamming pressure not acting in line with the guide frame.

### **5.3.3. Model Carrier**

Transparent PVC sheets are used to provide two-dimensional flow near the model. These plates are attached to the model carrier and travel with the model, thus allowing minimum clearance. If the plates were attached to the test sections, the force acting on the plates due to pressure drag and frictional resistance would be transferred via the load cells, and thus affect the measurements. As it is, only forces acting on the wedge section model are transmitted via the load sensors.

In the set-up for the earlier experiments, transparent PVC sheets were fitted close to each end of the section. These were fixed to a stationary frame, separated by a distance equal to the section width plus some clearance to prevent models from colliding with the plates. This clearance allowed water to be driven between the plates and the model, and thus affected the flow and the force measurement. It was therefor decided that the plates should travel with the model.

### **5.3.4. Sensors and Data Acquisition**

The earlier experiments highlighted the importance of using load cells with substantial dynamic response. Based on the estimated design case force vs time curve, the suppliers of the load cells, Graham and White, guaranteed that the DDE1000 had adequate dynamic response for the task. Adding the four load cells



gave a force capacity of 4000N, while the maximum estimated load for the design case was 4500N. However, a safe overload capacity of 50% guaranteed by Graham and White ensured that the load cells would not be damaged. Linearity between voltage output from the load cell and the excitation load is not guaranteed for the overload range, but a reduction of the velocity by 5 percent would keep the force within the rated capacity. Based on this, the 1000N capacity of the DDE100 would be sufficient. These particular load cells were not water submersible as originally intended. However, they were guaranteed to withstand substantial spray, and were modified with an improved sealing arrangement to allow short periods of submersion.

For the load cells to give a voltage reading that can be interpreted into a force, an excitation voltage is required. For these particular load cells, the optimum excitation was 10V. The output signal at this excitation is 20mV for a load equal to the rated capacity, i.e. 0.02mV per 1N load. Besides data sampling and recording, the Strawberry Tree data acquisition system also provided a complete system for voltage excitation, output signal amplifying and filtering.



## 5.4. Manufacture and Assembly

The steel components were manufactured from mild steel plating at the Mechanical Engineering Workshop at the University of Glasgow and the rig was partially assembled at the workshop and completed in the hydrodynamics laboratory.

### 5.4.1. Parts

For smooth travel of the guide shaft, tolerances for positioning of the linear ball bearings were very fine. The same applied to the assembly bars, where the faces on opposite sides of each bar needed to be parallel and spaced at exact relative distance. Any misalignment would cause a pre-bend and thus prevent smooth operation. The interface between the ball nut and its interface on the drive frame structure also required high accuracy during manufacture. Getting this surface squared to the ball bearing alignment and centred between the two shafts was vital to avoid an initial deflection in the ball screw. The accurate manufacture of the support frames and interfaces with the drive frame and sub carriage were important to assure correct orientation of the rig frame and thus guide frame movement perpendicular to the water surface. However, wider tolerances were accepted in these areas than in the manufacture of the guide system. Wider tolerances were also allowed for the motor interface on the drive assembly frame. This is due to the inherent flexibility in timing belt drives.

To manufacture the steel components to the required tolerances, all the faces on the drive frame and assembly bars were prepared by numerically controlled machining (NC).

On the model carrier the faces for mounting the four load cells needed to be in the same plane. Any misalignment of these faces would cause a gap between the model carrier and one load cell, and tightening the nuts to fix the load cells to the model carrier would then result in two and two diagonally facing cells being in tension or compression. It was also important to get the top face of the model



carrier parallel to the load cell faces to ensure correct test model orientation. To ensure that the transparent PVC sheets would be parallel to the test model and thus ensure clearance, it was necessary that the faces for plate mounting were perpendicular to the load cell faces. The necessity of accurate manufacture required that the model carrier also be machined by use of NC.

#### 5.4.2. Rig Assembly

The ball nut bearing is spigotted into its position on the drive assembly frame and secured by five screws inserted into holes tapped in the frame plate. This is seen in Figures 5-23 and 5-25. Figure 5-23 also shows the guide shafts mounted on to the drive frame via the linear ball bearings. The guide shaft ends are connected to the assembly bars via the support blocks, while the ball screw ends are connected via the manufactured interface components. This is shown for the upper assembly bar in Figure 5-24.

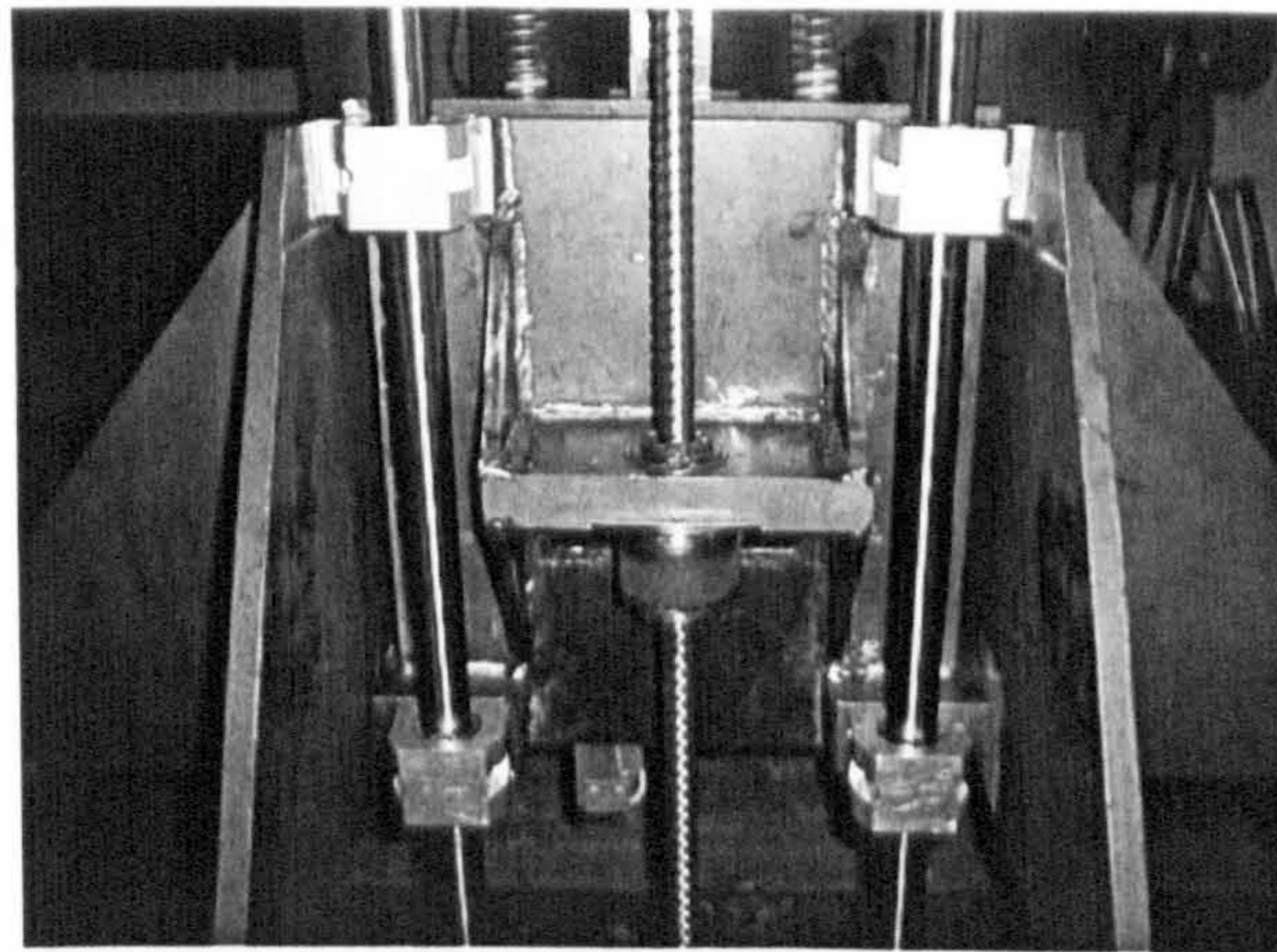


*Figure 5-23. Ball nut bearing spigotted into, and linear ball bearings bolted onto drive assembly frame.*



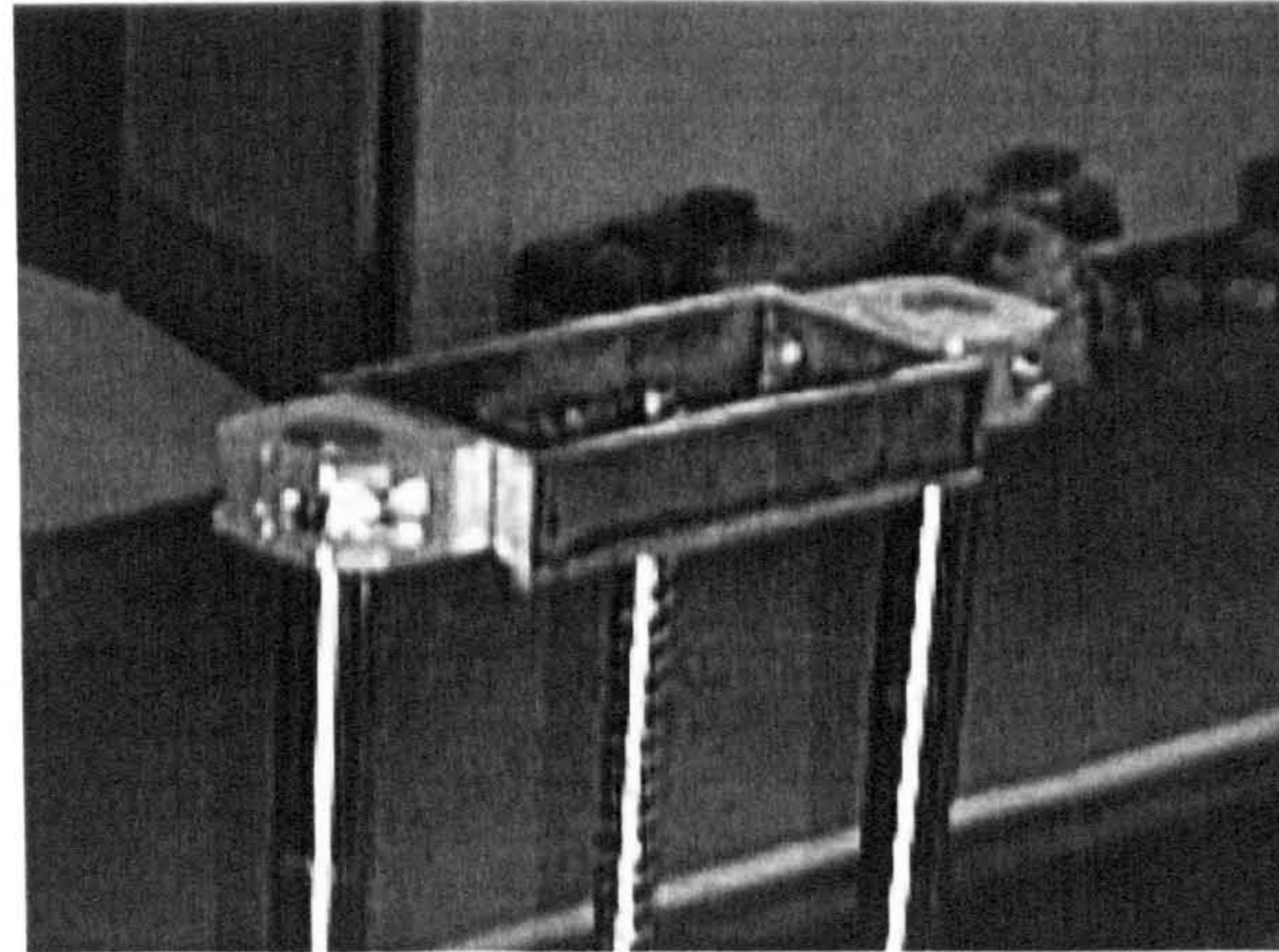


*Figure 5-24. Shaft, support blocks and threaded shaft mounted on the upper assembly bar.*

Holes drilled in the ball nut pulley accommodate bolts for mounting onto the ball nut as seen in Figure 5-25. Figure 5-26 shows the other pulley fitted to the motor shaft by use of a tapered bush after the motor is mounted onto its base of the drive assembly frame. The same picture shows the hole in the drive frame to provide a path for the timing belt between the two pulleys.

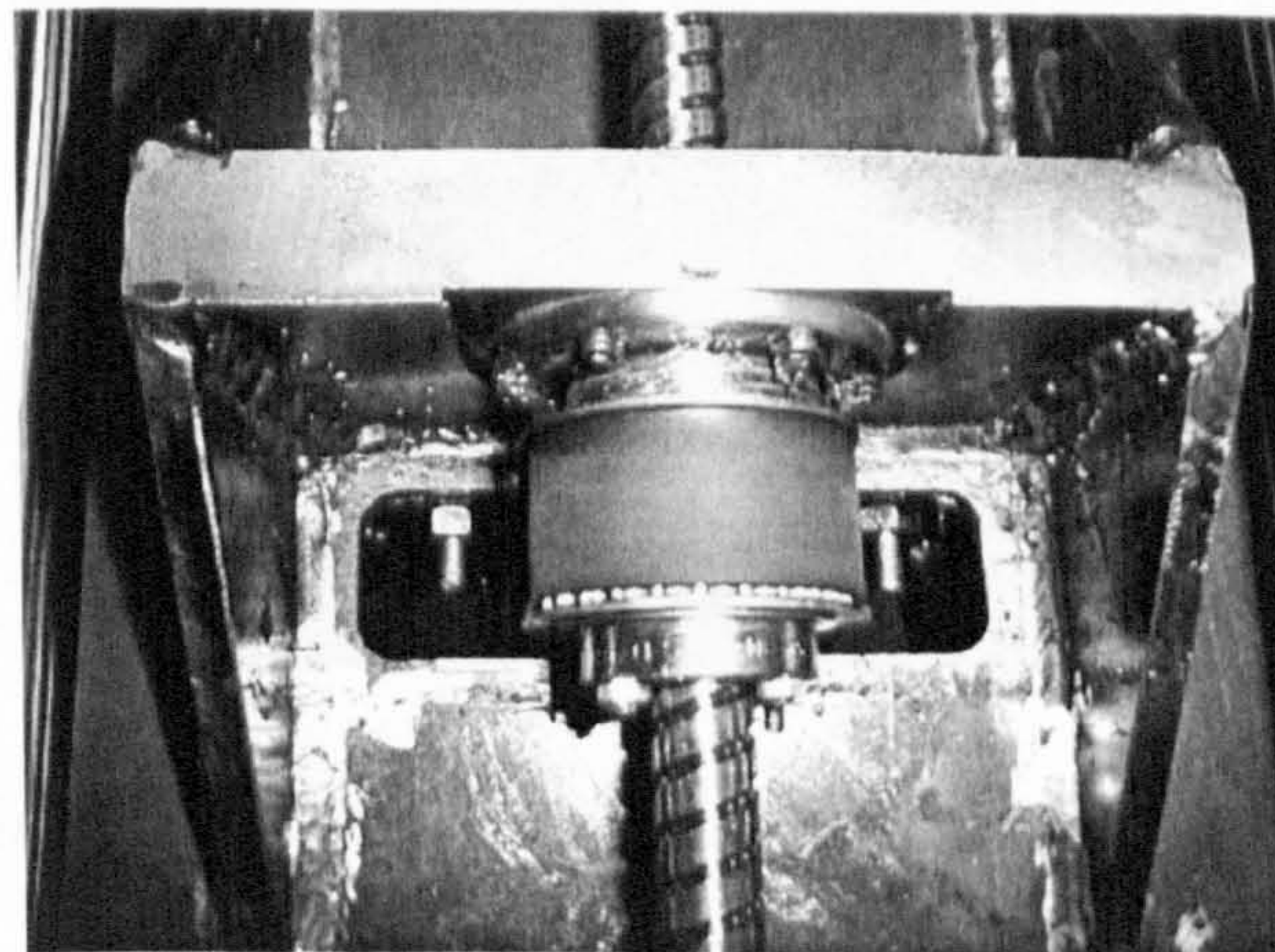


*Figure 5-25. Ball nut bearing flange screwed into the drive frame and pulley bolted to ball nut.*



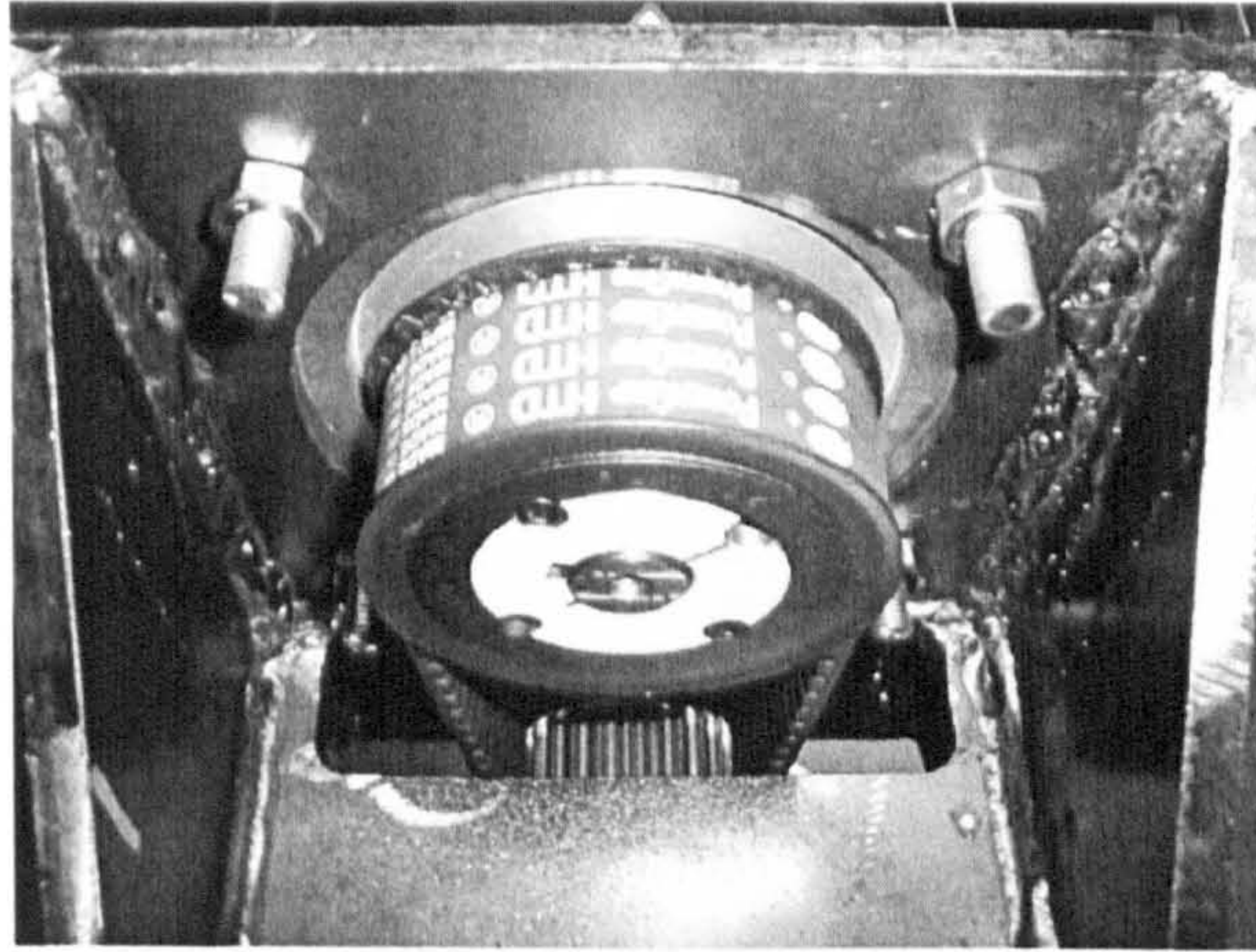


*Figure 5-26. Motor pulley and timing belt..*

The support frames were aligned and mounted on to the sub carriage over the test tank. Figure 5-27 shows the drive assembly frame of the complete test rig mounted between the support frames, and Figure 5-28 give views of the complete erected test rig.

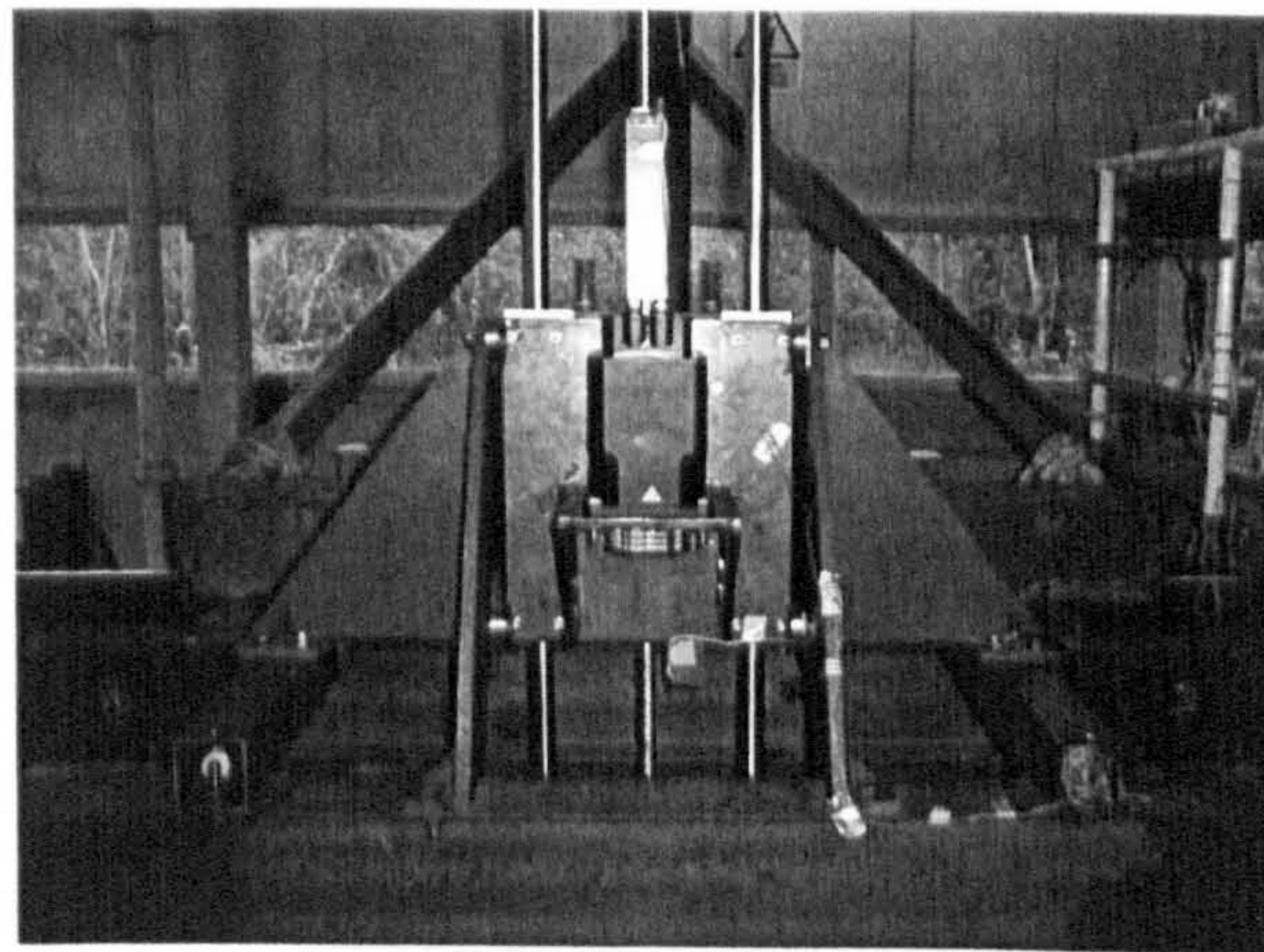


*Figure 5-27. Drive frame bolted on support frames.*



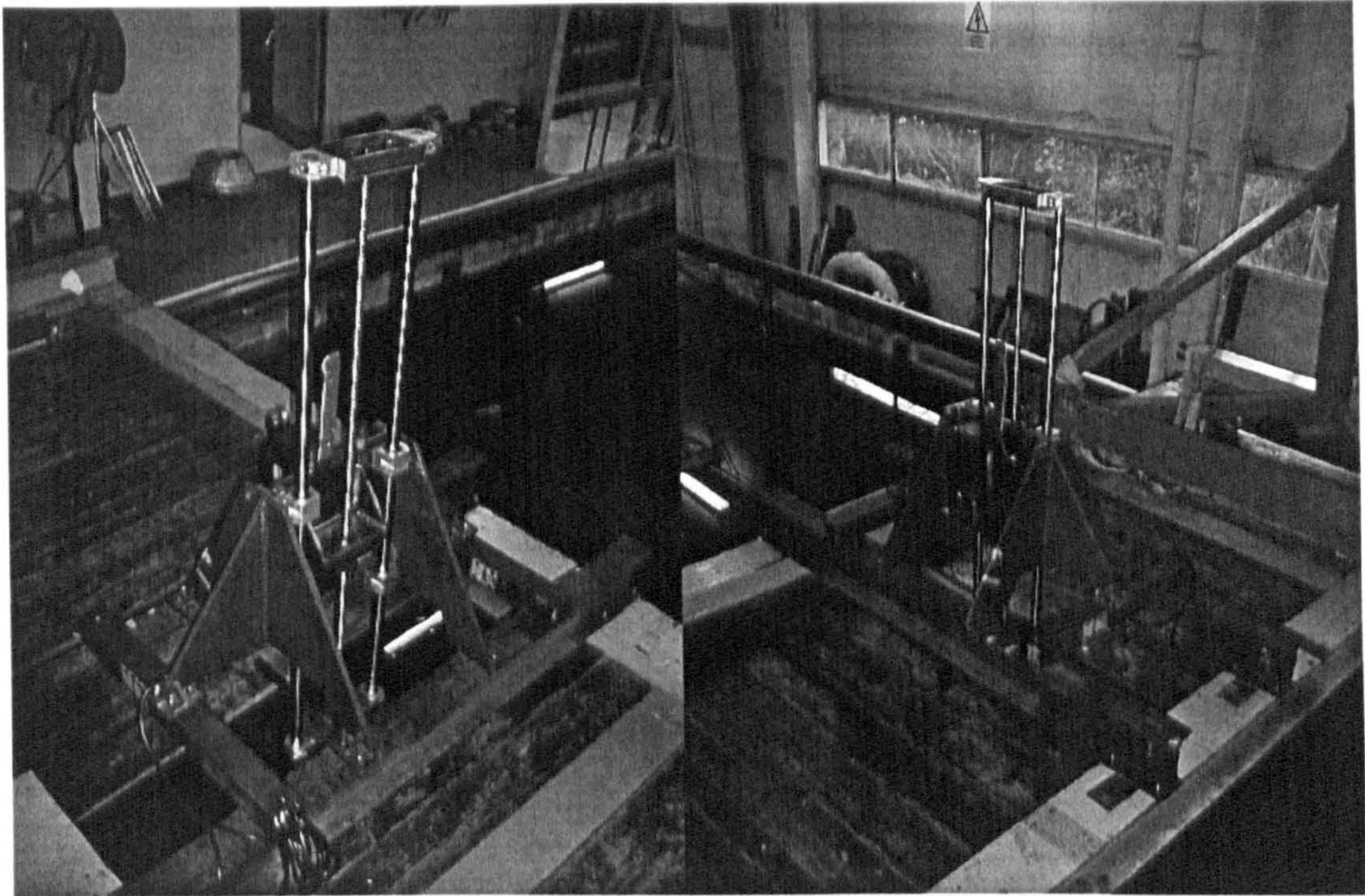


*Figure 5-28. Fully assembled test rig on support structure above the test tank.*

The transparent plates had to be fitted to the model carrier. Holes were drilled along the top of the plates so that they could be bolted on to the designated brackets on the model carrier. 10mm aluminium tube interconnected the corners of the transparent plates to provide lateral stiffness. In addition to this, three stays made of 2mm stainless steel rod were strapped between the two plates near to the wedge surface. The purpose of these was to reduce bulging of the plates due to high pressures near the wedge surface. Additional holes were drilled in the sheets at various locations to allow the stays to be placed differently for each wedge section tested. Figure 5-29 shows various views of the model carrier fitted with the transparent PVC sheets. The bolts seen on top of the model carrier are welded on and engage with the lower assembly bar when connected to the test rig.



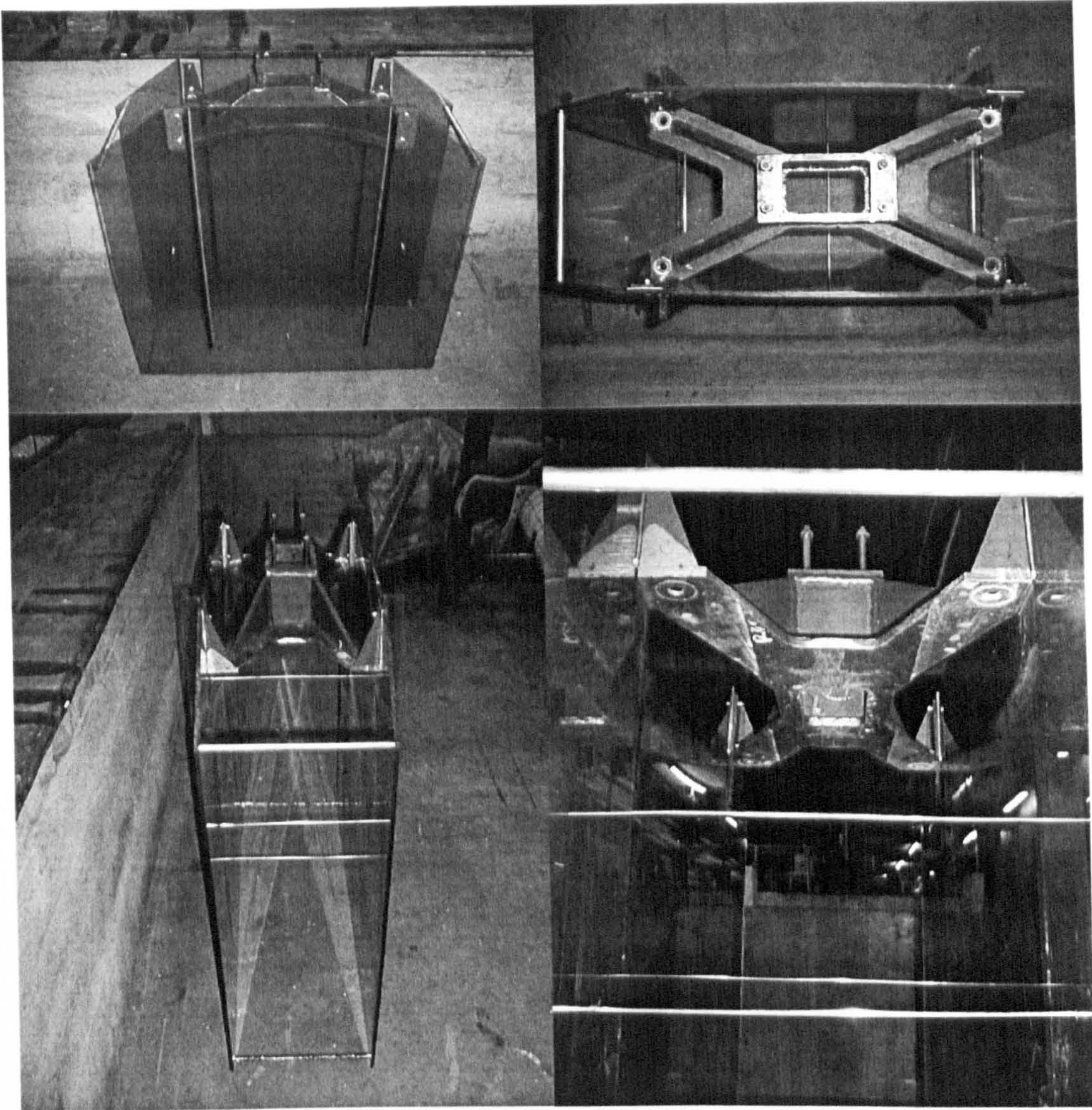


*Figure 5-29. Model carrier and transparent plates.*

Before bolting the model carrier to the lower assembly bar on the guide frame, the box section was fitted. The box section was connected to the model carrier via the four load cells as seen in Figure 5-30. All loads acting on the model section would therefore be transferred via the load cells. It was important to ensure that there was a clearance between the model section and the transparent sheet, and also that this clearance was kept to a minimum. The clearance was set at 2-3mm. A clearance was vital to avoid friction between plates and model, something that could cause a partial load to be transferred to the model carrier without being registered by the load cells. The clearance was kept as small as possible to avoid



water flow through the gap, something that would introduce three-dimensional flow effects.

For easy swapping of wedges between tests without disconnecting the box section from model carrier, the wedges were attached to the box section by band strapping. Figure 5-31 shows the strapping technique that was used.

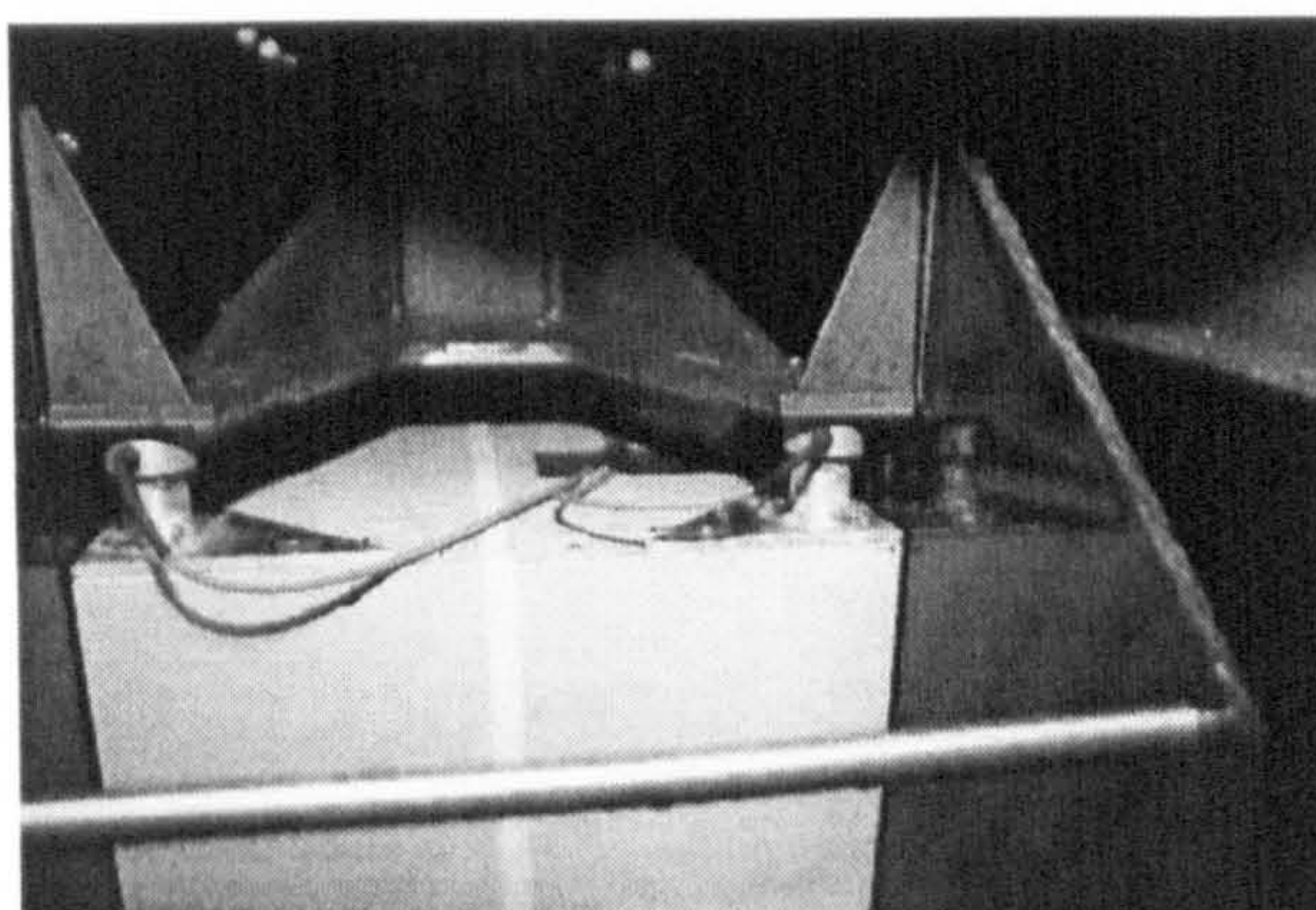


*Figure 5-30. Attachment of box section to model carrier via load cells.*

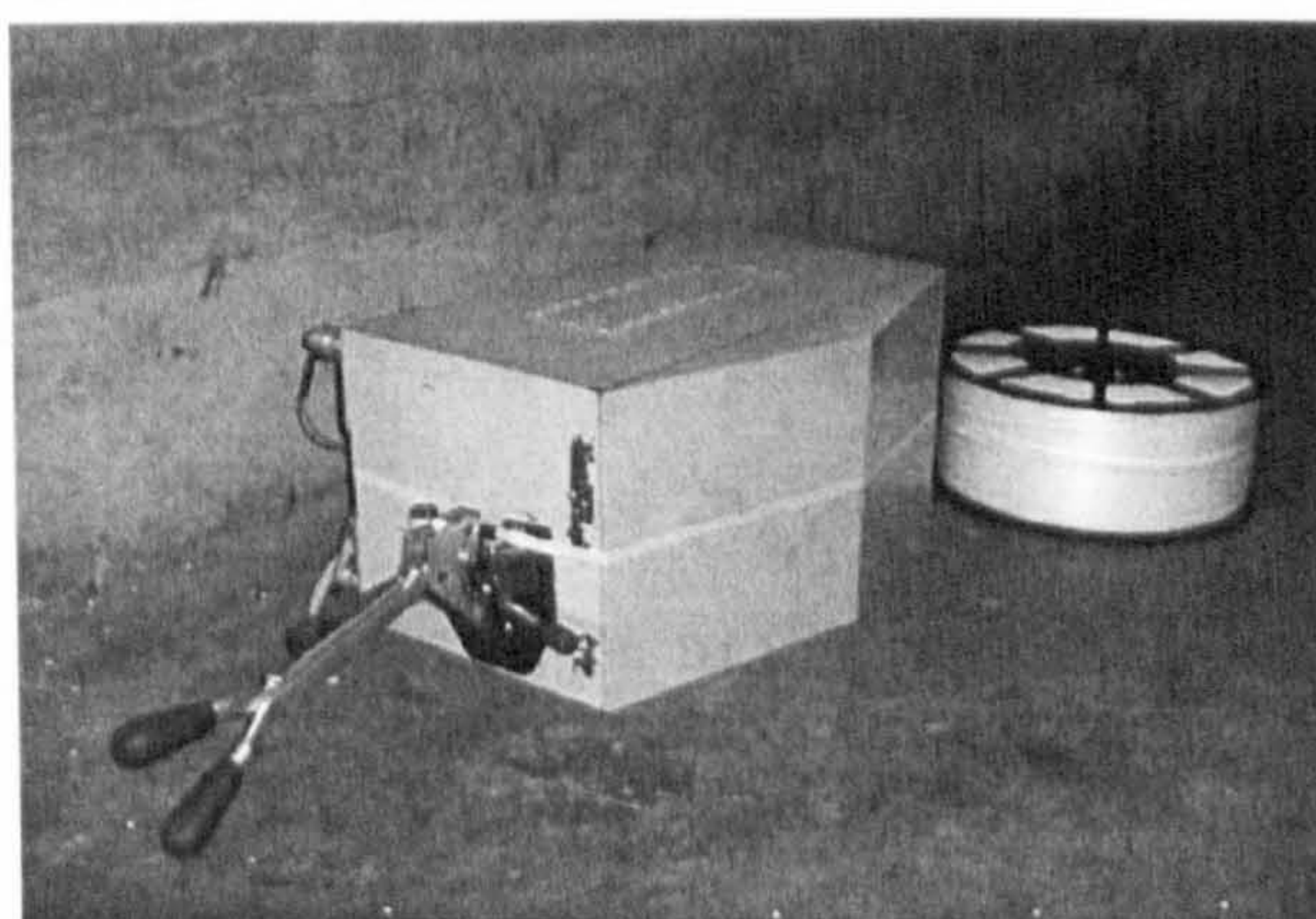


*Figure 5-31. Attachment of wedge section to box section by band strapping.*

The last assembly stage was to connect the model carrier to the test rig by bolting it on to the lower assembly bar. Figures 5-32 and 5-33 shows images of the complete test rig. Figure 5-32 also shows the control position on the main carriage in the background. The guide frame was in its upper position when the picture was taken. Note that the lower ends of the transparent plates were immersed before the



water entry motion was initiated to reduce any disturbance in the water before model section impact.

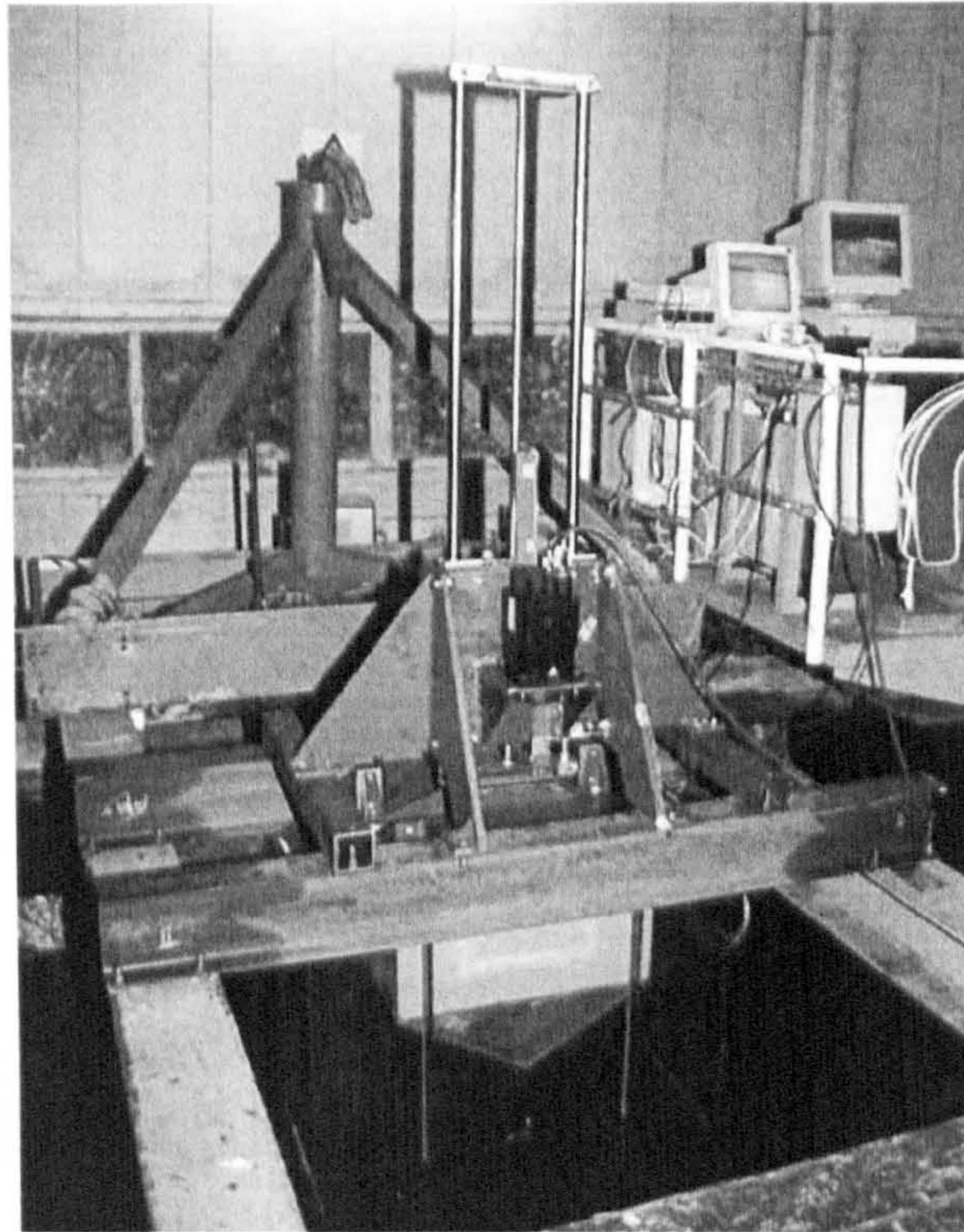


*Figure 5-32. Fully assembled rig with model carrier mounted on lower assembly bar, control station in the background.*



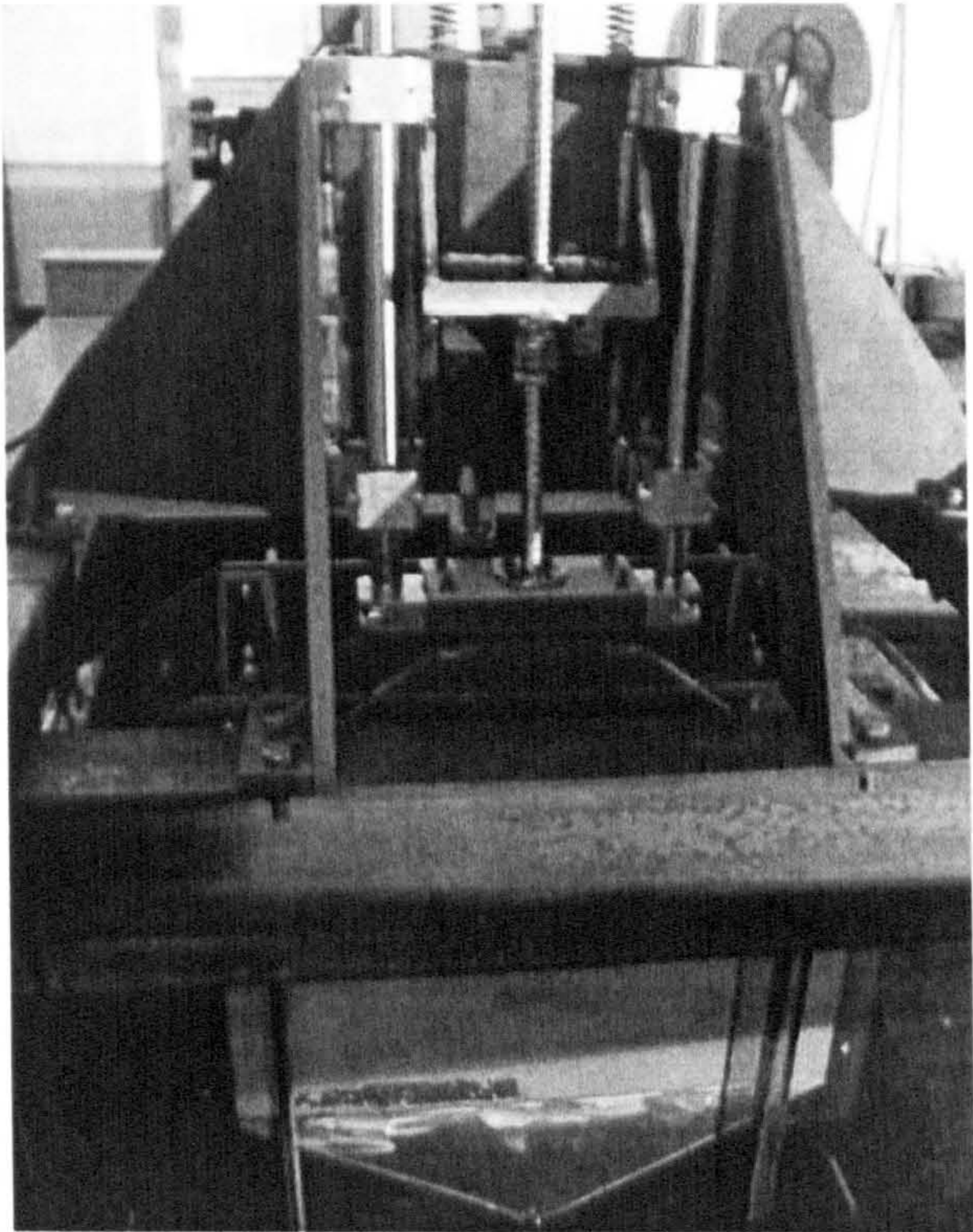


Figure 5-33. Assembled rig from reverse angle.



5.5. Operation of Test Rig

The software provided with the motor/controller system simplified commissioning and programming of the system. The user-friendly graphical interface (Figure 5-34) for programming of motion tasks made operation possible by personnel not qualified as control engineers.

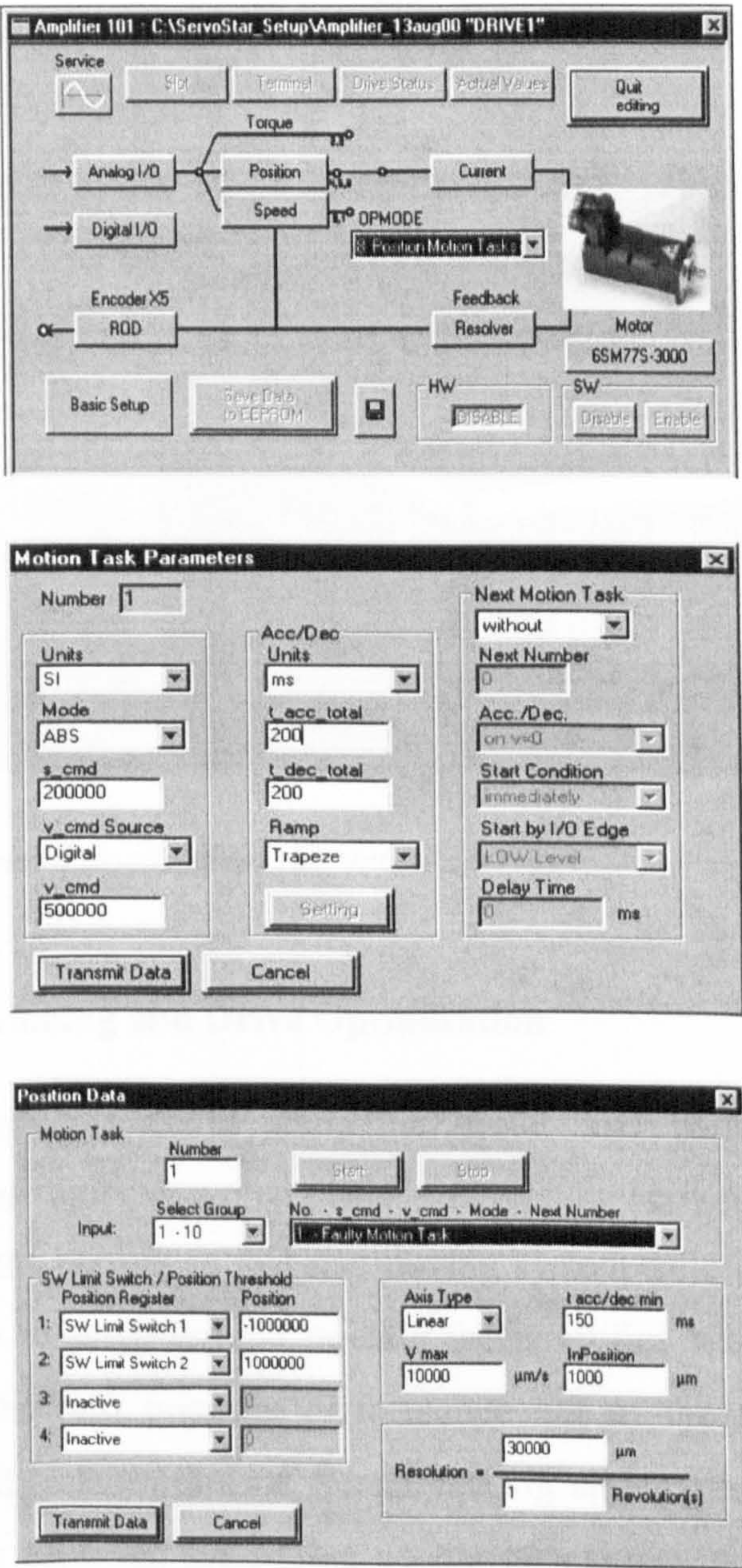
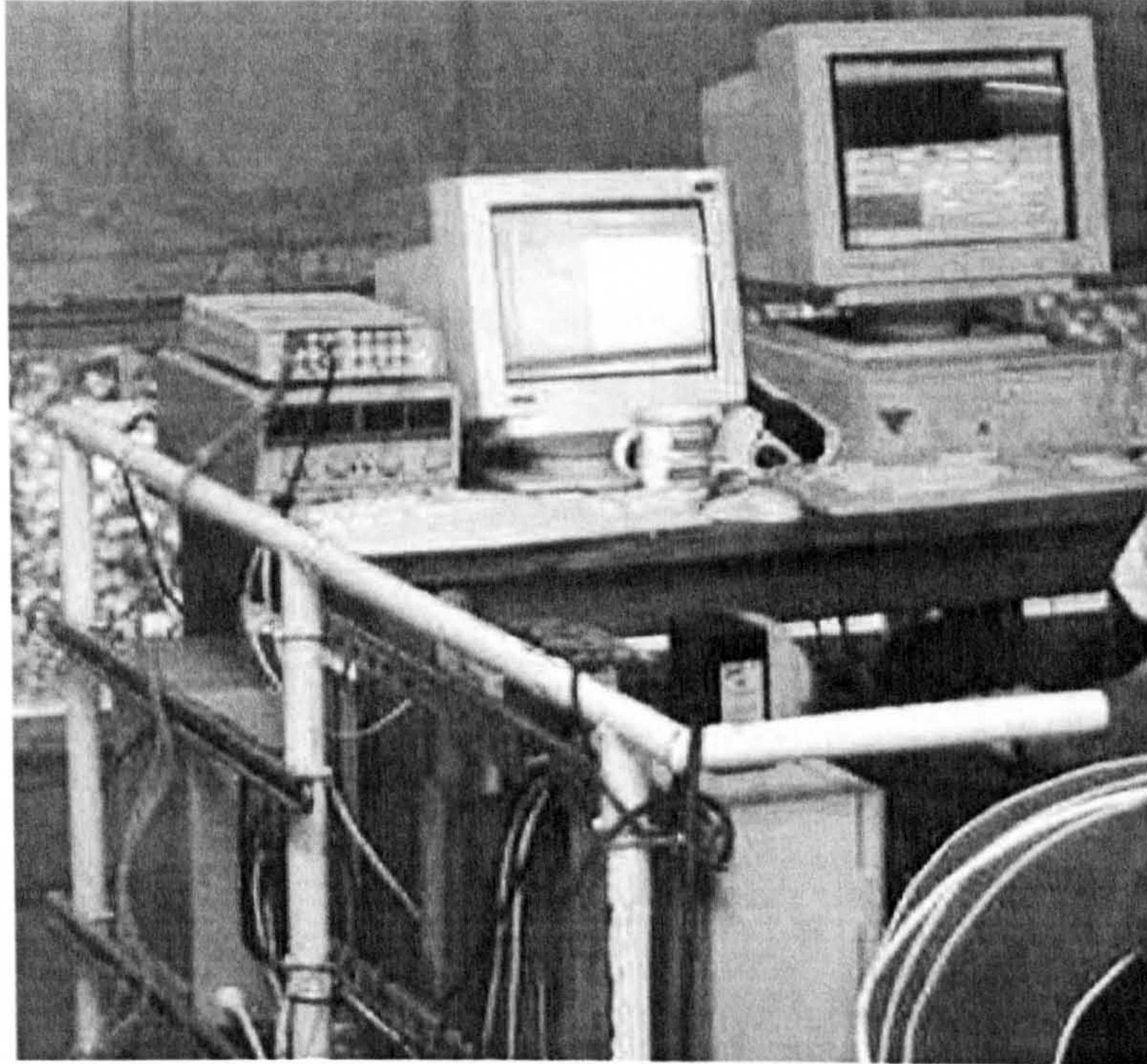


Figure 5-34. Graphical user interface for operation of Servostar digital servo amplifier.



One of the practical features was that pre-set ratios linked the linear motion to the rotary motion. This allowed all the operations to be programmed in terms of linear motion rather than rotational, which simplified the programming and handling in general. Figure 5-35 shows the control position on the main carriage, from where the rig was operated.



*Figure 5-35. Control position on the main carriage.*

#### **5.5.1. Commissioning and Drive Optimisation**

Before the experiments could start, the motor and controller system was commissioned. The digital servo amplifier controls the servomotor. The amplifier constantly varies the current so that the moving system follows a specific motion task. PC-software to program and operate the amplifier was supplied with the system. To get the best possible performance out of the system, the control parameters needed to be optimised for the test rig application. Guidelines in the user manual were followed for setting up the parameters, and then final tuning was carried out by trial and error. The velocity data showed a cyclic nature that was initiated by the impact, and an effort was made to minimise the range of these



fluctuations, aiming to maintain as constant velocity as possible during the water entry. However, it was found that a set-up that minimised the velocity deviation caused velocity fluctuations that were of low amplitude, but of high frequency, such that there were large fluctuating accelerations associated with the small velocity variations. Hence, there was trade off between the magnitude of the fluctuating acceleration and the range of the velocity fluctuations, i.e. the magnitude of the velocity deviation. The commissioning of the equipment involved fine-tuning of the control parameters. The most sensitive parameter, and the one having the greatest impact on how well the velocity was maintained during water entry tests, proved to be the proportional gain of the velocity controller,  $KP$ , which was set at 7. The proportional gain for the position controller was set at 0.25. The feed-forward factor that can be adjusted to ease the task of the position controller was set at 0.4. The final parameter, the integration time constant  $T_n$ , was set at 20. Motor parameters such as maximum speed and current were also programmed into the amplifier memory via the software.

### 5.5.2. Motion Tasks

The controller takes as its input a speed command, a current command or a position command. In the position command mode, various motion tasks can be programmed and executed successively. Once a position reference point is set, the controller can move the frame to an absolute position. Carrying out such a command also involves input of the speed required during the movement, the acceleration time up to the commanded speed and the time for decelerating before coming to rest at the commanded position. Upon successful execution of the first motion task, a new motion task can be executed either directly, or after a programmed delay time. The memory of the digital amplifier (controller) allows up to 180 motion tasks to be stored.

### 5.5.3. Limit Switches

The length of travel for the model carrier is limited to about 1.0m by the dimensions of the guide frame. This corresponds to about 33 revolutions for the servomotor. The peak current the amplifier is capable of delivering to the motor is

20A. The torque generated with this current input is 34Nm, which gives a linear force on the ball screw of 7.1kN. If an amplifier error or a fault in programming causes the guide frame to move outwith the physical limits of travel, this force would most certainly cause damage to the equipment. Also, this force is above the buckling strength of the ball screw. To prevent a failure, it is possible to program absolute end positions into the software, i.e. software limit switches. If the position comes outside these limits, an emergency brake with subsequent standstill torque is engaged. Because the angular position of the motor is used to find the position, such a safety system is not failsafe. If the reference point is set by error at a wrong position, or if there is a shift in pulley and motor shaft relative position, the software switches might not be engaged before end of travel is reached.

For a better guarantee of keeping the guide frame motion within the absolute limits of travel, hardware switches were installed. Setting a minimum emergency stop time configures the emergency brake sequence. Depending on the emergency stop time and the maximum velocity, the frame position at which the limit switches were to be activated was decided. Because of their easy installation and low cost, proximity switches were chosen as the limit switches for the test rig application. A proximity switch works such that if a magnet comes within certain proximity of a sensor, a circuit is broken. Designated 24V circuits for a positive and a negative limit switch are incorporated with the servo amplifier. If the negative circuit is broken, only movements in the positive direction are allowed and vice versa. Magnets were glued on to the upper and lower assembly bars. The hardware limit switches are located such that on upwards motion the emergency brake is engaged just before the lower assembly bar reaches the linear ball bearings on the drive frame, and on downward just before the load cells are immersed. The arrangement is shown in Figures 5-36 and 5-37.



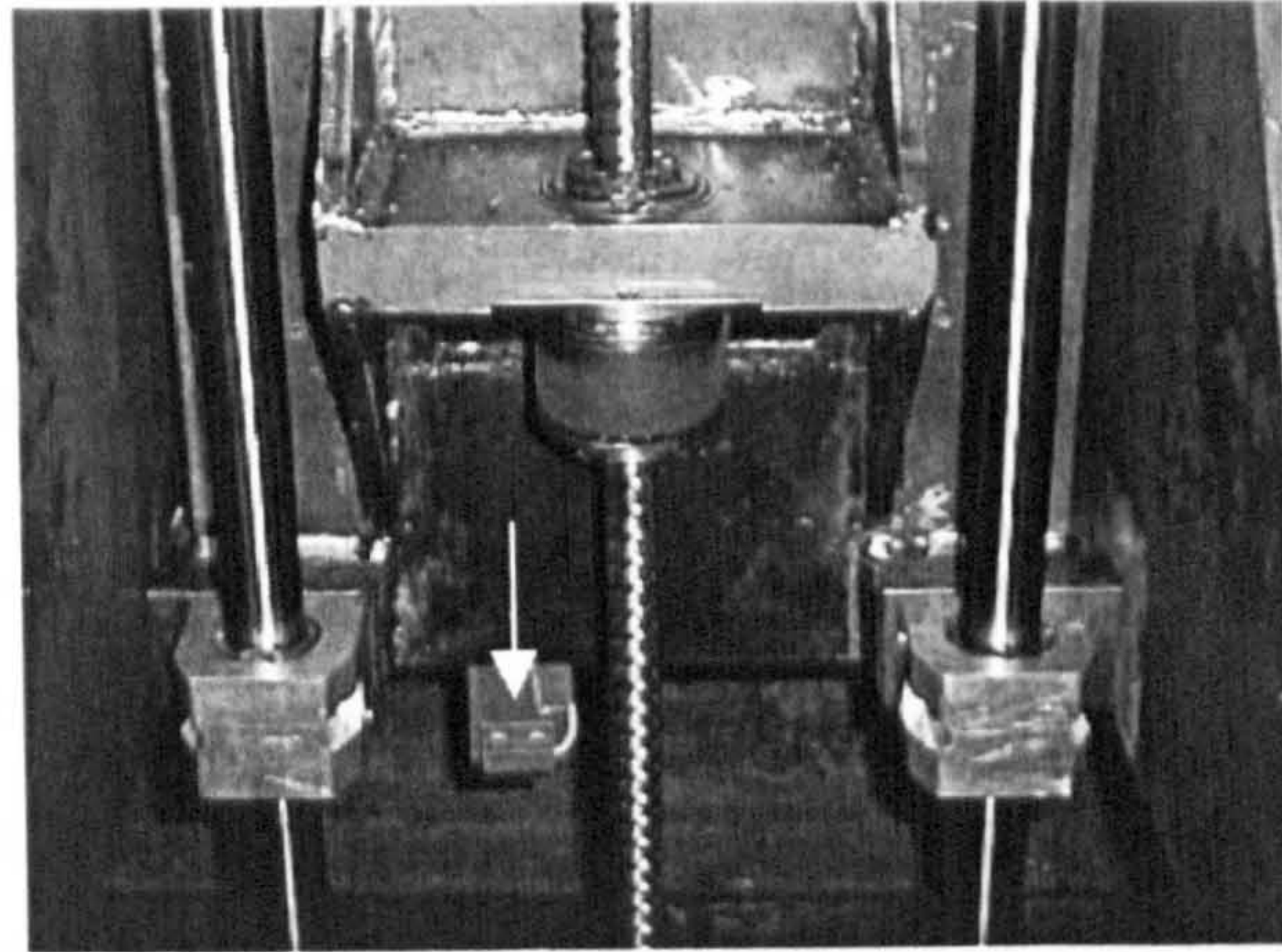


*Figure 5-36. Lower limit switch.*

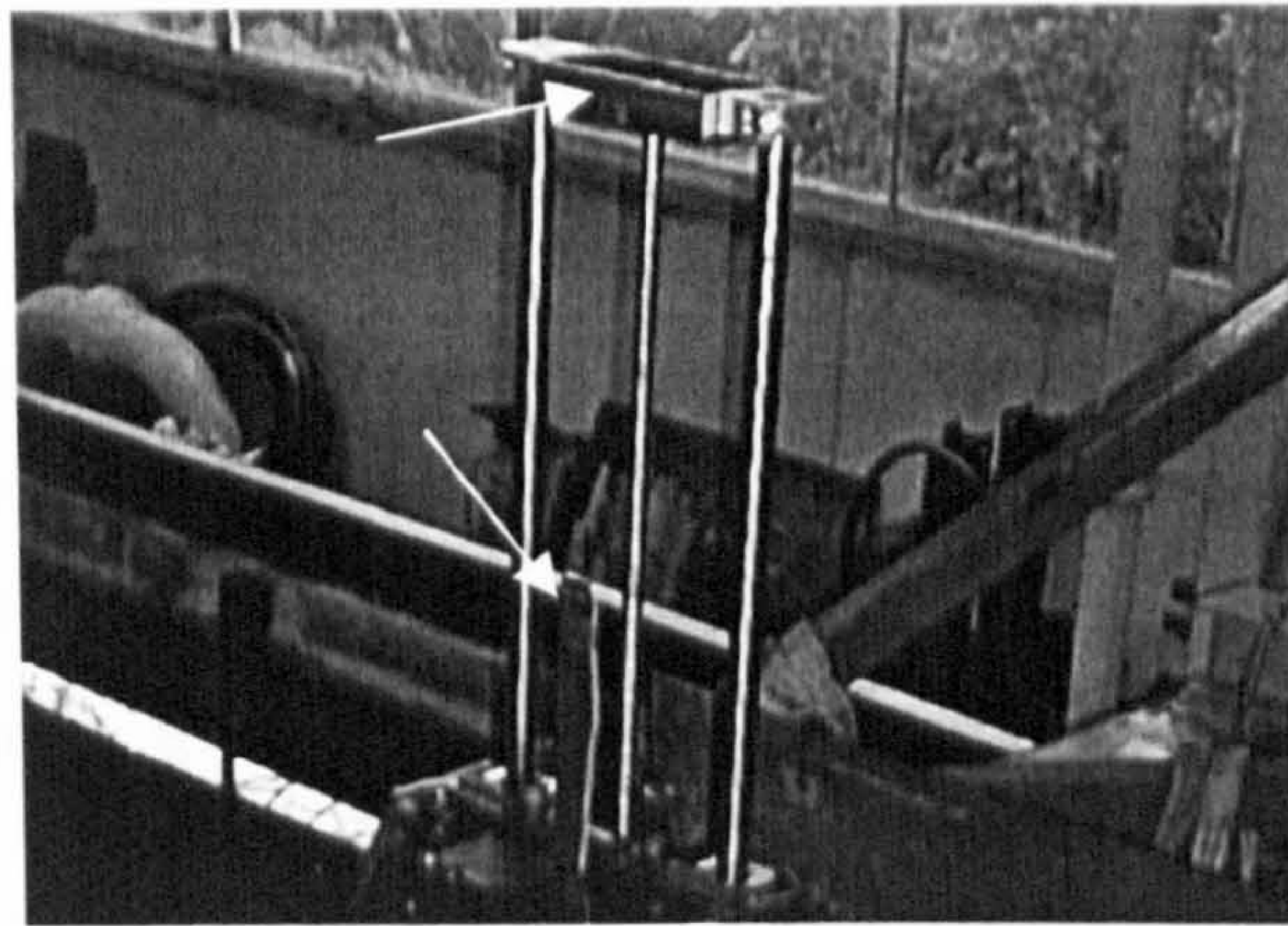


*Figure 5-37. Upper limit switch and magnet on assembly bar.*

#### **5.5.4. Data Acquisition**

The Strawberry Tree data acquisition system provides 16 channels for simultaneous data logging. In the present experimental set-up only 5 channels were used, 4 low voltage signals from the load cells and one  $\pm 10V$  signal of motor speed from the servo amplifier. Data logging was controlled via PC software. The low voltage output signal from the load cells depends on the excitation voltage into the cell. To ensure that the excitation voltage was the same for the tests as during calibration, the load cells were calibrated as connected to the data acquisition system. A practical feature of the data logger software was that the calibration data for each cell, consisting of the zero load voltage and the voltage



per kg, could be fed into the system. This allowed the calibrated load to be directly recorded for every sample instead of the load cell voltage.

### **5.5.5. Video Recording**

A video camera was set up just above the water level so that shape of the free surface during entry and exit tests could be monitored and recorded. The monitor and video recorder were positioned on the side of the test tank next to the control position on the main carriage so that one person could control all the equipment.

## **5.6. Test Program**

### **5.6.1. Constant Velocity Water Entry**

During the water entry tests, the servo amplifier was programmed to start the run from the guide frame's top position. The distance from the keel to the water surface when at this position varied with deadrise angle from less than 100mm with the largest angle to about 350mm with the smallest. The time allowed for acceleration was calculated and programmed such that entry velocity was achieved just before initial impact. Keeping the acceleration low minimises initiation of vibrations in the structure and thus reduces noise in the force signal from the load cells.

The constant velocity water entry motion task was programmed to stop downward motion before the load cells immersed. Deceleration time was set such that constant velocity was maintained until the whole of the wedge and approximately 2/3 of the box section was immersed. After 1 second stationary at the lowest position, the amplifier was programmed to do a slow ascent up to the top position. Next run commenced after a period of about 5 minutes to allow the water to calm down.

Every program was performed four times to check repeatability of the force readings. For each run, data recording started just before the entry motion program was engaged and stopped after the model had come to rest at the lowest

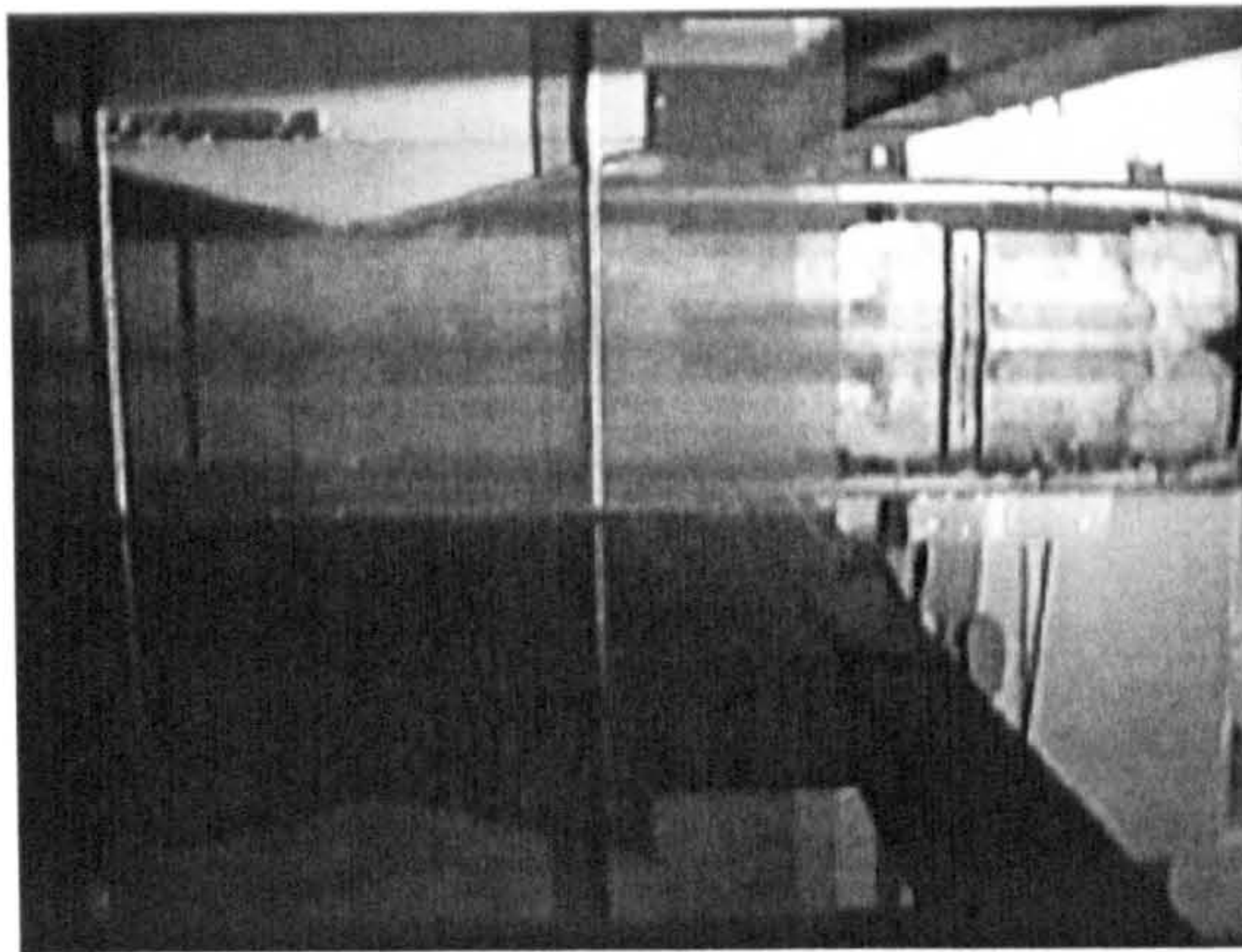


position. The sample rate varied from test case to test case. During the 5-degree wedge section water entry at the highest velocity (0.94m/s), the force increased from zero to peak in about 18ms. The sample rate applied for this case was 500Hz. This gave 9 recorded force measurements from initial impact to peak force occurrence. During the 30-degree wedge entry at the lowest velocity (0.48m/s), the time before peak force occurred was approximately 120ms. For this case the force measurements were sampled at a rate of 100Hz, which gave 12 recorded force measurements from initial impact to peak force occurrence. For all the other cases sample rates varied between 100Hz and 500Hz.

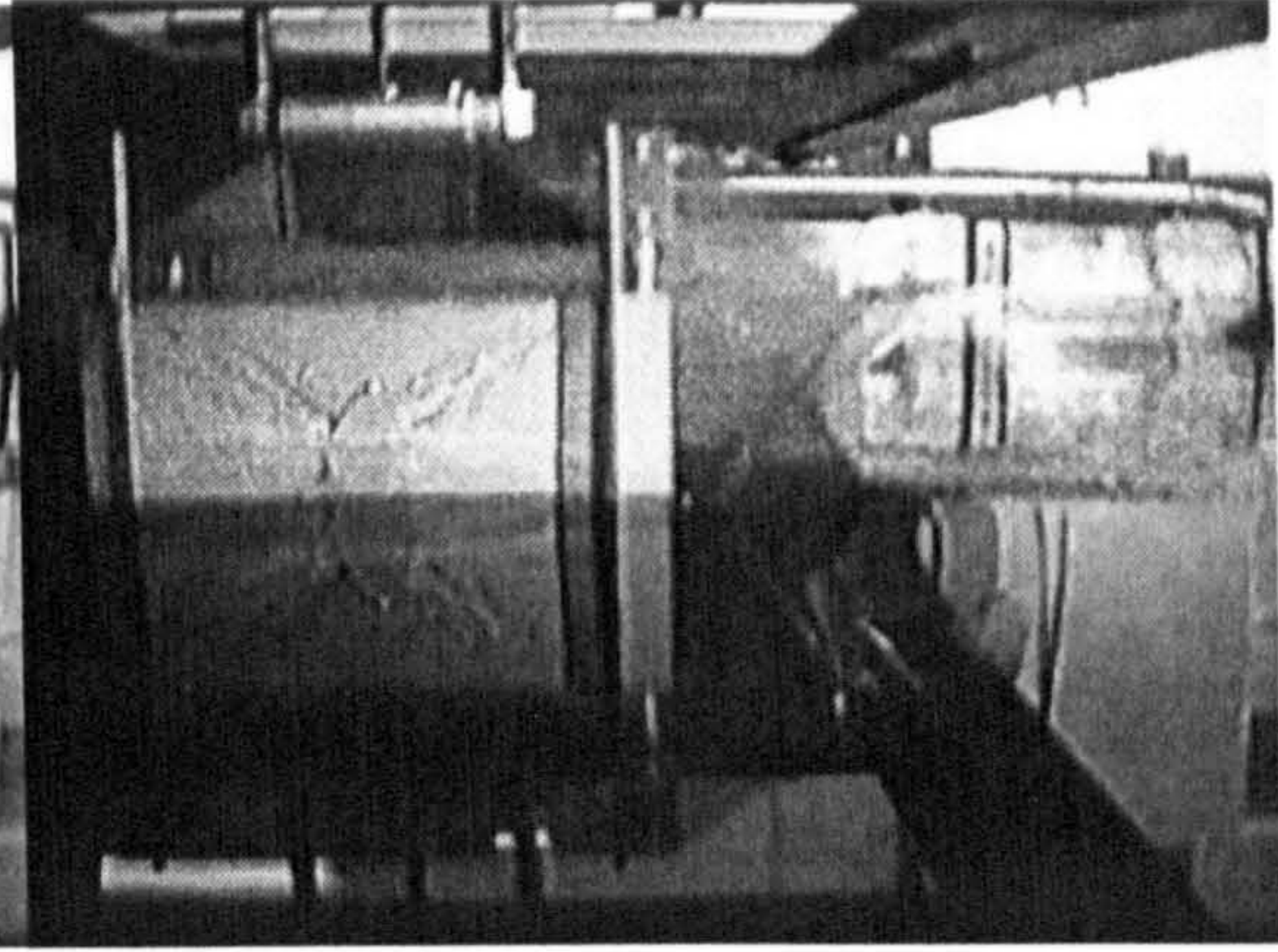
All but the 5 and 45 degree sections were tested at 0.48, 0.72 and 0.94m/s. The experimental results were to be used to extract the hydrodynamic force contribution. The greater the hydrodynamic contribution compared to the hydrostatic, the more accurate will be the results. How prominent the hydrodynamic force is depends on the angle of deadrise. It is known that the entry force acting on a low deadrise angle wedge is greater than the force acting on a high deadrise one. It is also known that the force drops quickly after chines are wetted. During the early stages after chines wetting, the hydrostatic force is greater for a high deadrise angle wedge than a low deadrise one due to more immersed volume to the undisturbed water level. Thus the 45-degree section requires higher entry velocities for the hydrodynamic force contribution to be prominent. The velocities with this section were therefore 0.72, 0.94 and 1.19m/s. When testing the 5 degree section the above mentioned relation between hydrodynamic and hydrostatic force contribution allowed the tests velocities to be somewhat lower. The velocities with this section were therefore 0.24, 0.48 and 0.94m/s.

Figure 5-38 shows an image of the 15 degree section in the initial position before the downward entry motion starts, and Figure 5-39 after some entry distance.





*Figure 5-38. At initial position.*



*Figure 5-39. After some immersion..*

### **5.6.2. Constant Velocity Water Exit**

All but the 30 and 45 degree sections were tested at exit velocities of 0.48 and 0.72m/s. The 30 degree section was only tested at 0.72m/s and the 45-degree section only at 0.94m/s. Also for the exit tests, the velocities were taken greater for high deadrise angle sections than low ones so that the hydrodynamic force would be prominent.

The motion program was set so that the section slowly moved to a depth at which the box section was about 80% immersed. Velocity during the immersion to the start position was set to 0.05m/s. It was set as low as this to minimise the disturbance of the water. A delay of 2 seconds was programmed, before an acceleration upwards was engaged. The acceleration time was set so that exit velocity was achieved after 0.1m of travel. Constant velocity was maintained until deceleration was engaged so that motion was stopped before end of limited upward travel. Figure 5-40 shows an image of the 15 degree section at rest in the lower position before upwards acceleration is engaged, while Figure 5-41 shows the section at constant exit velocity some distance above the calm water level.



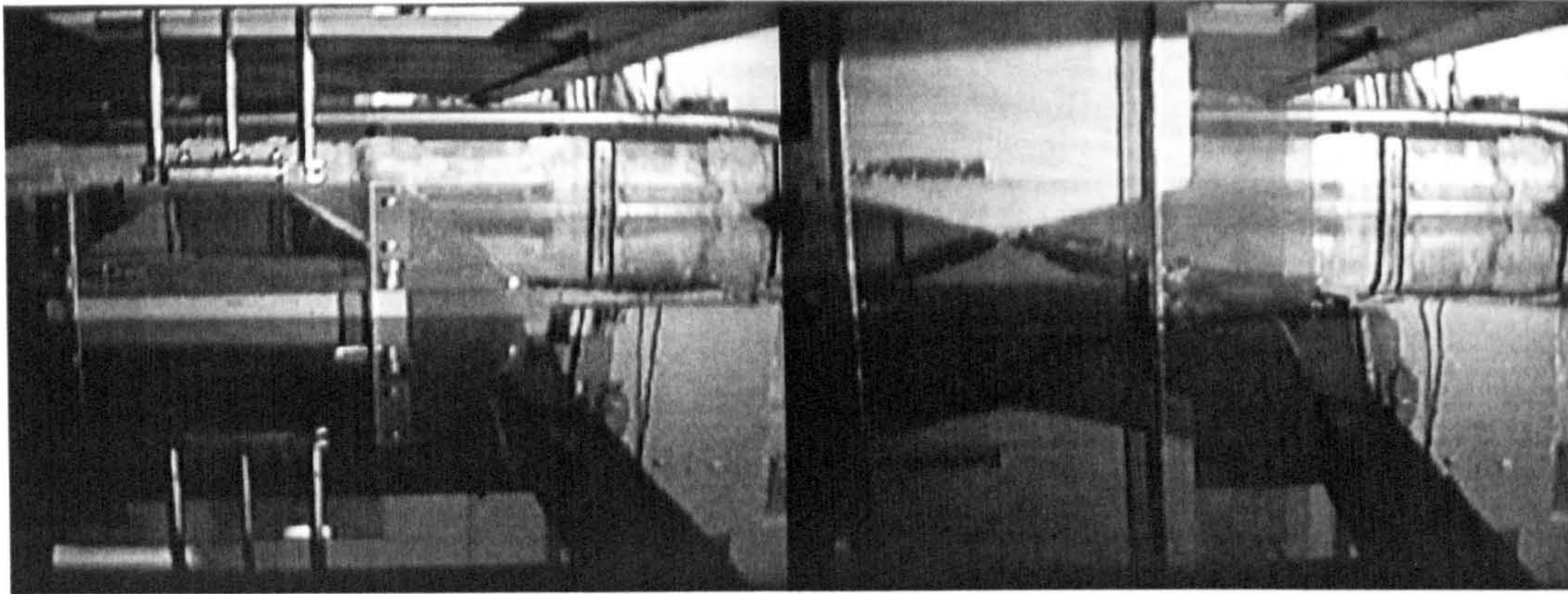


*Figure 5-40. At initial position.*

*Figure 5-41. After some exit travel.*

### **5.6.3. Accelerated/Decelerated Water Entry**

A series of water entries with acceleration or deceleration were carried out with the 15, 30 and 45 degrees sections. During the accelerated tests the initial position above the water level, before downward motion was engaged, varied for each case. This was done to obtain the desired velocity range during the dry chines stages of the entry. Each section was tested at two accelerations. The motion tasks were programmed such that there was constant acceleration until the chines were wetted, after which a deceleration was engaged to stop the movement. Then the program instructed the section back up to the starting position awaiting the water to calm down before a new test commenced.

The decelerated water entries were always started at the highest possible position. The motion task was programmed such that a certain velocity was achieved during the downward motion. This velocity was maintained until the instant of initial impact after which the motion task was programmed to engage a constant deceleration. This deceleration was maintained until the section came to rest, after which a slow ascent back to the start position was engaged.

### **5.6.4. Oscillation Tests**

The oscillating motion was conducted by repeatedly executing two motion tasks, one after the other. One task was programmed to move from an upper position to a lower position with a constant acceleration for half of the distance and a



constant deceleration for the other half. The other motion task was executed immediately upon the section reaching the lower position and was programmed such that there would be the same upward acceleration for half the distance toward the upper position and the same upward deceleration for the other half. During a complete cycle, all the accelerations/decelerations were of the same absolute magnitude. This created an oscillating motion where the acceleration is positive and constant when the section is above mid level and negative and constant when the section is below mid-level.

#### 5.6.4.1. Wet Chines

Wet chines oscillating tests were carried out with the 15- and 45-degrees sections and also with the bare flat-bottomed box section. For all three sections, the amplitude of the cycles was 0.025m and the maximum velocities at mid-level were  $\pm 0.3\text{m/s}$ . Given that the acceleration magnitude was constant it follows that the cycle period was 0.67s. All wet chines oscillations had approximately 0.2m chines immersion at mid-level. The force measurements were recorded for about 10 seconds at a sample rate of 200Hz.

#### 5.6.4.2. Dry Chines

The dry chines oscillations were carried out with the 15 and 45 degree sections. A small and large amplitude (relative to vertical keel to chine distance) test was carried out with both test sections. The 15 degree section large amplitude test had 0.035m immersion at mid-level and amplitude of 0.025m. Mid-level velocity was 0.3m/s and the cycle period was 0.67 second. The small amplitude test had 0.030m immersion at mid-level and amplitude of 0.01m. Mid-level velocity for the small amplitude tests was 0.2m/s and the cycle period was 0.4 seconds. The 45 degree section large amplitude test had 0.15m immersion at mid-level and amplitude of 0.1m. Mid-level velocity was 0.5m/s and the cycle period was 1.6 seconds. The small amplitude test had 0.225m immersion at mid-level and amplitude of 0.025m. Mid-level velocity for the small amplitude tests was 0.3m/s and the cycle period was 0.67s. Force measurements were recorded for about 10 seconds at a sampling rate of 200Hz for all the dry chines oscillation tests.



### 5.7. Test Rig Performance

The test rig performance has been evaluated by the maximum deviation from the initial velocity during the constant velocity water entry tests. These tests presented the most demanding tasks for the test rig's velocity control system due to the rapidly increasing nature of the dry chines impact force. The maximum deviations from the maximum velocity demands with the various test sections are given in Table 5-2.

$\beta$ [deg]	Velocity deviation
5	0.6 %
10	0.5 %
15	0.8 %
30	0.3 %
45	0.4 %

*Table 5-2. Maximum velocity deviation during constant velocity water entry.*

It is seen from the table that the 10 degree velocity deviation is 0.5 percent. This is equal to the estimate provided by the motor/controller supplier Heason Technology. However, their estimate was based on the predicted design case force. The maximum test velocity with the 10-degree section was 0.94m/s, and it is reasonable to assume that at the design case velocity of 1.5m/s the deviation would have been higher. It can therefore be argued that the supplier's estimate was rather optimistic. Nevertheless, the velocity deviation is less than 1 percent for all the test cases, i.e. less than the design requirement for the test rig.

## 5.8. Test Results

The data sets recorded with the data acquisition system consisted of the individual load cell readings and a reading of the angular speed of the servomotor transformed into the model carrier velocity. In addition to this, video recordings were made to study the free surface shape as the models entered and exited the water surface.

### 5.8.1. Vertical Position of Test Section

The experimental set up did not include a device for tracking of the absolute vertical position of the test sections during entry/exit. This was because access to such equipment was not available at the time the experiments were undertaken. The velocity data was used to obtain the vertical position. Integration of the recorded velocities gave the relative position of the test section. To allow the absolute position to be calculated, the initial position before engaging each test had to be known. This was done by carefully keeping the model carrier at the same distance from the water each time a reference point was set with the digital amplifier software. By doing so, the initial position of the carrier was always known when a motion program was started. An alternative and more direct approach would have been to use an analog output from the digital amplifier to give the position of the motor in terms of degrees from the reference. However, this would have involved re-programming of the digital amplifier, which could not be done in time for the slot that was given at the test tank facility. It was therefore decided to use the velocity integration approach for finding the position of the system. The accuracy of this method was evaluated by studying the plots of measured force against the vertical position obtained by velocity integration. During an entry test, once constant velocity was achieved but before the test section reached the water surface, the force was scattered (due to signal noise and structure vibrations) about a constant negative value corresponding to the weight of the test section. Once the test section penetrated the water, the force started to increase. By checking that the increase in force started at the same instant as when the position obtained by velocity integration showed zero immersion depth, the



method was evaluated. An example of such a plot is given in Figure 5-42. The nature of the scattered force data did not allow for quantification of the accuracy. However, visual judgement proved the method to be substantially accurate for the present experiments.

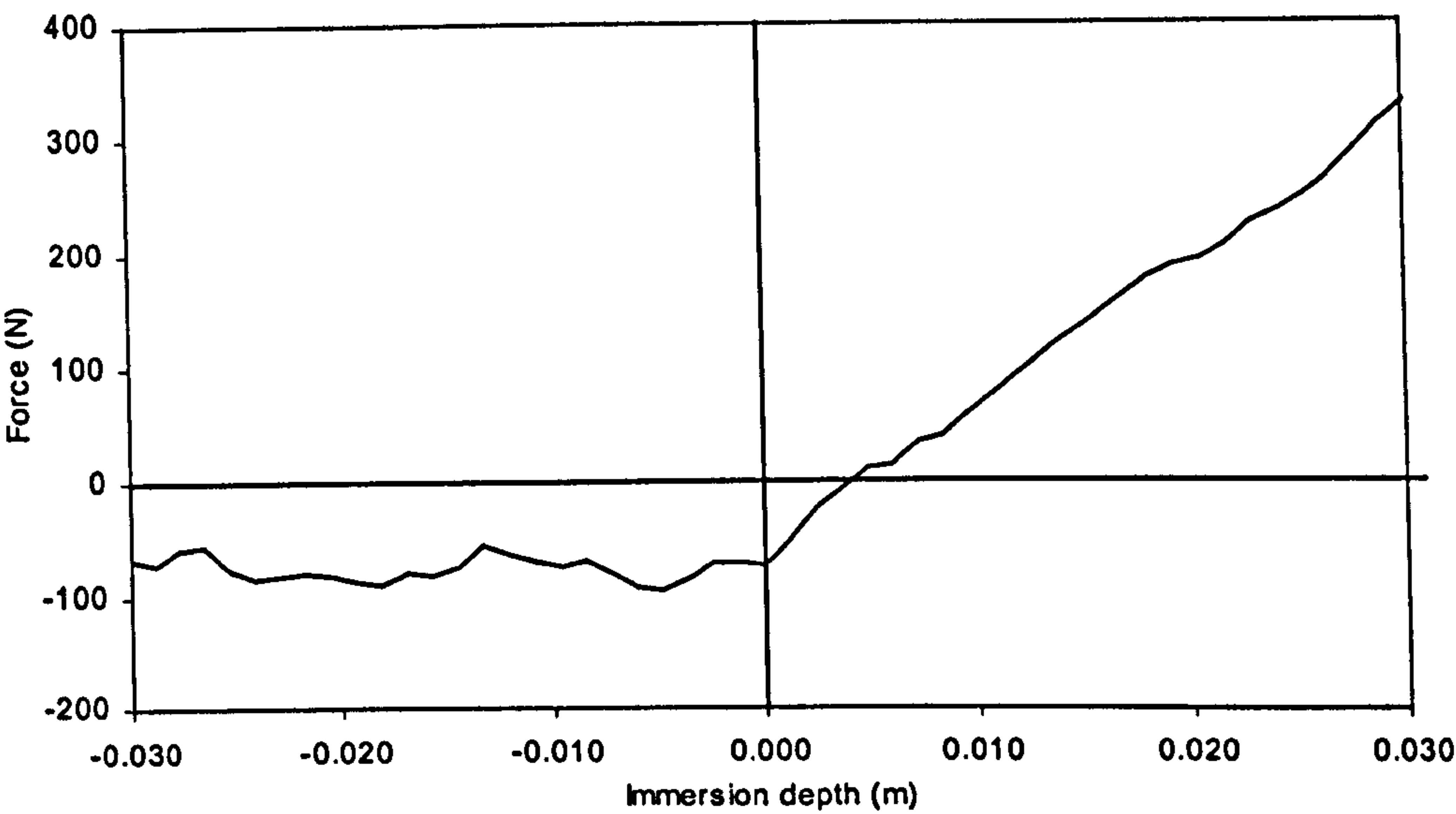


Figure 5-42. Evaluation of velocity integration method for position tracking.

**5.8.2. Viscous Force**

Included in the total water interaction force is the viscous resistance that acts parallel to the wedge surface. During a constant velocity water entry, the force contribution from viscous resistance will be at its largest relative to the dynamic pressure force component when the immersion depth is large, as shown in Figure 5-43.

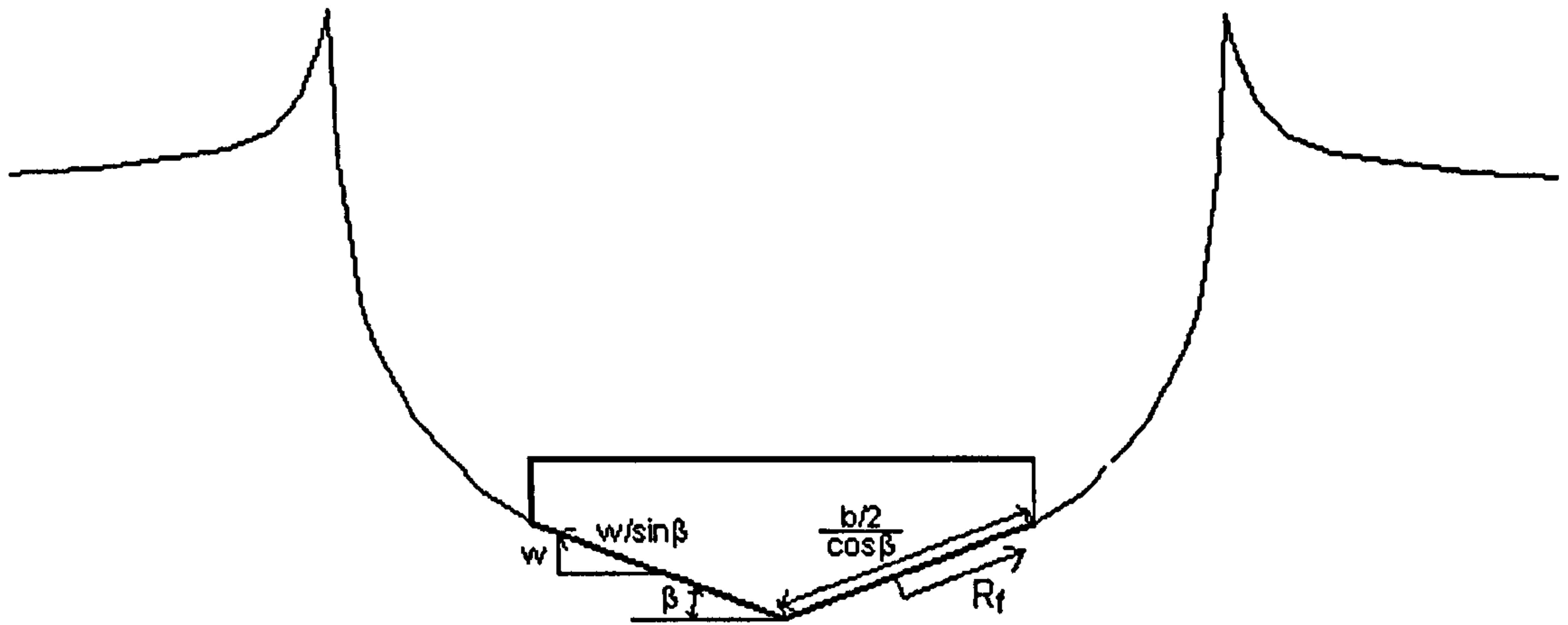


Figure 5-43. Frictional force component.

The viscous resistance coefficient  $C_f$  is Reynolds number dependent. For the purpose of calculating the viscous resistance force, the average velocity along the wedge is assumed to be such that its vertical component equals the entry velocity  $w$ . The velocity parallel to the wedge surface is then

$$V_{ws} = \frac{w}{\sin \beta} \quad (5-1)$$

The Reynolds number is therefore

$$R_n = \frac{V_{ws} \cdot l_{ws}}{\mu} = \frac{w \cdot \frac{b}{2}}{\sin \beta \cdot \cos \beta \cdot \mu} \quad (5-2)$$

Frictional resistance parallel to half-wedge surface

$$R_f = C_f \cdot \frac{1}{2} \rho V_{ws}^2 \cdot l_{ws}$$

$$R_f = C_f \cdot \frac{1}{2} \rho \frac{w^2}{\sin^2 \beta} \cdot \frac{b}{2 \cdot \cos \beta} \cdot l \quad (5-3)$$



Vertical component of the force due to viscous resistance

$$F_f = 2 \cdot R_f \cdot \sin \beta \tag{5-4}$$

Non-dimensional viscous vertical force, on beam

$$C_{F,b-f} = \frac{F_f}{\frac{1}{2} \rho w^2 \cdot b \cdot l} = \frac{C_f}{\sin \beta \cdot \cos \beta} \tag{5-5}$$

The ITTC-line has been applied for frictional resistance coefficient

$$C_f = \frac{0.075}{(\log R_n - 2)^2} \tag{5-6}$$

The frictional resistance coefficient increases with decreasing Reynolds number. Reynolds number is proportional to the velocity. Hence, lower velocity gives greater frictional resistance coefficient. The non-dimensional vertical component of the viscous force has been calculated for all the test deadrise angles. The viscous force as a proportion of the total force will be highest when the entry velocity is at its lowest and at deep immersions when the non-viscous force is at its lowest. The calculations were carried out for these conditions as a worst case. The deadrise angles, velocities and resulting non-dimensional vertical viscous forces are given in Table 5-3.

$\beta$	w	$C_{F,b-f}$
5	0.24	0.056
10	0.48	0.028
15	0.48	0.021
30	0.48	0.014
45	1.19	0.01

Table 5-3.      *Non-dimensional viscous force.*

The percentage contribution of the viscous resistance to the total hydrodynamic entry force has been calculated by use of CFD simulations of the test conditions that were carried out at a maximum non-dimensional immersion depth of  $z/d=3$ . The non-dimensional force, on beam, at this stage for the zero-gravity simulation is given in Table 5-4, together with the calculated percentage of viscous contribution.

$\beta$ [deg]	CFD $C_{F,b}$	VISCOUS/ TOTAL [%]
5	2.9	1.9
10	2.2	1.3
15	1.9	1.1
30	1.3	1.1
45	0.68	1.5

Table 5-4.     *Viscous contribution to the total force.*

Table 5-4 shows that the estimated viscous force is less than two percent of the total hydrodynamic force for all cases. Considering that the percentages in Table 5-4 are calculated using the highest expected viscous force contribution and lowest total force, it is concluded that the viscous force contribution can be regarded as negligible throughout.

**5.8.3.   Force Data**

The data logger was activated just before each test started, i.e. when the velocity was zero. The sum of the force readings from the four load cells, before motion is started, add up to the weight of the test section, comprising box and wedge, that was mounted under the model carrier via the load cells. This force is constant



throughout one test, and is therefore subtracted from the total force reading of all data sets in order to obtain the force due to interaction with the water.

For each test case, four runs were performed with the same motion program. In general, the results from the four runs compared well and demonstrated high repeatability. In Figure 5-44 the force data after subtracting the weight of the test section for four identical tests of constant velocity water entry are plotted as an example. The force data from the four identical tests were averaged for each case, before the force data were subjected to further analysis.

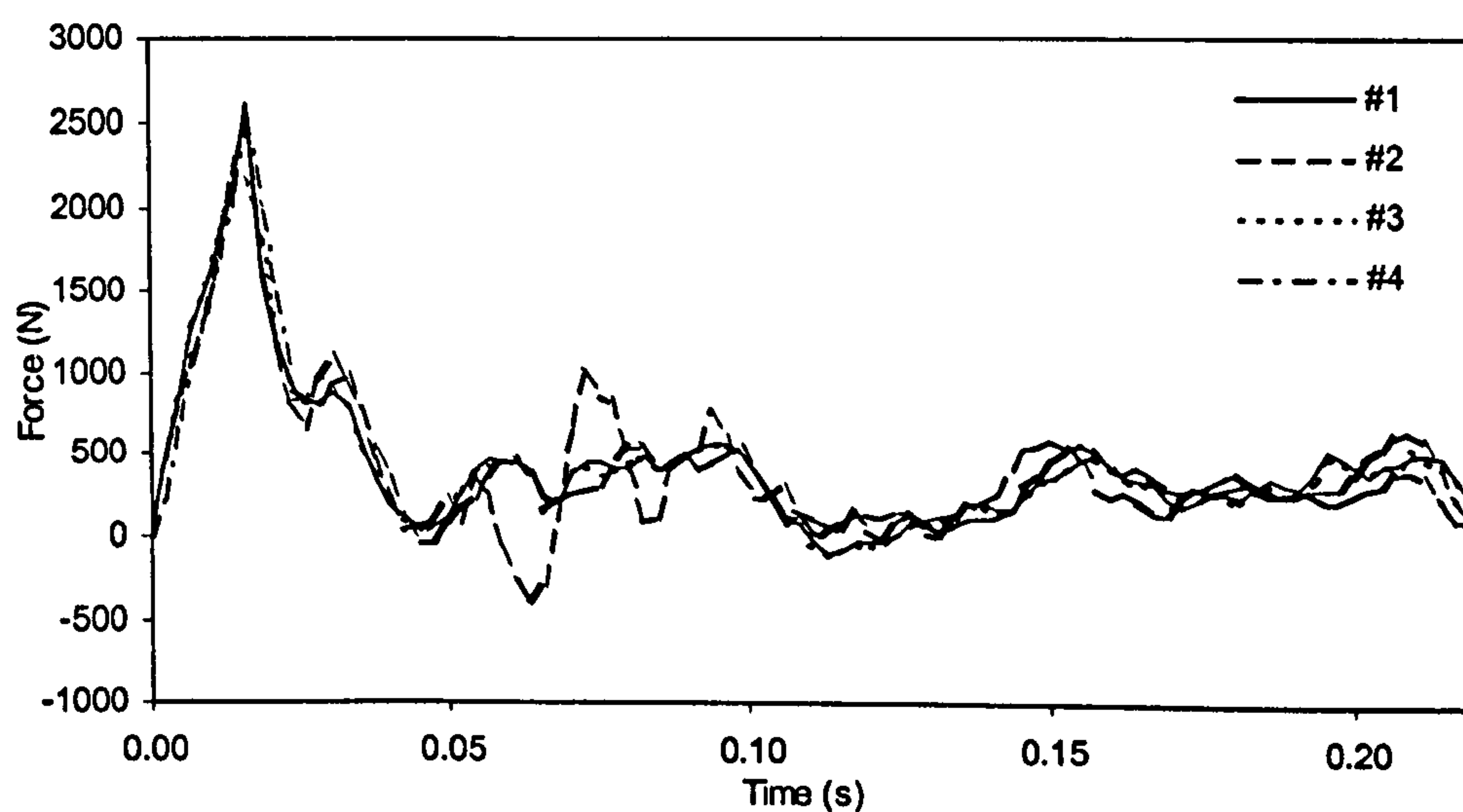


Figure 5-44. Force readings from four tests with 5 degrees wedge at 0.94 m/s.

#### 5.8.3.1. Constant Velocity Water Entry Tests

The force due to interaction with the water during a constant velocity water entry is

$$F = F_{4LC} - M_M \cdot g \quad (5-7)$$

where  $M_M$  is the mass of the test section and  $F_{4LC}$  is the sum of the load measured by the four load cells.

The resulting averaged forces obtained with the constant velocity water entry experiments are plotted for each test case in Figures 5-45 to 5-57. The velocity outputs from the digital amplifier are plotted in the same charts.

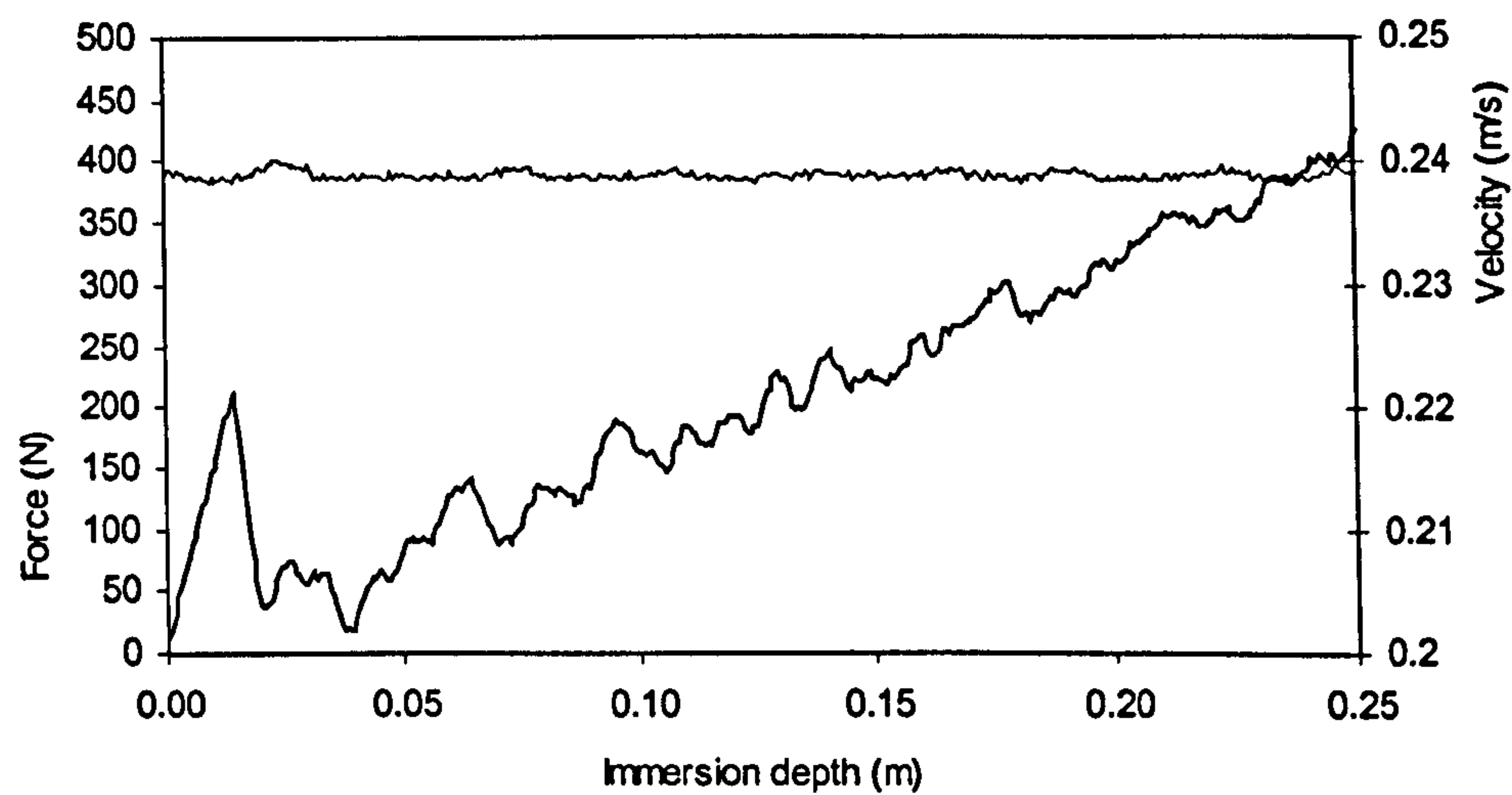


Figure 5-45. 5 degree constant velocity water entry at 0.24m/s.

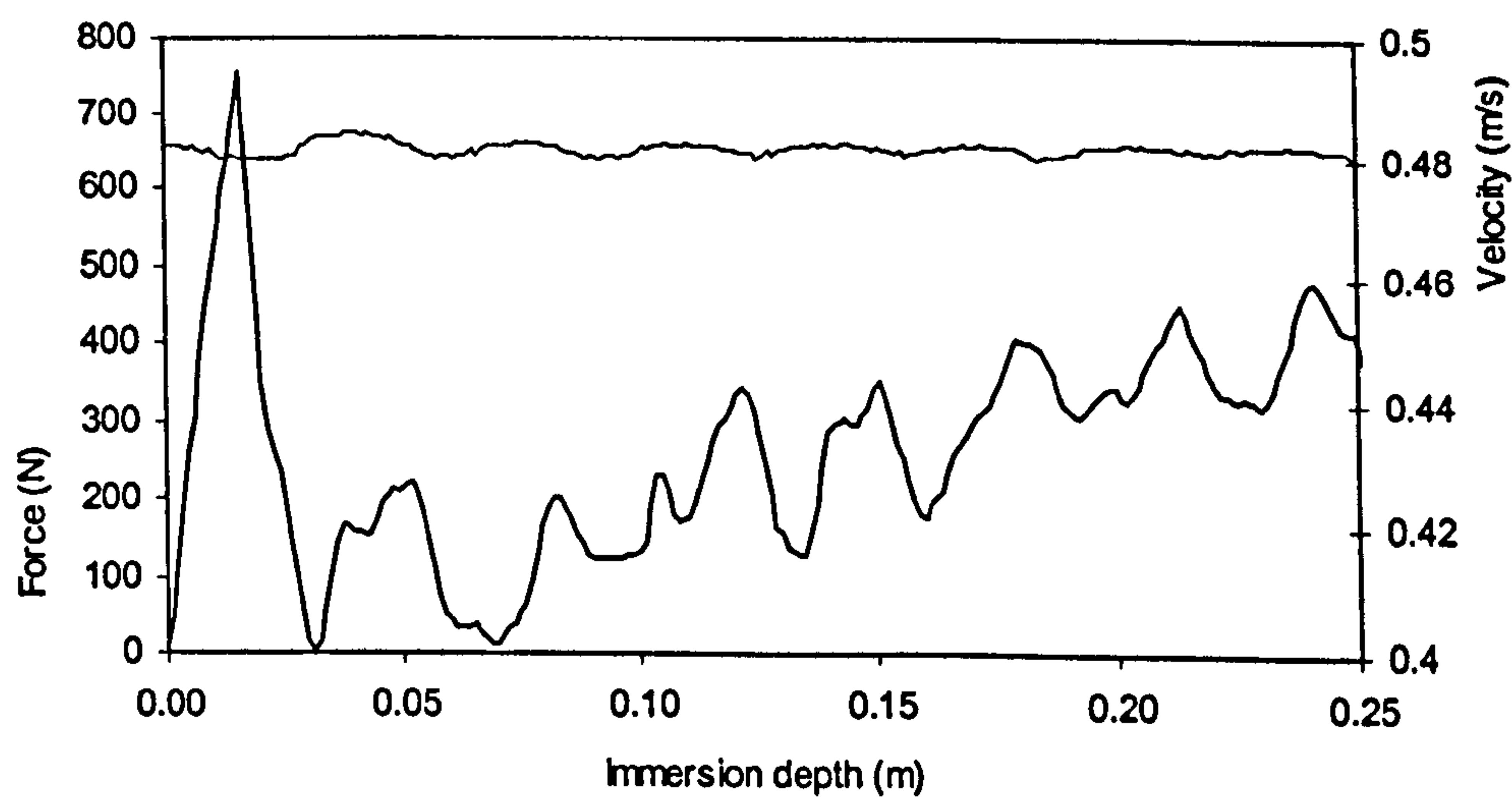


Figure 5-46. 5 degree constant velocity water entry at 0.48m/s.



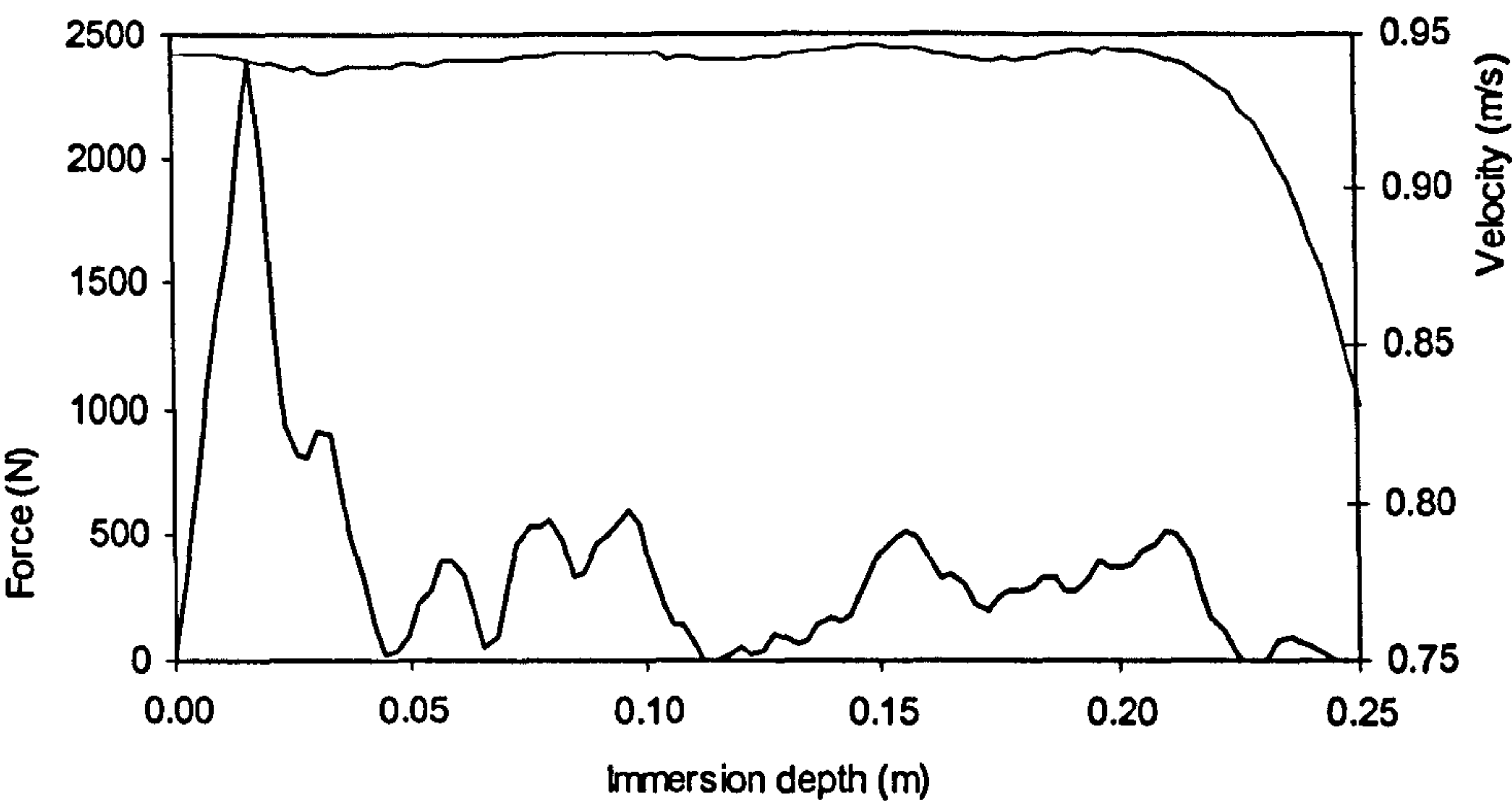


Figure 5-47. 5 degree constant velocity water entry at 0.94m/s.

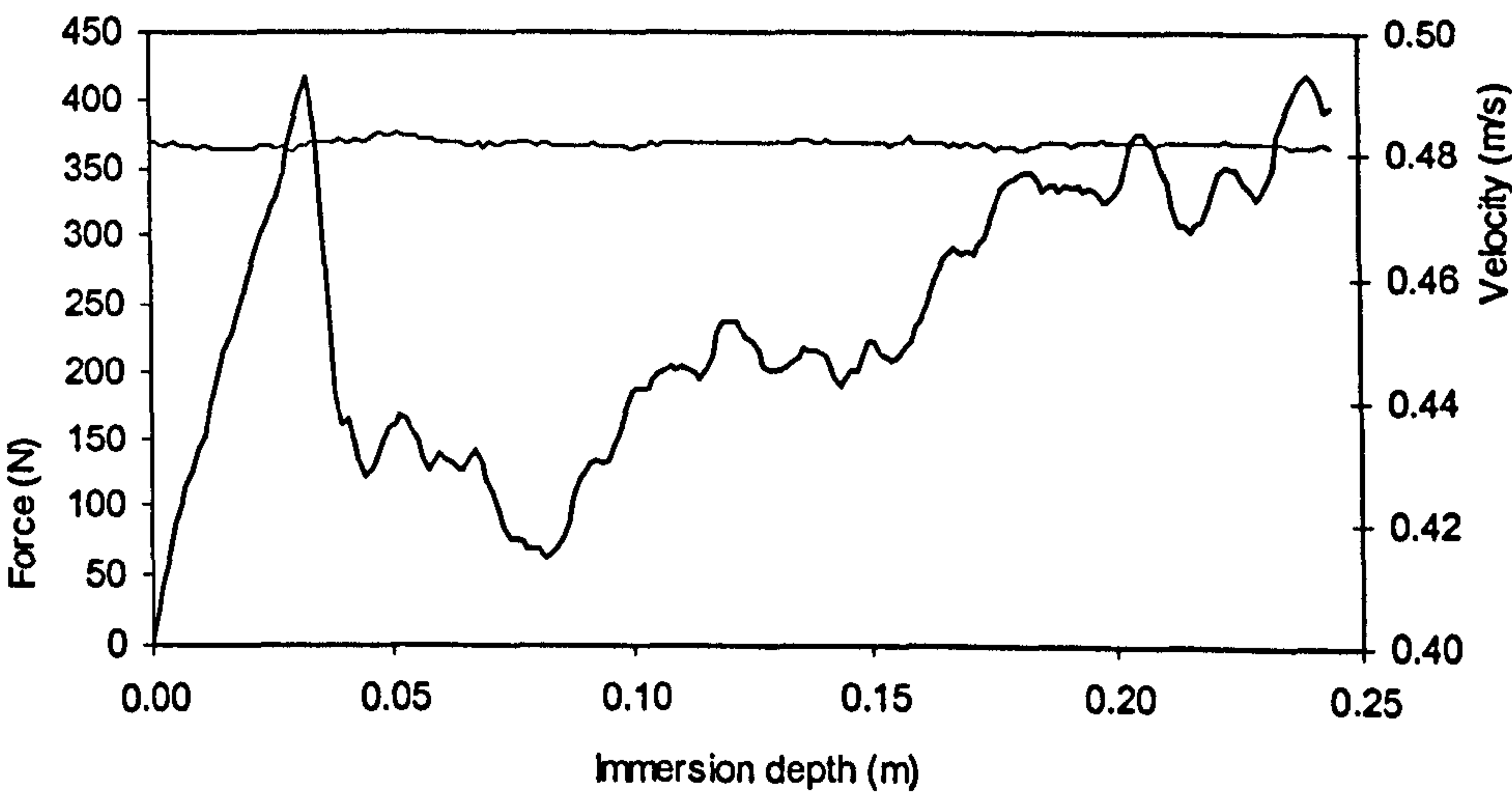


Figure 5-48. 10 degree constant velocity water entry at 0.48m/s.

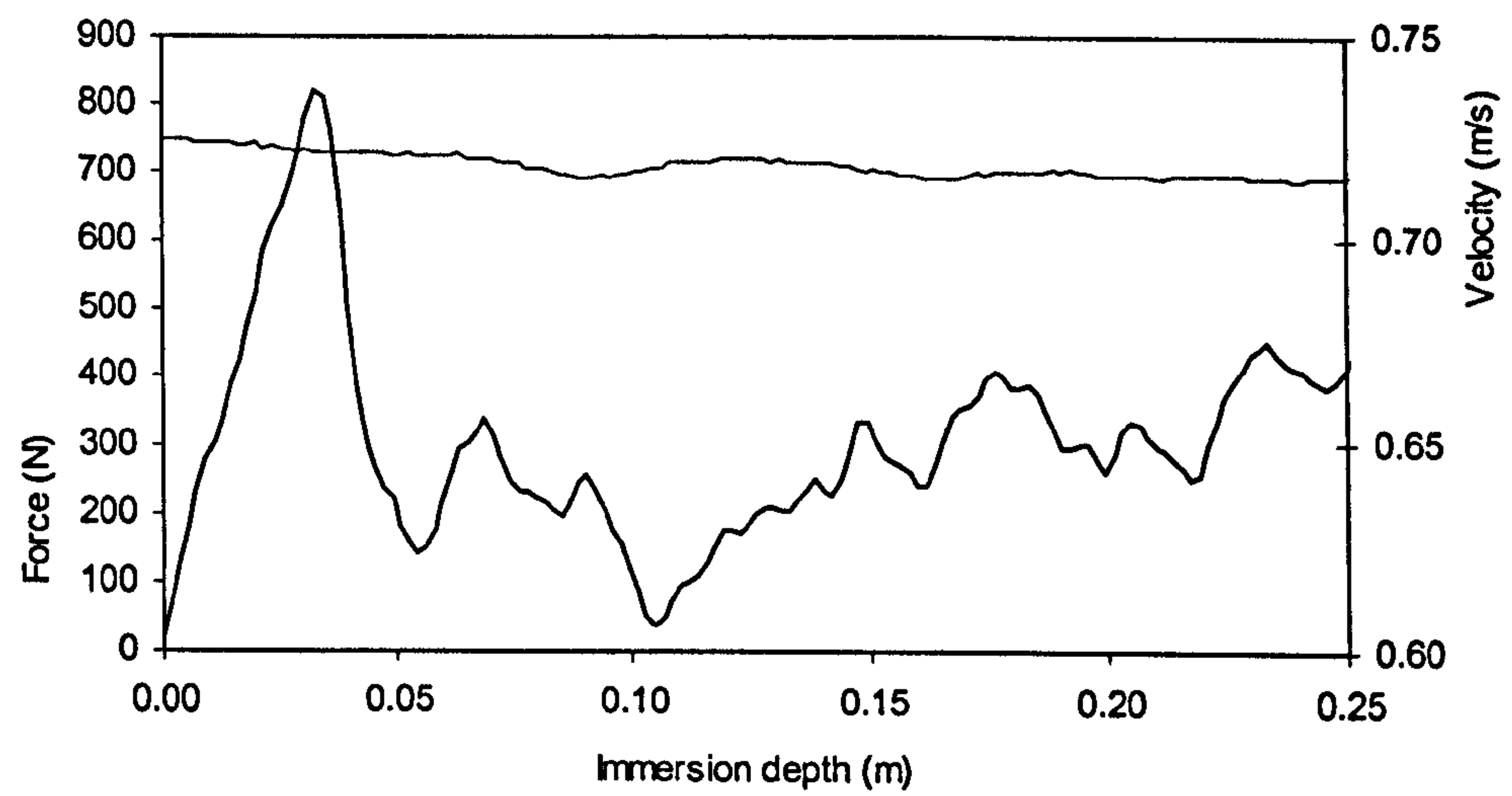


Figure 5-49. 10 degree constant velocity water entry at 0.72m/s.

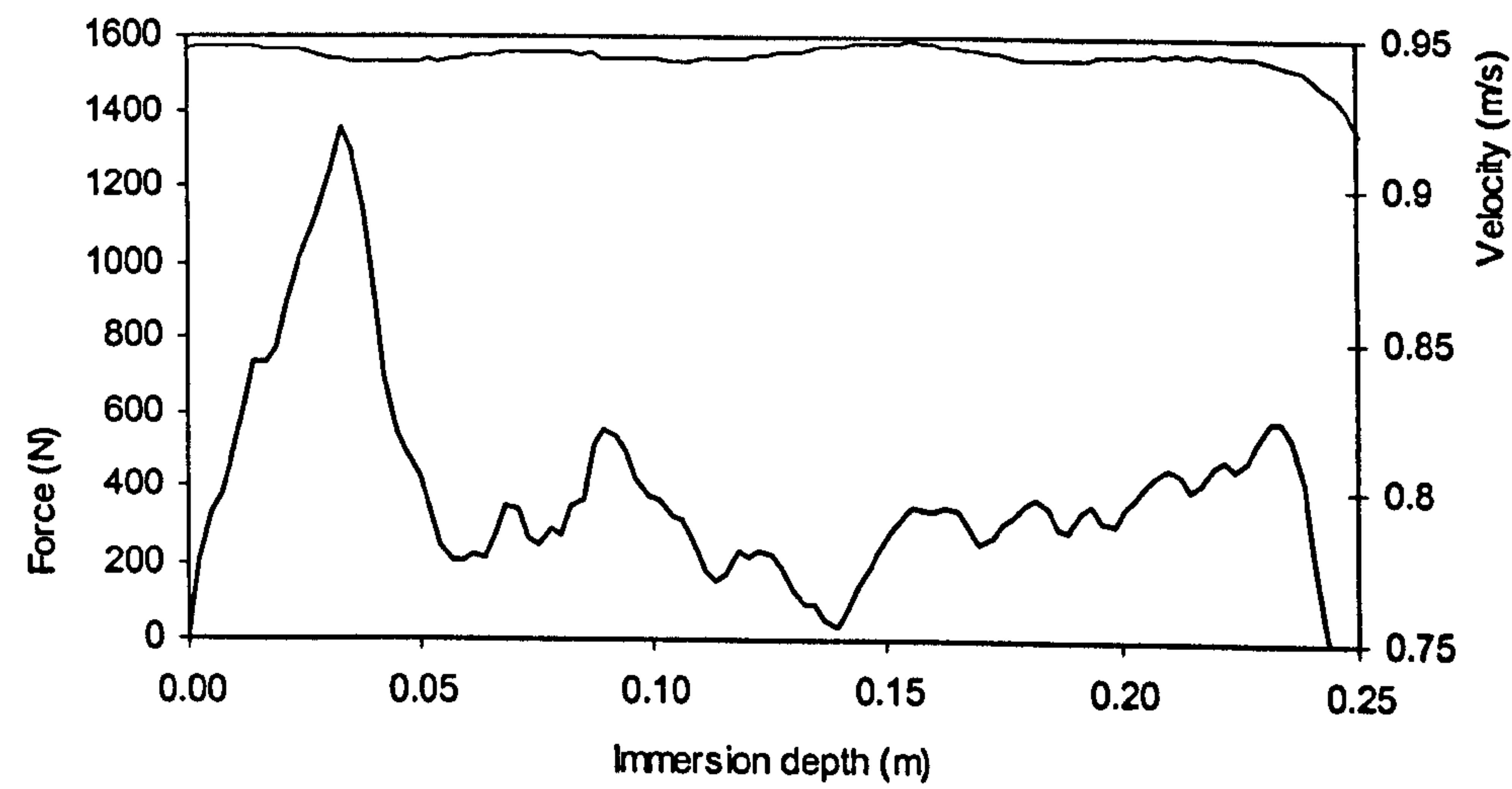


Figure 5-50. 10 degree constant velocity water entry at 0.94m/s.



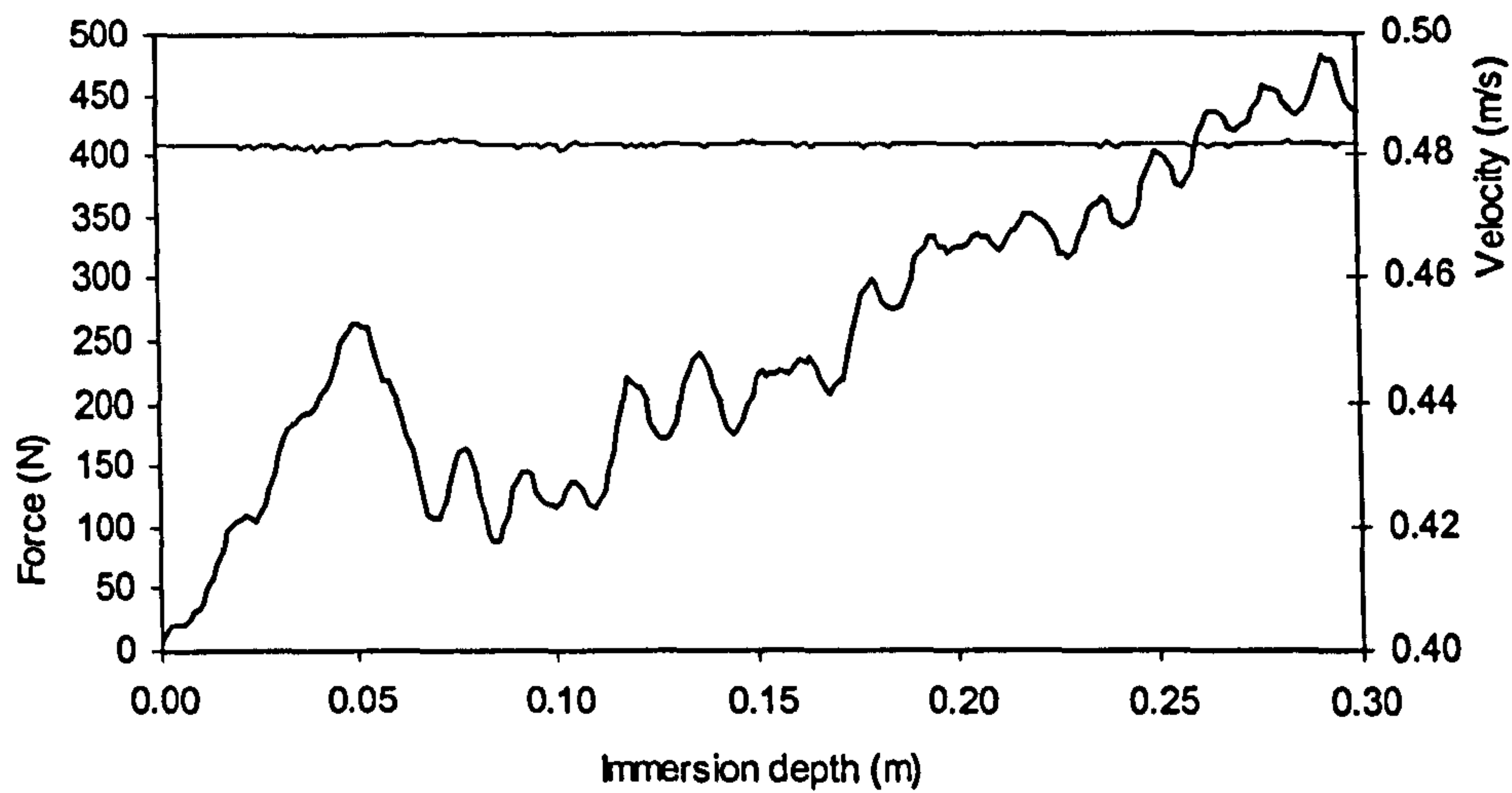


Figure 5-51. 15 degree constant velocity water entry at 0.48m/s.

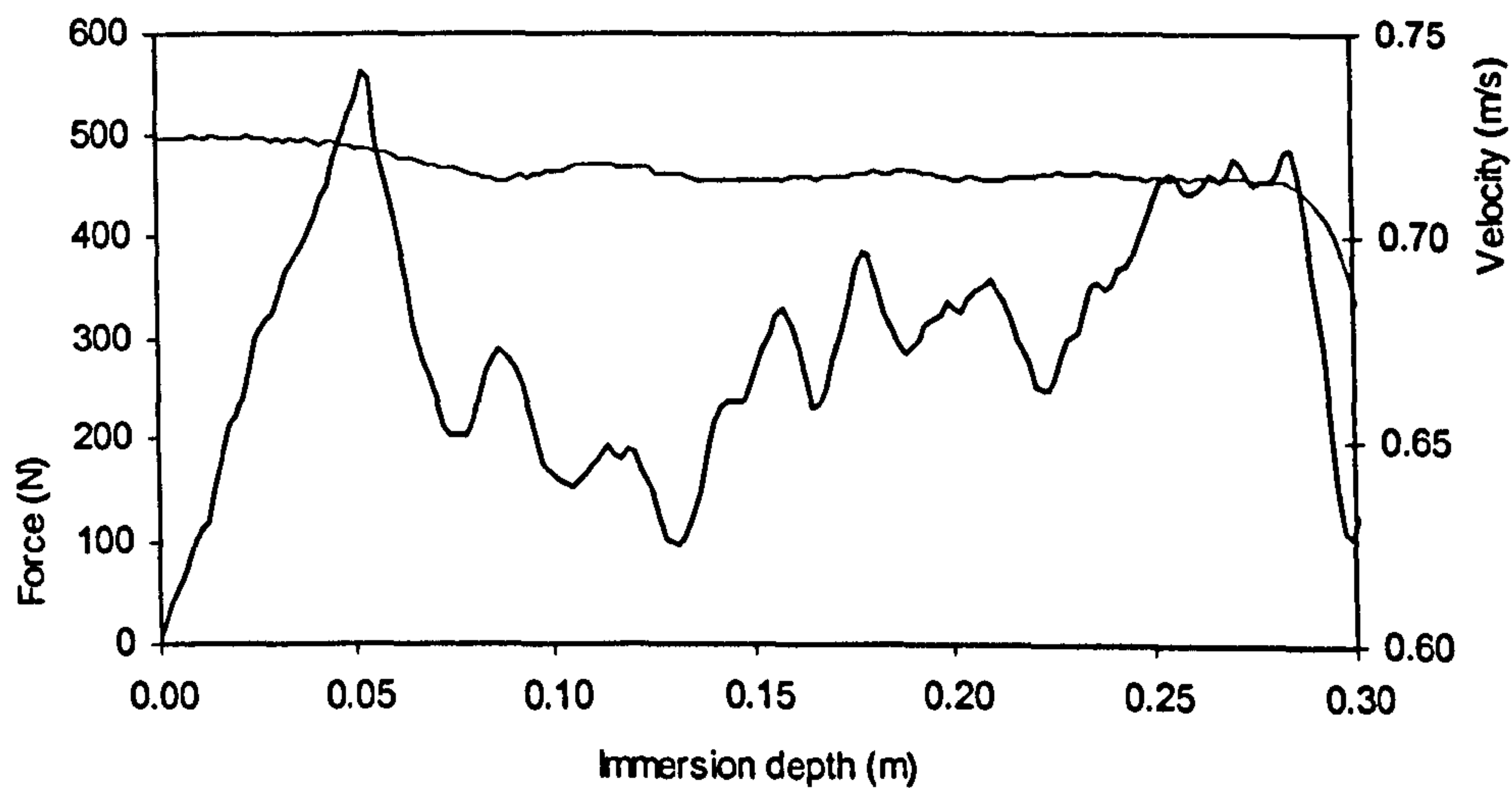


Figure 5-52. 15 degree constant velocity water entry at 0.72m/s.

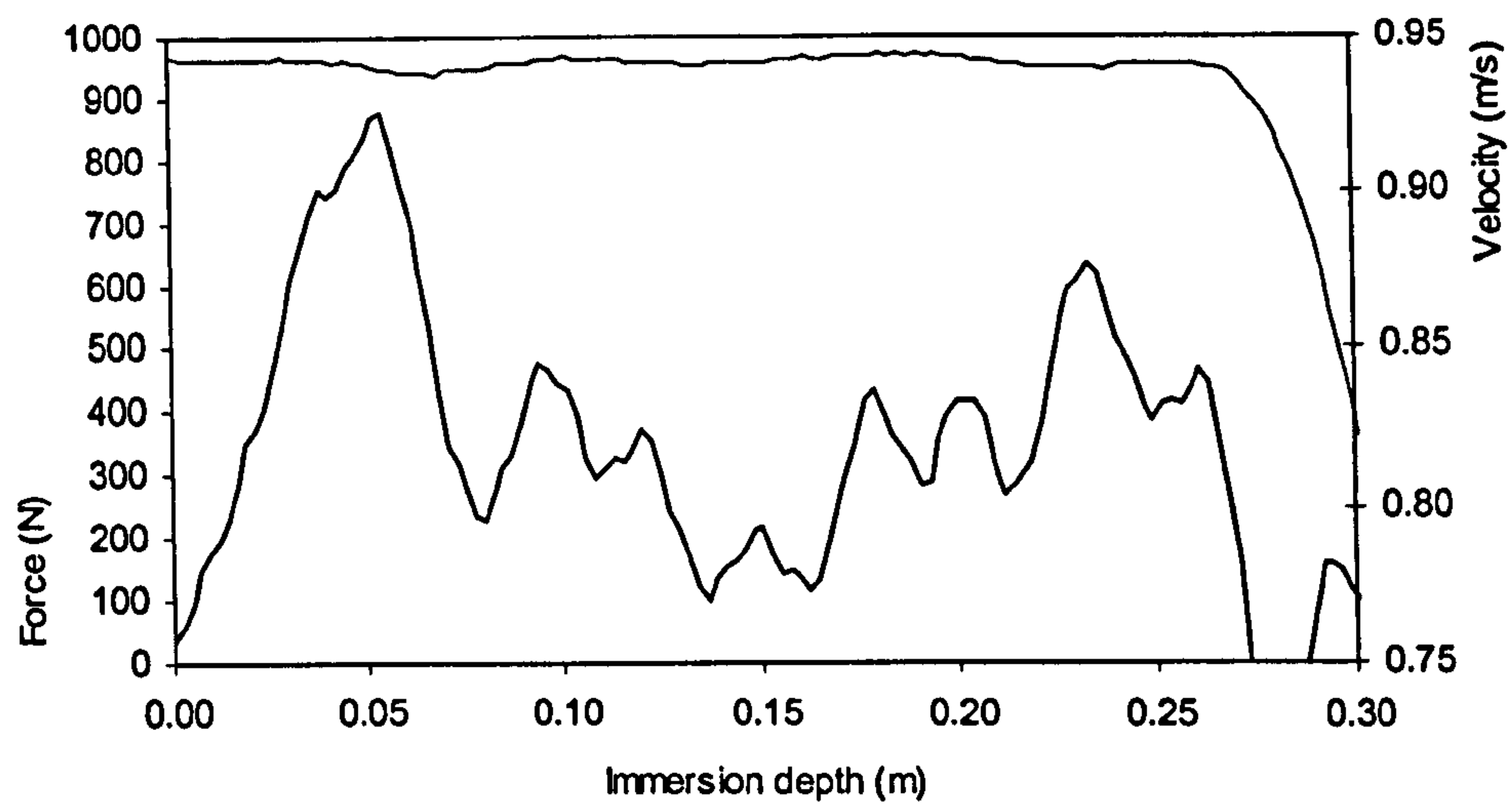


Figure 5-53. 15 degree constant velocity water entry at 0.94m/s.

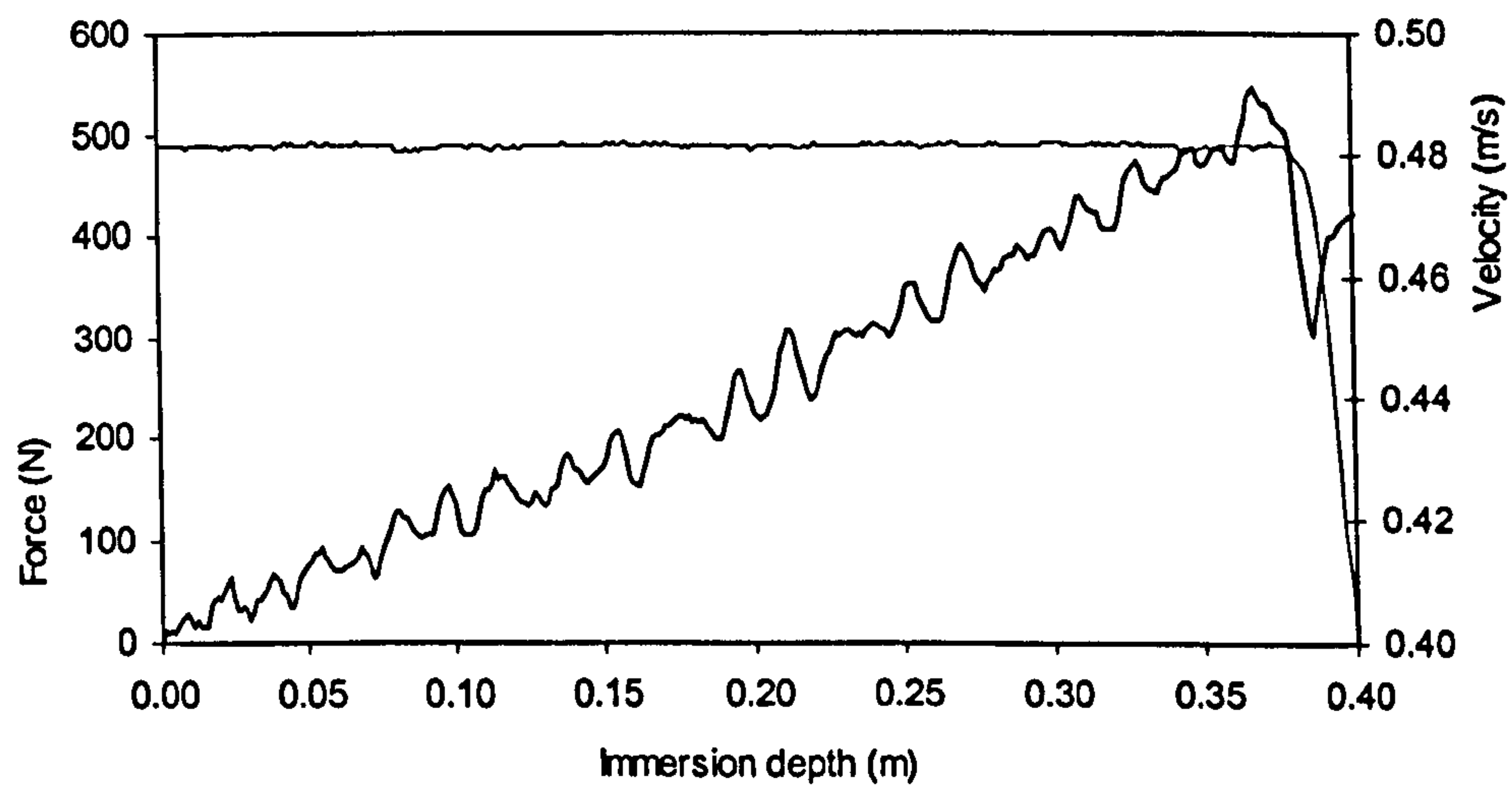


Figure 5-54. 30 degree constant velocity water entry at 0.48m/s.



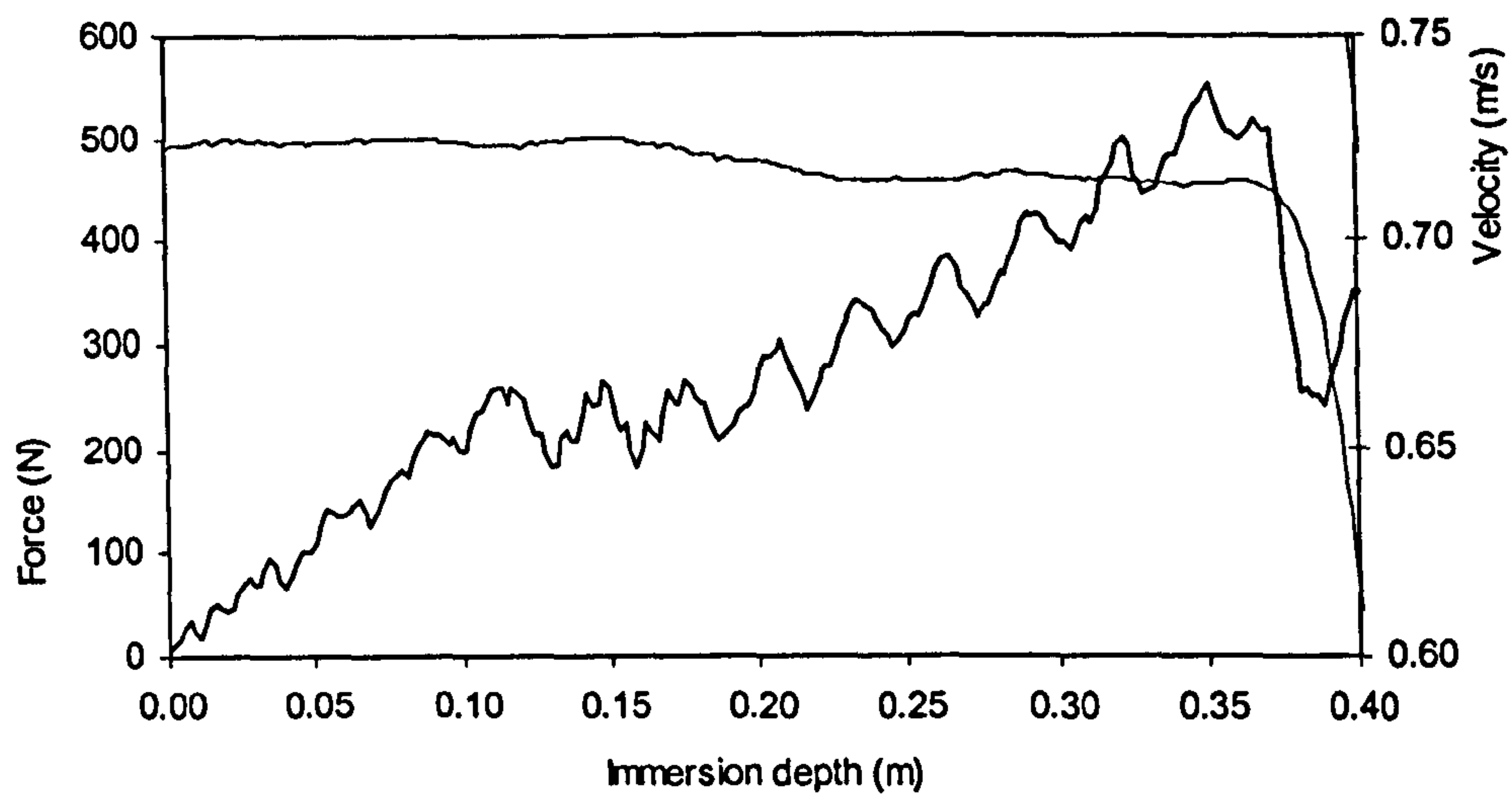


Figure 5-55. 30 degree constant velocity water entry at 0.72m/s.

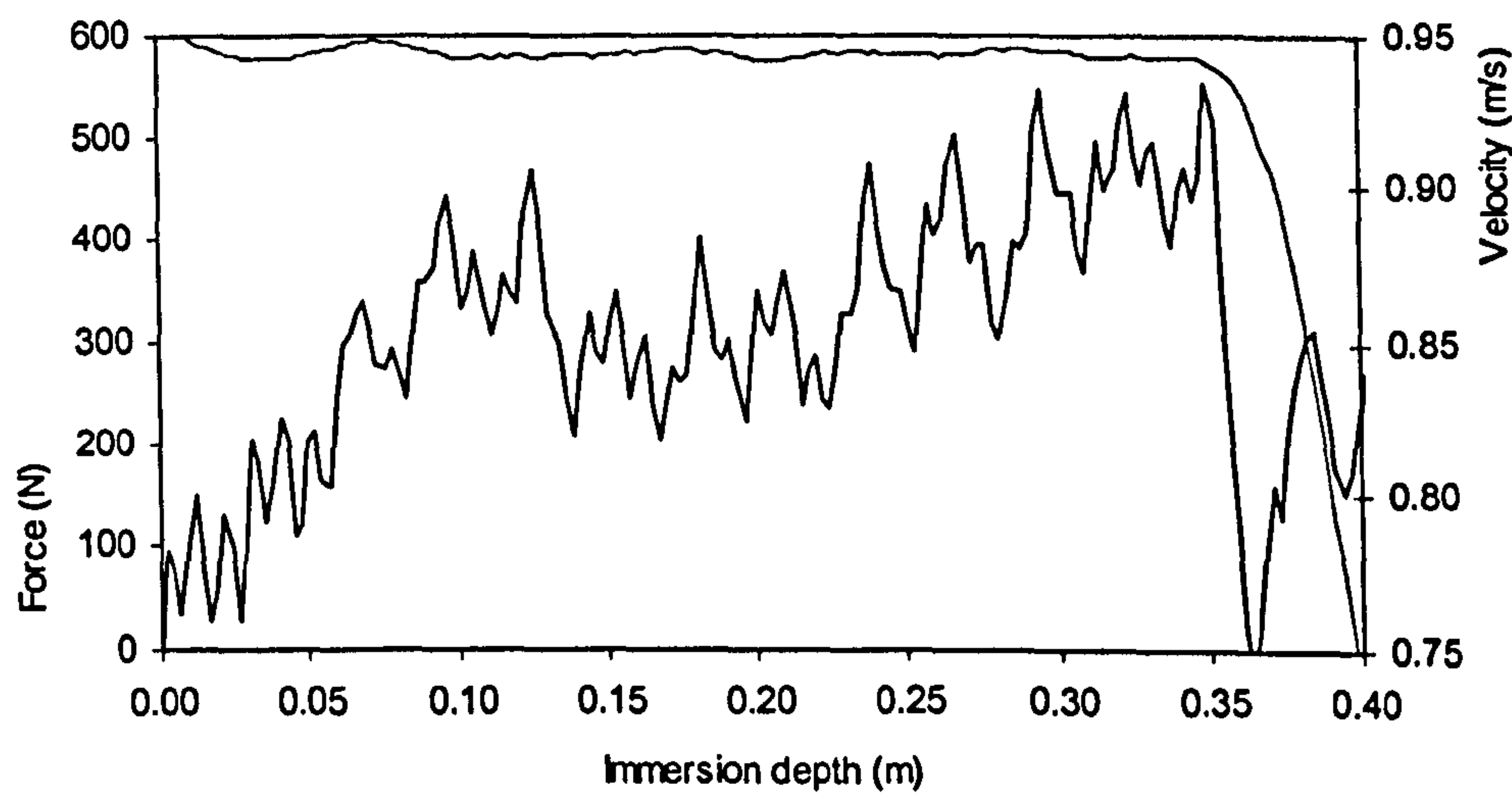


Figure 5-56. 30 degree constant velocity water entry at 0.94m/s.

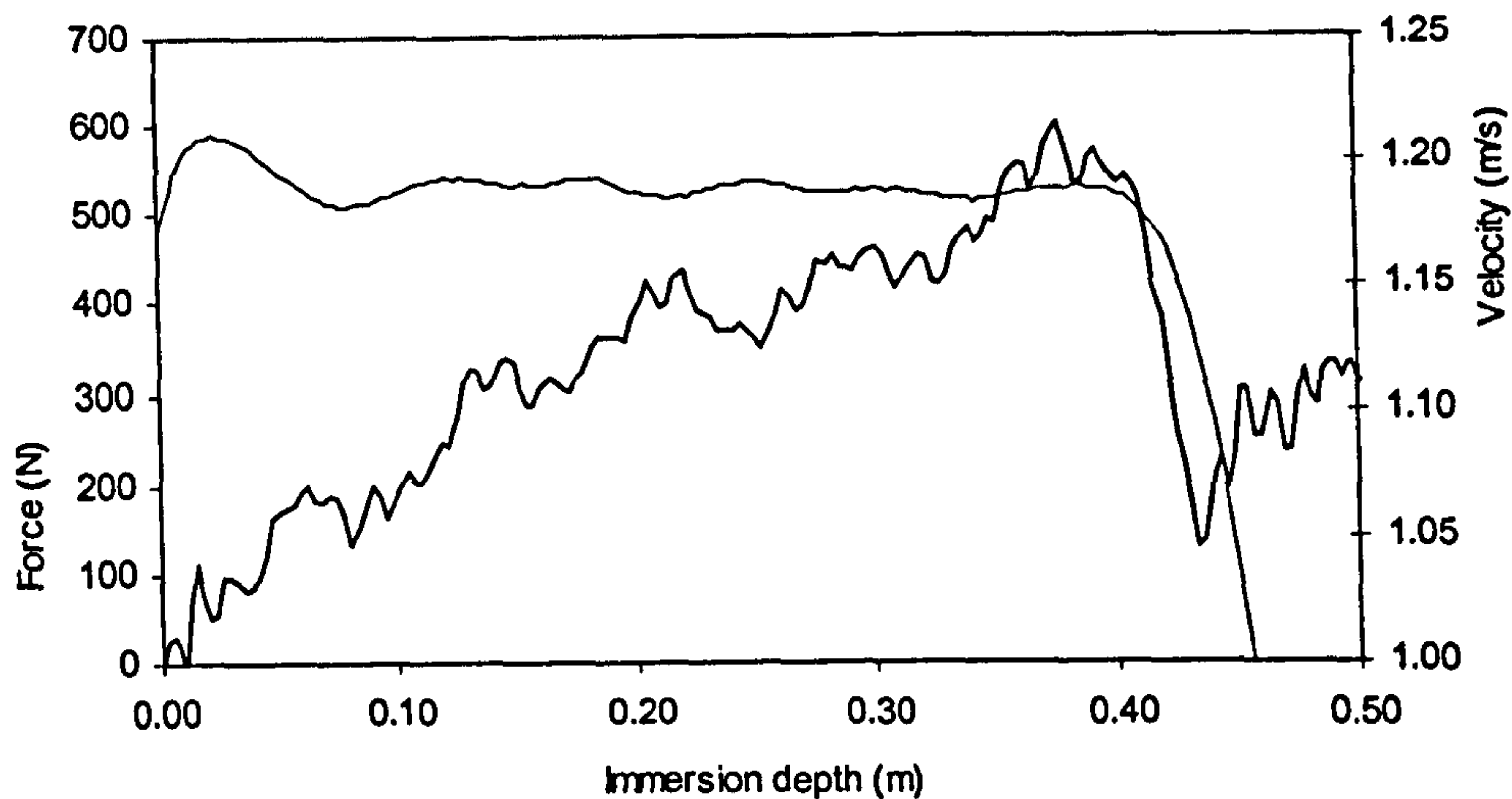


Figure 5-57. 45 degree constant velocity water entry at 1.19m/s.

Some of the force plots above show a step-like reduction in the measured force towards the end of the plotted range. This is when the test sections were decelerated as the model carrier reached the end of allowed travel. The deceleration is seen by the rapid reduction in velocity that starts at the same immersion depth as the force reduction.

The force plots have a cyclic nature that appears to be a composite of two different frequencies. The period of the higher frequency oscillation appears to vary between 0.02 and 0.05s, while the period of the low frequency oscillation varies between 0.07 and 0.16s. No distinct relation has been found between the period of the cyclic behaviour and the test parameters, velocity and deadrise angle. For some of the cases (Figures 5-46, 5-47, 5-50 and 5-53) the velocity fluctuations appear to be at the same frequency as the low frequency force cycles. During the initial stages of the water entry, the force rises rapidly. When the chines are wetted the force reduces again suddenly and rapidly. This impulse could initiate a cyclic motion of the drive that the controller cannot fully dampen. The effectiveness of the damping depends on the performance characteristics of the drive system. To be able to calculate the inertia force resulting from the velocity fluctuations, an estimate was made of the added mass of the test sections and added to their solid masses. The resulting inertia forces were only a fraction



of the observed amplitude of the measured force data. Figure 5-58 shows the calculated inertia forces along with the measured force for a 0.48m/s water entry with the 5 degrees test section.

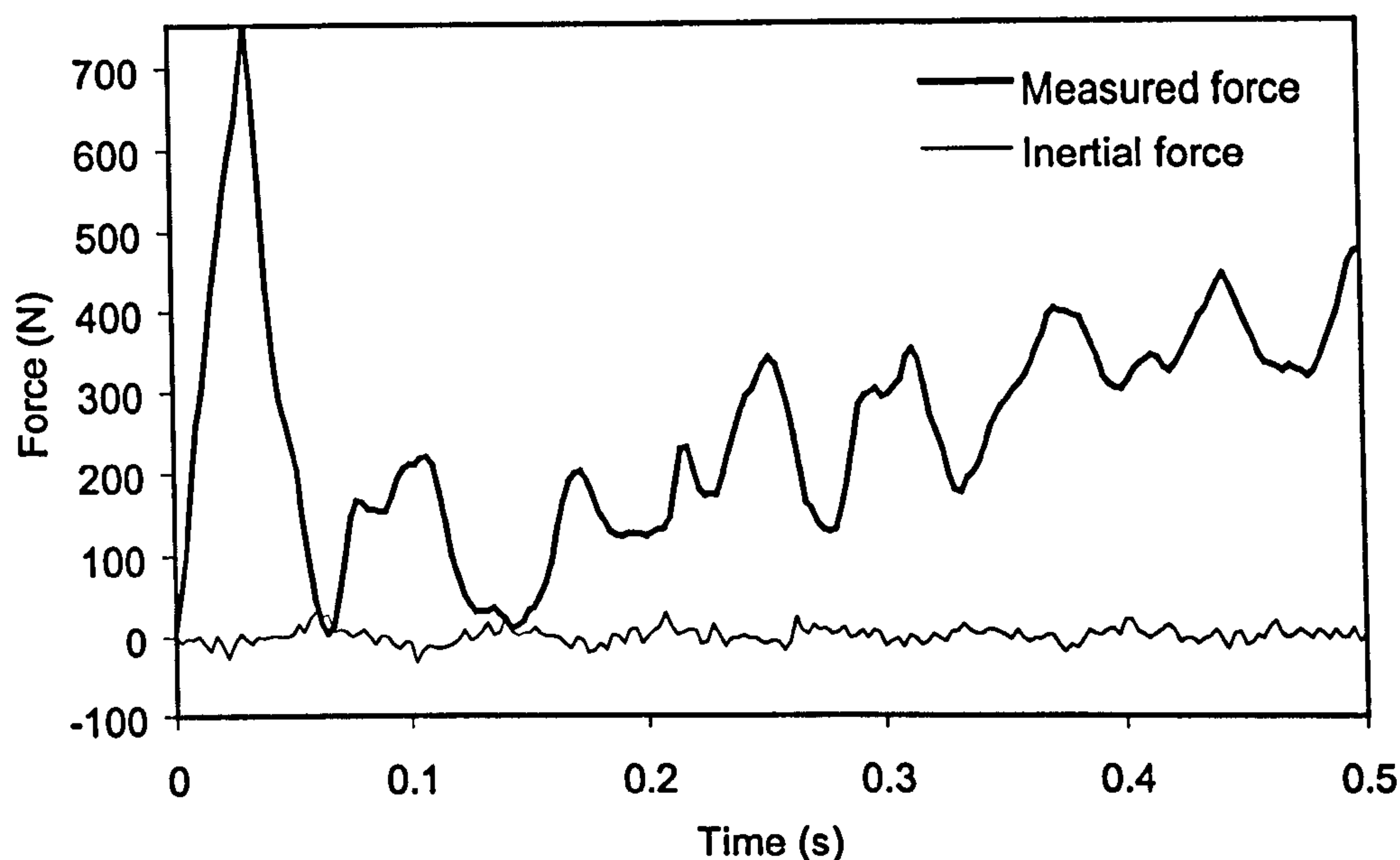


*Figure 5-58. Total measured force and inertia force associated with velocity fluctuations from 0.48m/s test with 5 degrees section.*

Although some of the force/velocity plots in Figures 5-45 to 5-57 indicate a relation between the periods of the velocity fluctuations and the low frequency cyclic nature of the force data, Figure 5-58 shows no such correlation between the magnitude of the measured force fluctuations and the magnitude of the inertial forces due to velocity variations.

In an attempt to find the source for the high frequency force fluctuations, the stiffness of the timing belt was investigated. The supplier of the timing belt drive provided a sheet giving the spring rate curve of the belt used on the test rig, which is shown in Figure 5-59.



## SPRING RATE CURVE 8MM HTD

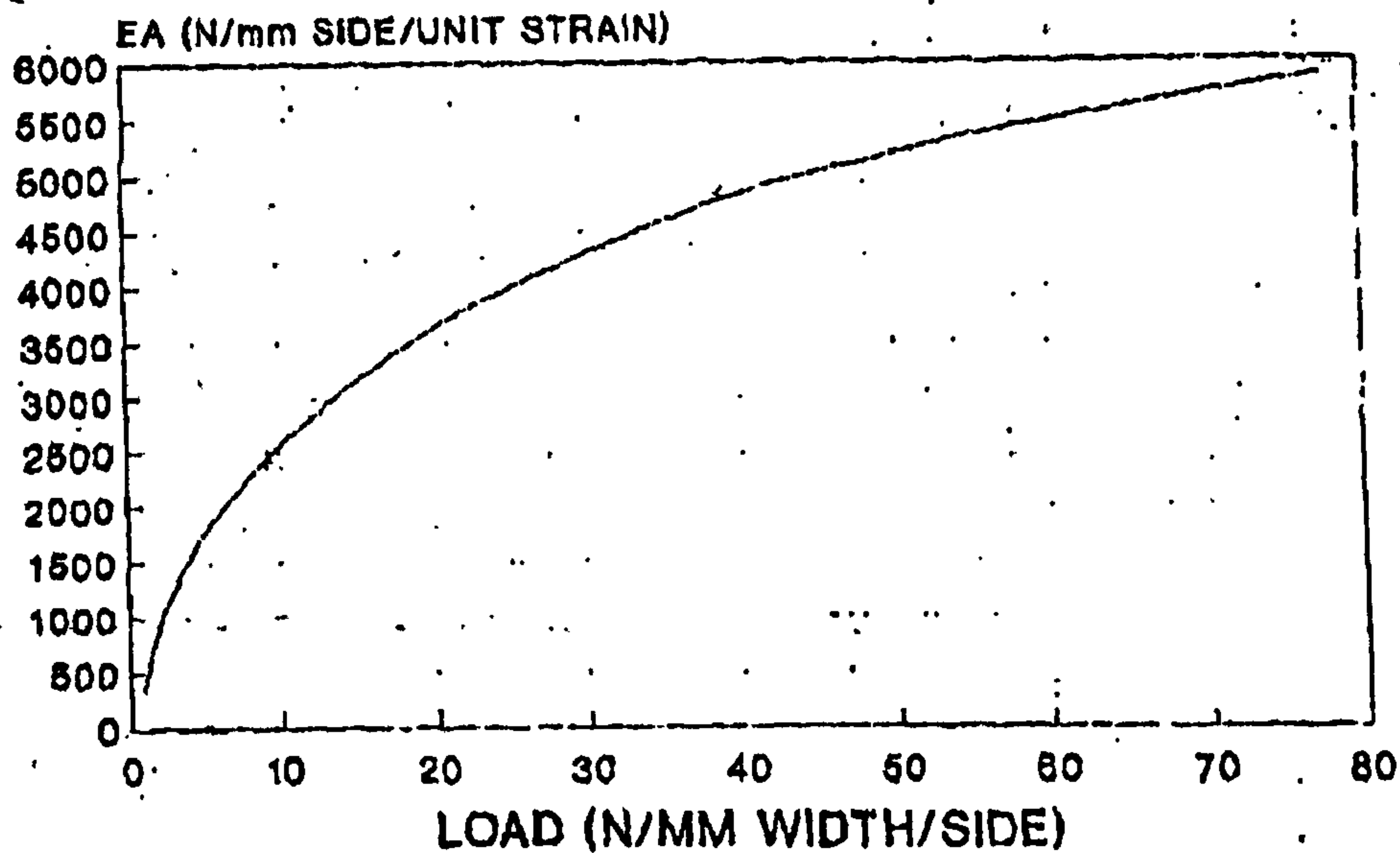


Figure 5-59. Timing belt spring rate curve.

It follows from the spring rate curve that the relation between elongation and load is non-linear, and hence the stiffness  $k_{lb}$  of the timing belt varies as the force varies during the water entry. The load on the belt during the downward motion is constant once constant velocity is obtained and before the wedge penetrates the water surface. This load is caused by the gravitational pull on the mass of the vertically moving parts. The total mass of these parts is approximately 70kg, with a small variation due to variation of test wedge mass. Correcting for the transmission ratio of 1:9.6 between the vertical movement and the belt movement, the belt load is found to be 72N during the initial stage of the water entry tests. The relation between strain and load per mm belt width was given by the

manufacturer as  $\epsilon = \frac{\sqrt{\text{load} / \text{width}}}{790}$ . For the 30mm wide belt the load divided by

the width equals 2.4N/mm. From this it follows that the belt strain is 0.002. Further, the loaded span length of the belt is 160mm, yielding an elongation of 0.32mm. The stiffness is calculated by dividing the known belt load with the known elongation, yielding  $k_{lb}=225\text{N/mm}$ . The natural frequency for a spring



mass system is given by  $f_n = \frac{1}{2\pi} \cdot \sqrt{\frac{k_{ib}}{m}}$ . The appropriate mass of the considered spring-mass system is the sum of the mass of the vertically moving parts, the added mass and the converted inertia of the ball nut and the pulley. The added mass is estimated to vary between 25 and 50kg depending on deadrise angle. The average of these values has been applied in the calculation. The masses and inertia have been converted to a mass of 1.66kg in the spring-mass system considered (conversion ratio for an inertial mass equals the square of the transmission ratio). Using the relation between mass and stiffness, the natural frequency is found to be 58Hz and the natural period is 0.017s.

The natural period estimated above is outside the experimentally observed range of 0.02 to 0.05s. However, the estimated and the experimentally observed periods are of the same order of magnitude, and, considering that the estimate has been obtained by a rather crude analysis, a relation between the natural frequency of the system and the high frequency cyclic behaviour of the force cannot be excluded.

Despite being stiffened by the cross rods, it is likely that the PVC sheets are bent away from the test section due to the high pressures built up during an impact. This could cause water flow between the sheets and the test section, thus reducing pressure. A reduction in pressure would again reduce the gap between sheets and test section, thus allowing pressure to increase. Although unlikely to cause a frequency as high as that observed, such a mechanism that causes pressure under the test section to vary, could cause the force acting on the tests section to fluctuate.

Further conclusions regarding the sources for the cyclic behaviour would involve a complicated analysis of the dynamics of the total system involving the spring-mass system of the belt and moving parts, the dynamics of the PVC sheets and the characteristics of the servo controller system. Such analysis would be impossible on basis of the currently available knowledge and data, and is beyond the scope of this work.

### 5.8.3.2. Oscillation Tests

The force readings from the oscillation experiments required an inertia force in addition to the test section weight to be subtracted from the measured forces in order to obtain the forces due to interaction with the water. The inertia force to accelerate the solid mass of the model section passes through the load cells. Using the recorded velocity output from the amplifier, the accelerations at any instant during the tests can be found. With the known test section mass, the inertia forces were calculated and subtracted from the total force readings. This gave data that represented the forces due to interaction between the test section and the water as

$$F = F_{4LC} - M_M \cdot g - M_M \cdot \frac{dw}{dt} \quad (5-8)$$

The extracted interaction force data for both the wet and dry chines oscillation tests are plotted in Figure 5-60 to 5-66 together with the immersion depth given by velocity integration. Note that the values on the immersion depth scale are in reverse order.



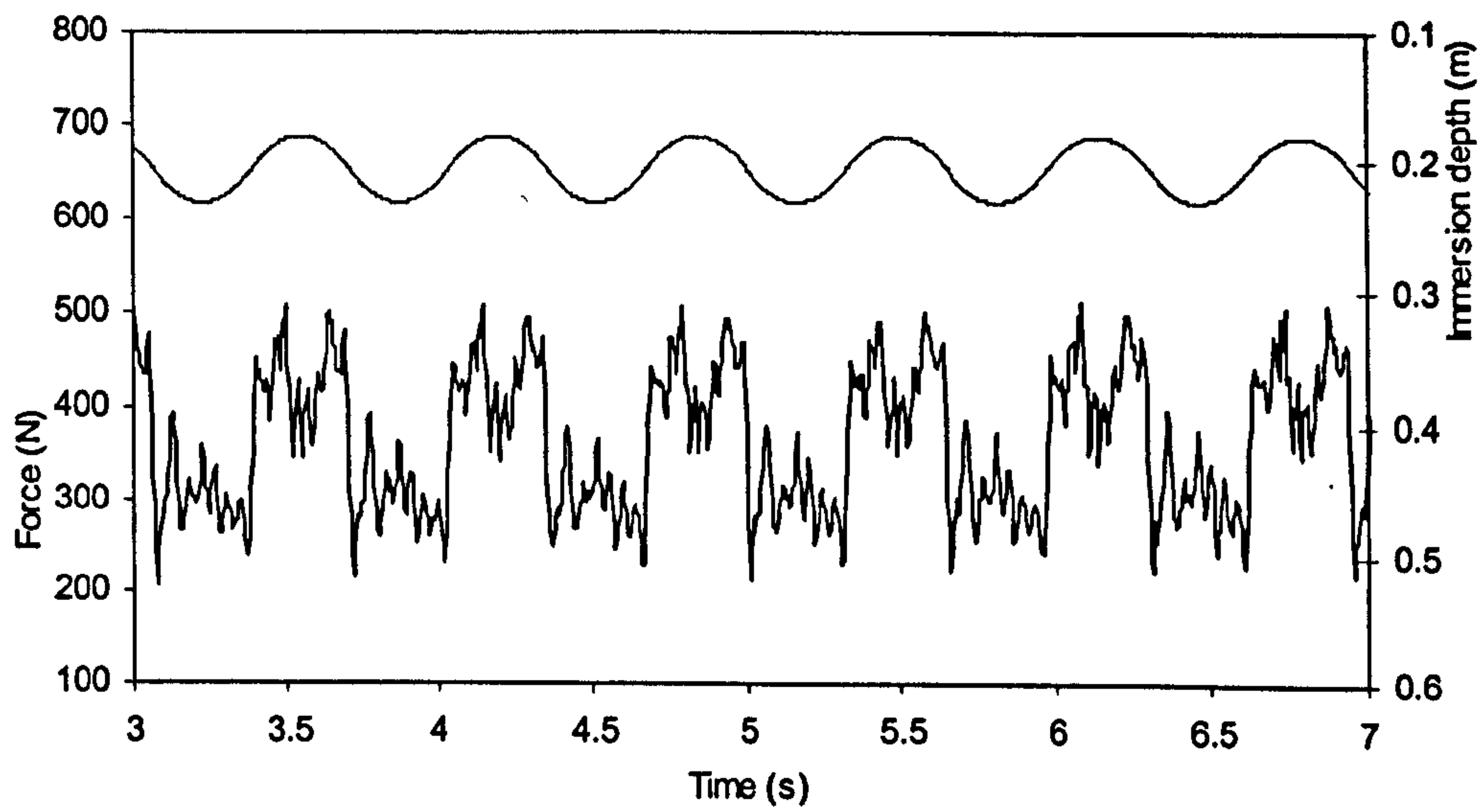


Figure 5-60. 0 degree wet chines oscillation,  $z=0.18-0.23m$ .

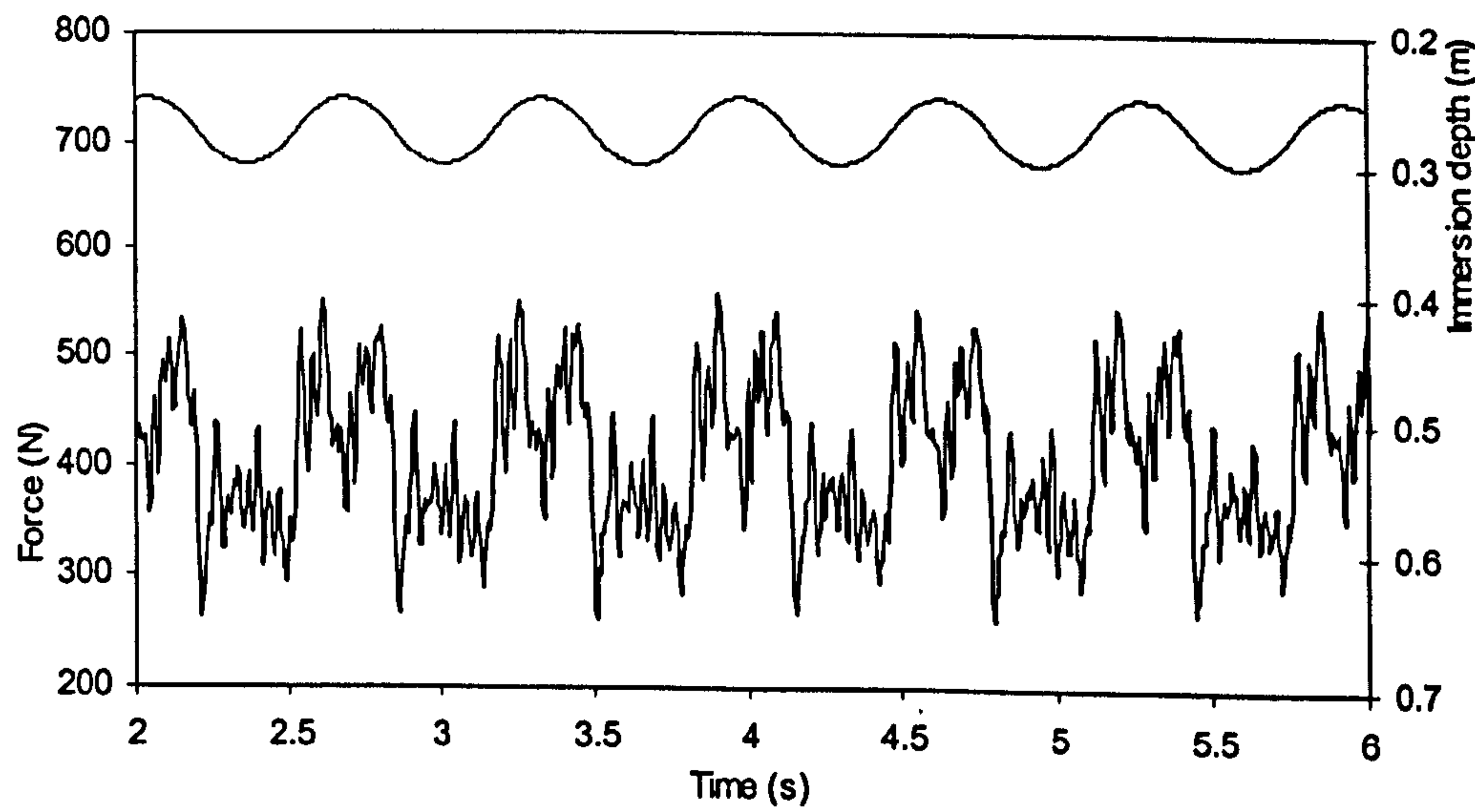


Figure 5-61. 15 degree wet chines oscillation,  $z=0.25-0.30m$ .

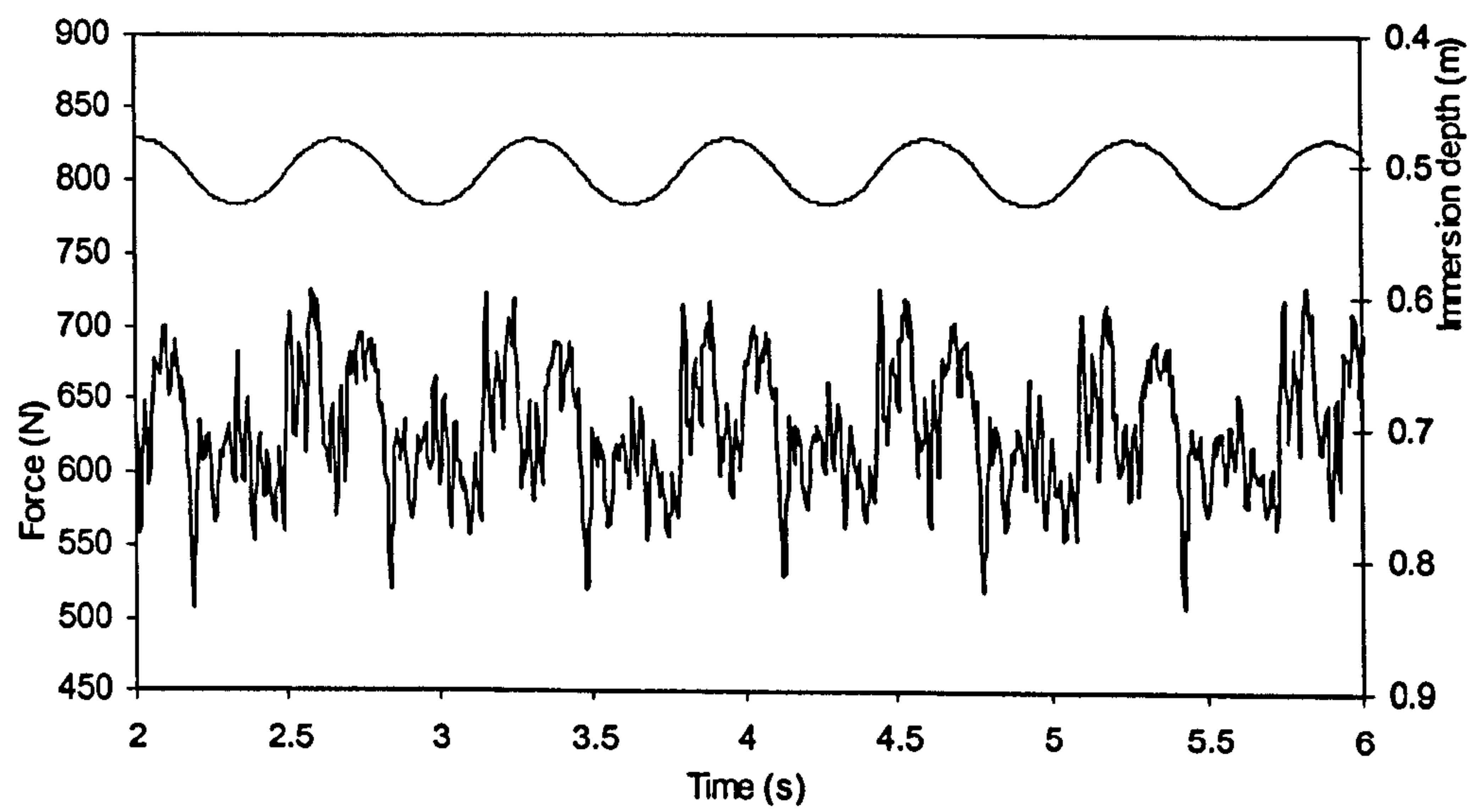


Figure 5-62. 45 degree wet chines oscillation,  $z=0.48-0.53m$ .

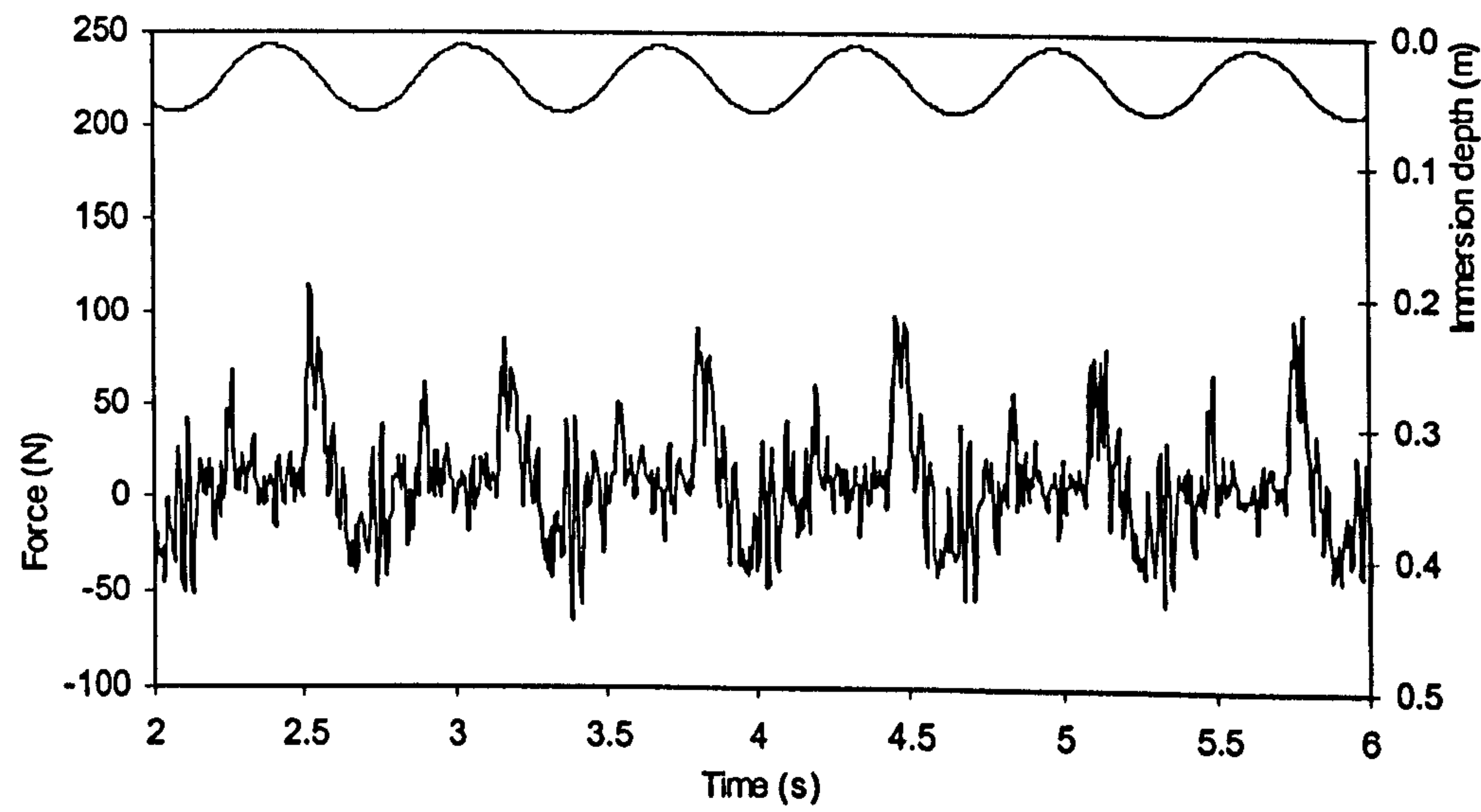


Figure 5-63. 15 degree dry chines oscillation,  $z=0.01-0.06m$ .



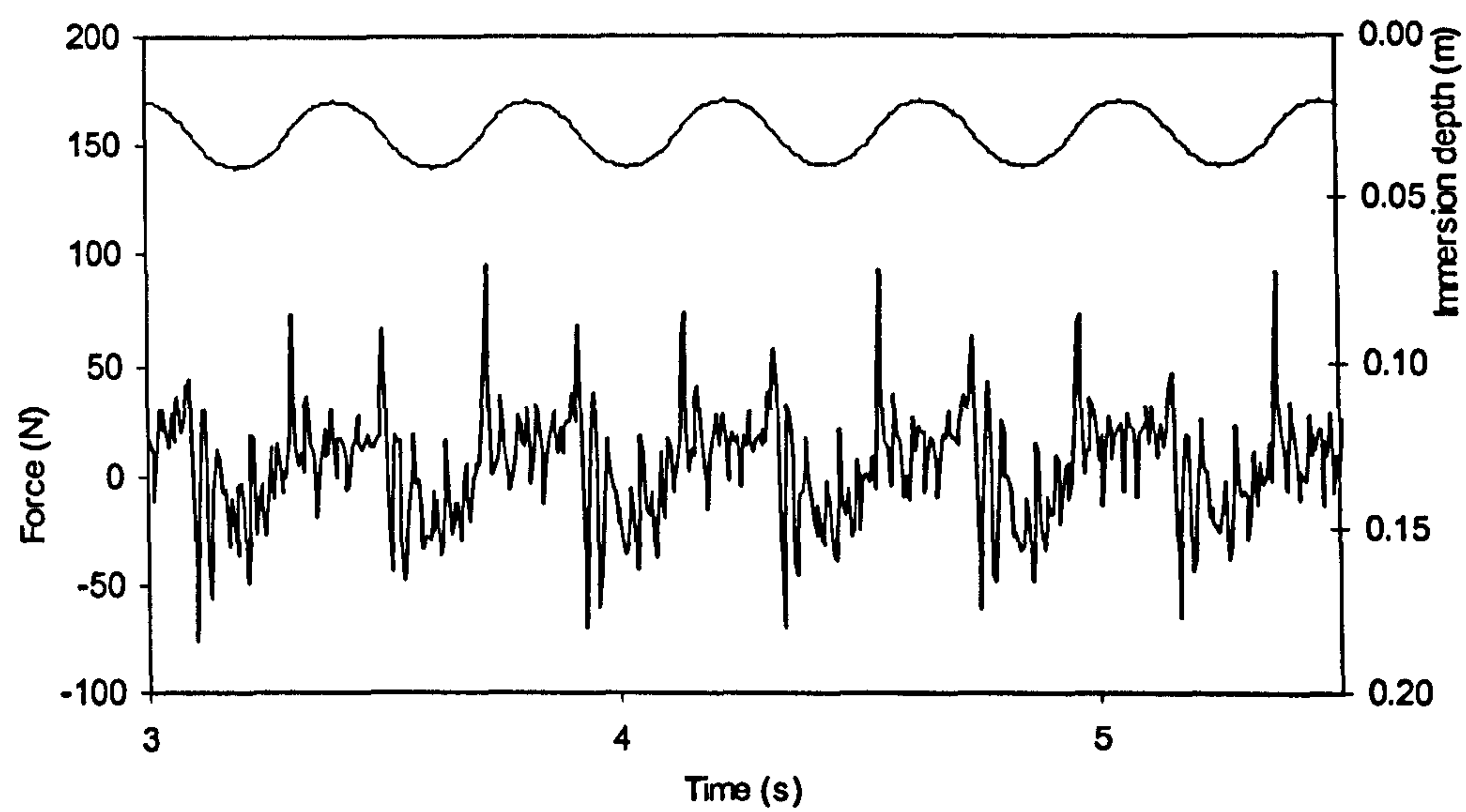


Figure 5-64. 15 degree dry chines oscillation,  $z=0.02-0.04m$ .

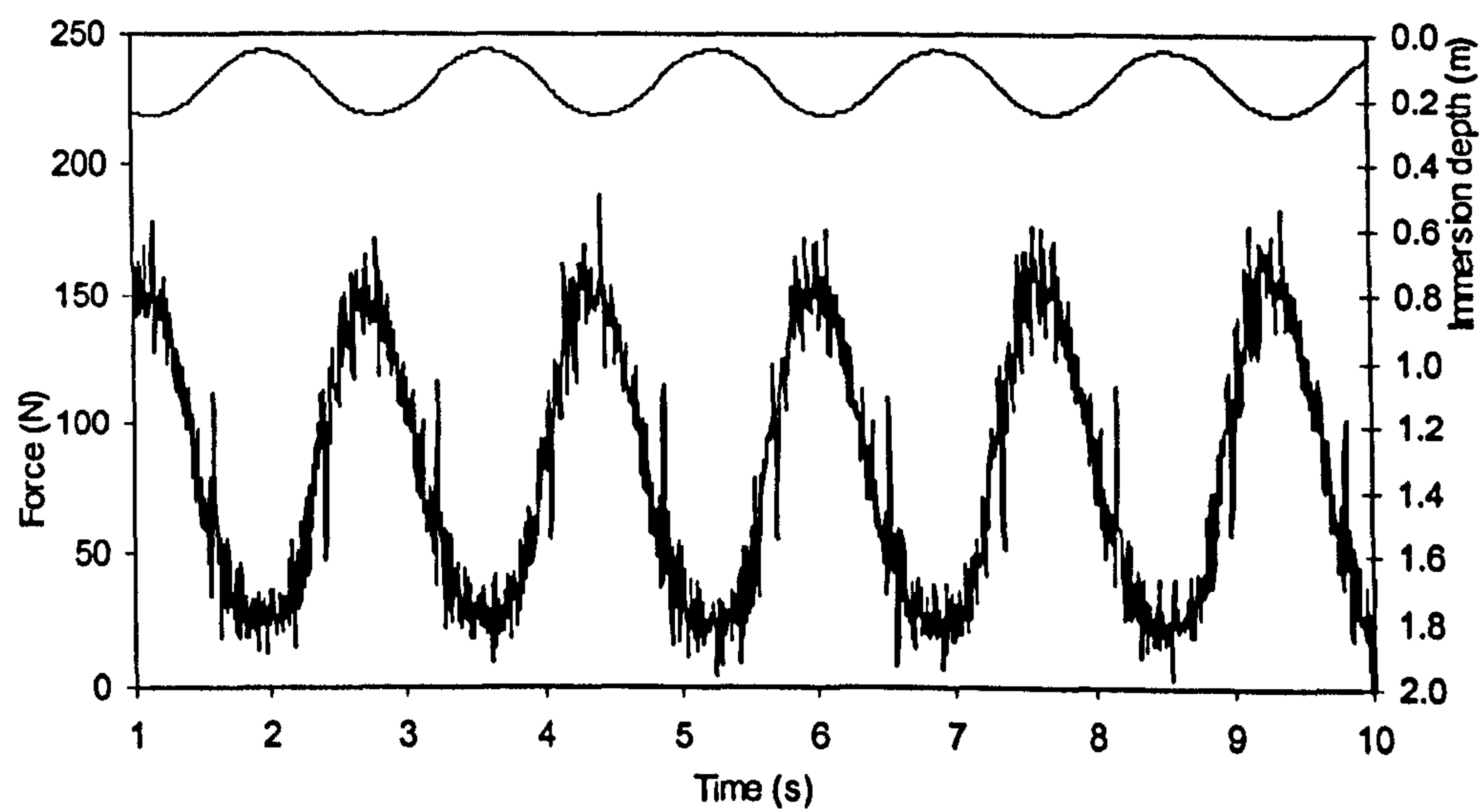
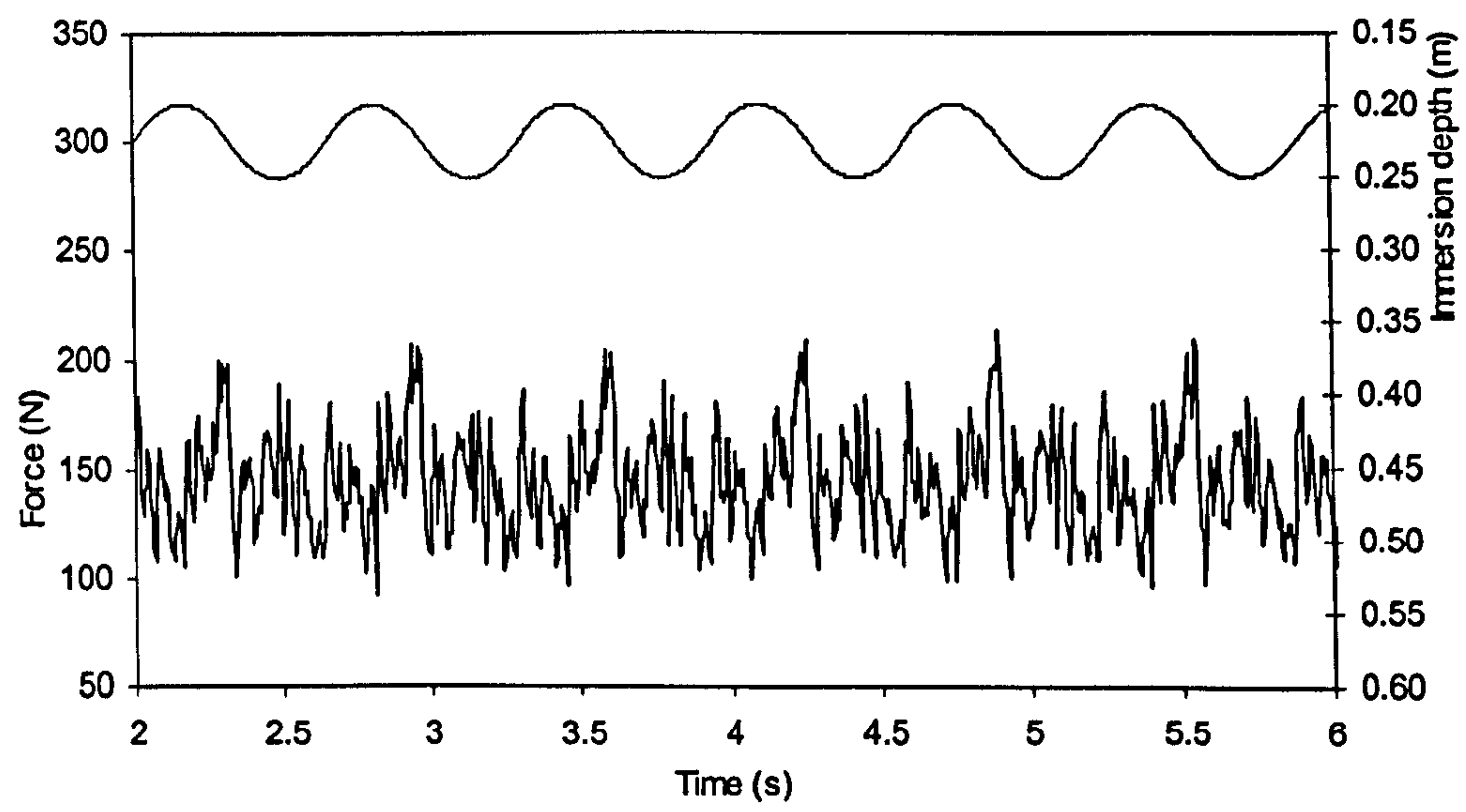


Figure 5-65. 45 degree dry chines oscillation,  $z=0.05-0.25m$ .



*Figure 5-66. 45 degree dry chines oscillation,  $z=0.20-0.25m$ .*

5.8.3.3. Accelerated Water Entry Tests

The measured data from the accelerated tests are also corrected by deducting the weight and the inertial force of the test sections, using Equation (5-8), in order to obtain the forces due to interaction with the water. The resulting force data for the accelerated entry tests are plotted in Figures 5-67 to 5-71 together with the velocity of the test section.



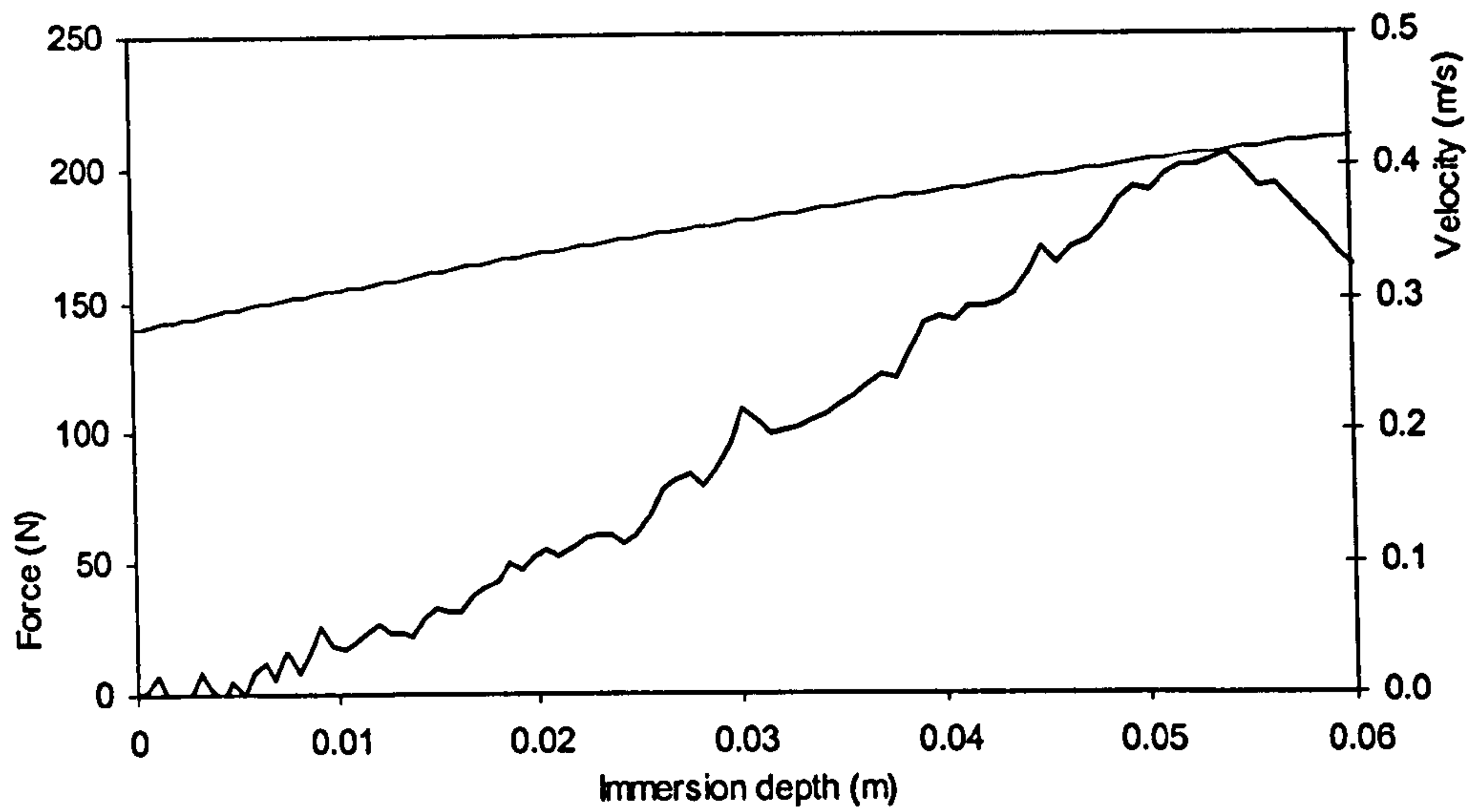


Figure 5-67. 15 degree accelerated water entry,  $a=0.83\text{m/s}^2$ .

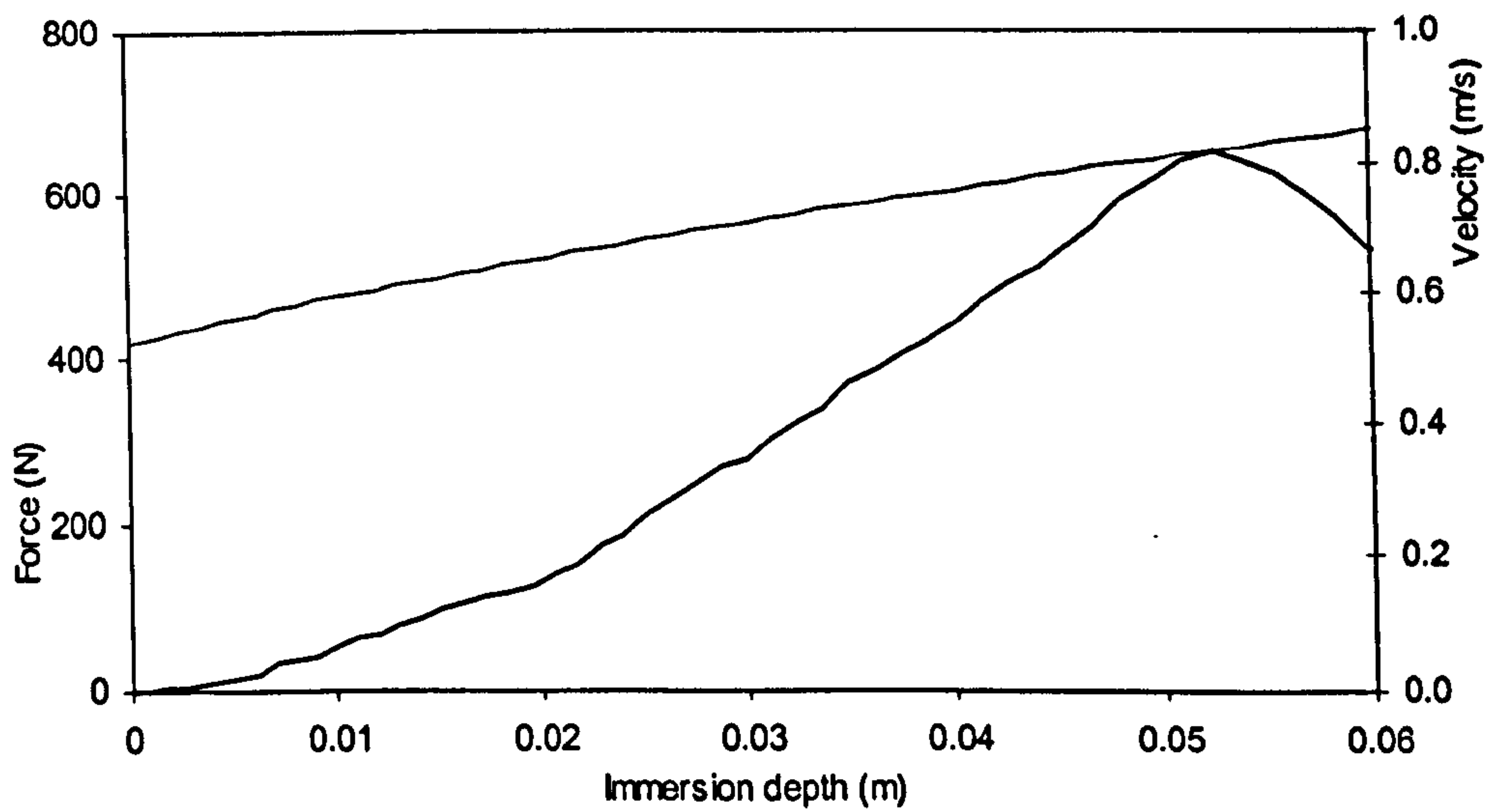


Figure 5-68. 15 degree accelerated water entry,  $a=3.33\text{m/s}^2$ .

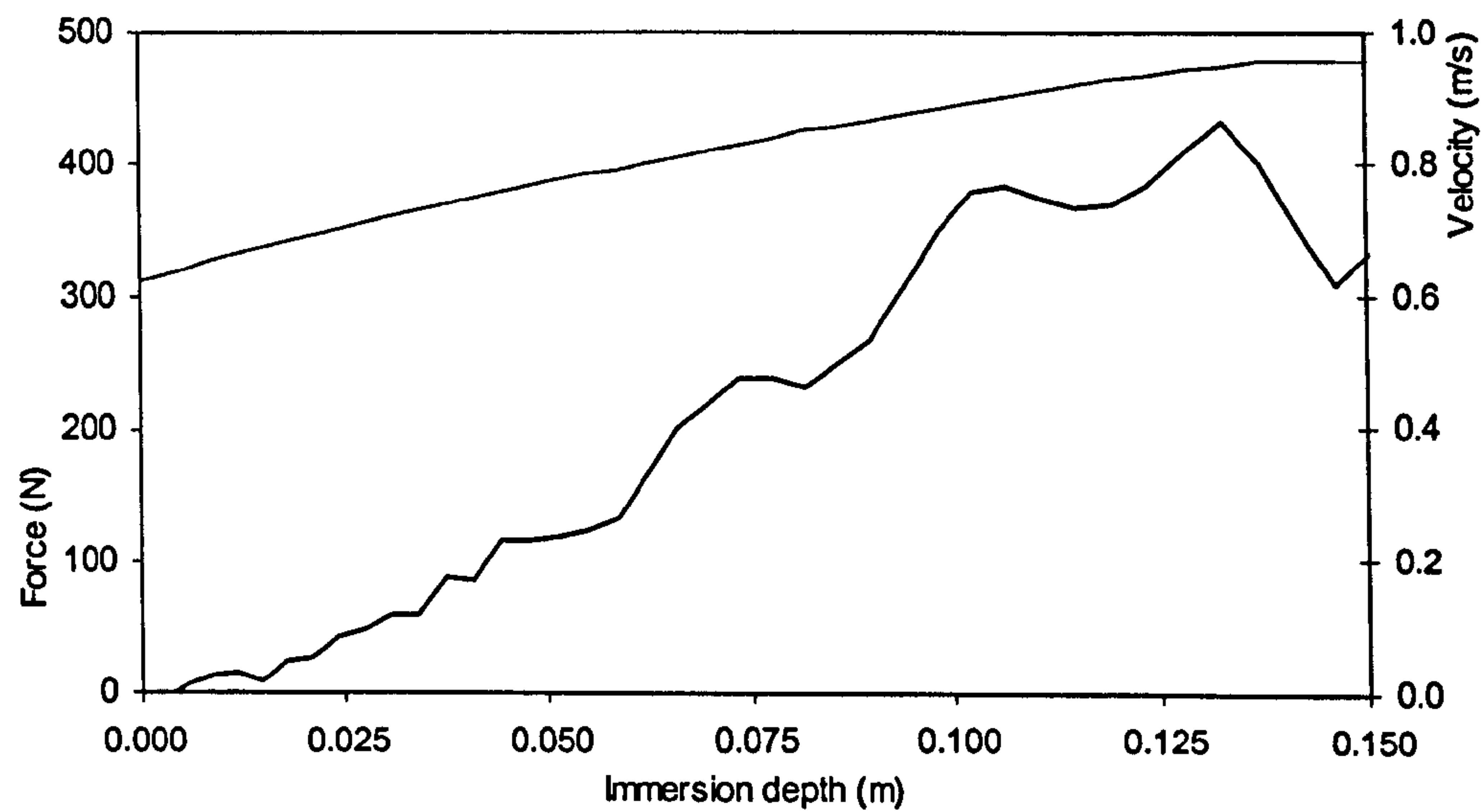


Figure 5-69. 30 degree accelerated water entry,  $a=2.50\text{m/s}^2$ .

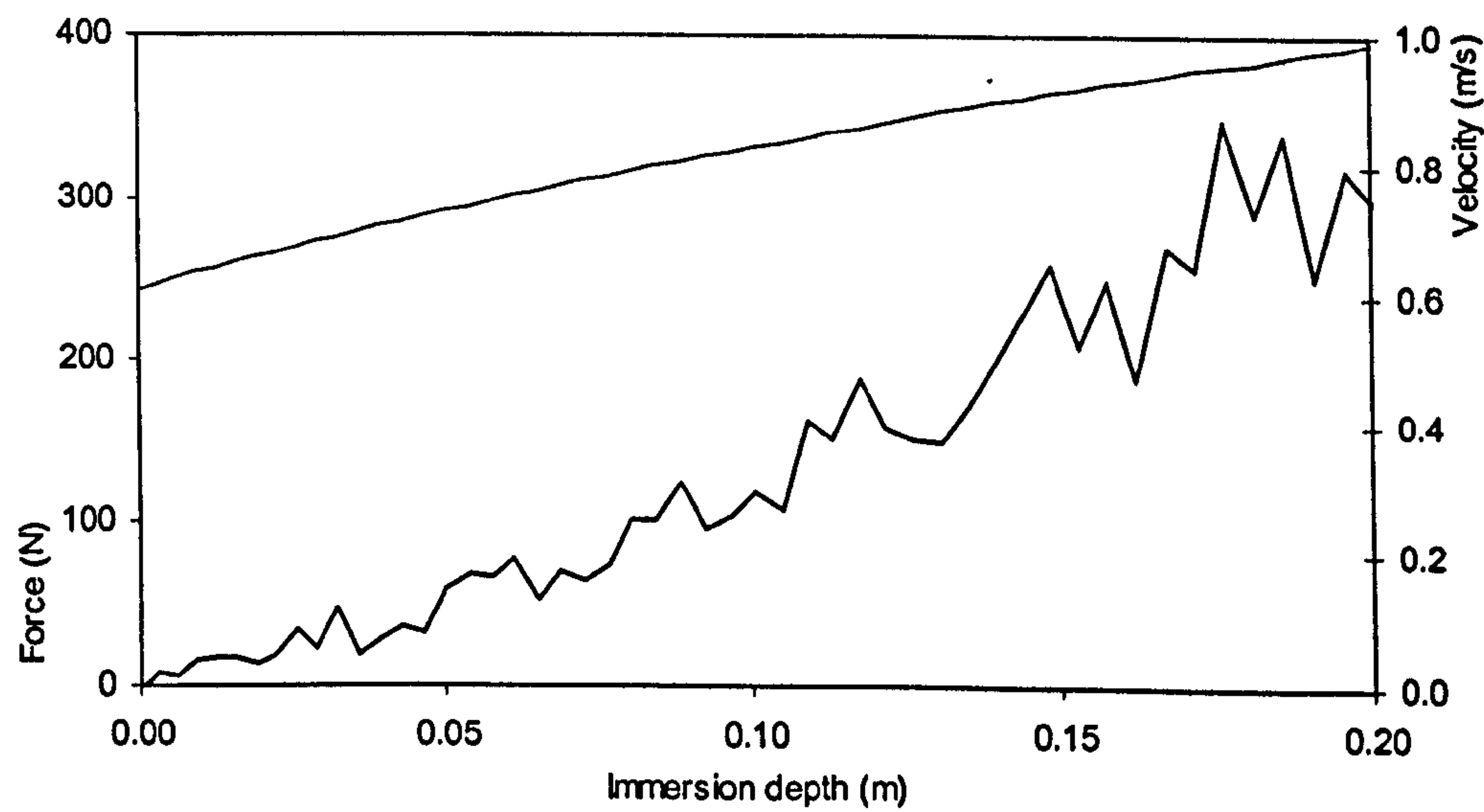


Figure 5-70. 45 degree accelerated water entry,  $a=1.71\text{m/s}^2$ .



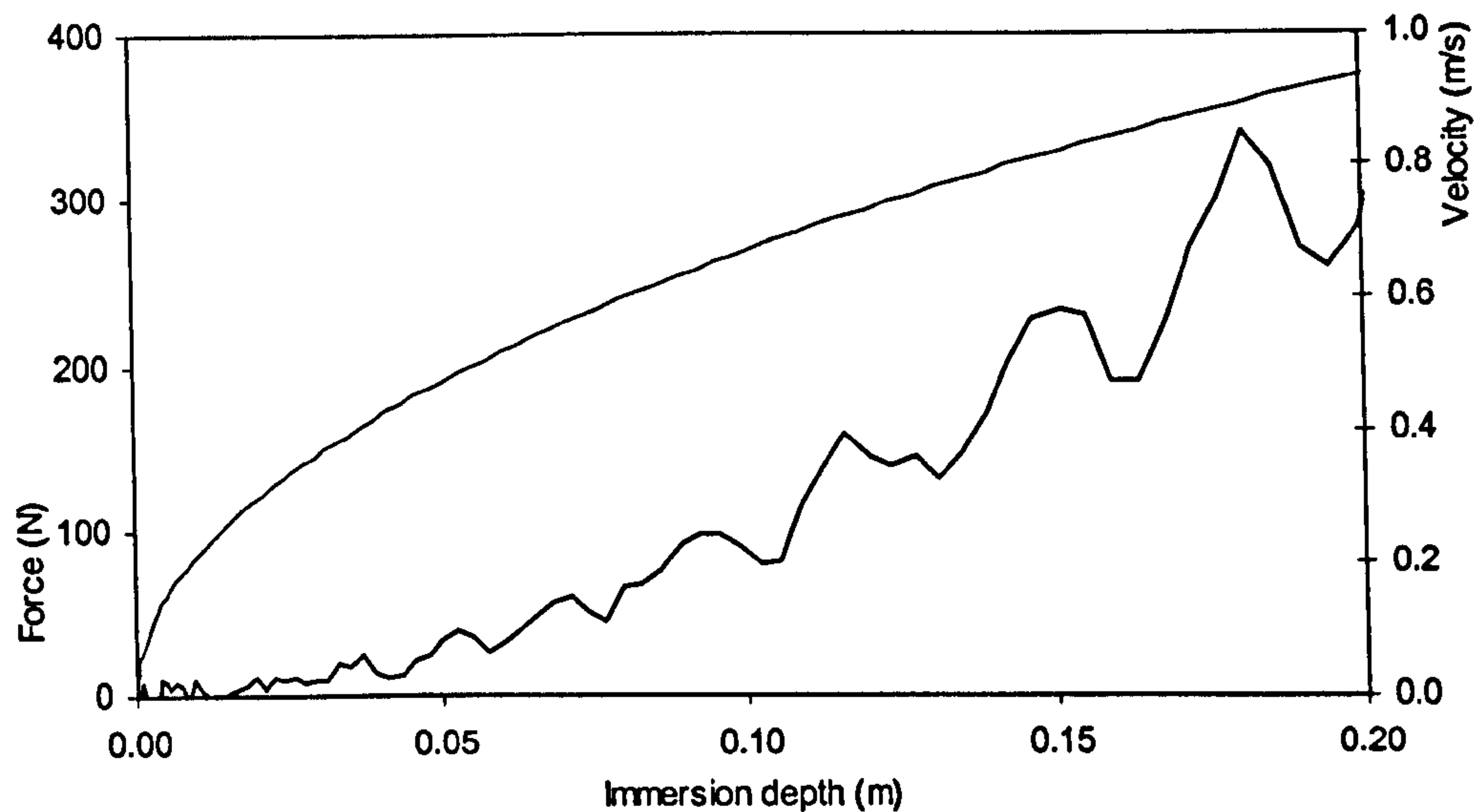


Figure 5-71. 45 degree accelerated water entry,  $a=2.40\text{m/s}^2$ .

#### 5.8.3.4. Constant Velocity Water Exit Tests

The force due to interaction with the water (once the test velocity is achieved) is found by subtracting the weight of the solid test section. The force data together with the recorded test velocity and the Archimedes buoyancy to the calm water level are plotted in Figures 5-72 to 5-75 for the period after constant velocity was achieved. Positive force is acting upwards. Thus the difference between the buoyancy force and the total force plotted is the dynamic force resisting upward movement. Note that the immersion depth is plotted on a reverse scale so that increase in time corresponds to moving from left to right in the charts.

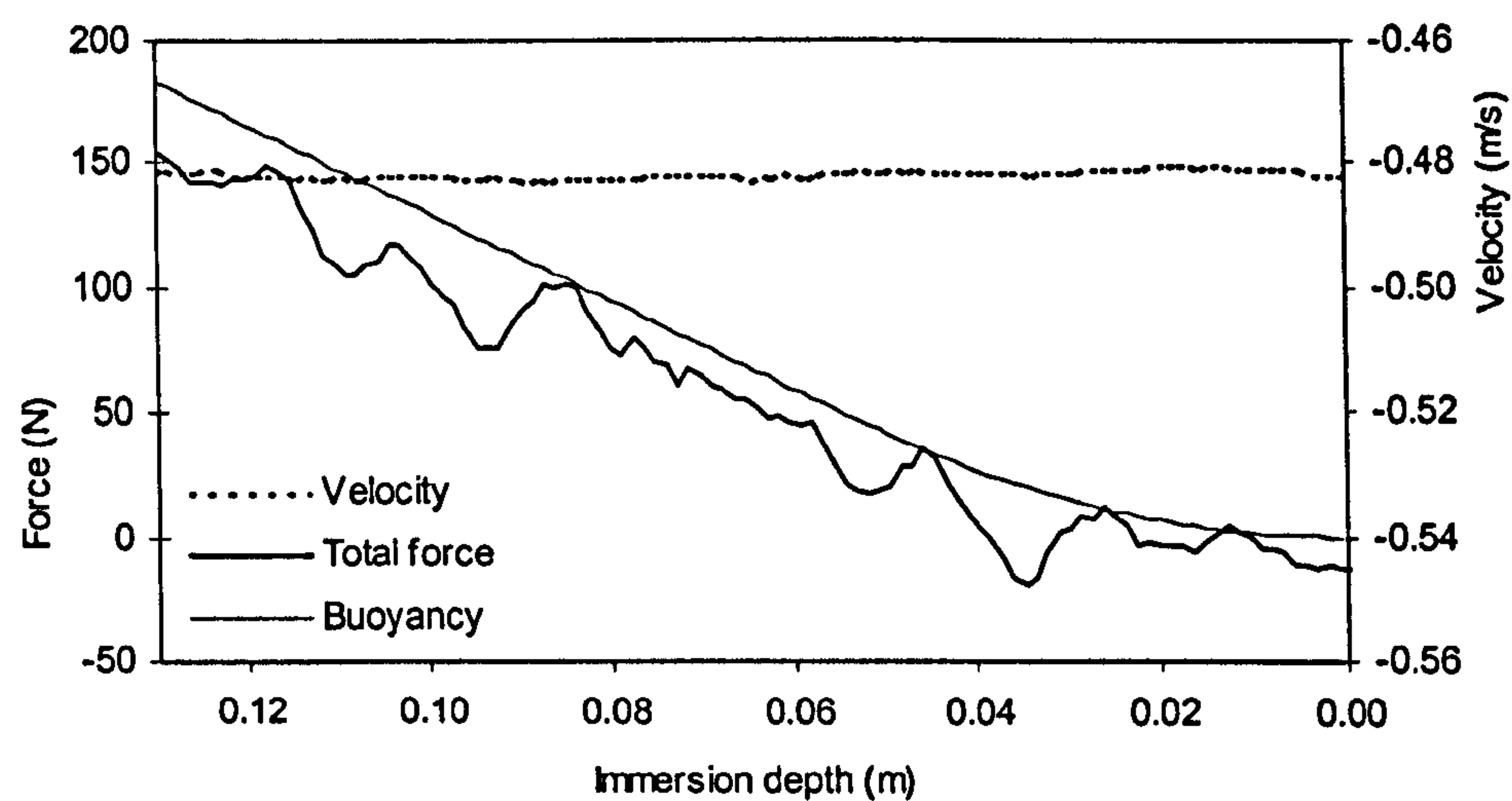


Figure 5-72. 10 degree constant velocity water exit at  $w=0.48\text{m/s}$ .

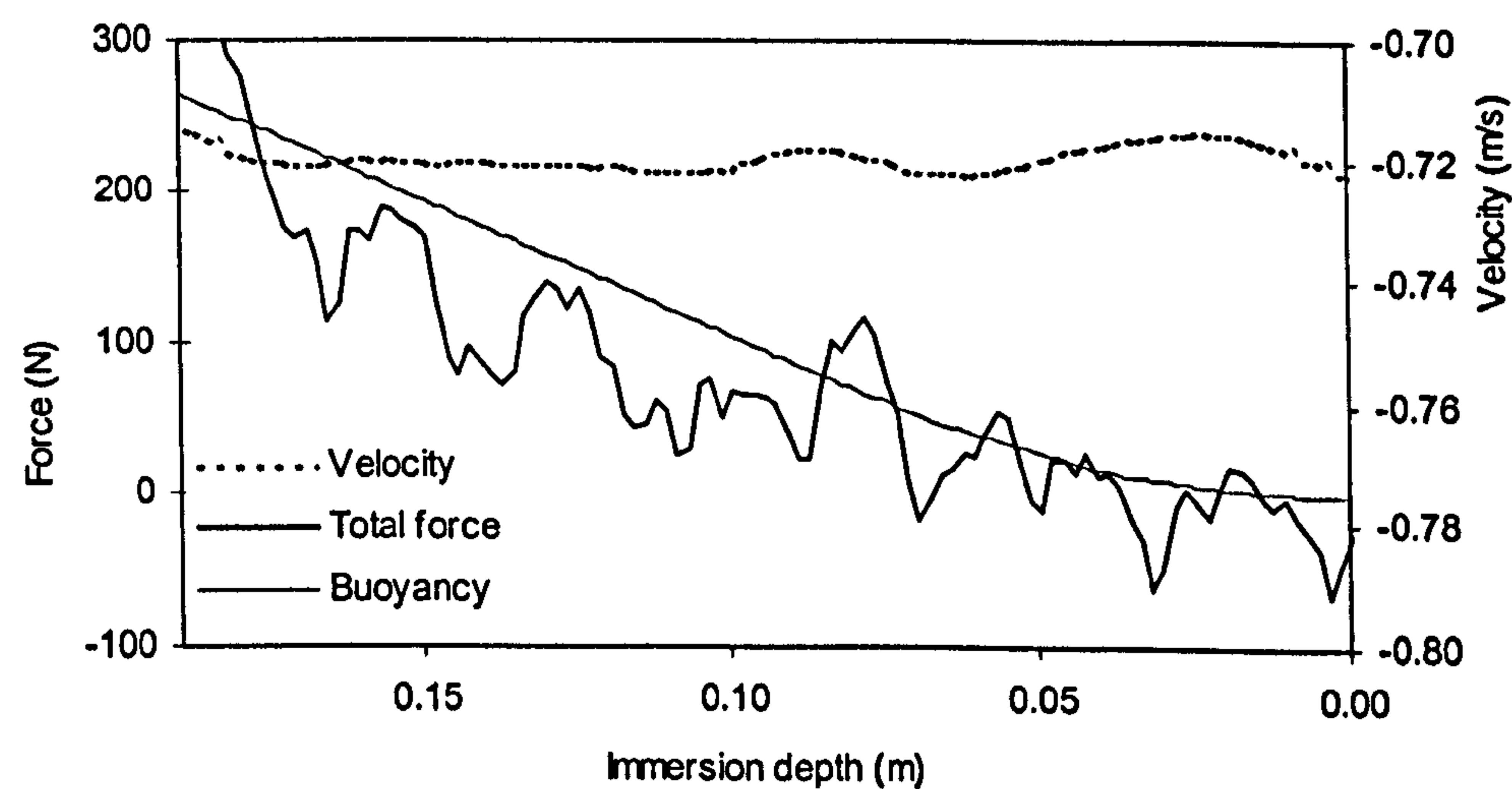


Figure 5-73. 15 degree constant velocity water exit at  $w=0.72\text{m/s}$ .



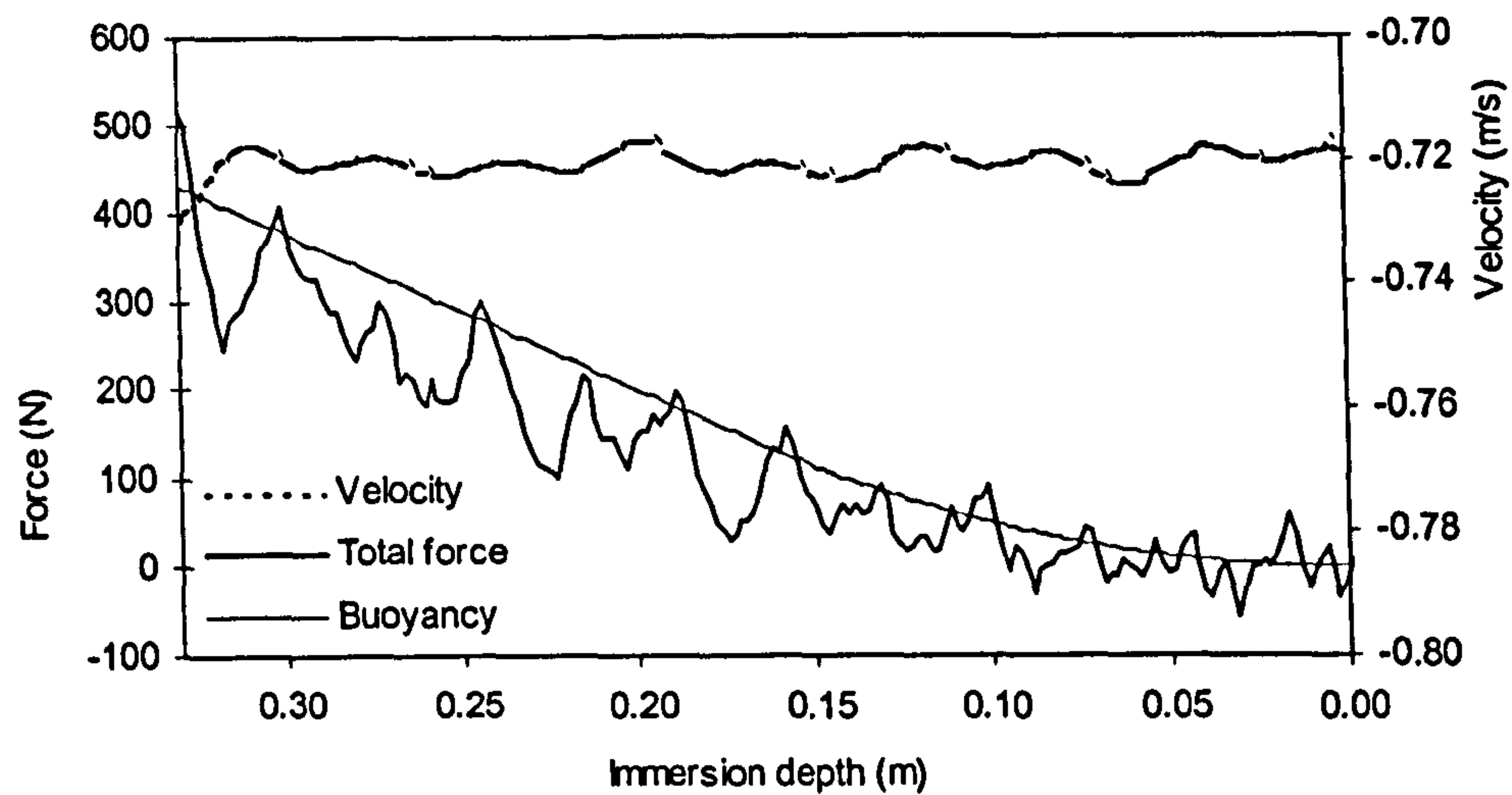


Figure 5-74. 30 degree constant velocity water exit at  $w=0.72\text{m/s}$ .

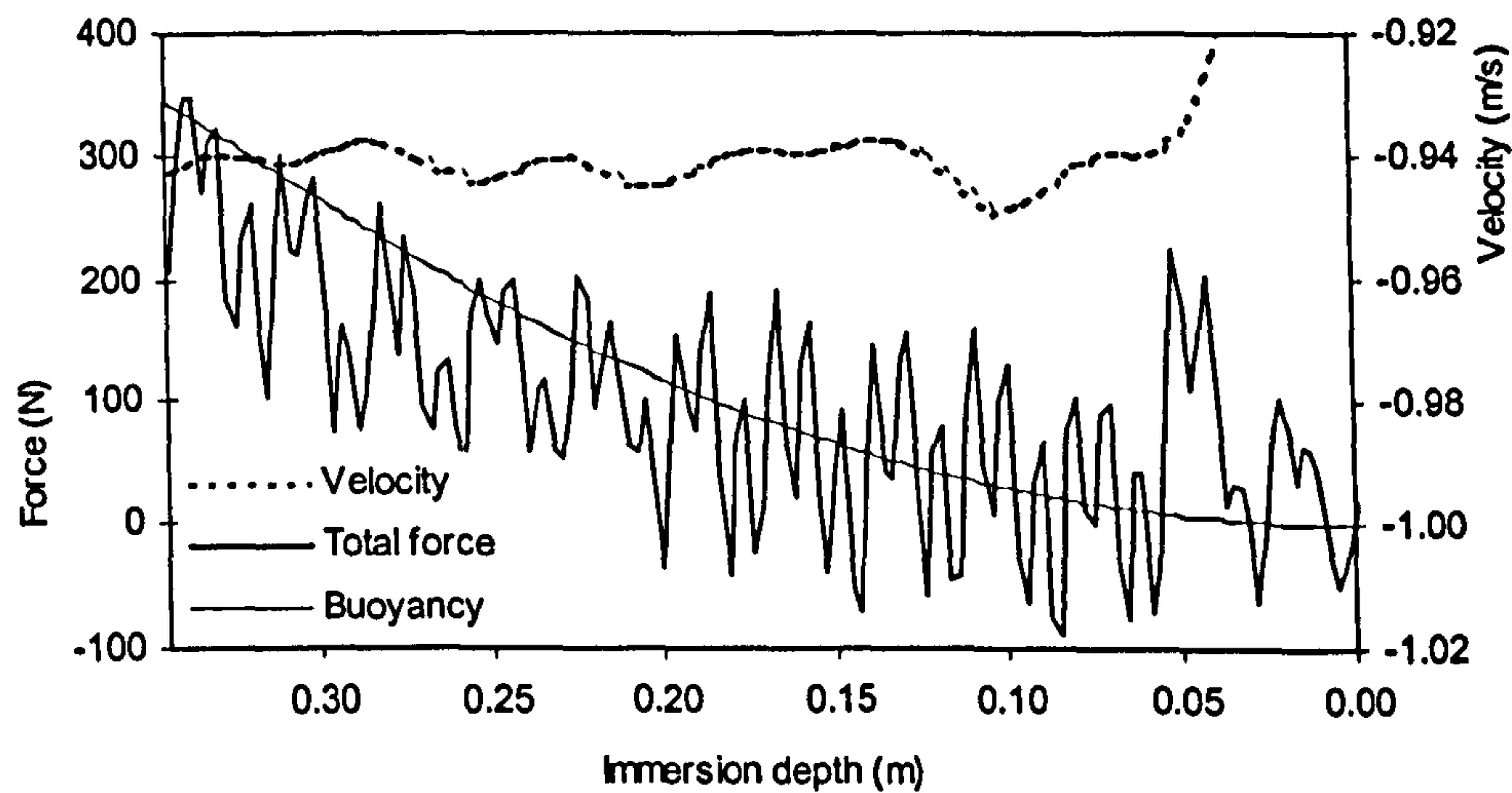


Figure 5-75. 45 degree constant velocity water exit at  $w=0.94\text{m/s}$ .

#### 5.8.4. Water Surface Shape

Video images of the constant velocity water entry and exit experiments were recorded to allow the comparison with the free surface shape from the CFD simulations, which are shown in Chapter 6.

#### 5.8.4.1. Water Entry

In Figures 5-76 to 5-80 a set of images captured from water entry sequences are presented. The sequences are captured from tests with the highest entry velocity of each wedge section.



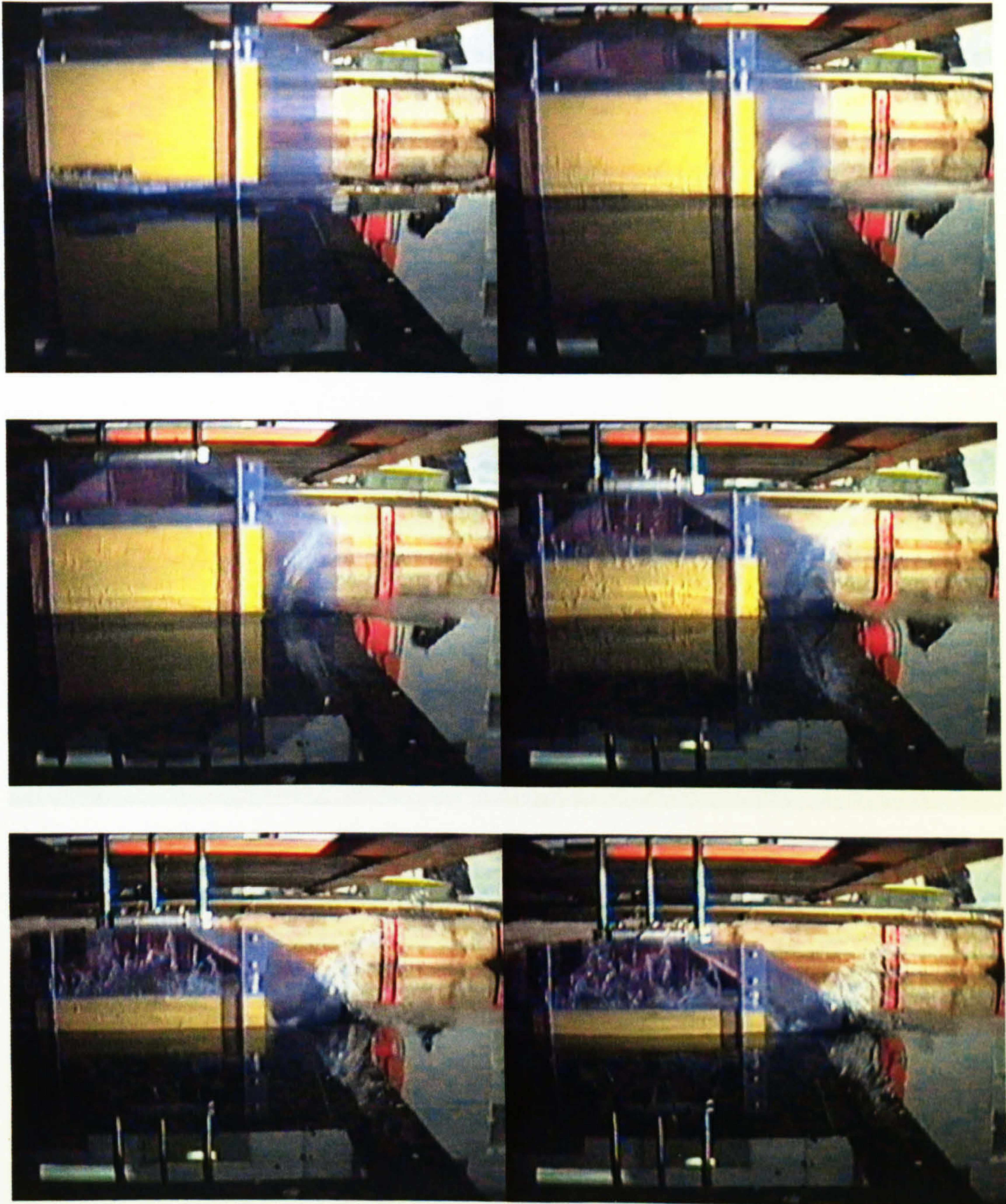
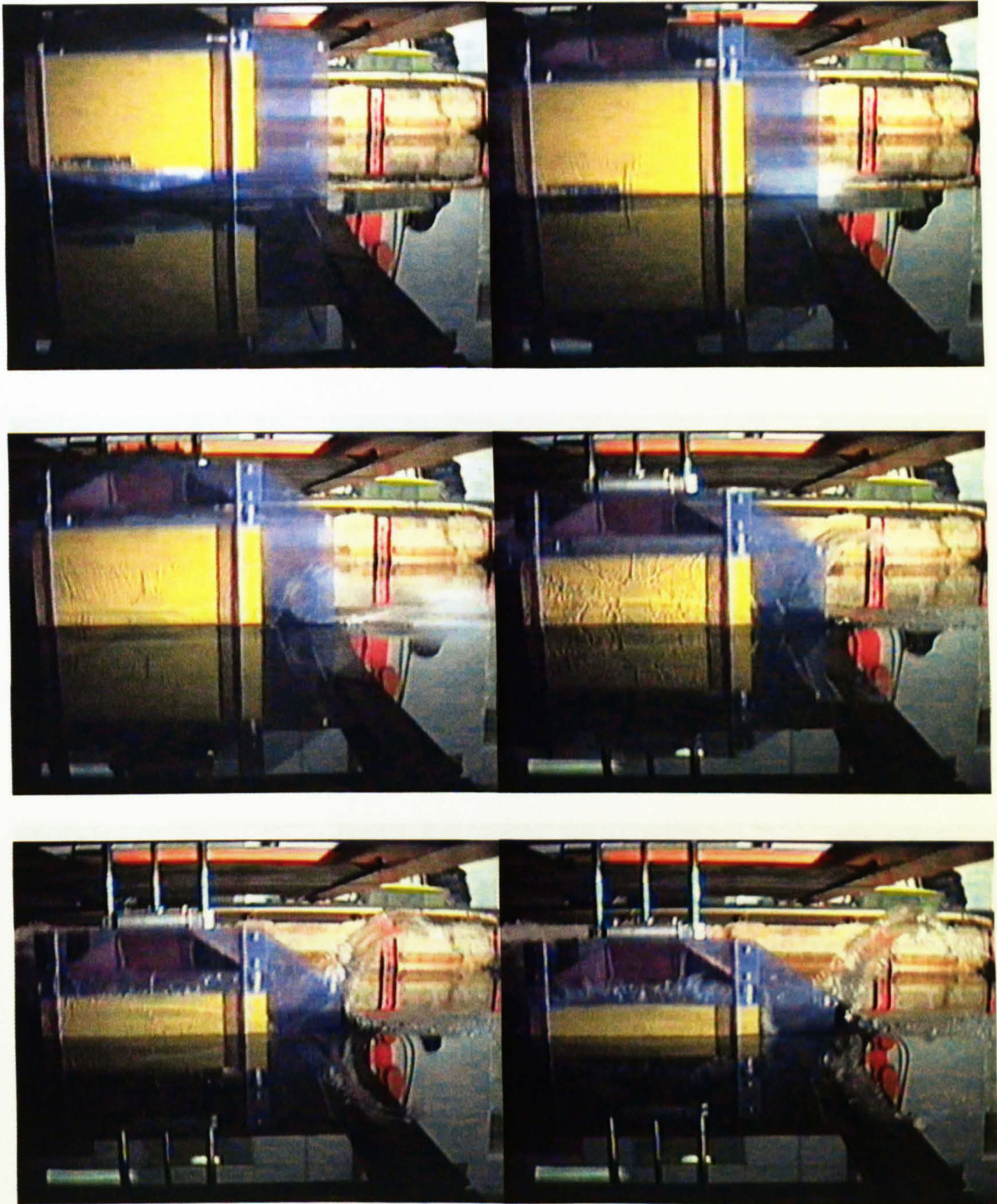


Figure 5-76. 5 degree constant velocity water entry.





*Figure 5-77. 10 degree constant velocity water entry.*





Figure 5-78. 15 degree constant velocity water entry.





*Figure 5-79. 30 degree constant velocity water entry.*





Figure 5-80. 45 degree constant velocity water entry.



5.8.4.2. Water Exit

One image from each of the 10, 15, 30 and 45 degree sections during water exit is shown in Figures 5-81 to 5-84 respectively. These images are captured when the vertical distance from undisturbed water surface to the chines is approximately half the section width. The images show that a large amount of water is moving entrained with the section to a level above the calm water surface.

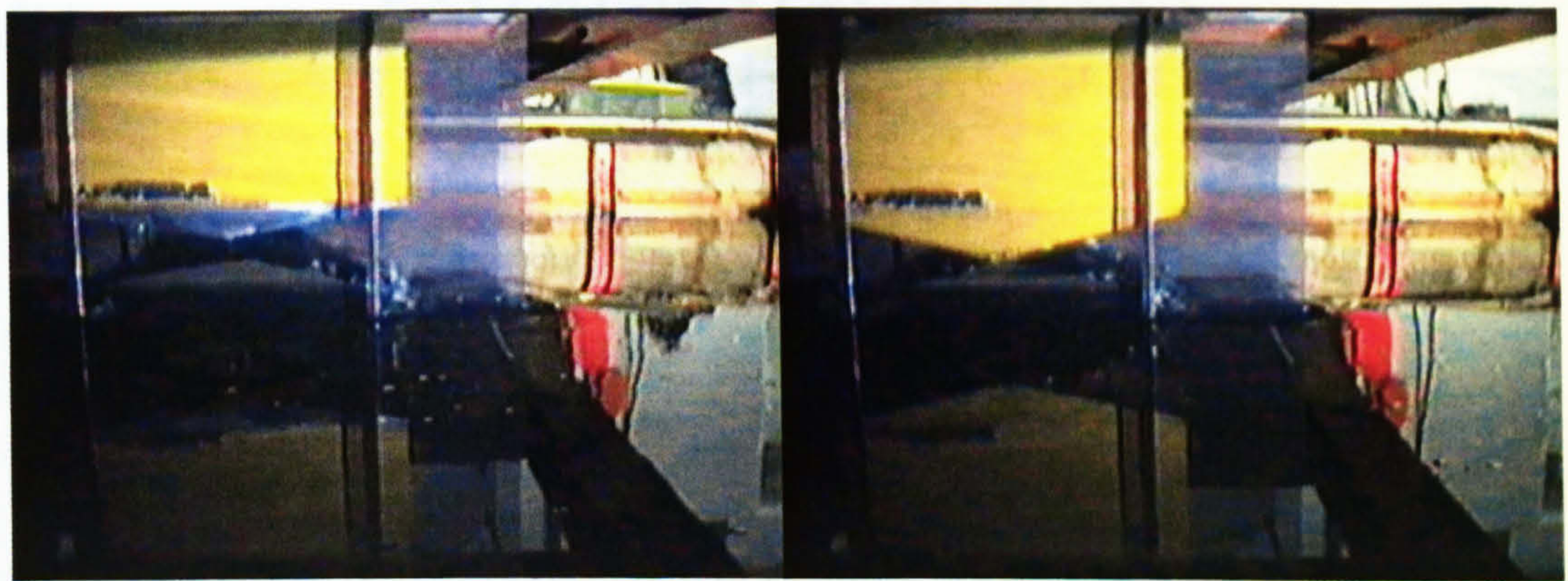


Figure 5-81. 10 degrees water exit.

Figure 5-82. 15 degrees water exit.



Figure 5-83. 30 degrees water exit.

Figure 5-84. 45 degrees water exit.



---

## **CHAPTER 6**

# **COMPARISON AND DISCUSSION OF CFD AND EXPERIMENTAL RESULTS**

---

In this chapter the experimental and CFD results are studied to find the most reasonable basis for development of a new theory. The experimental results are treated to extract the hydrodynamic force contribution from the interaction with the water from the load cells measurements, by removing the weight of the test section and the gravity dependent force that has been found from analysis of the CFD results. The hydrodynamic forces from the water entry experiments are compared with those obtained from the zero-gravity CFD simulation. Non-dimensional force coefficients for the dry chines cases are found from the experimental and CFD results, and these are compared in non-dimensional form with results from various other authors. Other aspects of the water entry problem, such as the pile up of water and the pressure distribution along the wedge surface, are also discussed and comparisons between experiments, CFD and other results are presented.

## **6.1. Comparison between CFD and Experiment**

### **6.1.1. Forces**

The exclusively hydrodynamic force, with flow unaffected by gravity during the constant velocity water entry, is obtained from the zero-gravity CFD simulations. However, the experimental results presented in Chapter 5 do not give the pure hydrodynamic force, but contain a hydrostatic component due to gravity, which is unavoidable in the test tank environment. The hydrostatic contribution to the total force during water entry depends on the velocity of the test section, the immersion depth and the deadrise angle. To be able to compare the zero-gravity hydrodynamic forces obtained from CFD simulation with those obtained experimentally, the hydrostatic term must be subtracted from the experimental data. The buoyancy ratio obtained by analysis of the data from the CFD simulations, described in Chapter 4, has been used to estimate the pure hydrodynamic contribution from the experimentally measured water entry forces. The full hydrostatic component is found by calculating the Archimedes buoyancy and multiplying this by the buoyancy ratio function as given in Equations (4-1) to



(4-3). Subtracting the full hydrostatic component from the experimental results yields the hydrodynamic force that acts on the section during entry. The hydrodynamic force, obtained with CFD simulations and experiments for all the test deadrise angles, is made non-dimensional on the maximum width of the test section and plotted against non-dimensional immersion depth  $z/d$  in Figure 6-1 to 6-5.

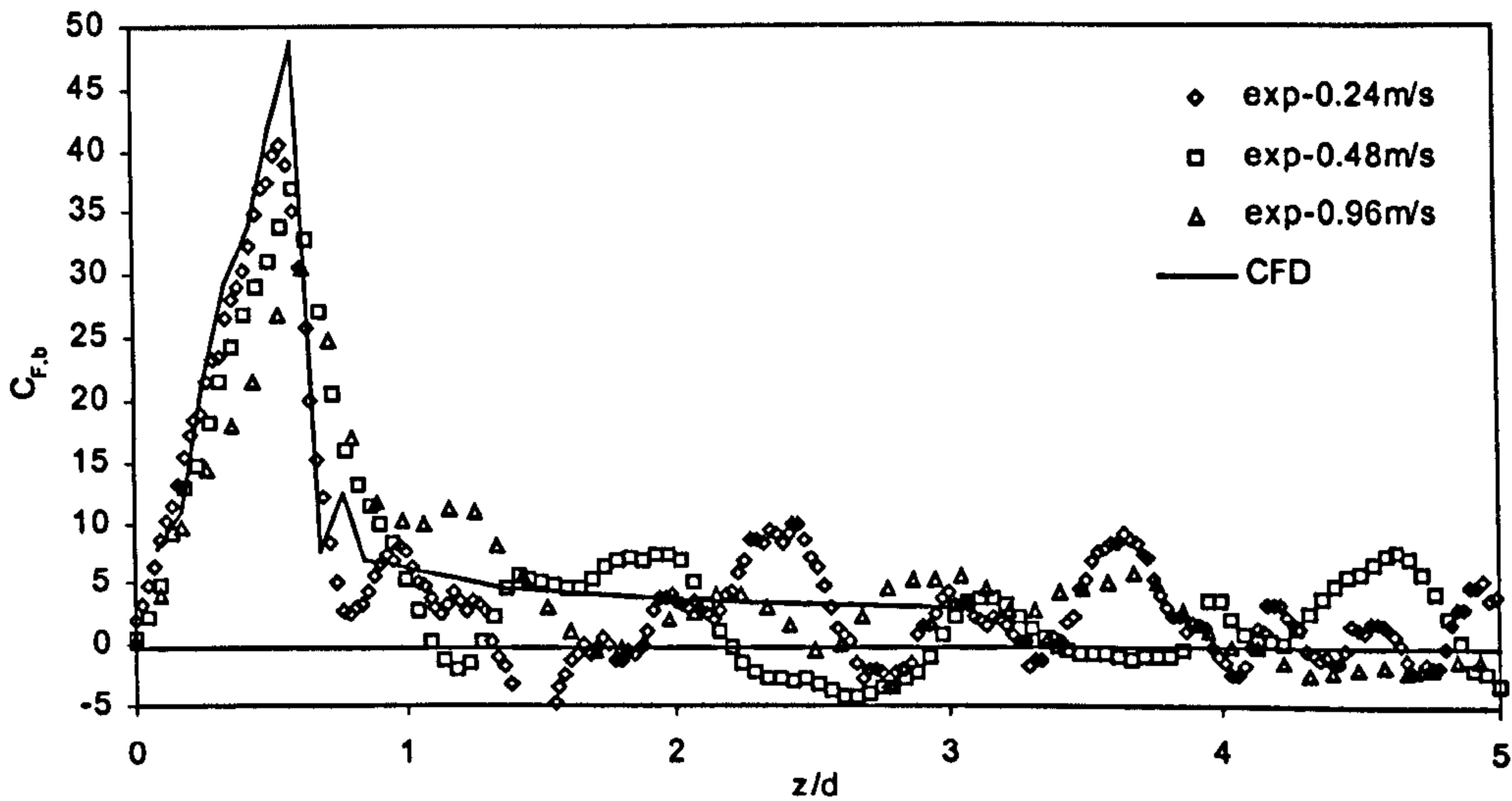


Figure 6-1. 5 degree constant velocity water entry, hydrodynamic force.

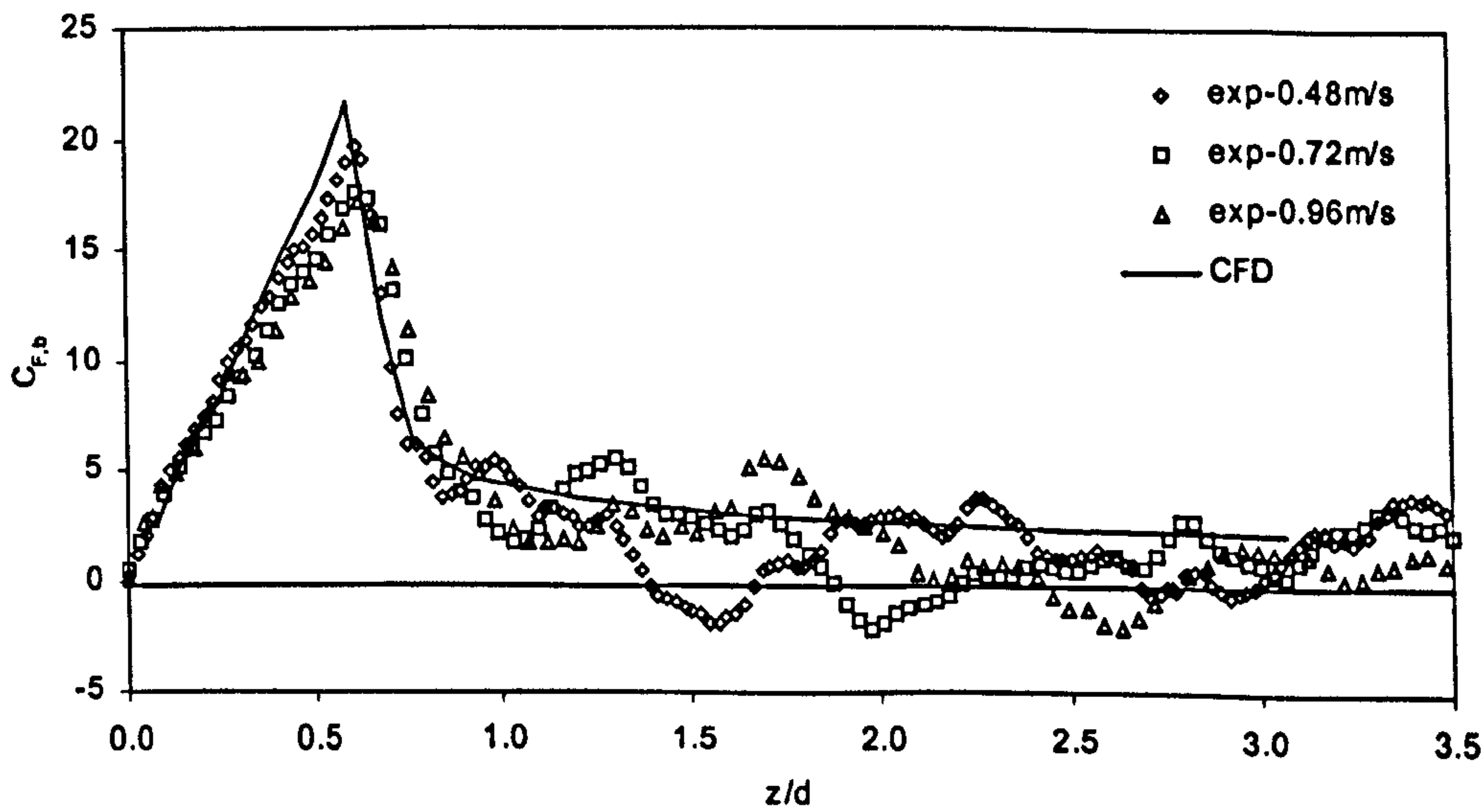


Figure 6-2. 10 degree constant velocity water entry, hydrodynamic force.

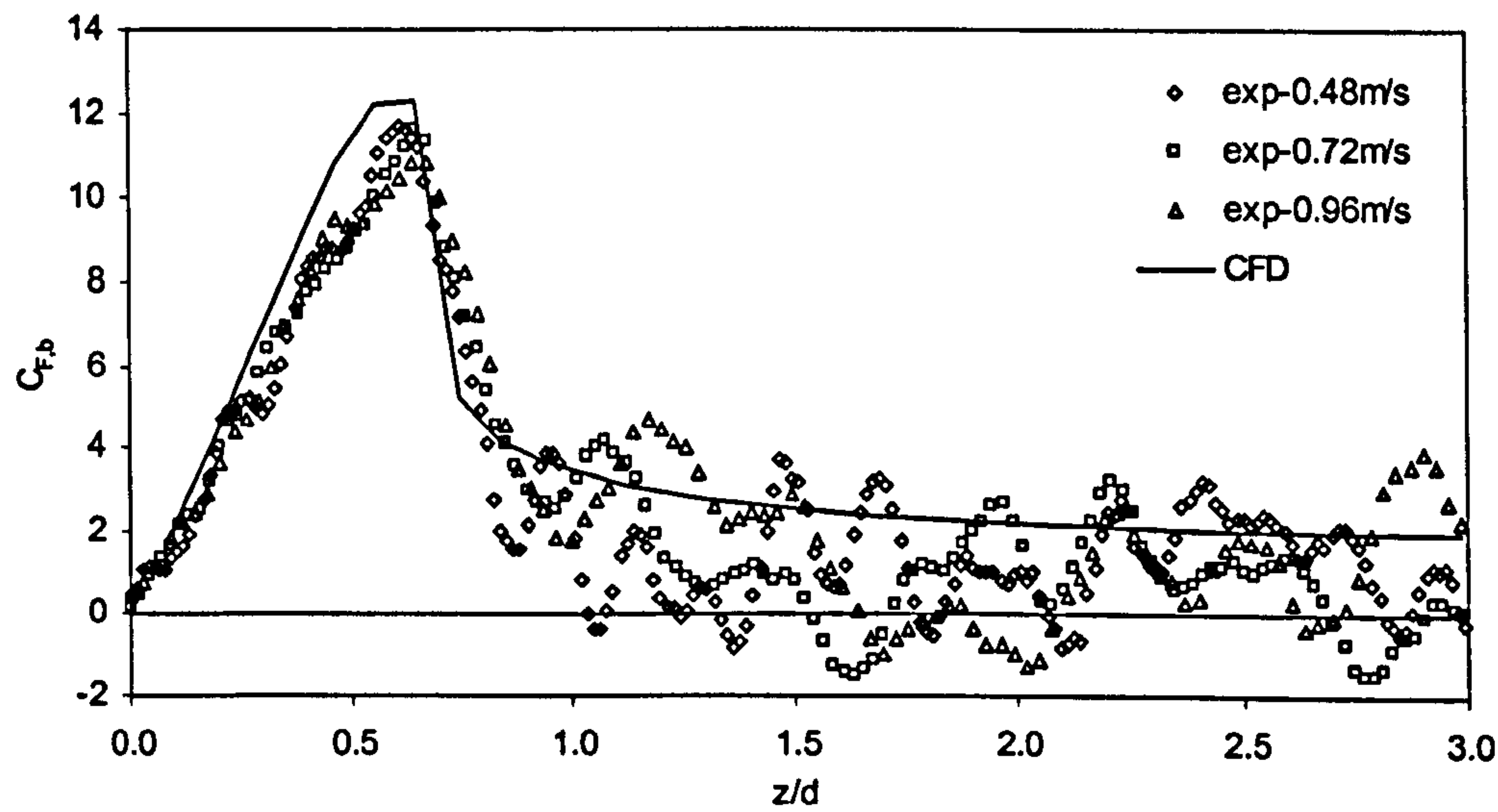


Figure 6-3. 15 degree constant velocity water entry, hydrodynamic force.

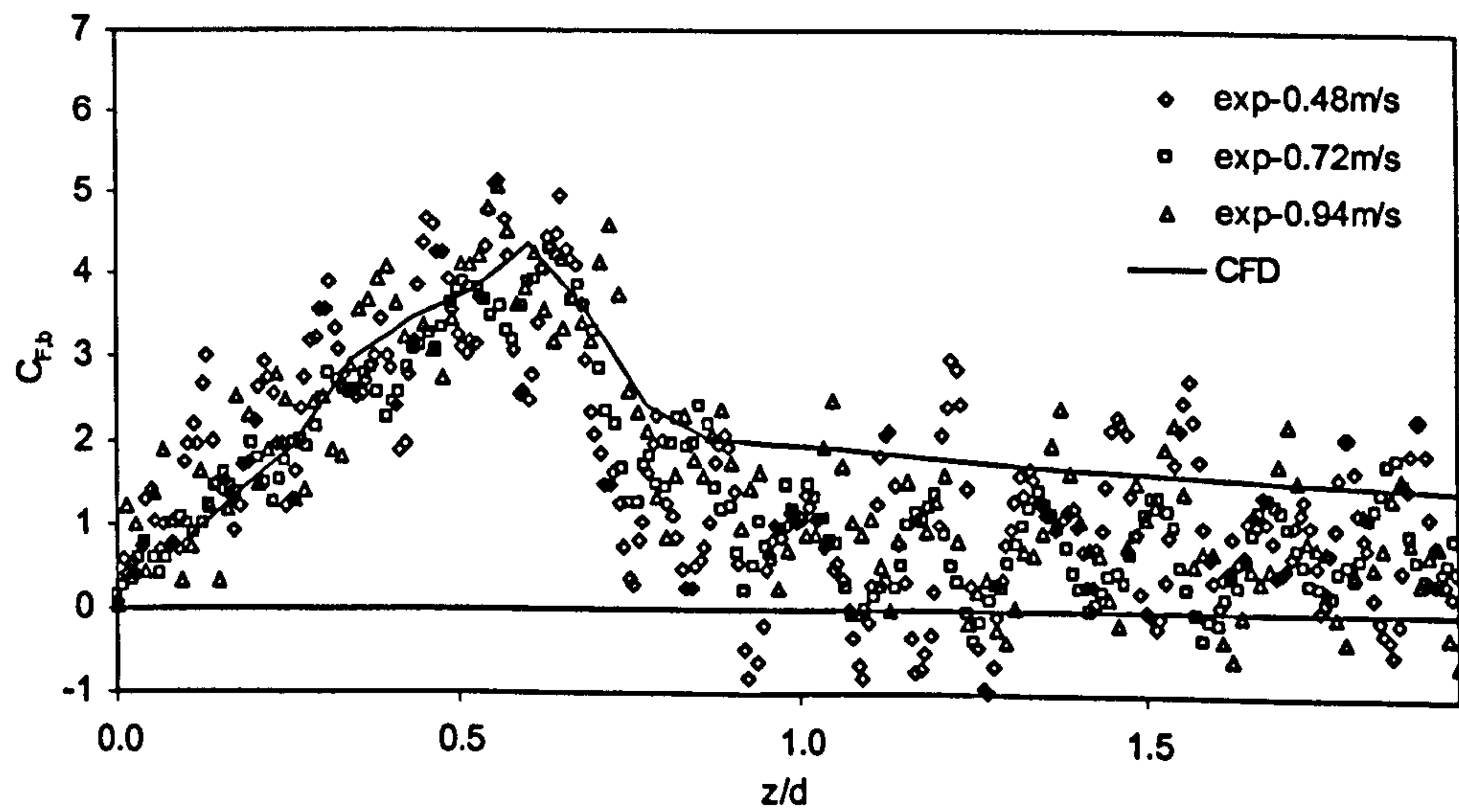


Figure 6-4. 30 degree constant velocity water entry, hydrodynamic force.



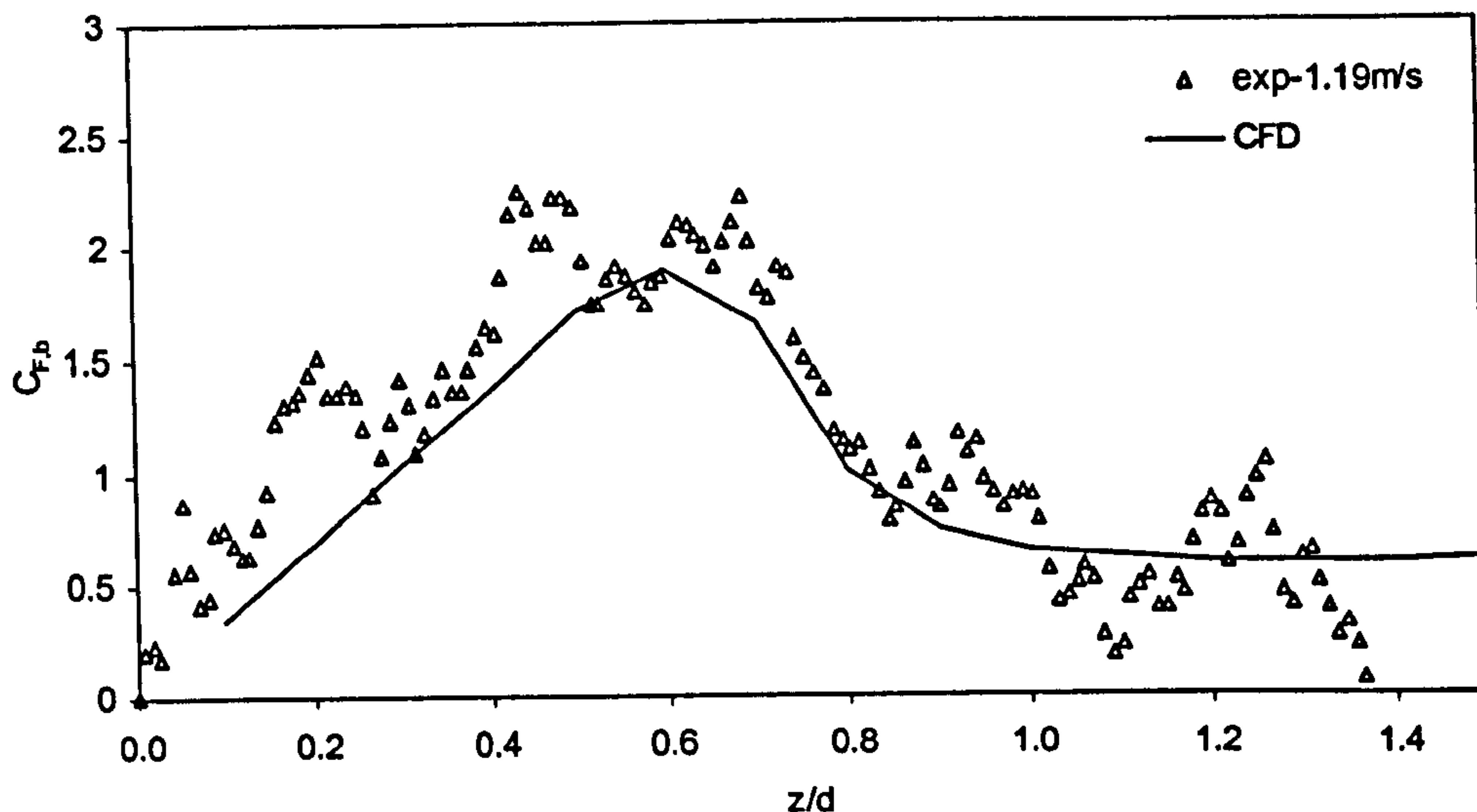


Figure 6-5. 45 degree constant velocity water entry, hydrodynamic force.

These force plots show that the forces obtained with CFD simulations are generally larger than those obtained experimentally, apart from the 45 degree results where the opposite is seen. The dry chines ( $z/d < 2/\pi$ ) forces obtained for each test section at different test velocities compare well for the 15 and 30 degree cases. For the 5 and 10 degree cases, the rate of increase of force from initial entry until the force peaks has a different slope for the three test velocities. This is more pronounced for the 5 degree case than the 10 degree case. During the 5 degree water entry at 0.94m/s, the force is rising from 0 to nearly 2500N in less than 18 ms. This exposes the load cells to a variation of more than 60% of their capacity in a short period of time. An explanation of the discrepancy between the dry chine forces obtained with different velocities for 5 and 10 degree sections may be an inadequate dynamic response of the load cells. If the sensors are exposed to a force that varies faster than the dynamic response, a lag will occur in the output signal. An increase in force will then appear as having lower slope than the actual rate of increase and the peak force will be lower.

The force acting on a wedge section during a dry chines constant velocity entry is commonly expressed in terms of a slamming force coefficient based on the immersion depth  $z$ . This slamming force coefficient is defined by

$$C_F = \frac{F'}{\rho w^2 z}$$

(6-1)

where  $F'$  is the hydrodynamic force per unit length of wedge section. Because of geometrical similarity, Equation (6-1) is expected to give constant values of  $C_F$  for  $z/d < 2/\pi$ .  $C_F$  values have been calculated for both the experimental and the CFD results. Each data point for immersion depths less than the depth at which the peak force occurs is made non-dimensional according to Equation (6-1), and the average value of these values of  $C_F$  is calculated separately for each deadrise angle. The resulting average slamming force coefficients are given in Table 6-1 together with the percentage difference between the CFD and experimental result.

$\beta$ [degrees]	$C_F$ - CFD	$C_F$ - Exp	Discrepancy
5	916	825	11 %
10	201	180	12 %
15	86.3	72.1	20 %
30	13.0	12.9	0.78 %
45	3.47	3.56	-2.5 %
60	0.818	-----	-----

Table 6-1.  $C_F$ , slamming force coefficients on immersion depth.

The force coefficients given in Table 6-1 show that the CFD simulation gives considerable higher force than obtained experimentally for low angles of deadrise, while for the 30 and 45 degree deadrises the discrepancy is much lower. The low discrepancy at high deadrise angles provides some validation for the dry chines higher deadrise angle CFD result.

The buoyancy ratio analysis described in Chapter 4 did not include the zero deadrise case. Therefore the hydrodynamic force from the experimental results



with the flat-bottomed section has been obtained by subtracting the full Archimedes' buoyancy. The resulting force is made non-dimensional on the section beam and is plotted in Figure 6-6 together with the zero-gravity CFD force data.

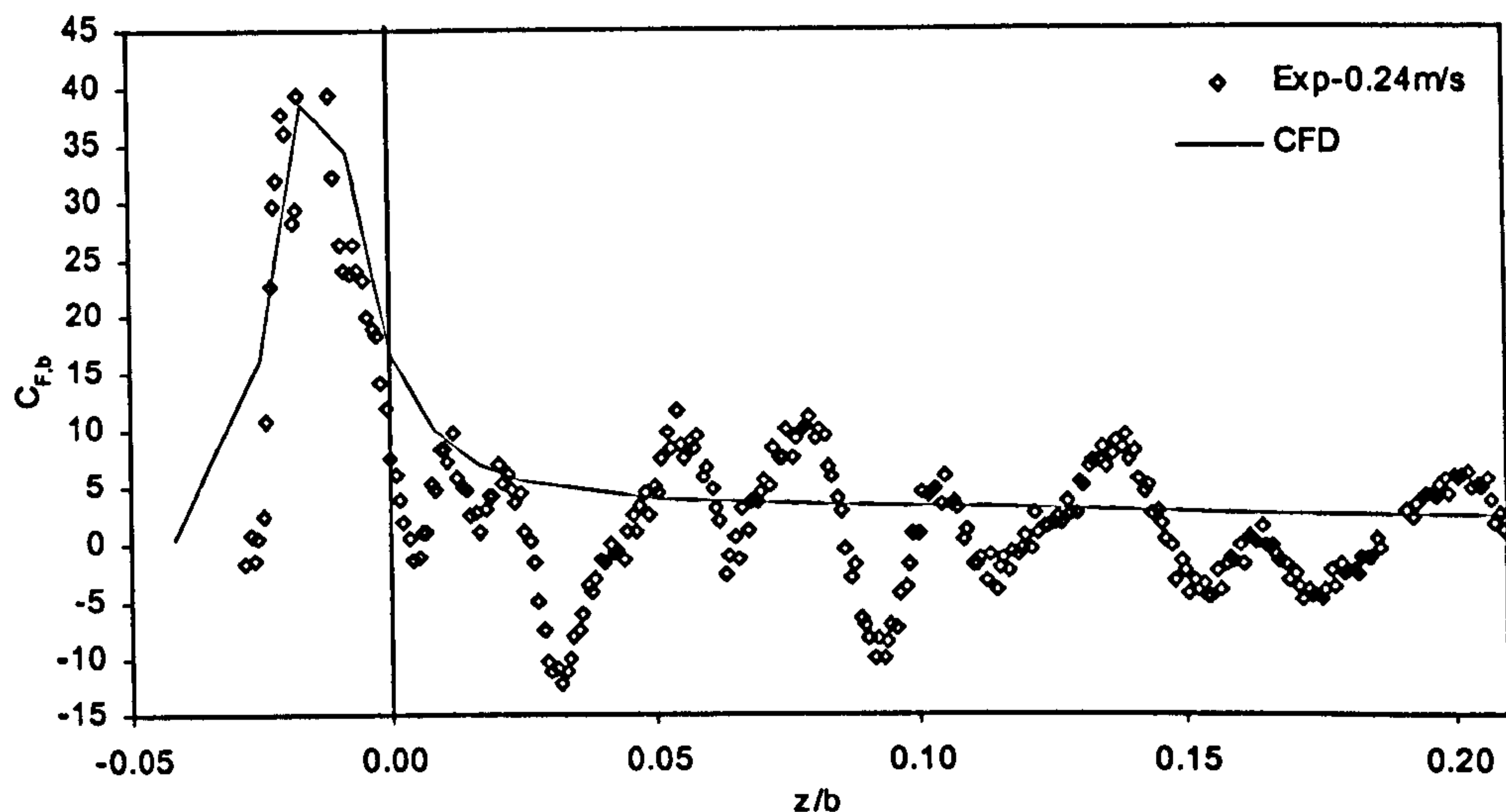


Figure 6-6. Flat-bottomed section water entry, hydrodynamic force.

It is seen that a force is present at negative immersion depth, i.e. before the section reaches the calm water level. This is due to pressure building up when air “escapes” from under the section, and hence deforms the water surface causing an advanced impact with the water (before the section crosses the calm water line). The force data from the CFD simulation show that the impact starts when the section is at a non-dimensional distance of  $z/b=0.042$  above the calm water level. Koehler and Kettleborough (1977) computed the surface deformations caused by the impact of a flat-bottomed two-dimensional section with water. This showed that impact initiated at an approximate non-dimensional distance  $z/b=0.05$  above the calm water surface. Ng and Kot (1992) found the same result by CFD simulation of the flat-bottomed water impact. The experimental data in Figure (6-6) show that the impact occurs at about  $z/b=-0.03$  above the calm water surface. The advanced impact force is not accounted for in the present theory. However, this effect is going to be substantially less in planing than for the two-dimensional water entry, as the air also “escapes” in the forward direction.

### 6.1.2. Wetting factor

The wetting factor  $WF$  is the ratio of wetted width to nominal width for a wedge during dry chines water entry. In the present work, the wetted width is defined as the distance between the pressure termination points. The termination of the geometric similarity condition during a wedge entry, i.e. the end of the dry chine condition, is then identified as when the wetted width coincides with the chines width. Hence, the wetting factor is found from the experimental data as the inverse of the non-dimensional immersion depth at the instant of peak force occurrence, i.e.  $WF=(z_{PF}/d)^{-1}$ . The wetting factor obtained with the CFD analysis is found more directly by studying the pressure distribution along the wedge. The non-dimensional immersion depths of peak force occurrence  $z_{PF}/d$ , obtained from the experimental data, and the non-dimensional pressure termination points  $Z_{pt}/z$ , obtained from the CFD analysis, are given in Table 6-2 ( $Z_{pt}$  is the ordinate of the pressure termination point from the keel). The table also gives the inverse of these values, i.e. the wetting factors according to the present definition. The results from both the experiments and the CFD show good agreement with Wagner's deadrise independent wetting factor,  $WF = \pi/2$ .



	Experiment			CFD	
$\beta$	w [m/s]	$\frac{z_{PF}}{d}$	WF	$\frac{Z_{pt}}{z}$	WF
5	0.24	0.57			
	0.48	0.60	1.67	0.64	1.56
	0.96	0.63			
10	0.48	0.61			
	0.72	0.65	1.59	0.64	1.56
	0.96	0.63			
15	0.48	0.64			
	0.72	0.68	1.50	0.61	1.64
	0.96	0.68			
30	0.48	0.68			
	0.72	0.69	1.52	0.65	1.54
	0.96	0.61			
45	1.19	0.71	1.60	0.60	1.67

Table 6-2. Wetting factors obtained with CFD and experiments.

### 6.1.3. Free Surface Elevation

It is of interest to compare the shape of the free surface as modelled in the CFD simulation with that captured with video recordings of the experiments. The position of segments of the free surface has been measured from large print outs of video images from the experiments. The shapes of the free surface during dry chines entry obtained from CFD simulations and from experiments are shown in Figure 6-7.

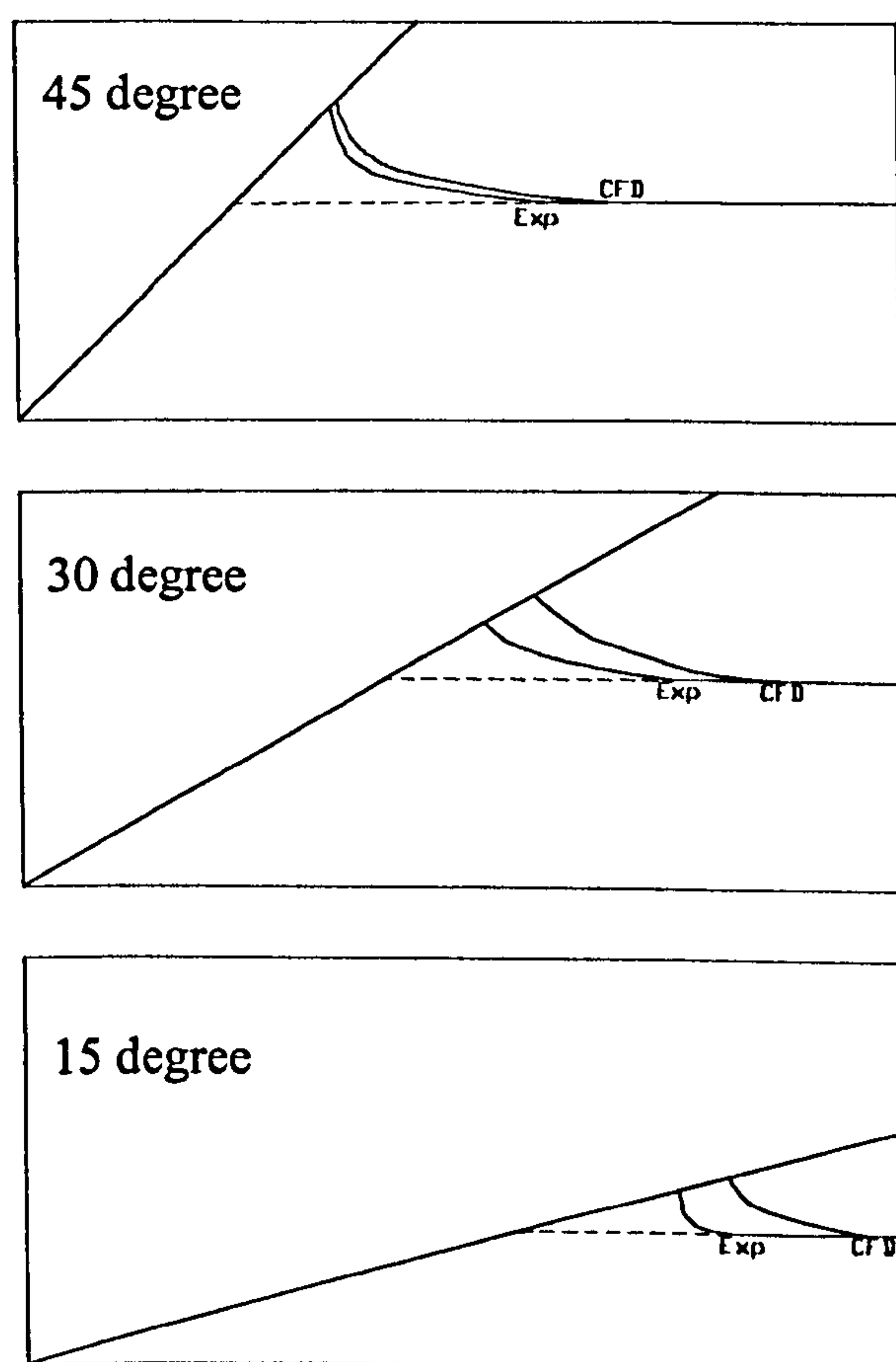


Figure 6-7. Water pile-up, shape of the free surface.

The comparison of the free surface shapes shows that the water pile-ups from the CFD simulations are greater than observed experimentally. The ratios of the green-water pile-up width to nominal width are given in Table 6-3.



$\beta$ [degrees]	Experiment	CFD
15	1.26	1.40
30	1.27	1.41
45	1.42	1.46

Table 6-3. Water pile up ratio, CFD and experiment.

The CFD free surface shapes presented in Figure 6-7 are from zero-gravity simulations while the experimental work obviously is carried out in a gravity environment. At low velocities the gravity will affect the flow, and hence affect the free surface shape. The images are captured from tests with entry velocity of 0.94m/s. Takemoto (1999) presents a theory for calculating the threshold velocity above which the gravity does not affect the flow significantly, and verified this with results from free-fall impact tests. This theory gives the threshold velocities for the three deadrise angles in Figure 6-7, at the immersion depths the images were captured, as less than 0.5m/s. Thus, if the threshold velocity from Takemoto is valid, the discrepancy between simulations and experiments in Figure 6-7 is not caused by gravity effects. However, Takemoto used free-fall tests to verify his theory. During free-fall tests the velocity during the water entry is not constant, and it is possible that thresholds during such entries differ from thresholds during constant velocity entry.

If gravity effects do not cause the difference in water pile-up, it may be that the free surface capturing (VOF) method applied in the CFD simulation has been inadequate, in which case the simulated free surface does not give a good representation of the phenomena. However, with the present definition, the agreement between experiments and CFD on wetting factor is quite good.

The plotted contour in Figure 6-7 represents the boundary of the green water. In the previous section the experimental data presented in Table 6-2 shows that the force peaks occur at non-dimensional immersion depths between 0.60 and 0.66.

This corresponds to a water pile-up between 1.52 and 1.67, i.e. considerably greater than the non-dimensional experimentally observed water pile-up presented in Table 6-3. From this it follows that there are high pressures in the spray region, above the green water boundary, that contribute significantly to the entry force.

## 6.2. Comparison With the Work of Others

The results obtained from the CFD and experimental work presented in the previous sections are compared in the following sections with results from other researchers.

### 6.2.1. Slamming Force Coefficient

The slamming force coefficients given in Table 6-1 are compared with various simulations in Figure 6-8. For better presentation, the coefficients are multiplied by  $\tan^2 \beta$ .

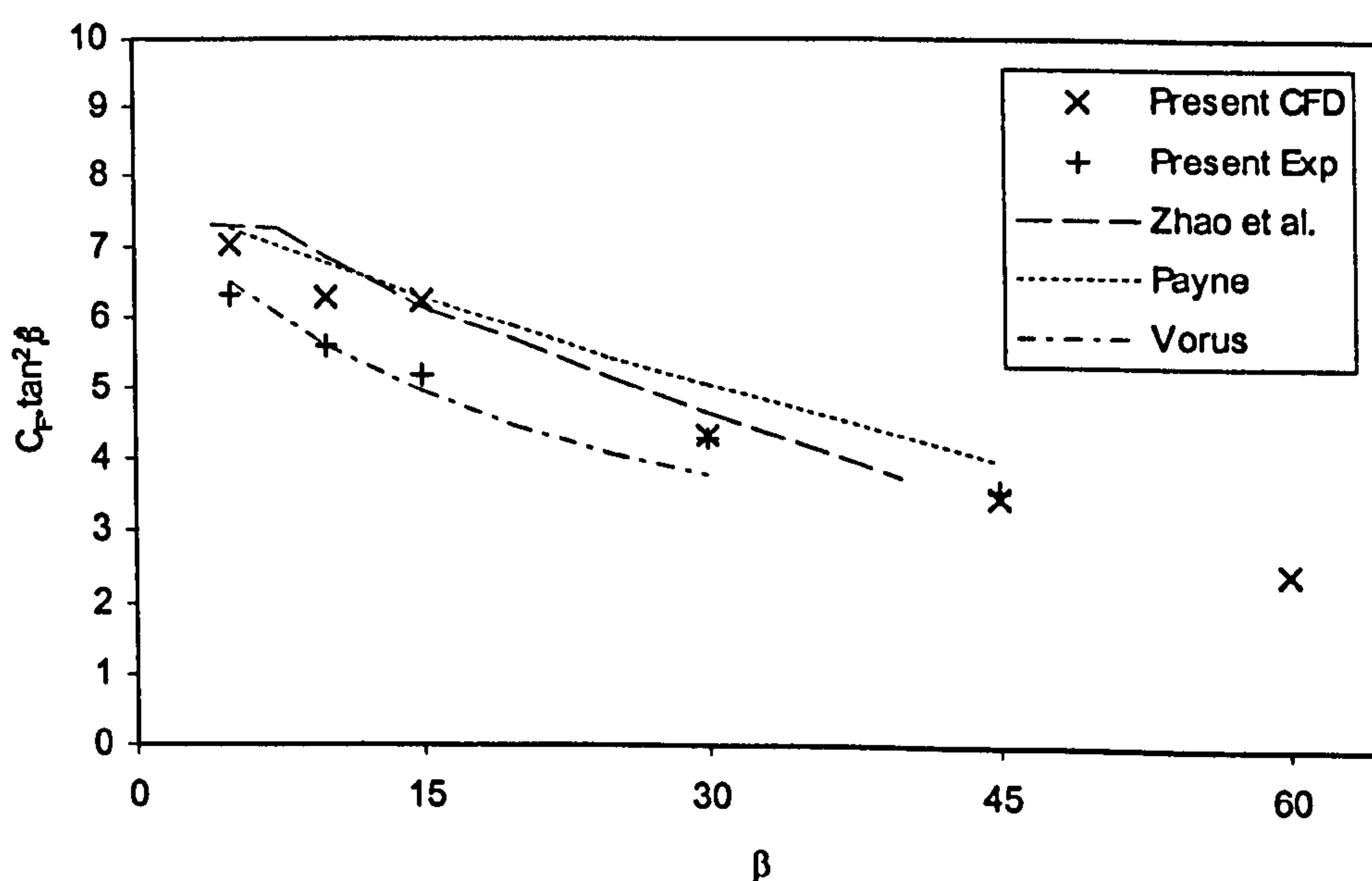


Figure 6-8. Slamming force coefficients.

It is seen that the experimental results agree best with the numerical approach by Vorus (1996) for low deadrise angle sections, while for the high deadrise angles



there is better agreement with the semi-analytical method from Payne (1994). The CFD results lie between those given by Vorus and the boundary element method of Zhao et al. (1993) with a tendency towards the latter.

### 6.2.2. Maximum Pressures

The point at which the peak pressure occur on the wedge, obtained from CFD simulations, is presented as a non-dimensional elevation  $Z_{p-max}/z$  in Figure 6-9 and compared with that given by Pierson (1954), Zhao and Faltinsen (1993) and Vorus (1996).  $Z_{p-max}$  is the vertical distance from the wedge apex up to the point of peak pressure and  $z$  is immersion depth.

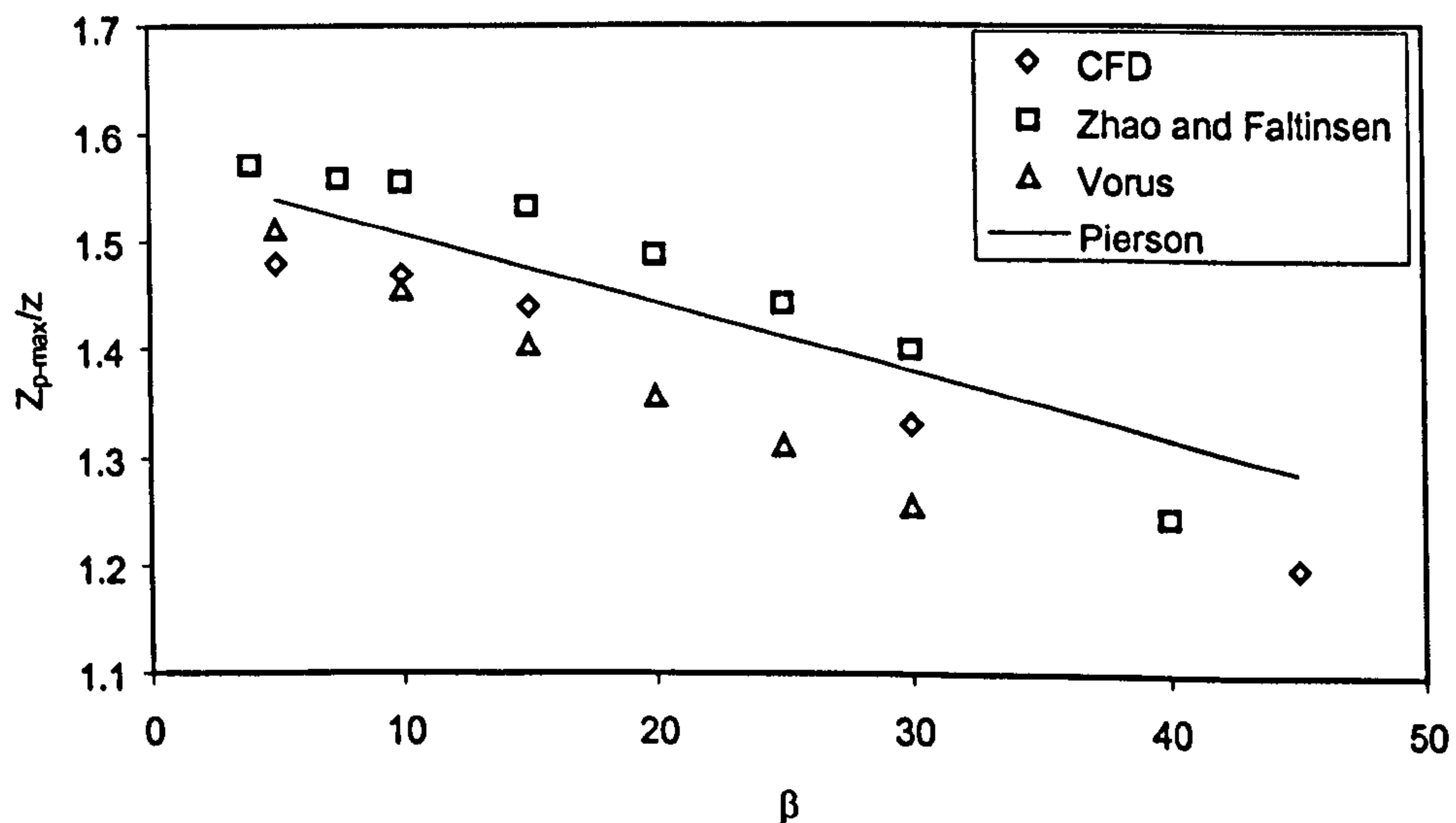


Figure 6-9. Peak pressure elevation.

It can be seen that the CFD results agree well with Vorus for low deadrise angles, while the higher deadrise angle data is closer to Zhao and Faltinsen.

The maximum pressure coefficients from the present CFD analysis, from Zhao and Faltinsen (1993) and from Vorus (1996) are compared with experimental data from slamming tests given by Chuang (1967) in Figure 6-10. The coefficients are multiplied by  $\tan\beta$  for better presentation.

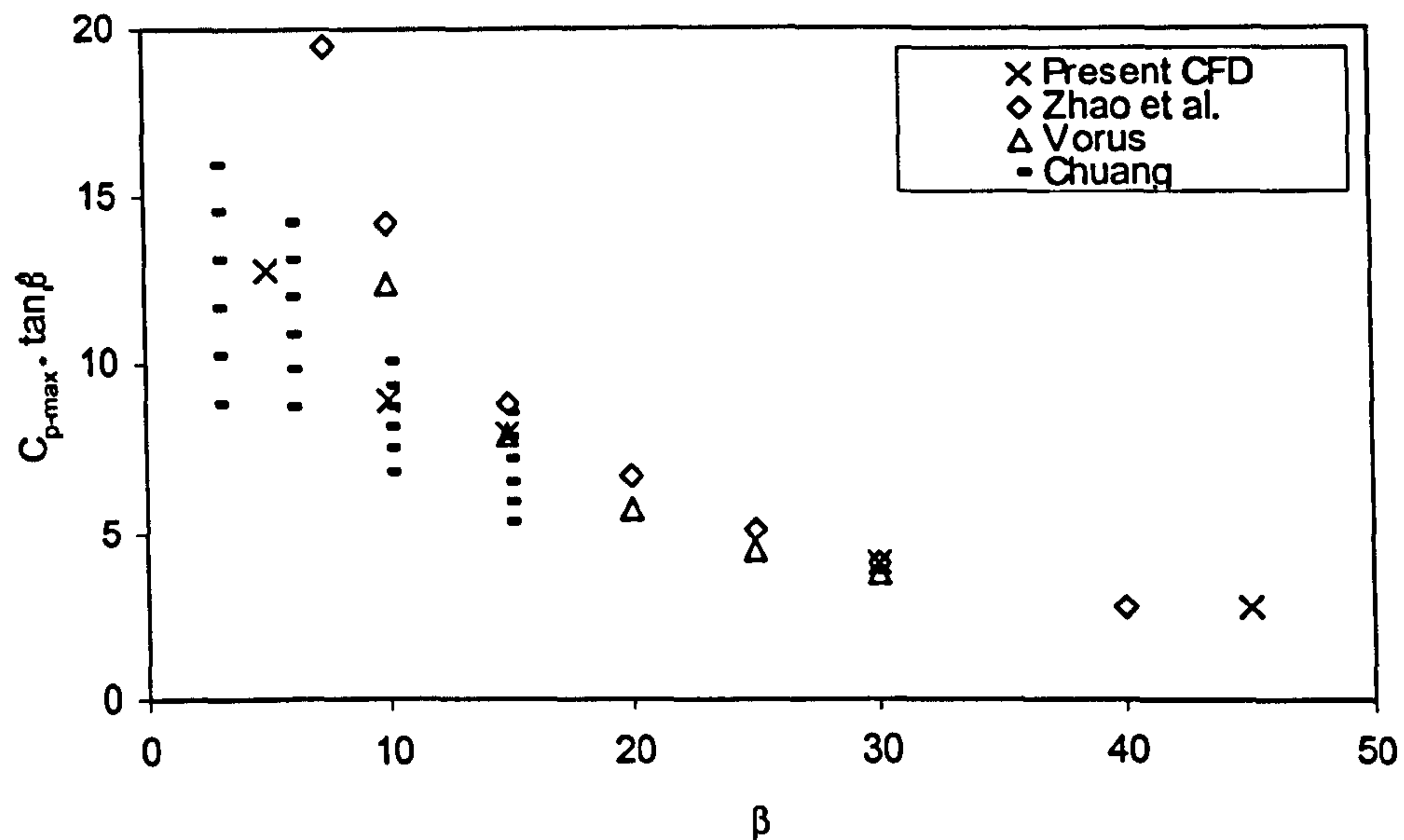


Figure 6-10. Maximum pressure coefficients.

There is good agreement between the three methods for deadrise angles above 15 degrees. At lower angles the CFD results are within the Chuang experimental scatter, while Vorus and Zhao and Faltinsen predict much higher values.

### 6.2.3. Wetting Factor

The definition of wetted width varies in the literature. Wagner (1932) calculated the shape of the free surface, and defined the wetted width by the intersection of the free surface and the wedge surface. Payne (1994) defines the wetted width as the distance between the stagnation lines, where the position of the stagnation line is adopted from Pierson (1954). Vorus (1996) defines the wetted width as the distance between the spray roots, i.e. the pressure termination points. The wetting factors WF (as defined in Section 6.1.2) obtained by CFD and by experiments are plotted in Figure 6-11, together with those given by Wagner (1932), Payne (1994) and Vorus (1996).



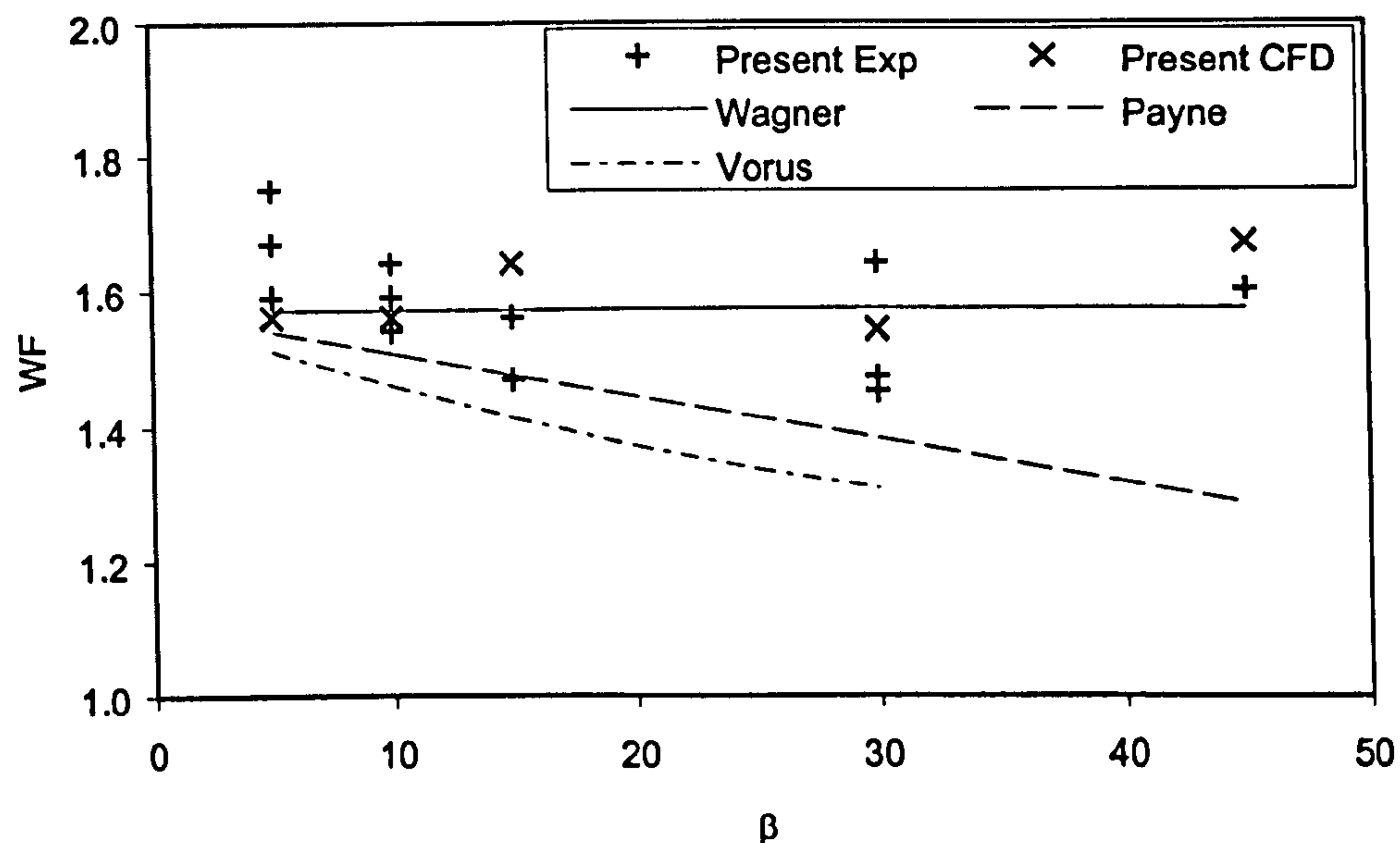


Figure 6-11. Wetting factors.

Both the experimental and the CFD data are scattered about a line representing Wagner's fixed wetting factor of  $\pi/2$ , while Vorus' and Payne's wetting factors decrease with increasing deadrise angle.

### 6.3. Validation of Buoyancy Ratio Function using CFD Data

The hydrodynamic force acting on a 30 degree wedge section during constant velocity water entry with two different velocities has been obtained by subtracting the Archimedes' buoyancy from the experimentally measured force and is plotted in non-dimensional form (on section beam) in Figure 6-12. The hydrodynamic force from the same test cases but obtained by subtracting the full gravity force effect (i.e. Archimedes' buoyancy multiplied by the buoyancy ratio) is plotted in Figure 6-13. The thin and the bold straight lines in the two figures represent an approximate smoothing of the irregular non-dimensional force data at the two water entry speeds. It is seen that the agreement between the non-dimensional hydrodynamic force is better in Figure 6-13 where the buoyancy ratio function has been applied. Since the hydrodynamic force should be independent of speed, this

lends some credence to the buoyancy ratio function, which was derived by comparison of gravity and zero-gravity CFD simulation force data.

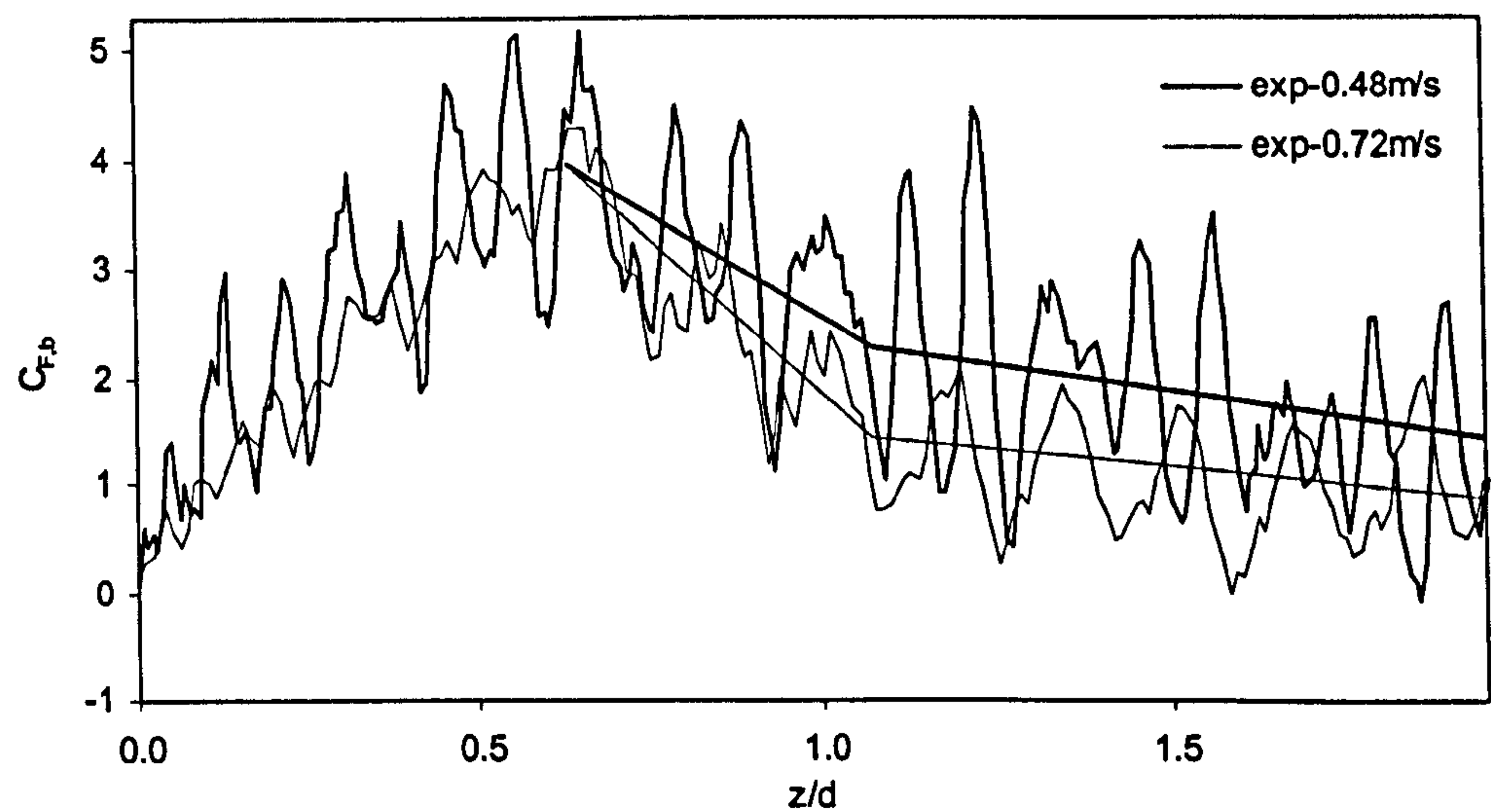


*Figure 6-12. Non-dimensional hydrodynamic force on 30 degree wedge section during constant velocity water entry obtained by subtracting the full Archimedes' buoyancy force.*



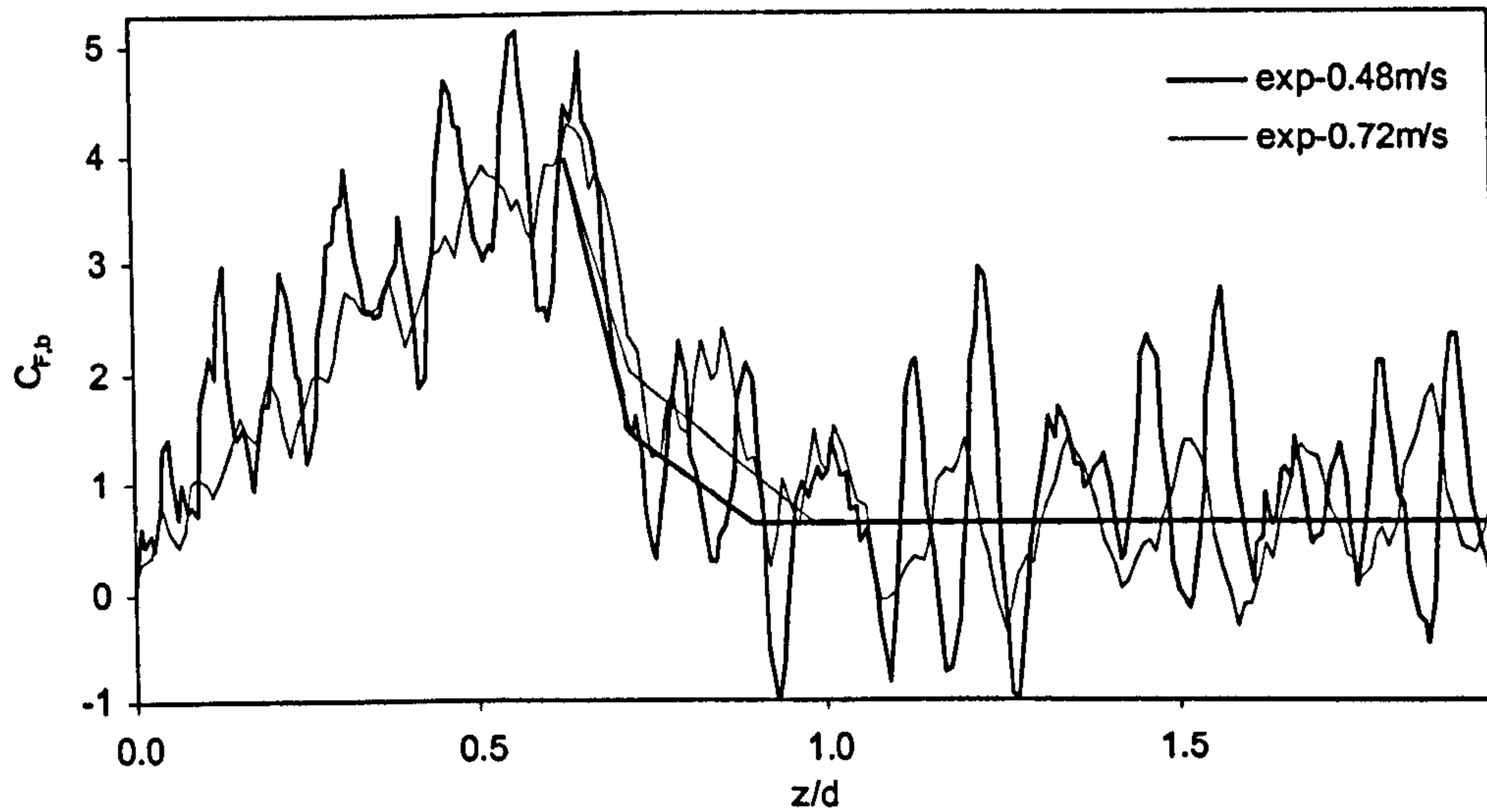


*Figure 6-13. Non-dimensional hydrodynamic force on 30 degree wedge section during constant velocity water entry obtained by subtracting the Archimedes' buoyancy times the buoyancy ratio.*

The hydrostatic force acting on a wedge section at a given non-dimensional immersion depth  $z/d$  is greater for a high deadrise angle section than a low deadrise angle section. On the other hand, the hydrodynamic force at a given  $z/d$  is greater for a low deadrise angle section than a high deadrise angle section. Thus, the contribution of the hydrostatic force to the total force decreases with decreasing deadrise angle. It was found that the hydrostatic force was only significant for force measurements from tests with the 30 and 45 degree deadrise angle sections.

#### 6.4. Most Reliable Source of Data for Development of Theory

The most reliable source of data for use in the development of the new theory has been decided on basis of the considerations that are discussed in the following paragraphs.

The results showed that there is reasonable agreement between the CFD and experiments for the dry chines stages of the water entry, but after the chines

immersion significant disagreement is seen. The fact that the results are consistent for dry chines stage while inconsistent for the wet chines stages can indicate simulation problems associated with the flow separation that occurs after the chines wetting. The experimental set-up was such that the end plates fitted to the model carrier provided two-dimensional flow, and hence the test events did not differ from the real two-dimensional water entry phenomenon that was to be investigated. Also, the high repeatability in the force measurements from different runs credits the quality of the set-up with regards to sensors and acquisition system. Further, apart from the case of the high velocity 5 degree wedge entry, the linear increase in force seen for the dry chines stage of the entry shows that the dynamic response of the load sensors are of substantially high dynamic response. These experiences and observations from the experiments give credibility to the results that have been obtained. On the other hand, CFD simulations by the volume of fluid method involves discretization of the fluid equations by the definition of a grid, and the accuracy of how well the computational domain represents the real flow domain depends on the grid quality. Also, the choice of interpolation schemes and solution parameters like time-stepping and convergence criteria have large impact on the simulation results in terms of quantities like pressures and velocities. In other words, there are more uncertainties regarding the CFD simulation than regarding the experiments. Thus, the experimental results have been regarded a more reliable source of data than the CFD results.

This choice of using the experimental data in the development of the new theory is validated in a later chapter where it is shown that the experimental results are consistent with slender body planing lift data. However, the dry chines high deadrise angle CFD results have been considered reliable on basis of issues discussed in the preceding sections, and have, along with the experimental data, been used in the development of the new theory.



---

**CHAPTER 7**

**ADDED MASS THEORY FOR WATER ENTRY  
AND EXIT**

---

This chapter describes the development of the present theory for water entry and exit, which has been obtained by analysis of the data given in the preceding chapters. Note that in this chapter viscous and gravity effects are neglected. All forces are per unit length of wedge sections. Velocities are positive downward, while forces acting on the section are positive upward.

The general purpose of the added mass theory is to have a model for separation of the hydrodynamic velocity and acceleration dependent forces, so that the full equation of motion for an object in a fluid can be established. Hypotheses were established to provide a basis for the data-analysis and development of the water entry theory. The validity of the water entry theory for use also in prediction of water exit forces is explored, leading to modifications of the theory for such cases. Further, the data from the oscillation tests and the accelerated/decelerated water entry tests are analysed to verify the added mass values derived in the present theory.

## 7.1. Water Entry Theory

In the added mass theory for the water entry of wedges by Von Karman (1924) and numerous subsequent researchers, the added mass has been taken as proportional to the half-width of the wedge squared. As the wedge immerses the width increases and hence the added mass increases. The force on an immersing wedge is expressed in Equation 3-2 as  $F' = m' \frac{dw}{dt} + w \frac{dm'}{dt}$ . In this equation both terms are associated with change in added mass momentum, i.e. only inertial forces, and when applied to wedges of finite width at constant velocity water entry, it gives zero force after the chines immerse. The experimental results given in Chapter 5 and 6 show that a force still exists after this occurs. It is the intention of the following hypotheses to provide a basis for separation of the constant velocity force into an added mass term and a flow momentum term that will explain the deep chines immersion force.



### 7.1.1. Hypothesis for Separation of Water Entry Forces

#### 7.1.1.1. Hypothesis 1 – Deep Chines Immersion Water Entry

Consider a wedge of finite width at deep immersion water entry. The added mass of a body moving vertically in water is proportional to the portion of the vertical momentum of the water particles whose velocity is affected by changes in the velocity of the body. The motion of the body does not affect water particles at a substantial distance from the body, and hence their momentum should not be included when calculating the added mass of the body. From the momentum theorem: “The net vertical force on a control volume equals the time rate of change of vertical momentum within the control volume plus the net vertical flow of momentum across its control surface”. During a constant velocity water entry, the flow within any chosen limits surrounding the finite width wedge and the water in its vicinity will approach steady state after adequate immersion depth. For steady state flow, the rate of change of momentum of the mass within the control volume is zero, and hence the force acting at constant velocity deep immersion should be represented as a flow momentum force. The experimental data presented in Chapters 5 and 6 show that after a certain non-dimensional immersion depth, depending on deadrise angle, the force acting on the wedge appears to be constant. It is hypothesised that when the force on the wedge appears to be constant there is steady state flow within some limits, where the velocity of the water particles is affected by the wedge section motion, so that the force due to rate of change of added mass momentum is zero. Thus the force at deep immersion can be treated exclusively as a flow momentum force, expressed in coefficient form as

$$C_{fm} = \frac{F'_{\text{deep-immersion}}}{\frac{1}{2} \rho w^2 \cdot b} \quad (7-1)$$

### 7.1.1.2. Hypothesis 2 – Dry Chines Water Entry

It is hypothesised that the flow momentum force is proportional to the nominal width of the wedge section with the same constant of proportionality throughout the water entry as for deep immersion depths, so that

$$F'_{fm} = C_{fm} \cdot \frac{1}{2} \rho w^2 \cdot 2y \quad , z < d \quad (7-2)$$

$$F'_{fm} = C_{fm} \cdot \frac{1}{2} \rho w^2 \cdot b \quad , z > d \quad (7-3)$$

where  $C_{fm}$  is given by Equation (7-1) and  $y = \frac{z}{\tan \beta}$ .

The difference between the total force and the flow momentum force is treated as being due to rate of change of added mass momentum. The separation of the force components, as hypothesised, are shown in Figure 7-1.

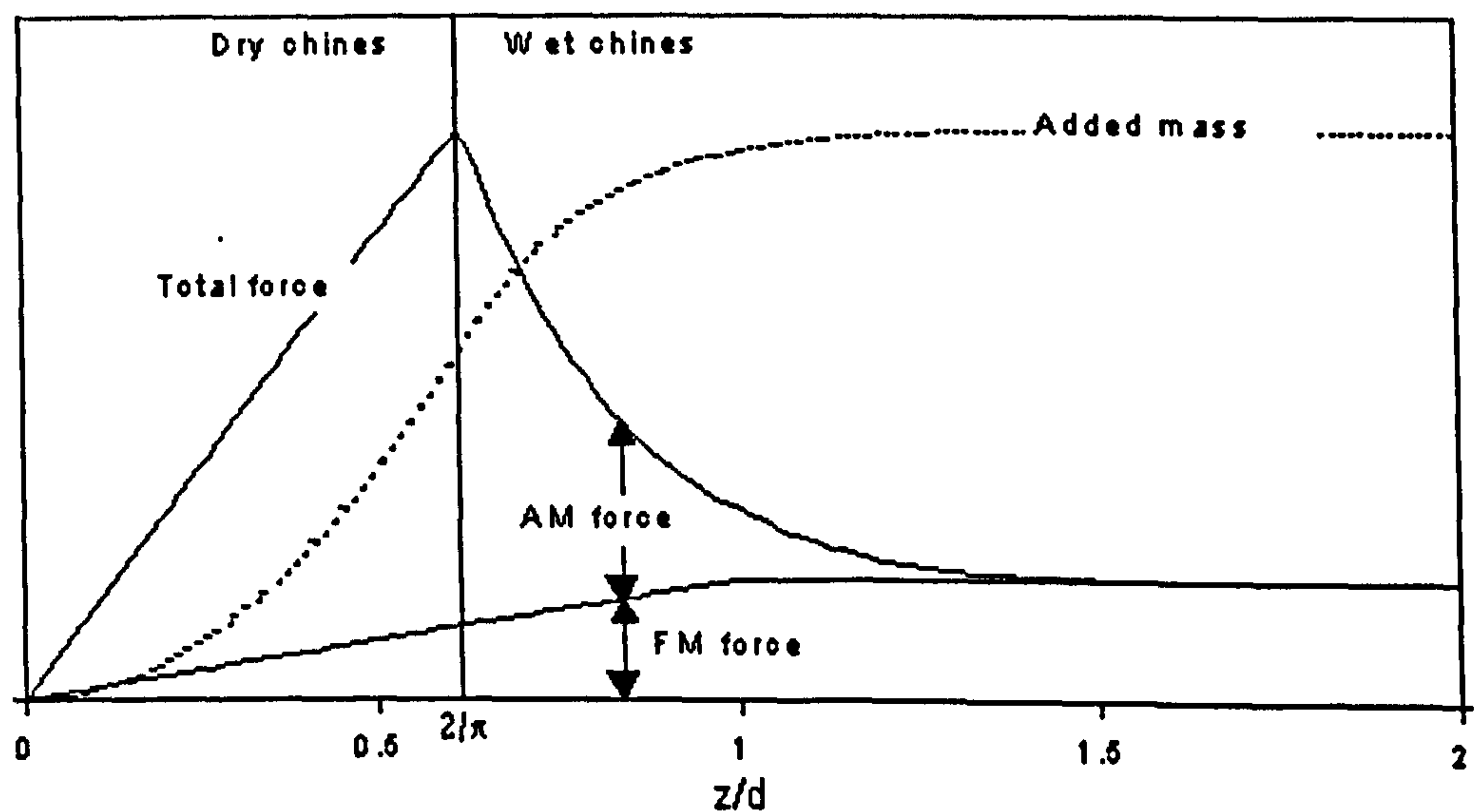


Figure 7-1. Force components on wedge section during constant velocity water entry.



## 7.1.2. Analysis of Constant Velocity Water Entry Data

### 7.1.2.1. Flow Momentum Force Component

The flow momentum coefficient, defined by Equation 7-1, has been obtained by analysis of the experimental data on the basis of the hypothesis in Section 7.1.1. Hypothesis 1 states that when the hydrodynamic force is constant with changing immersion, the force is entirely due to flow momentum. The experimentally obtained force coefficients on beam at non-dimensional immersion depths of  $z/d > 2$  for the 5 and 10 degree deadrise angle sections,  $z/d > 1.75$  for the 15 degree deadrise section,  $z/d > 1.25$  for the 10 degree deadrise and  $z/d > 1$  for the 45 degree deadrise, have been averaged separately for each test section. The averaged data are plotted in Figure 7-2 together with the function

$$C_{fm} = 1.08 \cdot \cos^2 \beta \quad (7-4)$$

which has been obtained by curve fitting to the experimental data.

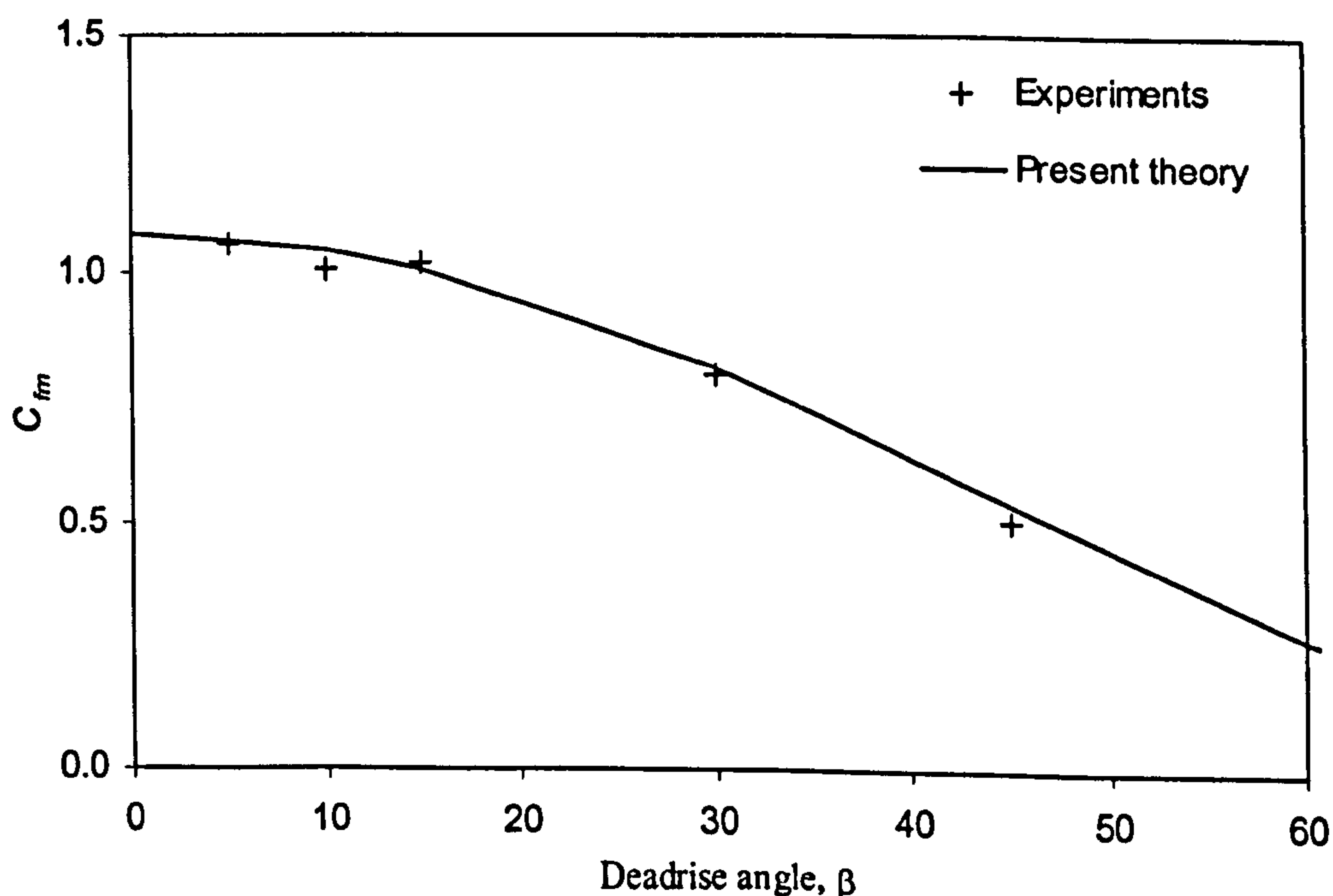


Figure 7-2. Deep immersion flow momentum coefficients.

Equation (7-4) gives a good fit to the experimentally based flow momentum coefficients.

Substitution of Equation (7-4) in Equation (7-2) and (7-3) gives the flow momentum force acting on a wedge section during water entry.

#### 7.1.2.2. Added Mass Force Component

Based on the known total hydrodynamic force from the constant velocity water entry experiments, and the extracted flow momentum force contribution from the preceding section, the added mass force component has been derived from

$$F'_m = F' - F'_{fm} \quad (7-5)$$

where  $F'_m$  denotes added mass force,  $F'_{fm}$  denotes flow momentum force and  $F'$  denotes total hydrodynamic force.

In Chapter 6 the slamming force coefficients  $C_F$  for dry chines wedge entry were obtained from the experimental data and are listed in Table 6-1. From Equation (6-1) the total hydrodynamic force is given by

$$F' = C_F \cdot \rho w^2 z \quad (7-6)$$

Equation (7-2) gives the flow momentum force for dry chines condition. Substituting this equation together with Equation (7-6) in Equation (7-5) and

setting  $y = \frac{z}{\tan \beta}$  gives

$$F'_m = C_F \cdot \rho w^2 z - C_{fm} \cdot \frac{1}{2} \rho w^2 \cdot \frac{2z}{\tan \beta} \quad (7-7)$$

where  $C_{fm}$  is given by Equation (7-4).

The force due to increase in added mass of a wedge during constant velocity water entry is given by



$$F'_{m'} = w^2 \cdot \frac{dm'}{dz} \quad (7-8)$$

For a wedge shape, the added mass is expressed in non-dimensional form as

$$C_{m'} = \frac{m'}{\frac{1}{2} \cdot \rho \pi y^2} \quad (7-9)$$

where  $y$  is the nominal width of the wedge section. Expressing Equation (7-9) in terms of  $m'$  and substituting  $y = \frac{z}{\tan \beta}$  gives

$$m' = C_{m'} \cdot \frac{1}{2} \cdot \rho \pi \cdot \frac{z^2}{\tan^2 \beta} \quad (7-10)$$

Substituting (7-10) in (7-8) and differentiating gives

$$F_{m'} = C_{m'} \cdot w^2 \cdot \rho \pi \cdot \frac{z}{\tan^2 \beta} \quad (7-11)$$

Substituting Equation (7-11) in (7-7) and solving in terms of the added mass coefficient gives

$$C_{m'} = \frac{C_F \cdot \tan^2 \beta}{\pi} - \frac{C_{fm} \cdot \tan \beta}{\pi} \quad (7-12)$$

Equation (7-12) has been used with the  $C_{fm}$  values determined by Equation (7-4) and  $C_F$  values taken from Table 6-1 to calculate the added mass coefficients given in Table 7-1.

$\beta$ [degrees]	$C_m$
5	1.98
10	1.72
15	1.56
30	1.22
45	0.961

---

*Table 7-1. Experimentally based dry chines added mass coefficients.*

In addition to the experimentally based added mass coefficients in Table 7-1, the added mass coefficient for a 60 degrees wedge has also been calculated, but by use of the slamming force coefficient  $C_F$  from the CFD results in Table 6-1. This gave the added mass coefficient as 0.632.

The added mass coefficients from Table 7-1 and the 60 degrees results from the CFD data are plotted in Figure 7-3. The Wagner –Sydow equation for added mass coefficient is adopted and found to give good fit to the data when multiplied by a factor of 0.89, as follows

$$C_m = 0.89 \cdot \left( \frac{\pi}{2\beta} - 1 \right)^2 \cdot \tan^2 \beta \quad (7-13)$$

Equation (7-13) is denoted ‘present theory’ in Figure 7-3.



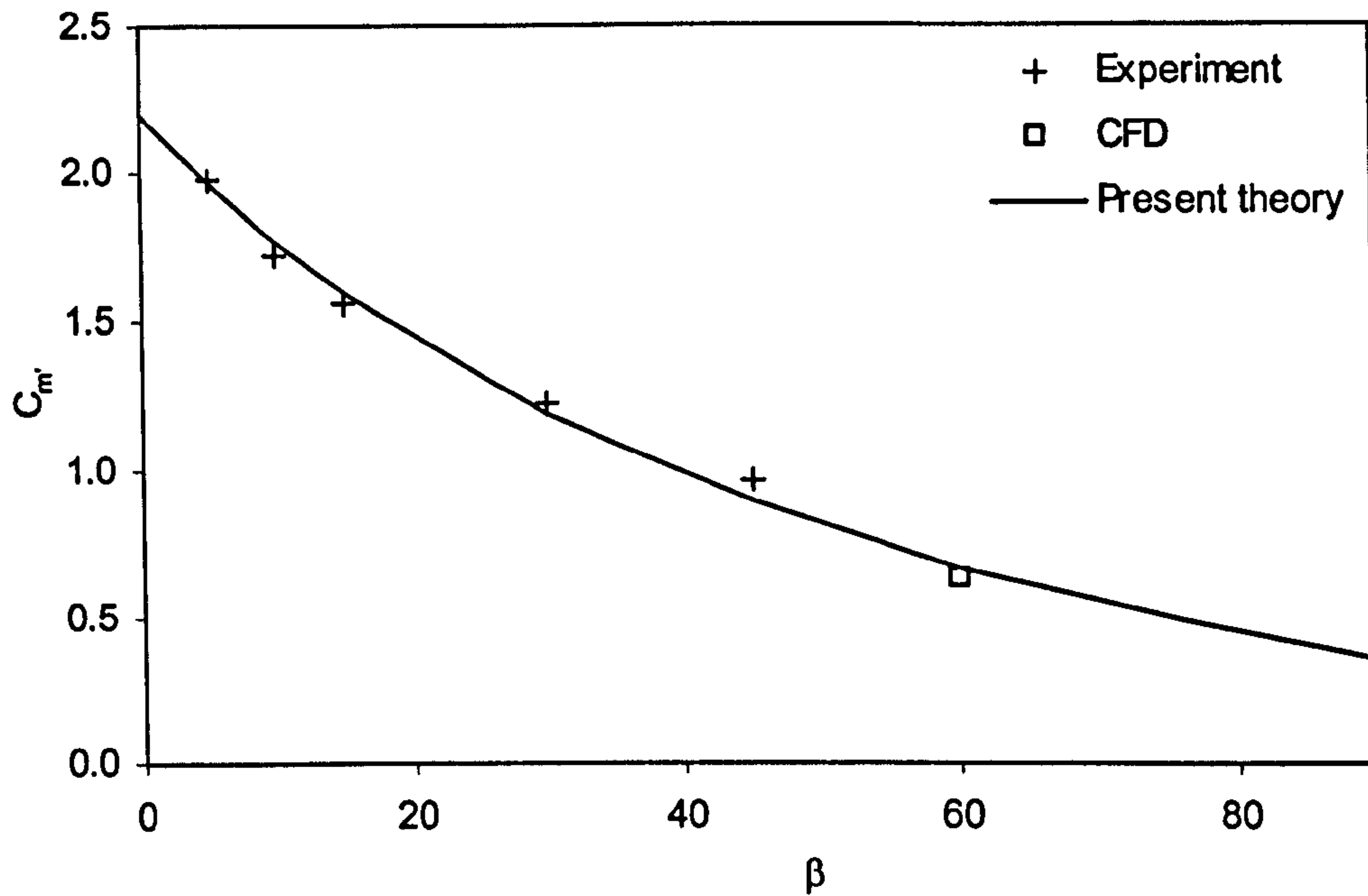


Figure 7-3. Added mass coefficients based on water entry experiment and CFD simulation.

It has earlier been hypothesised that at deep immersion, when the hydrodynamic constant velocity water entry force is constant, the force is entirely flow momentum associated. The dry chines added mass force,  $F'_{m'} = w^2 \frac{dm'}{dz}$ , holds for immersions up to the point at which the chines become wetted, i.e.  $z/d = 2/\pi$ . At this point the added mass is given by

$$m'_0 = C_{m'} \cdot \frac{1}{2} \rho \pi \cdot \left( \frac{b}{2} \cdot \frac{2}{\pi} \right)^2, \quad z/d = 2/\pi \quad (7-14)$$

The added mass continues to increase at greater immersions and is given by the empirical expression

$$m'_w = m'_0 \cdot \left( 1 + 0.57 \cdot \frac{\frac{z_c}{d}}{\frac{0.57}{\pi} + \frac{z_c}{d}} \right), \quad \frac{z}{d} > \frac{2}{\pi} \quad (7-15)$$

where  $z_c$  is the further immersion from chines wetting, given by  $z_c = z - \frac{2}{\pi}d \cdot m'_w$

from Equation (7-15) can be used in the equation  $F'_m = w^2 \frac{dm'_w}{dz_c}$  to give values

corresponding to  $F'_m = F' - F'_{fm}$  for the wet chines condition. The depth rate of change of added mass is given by

$$\frac{dm'}{dz} = \frac{dm'_w}{dz_c} = m'_0 \cdot \frac{\frac{0.57^2}{\pi}}{\frac{z_c^2}{d} + \frac{2 \cdot 0.57 \cdot z_c}{\pi} + \frac{0.57^2 \cdot d}{\pi^2}}, \quad \frac{z}{d} > \frac{2}{\pi} \quad (7-16)$$

The wet chines added mass function in Equation (7-15) provides continuity of  $dm'/dz$ . At the instant of chines wetting  $z = \frac{2}{\pi}d$  and  $z_c=0$ , and Equation (7-16) gives

$$\frac{dm'}{dz} = m'_0 \cdot \frac{\pi}{d} \quad (7-17)$$

Substituting Equation (7-14) in Equation (7-17) gives

$$\frac{dm'}{dz} = C_m \cdot \frac{1}{2} \rho \pi \cdot \frac{\left(\frac{2d}{\pi}\right)^2}{\tan^2 \beta} \cdot \frac{\pi}{d} = C_m \cdot \frac{2\rho d}{\tan^2 \beta} \quad (7-18)$$

Taking the derivative of the dry chines added mass given in Equation (7-10) with respect to immersion depth  $z$  gives

$$\frac{dm'}{dz} = C_m \cdot \rho \pi \cdot \frac{z}{\tan^2 \beta} \quad (7-19)$$



Substituting  $z = \frac{2}{\pi}d$  in Equation (7-19) gives

$$\frac{dm'}{dz} = C_{m'} \frac{2\rho d}{\tan^2 \beta}$$

which is identical to Equation (7-18). Thus continuity of  $dm'/dz$  at the instant of chines wetting is provided.

### 7.1.3. Comparison of Water Entry Theory with Present Experimental Results

#### 7.1.3.1. Wedge Sections

The total hydrodynamic force acting on a wedge section during a constant velocity water entry is given by the sum of added mass force  $F'_{m'}$  and flow momentum force  $F'_{fm}$ . The dry chines ( $z/d < 2/\pi$ ) added mass force is given by Equation (7-11). The wet chines added mass force is obtained by combining Equations (7-8), (7-14) and (7-16) to give

$$F'_{m'} = C_{m'} \cdot w^2 \cdot \rho \cdot \frac{b^2}{2\pi} \cdot \frac{\frac{0.57^2}{\pi}}{\frac{z_c^2}{d} + \frac{2 \cdot 0.57 \cdot z_c}{\pi} + \frac{0.57^2 \cdot d}{\pi^2}} \quad , z > \frac{2}{\pi} \cdot d \quad (7-20)$$

where  $C_{m'}$  is given by Equation (7-13). The wet chines flow momentum force is given by Equations (7-2) to (7-4).

The hydrodynamic forces acting on the test wedge sections during constant velocity water entry, calculated using this theory, are plotted in Figures (7-4) to (7-8). The experimental data are plotted in the same charts. The hydrodynamic force is made non-dimensional on maximum section width  $b$  as

$$C_{F,b} = \frac{F'}{\frac{1}{2} \rho w^2 b} \quad (7-21)$$

and is plotted against the non-dimensional immersion depth  $z/d$ .

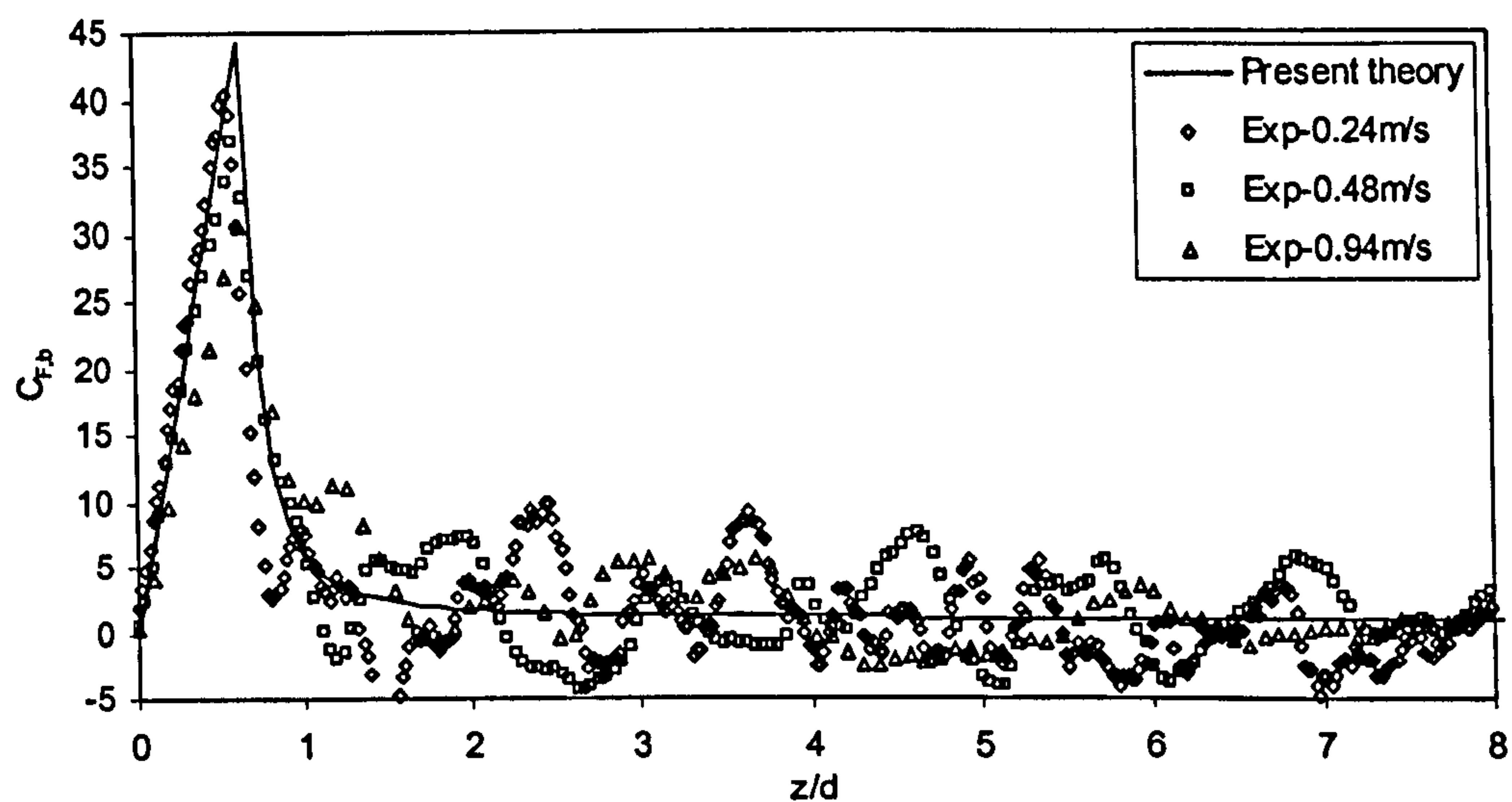


Figure 7-4. Constant velocity water entry of 5 degree wedge section.

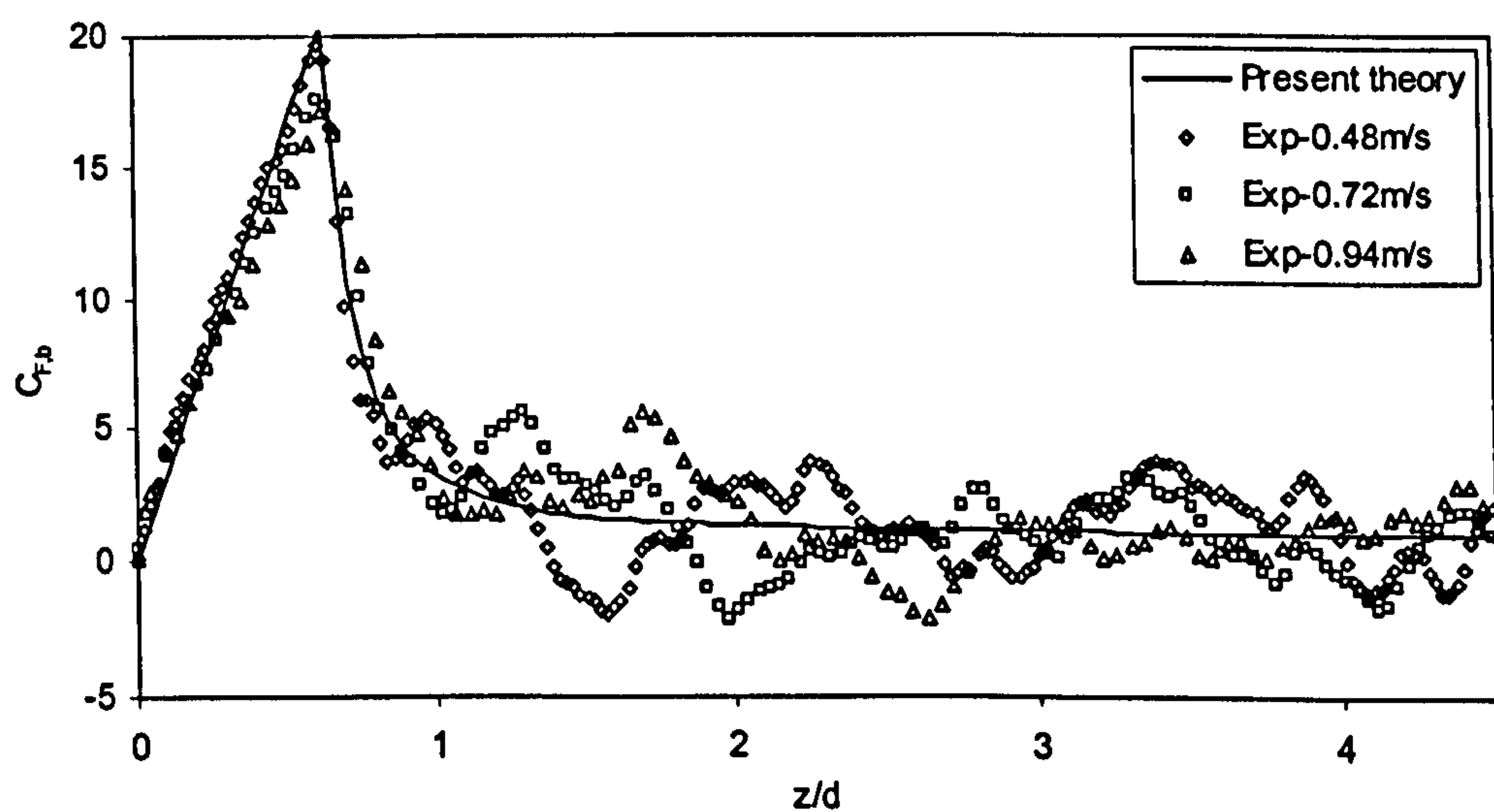


Figure 7-5. Constant velocity water entry of 10 degree wedge section.



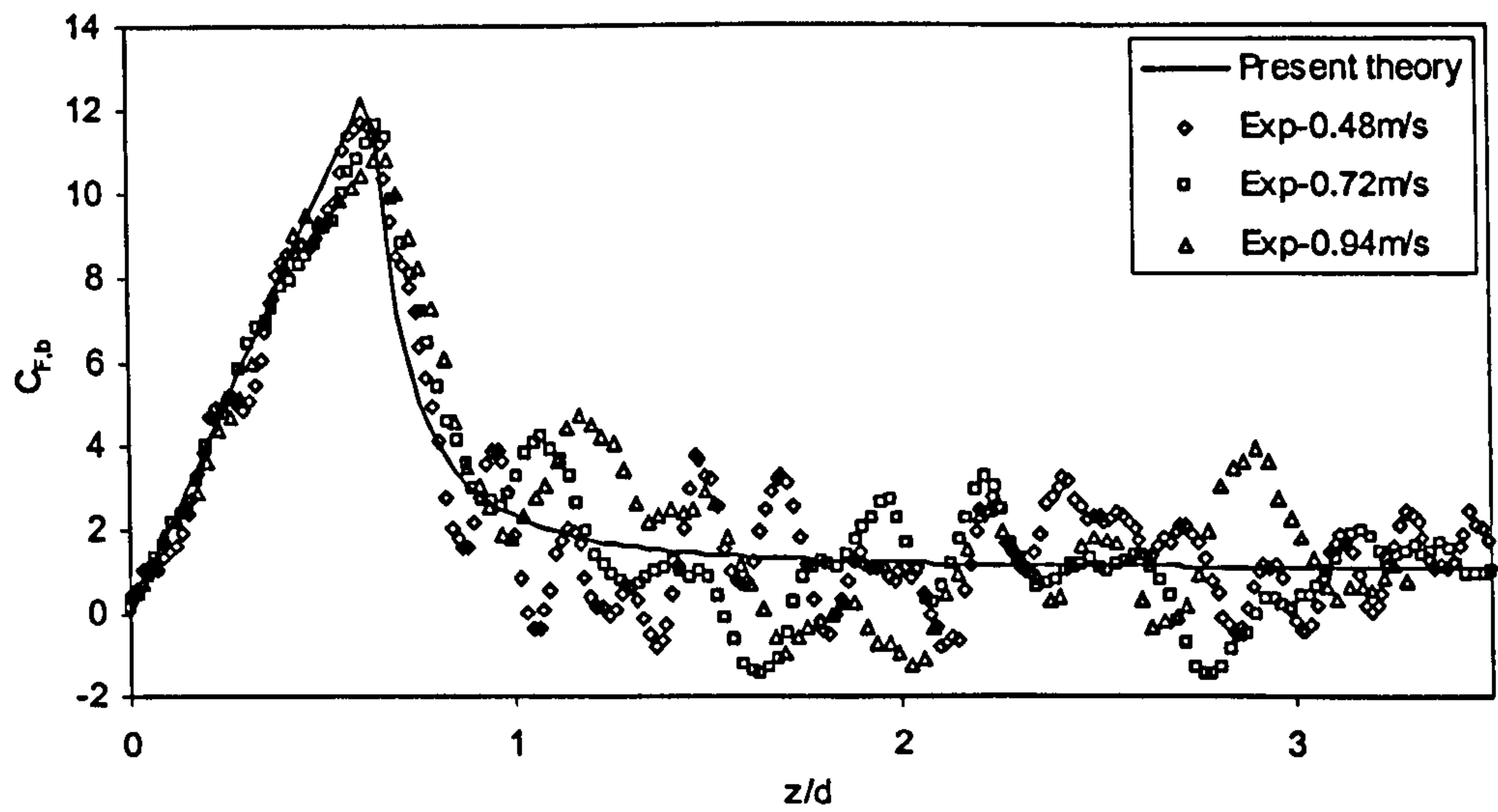


Figure 7-6. Constant velocity water entry of 15 degree wedge section.

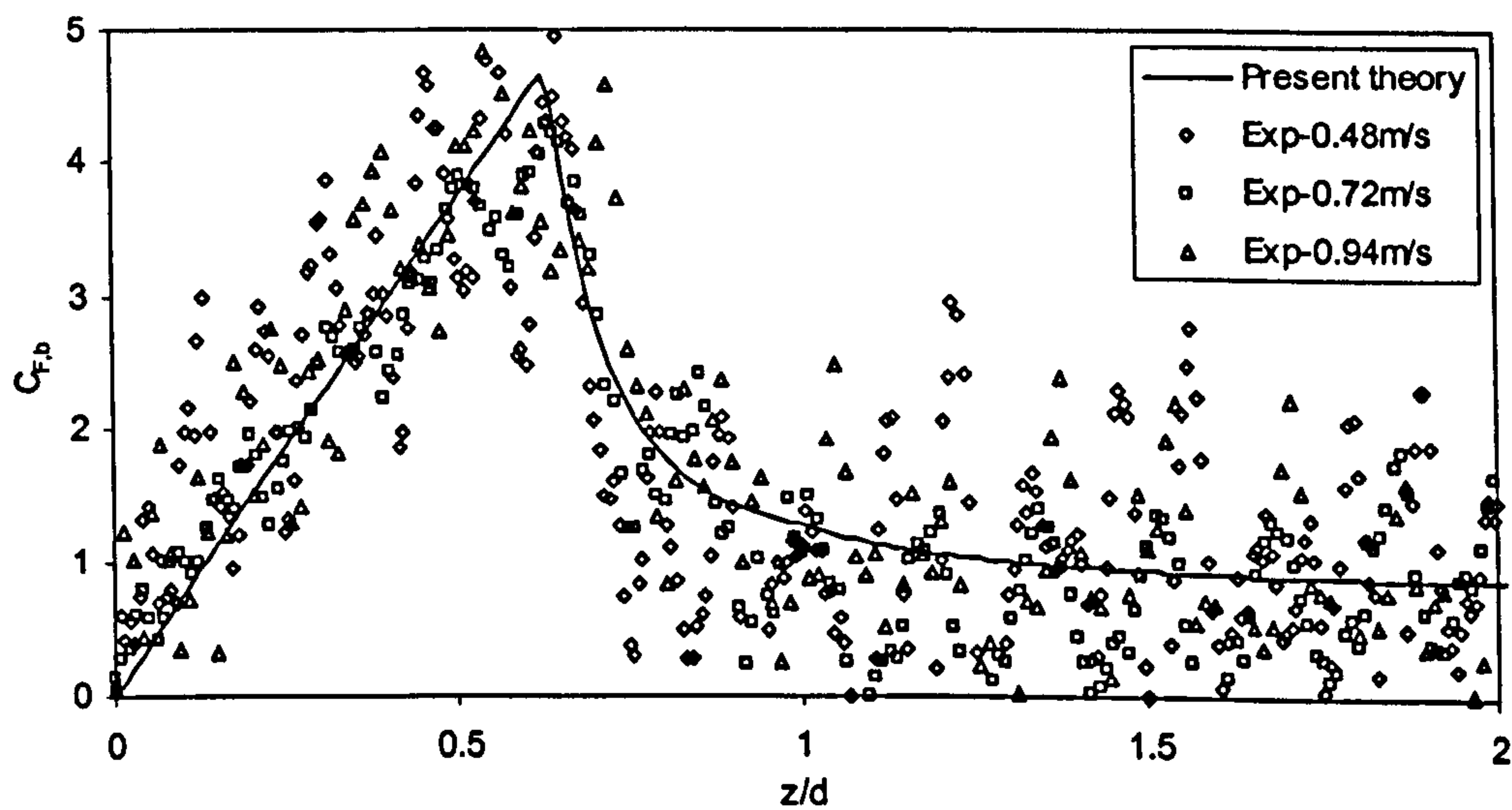


Figure 7-7. Constant velocity water entry of 30 degree wedge section.

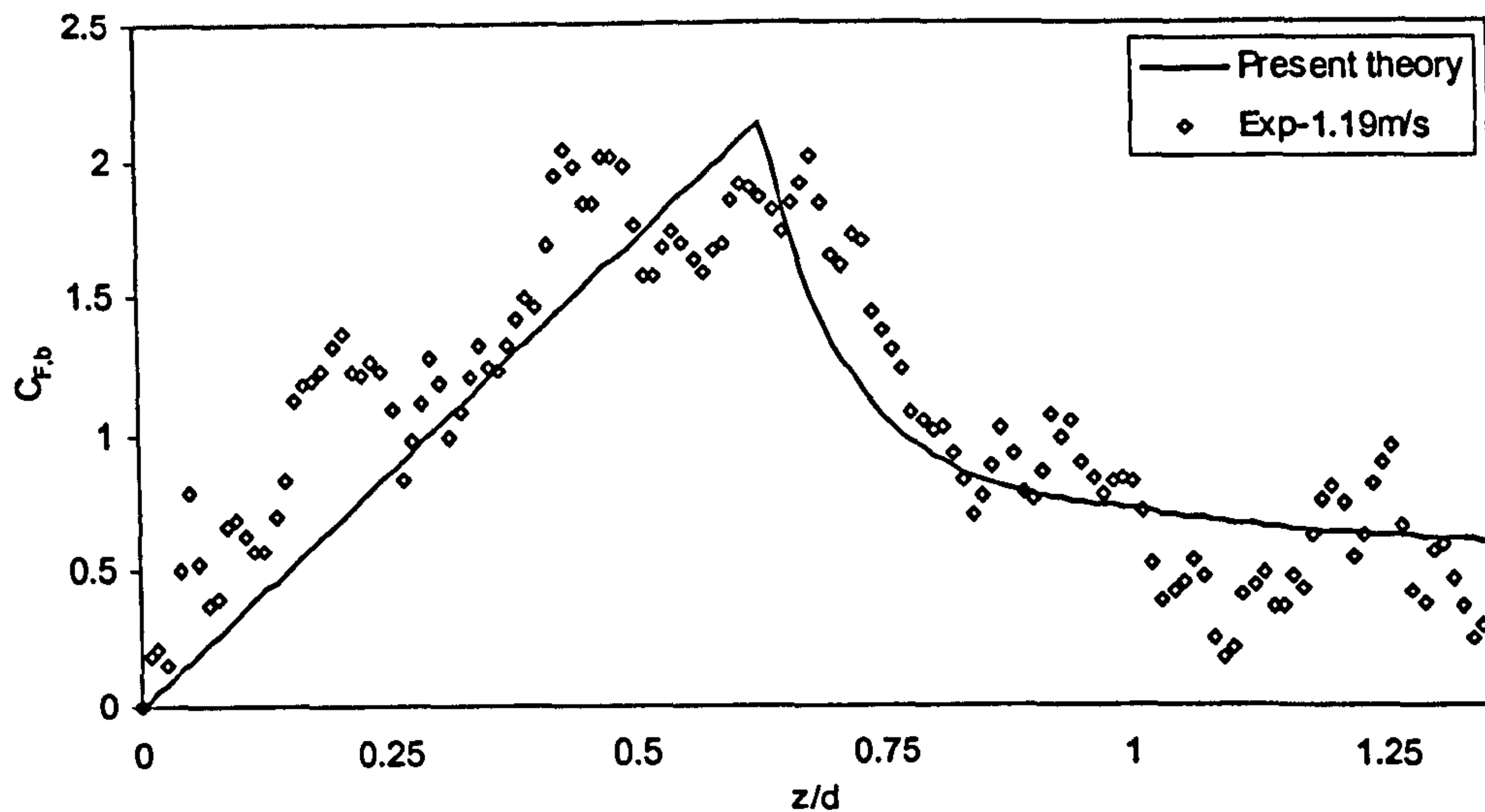


Figure 7-8. Constant velocity water entry of 45 degree wedge section.

The present theory generally gives a good fit to the experimental data. There is some discrepancy for low deadrise angle / high velocity, which is believed to be related to the dynamic response of the load sensors (as discussed in Section 6.1.1). Because of the added mass coefficient curve fitting shown in Figure 7-3 the present theory is slightly lower than the dry chines ( $z/d < 2/\pi$ ) experimental force for the 45 degree case.

#### 7.1.3.2. Flat-Bottomed Sections

The present theory added mass after chines immersion has been developed on the basis of test data obtained with wedge sections, i.e. non-zero deadrise angle sections. For zero deadrise angle sections (flat-bottomed), the non-dimensional immersion depth  $z/d$  is infinite for  $z > 0$  because  $d = 0$ . According to Equation (7-15) the added mass for a flat-bottomed section, where the chines immerse at  $z = 0$  is given by

$$m'_w = m'_0 \cdot 1.57 \quad (7-22)$$

Substituting Equation (7-14) in Equation (7-22) yields an expression that gives good correlation with data from the present experiments with the flat-bottomed section. The added mass for flat-bottomed sections is therefore given by



$$m'_w = C_{m'} \cdot \frac{1}{2} \rho \pi \cdot \left( \frac{b}{2} \cdot \frac{2}{\pi} \right)^2 \cdot 1.57 \quad (7-23)$$

where  $C_{m'}$  is given by Equation (7-13) as  $0.89 \cdot \frac{\pi^2}{4}$ . This is treated as a step increase in the added mass at the instant of initial impact with the water from zero to the value given by Equation (7-23) after which the added mass remains constant. Thus, the rate of change of added mass  $dm'/dz$  is zero after the initial impact (and step increase in added mass) of a flat-bottomed section. Therefore, the present theory accounts for the hydrodynamic force acting on a flat-bottomed section during constant velocity water entry entirely by the flow momentum force obtained by combining Equations (7-3) and (7-4) which gives

$$F' = 1.08 \cdot \cos^2 \beta \cdot \frac{1}{2} \rho w^2 \cdot b \quad (7-24)$$

The hydrodynamic force given by Equation (7-24) is plotted in Figure 7-9 together with data from the flat-bottomed section constant velocity water entry test of the present experiments. The hydrodynamic force is made non-dimensional on maximum section width  $b$  and is plotted against the non-dimensional immersion depth  $z/b$ . Note that only data from when the section is lower than the calm water level is included, i.e. the advanced impact force that is shown in Figure 6-6 is not included.

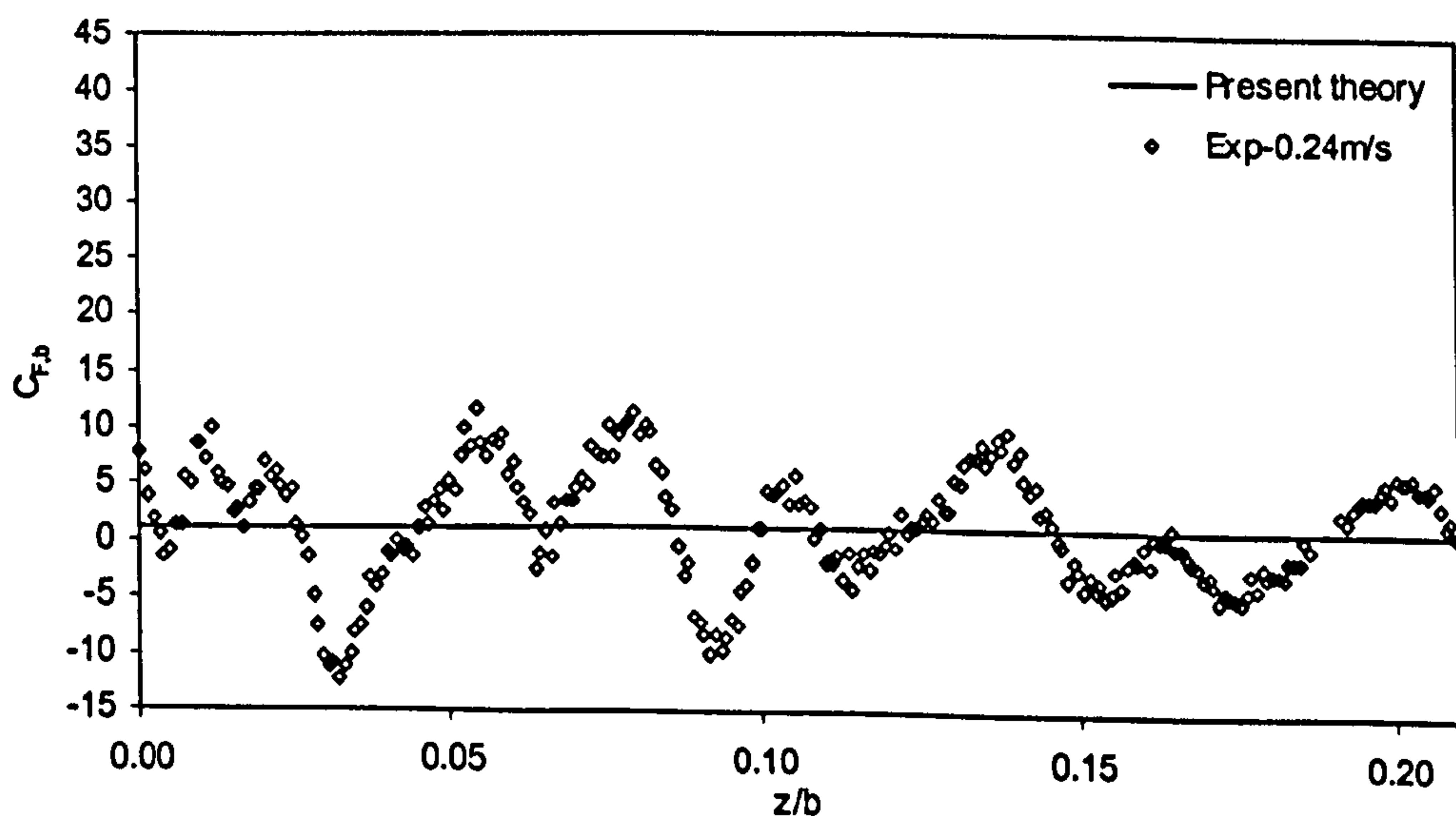


Figure 7-9. Constant velocity water entry of flat-bottomed section.

The average  $C_{F,b}$  of the experimental data in Figure 7-9 is 1.20. The present theory gives 1.08, which is 10 percent lower than the experimental average. This is a reasonable underestimate considering the highly scattered data and that the theory for flat-bottomed section is an extrapolation of a theory developed for deadrise sections.

#### 7.1.4. Comparison of Water Entry Theory with Results from the Present CFD Simulations and the Constant Velocity Simulations by Others

The force history from the simulations of constant velocity water entry of wedges has been presented for a 20 degree wedge by Vorus (1996) and Zhao et al. (1997b). The 20 degree wedge was not included in the present CFD simulations. However, it has been found that a flow momentum coefficient of  $C_{fm} = 2.0 \cdot \cos^2 \beta$  used with the new added mass theory for water entry provides a good basis for interpolation of the CFD force for all the deadrise angles in the simulation series. This has been used in the following comparison as the CFD result.

The hydrodynamic force acting on a 20 degree wedge section during a constant velocity water entry as given by the present theory is compared with the forces given by the various numerical simulations. The forces are plotted as coefficients on section beam against the non-dimensional immersion depth  $z/d$  in Figure 7-10.

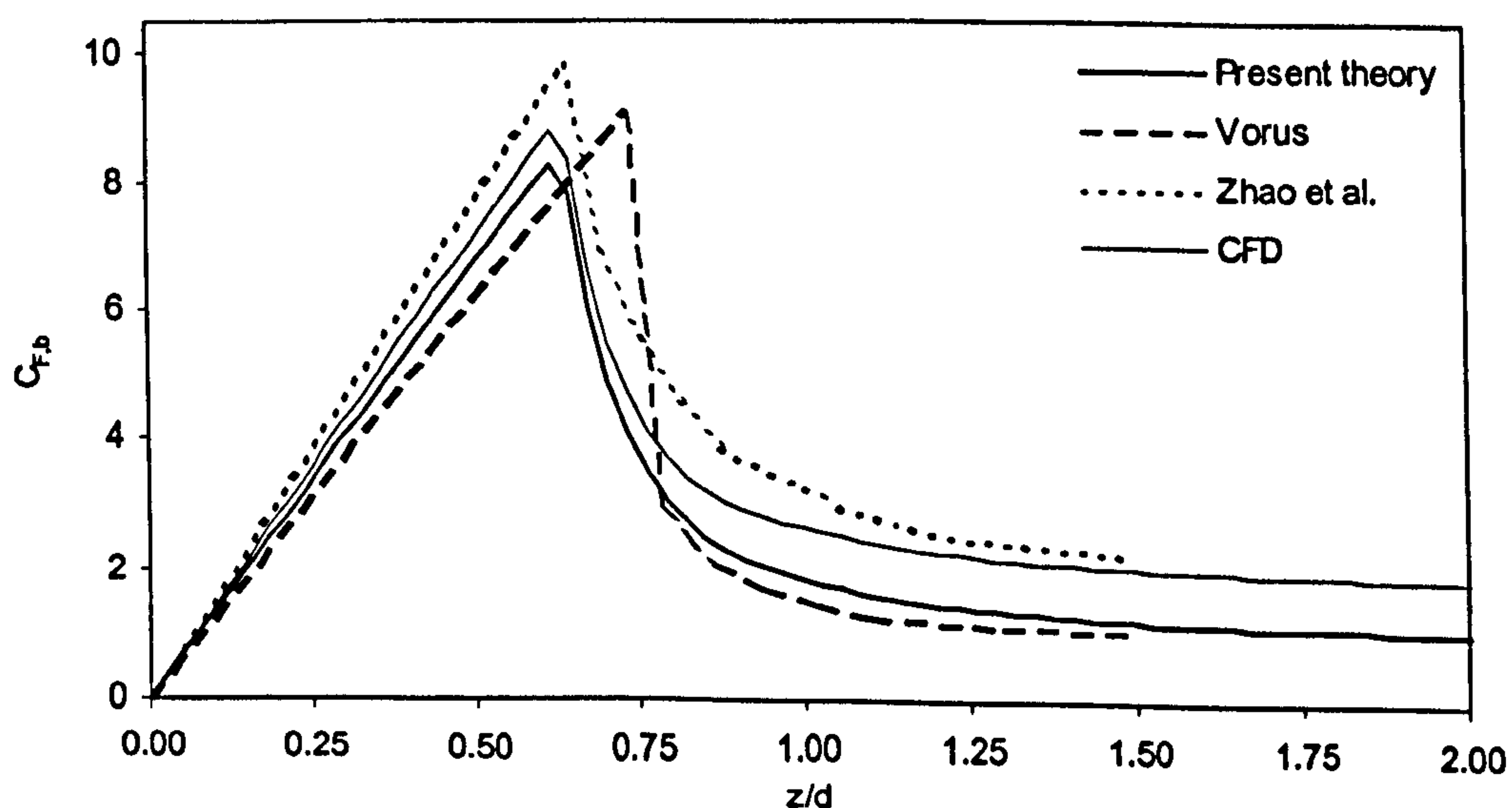




*Figure 7-10. Non-dimensional constant velocity water entry force for a 20 degree wedge section by present theory, Vorus (1996) and Zhao et al. (1997b) and present CFD.*

It has already been shown in Figures 7-4 to 7-8 that the present theory compares well with the experimentally obtained constant velocity water entry forces. A similar comparison was not done by Vorus or Zhao et al. as constant velocity water entry data has not previously been available. Although tests were not carried out with a 20 degree wedge section, it is reasonable to regard the curve denoted 'Present theory' in Figure 7-10 as a benchmark because the theory has shown good agreement with experimental results from tests with both 15 and 30 degree deadrise angle wedge sections. Figure 7-10 shows that the simulation result by Vorus is generally in better agreement with the present theory (and thus experiments), while the results from the simulations by Zhao et al. agrees more with the present CFD, particularly at higher  $z/d$ . An exception is at the stage of water entry just after chines wetting. It is seen that the peak force given by Vorus' simulation results occurs at a higher immersion depth than that given by the experiment. Thus, a significantly higher force is estimated at this stage by Vorus than measured experimentally. The instant of peak force occurrence predicted by Zhao et al. is in agreement with the experiment. The dry chines forces given by Zhao et al. are higher than the experimental forces, while the dry chines force given by Vorus is lower. However, it is seen that the dry chines results by Vorus are in better agreement with the experiments than the results given by Zhao et al.

## **7.2. Water Exit Theory**

### **7.2.1. Analysis of Constant Velocity Water Exit Data**

It was observed by studying the free surface shape during water exit tests that when the motion starts from a position where the chines are immersed, the water surface initially gets sucked down. Studying video material from the exit tests made these observations. It has proven difficult to demonstrate this effect on still

pictures captured from the available video material from these tests and thus such pictures are not presented herein. It is reasonable to assume that the immersion depth at which the chines exit from the water depends on the deadrise angle, the depth at which the section starts the exit from and the exit velocity. The immersion depths at which the chines exit the water have been found to coincide with the instant of a change in trend of the hydrodynamic force data. The hydrodynamic forces acting on the test sections during water exit are extracted from the experimental data by subtracting Archimedes' buoyancy from the total force. In Figures 7-11 to 7-14 (showing force made non-dimensional on the section beam) it is seen that at the highest depth range plotted (at the left-hand side of the graph), the force oscillates about some seemingly constant negative value. It is also seen that after a certain exit motion the trend of the force oscillating about a constant value is discontinued, which is when the chines emerges. Note that in Figures 7-11 to 7-14 the water depth is plotted on a reverse scale so that moving from left to right in the chart still corresponds to time increase, and that depth  $z$  is the distance from the wedge apex to the calm water level. Because forces are defined as positive upward, this implies that the net hydrodynamic force acting on the wedge section during the exit is working against the direction of motion.

At the instant the chines emerges, the non-dimensional mean force starts increasing at a seemingly constant rate to pass through zero force at zero depth. This increase starts at non-dimensional water depths of about 1.7 and 1.1 for the 10 and 15 degree deadrise sections respectively. In the plots for the 30 and 45 degree deadrise sections in Figures 7-13 and 7-14 the change in trend from a constant force to an increasing force does not occur until a non-dimensional depth of about 1.0, which is when the chines cross the calm water level. This indicates that the water surface is being less sucked down during exits with high deadrise angle sections than with lower ones, something expected when considering that the flow around a sharp corner causes greater pressure reduction than the flow around a lesser sharp corner.



In the present theory for constant velocity water entry, the hydrodynamic force consists of a rate of change of added mass term and a flow momentum term. When applying this theory to water exits it gives a net force acting in the same direction as the direction of motion, i.e. upward. The water entry theory would only be valid for exits if the flow was exactly the reverse of that during a water entry, which common sense suggests is unlikely. From the force plots in Figures 7-11 to 7-14 it is seen that the force is acting against the motion, and hence the water entry theory is clearly not valid for water exits.

The pictures of the water exits in Figures 5-81 to 5-84 show that a large amount of water follows the section to above the calm water level. This indicates that after the chines emerge from the water, the added mass is not given up as a force acting on the wedge, but acts to carry the water above the calm water level. Thus, the rate of change of added mass term from the water entry theory should be excluded from water exit calculations, yielding a constant velocity water exit force that is exclusively due to flow momentum. This was confirmed by studying the hydrodynamic force data from the exits. It was found that the magnitude of the mean force during the chines immersed stages of the exit is close to the deep immersion flow momentum force that was found for water entries, and that from the chines emerge the magnitude of the force is reducing linearly to give zero force at zero nominal immersion depth, i.e. at  $z=0$ . The force is therefore given by

$$F'_{fm} = C_{fm} \cdot \frac{1}{2} \rho w |w| \cdot b \quad , z > z_{ce} \quad (7-25)$$

for the wet chines stages of the exit, where  $z_{ce}$  is the immersion depth at the instant the chines emerge. The flow momentum coefficient is given by Equation (7-4). For the dry chines stages of the exit the force is expressed by

$$F'_{fm} = C_{fm} \cdot \frac{1}{2} \rho w |w| \cdot b \cdot \frac{z}{z_{ce}} \quad , z < z_{ce} \quad (7-26)$$

to give a linear decrease in water exit force from the instant the chines emerge.

The forces are calculate by Equations (7-25) and (7-26), made non-dimensional on section beam and are plotted together with the experimental data in Figures 7-11 to 7-14. It is seen that Equations (7-25) and (7-26) give a reasonable fit to the experimental data, apart from the lower depth range of the 45 degree deadrise plot, where the mean non-dimensional exit force appears to be positive, and in the immersed chines stages of the 10 degree deadrise exit, where the magnitude of the resisting exit force appears to be underestimated. At the low immersion depth stage of the 45 degree deadrise exit there was a reduction in the exit velocity due to the model carrier having to be decelerated as it approached the end of limited length of travel. Thus, the inertial forces associated with this deceleration have affected the force measurements. The velocity reduction is shown in Figure 5-74.



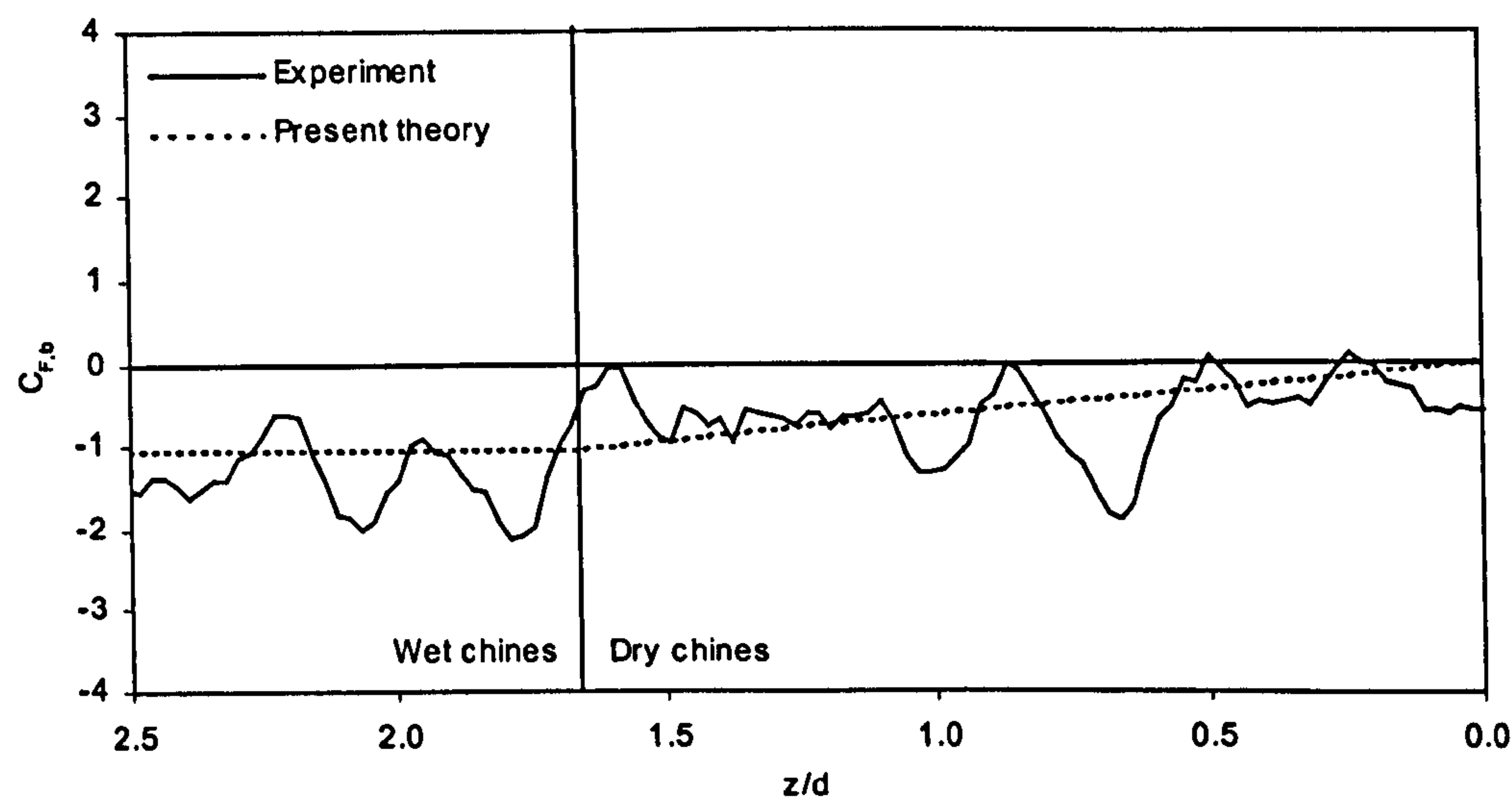


Figure 7-11. Non-dimensional water exit force, 10 degree wedge section.

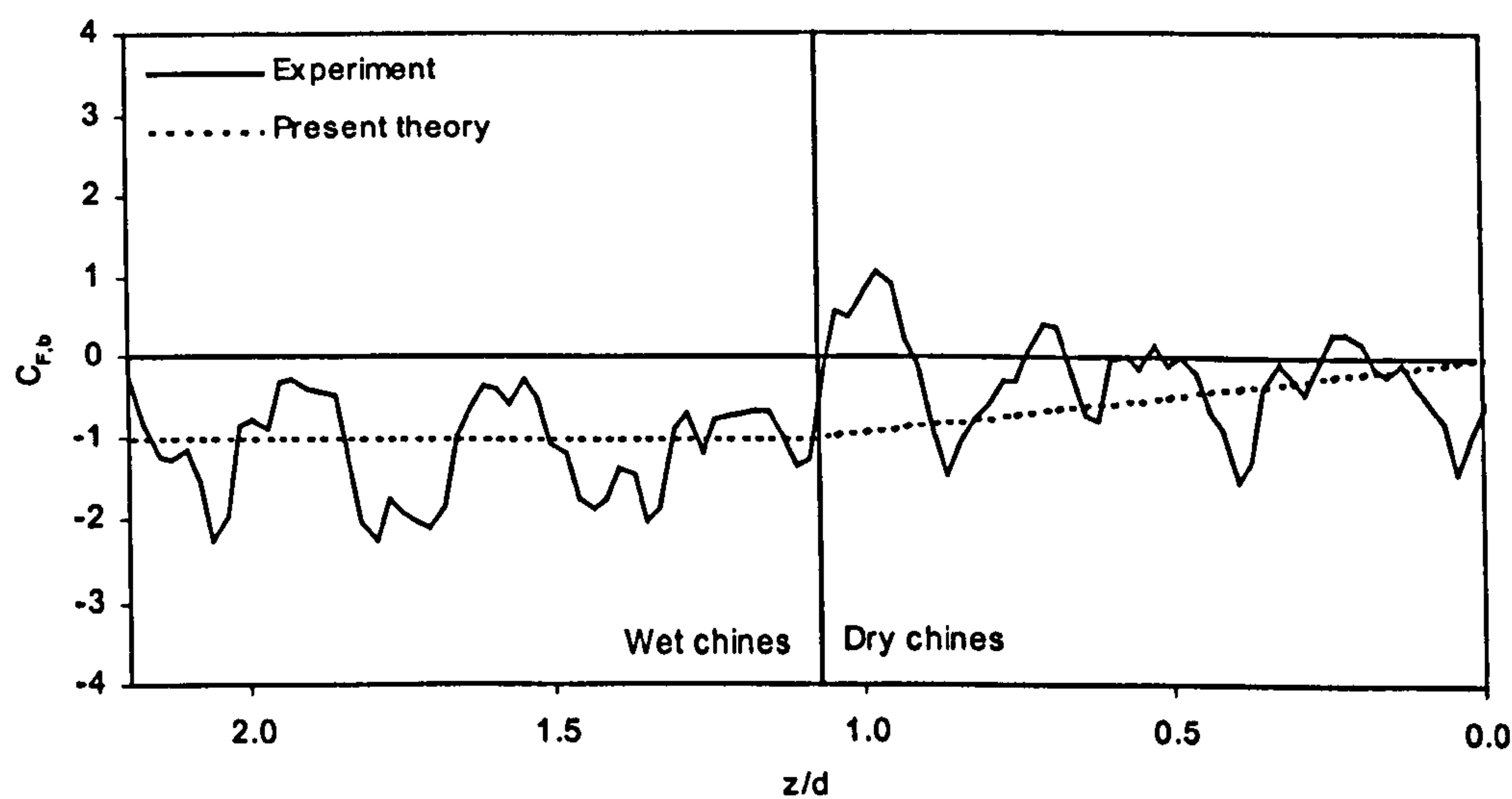


Figure 7-12. Non-dimensional water exit force, 15 degree wedge section.

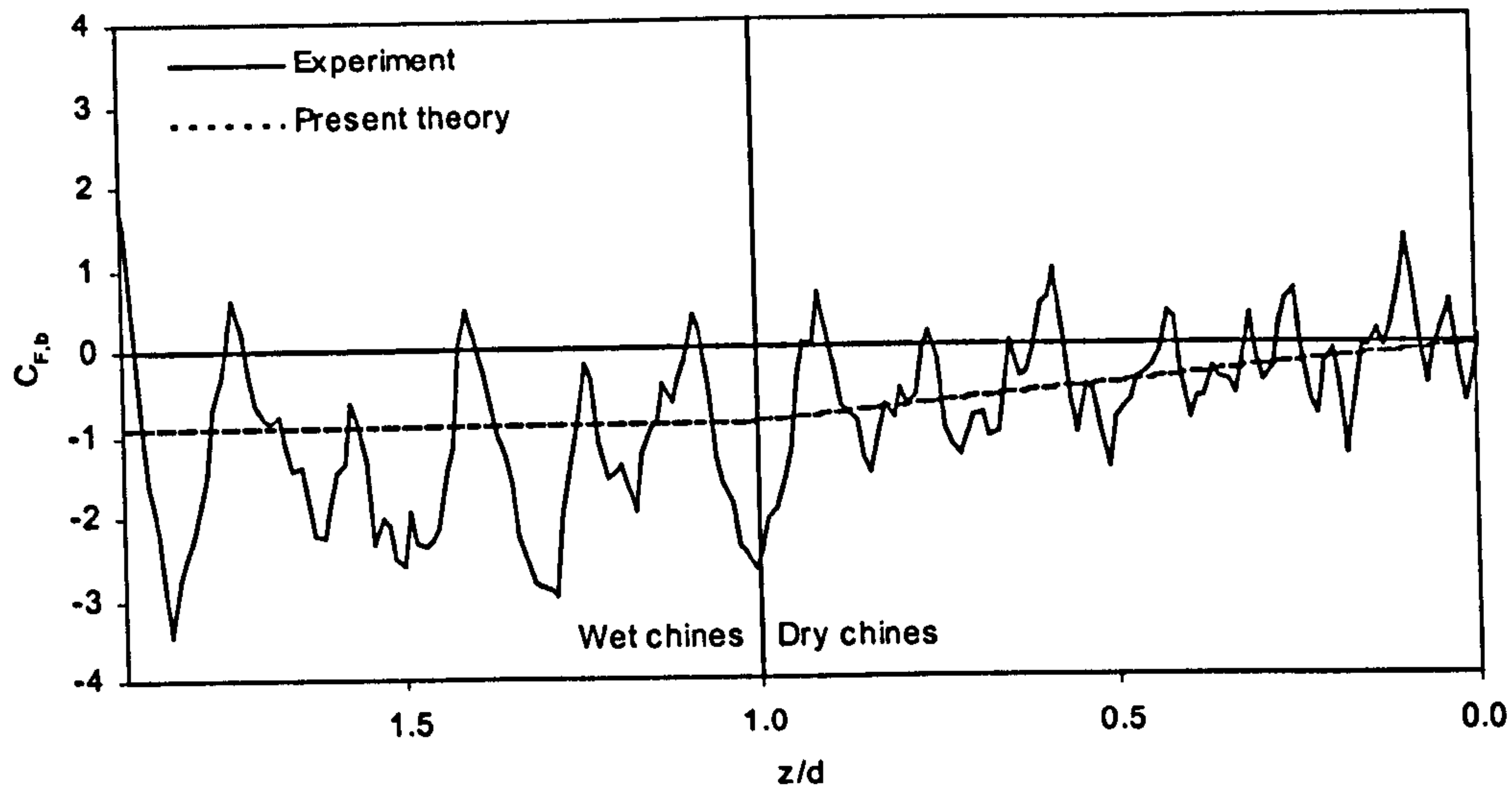


Figure 7-13. Non-dimensional water exit force, 30 degree wedge section.

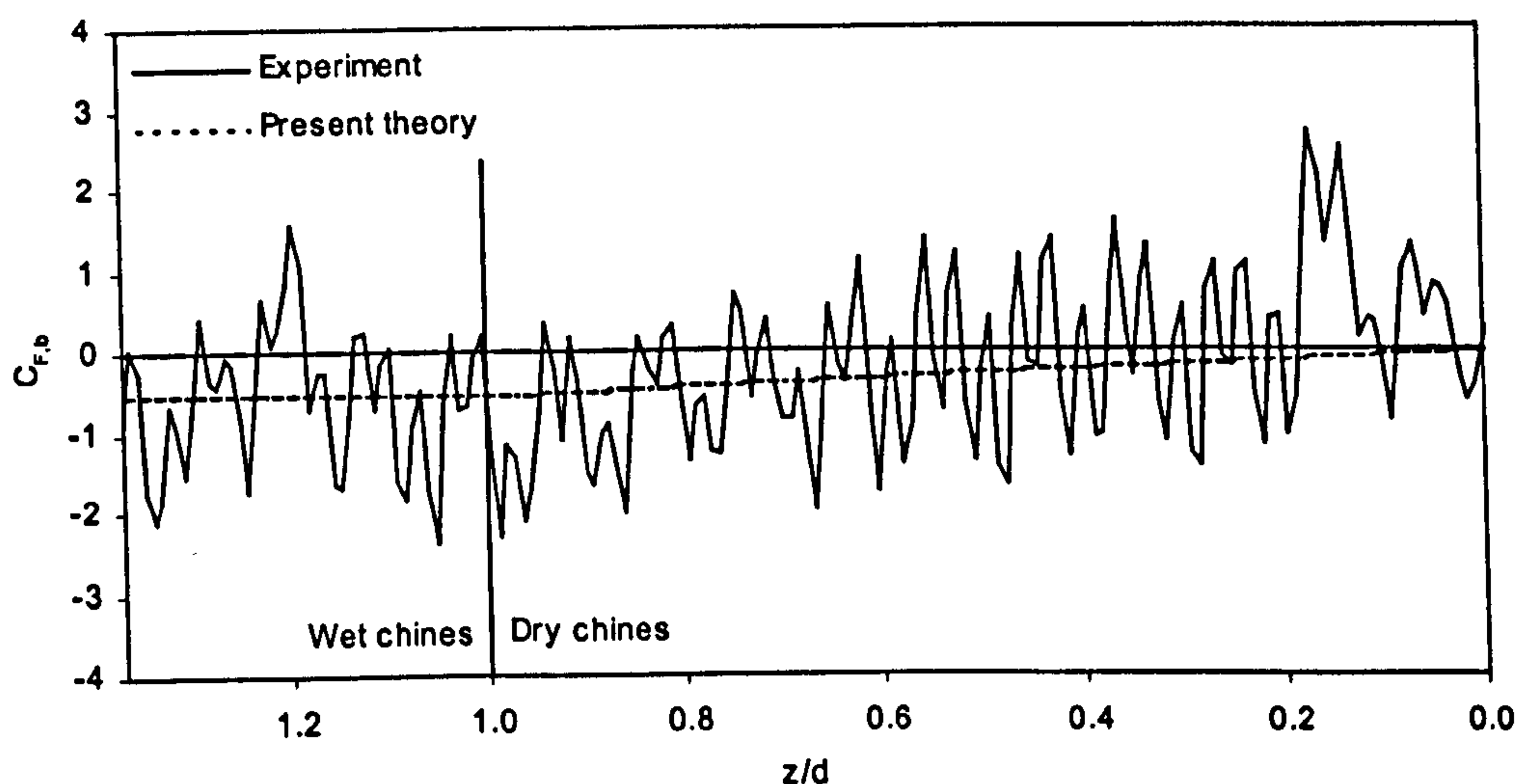


Figure 7-14. Non-dimensional water exit force, 45 degree wedge section.

### 7.3. Verification of Theory – Analysis of Remaining Test Data

The present theory has been validated by further analysis of the experimental data. For comparison with the present theory, deep chines immersion added mass values have been found using the wet chines oscillation results, and dry chines added mass values have been found using results from the accelerated/decelerated



water entry tests. Further, some experimental evidence of the flow momentum force component have been found from a consideration of the added mass values given by the present theory and those obtained by the present experiments.

### 7.3.1. Maximum Added Mass - Analysis of Wet Chines Oscillation Test Data

The hydrodynamic forces acting on the wet chines oscillating sections have been obtained by subtracting the Archimedes' buoyancy from the experimental data shown in Figures 5-60 to 5-62. Note that the data in these figures have been corrected to remove the weight and inertial force of the solid section mass.

During the wet chines oscillation tests, the maximum depth of the cycles was taken as large as the test rig would allow. The 0 degree deadrise section was oscillated from a depth of  $z/b=0.30$  to  $0.38$ , the 15 degree deadrise section from  $z/d=3.11$  to  $3.73$  and the 45 degree deadrise section from  $z/d=1.60$  to  $1.77$ . All the wet chines oscillation tests were performed with velocity varying linearly from  $-0.3\text{m/s}$  to  $+0.3\text{m/s}$  with constant acceleration of  $\pm 2.0\text{m/s}^2$ . According to Equation (7-15), the added mass value at the average depth of the 45 degree deadrise oscillations is only 5 percent below its asymptotic value, while for the 15 degree deadrise section the added mass is 2 percent below its asymptotic value. Therefore the added masses found from analysis of the wet chines oscillation data are considered to give a close estimate of the infinite depth added mass.

The flow momentum forces that were derived in Section 7.1 from the deep immersion force data are applied in a procedure for extracting the added masses from the wet chines oscillation test data. Because the added masses are considered to be constant at the mean water depths of these oscillation tests, the hydrodynamic force acting on the wedge section is given by

$$F' = m' \cdot \frac{dw}{dt} + C_{fm} \cdot \frac{1}{2} \rho \cdot |w| \cdot w \cdot b \quad (7-27)$$

where the first term is the inertial force resulting from acceleration of the added mass and the second is the flow momentum force term. The added mass of the

deeply immersed section is found by solving Equation (7-27) in terms of  $m'$  for every experimental data set recorded during a number of cycles. All the added mass values obtained for a given section are averaged and expressed in coefficient form by dividing by the mass of water in a half-cylinder of diameter equal to the section beam. The values obtained are given in Table 7-2.

$\beta$	$C_m$
0	1.23
15	1.02
45	0.602

*Table 7-2. Deep chines immersion added mass coefficients based on oscillation experiment data.*

The hydrodynamic forces have been calculated from Equation (7-27) by using the averaged added mass coefficients in Table 7-2, the flow momentum coefficients from Section 7.1 and velocity and accelerations calculated from the experimental data sets. The calculated forces are plotted together with the experimentally obtained hydrodynamic forces in Figures 7-15 to 7-17. The immersion depth ( $z$ ) of the test sections is also plotted. Note that the immersion depths are plotted on a reverse scale so that the curve indicates the vertical position of the test section.



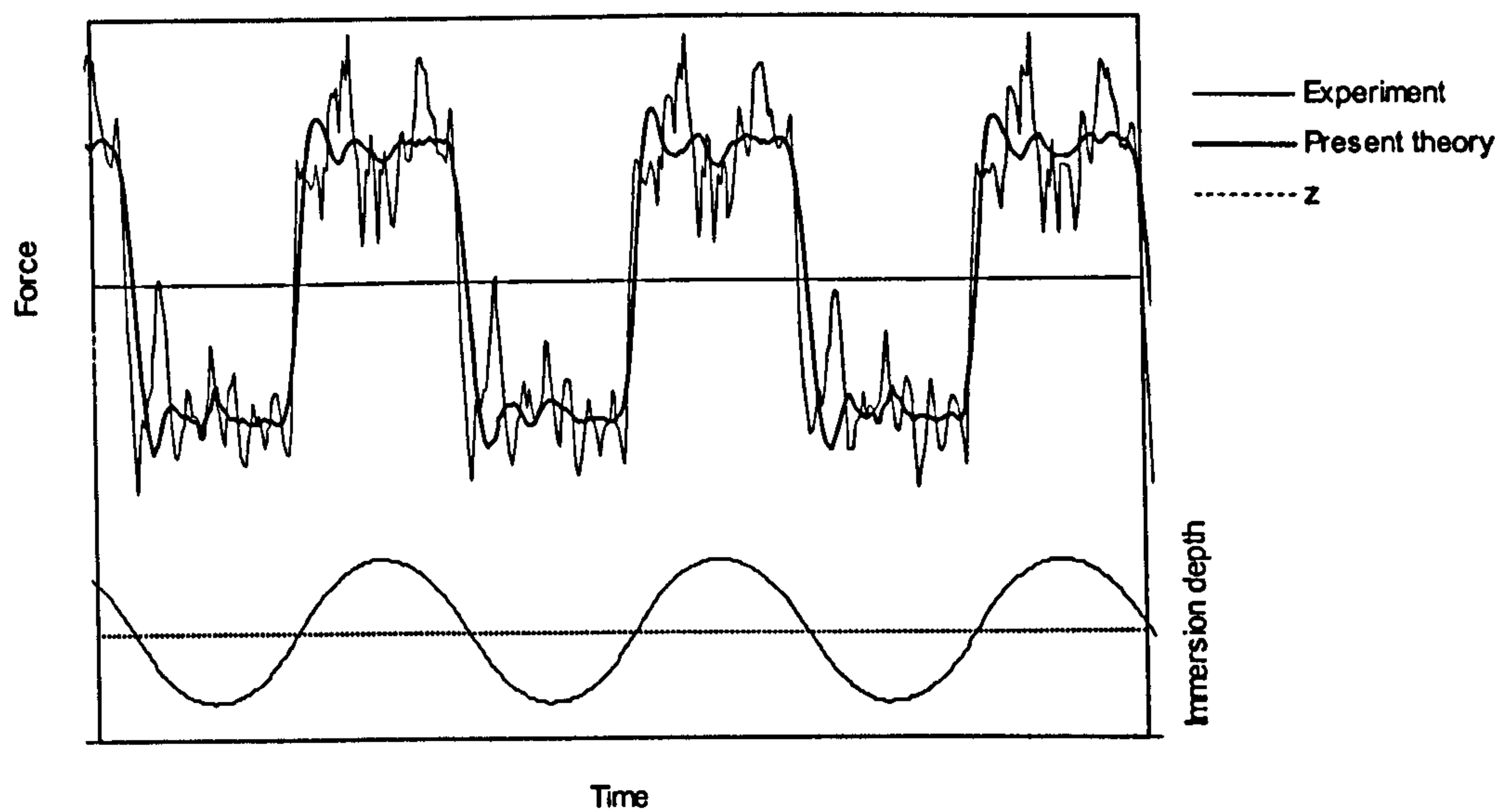


Figure 7-15. Wet chines oscillation of 0 degree section,  $z/b=0.30$  to  $0.38$ .

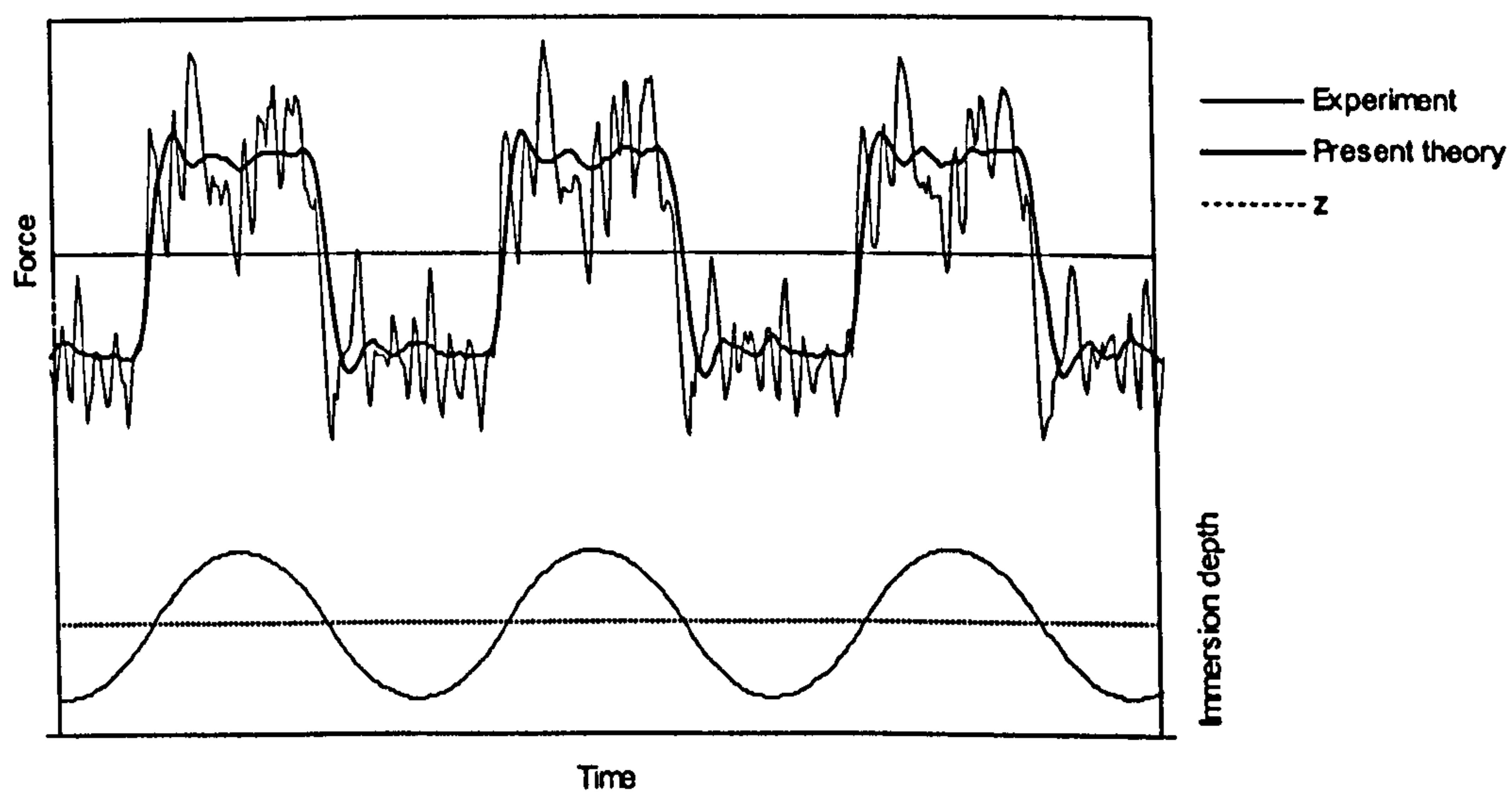


Figure 7-16. Wet chines oscillation of 15 degree section,  $z/d=3.11$  to  $3.73$ .

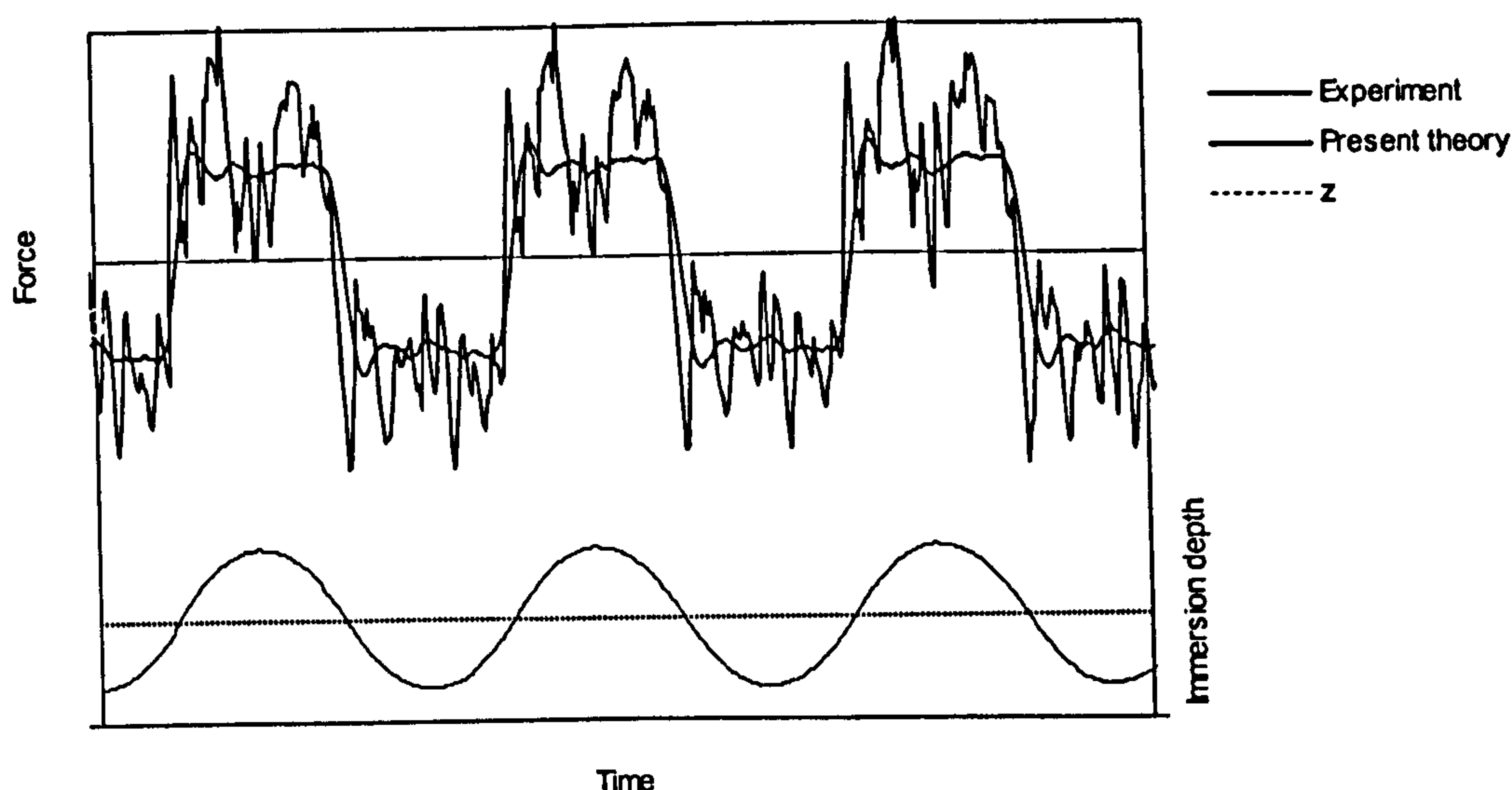


Figure 7-17. Wet chines oscillation of 45 degree section,  $z/d=1.60$  to  $1.77$ .

Combining Equations (7-14) and (7-15) gives the wet chines added mass as asymptotic to a value of

$$m'_{\infty} = 1.57 \cdot C_{m'} \cdot \frac{1}{2} \rho \pi \left( \frac{b}{\pi} \right)^2 \quad (7-28)$$

where  $C_{m'}$  is the dry chines added mass coefficient given by Equation (7-13). The wet chines added mass is made non-dimensional by dividing by the mass of water in a half-cylinder of diameter equal the section width  $b$ , giving

$$C_{m',\infty} = 1.57 \cdot \frac{4}{\pi^2} \cdot C_{m'} \quad (7-29)$$

Note that although the added mass at deep chines immersion is greater than for the dry chines condition, the added mass coefficients of the former are lower than the latter. This is because the added mass has been non-dimensionalised on the nominal half-width, and as the chines become wetted the rate of change of added mass decreases while the nominal half-width continues to increase with the same rate until  $z=d$ . Using Equation (7-29), the maximum added mass coefficients are calculated for the 0, 15 and 45 degree deadrise wedge sections. These are given in



Table 7-3 together with the percentage difference from those based on the wet chines oscillation experimental results given in Table 7-2.

$\beta$ [degrees]	$C_{m',\infty}$ -Theory	$C_{m',\infty}$ -Exp	Discrepancy
0	1.39	1.23	-13 %
15	1.01	1.02	-1 %
45	0.566	0.602	+6 %

*Table 7-3. Infinite depth added mass coefficient, present theory and experiment.*

The numbers in Table 7-3 show reasonable good agreement between the present theory values and those obtained by oscillation experiments for 15 and 45 degree deadrise angles. The greatest discrepancy is found for the zero deadrise angle case. This is not surprising since the immersed chines added mass expression has been developed by analysis of results from deadrise angle test data, and its application to zero deadrise angle sections is an extrapolation.

### **7.3.2. Dry Chines Added Mass - Analysis of Accelerated Water Entry Data**

The hydrodynamic forces acting on the sections during accelerated (and decelerated) water entry have been obtained by subtracting the Archimedes' buoyancy from the experimental data shown in Figures 5-66 to 5-70. Note that the data in these figures have been corrected to remove the weight and inertial force of the solid section mass.

During these tests the sections were subjected to a constant acceleration during the water entry. For each data set, the constant velocity force that corresponds to the velocity at each point of immersion was calculated using the slamming force coefficients  $C_F$  obtained from the constant velocity water entry test data and given in Table 6-1. This force was subtracted from the hydrodynamic force to obtain the inertial force component due to acceleration of the added mass. The added mass

was found by dividing the inertial force of the added mass by the acceleration. The results of added mass plotted against immersion depth were highly scattered for most test cases due to the small proportion of the total force that they represent. With the ratios of velocities to acceleration that was achieved during the tests, the constant velocity force was dominant relative to the force required to accelerate the added mass. The inertial force of the added mass of a two-dimensional wedge is expressed by

$$F'_{inertial} = m' \cdot a = C_m \cdot \frac{1}{2} \rho \pi \cdot \frac{z^2}{\tan^2 \beta} \cdot a \quad (7-30)$$

while the constant velocity force is expressed in terms of a slamming force coefficient as

$$F'_{steady} = C_F \cdot \rho \cdot w^2 \cdot z \quad (7-31)$$

The ratio of inertial force to steady force is therefore expressed by

$$\frac{F'_{inertial}}{F'_{steady}} = \frac{C_m \cdot \rho \cdot \pi \cdot z}{C_F \cdot 2 \cdot \tan^2 \beta \cdot w^2} \quad (7-32)$$

The inertial to steady force ratio was found to be less than 0.2 at an immersion depth equal to half that at which chines wetting occurred for all the test cases. Note that added mass coefficients from Equation 7-13 and the slamming force coefficients from Table 6-1 were used calculate the ratios given by Equation (7-32).

Reducing a scattered signal by values that are of magnitudes nearly as high, emphasises the scatter and results in the extremely scattered added mass inertial force data (both buoyancy and constant velocity force have been subtracted). However, some use could be made of the data from the tests with highest accelerations. The inertial forces from these tests were divided by the accelerations, and the resulting added mass data are shown in Figures 7-18 to 7-20. The added mass coefficient for each deadrise angle was calculated from a least squares fit to the function



$$m' = C_m \cdot \frac{1}{2} \rho \pi \cdot \frac{z^2}{\tan^2 \beta} \quad (7-33)$$

and the results are given in Table 7-4. The average of these added mass coefficients for each test section are also given in the table.

$\beta$ [degree]	Acc. [m/s <sup>2</sup> ]	$C_m$ of l.s.f	Average $C_m$
	-3.00	1.89	
15	0.83	1.37	1.54
	3.33	1.36	
30	2.50	1.46	1.46
45	2.4	1.31	1.09
	1.71	0.88	

Table 7-4. Dry chines added mass coefficients from accelerated water entry experiments.

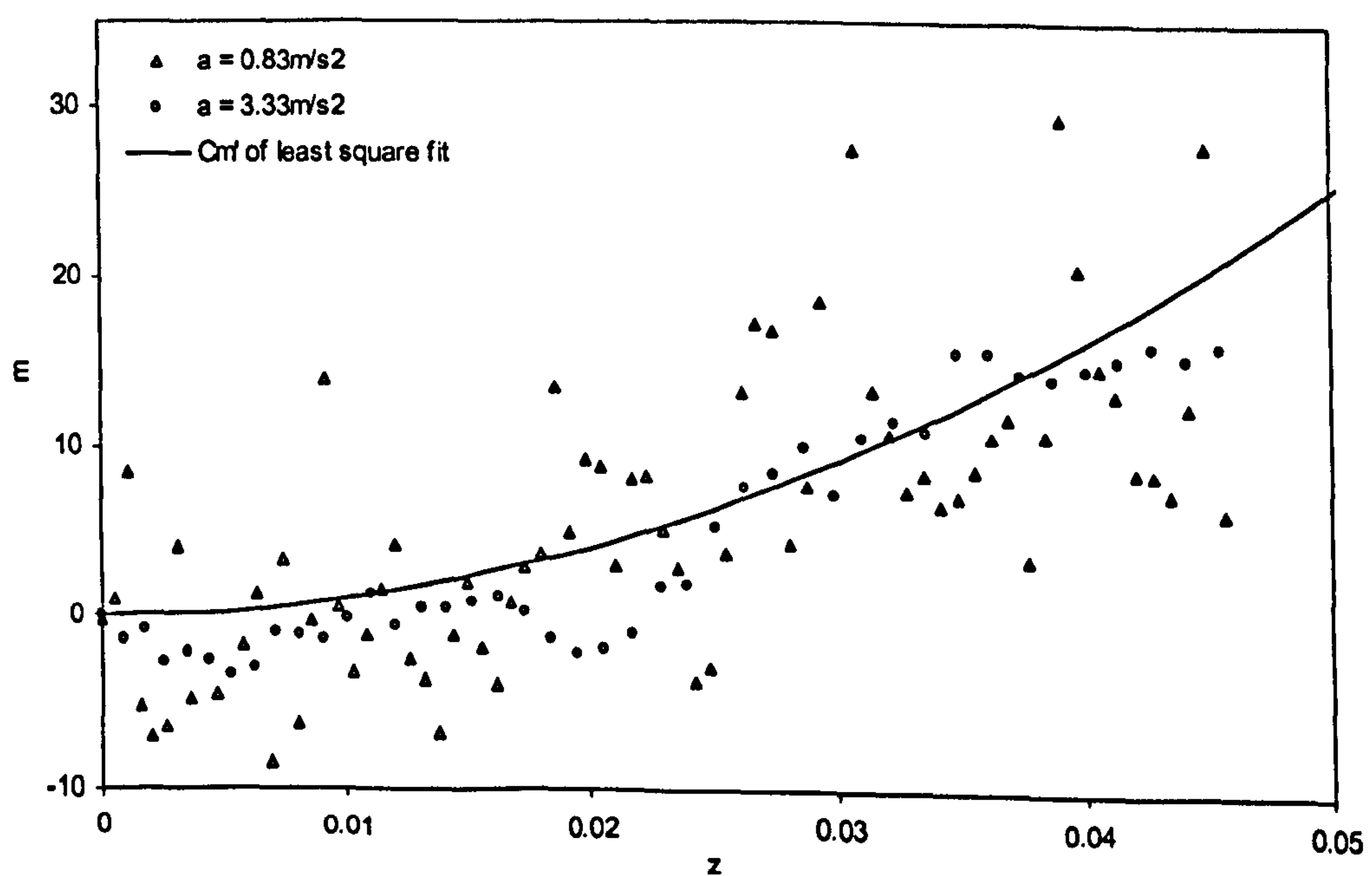


Figure 7-18. Accelerated water entry added mass of 15 degree wedge section.

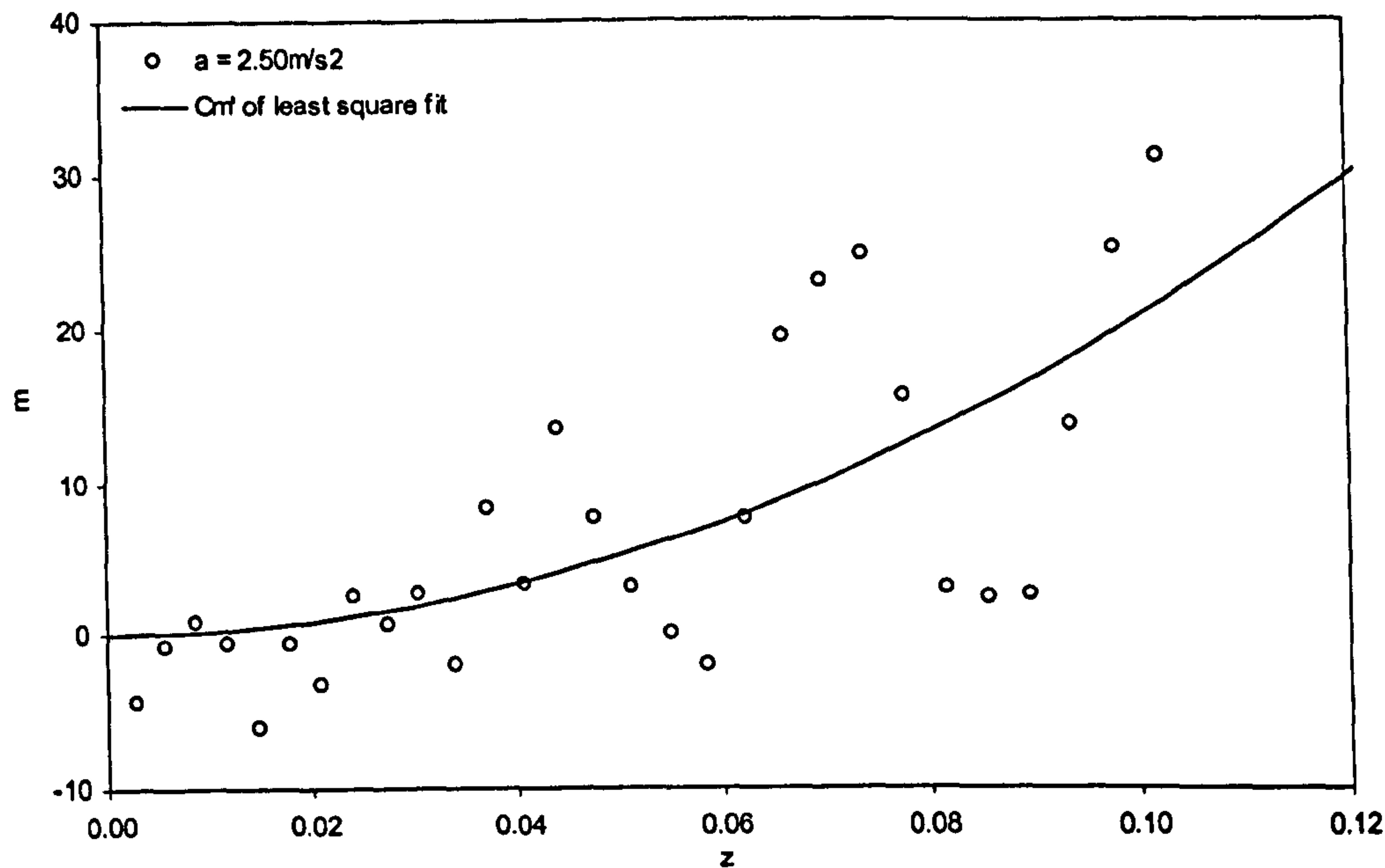


Figure 7-19. Accelerated water entry added mass of 30 degree wedge section.

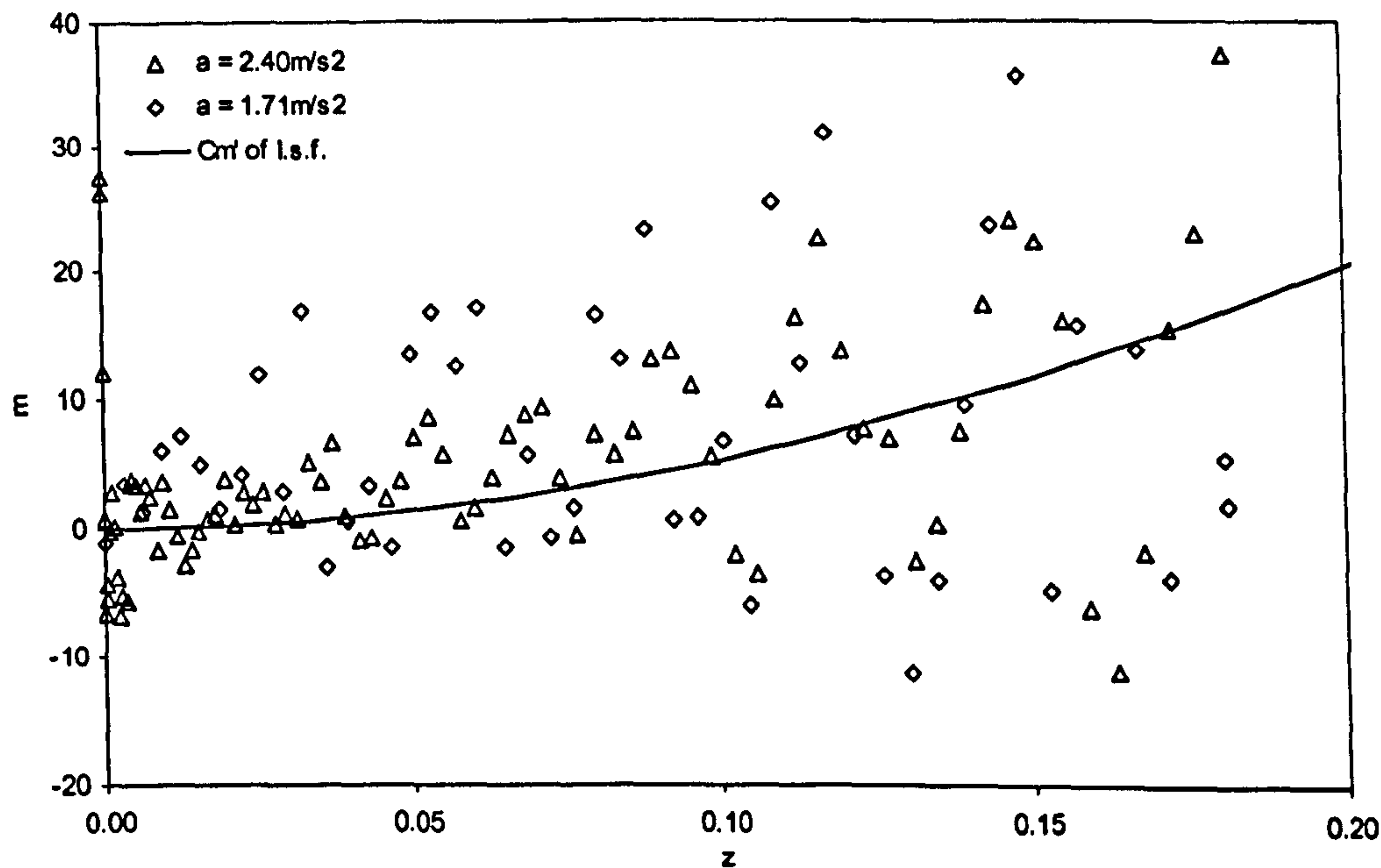


Figure 7-20. Accelerated water entry added mass of 45 degree wedge section.

These added mass coefficients compare well with the other experimentally obtained coefficients for the 15 degree deadrise angle sections. For the 30 and 45



degree cases, the added mass coefficients obtained from the accelerated water entry experiment was about 20 percent higher than the values calculated using the present theory and measured from the constant velocity water entry experiments.

### **7.3.3. Evidence of Flow Momentum Force**

It can be seen from Figure 7-1 that if the flow momentum contribution is excluded from the calculation of the hydrodynamic force acting on a wedge section during a water entry, then a higher rate of change of added mass will be predicted to account for this force. This will result in the added mass continuing to increase at deep immersion. This effect is calculated below. The flow momentum force to be accounted for by an additional rate of change of added mass is given in Equations (7-2) and (7-3) and can also be expressed by

$$F'_{fm} = C_{fm} \cdot \frac{1}{2} \rho w^2 \cdot \frac{2z}{\tan \beta} \quad , z < d$$

$$F'_{fm} = C_{fm} \cdot \frac{1}{2} \rho w^2 \cdot \frac{2d}{\tan \beta} \quad , z > d$$

For a constant velocity water entry, the added mass associated force equals the velocity squared times the depth rate of change of added mass, i.e.  $F'_{m'} = w^2 \frac{dm'}{dz}$ .

Thus the additional rate of change of added mass to account for the exclusion of flow momentum force is

$$\left( \frac{dm'}{dz} \right)_{add} = \frac{F'_{fm}}{w^2} \quad (7-34)$$

The additional added mass, at a given immersion depth  $z$ , due to this is

$$(m')_{add} = \int_0^z \frac{F'_{fm}}{w^2} dz = \int_0^d \frac{F'_{fm}}{w^2} dz + \int_d^z \frac{F'_{fm}}{w^2} dz = C_{fm} \cdot \rho \cdot \left( \int_0^d \frac{z}{\tan \beta} dz + \int_d^z \frac{z}{\tan \beta} dz \right) \quad (7-35)$$

And the additional added mass coefficient is

$$(C_{m'})_{add} = \frac{(m')_{add}}{\frac{1}{2} \rho \pi \cdot \left( \frac{d}{\tan \beta} \right)^2} = C_{fm} \cdot \frac{\frac{d^2}{2 \cdot \tan \beta} + \frac{d \cdot z}{\tan \beta} - \frac{d^2}{\tan \beta}}{\frac{1}{2} \pi \cdot \left( \frac{d}{\tan \beta} \right)^2} = \frac{C_{fm} \cdot \tan \beta}{\pi} \cdot \left( \frac{2z}{d} - 1 \right) \quad (7-36)$$

In the present oscillation tests, the 15 degree deadrise angle section was oscillated about an average depth of 0.275m and the 45 degree deadrise section was oscillated about an average depth of 0.505m. Analysis of the data from these tests gave added mass coefficients of 1.02 for the 15 degree deadrise section and 0.60



for the 45 degree deadrise section (also given in Table 7-3). At the depths these oscillations were carried out, the additional added mass coefficients, according to Equation (7-36), are 0.41 for the 15 degree deadrise section and 0.50 for the 45 degree deadrise section. Thus, not separating out the flow momentum force as a component of the total water entry force, results in a 40 percent overestimate of the added mass for the 15 degree deadrise section when compared with oscillation experiments and a 83 percent overestimate for the 45 degrees deadrise section. During a dry chine entry the force is predominantly due to added mass, and therefore errors here are small.

## 7.4. Comparison of added mass coefficients

### 7.4.1. Dry Chines

The dry chines added mass coefficients that have been obtained by analysis of the constant velocity and the accelerated water entry data, and by the 60 degrees deadrise CFD data are presented in Figure 7-21 together with present theory and the theories of other authors. The letters CVWE in the data legend denote “Constant Velocity Water Entry”, and the letters AWE denote “Accelerated Water Entry”.

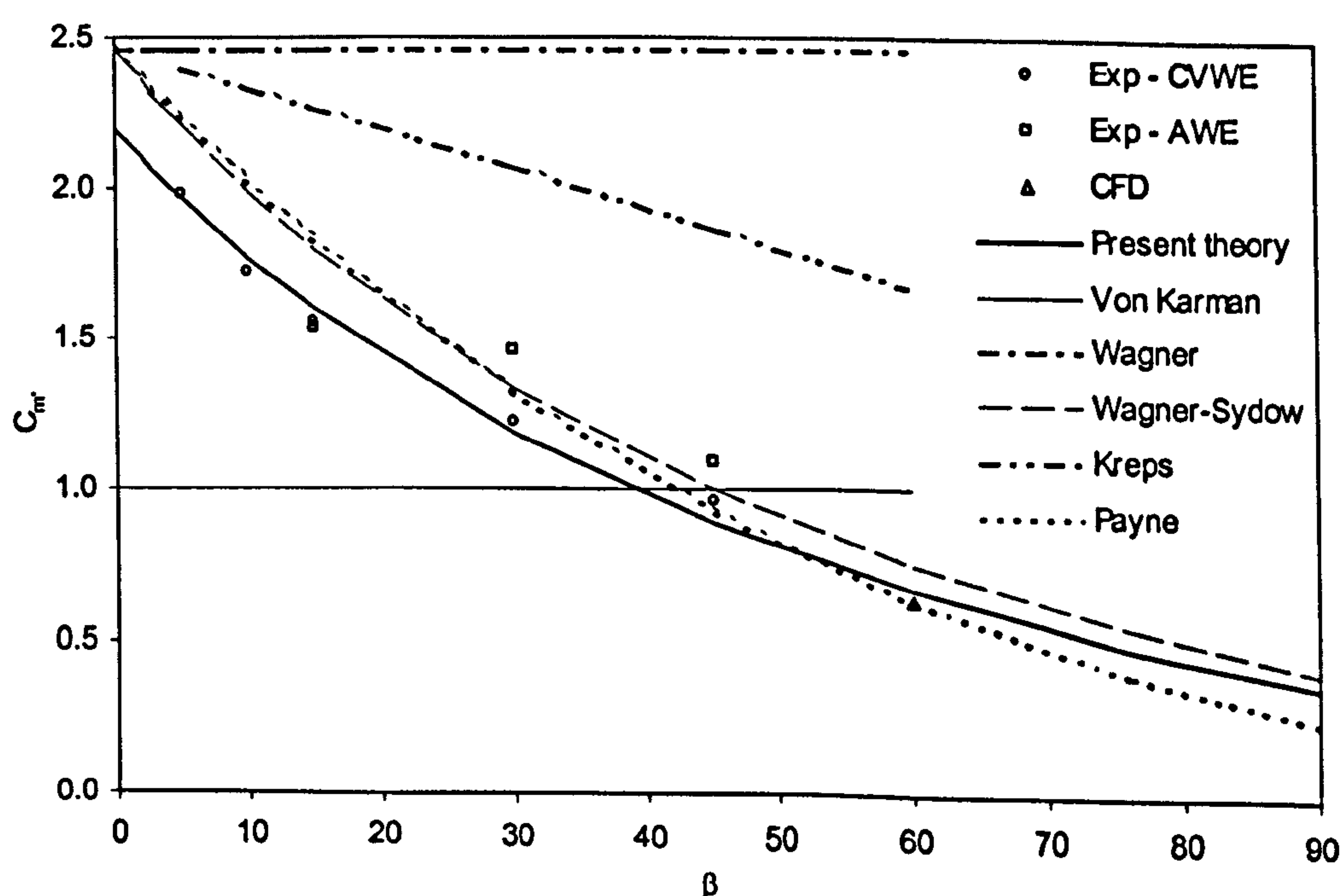


*Figure 7-21. Dry chines added mass coefficients from present theory, present experiments and by various other authors.*

It is seen that the added mass coefficients based on the accelerated water entry data are somewhat higher than those based on analysis of the constant velocity water entry data. However, the data from the accelerated tests were extremely scattered, and hence do not provide a reliable basis for adjustment of the present theory added mass coefficient function.

#### 7.4.2. Wet Chines

The added mass coefficients obtained from the wet chines oscillation tests given in Table 7-3 are plotted in Figure 7-22 together with a curve representing the present theory infinite depth added mass coefficients given by Equation (7-13) and (7-29).

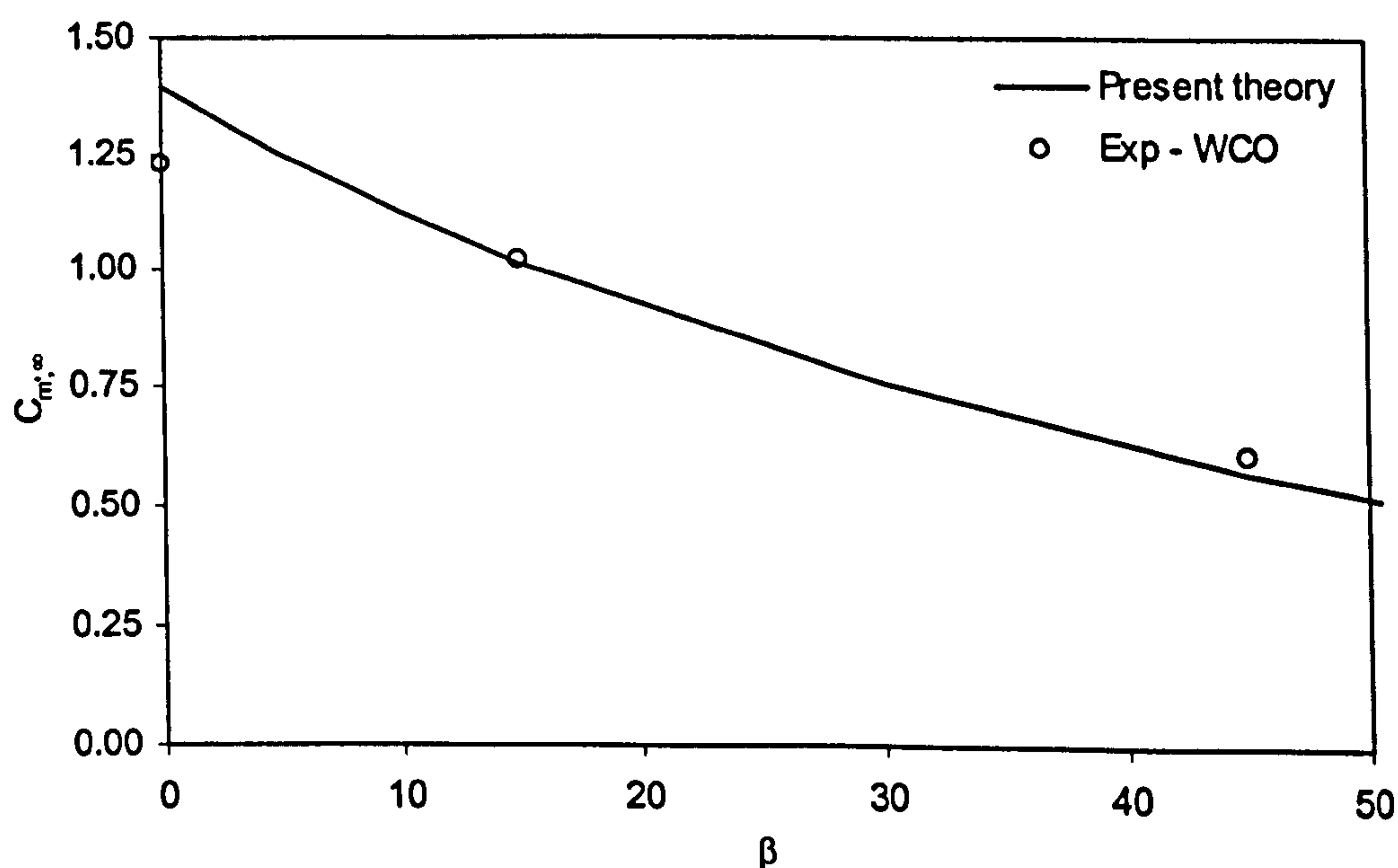


*Figure 7-22. Deep immersion added mass coefficients from theory and wet chines oscillation tests.*



## 7.5. Prediction of Dry Chines Oscillation Forces – Comparison with Dry Chines Oscillation Experiment

The hydrodynamic forces acting on the dry chines oscillating sections have been obtained by subtracting the Archimedes' buoyancy from the experimental data shown in Figures (5-62) to (5-65). Note that the data in these figures have been corrected to remove the weight and inertial force of the solid section mass.

Two different deadrise angle sections were tested, the 15 and the 45 degree deadrise sections. Both sections were tested with two different amplitudes. The 15 degree deadrise section oscillations were performed at depth range  $z/d=0.124$  to  $0.746$  and  $z/d=0.249$  to  $0.498$ , while the 45 degree section at  $z/d=0.167$  to  $0.833$  and  $z/d=0.667$  to  $0.833$ . During the large amplitude 15 degree section oscillations, the velocity was varied linearly from  $-0.3\text{m/s}$  to  $+0.3\text{m/s}$ , while during the small amplitude oscillations the velocity was varied linearly from  $-0.2\text{m/s}$  to  $+0.2\text{m/s}$ . In both 15 degree section cases the acceleration was constant at  $\pm 2.0\text{m/s}^2$ . During the 45 degree section large amplitude test, the velocity varied linearly from  $-0.5\text{m/s}$  to  $+0.5\text{m/s}$ , while during the small amplitude test the velocity was varied linearly from  $-0.3\text{m/s}$  to  $+0.3\text{m/s}$ . In the large amplitude 45 degree section test the acceleration was constant with magnitude of  $\pm 1.25\text{m/s}^2$ , while in the small amplitude case the magnitude of the acceleration was  $\pm 2.0\text{m/s}^2$ .

The results from these tests have not been used in the analysis to quantify the force components of the present theory. However, the theory has been applied to the test conditions to obtain the forces for comparison with the test force data. The purpose of this is to evaluate the quality of the present theory for prediction of the hydrodynamic forces acting on dry chines wedge sections during cyclic motions.

The value of added mass of a wedge section is associated with its nominal width, i.e. the distance between the intersection of the wedge and the calm water surface. The force Equation (7-27) is expanded to account for the variation in added mass as result of the varying width. The hydrodynamic force for dry chines oscillations can thus be expressed as

$$F' = m' \cdot \frac{dw}{dt} + w^2 \cdot \frac{dm'}{dz} + C_{fm} \cdot \frac{1}{2} \rho w^2 \cdot \frac{2z}{\tan \beta} \quad , \quad w > 0 \quad (7-37)$$

where  $dm'/dz$  is given by the derivative of Equation (7-10) with respect to  $z$ , and expressed by

$$\frac{dm'}{dz} = C_{m'} \cdot \rho \pi \cdot \frac{z}{\tan^2 \beta} \quad (7-38)$$

Equation (7-37) is only applied to the entry half-cycles of the oscillations. In Section 7.2 it was shown that force predictions that correlate well with experimental data from exit tests can be obtained by excluding the rate of change of added mass force component. The exit half-cycle force can therefore be expressed as

$$F' = m' \cdot \frac{dw}{dt} + C_{fm} \cdot \frac{1}{2} \rho w^2 \cdot \frac{2z}{\tan \beta} \quad , \quad w < 0 \quad (7-39)$$

In both Equations (7-37) and (7-39)  $C_{fm}$  is given by Equation (7-4). The hydrodynamic forces acting on the dry chines oscillating sections are plotted together with the predictions given by Equations (7-37) and (7-39) in Figures 7-23 to 7-26. Equations (7-37) and (7-39) are calculated using depth, velocity and accelerations derived from the recorded velocities. The immersion depths  $z$  is plotted in the lower area of the figures. The curve given by Equations (7-37) and (7-39) is denoted 'Present theory'. Note that the immersion depths are plotted on a reverse scale so that the curve indicates the vertical position of the test section.



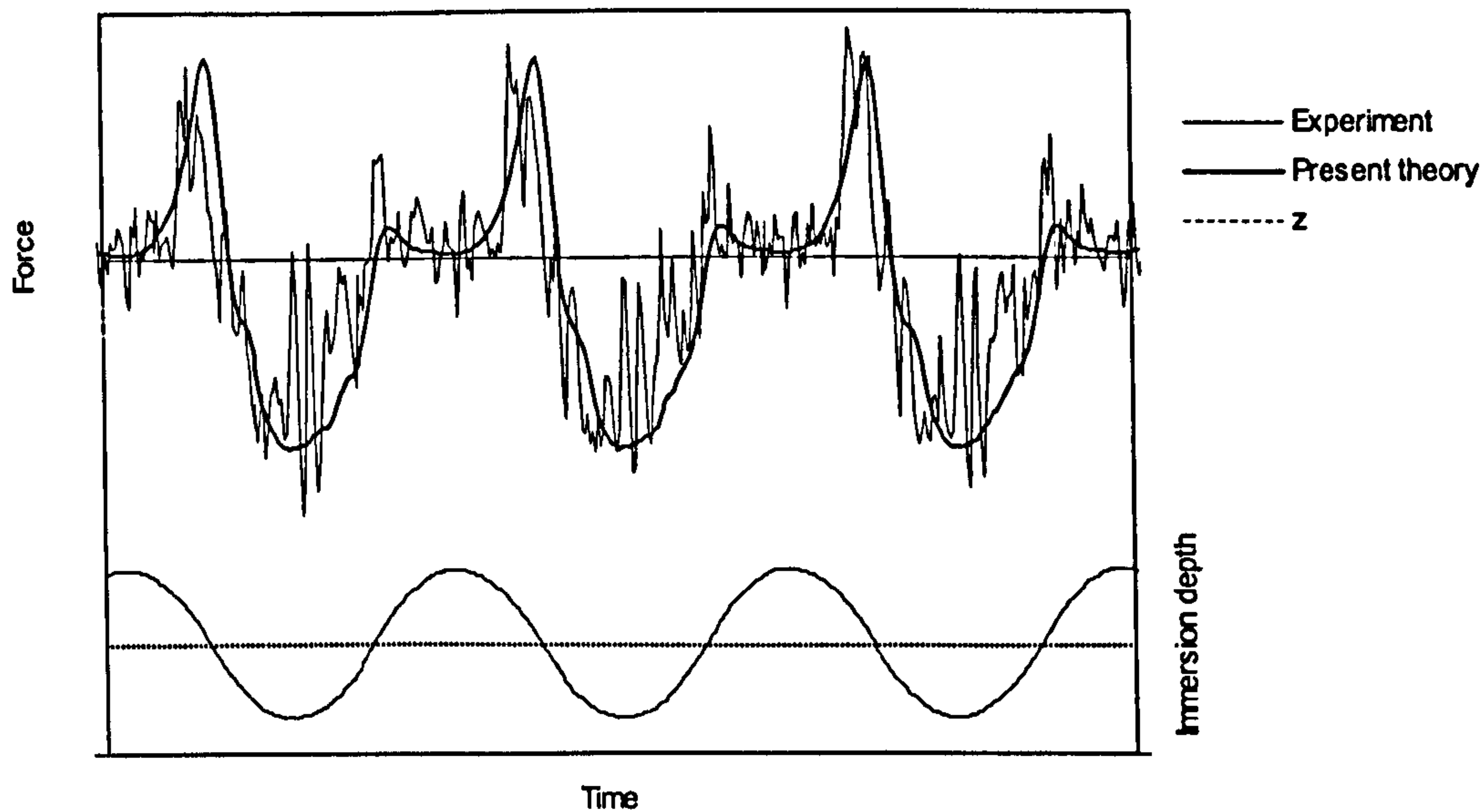


Figure 7-23. Dry chines oscillation of 15 degree wedge section,  $z/d=0.124$  to 0.746.

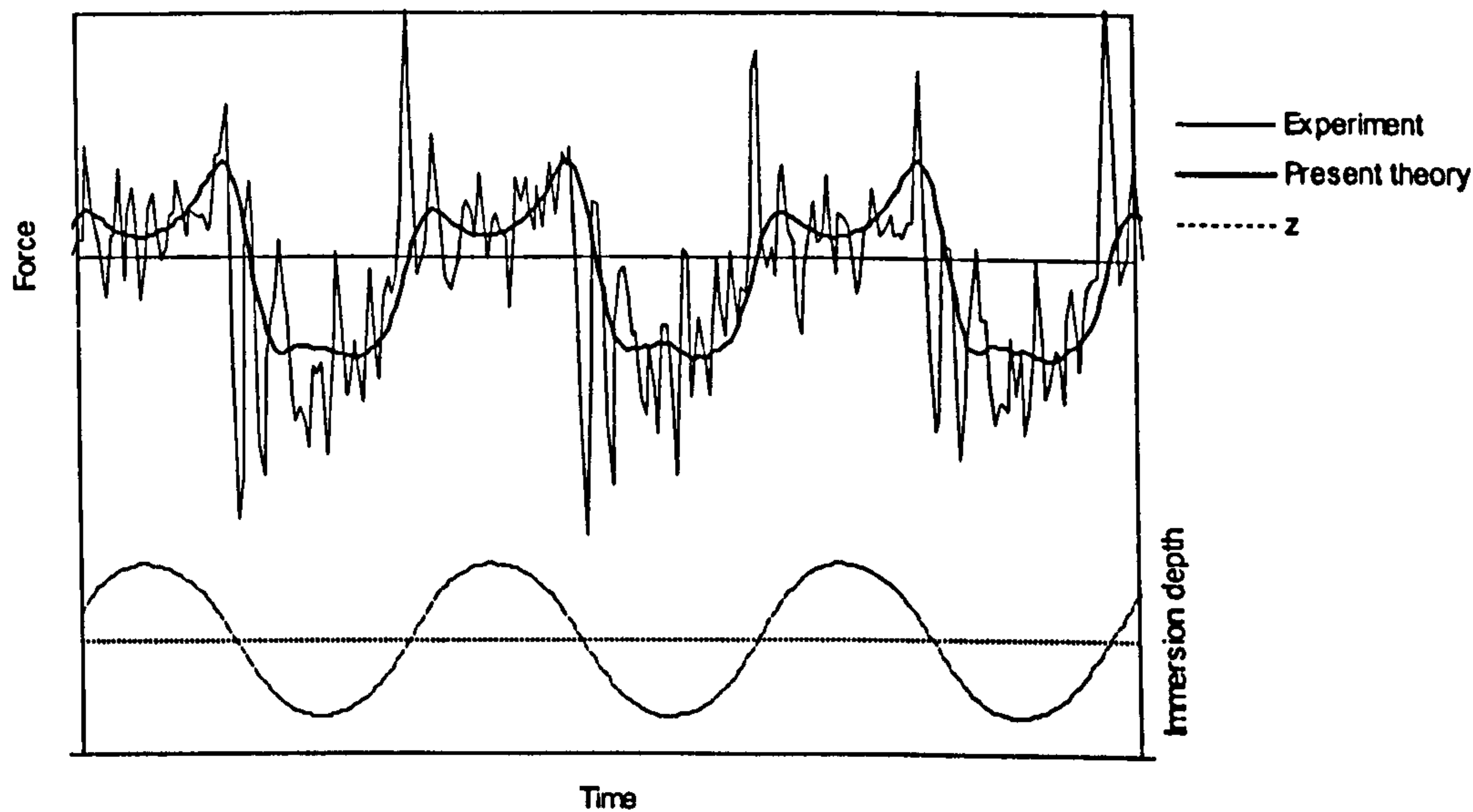


Figure 7-24. Dry chines oscillation of 15 degree wedge section,  $z/d=0.249$  to 0.498.

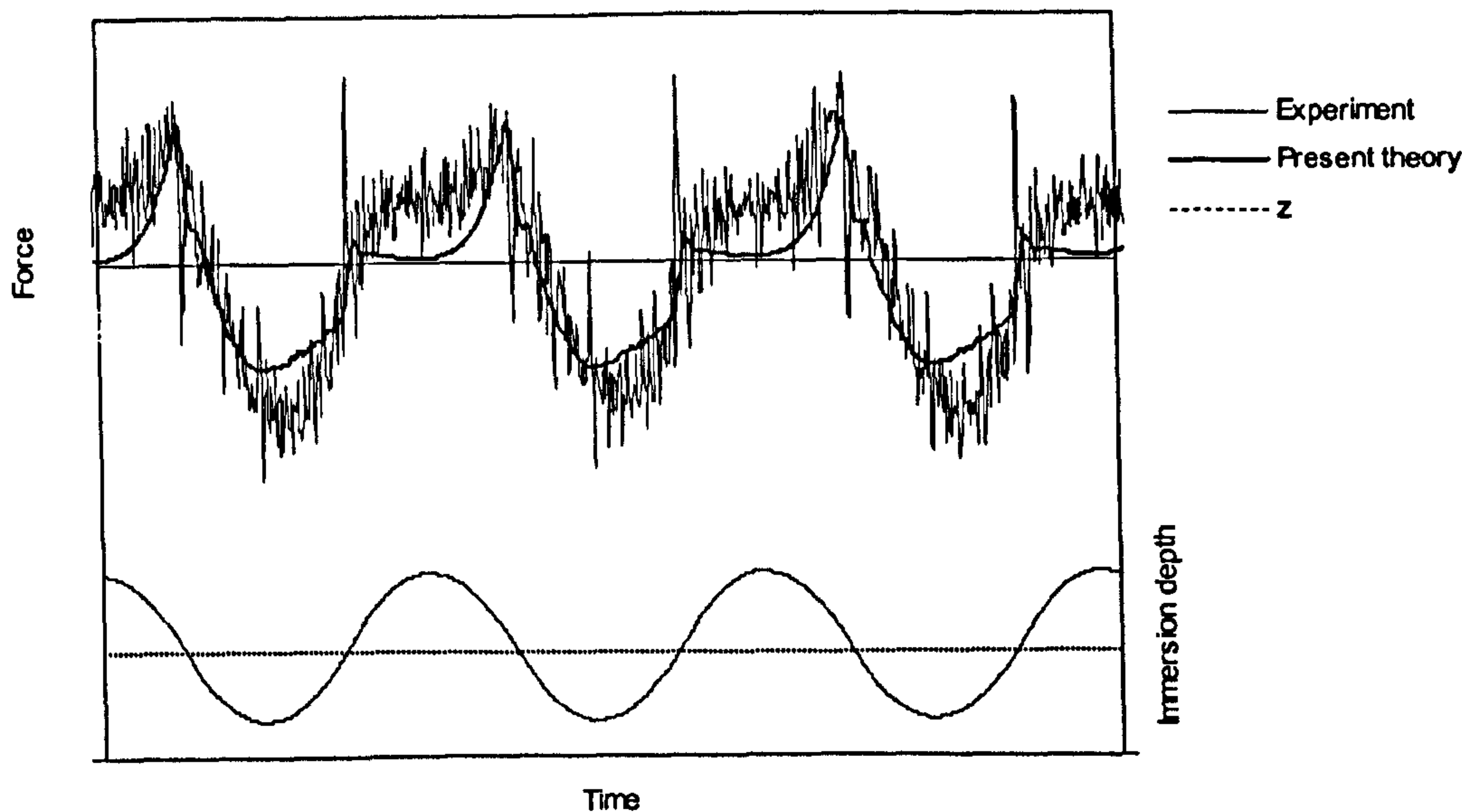


Figure 7-25. Dry chines oscillation of 45 degree wedge section,  $z/d=0.167$  to  $0.833$ .

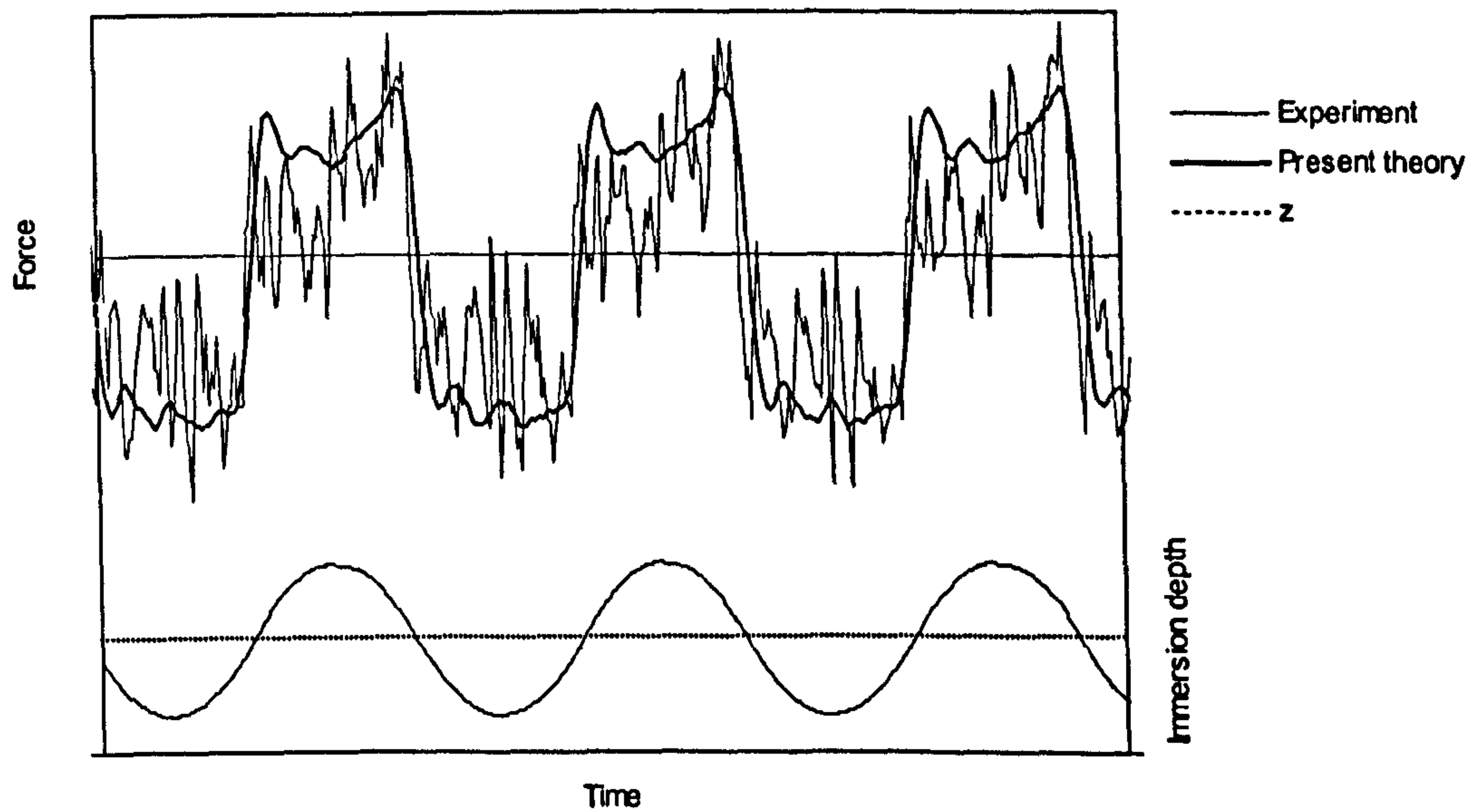


Figure 7-26. Dry chines oscillation of 45 degree section,  $z/d=0.667$  to  $0.833$ .

Figures 7-23 and 7-26 show that the present theory predicts the forces satisfactorily for the 15 degree section cyclic motion. In Figure 7-26 it is seen that also the predicted forces agree reasonably well with the measurements for the 45 degree small amplitude oscillations if disregarding the exit stages above mean



depth. For the 45 degree large amplitude oscillations in Figure 7-25 it is seen that there are generally significant disagreement between predicted and measured force with the exception of the water entry stages below mean depth.

Pictures from the water exit tests have shown that a large amount of water follows the test section above the calm water level. This could explain the large force (relative to the predicted force) measured at the lowest immersion depths during large amplitude oscillations of the 45 degree section seen in Figure 7-25. As the section is given a positive acceleration during the final exit stages to slow the upward motion which is followed by an accelerated downward motion, the water that has followed the section above the calm water level represents an additional inertia, which is not accounted for by the theory. Thus the force during this stage of these oscillations are largely underestimated.

Application of the added mass theory for prediction of cyclic motion forces implies that an undisturbed water surface is assumed each time the motion changes direction. Thus the added mass theory clearly breaks down for prediction of cyclic motion for cases when the disturbance of the free surface is large, and this is causing the disagreement shown in Figure 7-25. However, the theory seems to be consistent with the experimental data for the 15 degree deadrise angle dry chines cyclic motion cases. It is expected that there will be less disturbance of the free surface during dry chines cyclic motion of a low deadrise section than that during cyclic motion of a high deadrise angle section. This is because of the lesser variation in displaced and thus less water that flows to and from.

The instant of the sudden change in sign of acceleration, i.e. at maximum absolute velocity magnitude and mean immersion depth, induces the positive peak force seen on the exit and the negative peak seen on the entry.

The data from the low amplitude tests, shown in Figures 7-24 and 7-26, are more scattered than the large amplitude test data, shown in Figures 7-23 and 7-25. This is caused by there being greater fluctuations in the acceleration magnitude during the large amplitude tests than during the small amplitude tests. These fluctuations are induced by the acceleration sign changeovers that have been programmed to

create the oscillating motion. For the large amplitude oscillations, the period between acceleration sign changeovers is longer, allowing the fluctuations to decay in between, and thus resulting in less scattered force data.



PAGE NUMBERING AS IN THE  
ORIGINAL THESIS

---

**CHAPTER 8**

**APPLICATION OF WATER ENTRY THEORY**

**IN PLANING**

---



This chapter describes the application of the present water entry theory in a procedure to predict steady planing lift on slender body planing surfaces. The accuracy of this procedure is evaluated by comparison with experimental results from the literature, which are also used to quantify the effect of longitudinal flow on the lift force for non-slender planing surfaces.

### 8.1. Hydrodynamic Lift on Slender Planing Surfaces

It has been demonstrated with Figure 3-1 that the steady planing of a prismatic hull is hydrodynamically similar to the constant velocity water entry of a wedge section. The force acting on elements of the hull perpendicular to the trimmed keel line can be found by considering each hull element as a two-dimensional section entering the water with a velocity equal to the hull velocity component acting normal to the planing surface, i.e.  $U_0 \cdot \sin \tau$ , where  $U_0$  is the forward speed of the hull and  $\tau$  is the trim angle. Integration of the elemental forces along the hull gives the total hydrodynamic force acting normal to the planing surface.

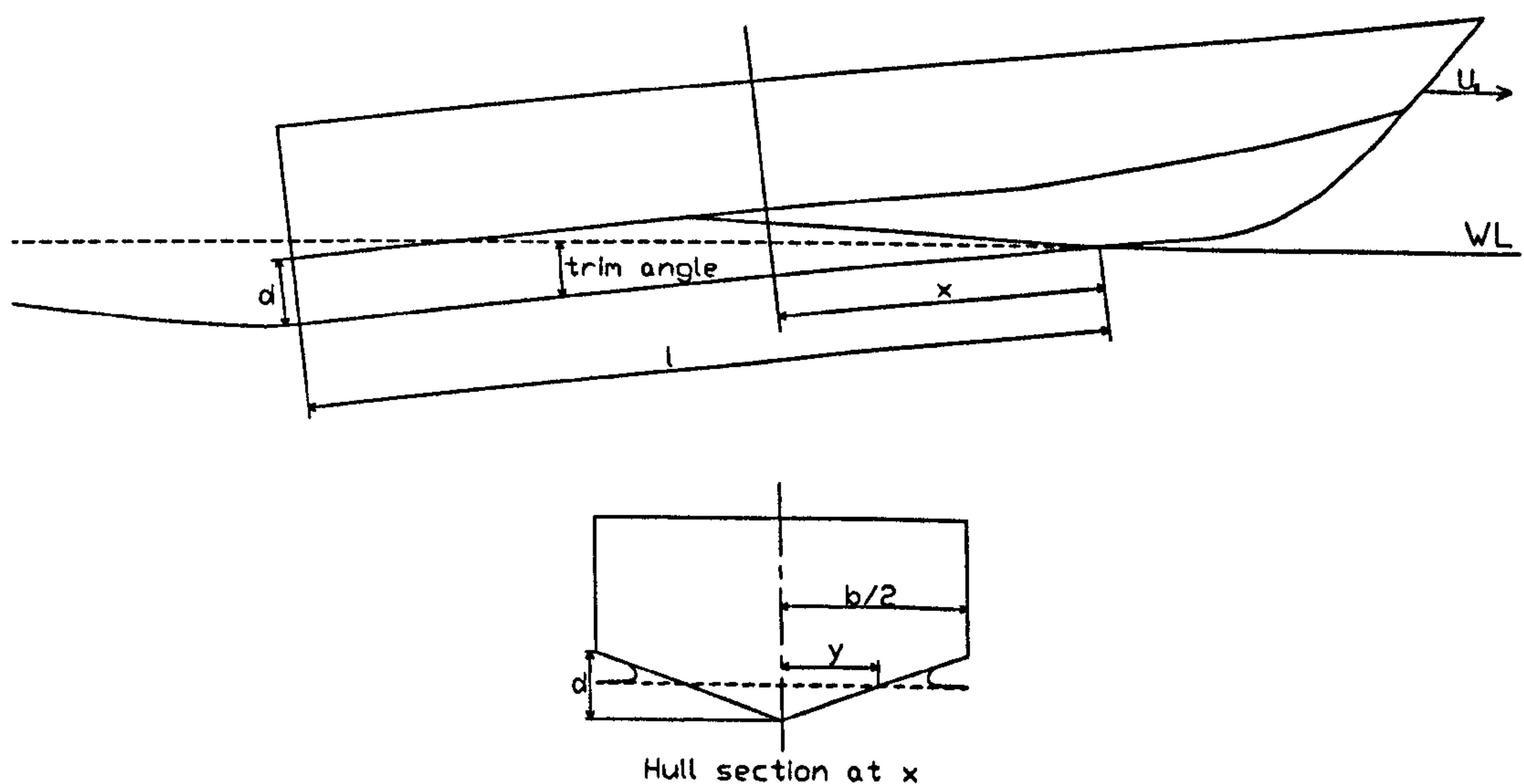


Figure 8-1. Coordinate system and notation for the planing equations.

The force acting on a two-dimensional wedge section during a constant velocity water entry is the sum of the added mass force and the flow momentum force given by Equations (7-8) and (7-2) respectively. The force acting on a section of a planing hull with elemental length  $dx$  (normal to the keel line) is from a water entry consideration therefore given by

$$\frac{dN}{dx} = (U_0 \cdot \sin \tau)^2 \cdot \frac{dm'}{d(x \cdot \tan \tau)} + C_{fm} \cdot \frac{1}{2} \rho \cdot (U_0 \cdot \sin \tau)^2 \cdot 2y \quad (8-1)$$

where  $N$  is the total hydrodynamic force acting on the hull normal to the keel line, and  $U_0 \sin \tau$  and  $x \cdot \tan \tau$  are the water entry velocity and immersion depth in the plane of the hull section corresponding to  $w$  and  $z$  respectively. The lateral dimension  $y$  in the flow momentum term is given by the lesser value of  $b/2$  and  $\frac{x \cdot \tan \tau}{\tan \beta}$ , where  $\beta$  is the deadrise angle in the plane of the hull section. The total

normal force is found by integrating Equation (8-1) along the planing surface from the forward intersection of the calm water level and the keel to the trailing edge

$$\begin{aligned} N &= \int_{x=0}^{x=l} \frac{dN}{dx} dx = \frac{(U_0 \cdot \sin \tau)^2}{\tan \tau} \cdot \int_{x=0}^{x=l} dm' + C_{fm} \cdot \frac{1}{2} \rho \cdot (U_0 \cdot \sin \tau)^2 \cdot \int_{x=0}^{x=l} 2y(x) dx \\ &= \frac{(U_0 \cdot \sin \tau)^2}{\tan \tau} \cdot m'_x + C_{fm} \cdot \frac{1}{2} \rho \cdot (U_0 \cdot \sin \tau)^2 \cdot S \end{aligned} \quad (8-2)$$

In Equation (8-2),  $m'_x$  is the value of the two-dimensional added mass at the trailing edge and  $S$  is the waterplane area defined by the trailing edge, the chines and/or the intersection of hull and calm water level (depending on wet or dry chines planing). The lift force is the vertical component of the normal force. Thus the lift is given by

$$L = N \cdot \cos \tau = \left( \frac{(U_0 \cdot \sin \tau)^2}{\tan \tau} \cdot m'_x + C_{fm} \cdot \frac{1}{2} \rho \cdot (U_0 \cdot \sin \tau)^2 \cdot S \right) \cdot \cos \tau \quad (8-3)$$



With a wetting factor, as defined in Chapter 6,  $WF = \pi/2$ , the chines are dry when the nominal length of a prismatic planing surface is less than  $\frac{b \cdot \tan \beta}{\pi \cdot \tan \tau}$ . The dry chines added mass is given by Equation (7-10) as

$$m' = C_m \cdot \frac{1}{2} \rho \pi \frac{z^2}{\tan^2 \beta}$$

and the normal depth  $z$  at the trailing edge is given by  $l \cdot \tan \tau$ . Note that “normal depth” denotes that the dimension is taken normal to the keel-line. Thus the trailing edge added mass for a dry chines prismatic planing surface is expressed as

$$m'_x = C_m \cdot \frac{1}{2} \rho \pi \cdot l^2 \frac{\tan^2 \tau}{\tan^2 \beta}, \quad l < \frac{b \cdot \tan \beta}{\pi \cdot \tan \tau} \quad (8-4)$$

The wet chines added mass is given by Equations (7-14) and (7-15) as

$$m'_w = C_m \cdot \frac{4}{\pi^2} \cdot \left( 1 + 0.57 \cdot \frac{\frac{z_c}{d}}{\frac{0.57}{\pi} + \frac{z_c}{d}} \right) \cdot \frac{1}{2} \rho \pi \left( \frac{b}{2} \right)^2.$$

The normal chines immersion  $z_c$  has previously been defined as the normal immersion depth  $z$  minus the depth at which the chines get wetted, i.e.

$z_c = z - \frac{2}{\pi} d$ , where  $d = \frac{b}{2} \tan \beta$  and  $z = x \cdot \tan \tau$ . This yields

$$\frac{z_c}{d} = \frac{2z}{b \cdot \tan \beta} - \frac{2}{\pi} = \frac{l}{b} \cdot \frac{2 \tan \tau}{\tan \beta} - \frac{2}{\pi} \quad (8-5)$$

Thus the trailing edge added mass for a wet chines prismatic planing surface is given by

$$m'_x = C_m \cdot \frac{4}{\pi^2} \cdot \left( 1 + 0.57 \cdot \frac{\frac{l}{b} \cdot \frac{2 \tan \tau}{\tan \beta} - \frac{2}{\pi}}{\frac{l}{b} \cdot \frac{2 \tan \tau}{\tan \beta} - \frac{1.43}{\pi}} \right) \cdot \frac{1}{2} \rho \pi \left( \frac{b}{2} \right)^2, \quad l > \frac{b \cdot \tan \beta}{\pi \cdot \tan \tau} \quad (8-6)$$

Substituting Equations (8-4) and (8-6) in Equation (8-3) gives the lift force for dry and wet chines prismatic planing surfaces respectively. It is common to non-dimensionalise the lift force on dry chines planing surfaces on the nominal length squared, giving

$$C_{L_l} = \frac{L}{\frac{1}{2} \rho U_0^2 \cdot l^2} = C_m \cdot \pi \cdot \frac{\sin^3 \tau}{\tan^2 \beta} + C_{fm} \cdot \frac{\sin^3 \tau}{\tan \beta}, \quad \frac{l}{b} < \frac{\tan \beta}{\pi \cdot \tan \tau} \quad (8-7)$$

The lift force on wet chines planing surfaces is commonly made non-dimensional on beam squared, giving

$$C_{L_b} = C_m \cdot \frac{\sin \tau \cdot \cos^2 \tau}{\pi} \cdot \left( 1 + 0.57 \cdot \frac{\frac{l}{b} \cdot \frac{2 \tan \tau}{\tan \beta} - \frac{2}{\pi}}{\frac{l}{b} \cdot \frac{2 \tan \tau}{\tan \beta} - \frac{1.43}{\pi}} \right) + C_{fm} \left( \frac{l}{b} \right)^2 \cdot \frac{\sin^3 \tau}{\tan \beta}$$

$$\frac{\tan \beta}{\pi \cdot \tan \tau} < \frac{l}{b} < \frac{\tan \beta}{2 \cdot \tan \tau} \quad (8-8)$$

and

$$C_{L_b} = C_m \cdot \frac{\sin \tau \cdot \cos^2 \tau}{\pi} \cdot \left( 1 + 0.57 \cdot \frac{\frac{l}{b} \cdot \frac{2 \tan \tau}{\tan \beta} - \frac{2}{\pi}}{\frac{l}{b} \cdot \frac{2 \tan \tau}{\tan \beta} - \frac{1.43}{\pi}} \right) + C_{fm} \cdot \sin^2 \tau \cdot \cos \tau \cdot \left( \frac{l}{b} - \frac{\tan \beta}{4 \tan \tau} \right)$$



$$\frac{l}{b} > \frac{\tan \beta}{2 \cdot \tan \tau} \quad (8-9)$$

The discontinuity in the lift coefficient expression for wet chines surfaces at  $\frac{l}{b} = \frac{\tan \beta}{2 \cdot \tan \tau}$  results from the flow momentum force in Equation (7-3) being defined as a function of the nominal width  $2y$ , and not the wetted width  $2y_w$ . The coefficients  $C_{fm}$  and  $C_m$  in the above expressions are given by Equations (7-4) and (7-13) respectively.

On flat planing plates the chines are always wet and  $l/b$  is always greater than  $\frac{\tan \beta}{2 \cdot \tan \tau}$  (because  $\tan \beta = 0$ ), and hence only Equation (8-9) is applicable. The function within the parentheses of the first term of Equation (8-9) always yields 1.57 for flat plates (also due to  $\tan \beta = 0$ ). Thus for flat plates, the dynamic lift component is given by:

$$C_{L_b} = C_m \cdot \frac{\sin \tau \cdot \cos^2 \tau}{\pi} \cdot 1.57 + C_{fm} \cdot \sin^2 \tau \cdot \cos \tau \cdot \frac{l}{b} \quad (8-10)$$

## 8.2. Hydrostatic Lift on Planing Surfaces

The lift forces measured during planing experiments necessarily include a hydrostatic contribution, the significance of which, relative to the dynamic lift, depends on the planing velocity. To allow comparison of the above planing equations with results from various published planing experiments, the hydrostatic lift terms derived below are added to the dynamic lift as given by Equations (8-7) to (8-10).

### 8.2.1. Flat Plates

For a rectangular flat plate the Archimedes' buoyancy force is expressed as

$$L_{AB} = \frac{1}{2} \rho g \cdot b \cdot l^2 \cdot \sin \tau \cdot \cos \tau \quad (8-11)$$

And in non-dimensional form (on beam squared)

$$C_{AB_b} = \frac{L_{AB}}{\frac{1}{2} \rho U_0^2 b^2} = \left( \frac{l}{b} \right)^2 \cdot \frac{\sin \tau \cdot \cos \tau}{C_v^2} \quad (8-12)$$

Archimedes' law only applies when the water surface is planar and undisturbed, i.e. static condition. The transom of a planing hull is dry when in its planing regime. Hence the pressure at the trailing edge of the planing surface is equal to the atmospheric pressure instead of  $\rho g l \cdot \sin \tau$  as the application of Archimedes' law implies. The hydrostatic lift force acting on a flat planing plate is therefore somewhere between zero and that given by Equation (8-12). The non-dimensional hydrostatic lift is therefore expressed as:

$$C_{HS_b} = \left( \frac{l}{b} \right)^2 \cdot \frac{\sin \tau \cdot \cos \tau}{C_v^2} \cdot \phi_0 \quad (8-13)$$

where  $\phi_0$  is the buoyancy ratio, a function varying from 0 to 1. Payne (1995) derived an expression for the buoyancy ratio, and this has been adopted in the present approach. Payne used low-speed planing data by Savitsky and Neidinger to prove a relation between buoyancy ratio and length to beam ratio, which is expressed by

$$\phi_0 = 1 - \frac{b}{l} \quad (8-14)$$

In deriving this relation, Payne (1995) used dynamic lift equations that Payne (1994) had shown to give excellent agreement with high-speed planing data by Shuford, in which buoyancy force is negligible relative to the dynamic lift. Thus credence can be given to Equation (8-14).



Substituting Equation (8-14) in Equation (8-13) yields the hydrostatic lift coefficient for a flat planing plate

$$C_{HS_b} = \frac{\sin \tau \cdot \cos \tau}{C_V^2} \cdot \left(\frac{l}{b}\right)^2 \cdot \left(1 - \frac{b}{l}\right) \quad (8-15)$$

### 8.2.2. Prismatic Surfaces

It can easily be shown with trigonometry that the Archimedes' buoyancy force on a prismatic hull shape is given by

$$L_{AB} = \rho g \cdot \left(\frac{bl^2 \tan \tau}{6}\right) \quad , \frac{l}{b} < \frac{\tan \beta}{2 \cdot \tan \tau} \quad (8-16)$$

and

$$L_{AB} = \rho g \cdot \left(\frac{b^3 \tan^2 \beta}{24 \tan \tau} + \frac{b^2 \tan \beta}{4} \cdot \left(l - \frac{b \tan \beta}{2 \tan \tau}\right) + \frac{b}{2} \cdot \left(l \tan \tau - \frac{b \tan \beta}{2}\right) \cdot \left(l - \frac{b \tan \beta}{2 \tan \tau}\right)\right)$$

$$, \frac{l}{b} > \frac{\tan \beta}{2 \cdot \tan \tau} \quad (8-17)$$

where the discontinuity is introduced by the chines submergence (calm water level).

Payne (1995) claims (without presenting evidence) that Equation (8-14) also provides a good representation of buoyancy ratios extracted using low-speed data from planing experiments with deadrise surfaces undertaken by Savitsky and Neidinger.

The corrected hydrostatic lift contribution, non-dimensionalised on beam squared, is given by

$$C_{HS_b} = \frac{L_{AB} \cdot \phi_0}{\frac{1}{2} \rho U_0^2 b^2} \quad (8-18)$$

It can easily be shown that substituting Equations (8-14) and (8-16) in Equation (8-18) yields

$$C_{HS_b} = \frac{1}{C_v^2} \cdot \left(\frac{l}{b}\right)^2 \cdot \frac{\tan \tau}{3} \cdot \left(1 - \frac{b}{l}\right) \quad , \quad \frac{l}{b} < \frac{\tan \beta}{2 \cdot \tan \tau} \quad (8-19)$$

And substituting Equations (8-14) and (8-17) in Equation (8-18) yields

$$C_{HS_b} = \frac{1}{C_v^2} \cdot \left( \left(\frac{l}{b}\right)^2 - \frac{l}{b} \cdot \frac{\tan \beta}{2 \tan \tau} + \frac{\tan^2 \beta}{12 \tan \tau} \right) \cdot \left(1 - \frac{b}{l}\right) \quad , \quad \frac{l}{b} > \frac{\tan \beta}{2 \cdot \tan \tau} \quad (8-20)$$

### 8.3. Comparison of Present Slender Body Theory with planing Data

The planing equations derived using the water entry approach are compared with lift data from various planing experiments. The hydrodynamic lift components have been extracted from the experimental data using Equations (8-15), (8-19) and (8-20). As expected, the theory fails to give good predictions at low length to beam ratio, where the slender body assumptions are no longer valid.

#### 8.3.1. Flat Plates

Sottorf's (1929) and Shuford's (1958) planing lift data are used for comparison with flat plate lift calculated using Equations (8-10) and (8-15). Sottorf's results include very high aspect ratio data that are presented together with carefully measured nominal and wetted lengths, while Shuford's data are from tests of large length to beam ratio planing plates. Thus the two experiments together provide lift data for both extremes of high aspect ratio and large length to beam ratio. However, Shuford did not measure the nominal length during his tests. For



application of Equations (8-10) and (8-15), the nominal length to beam ratio is required.

Savitsky (1964) presented a relationship between the wetted and nominal length to beam ratios based on various flat plate experimental data (sources not specified). For nominal length to beam ratios above 1.0 the relationship between wetted and nominal length was given by

$$\frac{l_w}{b} = \frac{l}{b} + 0.3 \quad , \frac{l}{b} > 1.0 \quad (8-21)$$

The above equation allowed the nominal length to beam ratios in Shuford's data to be estimated from the wetted length to beam ratios given.

The ratio of predicted lift using the present theory to measured lift  $\Phi$  is plotted in Figure 8-2. Sottorf employed a test protocol that was highly unusual. The lift coefficient on beam was held constant, at one of four values, while load and speed varied to obtain these values. The numbers in the data legend, next to the shortened names of Shuford and Sottorf, denote trim angle in degrees and speed coefficient  $C_V$  respectively.

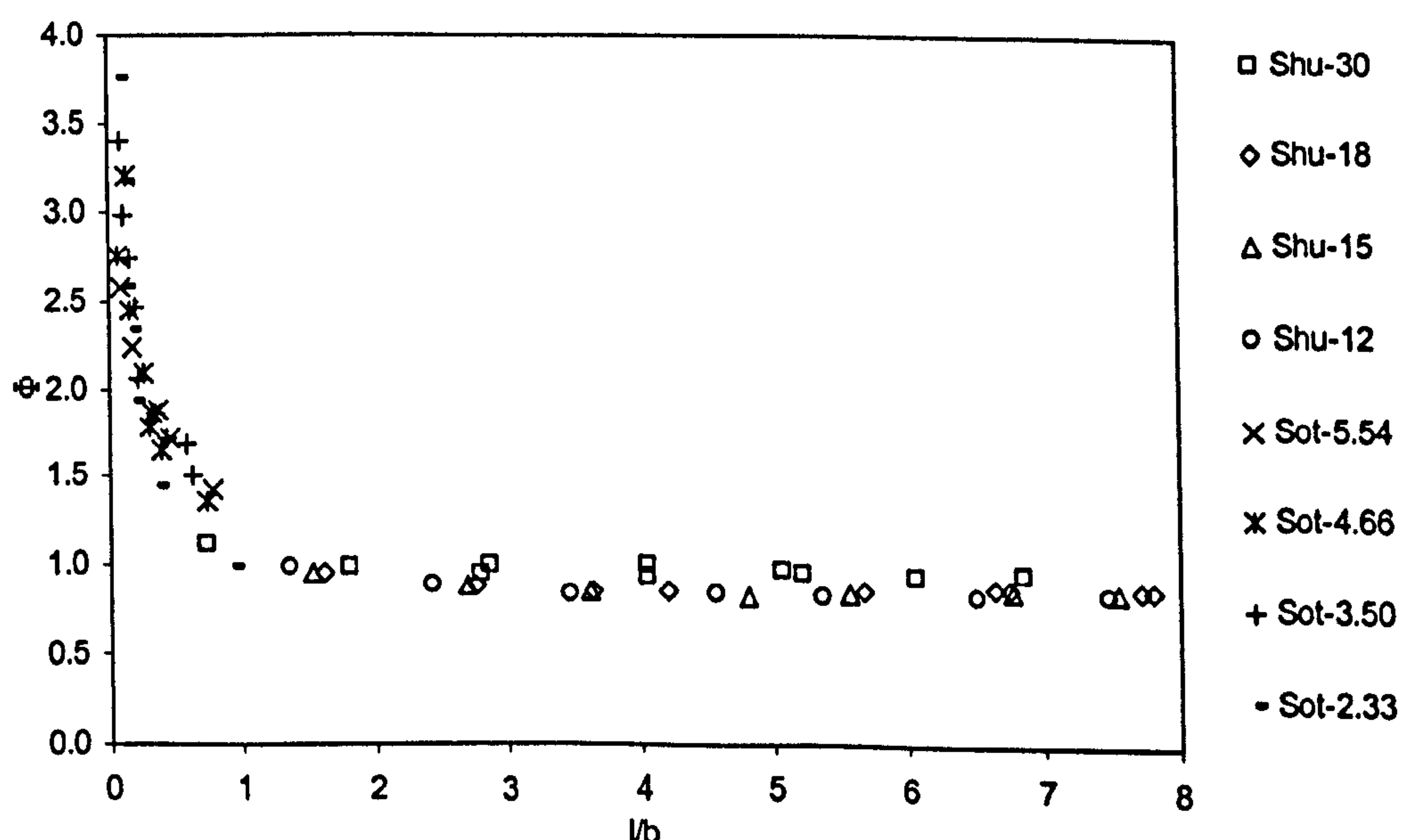


Figure 8-2. Predicted lift divided by measured lift for flat plates.

It is seen that there is agreement between prediction and measurement for length to beam ratios greater than about 2. At ratios less than this value, the present slender body planing theory predicts lift forces greater than measured experimentally, especially at the lowest length to beam ratios, i.e. highest aspect ratios.

8.3.2. Wet Chines Prismatic Surfaces

The slender body wet chines prismatic surface lift force calculated using Equations (8-8), (8-9), (8-19) and (8-20) is compared with experimental data given by Shoemaker (1934), Chambliss and Boyd (1953) and Shuford (1958). The ratio of predicted lift to measured lift  $\Phi$  is plotted in Figures 8-3 to 8-6. The numbers next to the shortened experimenter's name in the data legend denote trim angle in degrees.

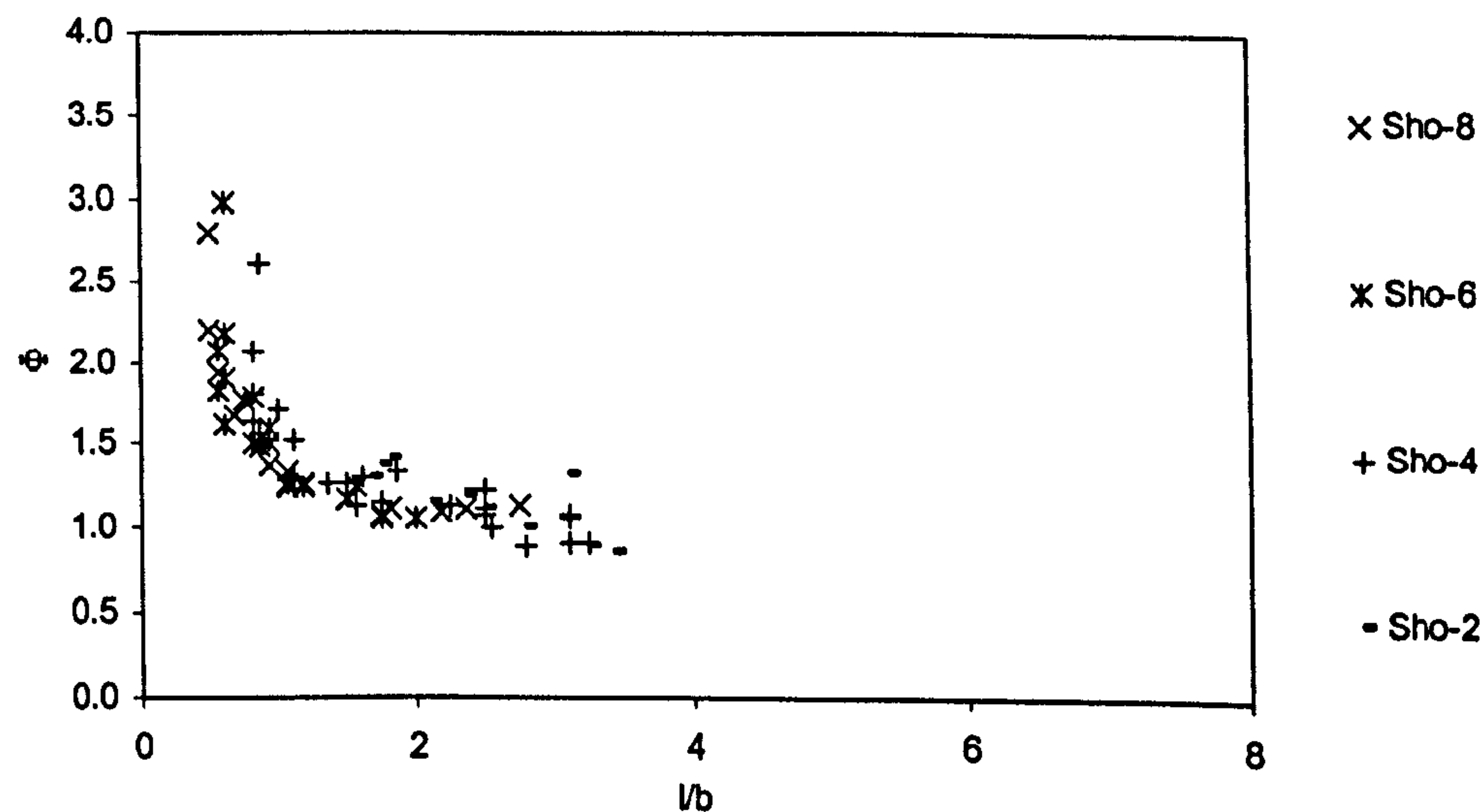


Figure 8-3. Predicted lift divided by measured lift for 10 degrees deadrise, wet chines.



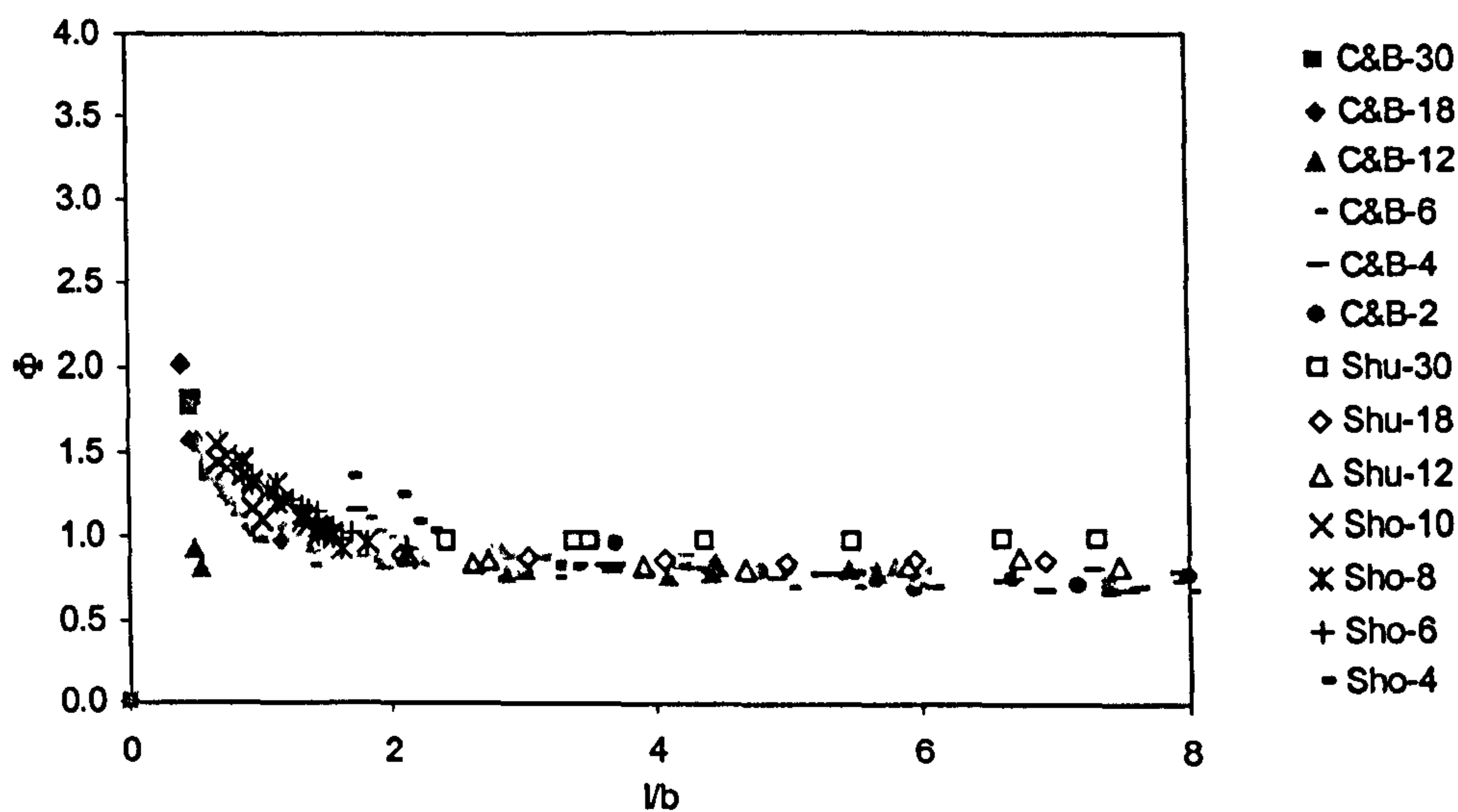


Figure 8-4. Predicted lift divided by measured lift for 20 degrees deadrise, wet chines.

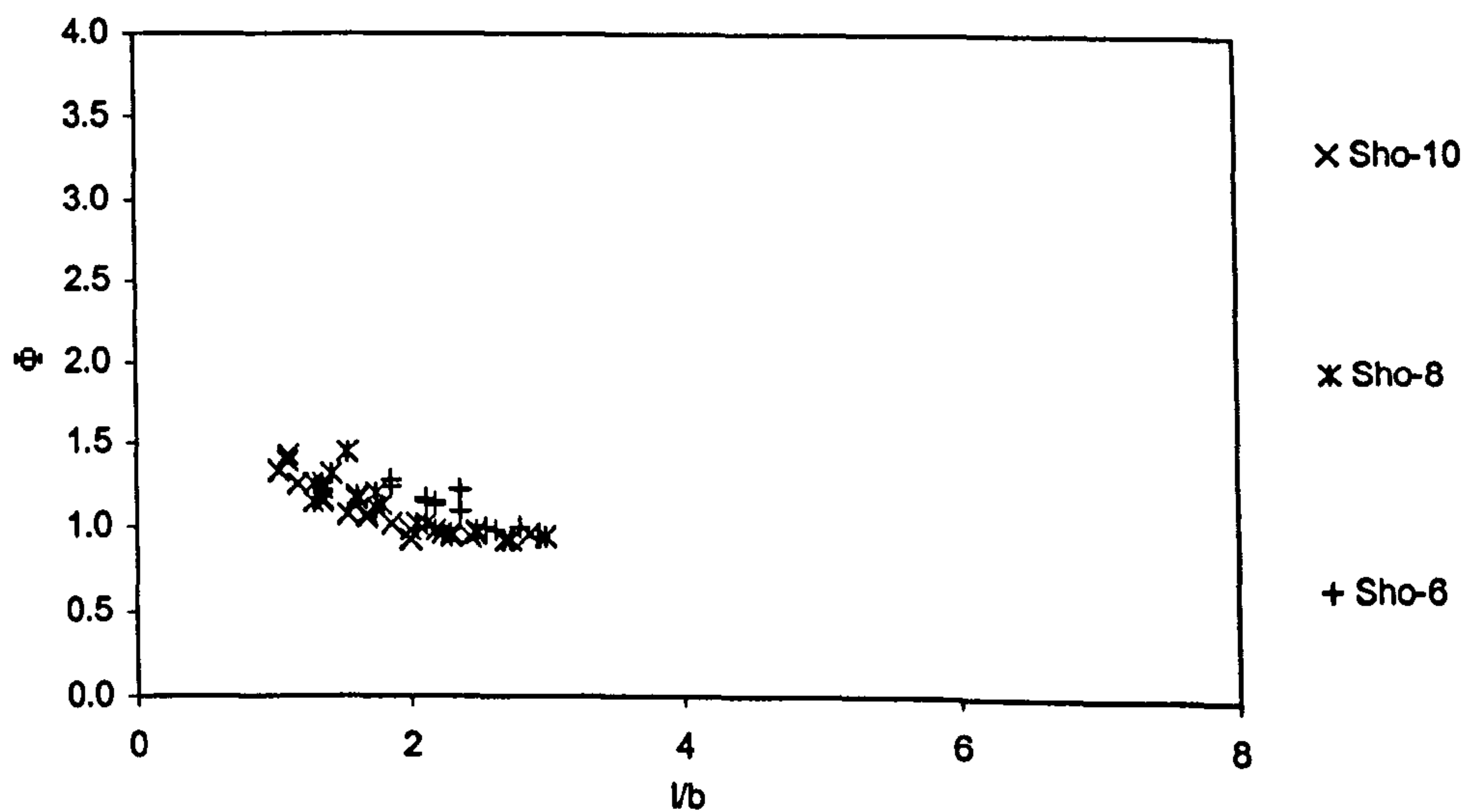


Figure 8-5. Predicted lift divided by measured lift for 30 degrees deadrise, wet chines.

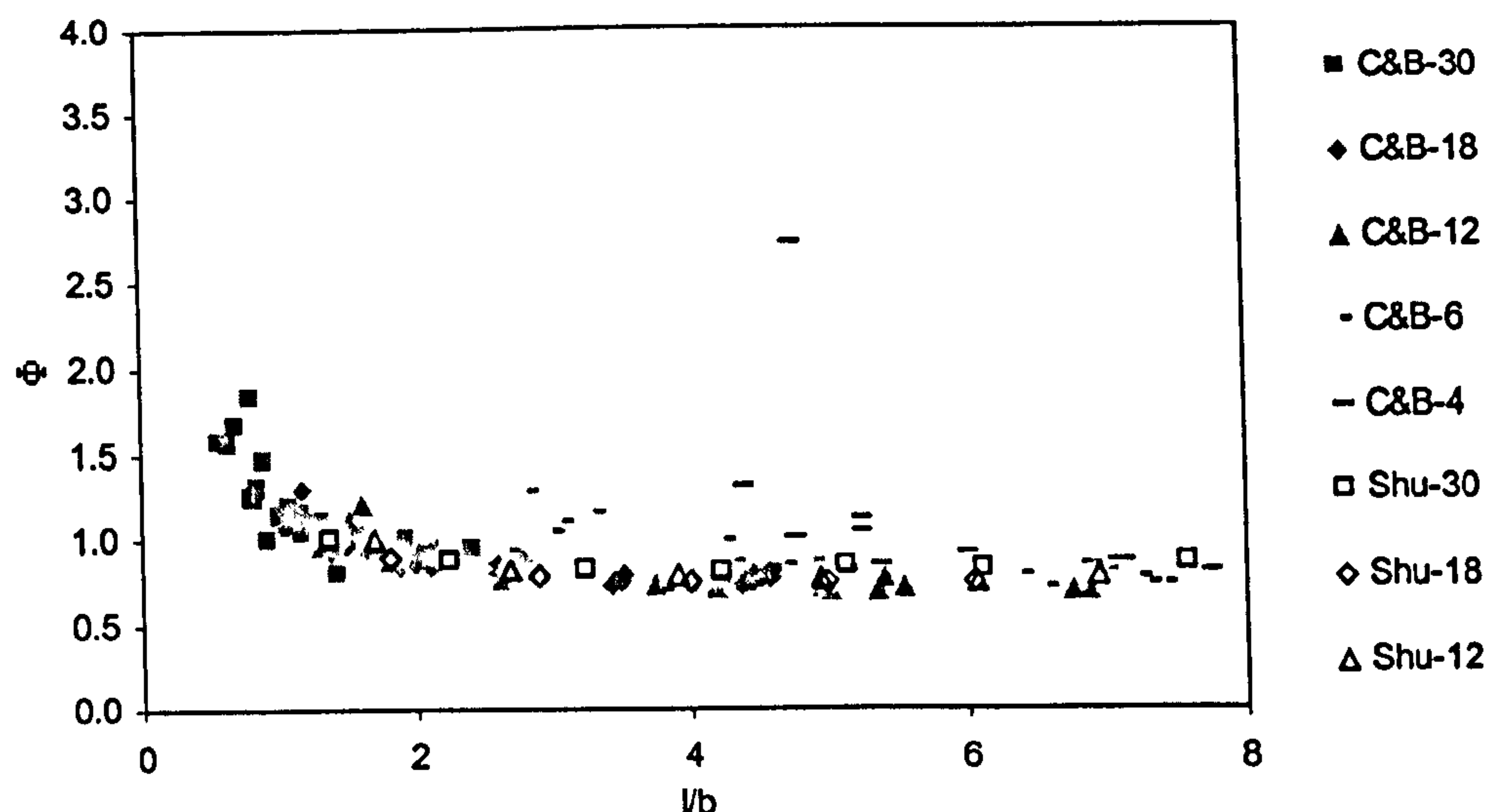


Figure 8-6. Predicted lift divided by measured lift for 40 degrees deadrise, wet chines.

The data for hulls with deadrise are more scattered than the flat plate data. There is generally a satisfactory agreement between prediction and measurement for length to beam ratios greater than 2, while overpredictions are made at the lower length to beam ratios. However, the predicted lift force is on average about 15 percent lower than the measured force for the 20 and 40 degree cases for length to beam ratios greater than about 2.

### 8.3.3. Dry Chines Prismatic Surfaces

Predictions using Equation (8-7) and (8-19) are compared with experimental lift data published by Shoemaker (1934), Chambliss and Boyd (1953), Pierson (1954) and Springston and Sayre (1955). The ratio of predicted lift to measured lift  $\Phi$  is plotted against length to beam ratio in Figure 8-7, while in Figure 8-8 the same data is plotted against trim angle. The number in the data legend in these figures denotes deadrise angle in degrees.



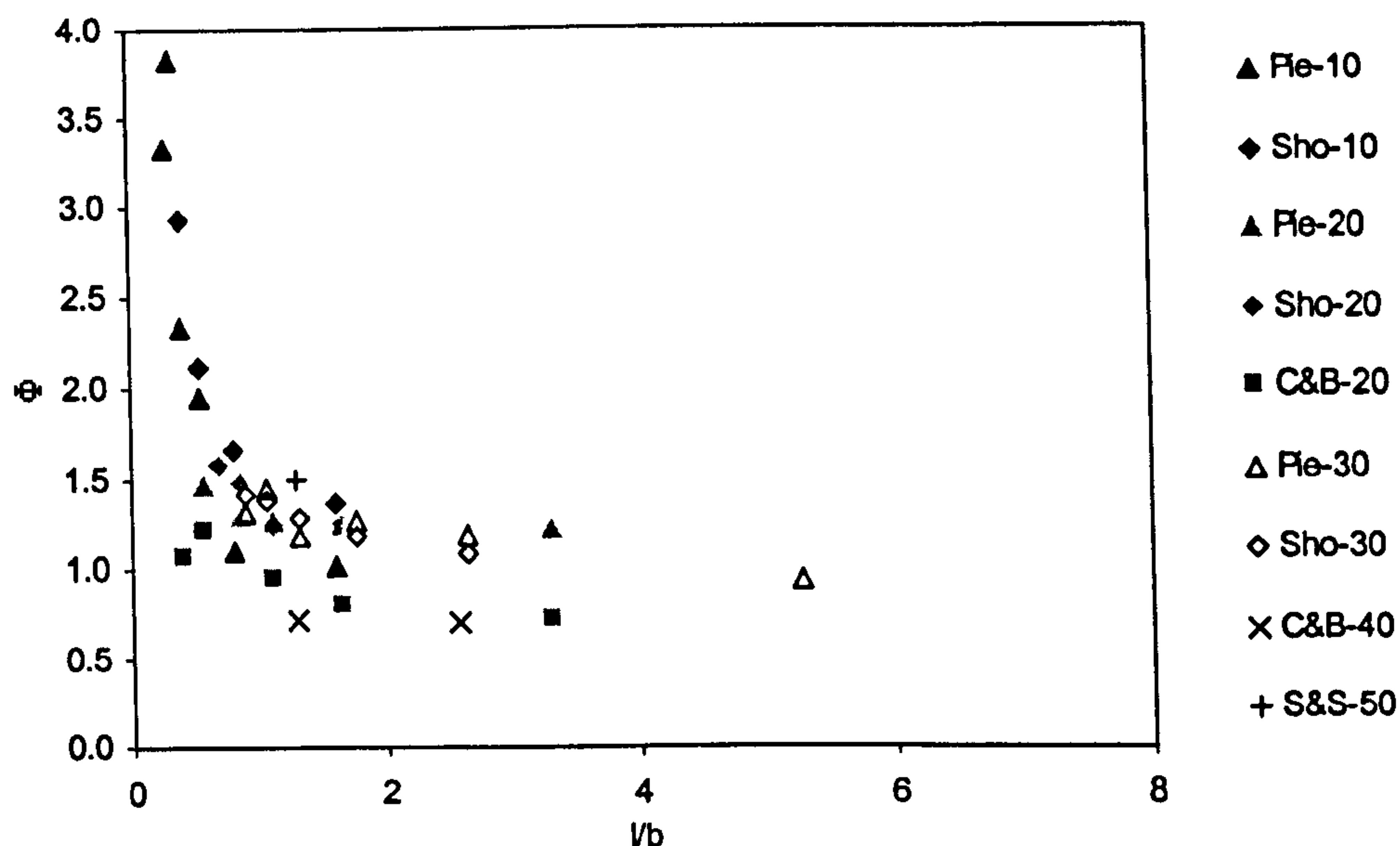


Figure 8-7. Predicted lift divided by measured lift for dry chines planing.

The dry chines data are even more scattered than the wet chines data plotted in the preceding figures. However, like the comparison with the flat plate and wet chines prismatic data, Figure 8-7 also shows significant disagreement between theory and measurement at low length to beam ratios. At high length to beam ratios the predicted and measured values agree reasonably well within the scatter of the experimental data. Note that the measurements given by Chambliss and Boyd (1953) appear to be considerably lower than the others' data.

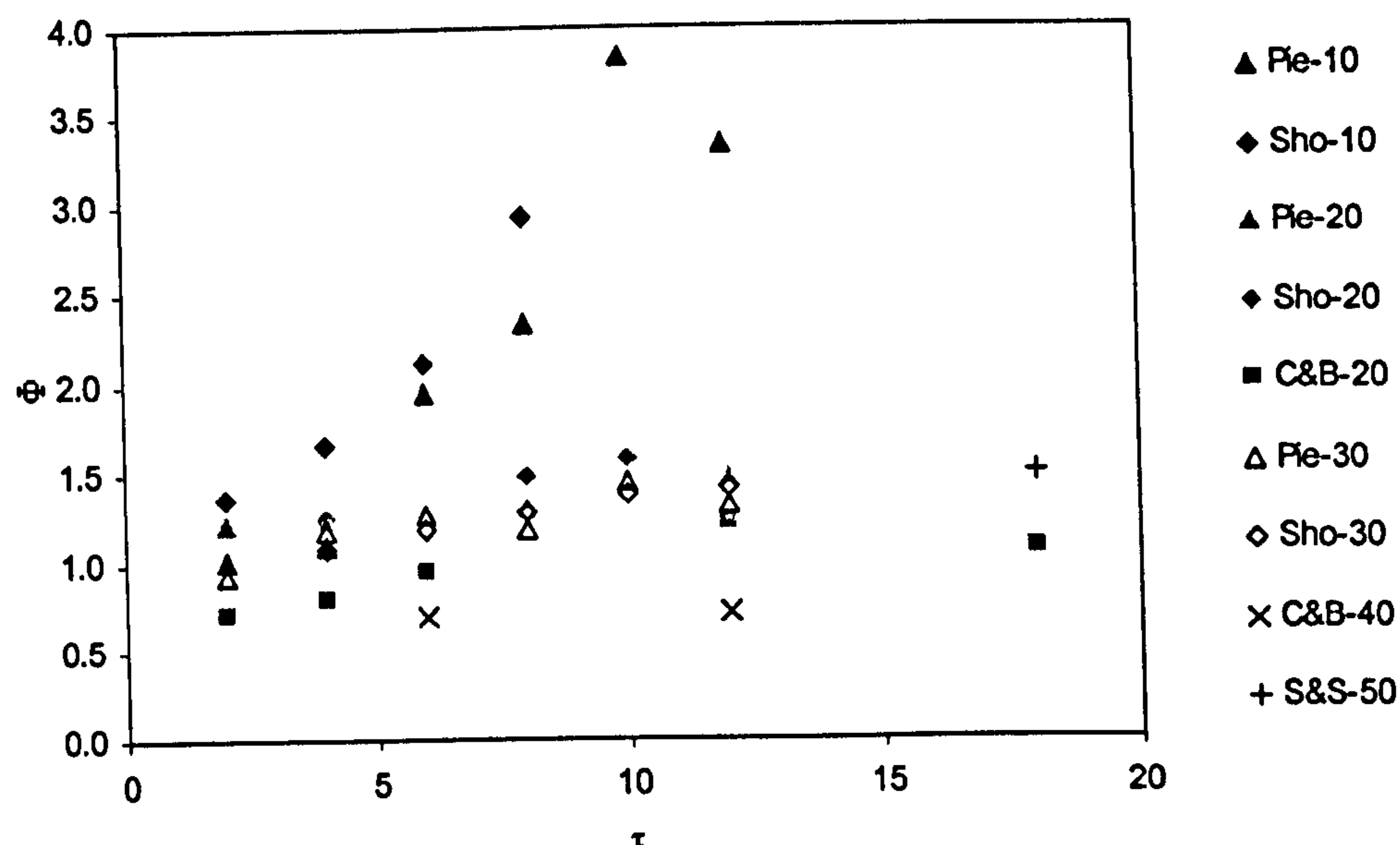


Figure 8-8. Predicted lift divided by measured lift for dry chines planing, plotted against trim angle.

In Figure 8-8 it is seen that in general, if neglecting the 20 degree results by Chambliss and Boyd, for a given trim angle, the predicted to measured lift ratio is higher for low angles of deadrise than for high angles of deadrise. The sweep back angle of the spray line is greater for a hull of high deadrise angle than for a low deadrise angle hull, and hence has a higher length to beam ratio. Thus the high deadrise angle hull is in effect more slender and the predicted to measured lift ratio is closer to unity than for low deadrise angle.

#### 8.4. Hydrodynamic Lift on Non-Slender Planing Surfaces

Slender body theory presupposes that there is flow only in planes that are normal to the body axis (which, in planing theory, is taken as the keel), i.e. no longitudinal flow occurs. This is known to be a reasonable assumption only at higher length to beam ratios and at moderate trim angles. The present slender body planing theory expressed in Equations (8-7) to (8-10) has, in the above section, been shown to compare well with experimental data at length to beam ratios greater than about 2 for flat plate and wet chines prismatic planing.



Although this is not concluded as firmly for dry chines planing, the scattered data in Figure 8-7 suggests a similar relation for dry chines cases. Thus planing surfaces are herein considered slender when  $l/b > 2$  for the range of trim covered by the data, i.e.  $\tau < 30$  degrees. Planing surfaces of length to beam ratio less than 2 are herein referred to as non-slender planing surfaces.

The slender body approach implies that there is a sectional lift force acting on the transom section of a planing hull. For a planing hull at high velocity the flow separates at the trailing edge and the transom is dry. It follows from the dynamic free surface boundary condition that the pressure at the trailing edge is zero, i.e. the sectional lift force on the transom section is zero. To comply with this condition there must be a longitudinal flow (relative to the undisturbed water) in the aft region that causes the pressure drop to zero (Bernoulli effect). Thus, there is a lift reduction from the lift calculated using the slender body approach. Part of the lift reduction due to longitudinal flow effect is proportional to the Archimedes buoyancy force and has been accounted for by the buoyancy ratio function in the hydrostatic force term. However, the remaining lift reduction due to longitudinal flow effect is proportional to the forward velocity squared and needs to be accounted for. In slender planing, the latter is insignificant compared to the total dynamic lift component. In non-slender planing, the loss of lift due to longitudinal flow effect has a significant bearing on the total hydrodynamic lift force, and this causes the discrepancy between predicted and measured lift for low length to beam ratios, as seen in Figures 8-2 to 8-7.

Payne's planing theory is also based on the slender body concept. Payne (1981a and subsequent work) modifies the slender body theory to fit high aspect ratio experimental data by assuming that the added mass stream tube is not deflected by the full trim angle  $\tau$ . Thus, there is less vertical momentum imparted to the downwash and hence a reduction in the added mass momentum of the hull. Payne (1995) presents an aspect ratio correction of the added mass that was derived from an empirical fit to the various planing data available in the literature, and thus makes the theory applicable for high aspect ratios.

The present theory also uses an aspect ratio correction to account for the effect of longitudinal flow and thus achieve correlation with experimental planing data at high aspect ratios. While the dynamic lift force on slender surfaces, according to Payne (1995), is entirely added mass associated, the present theory involves an additional lift component not associated with added mass, i.e. the flow momentum term. The flow momentum lift component is small relative to the added mass component at low length to beam ratios, which is when an aspect ratio correction is required for correlation with experimental lift measurements. Thus, only the added mass component need to be corrected for aspect ratio, yielding

$$C_{L_b} = C_{L,m'_b} \cdot f(A) + C_{L,fm_b} + C_{HS_b} \quad (8-22)$$

for flat plates and wet chines prismatic planing surfaces, which are made non-dimensional on the beam squared), and

$$C_{L_l} = C_{L,m'_l} \cdot f(A) + C_{L,fm_l} + C_{HS_l} \quad (8-23)$$

for dry chines prismatic planing surface, (which are made non-dimensional on length squared).

#### 8.4.1. Flat Plate Theory

Values of the aspect ratio correction factor  $f(A)$  have been calculated for a range of length to beam ratios from the flat plate data given by Shoemaker (1934) and Shuford (1954), using Equation (8-22) with the appropriate flat plate expressions. For flat plates,  $C_{L,m'_b}$  is given by the first term of Equation (8-10),  $C_{L,fm_b}$  is given by the second term of the same equation and  $C_{HS_b}$  is given by Equation (8-15). Thus the total lift coefficient is given by

$$C_{L_b} = C_m \cdot \frac{\sin \tau \cdot \cos^2 \tau}{\pi} \cdot 1.57 f(A) + C_{fm} \sin^2 \tau \cdot \cos \tau \cdot \frac{l}{b} + \frac{\sin \tau \cdot \cos \tau}{C_v^2} \cdot \left(\frac{l}{b}\right)^2 \cdot \left(1 - \frac{b}{l}\right) \quad (8-24)$$



and values of  $f(A)$  can be calculated by inserting experimental values of  $C_{L_b}$  into this equation. The resulting  $f(A)$  values are plotted in Figure 8-9 below. On low length to beam ratio planing plates the wetted length is significantly higher than the nominal. This reduces the aspect ratio of the planing surface. The  $f(A)$  values are therefore plotted against wetted length to beam ratio. The curve denoted 'Present theory' in Figure 8-9 represents the function

$$f(A) = \frac{1}{\sqrt{1 + \left(\frac{2}{3}A\right)^2}} \quad (8-25)$$

where the aspect ratio for the flat plate is defined by the wetted length as  $A = b/l_w$ . This function provides a good fit to the  $f(A)$  data.

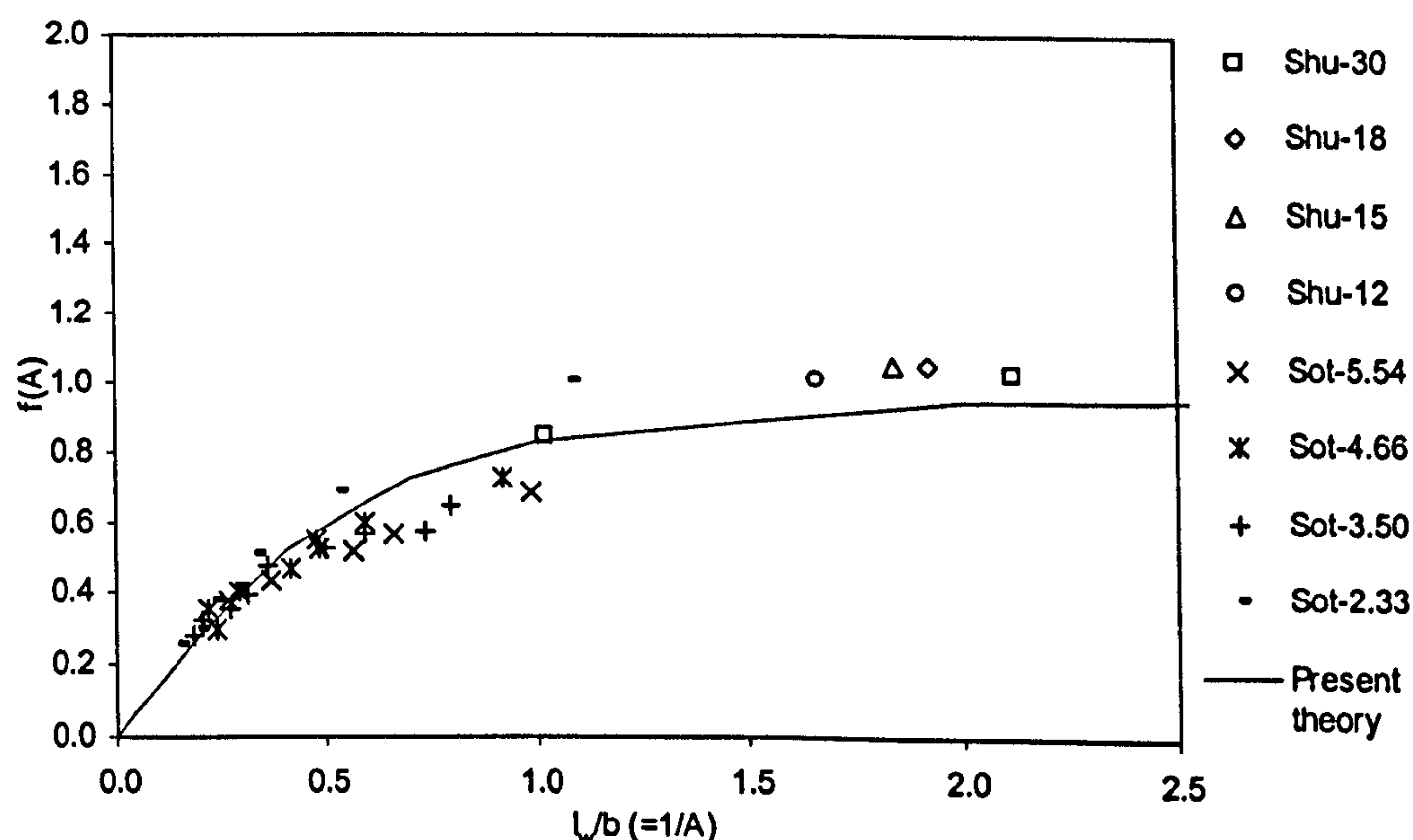


Figure 8-9.  $f(A)$  from (8-24) by use of Sottorf's and Shuford's flat plate data.

#### 8.4.2. Two-Dimensional Planing Plate

For plates with large aspect ratios, Equation (8-24), with substitution of Equation (8-25), can be reduced to

$$C_{L_b} = C_{m'} \cdot \frac{\sin \tau \cdot \cos^2 \tau}{\pi} \cdot 1.57 \cdot \frac{1}{\sqrt{1 + \left(\frac{2}{3}A\right)^2}} \approx C_{m'} \cdot \frac{\sin \tau \cdot \cos^2 \tau}{\pi} \cdot 1.57 \cdot \frac{3}{2A} \quad (8-26)$$

and when non-dimensionalising on wetted surface area,  $S_w = l_w \cdot b$ , rather than beam squared

$$C_{L_{sw}} = C_{L_b} \cdot \frac{b}{l_w} = C_{m'} \cdot \frac{\sin \tau \cdot \cos^2 \tau}{\pi} \cdot 1.57 \cdot \frac{3}{2} \quad (8-27)$$

Equations (7-13) and (7-23) give  $C_{m'}$  for a flat plate as  $0.89 \cdot \frac{\pi^2}{4}$ , and substituting in Equation (8-27) gives

$$C_{L_{sw}} = 0.524 \cdot \pi \cdot \sin \tau \cdot \cos^2 \tau \quad (8-28)$$

which for small angles of trim can be expressed as

$$C_{L_{sw}} = 0.524 \cdot \pi \cdot \tau \quad (8-29)$$

Thus giving the two-dimensional lift curve slope as

$$\frac{\partial C_{L_{sw}}}{\partial \tau} = 0.524\pi \approx 1.65 \quad (8-30)$$

In Figure 8-10 data given by Sottorf are presented in terms of a lift-curve slope of

$$\text{the form } \frac{C_{L_{sw}}}{\tau} = \frac{C_{L_b} \cdot \frac{b}{l_w}}{\tau}.$$



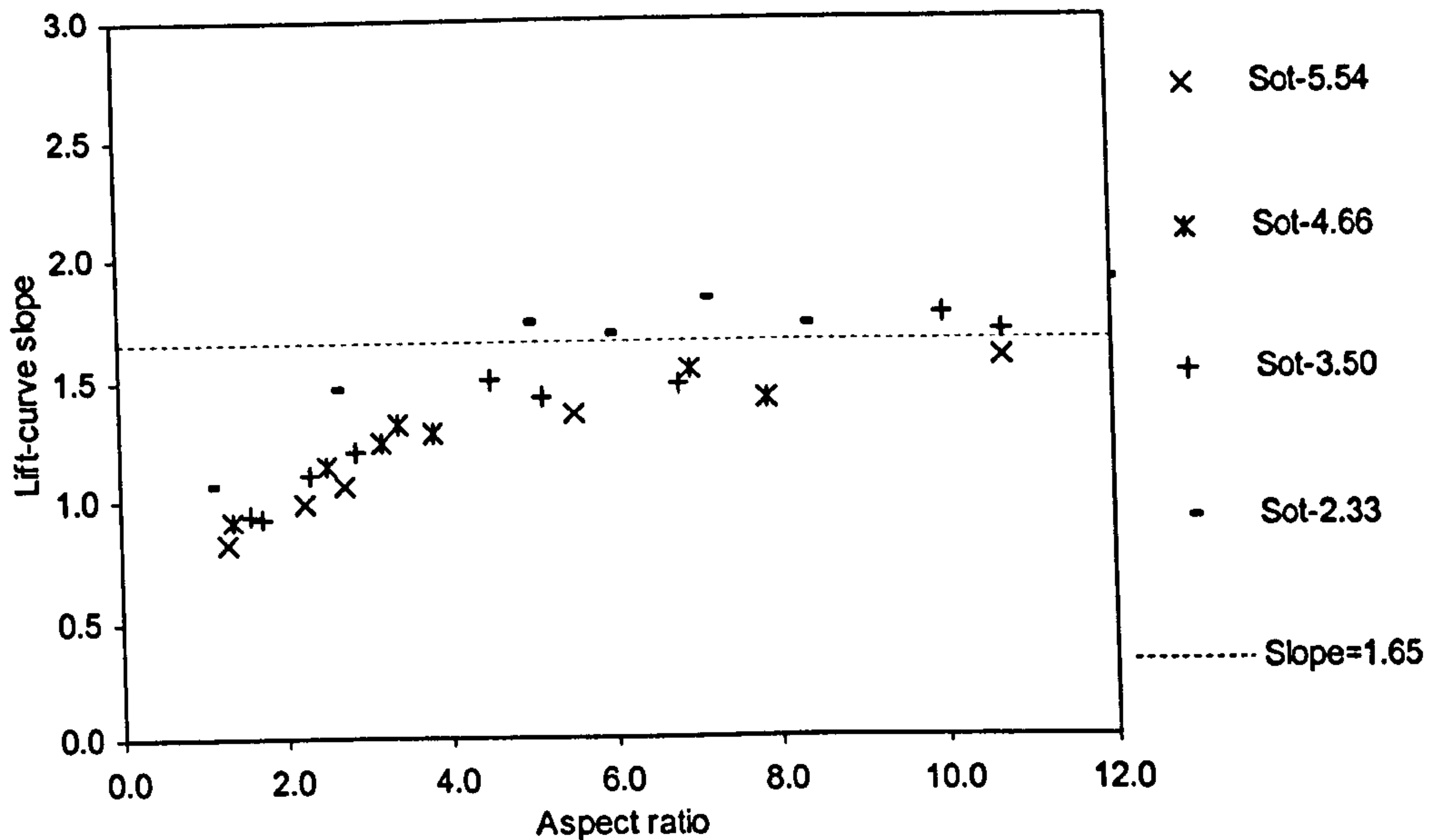


Figure 8-10. Lift-curve slope derived from the flat plate data by Sottorf.

It is seen that the present theory value of 1.65 for the two-dimensional plate correlates well to an average of the scattered high aspect ratio lift-curve slopes derived from Sottorf's data.

In Payne (1994) the two-dimensional plate lift-curve slope is given by

$$\frac{dC_{L_s}}{d\tau} = \left( \frac{C_P}{C_{P_0}} \right) \cdot \pi \quad , \text{ where } \quad \left( \frac{C_P}{C_{P_0}} \right) = -\frac{1}{2}\pi\tau + \sqrt{1 + \frac{1}{4}\pi^2\tau^2}$$

Thus Payne's lift curve slope varies from  $0.94\pi$  at 2 degrees trim to  $0.8\pi$  at 8 degrees trim. Payne derived the aspect ratio correction so that it would correlate to the two-dimensional theoretical result from Pierson and Leshnover's (1948) analytical solution to the potential flow about a planing surface (based on the

theory of Wagner (1932)), i.e.  $\frac{dC_{L_s}}{d\tau} = \pi$  (for small  $\tau$ ). However, the value of 1.65

is approximately half of the result obtained by Pierson and Leshnover. Hence, Payne adopted a two-dimensional lift-curve slope that is about twice of that indicated by the data of Sottorf in Figure 8-10. Figure 8-11 shows a graph taken from Payne (1995) where his own theory is compared with data given by

Weinstein and Kapryan (1953) that includes high aspect ratio measurements. Note that only the solid symbols represent values obtained using Payne's equation.

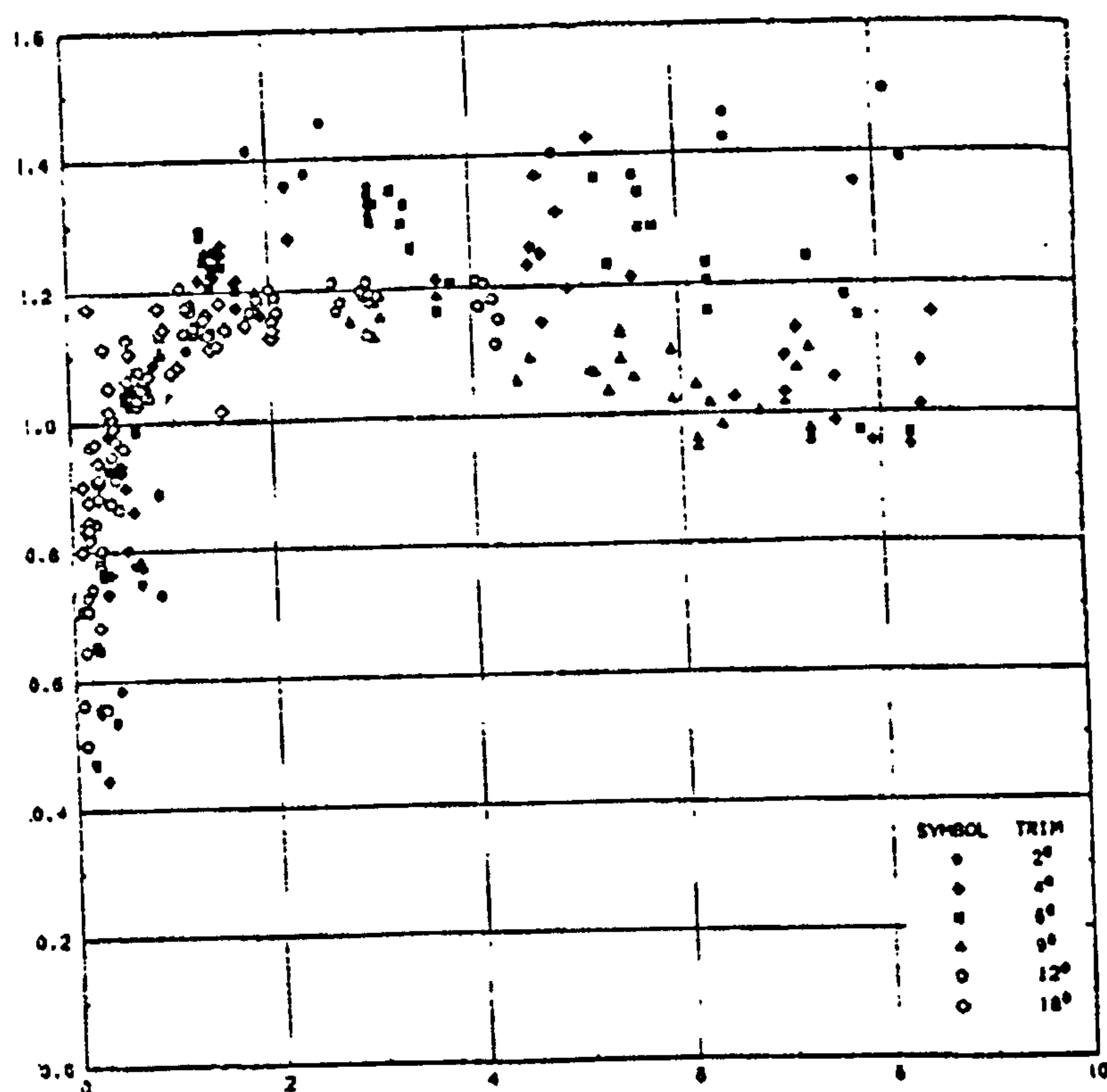


Figure 8-11. Figure taken from Payne (1995) showing lift measurements by Weinstein and Kapryan (1953) divided by lift predicted by Payne plotted against length to beam ratios.

It is seen from Figure 8-11 that at very high aspect ratios (low length to beam ratios, i.e. at l.h.s. of the chart), Payne's theory gives the lift as about twice the measured values. Payne claims that the small scale of the models used by Weinstein and Kapryan caused difficulties in measuring the wetted lengths, and excludes all data for  $l/b < 1$  in the validation of his theory.

Figure 8-12 shows another graph taken from Payne (1995), where his theory is compared with the data given by Sottorf (1929).



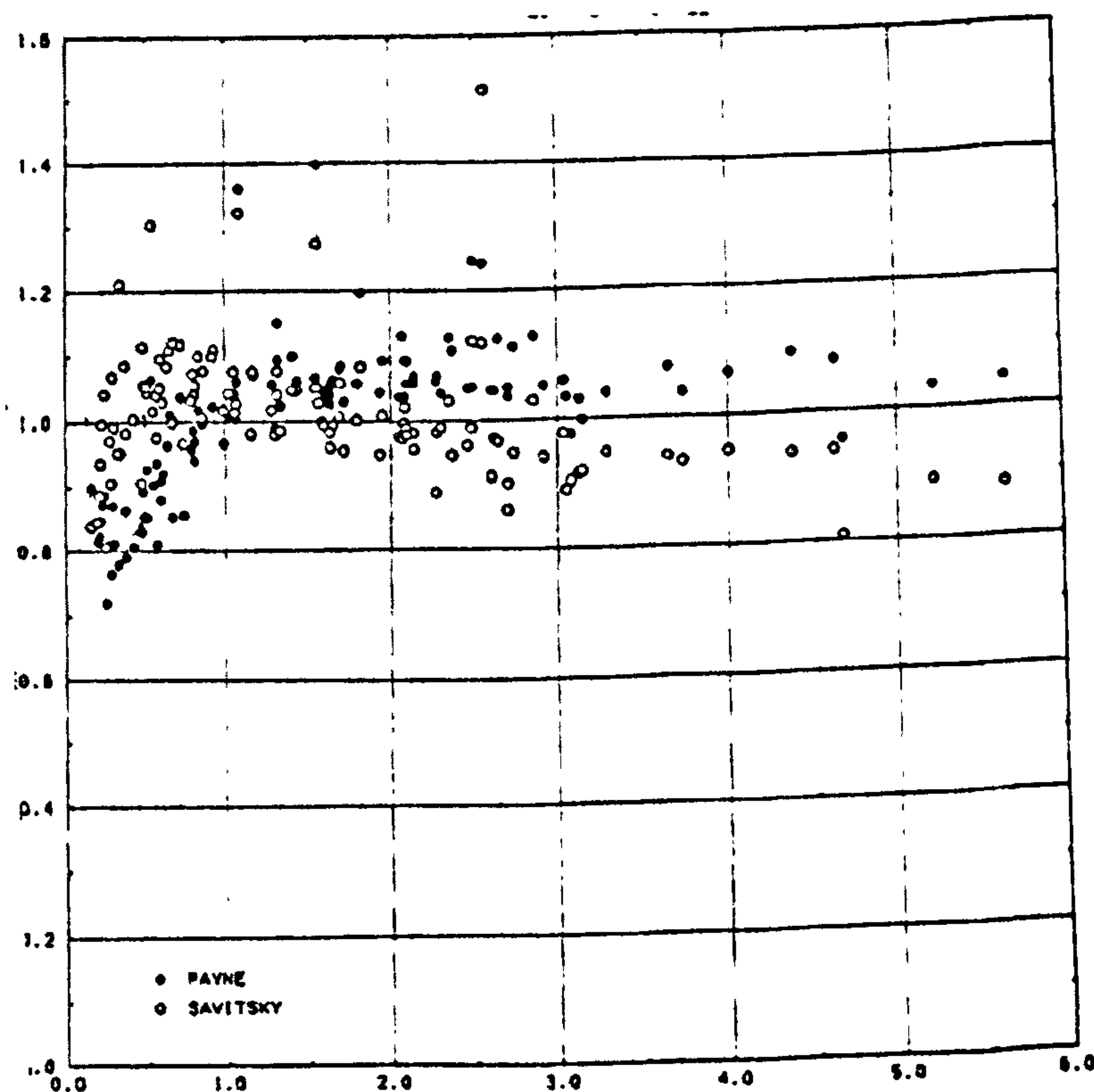


Figure 8-12. Figure taken from Payne (1995) showing lift measurements by Sottorf (1929) divided by lift predicted by Payne plotted against length to beam ratios.

The data plotted in Figure 8-12 do not include aspect ratios as high as in Figure 8-11, but it can again be seen that Payne's theory breaks down for high aspect ratios.

#### 8.4.3. Prismatic Theory, Wet Chines

Lift data from experiments with wet chines deadrise planing surfaces by Shoemaker (1934), Chambliss & Boyd (1953) and Shuford (1958) have been used in Equation (8-22) (with the appropriate wet chines expressions for  $C_{L,m'}$ ,  $C_{L,fb}$  and  $C_{HS_b}$ ) to calculate  $f(A)$  values for low length to beam ratio prismatic planing surfaces in the same manner as for flat plates. For wet chines,  $C_{L,m'}$  is given by the first term of Equation (8-8) and (8-9),  $C_{L,fb}$  is given by the second term of

the same equations and  $C_{HS_b}$  is given by Equation (8-19) and (8-20). These equations give

$$C_{L_b} = C_m \cdot \frac{\sin \tau \cdot \cos^2 \tau}{\pi} \cdot \left( 1 + 0.57 \cdot \frac{\frac{l}{b} \cdot \frac{2 \tan \tau}{\tan \beta} - \frac{2}{\pi}}{\frac{l}{b} \cdot \frac{2 \tan \tau}{\tan \beta} - \frac{1.43}{\pi}} \right) \cdot f(A) \quad (8-31)$$

$$+ C_{fm} \left( \frac{l}{b} \right)^2 \cdot \frac{\sin^3 \tau}{\tan \beta} + \left( 1 - \frac{b}{l} \right) \cdot \frac{1}{C_v^2} \cdot \left( \frac{l}{b} \right)^2 \cdot \frac{\tan \tau}{3}$$

$$, \frac{\tan \beta}{\pi \cdot \tan \tau} < \frac{l}{b} < \frac{\tan \beta}{2 \cdot \tan \tau}$$

and

$$C_{L_b} = C_m \cdot \frac{\sin \tau \cdot \cos^2 \tau}{\pi} \cdot \left( 1 + 0.57 \cdot \frac{\frac{l}{b} \cdot \frac{2 \tan \tau}{\tan \beta} - \frac{2}{\pi}}{\frac{l}{b} \cdot \frac{2 \tan \tau}{\tan \beta} - \frac{1.43}{\pi}} \right) \cdot f(A)$$

$$+ C_{fm} \cdot \sin^2 \tau \cdot \cos \tau \cdot \left( \frac{l}{b} - \frac{\tan \beta}{4 \tan \tau} \right) + \left( 1 - \frac{b}{l} \right) \cdot \frac{1}{C_v^2} \cdot \left( \left( \frac{l}{b} \right)^2 - \frac{l}{b} \cdot \frac{\tan \beta}{2 \tan \tau} + \frac{\tan^2 \beta}{12 \tan \tau} \right)$$

$$, \frac{l}{b} > \frac{\tan \beta}{2 \cdot \tan \tau} \quad (8-32)$$

The resulting values are plotted in Figure 8-12 to 8-15 below, where the curve denoted 'Present theory' represents the function

$$f(A) = \frac{1}{\sqrt{1 + A^2}} \quad (8-33)$$

where the aspect ratio is defined by the nominal length as  $A=b/l$ . Note that  $l$  is given by the distance from the intersection of the calm water line and the keel-line to the trailing edge.



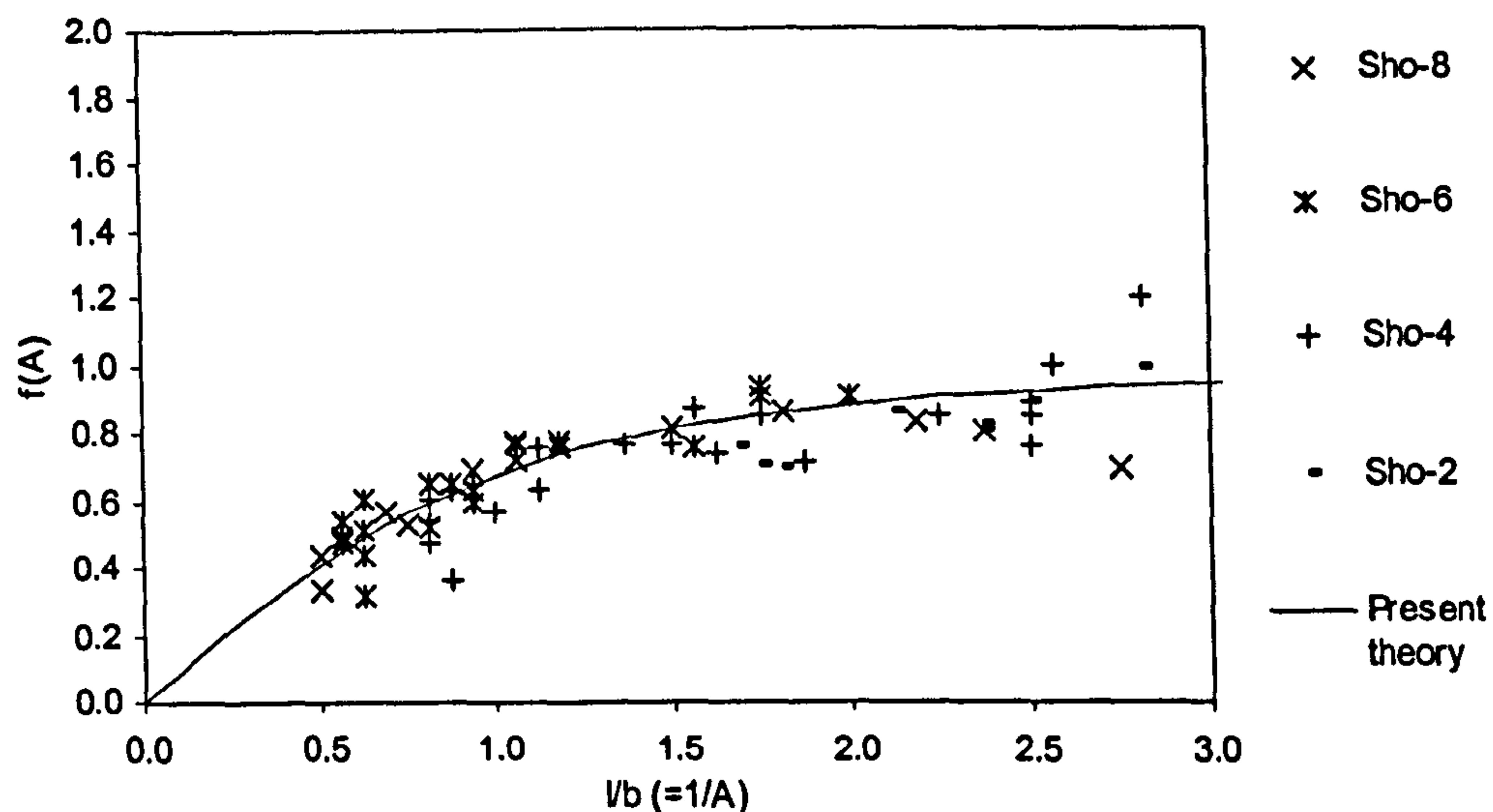


Figure 8-13.  $f(A)$  from Equations (8-31) and (8-32) by use of Shoemaker's 10 degree data.

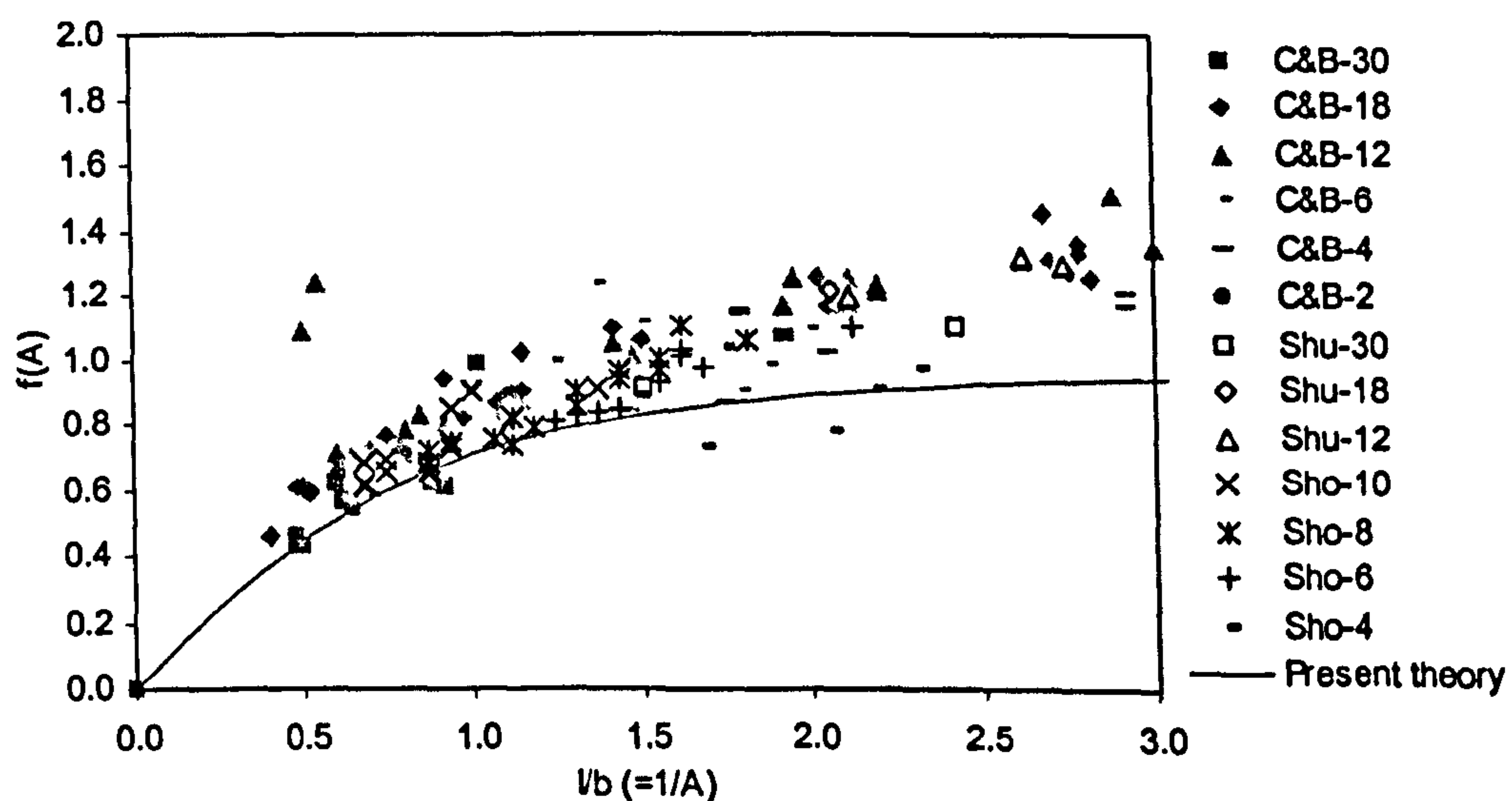


Figure 8-14.  $f(A)$  from Equations (8-31) and (8-32) by use of Shoemaker's, Shuford's and Chambliss and Boyd's 20 degrees data.

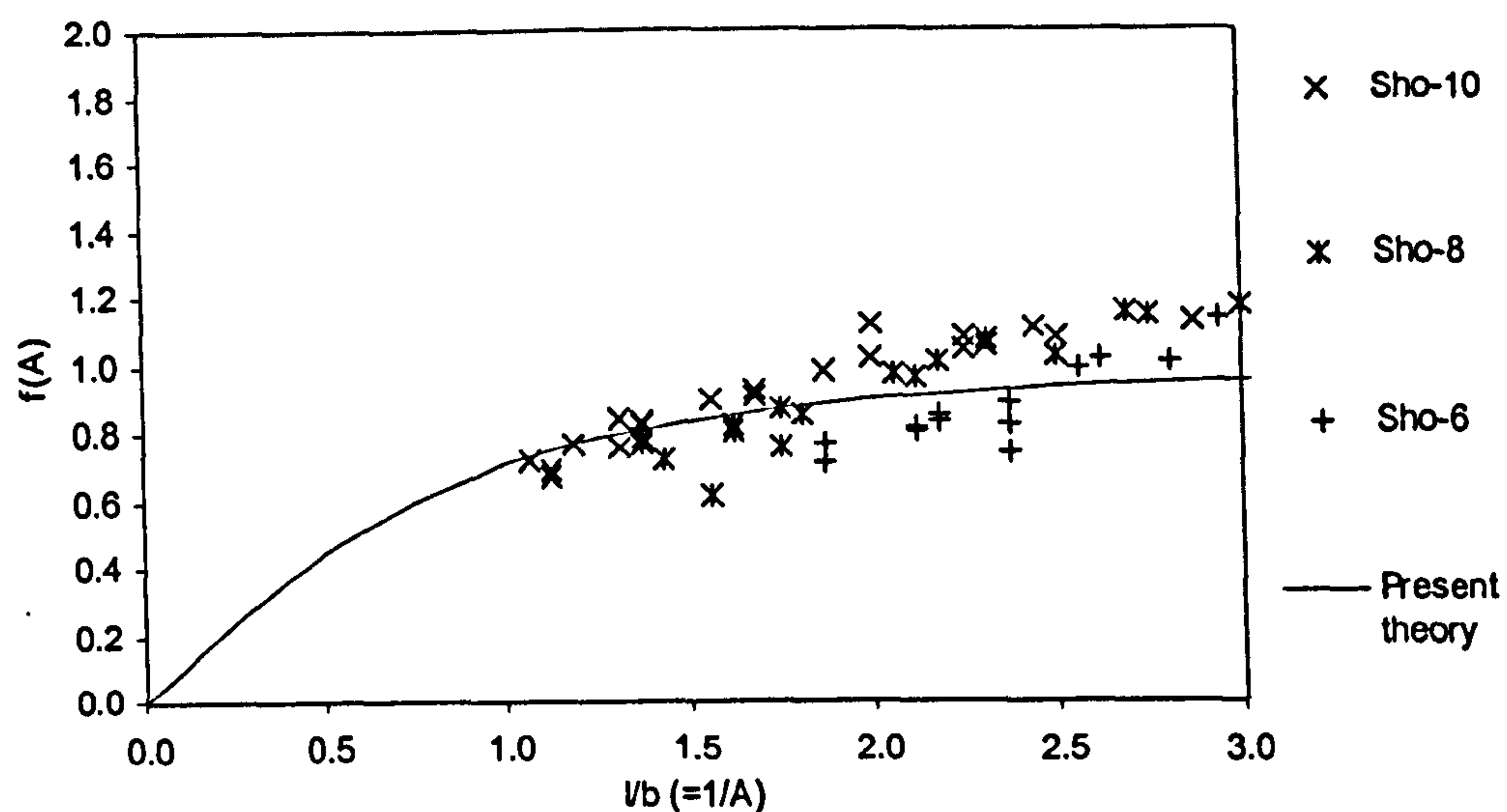


Figure 8-15.  $f(A)$  from Equations (8-31) and (8-32) by use of Shoemaker's 30 degrees data.

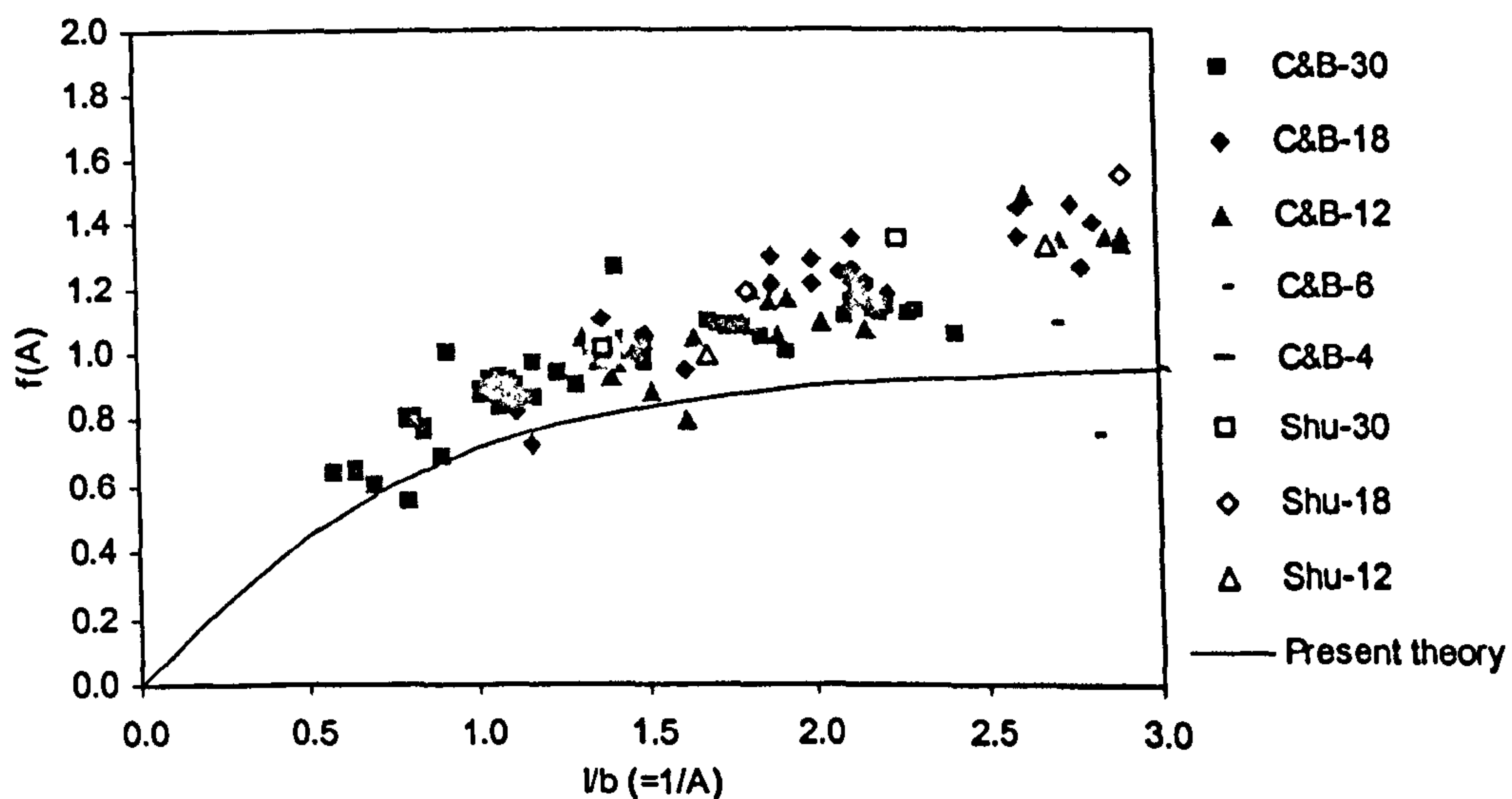


Figure 8-16.  $f(A)$  from Equations (8-31) and (8-32) by use of Shuford's and Chambliss and Boyd's 40 degrees data.

Equation (8-33) provides a reasonable fit to the  $f(A)$  values calculated from lift measurements, apart from in the upper length to beam range plotted for the 20 and



40 degree cases. The  $f(A)$  values calculated from the measurements are greatly scattered. However, the trend of the values calculated for deadrise angles of 20 and 40 degree, indicates that at length to beam ratios above approximately 1.5, the  $f(A)$  required to obtain correlation between predicted lift and measured lift is above unity. It was shown in Section 8.3.2 and Figures 8-4 and 8-6 that at high length to beam ratios, the lift predicted using slender body theory (without aspect ratio correction) is slightly smaller than the measured lift. The added mass lift contribution, relative to the total dynamic lift, decreases with an increase in length to beam ratio. The aspect ratio correction is defined as a factor in the added mass term. It follows that although  $f(A)$  values calculated from measurements at large length to beam ratios are well above the  $f(A)$  function (as seen in Figures 8-14 and 8-16), the predicted lift will only be a small percentage lower than the measured lift (as seen in Figures 8-4 and 8-6).

#### 8.4.4. Prismatic Theory, Dry Chines

Lift data from experiments with dry chines deadrise planing surfaces by Shoemaker (1934), Chambliss and Boyd (1953), Pierson (1954) and Springston and Sayre (1955) have been used in Equation (8-23) to calculate  $f(A)$  values for low length to beam ratios in the same manner as for flat plates. For dry chines,  $C_{L,m'l}$  is given by the first term of Equation (8-7),  $C_{L,fm'l}$  is given by the second term of the same equation,  $C_{HS'l}$  is given by dividing Equation (8-19) by  $(l/b)^2$  to obtain non-dimensionalising on length squared rather than beam squared. Thus yielding the lift coefficient for dry chines planing as

$$C_{L_l} = \frac{L}{\frac{1}{2} \rho U_0^2 \cdot l^2} = C_{m'} \cdot \pi \cdot \frac{\sin^3 \tau}{\tan^2 \beta} \cdot f(A) + C_{fm'} \cdot \frac{\sin^3 \tau}{\tan \beta} + \left(1 - \frac{b}{l}\right) \cdot \frac{1}{C_v^2} \cdot \frac{\tan \tau}{3} \quad (8-34)$$

The resulting values are plotted in Figure 8-17, where the curve denoted 'Present theory' represents Equation (8-34).

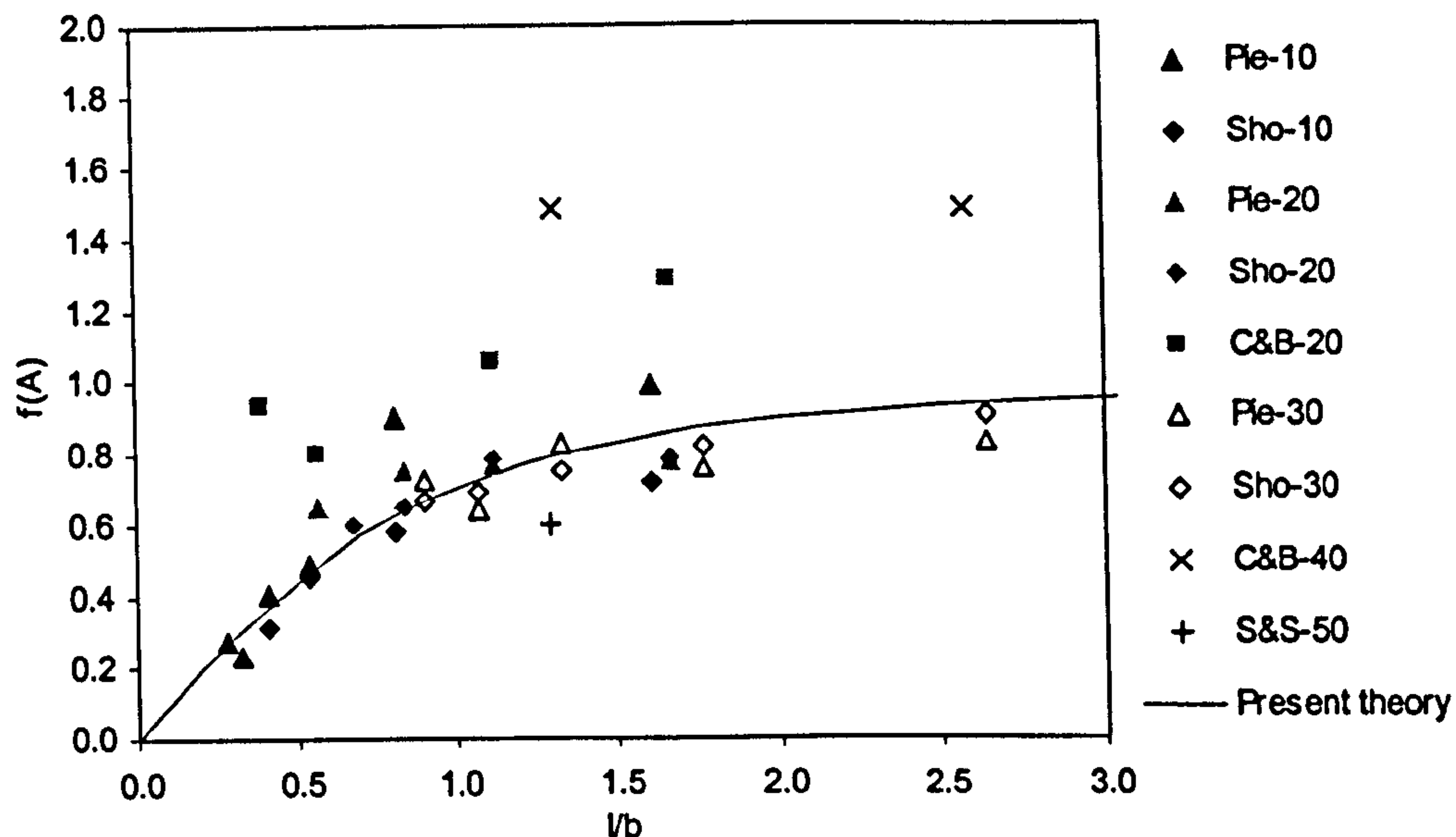


Figure 8-17.  $f(A)$  from (6-34) by use of Shoemaker's, Chambliss and Boyd's, Pierson's and Springston and Sayre's data.

Although the  $f(A)$  values in Figure 8-17 are generally scattered, Chambliss and Boyd's measurements are in disagreement with those of the other sources. Disregarding these points, (8-34) gives a satisfactory fit within the scatter of the calculated  $f(A)$  values.

### 8.5. Validation of the Applied Hydrostatic Lift Component

In order to validate the buoyancy ratio estimate for prismatic planing surfaces given by Equation (8-14),  $f(A)$  values have been calculated for 10 and 30 degree deadrise planing surfaces using the same dynamic lift terms as in the sections above, but first with no buoyancy included and then with the full Archimedes' buoyancy used for the hydrostatic term. The results are plotted in Figures 8-18 and 8-19.



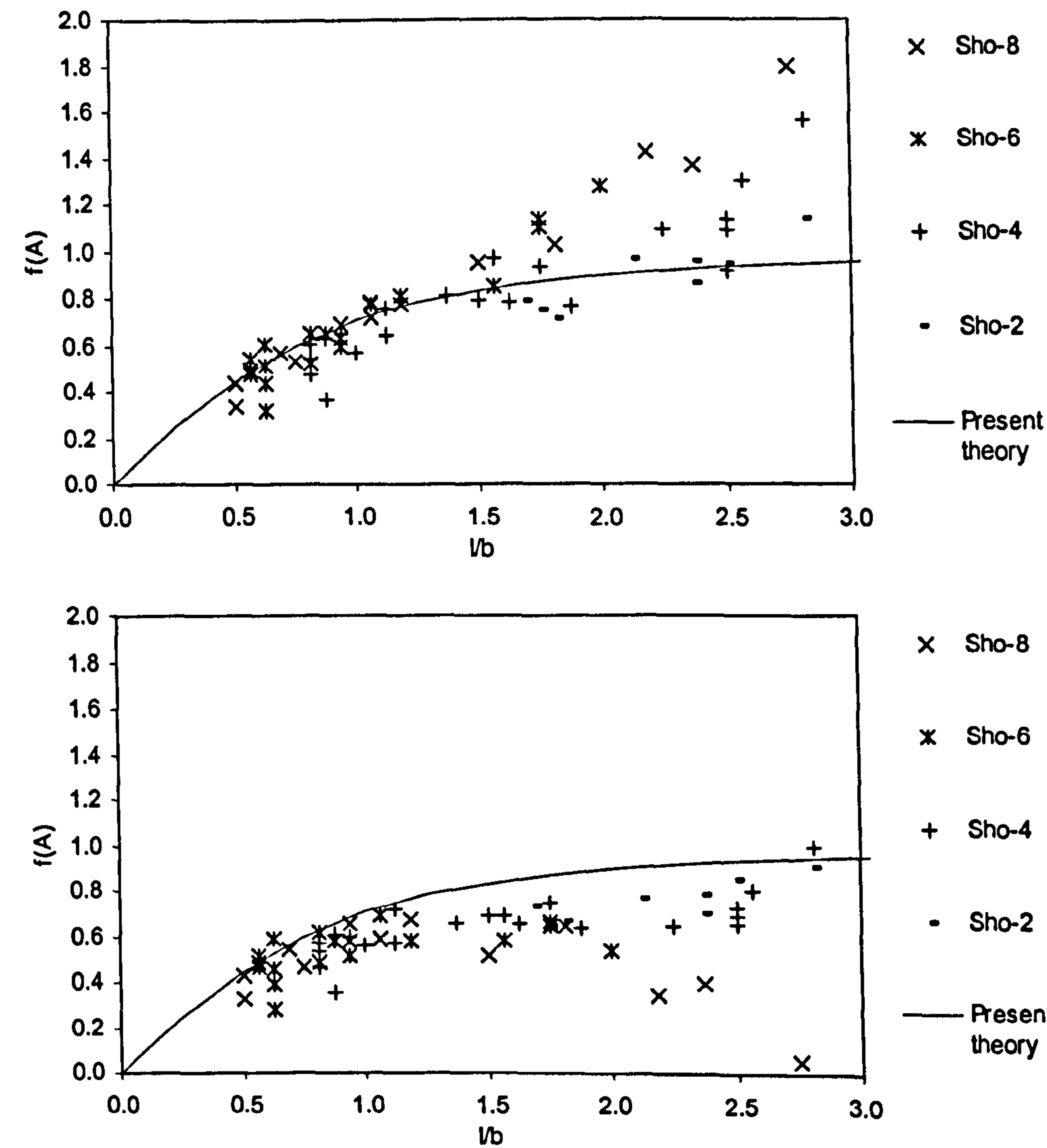


Figure 8-18. Top: 10 degrees  $f(A)$  values derived using zero buoyancy.  
Bottom: 10 degrees  $f(A)$  values derived using the full Archimedes' buoyancy.

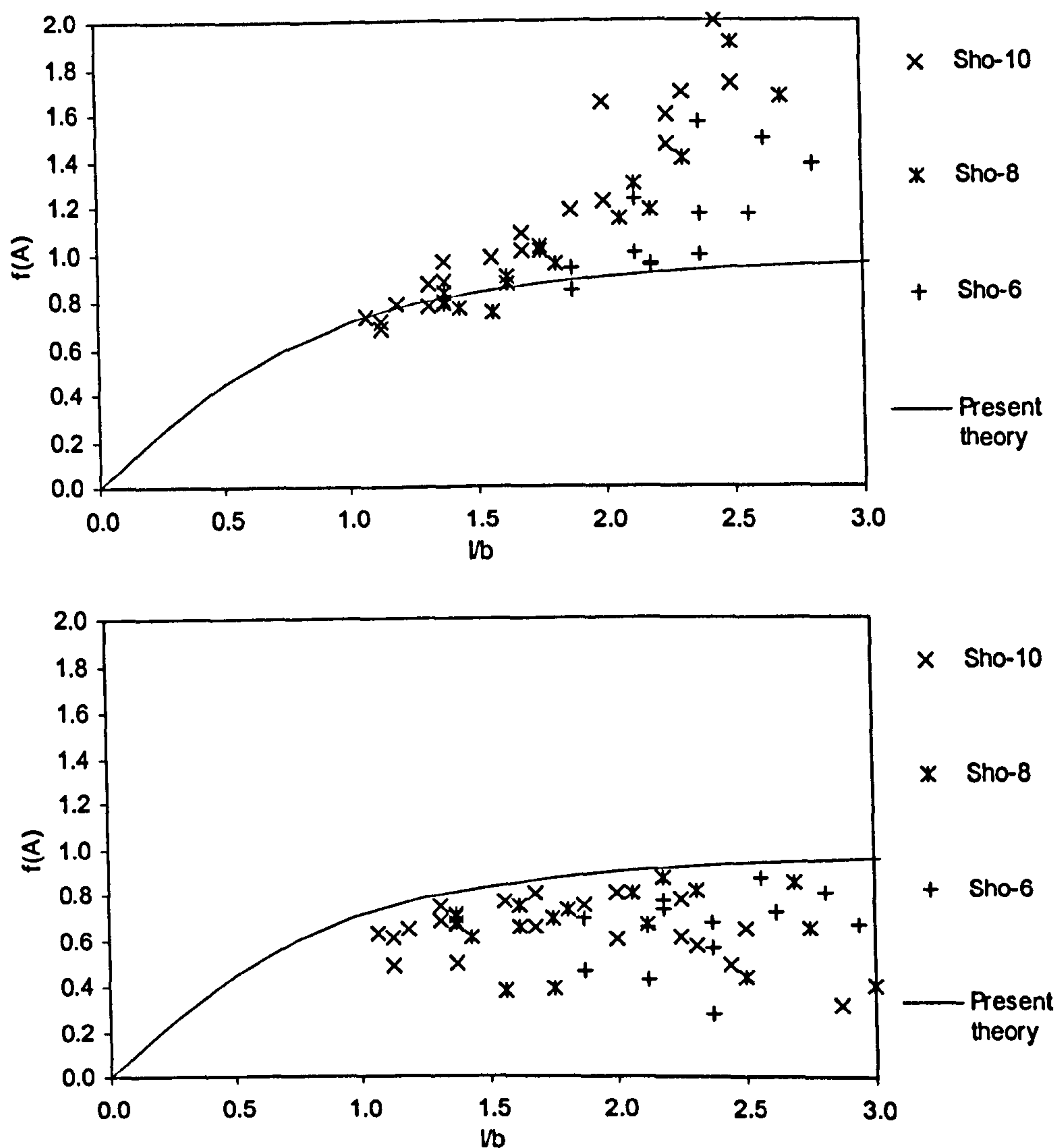


Figure 8-19. Top: 30 degrees  $f(A)$  values derived using zero buoyancy.

Bottom: 30 degrees  $f(A)$  values derived using the full Archimedes' buoyancy.

It is seen that when using zero buoyancy or when using the full Archimedes' buoyancy to calculate  $f(A)$ , the scatter is increased considerably compared to the relatively low-scattered values plotted in Figures 8-13 and 8-15, where the buoyancy ratio Equation (8-14) has been applied. The fact that the values obtained when applying the buoyancy ratio equation are less scattered than when applying  $\phi_0=0$  or  $\phi_0=1$  provides some justification for its use.



## 8.6. Comparison of Non-Slender Body Equations with Experiments

The same planing data used in the previous sections are used for comparison with the complete equations of the present theory (slender body theory with aspect ratio correction) for steady planing lift predictions of flat plates and prismatic hulls. Predicted lift to measured lift ratio is given in Figures 8-20 to 8-25. Note that also the predicted to measured ratios for flat plates are plotted against the nominal length to beam ratio  $l/b$ .

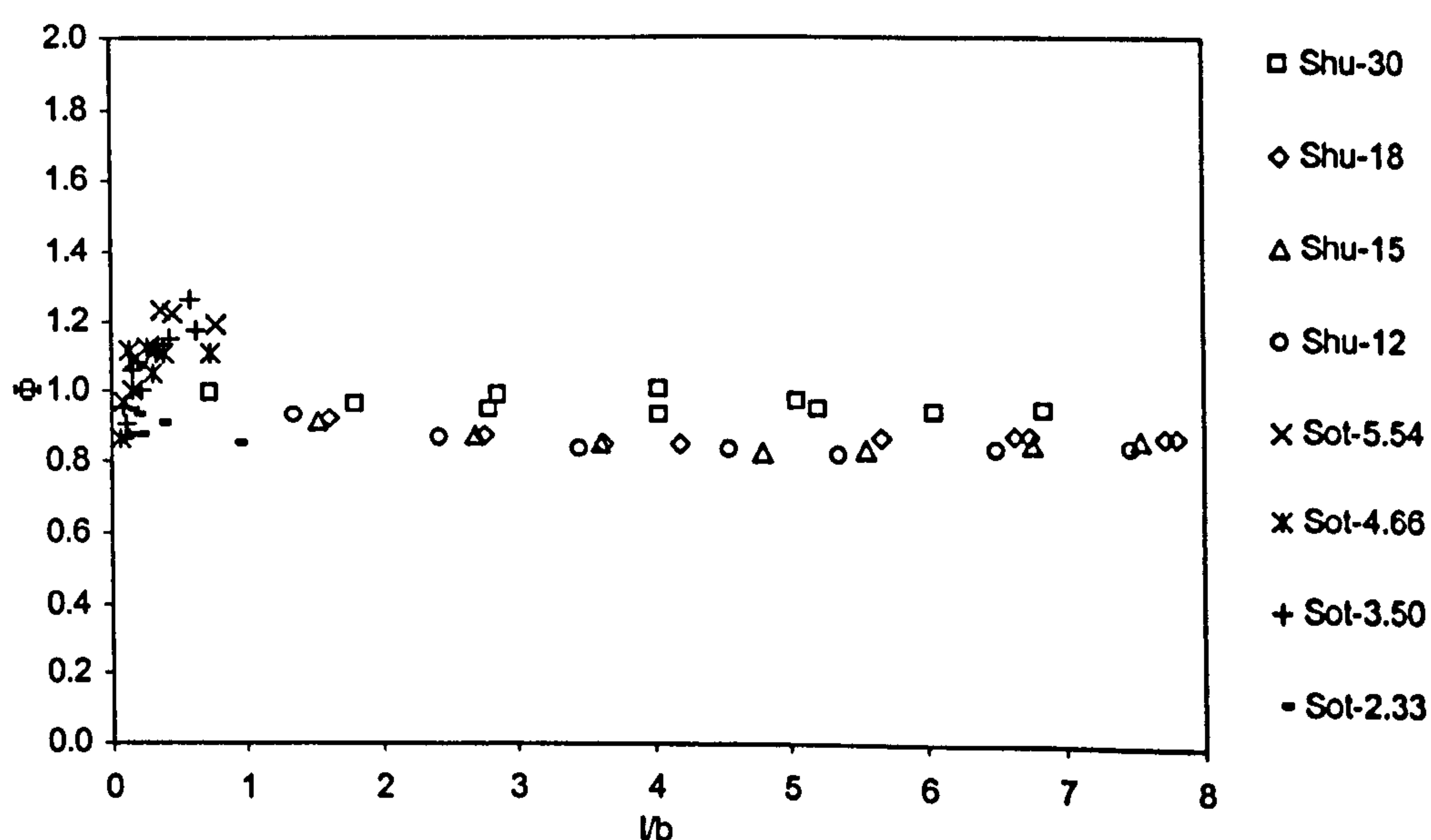


Figure 8-20. Predicted lift divided by measured lift for flat plates.

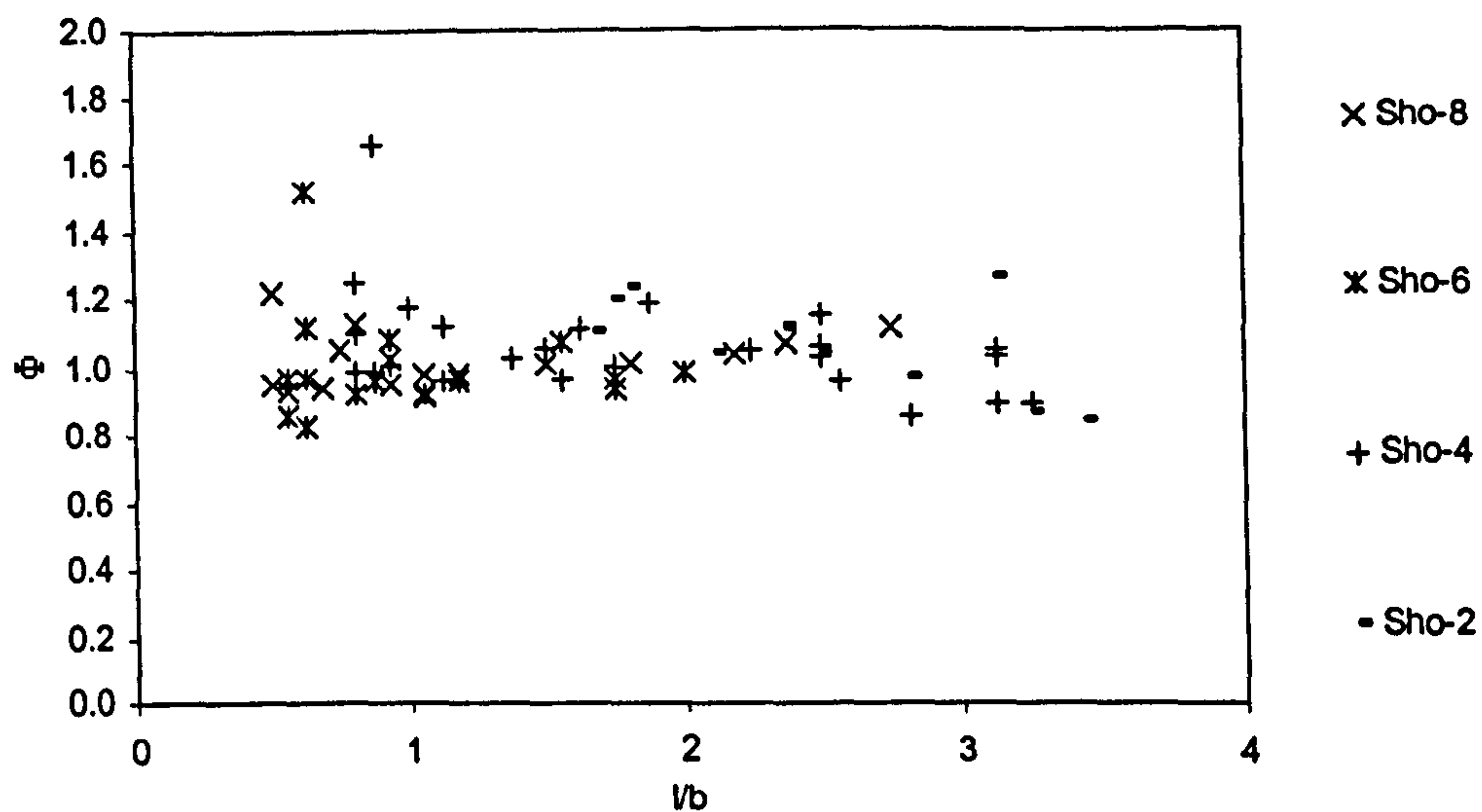


Figure 8-21. Predicted lift divided by measured lift for 10 degrees deadrise, wet chines.

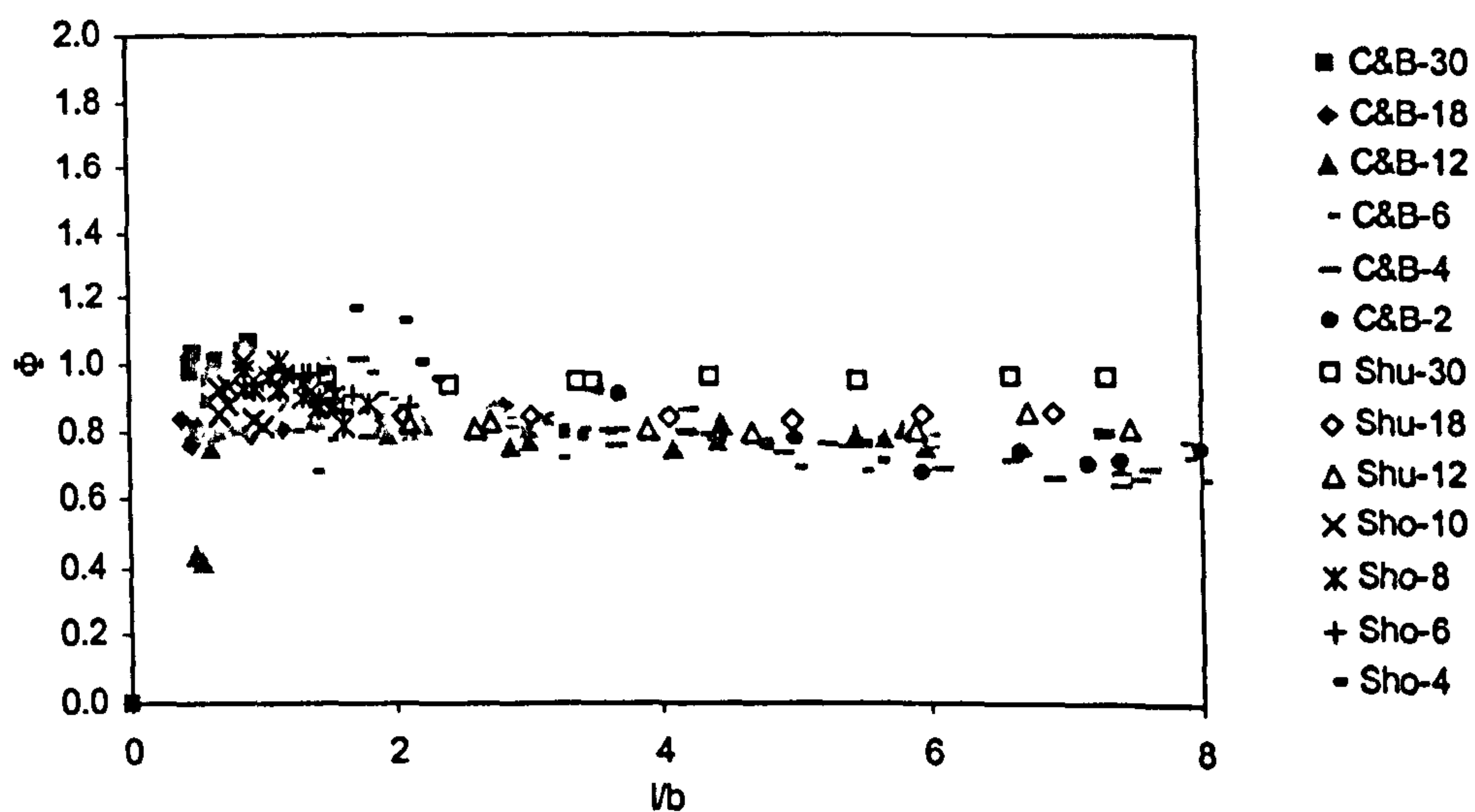


Figure 8-22. Predicted lift divided by measured lift for 20 degrees deadrise, wet chines.



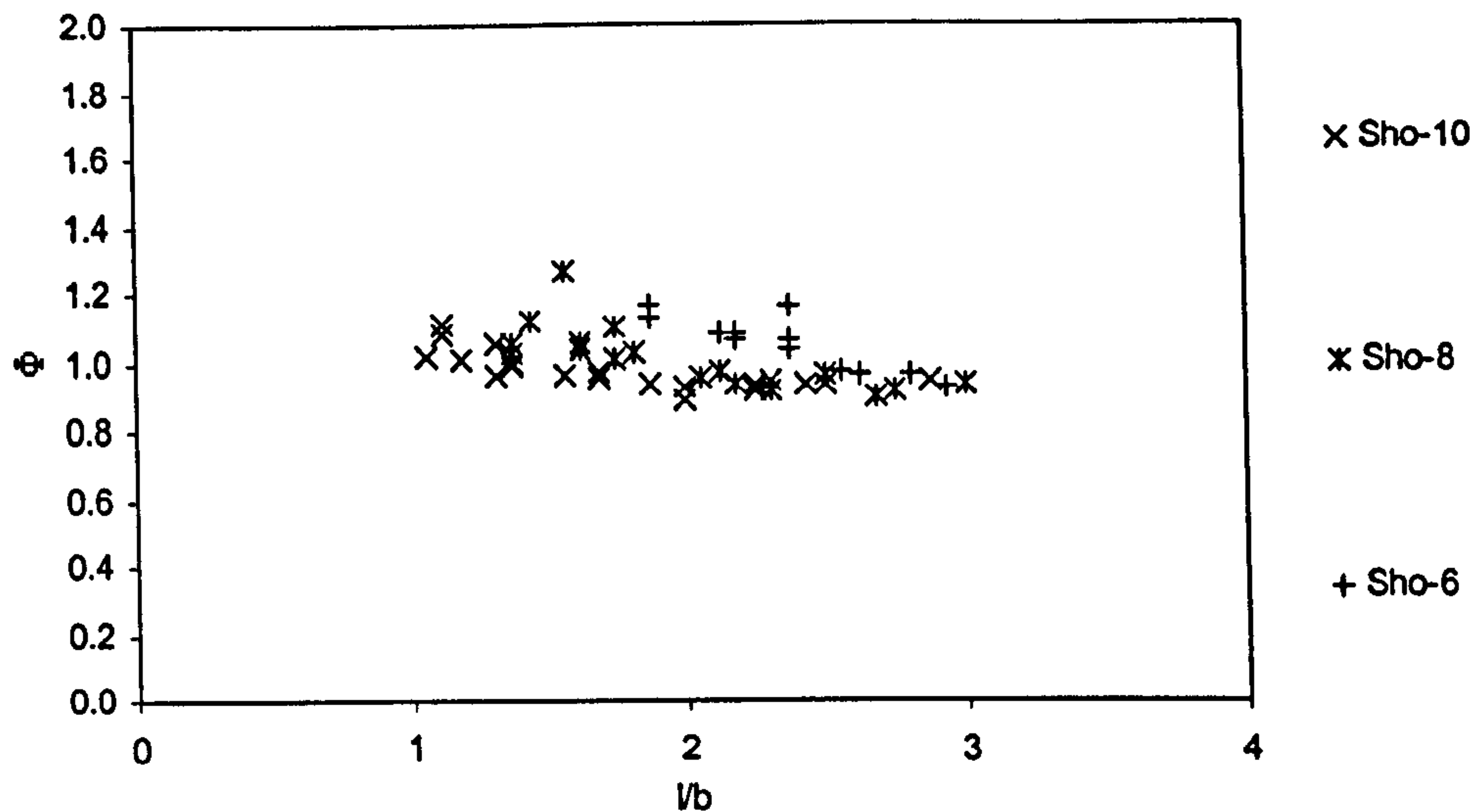


Figure 8-23. Predicted lift divided by measured lift for 30 degrees deadrise, wet chines.

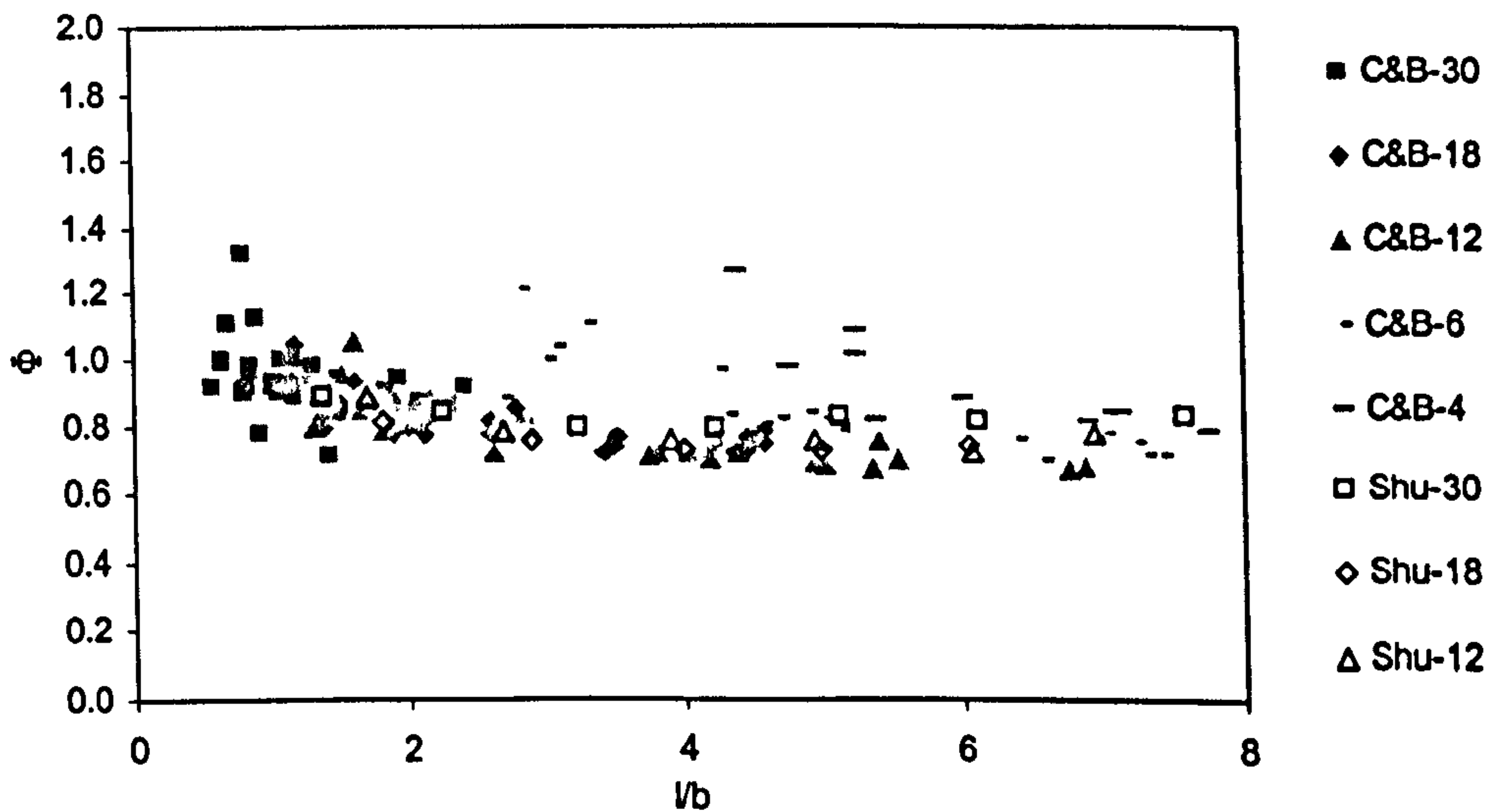
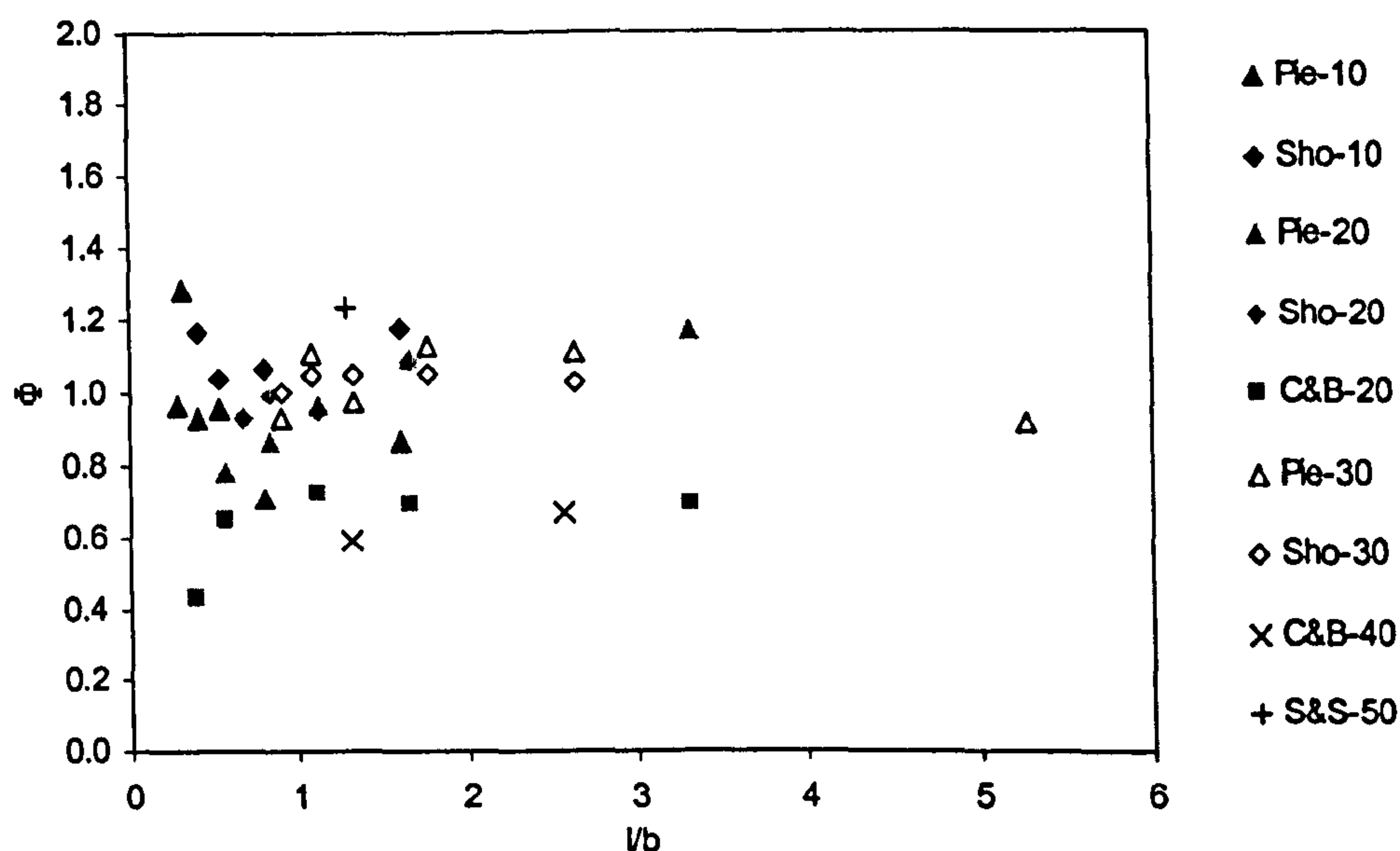


Figure 8-24. Predicted lift divided by measured lift for 40 degrees deadrise, wet chines.





---

**CHAPTER 9**

**CONCLUSIONS AND RECOMMENDATIONS**

---

## 9.1. Conclusions

Numerical simulations and experimental work on the vertical motion of wedge shaped sections moving through a free surface have been presented in this thesis. This work has provided force data for constant velocity water entry and exit of wedge shaped bodies, something not previously available from the literature. The data have been analysed to develop a quasi-empirical added mass theory for water entry and exit of such sections. Thus providing a basis for application of the added mass theory to predict the unsteady motion forces acting on transverse sections of a planing craft. Further, the water entry theory has been used to estimate the steady planing lift force on flat plates and prismatic hulls. Comparison with experimental lift data from the literature has been carried out, and an empirical expression has been fitted to give correlation between non-slender lift data and theory.

A test rig has been designed and manufactured to carry out controlled velocity water entry and exit tests. The new test rig has proven to be capable of producing the results required for the present investigation on the added mass theory. Some oscillations in the load cell readings are thought to be due to flexing in the timing belt transmission between the motor and the test section. However, the force fluctuations caused by the flexing were averaged and did not have an important impact on the analysis of the measured forces. The operation of the test rig proved successful and the rig provides a useful facility for other experiments involving controlled linear motion.

The comparison of the constant velocity water entry results showed that the forces obtained by CFD for the dry chines stage of the entry were in reasonably good agreement with the experimental data for low angles of deadrise (discrepancy between 10 and 20 percent). For high angles of deadrise the dry chines CFD forces were in excellent agreement the experimental data (discrepancy < 3 percent). After chines wetting, the CFD obtained forces were significantly higher than those measured experimentally. The development of the present added mass



theory for water entry during both the dry and the wet chines stages has been developed mainly by analysis of the experimental results. The force at deep immersions, non-dimensionalised on section length times beam, was found to be well represented by Equation (6-4). The dry chines added mass coefficient was found to be well represented by the Wagner-Sydow equation multiplied by a factor of 0.89.

Both the CFD and the experimental force data show that the peak force occurred at the point at which the chines become wetted, which was at a non-dimensional immersion depth of about  $z/d=2/\pi$  for all angles of deadrise within the range of the test series, i.e.  $\beta < 45$  degree. The wetting factor was found to have a constant value of  $\pi/2$  up to the point of chine immersion.

The theory presented for the constant velocity water entry of wedge shaped sections has been shown to be consistent with added mass data obtained by oscillation tests with sections at large immersion depths. Also, it has been shown that the inclusion of a flow momentum term in the theory is necessary since the added mass would otherwise have been greatly overestimated to account for the deep immersion forces.

If the water entry theory is applied to estimate water exits, a large force that acts in the direction of motion is found, something that is in contradiction with common sense and is also proven wrong by the experimental water exit data. However, it was shown that exclusion of the rate of change of added mass term yielded an expression that gave forces that correlate with the water exit experiments. The pictures captured during water exit tests show that a large amount of water follows the wedge section above the calm water level. This observation is consistent with excluding the rate of change of added mass term as it proves that the momentum of the added mass is not given back as an impulse imparted on the wedge but is used to carry the water above the calm water level.

Thus, the aims 1 to 4 from Section 1.4. have been achieved:

1. The forces acting on a wedge during water entry due to changes in added mass momentum and due to flow momentum have been separated.
2. The increase in added mass after chines wetting has been evaluated.
3. A revised quasi-empirical theory for constant and non-constant velocity water entry of both dry chines and wet chines stages has been developed.
4. The validity of the water entry theory for prediction of exit forces has been explored, and the theory modified on basis of comparison with experimental force data and visual observations of the free surface.

Although the added mass coefficients obtained by the accelerated water entry tests were highly scattered, comparison of these with the coefficients extracted from the constant velocity results, after subtracting the estimated contribution from flow momentum, indicates that the contribution from a dry chines flow momentum force, if any, had to be small compared to the dry chines added mass contribution. Unlike the proof established for the presence of a wet chines flow momentum force during water entry, proof has not been established for the flow momentum force during the dry chines stages of the entry. However, it has been argued that the dry chines flow momentum term is small relative to the added mass term, and hence a poor estimate of the flow momentum contribution will only have minor impact on the total hydrodynamic force estimate. Also, it has been shown experimentally that the flow momentum term gives a force that is consistent with the hydrodynamic force acting on wedge sections during constant velocity water exits. Thus, the inclusion of a dry chines flow momentum term has given a theory that is consistent with both exit and entry data.

The quasi-empirical constant velocity water entry equation has been applied in a slender body approach to derive expressions for the slender body steady planing lift forces on flat plates and prismatic hulls. Comparison with published experimental planing lift data shows that at length to beam ratios greater than



about 2, the slender body equations are consistent with measurements. At length to beam ratios of less than about 2, the slender body equations overpredict the lift force. The introduction of an aspect ratio correction to the added mass in the slender body equations gave correlation between theory and experiments at the lowest length to beam ratios at which planing data is available, i.e. correlation at high aspect ratios. Thus, aim 5 and 6 from Section 1.4. have been achieved:

5. The water entry theory has been applied to derive slender body steady planing lift equations that are shown to compare well with planing data at length to beam ratios above 2.
6. An aspect ratio correction has been introduced to give correlation with the highest aspect ratio planing data available from the literature.

Application to predict slender body planing lift has shown that the new added mass theory is consistent with published planing data at high length to beam ratios, and this justifies the decision made regarding the reliability of the two data sources. If the new water entry theory had been based on the CFD data instead of the experimental data, the resulting flow momentum coefficients from the data analysis would have been nearly twice the values of the present theory. It follows that at large length to beam ratios, when the corresponding non-dimensional draft at the transom ( $z/d$ ) is large and thus a large part of the lift force is due to flow momentum, this would result in the lift forces being highly overpredicted compared with the planing data.

Zhao et al. (1997b) applied their water entry simulation results to predict the lift force on slender body planing surfaces. It has been shown that the forces acting during the wet chines stages of a constant velocity water entry as given by Zhao et al. is much greater than those found by the present experiments and agrees better with the present CFD. This can explain the overpredictions of lift made by Zhao et al. when compared with the well recognised empirical equations of Savitsky (1964).

## 9.2. Recommendations for future work

The following paragraphs give the author's opinion of necessary further research related to the added mass planing theory.

A fuller treatment of the equations for force acting on wedge sections during constant velocity water entry would give the longitudinal distribution of lift force on a slender body planing plate or prismatic hull. It would be of interest to compare the centre of lift from this approach to that measured experimentally for low length to beam ratio planing surfaces, and hence obtain the centre of the "loss of lift" which herein has been treated as a correction to the added mass. This would highlight in which region of the planing surface the three-dimensional flow effect is of greatest significance, and would allow the centre of lift to be predicted also for high aspect ratio planing surfaces.

Further investigation should be carried out into the exit phenomena. The force on a wedge section during a water exit, as given herein, requires that the point of chines emergence, i.e. when chines become dry, is known. Therefore, for application in prediction of forces on sections during periodic water exit, i.e. cyclic motion, an assumption of when this occurs must be made, e.g. when the chines cross the calm water level. The instant of chines emerging is also under influence of the disturbance of the water surface before exit motion is engaged. Knowledge of the variation of the immersion depth of chines emergence with variation in velocity, deadrise and the initial depth before the exit motion is engaged, would be advantageous for application of the water exit theory to cases involving cyclic motion and large disturbances of the free surface.

Prediction of the lift force on non-prismatic hull forms, e.g. warped hulls, by the water entry approach requires the forces acting on wedge sections on which the deadrise angle varies with immersion depth to be known. The present investigation has shown that the CFD approach produces reliable results for the dry chines stages of the entry. Thus, an investigation could be based on results from CFD simulations of such water entries. Such simulations would require regeneration of the grid as the simulation progresses.



### **9.3. Closure**

A research investigation into added mass theory for water entry and exit and its application in planing has been successfully completed and reported. New data for the water entry and exit of wedge shaped bodies have been produced and analysed to develop a new added mass theory that handles both the entry and exit motion. It is believed that the presented work provides a useful basis for prediction of the unsteady motion forces of planing craft, and it is hoped that further research along these lines will be carried out to develop an added mass strip method for seakeeping analysis of planing craft.

---

**APPENDIX A**

**EARLIER WATER ENTRY EXPERIMENTS**

---



Prior to the design of the main test rig, some velocity controlled drop tests were carried out using a rather simple experimental set-up. The objective of these experiments was, as with the main experiments described in Chapter 4, to measure the total force acting on wedge shaped sections during constant velocity water entry. The experimental set-up for these earlier water entry experiments is sketched in Figure A-1.

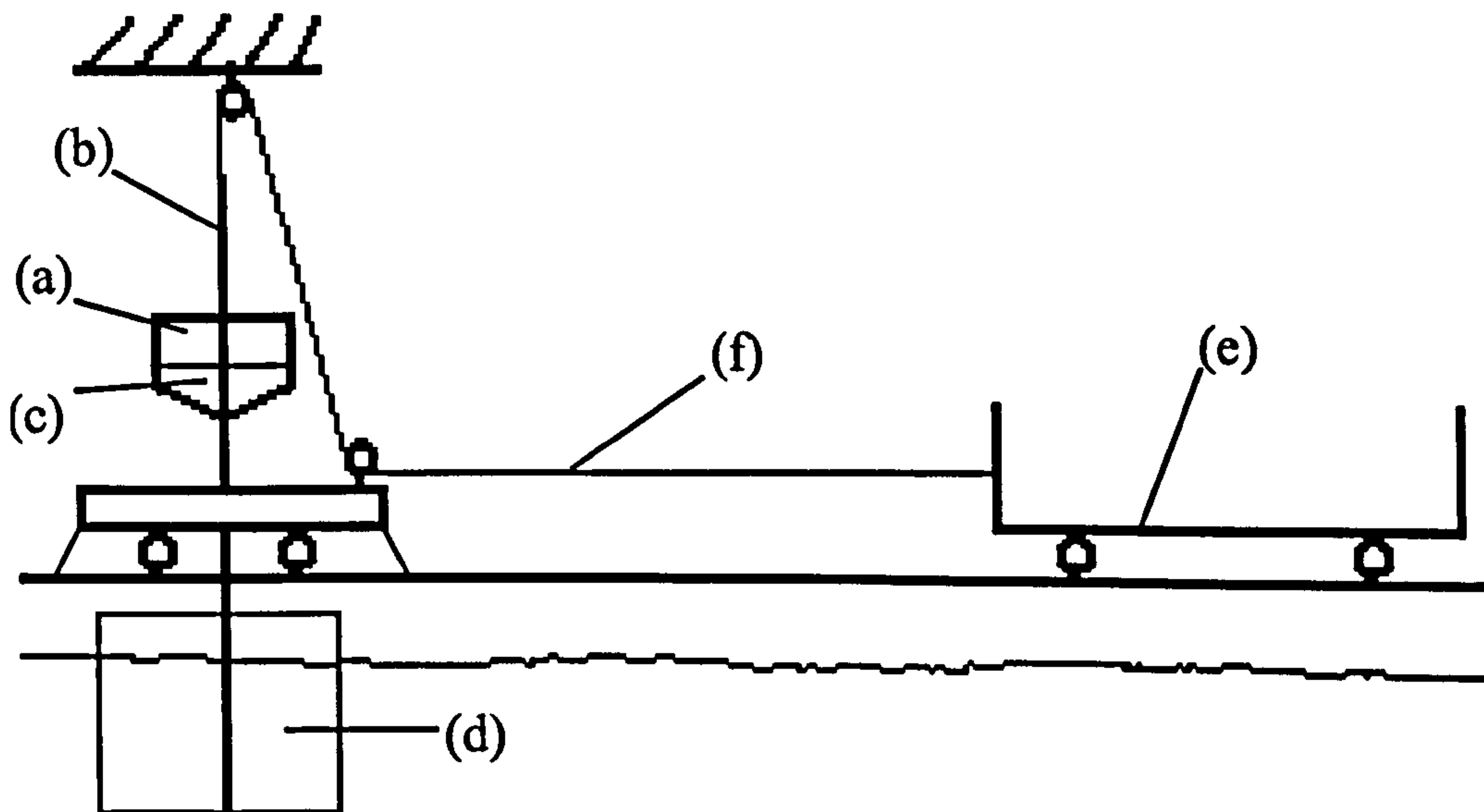


*Figure A-1 Experimental set-up for the earlier experiments.*

The test equipment, shown in Figure A-1, consisted of a model carrying trolley (a), free to move vertically along guide rails (b) fixed above the water in the hydrodynamic laboratory towing basin. The hull section models (c) to be tested were mounted under the model carrier via four load cells, one in each corner. The load cells were connected to an amplifier and a PC computer for recording of the data. Visual recordings were also taken using video cameras mounted both above and under the water for recording of the tests.

To achieve two-dimensional flow, two transparent plates (d) were positioned on the guide rails at a distance apart that was just enough for the models to slide down between. Velocity of the trolley during the water entry was controlled by using the basin towing carriage (e) to provide a range of constant speeds up to



about 1.5m/s. A steel cable (f) was led from the top of the model carrier through two pulleys to the towing carriage. The model carrier was ballasted to keep the cable tight so that, as the towing carriage moved towards the test rig at constant velocity, it was lowered towards the water at a velocity that was constant, subject to any cable stretch with varying load and provided the net force on the model carrier was acting downwards. The speed of the carriage was recorded together with the load cell readings.

Figure A-2 shows a picture of the guide rails, the model carrier/trolley and a test section connected via load cells.

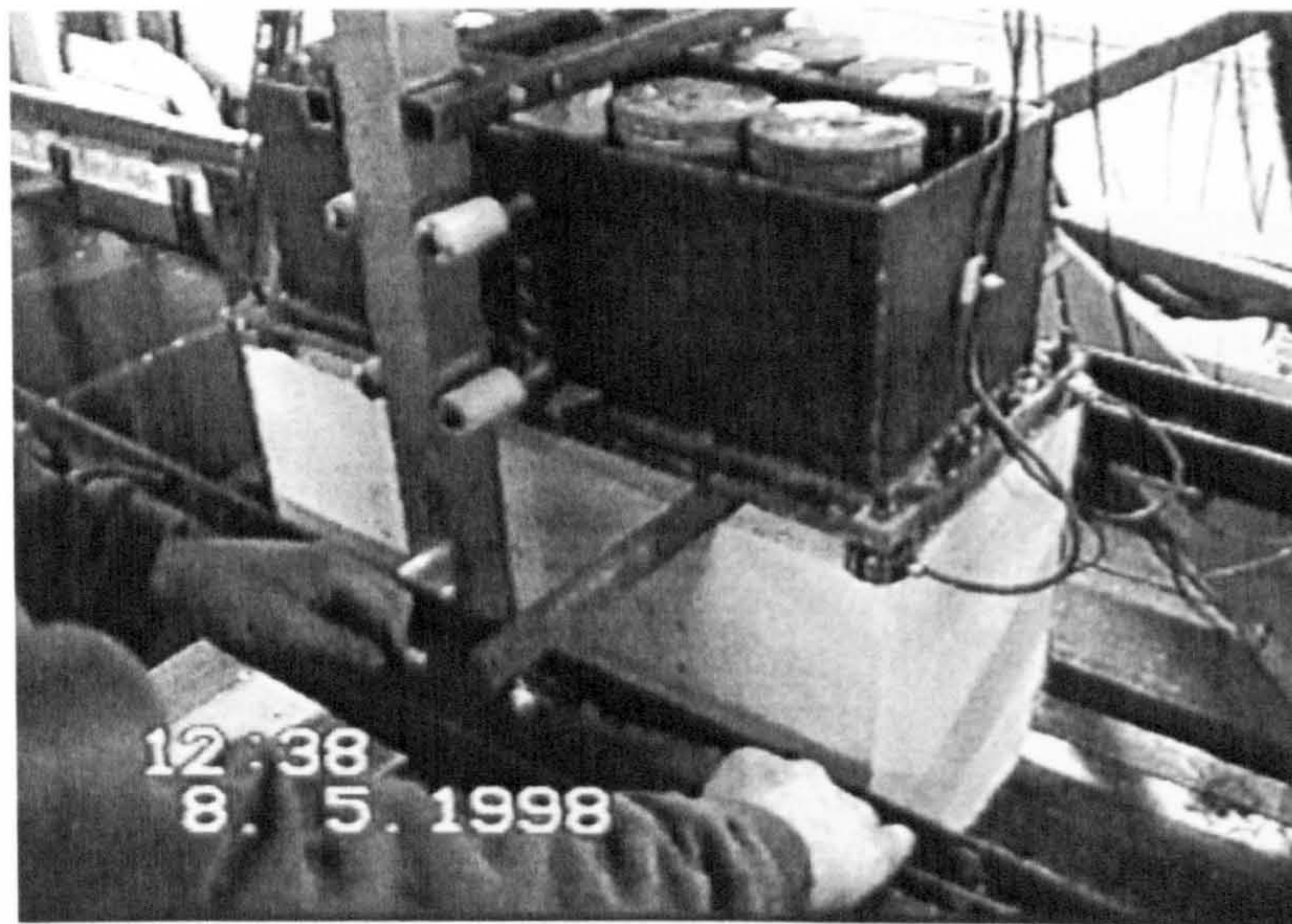


*Figure A-2. Trolley box and tests section between vertical guide rails.*

Figure A-3 and A-4 shows pictures captured from the video cameras positioned above and under the water respectively.



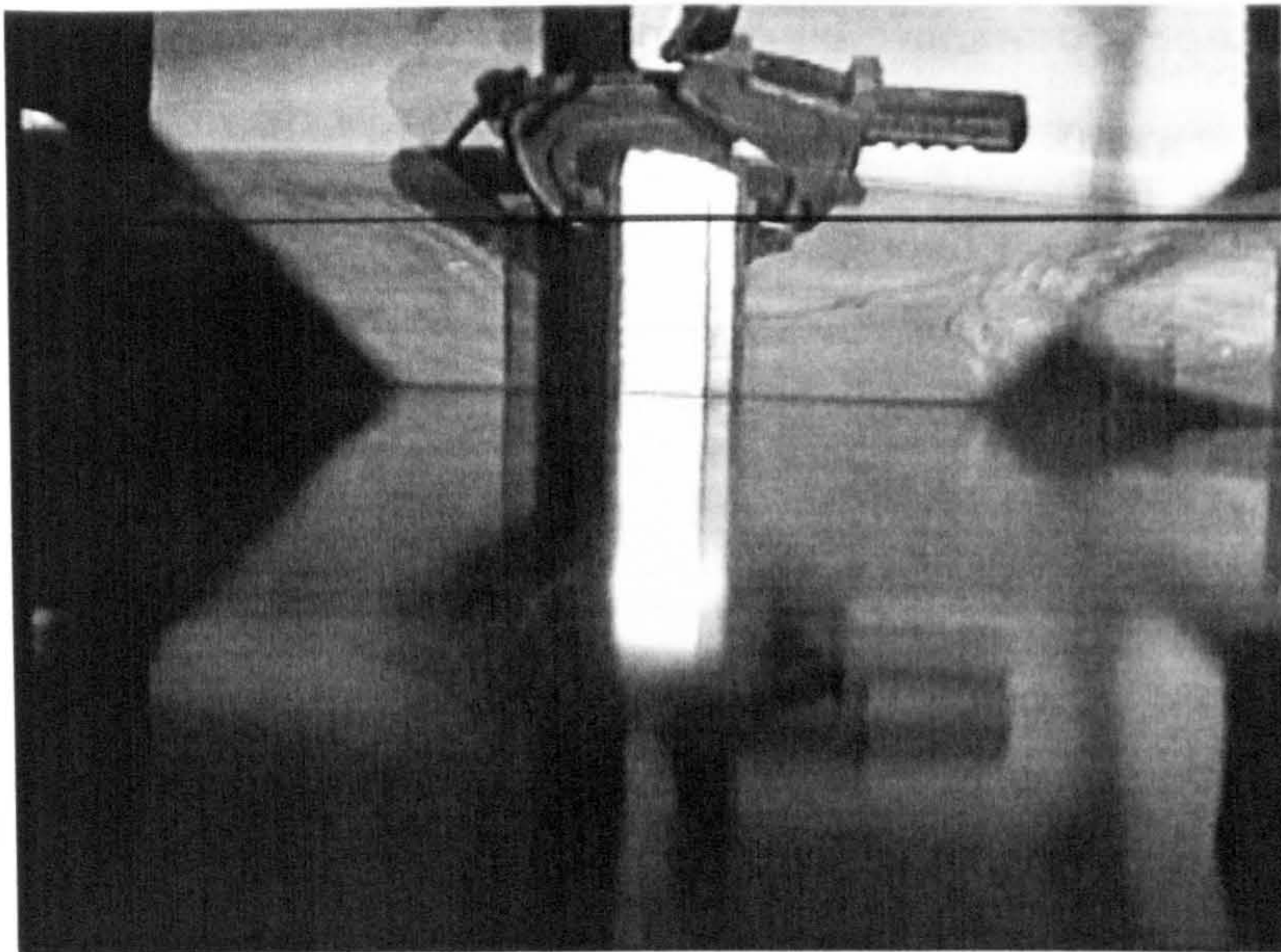


*Figure A-3. Picture captured during a 45 degree wedge water entry.*



*Figure A-4. Underwater picture captured during a 30 degree wedge water entry.*

Wedge sections of 5, 10, 15, 30 and 45 degree deadrise were tested, some of which were made of PVC sheets and some of aluminium plates. Some results from these tests are shown in Figures A-5 to A-9. The hydrodynamic force coefficient ( $C_{F,b}$ ) plotted in these figures has been obtained by subtracting



Archimedes' buoyancy force from the total measured force and non-dimensionalising on section length times maximum beam.

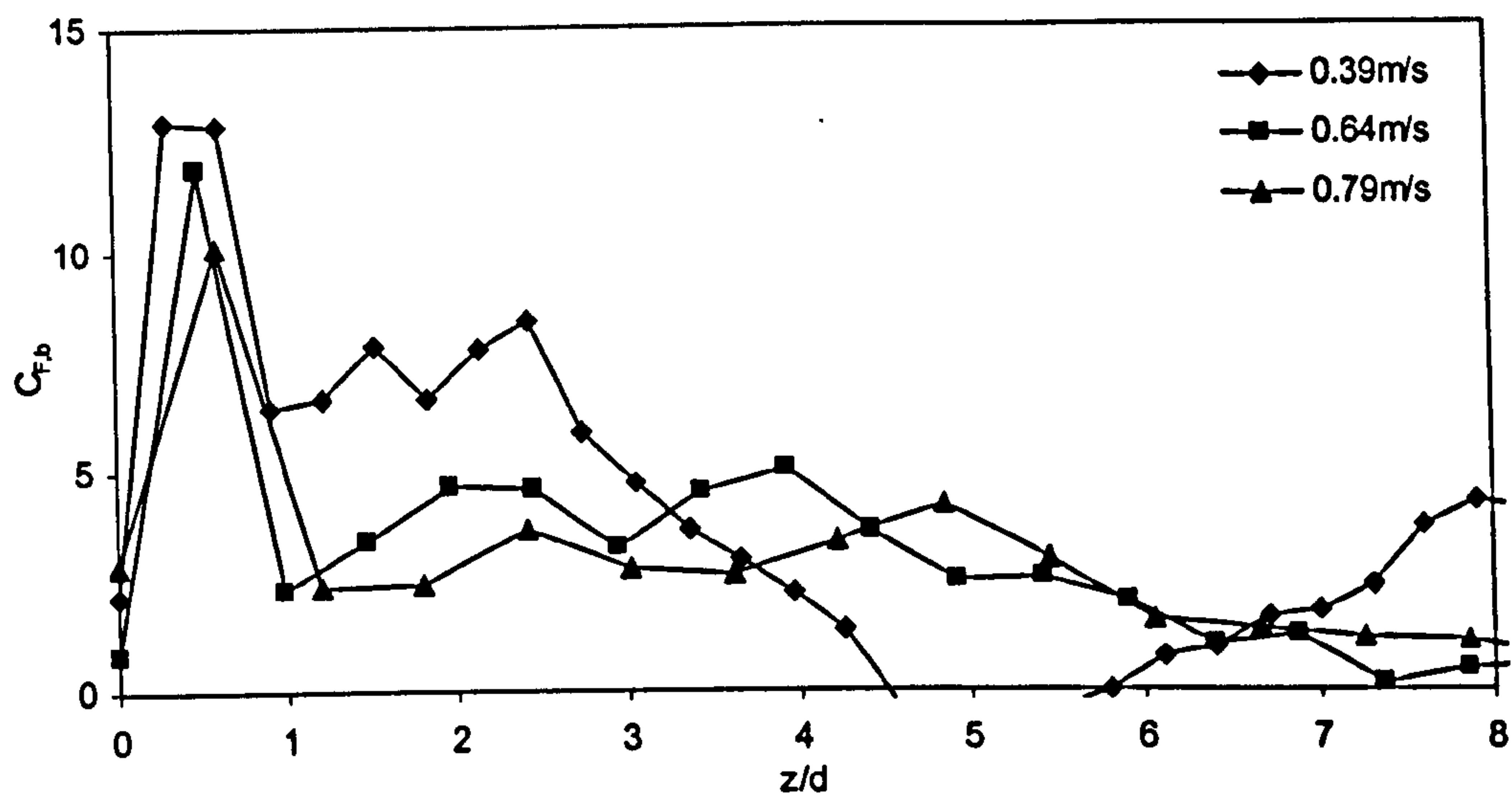


Figure A-5. Non-dimensional water entry force on 5 degree wedge sections.

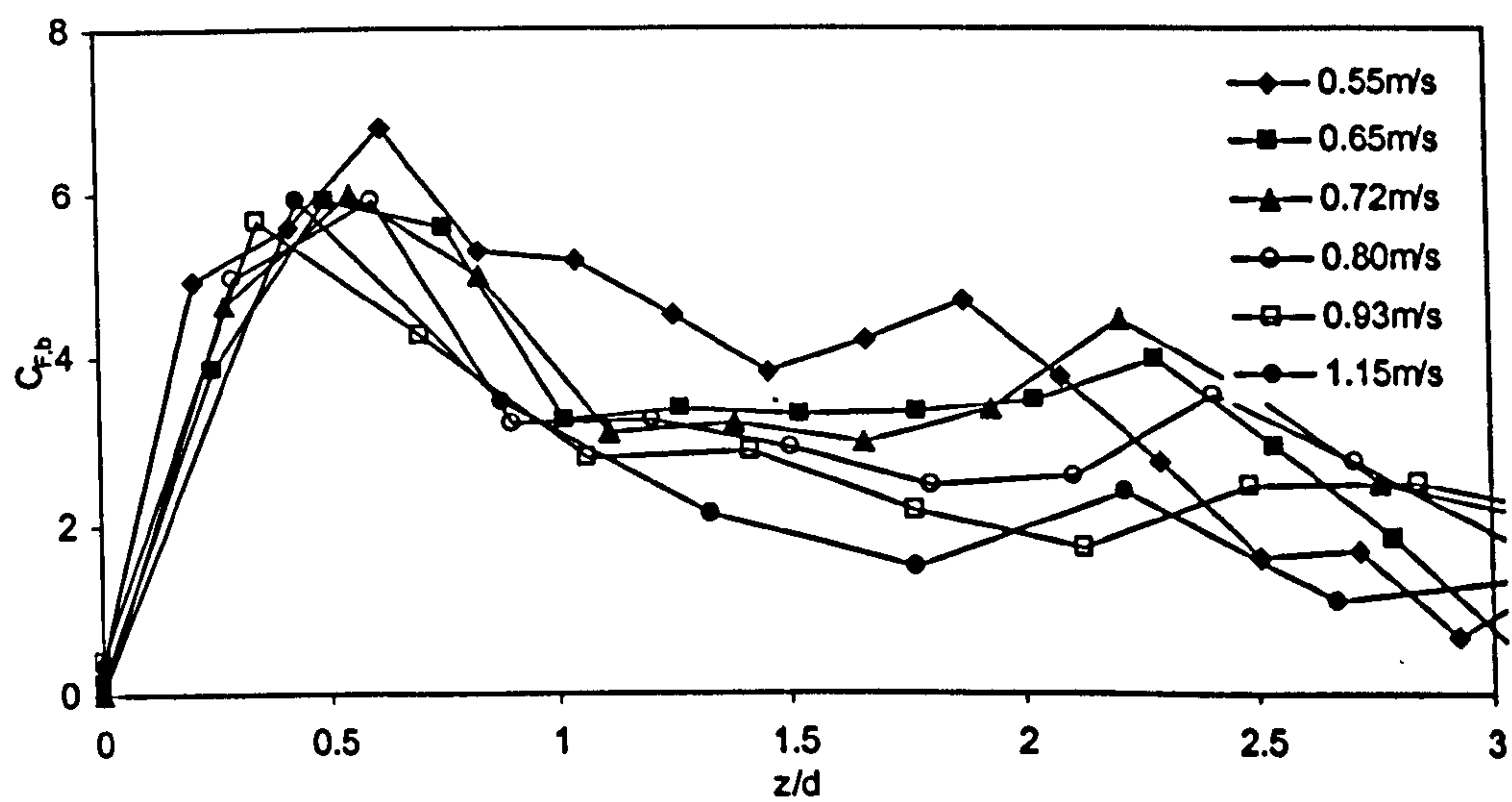


Figure A-6. Non-dimensional water entry force on 10 degree wedge sections.



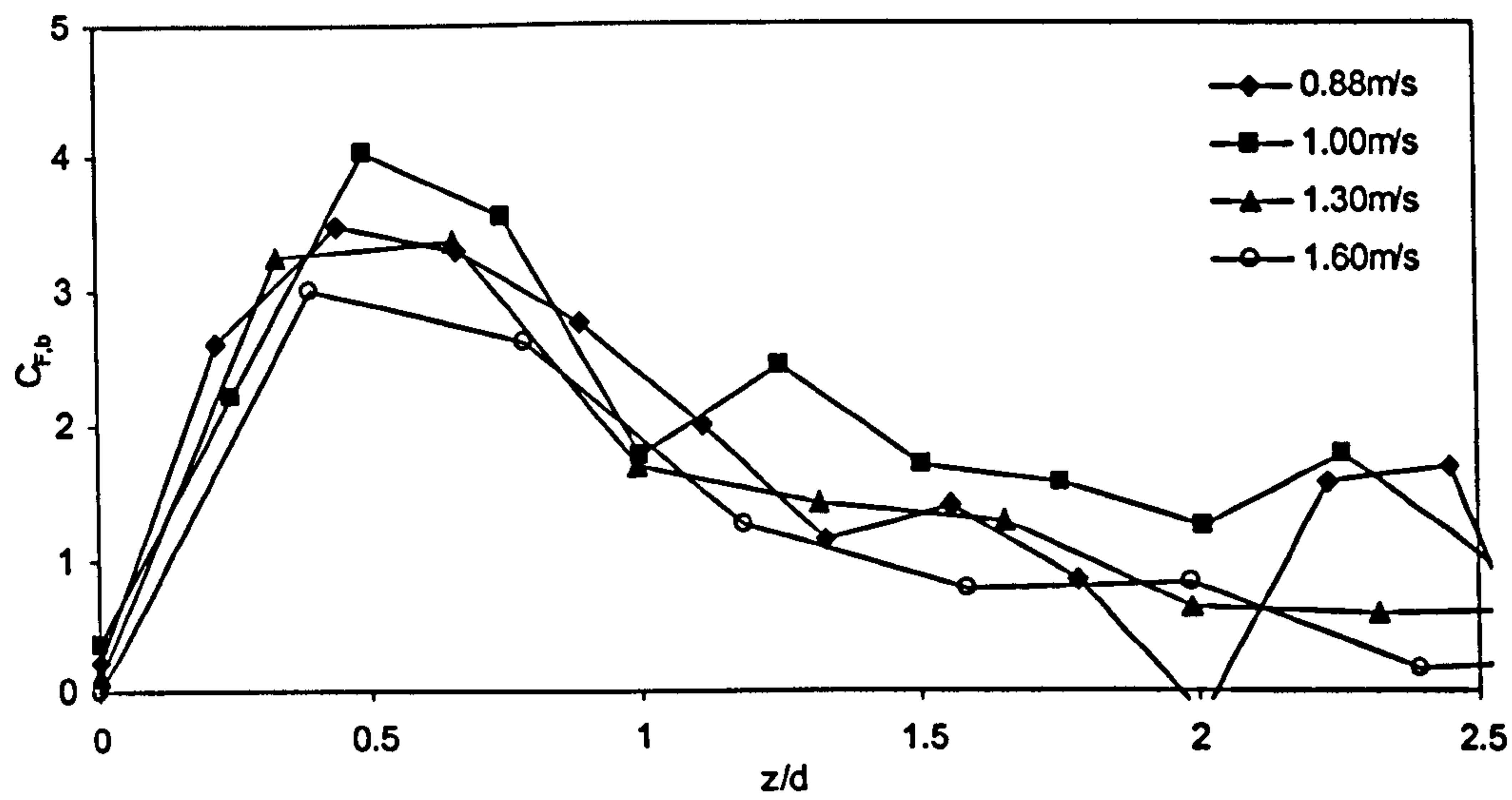


Figure A-7. Non-dimensional water entry force on 15 degree wedge sections.

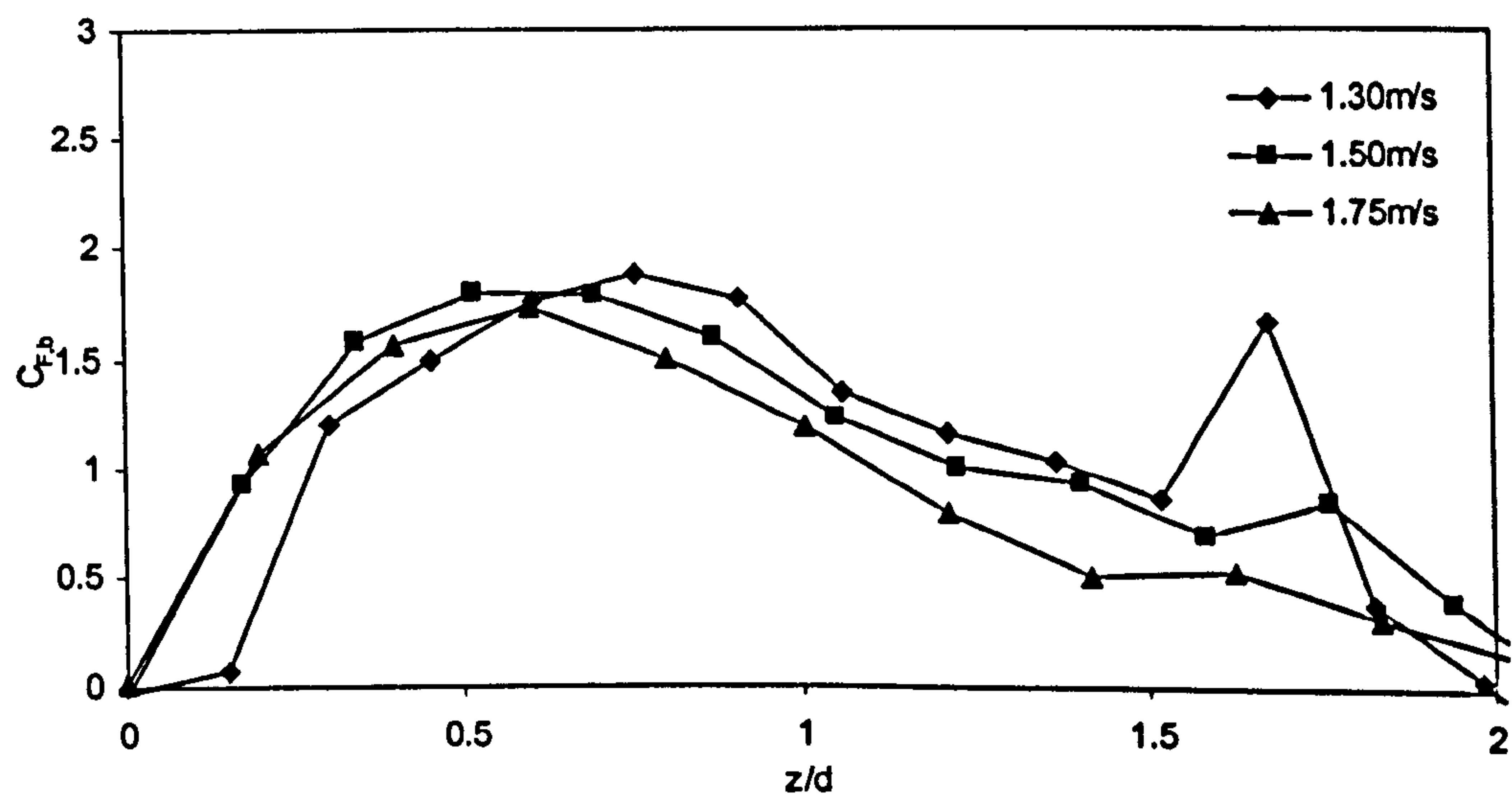


Figure A-8. Non-dimensional water entry force on 30 degree wedge sections.

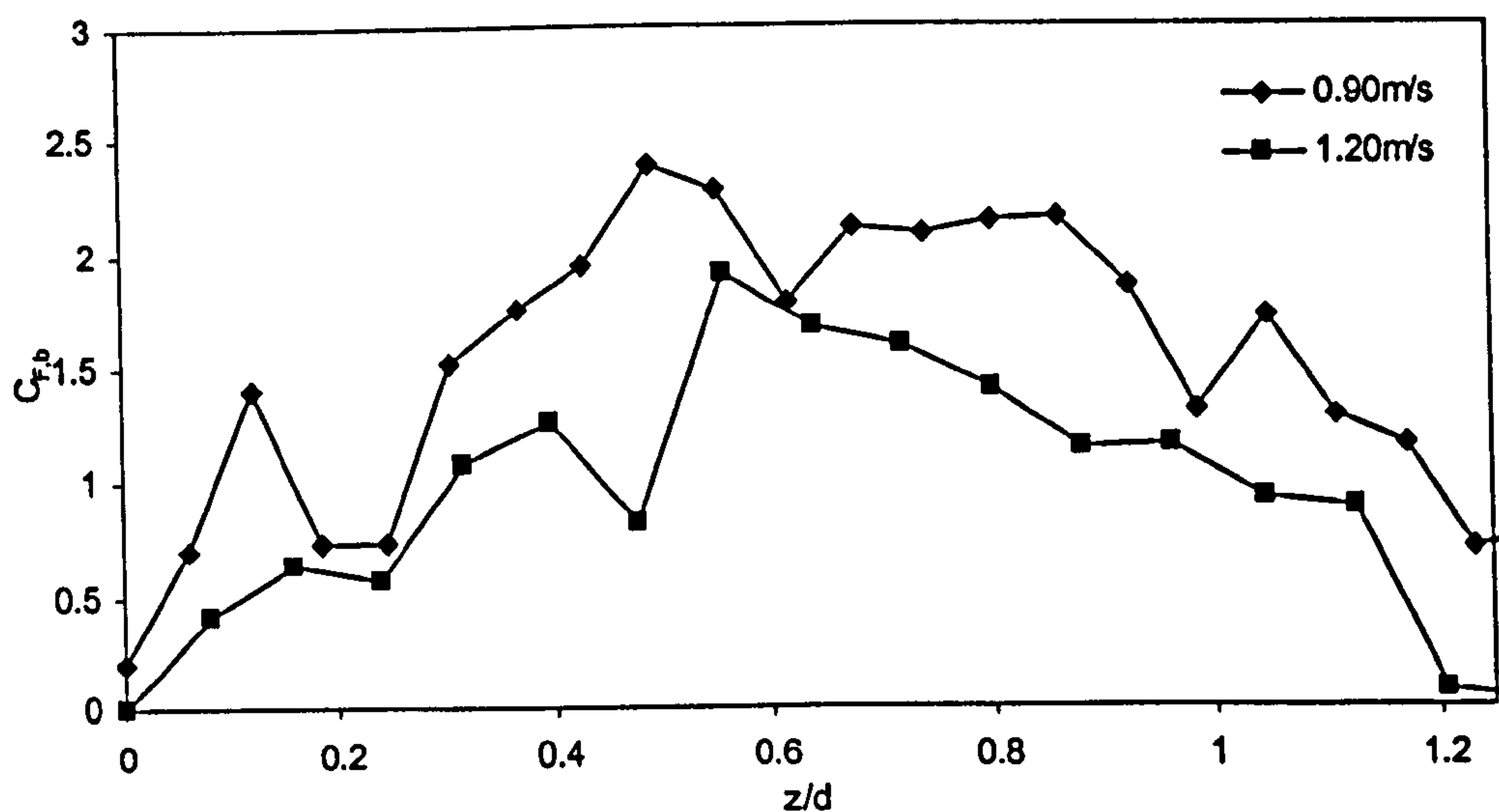


Figure A-9. Non-dimensional water entry force on 45 degree wedge sections.

The load cells used for force measurements in these earlier experiments were not of high dynamic response. Due to this, the rapidly increasing force during the early stages was not recorded, and hence the peak force occurring at the instant of chines wetting was much lower than actually experienced by the test section. This is seen if comparing the magnitude of the peak obtained in the main experiments in Figures 5-2 to 5-5 with those seen in Figures A-5 to A-9. It is seen that the force obtained with the earlier experiments, for the initial stages of the entry, is far too low.

A problem also experienced with the set-up of the earlier experiments was stretch in the cable connecting the towing carriage and test section. The high loads acting, particularly for low angle of deadrise, during the initial stages reduced the cable tension and thus also the stretch. After peak force occurrence the cable tension again increased, inducing oscillating motion of the test section.

Also, the guide system providing linear vertical motion during the water entry was not substantially rigid. For this reason, the plates positioned in the water, for the test sections to slide down between and provide two-dimensional flow, were placed with extra clearance to prevent collision with the impacting section. It is



likely that the unnecessary large clearance allowed water to escape between the test section and these plates, resulting in pressure reduction and thus force reduction.

The main conclusions from the earlier water entry experiment were as follows:

- The design of the test rig caused unreliable results.
- A better test rig was required for further experiments.
- The connection between model and velocity controller had to be more rigid.
- High dynamic response load cells were needed.
- Two-dimensional flow providing plates had to travel with the test section to allow minimal clearance.

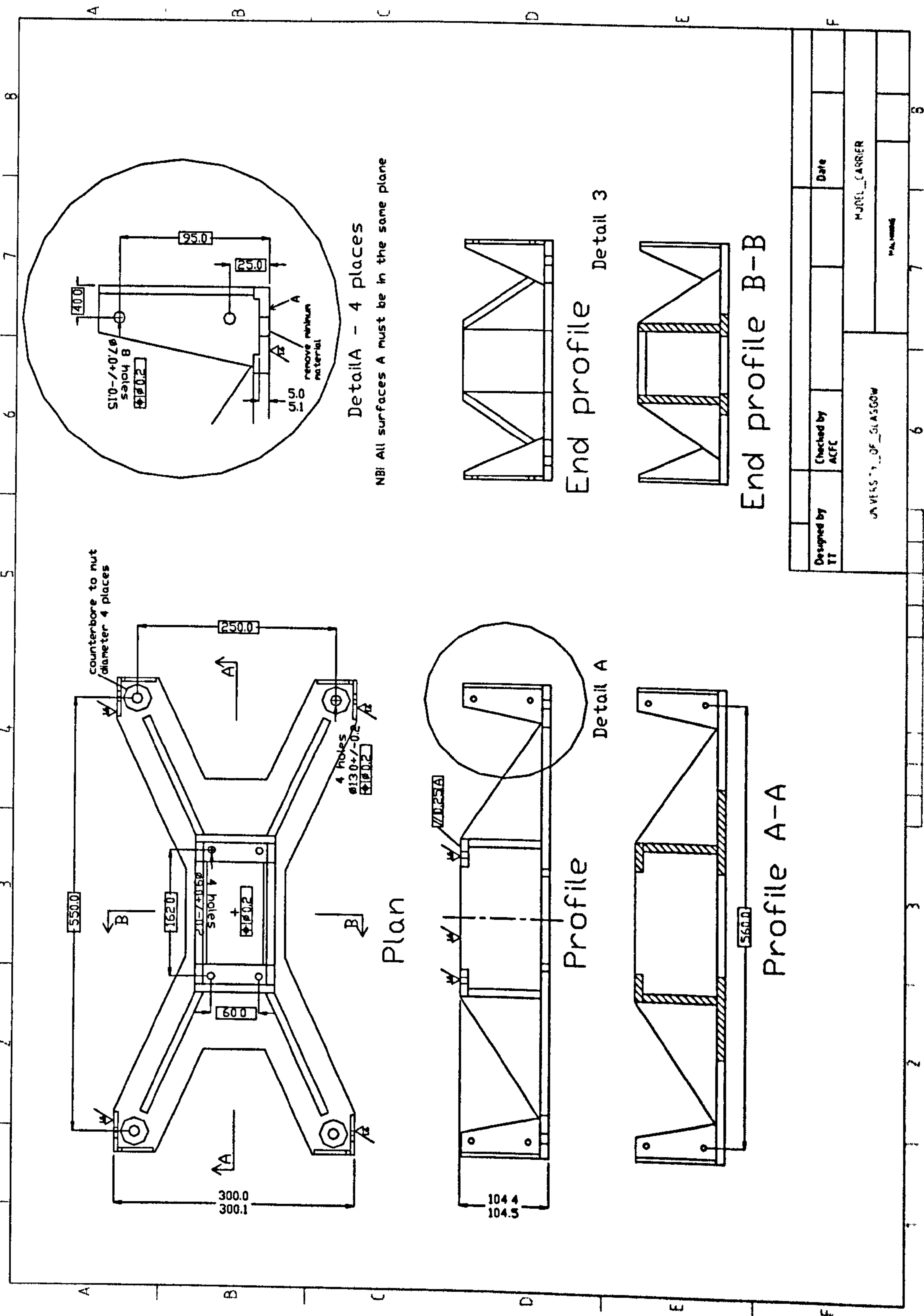
---

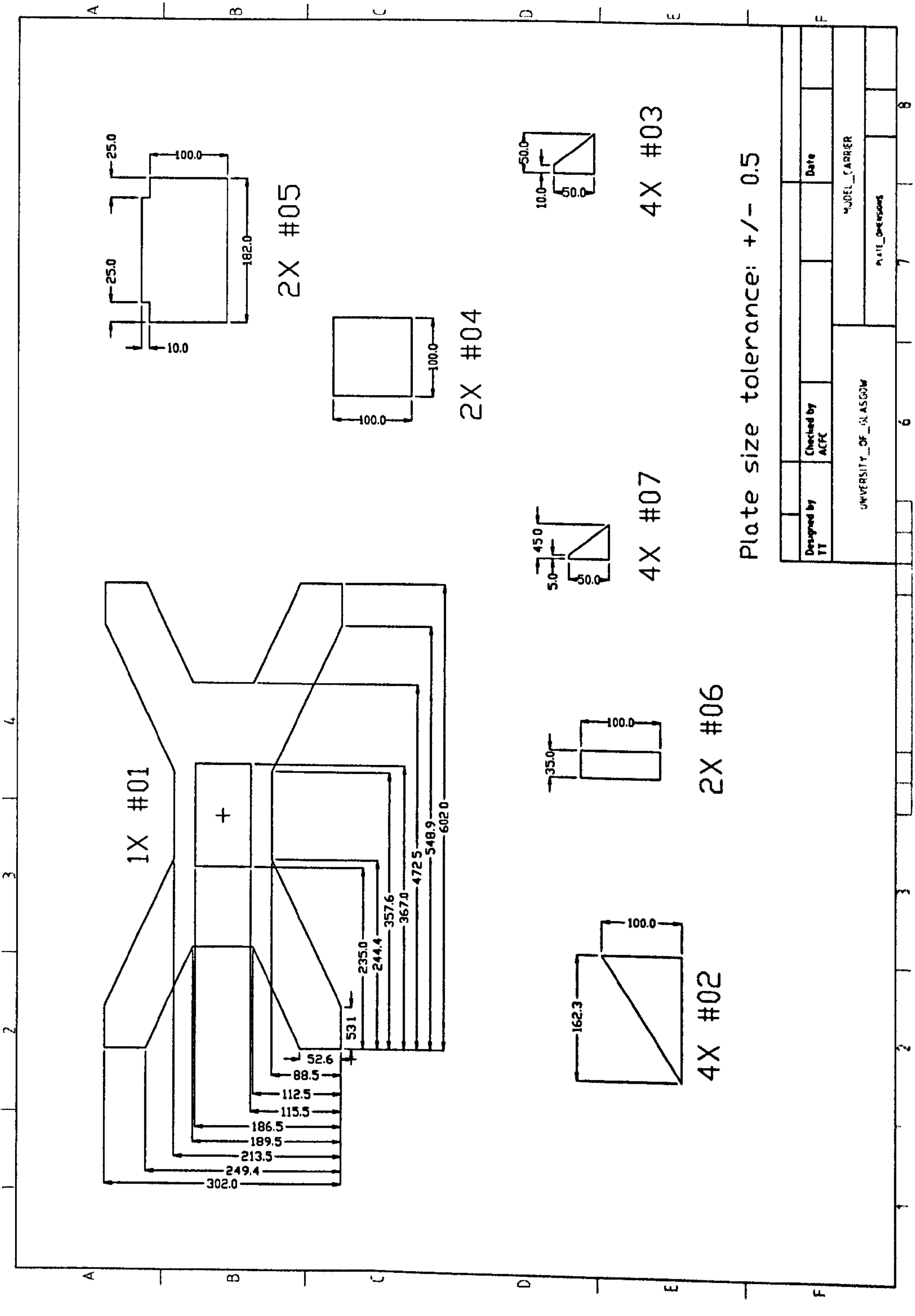
**APPENDIX B**

**TEST RIG MANUFACTURE DRAWINGS**

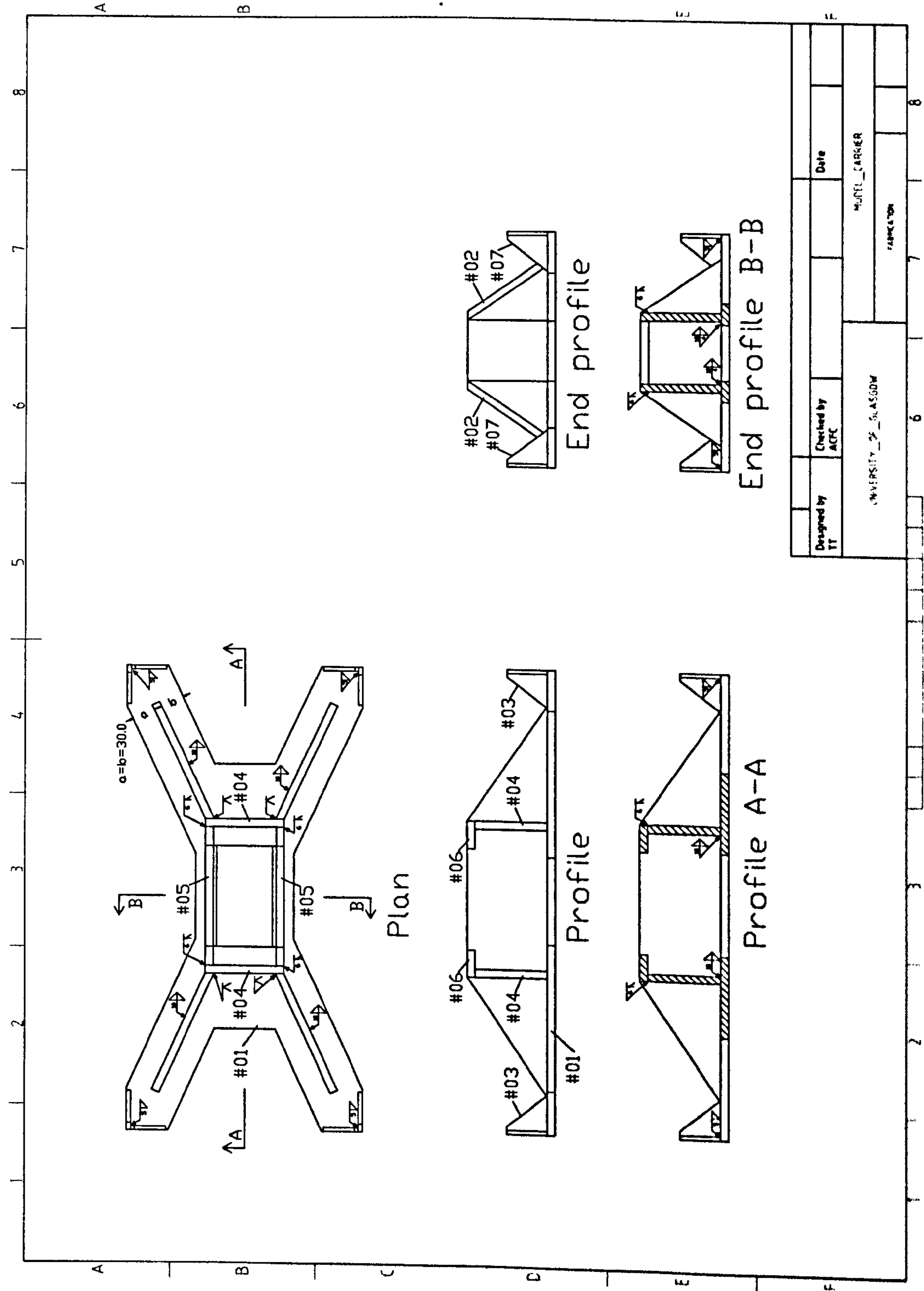
---

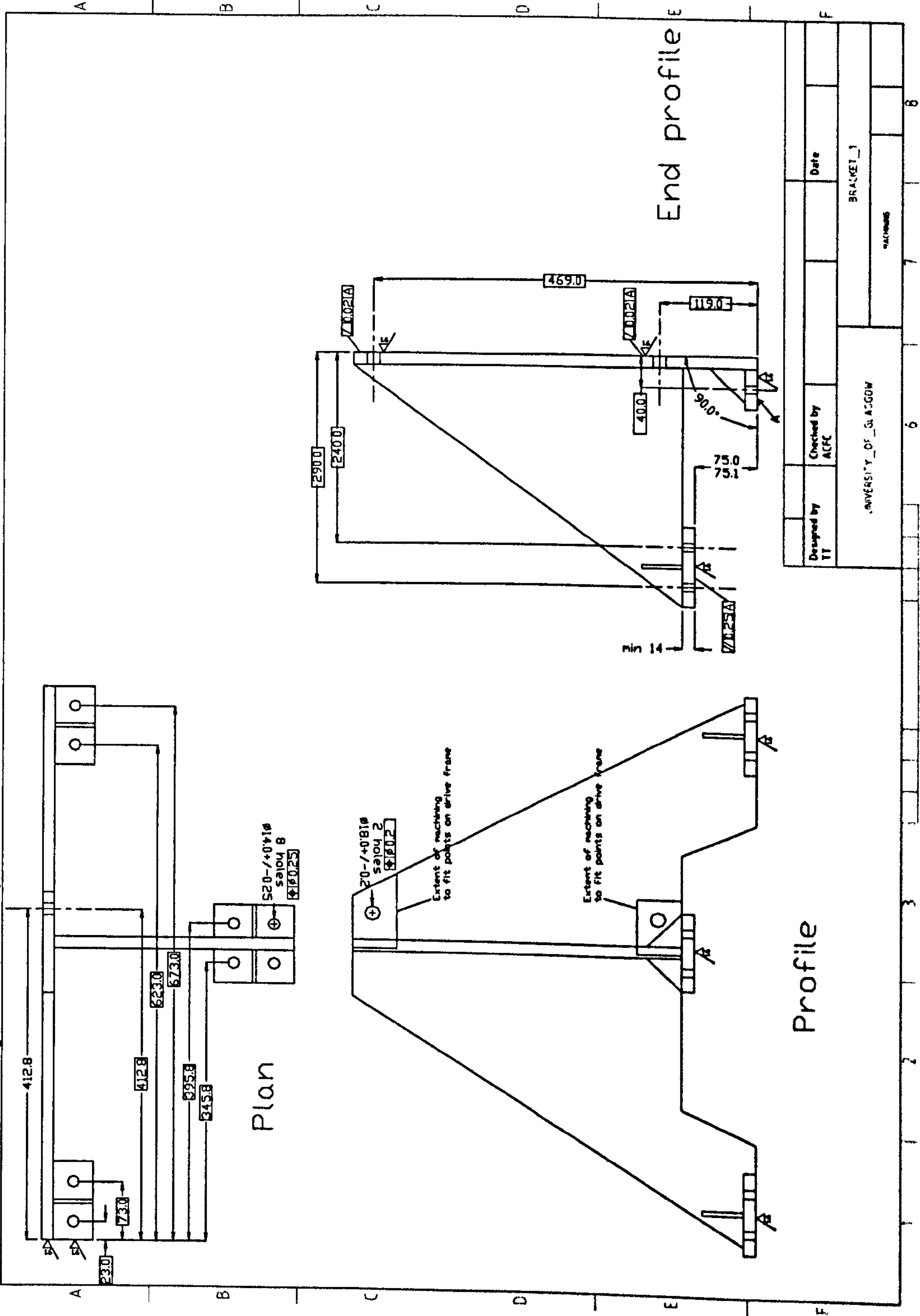




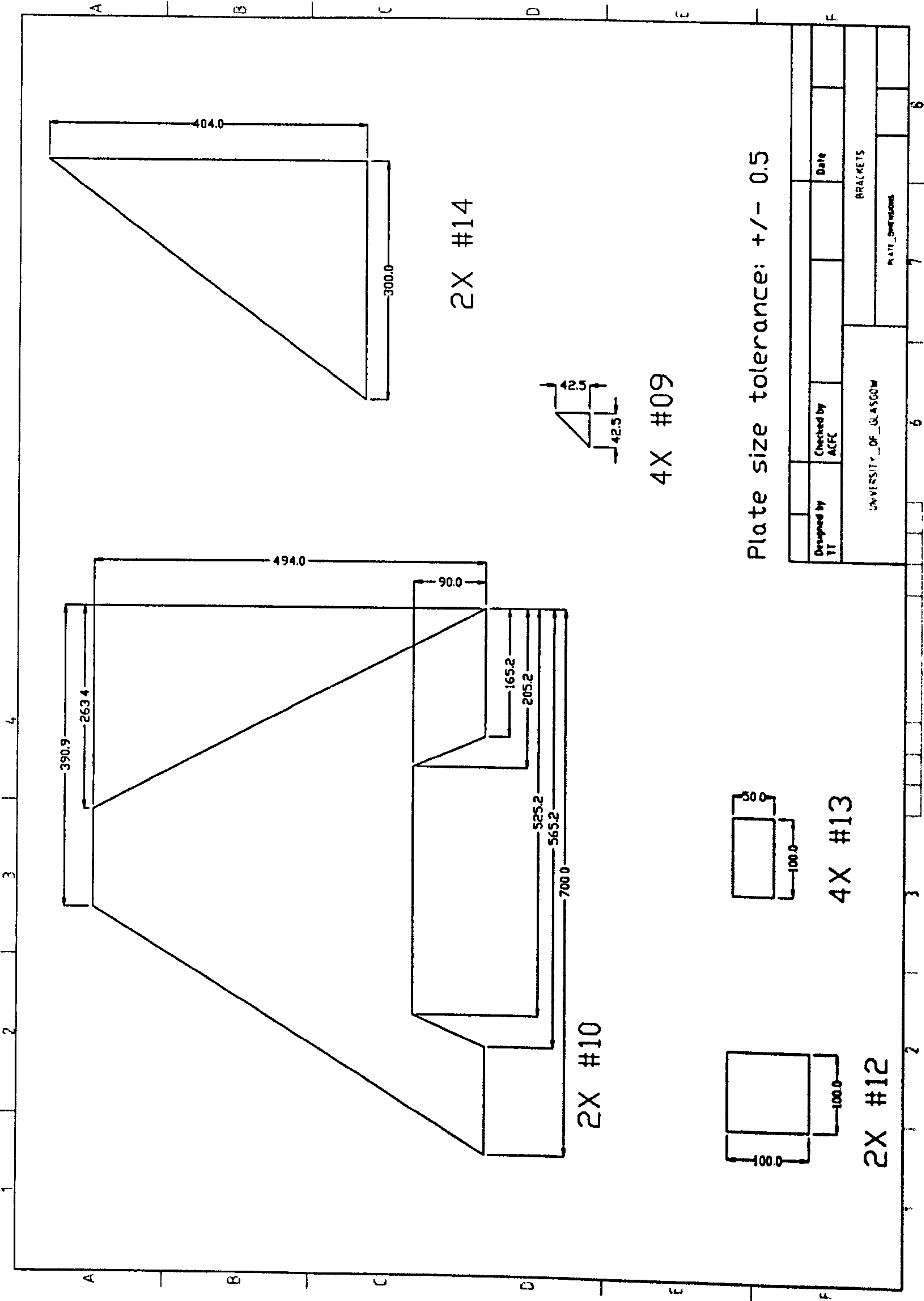


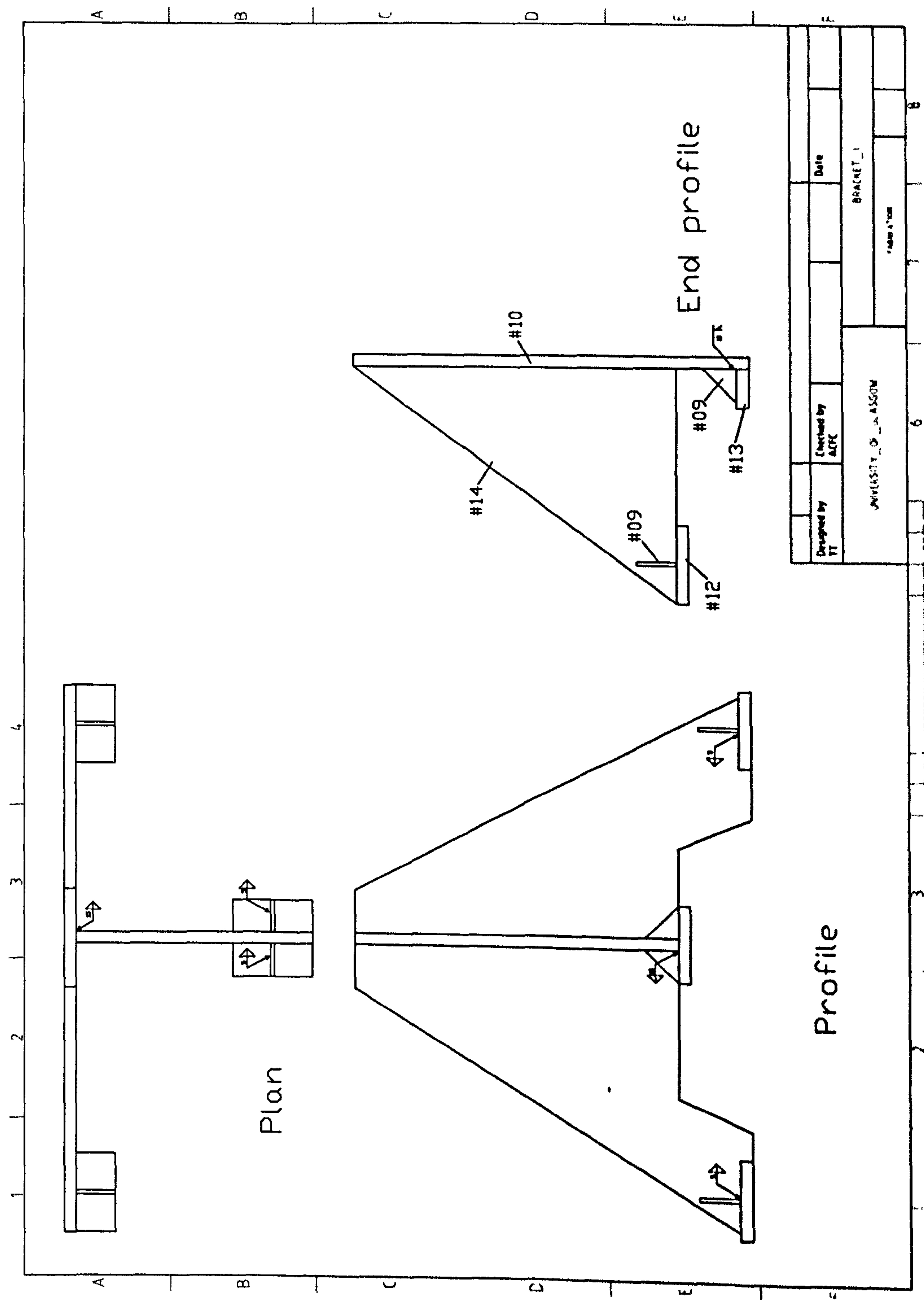






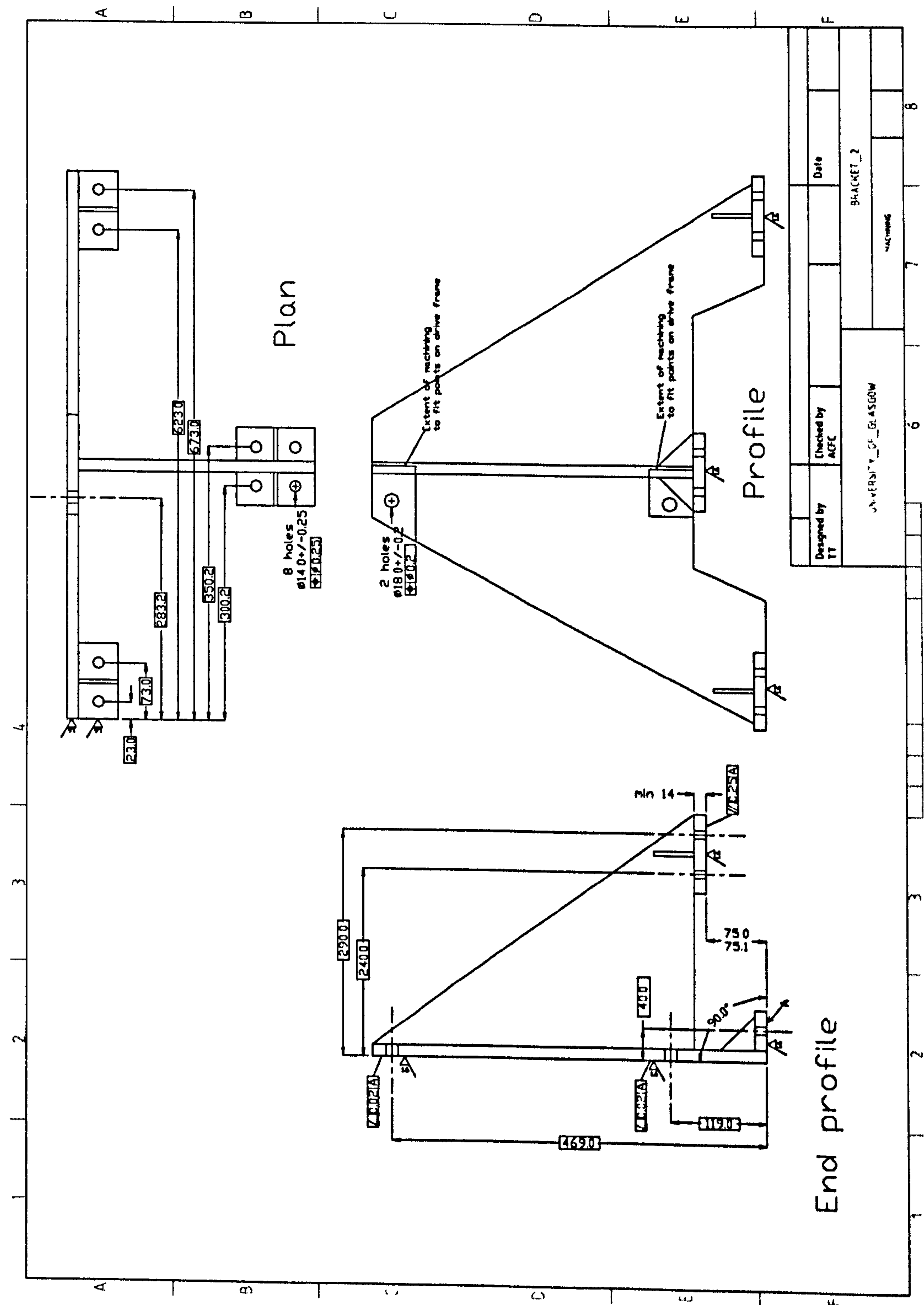


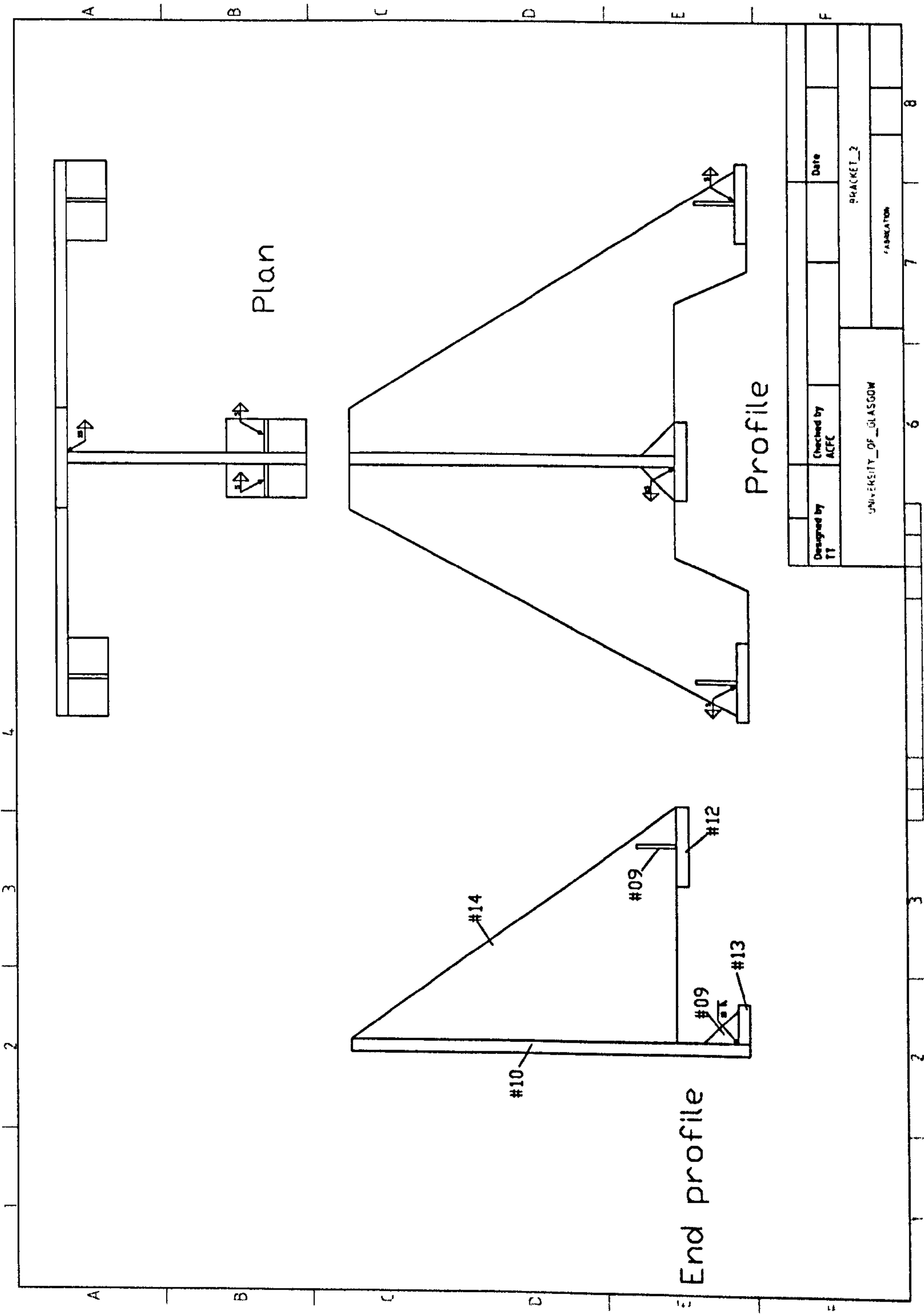




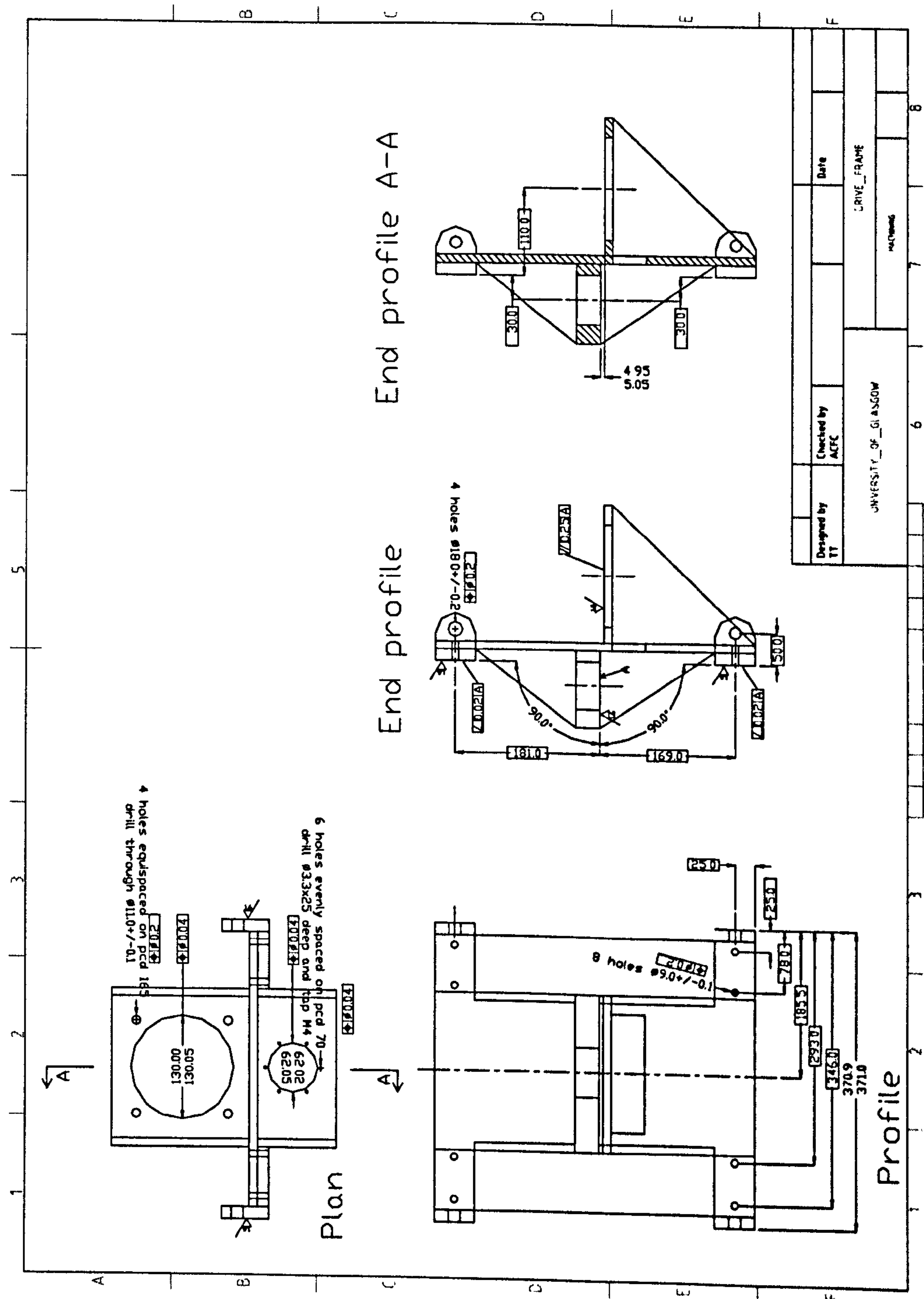
Drawn by	Checked by	Date	BRACKET 1	
TT	ACFC		UNIVERSITY OF ALABAMA	
			Revision	8

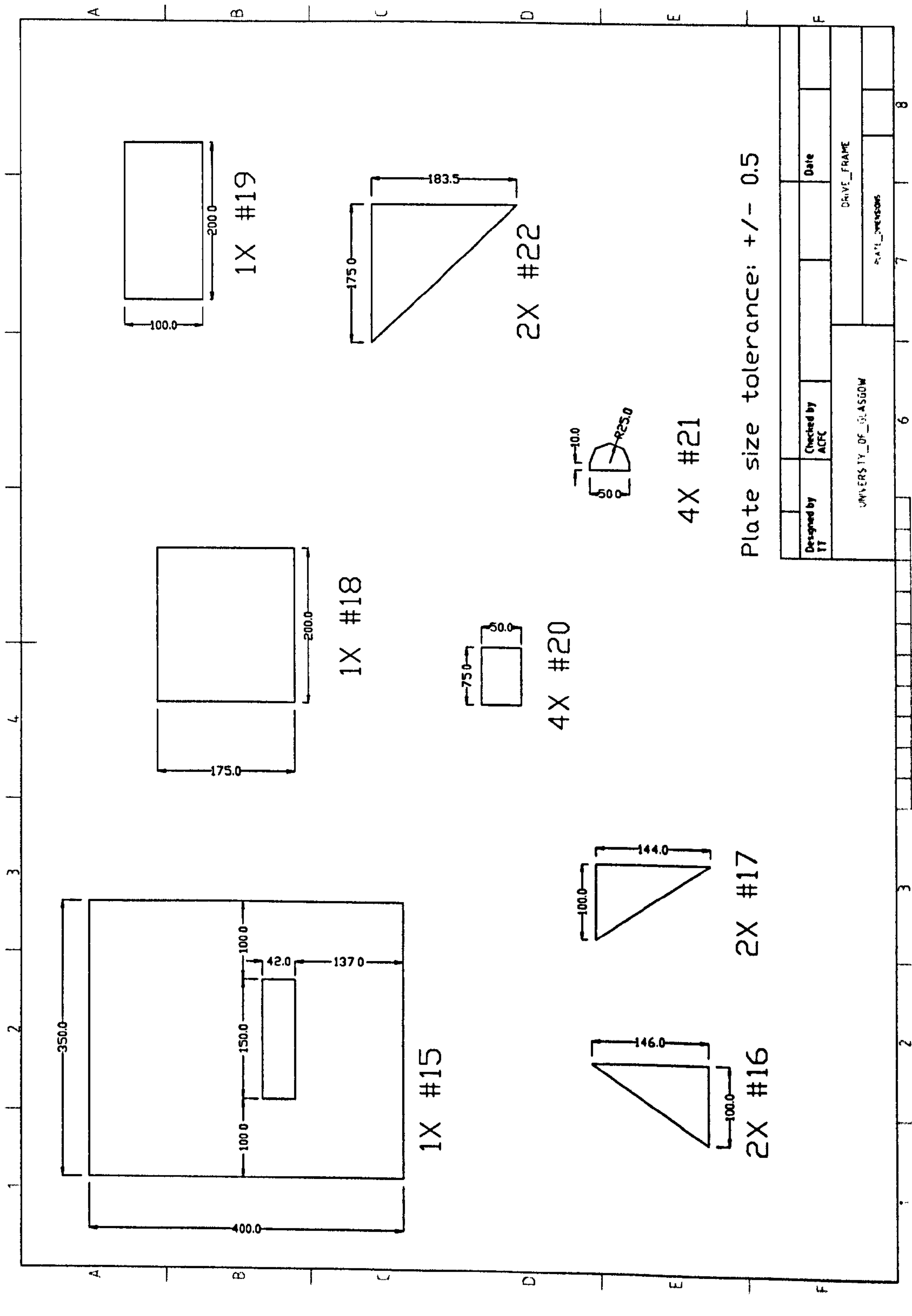




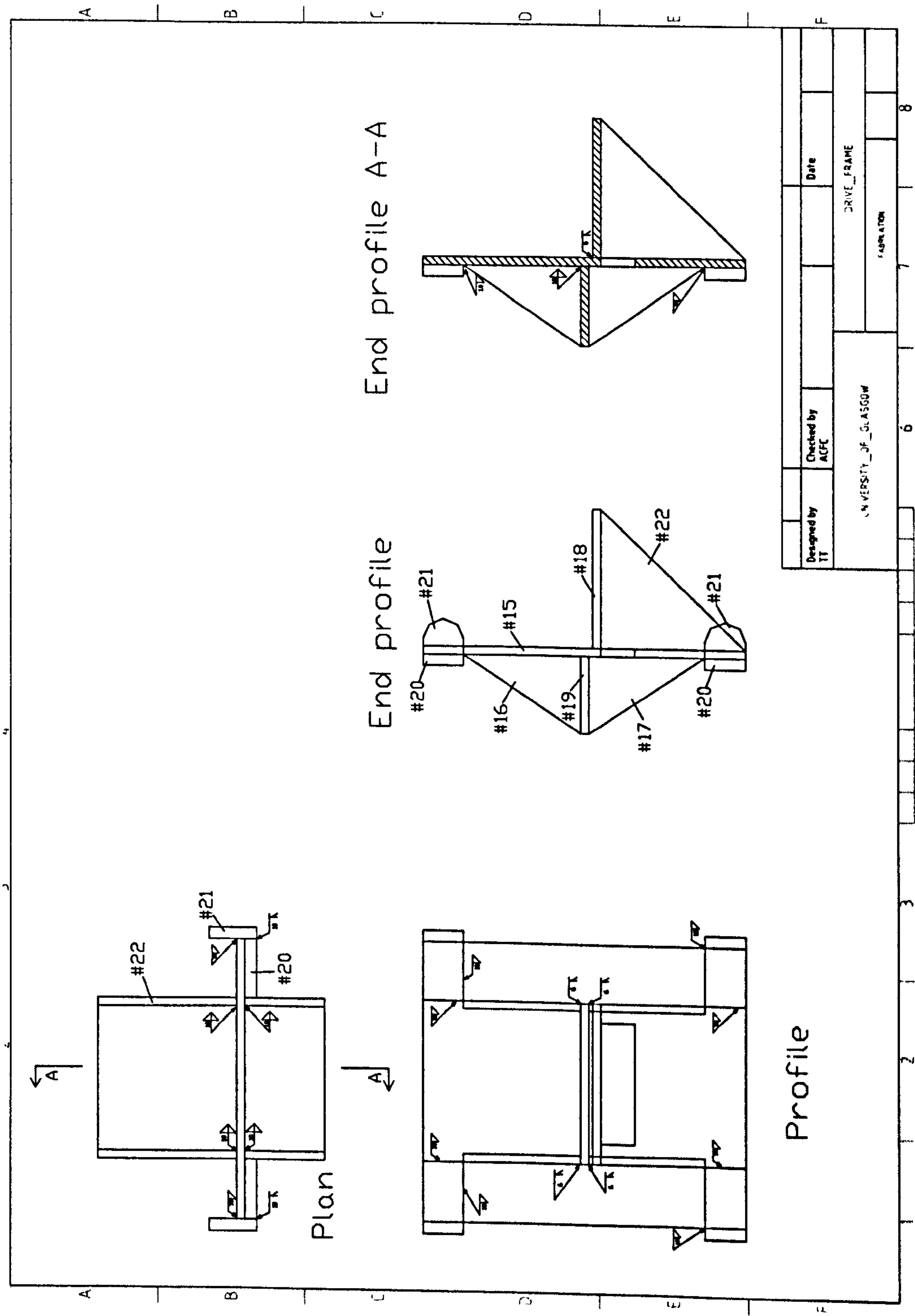


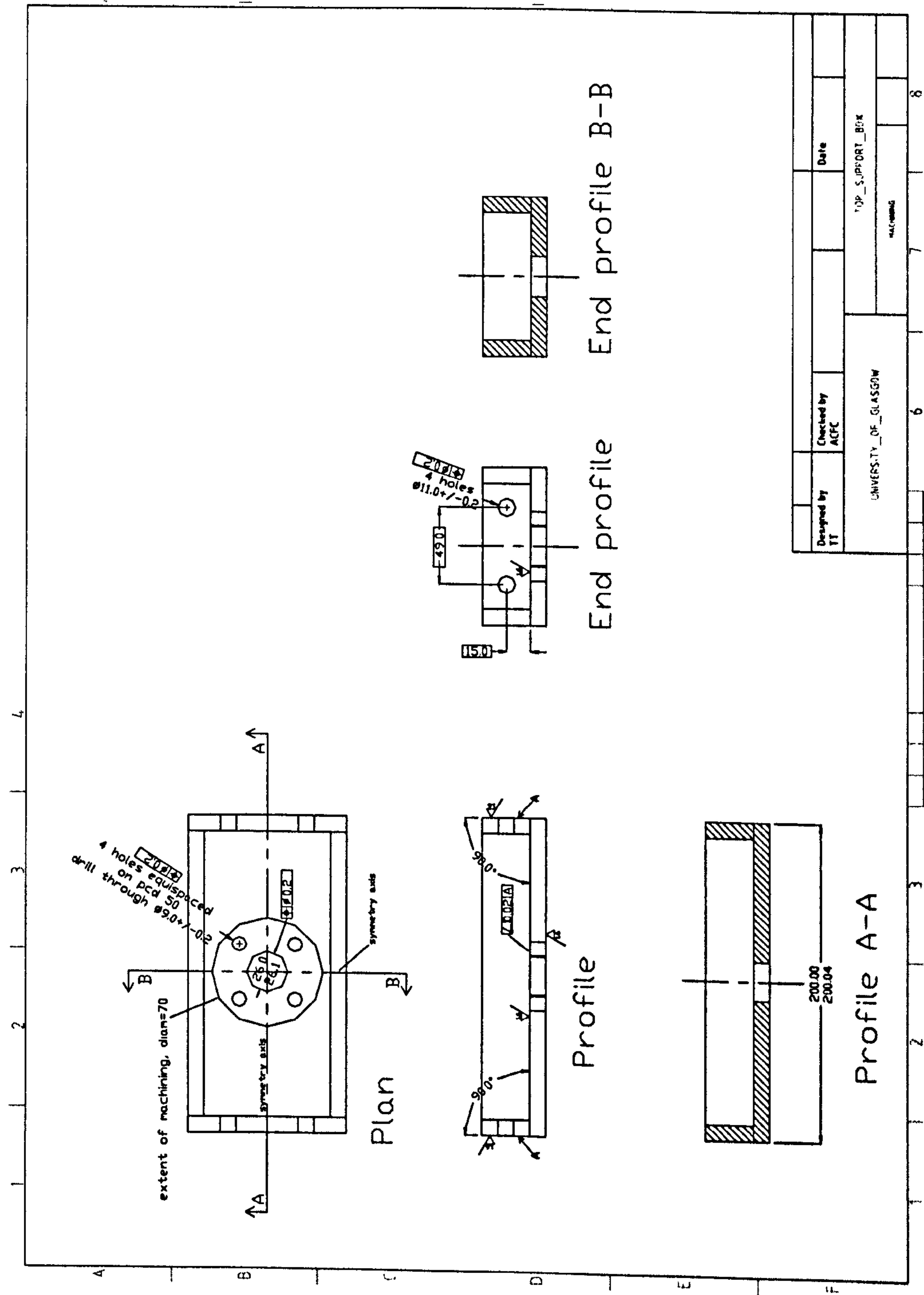




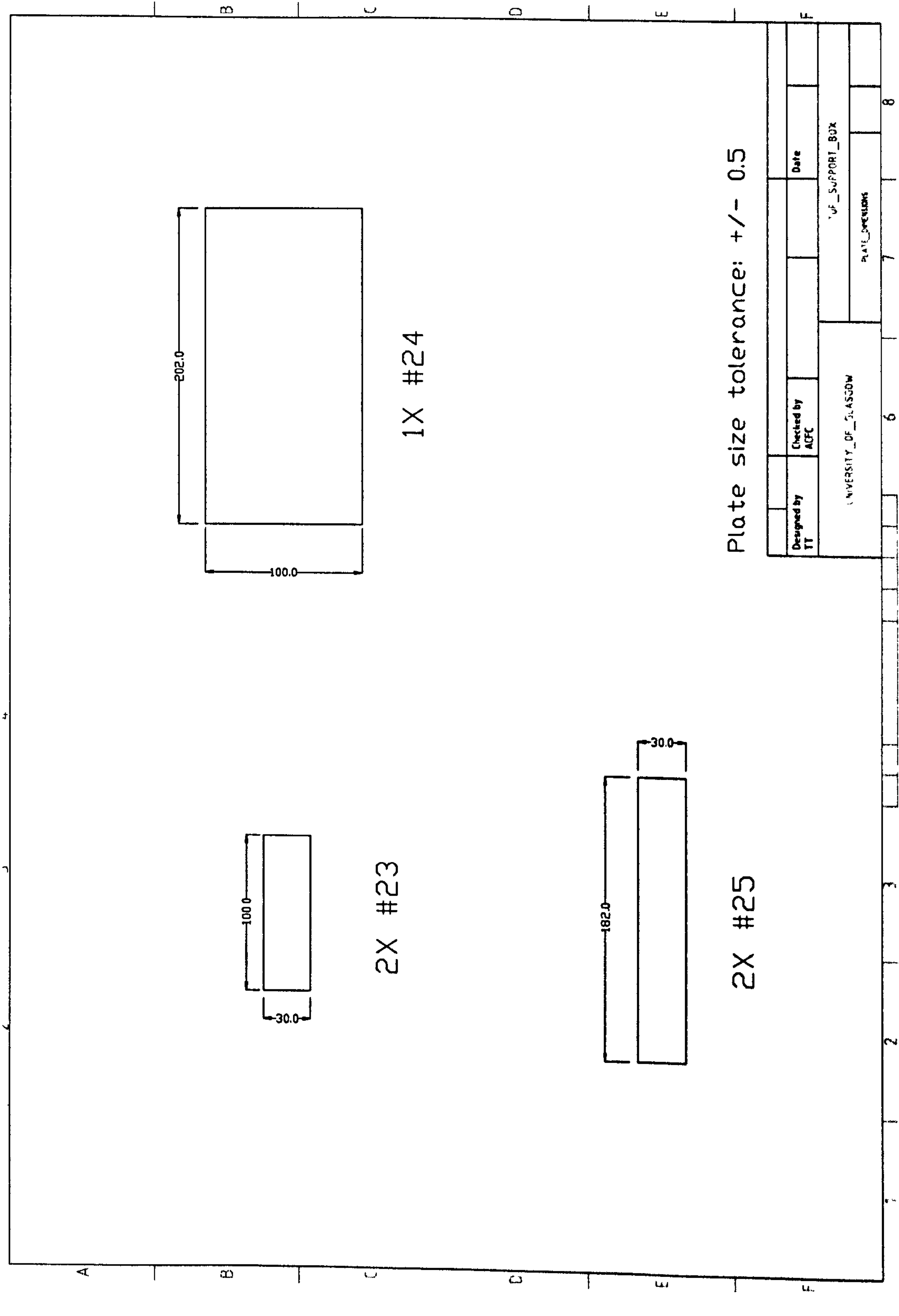




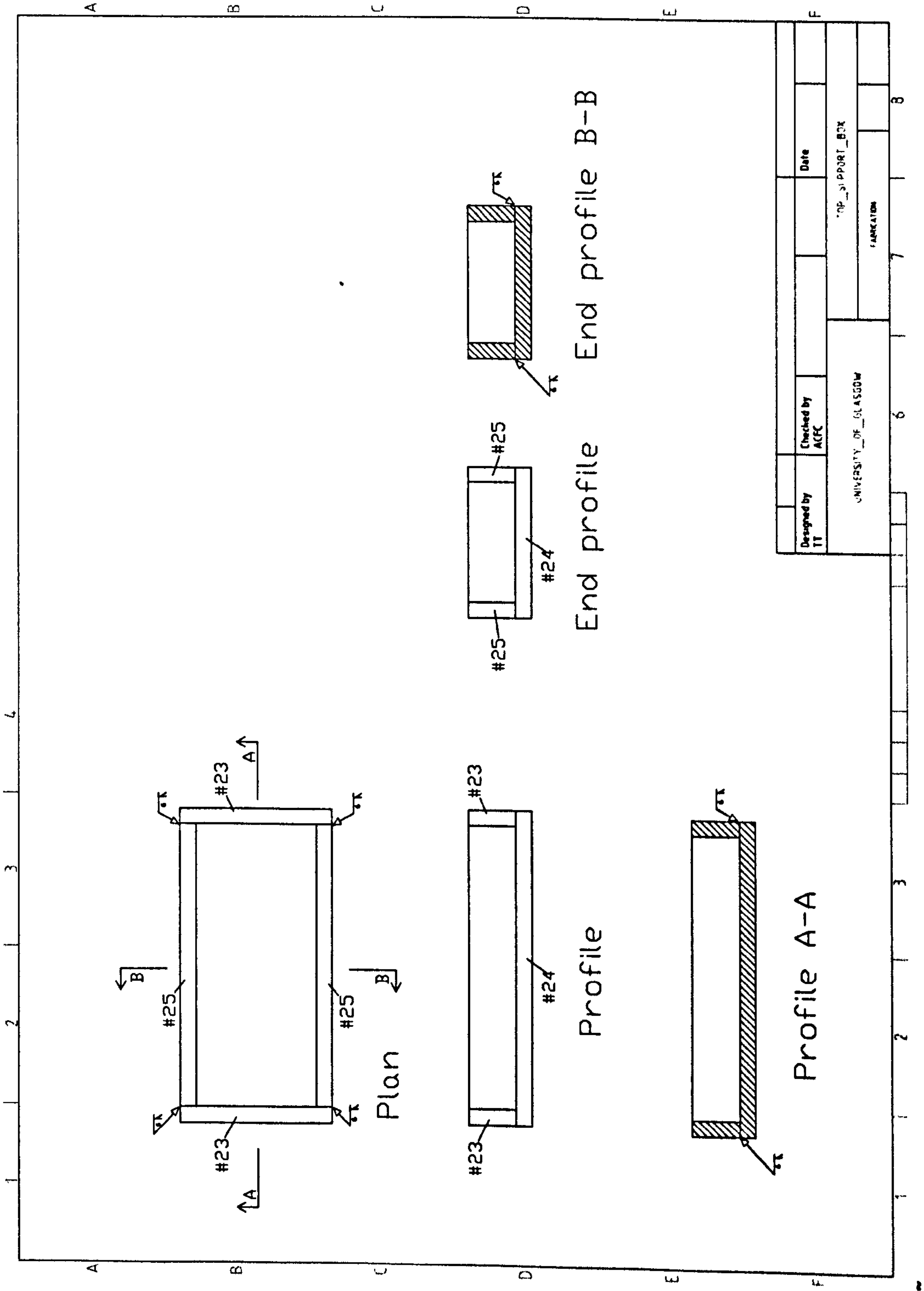




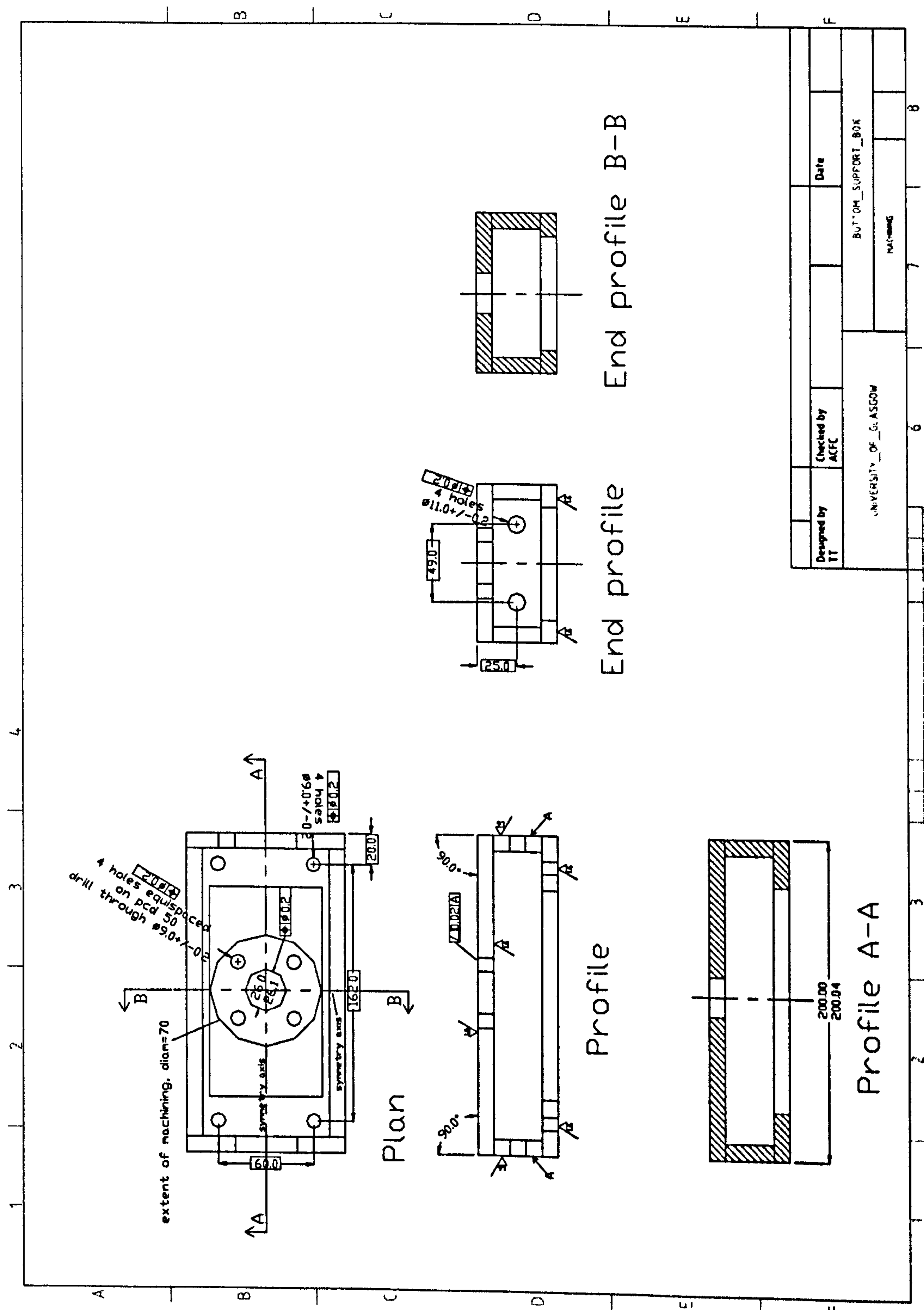


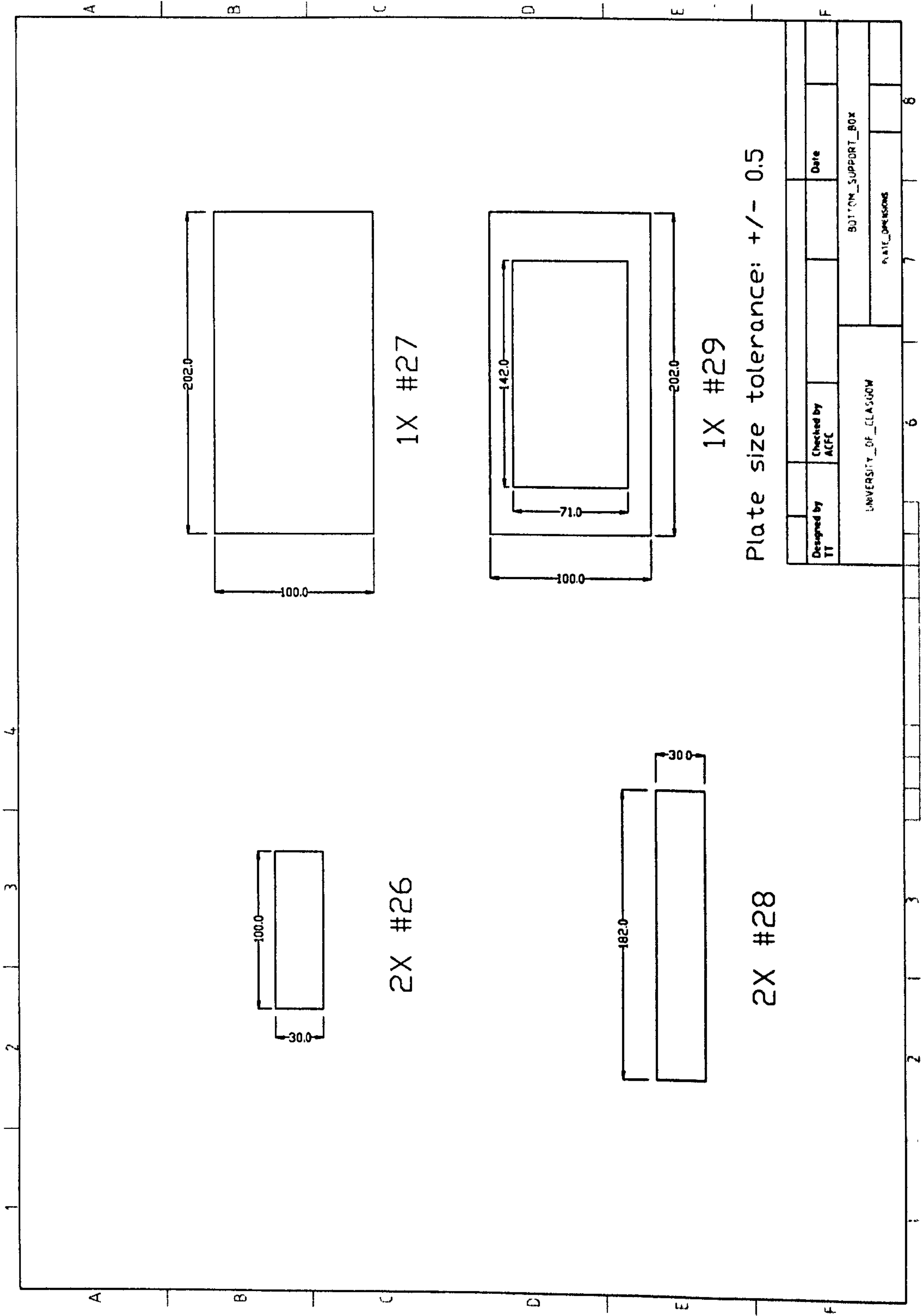


Designed by TT	Checked by AFC	Date	
UNIVERSITY OF GLASGOW		PLATE SPECIFICATIONS	
		UF_SUPPORT_BOX	

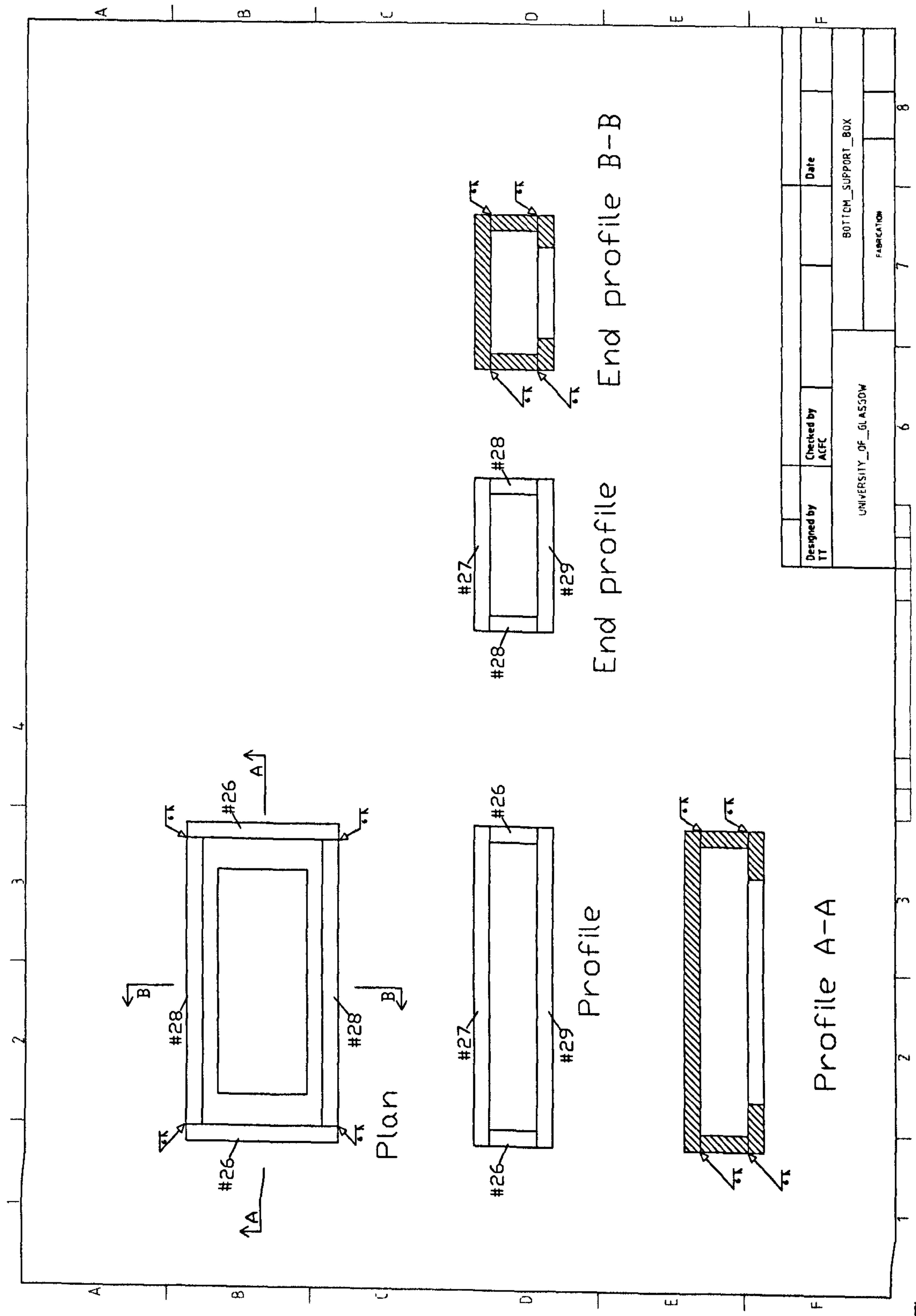


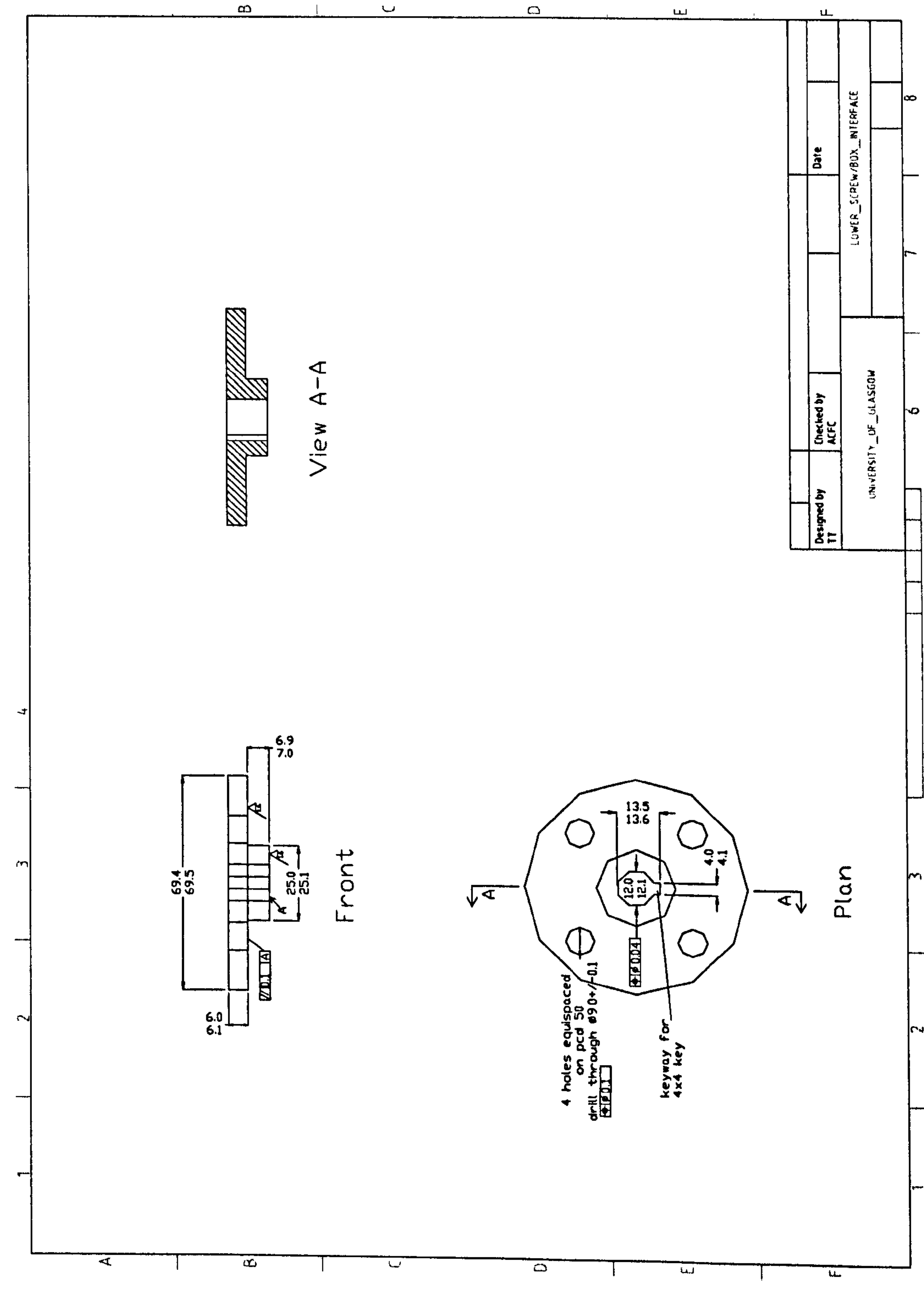




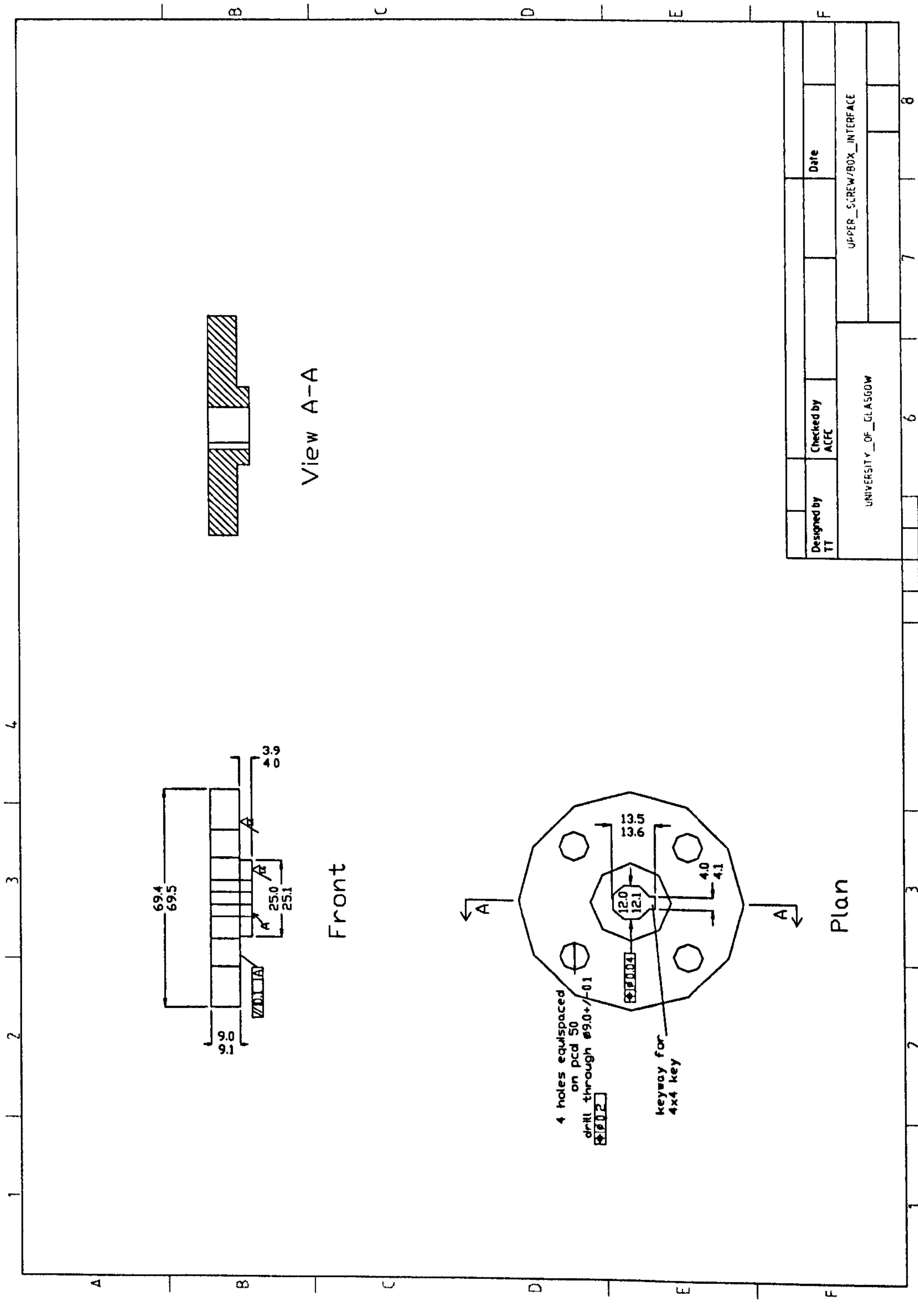












---

**APPENDIX C**

**TEST RIG EQUIPMENT SHEETS**

---



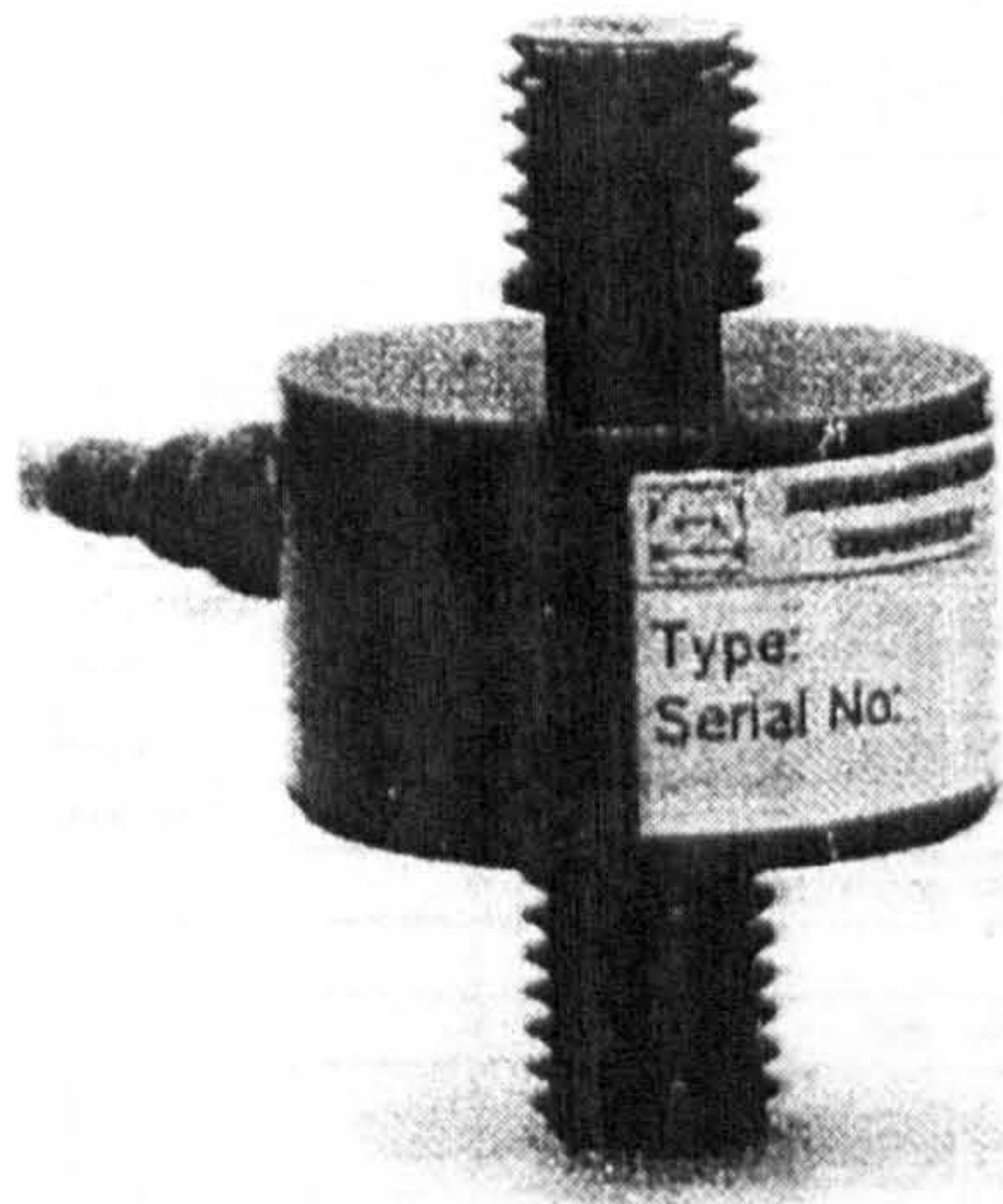
C.1. DDE1000 Load Cell – Datasheet

**GW**

**DDE** SERIES

MINIATURE LOW PROFILE  
TENSION & COMPRESSION

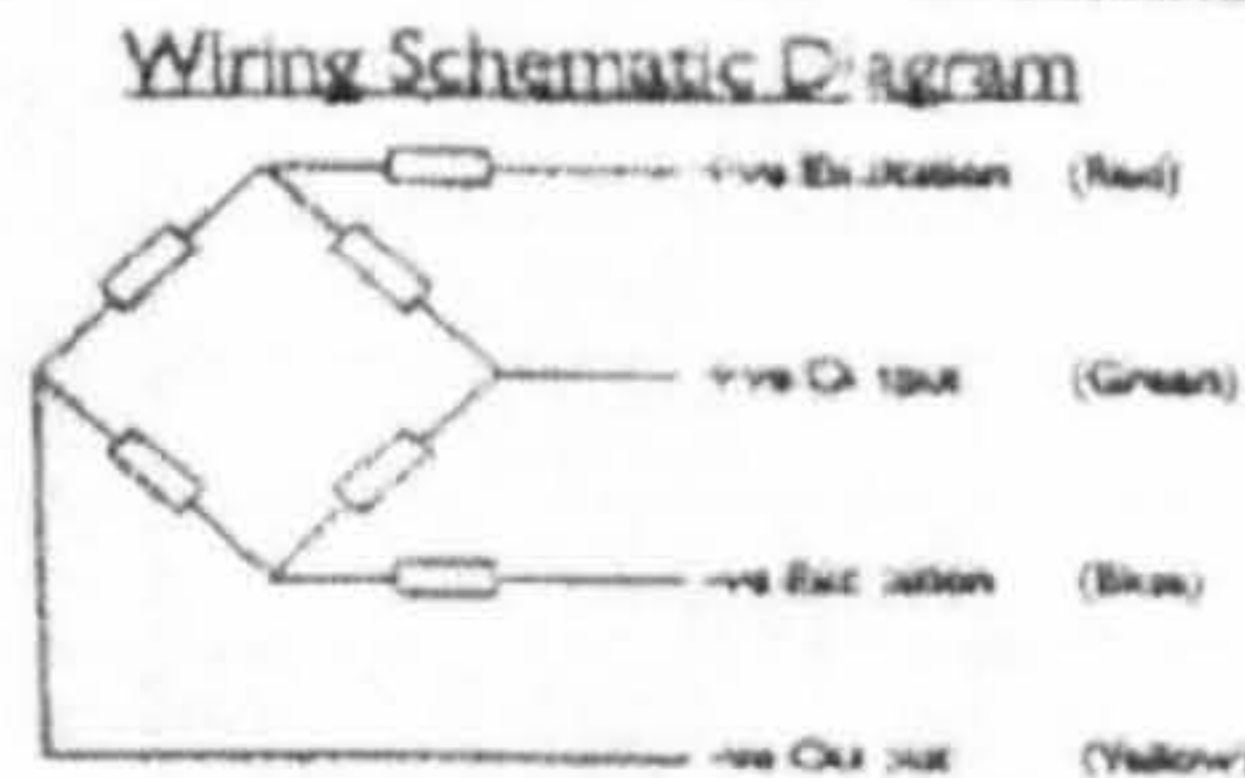
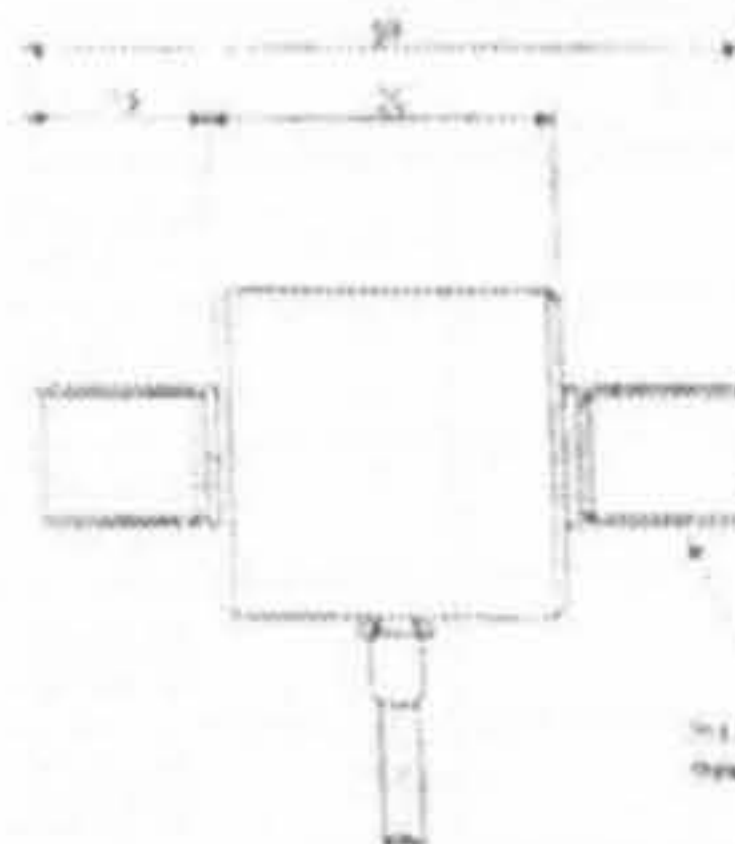
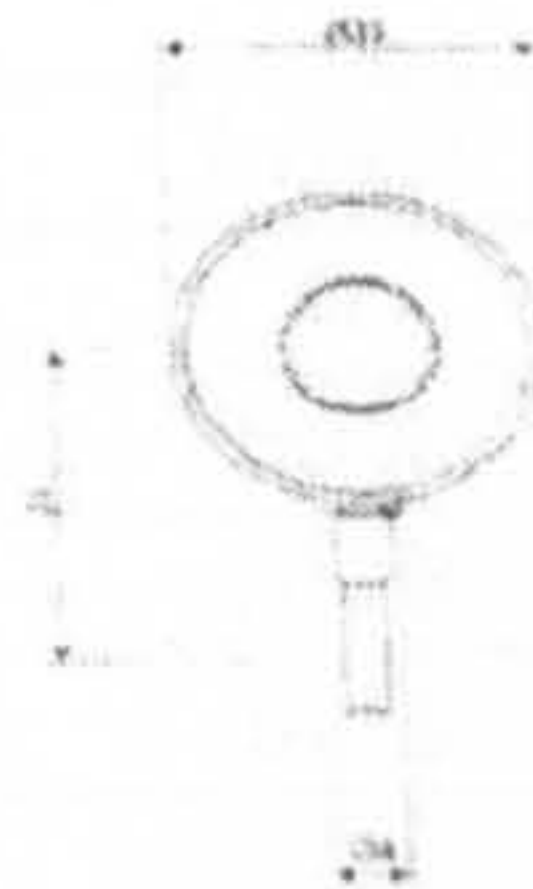
CAPACITIES AVAILABLE:  
10KG to 2 tonne (100N to 20kN)



The DDE range of low profile load cells are designed for the measurement of tensile or compressive forces.

The DDE design enables in-line mounting of the load cell in a variety of industrial, research and development applications. It's compact size makes it advantageous in applications where it is not possible to fit conventional load cells, i.e. "S" type load cells.

The low deflection and high natural frequency of the DDE offers particular benefits in material testing and cable monitoring applications.




**Specification**

Rated Capacities.....	100, 200, 500, 2000, 5000, 10000, 20000N
Rated Output.....	2.0mV/Vnominal
Zero Balance.....	±1% of rated output
Nonlinearity.....	±0.25% of rated output
Hysteresis.....	0.30% of rated output
Temperature effect on output.....	±0.005% of applied load/ °C
Temperature effect on zero.....	±0.005% of rated output/°C
Safe temperature range.....	-20°C to +80°C
Temperature compensated.....	0°C to +70°C
Safe overload.....	150% of rated capacity
Ultimate overload.....	200% of rated capacity
Input impedance.....	375ohm
Output impedance.....	350ohm
Insulation impedance.....	>500 megohms
Recommended excitation.....	10V DC/AC
Maximum excitation.....	15V DC/AC
Construction.....	N-2kN aluminium alloy, 5kN-20kN Stainless Steel
Environmental protection.....	IP65
Cable.....	2 Metre 4 core screened



C.2. Load Cell 1 – Calibration Sheet



**GRAHAM & WHITE INSTRUMENTS LTD.**

135 HATFIELD ROAD, ST. ALBANS, HERTFORDSHIRE, AL1 4LZ ENGLAND  
TEL: (01727) 859373  
FAX: (01727) 844272


Certificate of Test and Calibration

Calibration Record Number
8676

Serial No.	55764	Customer Order No.	ET-002
Type	DDE	Job No.	398

Load	Read 1.	Read 2.	.BSL	Error
0	0.000		0.000	0.000
50%	9.984		9.990	-0.006
100%	19.980		19.980	0.000
50%	9.989		9.984	0.005
0	0.000		0.000	0.000

Load Rating	1000N	Proof Rating	150%
Sensitivity	1.998mv/v	Linearity (FRO)	-0.030%
Input Resist	400Ω	Hysteresis (FRO)	0.025%
Output Resist	350Ω	Insulation Resist	<1000 MΩ
Zero	-0.075mv	Compensated temp. Range	As Spec.

Name	N.Brock
Signed	
Date	27/08/99

Colour Code	
Pos. Supply	Red
Neg. Supply	Blue
Pos. Output	Green
Neg. Output	Yellow



C.3. Load Cell 2 – Calibration Sheet



**GRAHAM & WHITE INSTRUMENTS LTD.**  
135 HATFIELD ROAD, ST. ALBANS, HERTFORDSHIRE, AL1 4LZ ENGLAND  
TEL: (01727) 859373 FAX: (01727) 844272


Certificate of Test and Calibration

Calibration Record Number
8677

Serial No. 55765	Customer Order No. ET-002
Type DDE	Job No. 398

Load	Read 1.	Read 2.	.BSL	Error
0	0.000		0.000	0.000
50%	10.004		10.010	-0.006
100%	20.020		20.020	0.000
50%	10.009		10.004	0.005
0	0.000		0.000	0.000

Load Rating	1000N	Proof Rating	150%
Sensitivity	2.002mv/v	Linearity (FRO)	-0.030%
Input Resist	400Ω	Hysteresis (FRO)	0.025%
Output Resist	350Ω	Insulation Resist	<1000 MΩ
Zero	-0.126mv	Compensated temp. Range	As Spec.

Name	N.Brock
Signed	
Date	27/08/99

Colour Code	
Pos. Supply	Red
Neg. Supply	Blue
Pos. Output	Green
Neg. Output	Yellow

C.4. Load Cell 3 – Calibration Sheet



**GRAHAM & WHITE INSTRUMENTS LTD.**

135 HATFIELD ROAD, ST. ALBANS, HERTFORDSHIRE, AL1 4LZ ENGLAND  
TEL: (01727) 859373      FAX: (01727) 844272


Certificate of Test and Calibration

Calibration Record Number
8678

Serial No. 55766	Customer Order No. ET-002
Type DDE	Job No. 398

Load	Read 1.	Read 2.	.BSL	Error
0	0.000		0.000	0.000
50%	9.996		9.991	-0.005
100%	19.982		19.982	0.000
50%	10.000		9.996	0.004
0	0.000		0.000	0.000


Load Rating	1000N	Proof Rating	150%
Sensitivity	1.998mv/v	Linearity (FRO)	-0.025%
Input Resist	400Ω	Hysteresis (FRO)	0.020%
Output Resist	350Ω	Insulation Resist	<1000 MΩ
Zero	-0.127mv	Compensated temp. Range	As Spec.

Name	N.Brock
Signed	
Date	27/08/99

Colour Code	
Pos. Supply	Red
Neg. Supply	Blue
Pos. Output	Green
Neg. Output	Yellow



C.5. Load Cell 4 – Calibration Sheet



**GRAHAM & WHITE INSTRUMENTS LTD.**  
135 HATFIELD ROAD, ST. ALBANS, HERTFORDSHIRE, AL1 4LZ ENGLAND  
TEL: (01727) 859373 FAX: (01727) 844272


Certificate of Test and Calibration

Calibration Record Number
8679

Serial No. 55767	Customer Order No. ET-002
Type DDE	Job No. 398

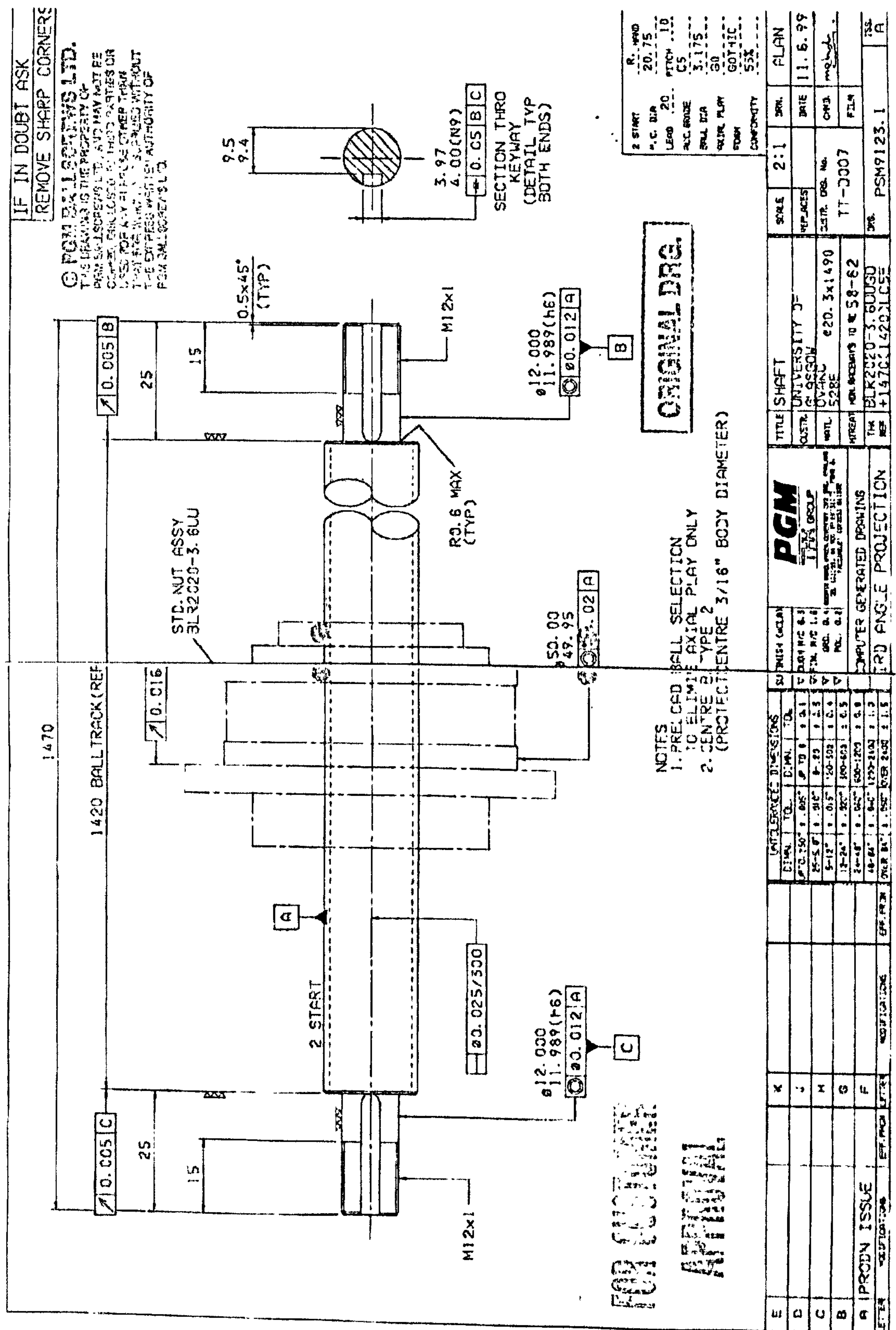
Load	Read 1.	Read 2.	.BSL	Error
0	0.000		0.000	0.000
50%	10.014		10.009	-0.005
100%	20.018		20.018	0.000
50%	10.019		10.014	0.005
0	0.000		0.000	0.000

Load Rating 1000N	Proof Rating 150%
Sensitivity 2.002mv/v	Linearity (FRO) -0.025%
Input Resist 400Ω	Hysteresis (FRO) 0.025%
Output Resist 350Ω	Insulation Resist <1000 MΩ
Zero -0.054mv	Compensated temp. Range As Spec.

Name	N.Brock
Signed	
Date	27/08/99

Colour Code	
Pos. Supply	Red
Neg. Supply	Blue
Pos. Output	Green
Neg. Output	Yellow

### C.6. Ball Screw – Drawing





C.7. Timing Belt Drive – Calculation

Data			
Power	6.28 KW		
Ratio	1.15 speed increase		
input speed	3000.00 RPM		
Calculated torque	n/a	Nm	
Stated max input torque	20.00 Nm		
duty cycle	Test rig, infrequent operation, heavy impact load		
centre distance	?	m	
driver type	Class 1		
load type	heavy shock		
basic service factor	1.70		
additional service factors			
idler?			
intermittent?			
speed increaser?	0.10		
Total service factor	1.80		
Design Power		11.31 KW	
pulley style	PGGT		
Pitch Size	8.00		
Smaller pulley	24.00 teeth		
Larger pulley	36.00 teeth		
smaller pulley power rating at	4500.00 rpm	=	11.3 W
Belt width factor	1.57	(30 MM BELT)	
smallest pulley rating	17.74 KW		
Pitch			8.00
No teeth large pulley			36.00
No teeth small pulley			24.00
Large pulley	Pitch dia	91.6733	
Small pulley	Pitch dia	61.1155	
Centre distance - nominal			32.000
Belt Cat No - if known	N/A		
MINIMUM CRITICAL DISTANCE BETWEEN PULLEYS			
(excluding flange diameters)			76.3944
Ratio			1.5000
Knowing belt length.			
Where belt length equals	800.0000	600	480
Centre distance equals	279.6433	179.4101	128
Teeth in mesh	11.56291425	11.31872	

C.8. Servomotor – Datasheet

Data	Sym	Dim	6SM27M-4000	6SM37S-6000	6SM37M-6000	6SM37L-4000	6SM37VL-6000	6SM37VL-6000-09	6SM47L-3000	6SM57S-3000	6SM57M-3000	6SM77K-3000	6SM77S-3000	6SM107K-3000	6SM107S-3000
Standstill torque	M <sub>0</sub>	Nm	0,32	0,5	1	1,5	3	3	3	4,6	8	11	17	26	32
Standstill current	I <sub>0rms</sub>	A	0,8	1	1,6	1,6	3,8	3,8	2,3	2,8	4,3	6	10	16	20
Rated speed	n <sub>n</sub>	min <sup>-1</sup>	4000	6000	6000	4000	6000	6000	3000	3000	3000	3000	3000	3000	3000
Torque constant	K <sub>Trms</sub>	Nm/A	0,41	0,5	0,62	0,96	0,79	0,79	1,33	1,65	1,85	1,85	1,70	1,6	1,6
Voltage constant	K <sub>Erms</sub>	mV/min	25	30	38	58	48	48	81	97	112	112	103	97	97
Mains voltage	U <sub>n</sub>	V	400 / 460												
Rated torque at n <sub>n</sub>	M <sub>n</sub>	Nm	0,3	0,4	0,8	1,2	2	2	2,2	3	6	8,5	12	20	23
Rated current	I <sub>n</sub>	A	0,75	0,95	1,5	1,5	2,8	2,8	2	2,7	4	5	8	14	16
Rated power	P <sub>n</sub>	kW	0,13	0,25	0,5	0,5	1,2	1,2	0,47	0,95	1,9	2,7	4	6,3	7,2
Peak current	I <sub>0max</sub>	A	3,5	4,0	6,5	6,4	15,2	15,2	9	11	17	24	40	70	85
Motor pole no.	P <sub>Mot</sub>	-	6												
Resolver pole no.	P <sub>Res</sub>	-	2												
Winding resistance Phase-Phase	R <sub>20</sub>	Ω	31	36	12,8	15,5	3,65	3,65	11	6,3	3,9	2,2	1,1	0,45	0,37
Winding inductance Phase-Phase	L	mH	21	32	21	30	8	8	25	35	24	18	8,3	4,4	3,6
Insulation class	-	-	F(DIN 57530)												
Switch point thermal contact	-	°C	145 ±5												
Design	-	-	IM B5(V1,V3), DIN 42950												
Rotor moment of inertia	J	kgcm <sup>2</sup>	0,08	0,45	0,7	1,0	1,6	1,6	1,6	3,1	4,5	12	18	82	104
Static friction torque	M <sub>R</sub>	Nm	0,02	0,02	0,02	0,03	0,05	0,05	0,05	0,12	0,15	0,25	0,30	0,40	0,50
Radial load permitted at shaft end with n <sub>n</sub>	F <sub>R</sub>	N	90	270	270	270	270	270	270	650	650	730	730	870	870
Axial load permitted at shaft end with n <sub>n</sub>	F <sub>A</sub>	N	30	90	90	90	90	90	90	180	180	210	210	360	360
Tolerance class flange	-	-	R, DIN 42955												
Vibration class	-	-	N, DIN ISO 2373												
Thermal time constant	t <sub>TH</sub>	min	10	10	15	15	15	15	15	20	20	25	30	30	40
Weight standard	G	kg	1,1	1,9	2,3	2,9	3,5	3,5	3,5	5,7	7,6	9,8	14	28	32,5
Order number standard	-	-	83212	83205	83207	83210	90702	90578	87528	87087	86477	87528	89835	89836	89837
EMV-RES connector	-	-	12 poles, round												
RES cable, shielded	-	mm <sup>2</sup>	4 x 2 x 0,25												
Power connection	-	plug	4 + 4-poles, angled												
Motor cable, shielded	-	mm <sup>2</sup>	4x1 or 4x1,5											4x1,5	4x2,5
Holding torque	M <sub>BR</sub>	Nm	1	2,5						6		12		20	
Operating voltage	U <sub>BR</sub>	V=	24 +6/-10%												
electrical power	P <sub>BR</sub>	W	8	14						16		18		22	
Moment of inertia	J <sub>BR</sub>	kgcm <sup>2</sup>	0,07	0,38						1,08		3,6		9,5	
Release delay time	t <sub>BRH</sub>	ms	15-20	10-15						10-30		30-60		20-60	
Application delay time	t <sub>BRL</sub>	ms	5-10	10-15						5-15		10-20		10-35	
Weight of the brake	G <sub>BR</sub>	kg	0,3	0,4						0,6		1,5		3,3	
Motor cable with brake, shielded	-	mm <sup>2</sup>	4x1 + 2x0,75 or 4x1,5 + 2x0,75											4x1,5+ 2x0,75	4x2,5 + 2x1
Order number with -G-	-	-	83213	83206	83209	83211	90703	90673	87529	86792	87088	87527	89864	89865	89866



C.9. Digital Servo Amplifier – Datasheet

		SERVOSTAR™					
Rated data	DIM	601	603	606	610	614	620
Rated supply voltage	V~	3 x 230V <sub>-10%</sub> ... 480V <sub>-10%</sub> , 50 ... 60 Hz					
Rated installed load for S1 operation	kVA	1	2	4	7	10	14
Rated DC-link voltage	V=	310 - 675					
Rated output current (rms value, ± 3%)	A <sub>rms</sub>	1,5	3	6	10	14	20
Peak output current (max. ca. 5s, ± 3%)	A <sub>rms</sub>	3	6	12	20	28	40
Clock frequency of the output stage	kHz	8					
Technical data for regen circuit	—	⇒ 1.10					
Overvoltage protection treshold	V	450...900					
Form factor of the output current (at rated data and min. load inductance)	—	1.01					
Bandwidth of subordinate current control- ler	kHz	> 1,2					
Residual voltage drop at rated current	V	5					
Quiescent dissipation, output stage dis- abled	W	15					
Dissipation at rated current (incl. power supply losses, without regen dissipation)	W	30	40	60	90	160	200
Internal fusing (external fusing ⇒ 1.7.1)							
Auxiliary supply 24V	—	internal 3,15 AT					
Regen resistor	—	Internal, electronic					
Inputs							
Setpoint 1/2, resolution 14bit/12bit	V	±10					
Common-mode voltage max.	V	±10					
Input resistance	kΩ	20					
Digital inputs	V	low 0...7 / high 12...36					
	mA	7					
Aux. power supply, electrically isolated without brake	V	20...36					
	A	1					
Aux. power supply, electrically isolated with brake	V	24 (-0% +15%)					
	A	3					
Max. output current, brake	A	2					
Connections							
Control signals	—	Combicon 5,08 / 18 pole , 2,5mm²					
Power signals	—	Power Combicon 7,62 / 4x4 + 1x6-pole, 4mm²					
Resolver input	—	SubD 9pole (socket)					
Sine-cosine encoder input	—	SubD 15pole (socket)					
PC-interface, CAN	—	SubD 9pole (plug)					
Encoder emulation, ROD/SSI	—	SubD 9pole (plug)					
Mechanical							
Weight	kg	4				5	7,5
Height without connectors	mm	275					
Width	mm	70				100	120
Depth without connectors	mm	265					

External fusing

Fusible cutouts or similar	SERVOSTAR™ 601 / 603	SERVOSTAR™ 606 / 610	SERVOSTAR™ 614 / 620
AC supply F <sub>N1/2/3</sub>	6 AT	10 AT	20 AT
24V supply F <sub>H1/2</sub>	max. 16 AF		
Regen resistor F <sub>B1/2</sub>	4 AF	6 AF	6 AF

---

## LIST OF FIGURES

---

Figure 1-1.	Forces acting on a planing craft.	20
Figure 3-1.	The analogy of the impact/water entry and the planing phenomena.	31
Figure 4-1.	Control volume for conservation of mass.	59
Figure 4-2.	Control volume for conservation of momentum.	59
Figure 4-3.	Simulation domain.	64
Figure 4-4.	Grid topology for 15 to 60 degrees deadrise simulations.	66
Figure 4-5.	Grid close to a wedge of 30 degrees deadrise.	66
Figure 4-6.	Grid topology for 0 to 10 degrees deadrise simulations.	68
Figure 4-7.	Non-dimensional water entry force, flat-bottomed section, zero gravity.	73
Figure 4-8.	Non-dimensional water entry force, 5 degree wedge section.	73
Figure 4-9.	Non-dimensional water entry force, 10 degree wedge section.	74
Figure 4-10.	Non-dimensional water entry force, 15 degree wedge section.	74
Figure 4-11.	Non-dimensional water entry force, 30 degree wedge section.	75
Figure 4-12.	Non-dimensional water entry force, 45 degree wedge section.	75
Figure 4-13.	Non-dimensional pressure along wedge surface.	76



Figure 4-14.	5 degree wedge.	78
Figure 4-15.	10 degree wedge.	78
Figure 4-16.	15 degree wedge.	78
Figure 4-17.	30 degree wedge.	79
Figure 4-18.	45 degree wedge.	79
Figure 4-19.	60 degree wedge.	79
Figure 4-20.	5 degree wedge section at 0.5m/s.	81
Figure 4-21.	5 degree wedge section at 1.0m/s.	82
Figure 4-22.	5 degree wedge section at 1.5m/s.	83
Figure 4-23.	5 degree wedge section at zero gravity.	84
Figure 4-24.	10 degree wedge section at 0.5m/s.	85
Figure 4-25.	10 degree wedge section at 1.0m/s.	86
Figure 4-26.	10 degree wedge section at 1.5m/s.	87
Figure 4-27.	10 degree wedge section at zero gravity.	88
Figure 4-28.	15 degree wedge section at 0.5m/s.	89
Figure 4-29.	15 degree wedge section at 1.0m/s.	90
Figure 4-30.	15 degree wedge section at 1.5m/s.	91
Figure 4-31.	15 degree wedge section at zero gravity.	92
Figure 4-32.	30 degree wedge section at 0.5m/s.	93
Figure 4-33.	30 degree wedge section at 1.0m/s.	94
Figure 4-34.	30 degree wedge section at 1.5m/s.	95

Figure 4-35.	30 degree wedge section at zero gravity.	96
Figure 4-36.	45 degree wedge section at 0.5m/s.	97
Figure 4-37.	45 degree wedge section at 1.0m/s.	98
Figure 4-38.	45 degree wedge section at 1.5m/s.	99
Figure 4-39.	45 degree wedge section at zero gravity.	100
Figure 4-40.	Buoyancy ratios extracted from the CFD results.	102
Figure 4-41	buoyancy ratio for 15 degree, 0.5m/s case.	104
Figure 4-42.	Curve fitting to the average buoyancy ratio data.	106
Figure 5-1.	Experimental set-up.	109
Figure 5-2.	Side views of the test rig.	110
Figure 5-3.	Front and back views of test rig.	111
Figure 5-4.	Design case - load against immersion.	113
Figure 5-5.	Servomotor.	116
Figure 5-6.	Digital servo amplifier.	116
Figure 5-7.	Nut rotating ball screw unit.	117
Figure 5-8.	Ball nut / ball bearing construction.	118
Figure 5-9.	Timing belt drive by davall gears.	119
Figure 5-10.	Linear ball bearing.	120
Figure 5-11.	Shaft support block.	120
Figure 5-12.	Drive assembly frame.	121
Figure 5-13.	Support bracket.	121



Figure 5-14.	Upper assembly bar.	122
Figure 5-15.	Lower assembly bar.	122
Figure 5-16.	Upper assembly bar/ball screw interface.	123
Figure 5-17.	Lower assembly bar/ball screw interface.	123
Figure 5-18.	Box section.	124
Figure 5-19.	Wedge sections.	124
Figure 5-20.	Model carrier.	126
Figure 5-21.	Tension/compression load cell, dde1000.	127
Figure 5-22.	Data acquisition by strawberry tree.	127
Figure 5-23.	Ball nut bearing spigotted into, and linear ball bearings bolted onto drive assembly frame.	134
Figure 5-24.	Shaft, support blocks and threaded shaft mounted on the upper assembly bar.	135
Figure 5-25.	Ball nut bearing flange screwed into the drive frame and pulley bolted to ball nut.	135
Figure 5-26.	Motor pulley and timing belt.	136
Figure 5-27.	Drive frame bolted on support frames.	136
Figure 5-28.	Fully assembled test rig on support structure above the test tank.	137
Figure 5-29.	Model carrier and transparent plates.	138
Figure 5-30.	Attachment of box section to model carrier via load cells.	139
Figure 5-31.	Attachment of wedge section to box section	

by band strapping.	139
Figure 5-32. Fully assembled rig with model carrier mounted on lower assembly bar, control station in the background.	140
Figure 5-33. Assembled rig from reverse angle.	141
Figure 5-34. Graphical user interface for operation of servostar digital servo amplifier.	142
Figure 5-35. Control position on main carriage.	143
Figure 5-36. Lower limit switch.	146
Figure 5-37. Upper limit switch and magnet on assembly bar.	146
Figure 5-38. At initial position.	149
Figure 5-39. After some immersion.	149
Figure 5-40. At initial position.	150
Figure 5-41. After some exit travel.	150
Figure 5-42. Evaluation of velocity integration method for position tracking.	154
Figure 5-43. Frictional force component.	155
Figure 5-44. Force readings from four tests with 5 degrees wedge at 0.94 m/s.	158
Figure 5-45. 5 degree constant velocity water entry at 0.24m/s.	159
Figure 5-46. 5 degree constant velocity water entry at 0.48m/s.	159
Figure 5-47. 5 degree constant velocity water entry at 0.94m/s.	160
Figure 5-48. 10 degree constant velocity water entry at 0.48m/s.	160



Figure 5-49.	10 degree constant velocity water entry at 0.72m/s.	161
Figure 5-50.	10 degree constant velocity water entry at 0.94m/s.	161
Figure 5-51.	15 degree constant velocity water entry at 0.48m/s.	162
Figure 5-52.	15 degree constant velocity water entry at 0.72m/s.	162
Figure 5-53.	15 degree constant velocity water entry at 0.94m/s.	163
Figure 5-54.	30 degree constant velocity water entry at 0.48m/s.	163
Figure 5-55.	30 degree constant velocity water entry at 0.72m/s.	164
Figure 5-56.	30 degree constant velocity water entry at 0.94m/s.	164
Figure 5-57.	45 degree constant velocity water entry at 1.19m/s.	165
Figure 5-58.	Total measured force and inertia force associated with velocity fluctuations from 0.48m/s test with 5 degrees section.	166
Figure 5-59.	Timing belt spring rate curve.	167
Figure 5-60.	0 degree wet chines oscillation, $z=0.18-0.23\text{m}$ .	170
Figure 5-61.	15 degree wet chines oscillation, $z=0.25-0.30\text{m}$ .	170
Figure 5-62.	45 degree wet chines oscillation, $z=0.48-0.53\text{m}$ .	171
Figure 5-63.	15 degree dry chines oscillation, $z=0.01-0.06\text{m}$ .	171
Figure 5-64.	15 degree dry chines oscillation, $z=0.02-0.04\text{m}$ .	172
Figure 5-65.	45 degree dry chines oscillation, $z=0.05-0.25\text{m}$ .	172
Figure 5-66.	45 degree dry chines oscillation, $z=0.20-0.25\text{m}$ .	173
Figure 5-67.	15 degree accelerated water entry, $a=0.83\text{m/s}^2$ .	174
Figure 5-68.	15 degree accelerated water entry, $a=3.33\text{m/s}^2$ .	174

Figure 5-69.	30 degree accelerated water entry, $a=2.50\text{m/s}^2$ .	175
Figure 5-70.	45 degree accelerated water entry, $a=1.71\text{m/s}^2$ .	175
Figure 5-71.	45 degree accelerated water entry, $a=2.40\text{m/s}^2$ .	176
Figure 5-72.	10 degree constant velocity water exit at $w=0.48\text{m/s}$ .	177
Figure 5-73.	15 degree constant velocity water exit at $w=0.72\text{m/s}$ .	177
Figure 5-74.	30 degree constant velocity water exit at $w=0.72\text{m/s}$ .	178
Figure 5-75.	45 degree constant velocity water exit at $w=0.94\text{m/s}$ .	178
Figure 5-76.	5 degree constant velocity water entry.	180
Figure 5-77.	10 degree constant velocity water entry.	181
Figure 5-78.	15 degree constant velocity water entry.	182
Figure 5-79.	30 degree constant velocity water entry.	183
Figure 5-80.	45 degree constant velocity water entry.	184
Figure 5-81.	10 degrees water exit.	185
Figure 5-82.	15 degrees water exit.	185
Figure 5-83.	30 degrees water exit.	185
Figure 5-84.	45 degrees water exit.	185
Figure 6-1.	5 degree constant velocity water entry, hydrodynamic force.	188
Figure 6-2.	10 degree constant velocity water entry, hydrodynamic force.	188
Figure 6-3.	15 degree constant velocity water entry, hydrodynamic force.	189



Figure 6-4.	30 degree constant velocity water entry, hydrodynamic force.	189
Figure 6-5.	45 degree constant velocity water entry, hydrodynamic force.	190
Figure 6-6.	Flat-bottomed section water entry, hydrodynamic force.	192
Figure 6-7.	Water pile-up, shape of the free surface.	195
Figure 6-8.	Slamming force coefficients.	197
Figure 6-9.	Peak pressure elevation.	198
Figure 6-10.	Maximum pressure coefficients.	199
Figure 6-11.	Wetting factors.	200
Figure 6-12.	Non-dimensional hydrodynamic force on 30 degree wedge section during constant velocity water entry obtained by subtracting the full Archimedes' buoyancy.	201
Figure 6-13.	Non-dimensional hydrodynamic force on 30 degree wedge section during constant velocity water entry obtained by subtracting the full Archimedes' buoyancy.	202
Figure 7-1.	Force components on wedge section during constant velocity water entry.	207
Figure 7-2.	Deep immersion flow momentum coefficients.	208
Figure 7-3.	Added mass coefficients based on water entry experiment and CFD simulation.	212
Figure 7-4.	Constant velocity water entry of 5 degree wedge section.	215

Figure 7-5.	Constant velocity water entry of 10 degree wedge section.	215
Figure 7-6.	Constant velocity water entry of 15 degree wedge section.	216
Figure 7-7.	Constant velocity water entry of 30 degree wedge section.	216
Figure 7-8.	Constant velocity water entry of 45 degree wedge section.	217
Figure 7-9.	Constant velocity water entry of flat-bottomed section.	218
Figure 7-10.	Non-dimensional constant velocity water entry force on a 20 degree wedge section.	220
Figure 7-11.	Non-dimensional water exit force, 10 degree wedge section.	224
Figure 7-12.	Non-dimensional water exit force, 15 degree wedge section.	224
Figure 7-13.	Non-dimensional water exit force, 30 degree wedge section.	225
Figure 7-14.	Non-dimensional water exit force, 45 degree wedge section.	225
Figure 7-15.	Wet chines oscillation of 0 degree section, $z/b=0.30$ to $0.38$ .	228
Figure 7-16.	Wet chines oscillation of 15 degree section, $z/d=3.11$ to $0.73$ .	228
Figure 7-17.	Wet chines oscillation of 45 degree section, $z/d=1.60$ to $1.77$ .	229
Figure 7-18.	Accelerated water entry added mass of 15 degree wedge section.	233



Figure 7-19.	Accelerated water entry added mass of 30 degree wedge section.	233
Figure 7-20.	Accelerated water entry added mass of 45 degree wedge section.	234
Figure 7-21.	Dry chines added mass coefficients from present theory, present experiments and by various other authors.	237
Figure 7-22.	Deep immersion added mass coefficients from theory and wet chines oscillation tests.	238
Figure 7-23.	Dry chines oscillation of 15 degree wedge section, $z/d=0.124$ to $0.746$ .	241
Figure 7-24.	Wet chines oscillation of 15 degree wedge section, $z/d=0.249$ to $0.498$ .	241
Figure 7-25.	Wet chines oscillation of 45 degree wedge section, $z/d=0.167$ to $0.833$ .	242
Figure 7-26.	Wet chines oscillation of 45 degree section, $z/d=0.667$ to $0.833$ .	242
Figure 8-1.	Coordinate system and notation for the planing equations.	246
Figure 8-2.	Predicted lift divided by measured lift for flat plates.	254
Figure 8-3.	Predicted lift divided by measured lift for 10 degrees deadrise, wet chines.	255
Figure 8-4.	Predicted lift divided by measured lift for 20 degrees deadrise, wet chines.	256
Figure 8-5.	Predicted lift divided by measured lift for 30 degrees deadrise, wet chines.	256

Figure 8-6.	Predicted lift divided by measured lift for 40 degrees deadrise, wet chines.	257
Figure 8-7.	Predicted lift divided by measured lift for dry chines planing.	258
Figure 8-8.	Predicted lift divided by measured lift for dry chines planing, plotted against trim angle.	259
Figure 8-9.	F(A) from (8-24) by use of sottorf's and shuford's flat plate data.	262
Figure 8-10.	Lift-curve slope derived from the flat plate data by shoemaker.	264
Figure 8-11.	Figure taken from Payne (1995) showing lift measurements by Weinstein and Kapryan (1953) divided by lift predicted by Payne plotted against length to beam ratios.	265
Figure 8-12 .	Figure taken from Payne (1995) showing lift measurements Sottorf (1929) divided by lift predicted by Payne plotted against length to beam ratios.	266
Figure 8-13.	F(A) from equations (8-31) and (8-32) by use of Shoemaker's 10 degree data.	268
Figure 8-14.	F(A) from equations (8-31) and (8-32) by use of Shoemaker's, Shuford's and Chambliss and Boyd's 20 degrees data.	268
Figure 8-15.	F(A) from equations (8-31) and (8-32) by use of Shoemaker's 30 degrees data.	269
Figure 8-16.	F(A) from equations (8-31) and (8-32) by use of Shuford's and Chambliss and Boyd's 40 degrees data.	269
Figure 8-17.	F(A) from (6-34) by use of Shoemaker's, Chambliss and Boyd's, Pierson's and Springston and Sayre's data.	271



- Figure 8-18. Top: 10 degrees  $f(A)$  values derived using zero buoyancy.  
Bottom: 10 degrees  $f(A)$  values derived using the  
full Archimedes' buoyancy. 272
- Figure 8-19. Top: 30 degrees  $f(A)$  values derived using zero buoyancy.  
Bottom: 30 degrees  $f(A)$  values derived using the  
full Archimedes' buoyancy. 273
- Figure 8-20. Predicted lift divided by measured lift for flat plates. 274
- Figure 8-21. Predicted lift divided by measured lift for 10 degrees deadrise,  
wet chines. 275
- Figure 8-22. Predicted lift divided by measured lift for 20 degrees deadrise,  
wet chines. 275
- Figure 8-23. Predicted lift divided by measured lift for 30 degrees deadrise,  
wet chines. 276
- Figure 8-24. Predicted lift divided by measured lift for 40 degrees deadrise,  
wet chines. 276
- Figure 8-25. Predicted lift divided by measured lift for dry chines. 277

---

**LIST OF TABLES**

---

Table 4-1.	Maximum pressure coefficients.	77
Table 4-2.	Buoyancy ratio curve fitting parameters.	106
Table 5-1.	Mass of test sections.	125
Table 5-2.	Maximum velocity deviation during constant velocity water entry.	152
Table 5-3.	Non-dimensional viscous force.	156
Table 5-4.	Viscous contribution to the total force.	157
Table 6-1.	$C_f$ , slamming force coefficients on immersion depth.	191
Table 6-2.	Wetting factors obtained with CFD and experiments.	194
Table 6-3.	Water pile up ratio, CFD and experiment.	196
Table 7-1.	Experimentally based dry chines added mass coefficients.	211
Table 7-2.	Deep chines immersion added mass coefficients based on oscillation experiment data.	227
Table 7-3.	Infinite depth added mass coefficient, present theory and experiment.	230
Table 7-4.	Dry chines added mass coefficients from accelerated water entry experiments.	232



---

## REFERENCES

---

BISPLINGHOF, R.L. and DOHERTY, C.S. 1950. Some studies of the impact of vee wedges on a water surface. Journal of the Franklin Institute.

BOBYLEFF, D. 1881. Journal of Russian Physio-Chemical Society, 13.n

CHAMBLISS, D.B and BOYD, G.M. Jr 1953. The planing characteristics of two v-shaped prismatic surfaces having angles of deadrise of 20 degree and 40 degree. NACA TN2876.

CHUANG, S.L. 1967. Experiments on slamming of wedge shaped bodies. Journal of Ship Research, 11.

HOERNER, S.F. 1965 Fluid Dynamic Drag. Midland Park, Midland Park, New Jersey.

JONES, R.T. 1946. Properties of low-aspect ratio pointed wings at speeds below and above the speed of sound, NACA TR 835.

KORVIN-KROUKOVSKY, B.V. 1950. Lift of planing surfaces. J. Aero. Sci. 17.

KREPS, R.L. 1943. Experimental investigation of impact in landing on water. NACA 1046.

LAMB, H. 1932. Hydrodynamics. Cambridge Univ. Press.

LEWIS, F.M. 1929. The inertia of the water surrounding a vibrating ship. SNAME Transactions 37.

MAYO, W.L. 1943. Analysis and modification of theory for impact of seaplanes on water. NACA TN 1008.

MUNK, M. 1924. The aerodynamic forces on airship hulls. NACA TR 184.

- NG, C.O. and KOT, S.C. 1992. Computations of water impact on a two-dimensional flat-bottomed body with a volume of fluid method. *Ocean Engng*, 19.
- PABST, W. 1931. Theory of the landing impact of seaplanes. NACA TM 580.
- PABST, W. 1932. Landing impact of seaplanes. NACA TM 624.
- PAYNE, P.R. 1981. The normal force on a flat planing plate, including low length to beam ratios. *Ocean Engng* 8.
- PAYNE, P.R. 1982. Contributions to the virtual mass theory of hydrodynamic planing. *Ocean Engng* 9.
- PAYNE, P.R. 1988. Design of high-speed boats, Volume 1: Planing, Fishergate, Inc., Annapolis, Maryland USA.
- PAYNE, P.R. 1992. A unification in the added mass theory of planing. *Ocean Engng* 19.
- PAYNE, P.R. 1994. Recent developments in "added-mass" planing theory. *Ocean Engng* 21.
- PAYNE, P.R. 1995. Contributions to planing theory. *Ocean Engng* 22.
- PIERSON, J.D. 1951. On the virtual mass of water associated with an immersing wedge. *Journal of Aeronautical Sciences*. June 1951.
- PIERSON, J.D., DINGEE, D.A and NEIDINGER, J.W. 1954. A hydrodynamic study of the chines-dry planing body. Stevens Institute of Technology, Davidson Laboratory Report SIT-DL-54-492.
- PIERSON, J.D. and LESHNOVER, S. 1948. An analysis of the fluid flow in the spray root and wake regions of flat planing surfaces. Steven Institute of Technology, Report 335.
- PRANDTL, L. 1905. Über flüssigkeiten bei sehr kleiner reibung. *Verh. III Internat. Math. Kongr., Heidelberg*.



SAMBRAUS, A. 1936. Planing – NACA TM 848.

SAVITSKY, D. 1964. Hydrodynamic design of planing hulls. Marine Technology, 1.

SAVITSKY, D and NEIDINGER, J.W. 1954. Wetted area and center of pressure of planing surface at very low speed coefficients. Stevens Institute of Technology, Report No. 493.

SCHNITZER, E. 1953. Theory and procedure for determining loads and motions in chine-immersed hydrodynamic impacts of prismatic bodies. NACA Report 1152.

SELLARS, F.H. 1967. Water impact loads. Marine Technology, 13.

SHOEMAKER, J.M. 1934. Tank tests of flat and v-bottom planing surfaces. NACA TN 509.

SHUFORD, C.L. 1954. A review of planing theory and experiment with a theoretical study of pure-planing lift of rectangular flat plates. NACA TN 3233.

SHUFORD, C.L. 1958. A theoretical and experimental study of planing surfaces including effects of cross-section and plan form. NACA Report 1355.

SOTTORF, W. 1929 Experiments with planing surfaces. NACA TM 661.

SPRINGSTON, G.B. and SAYRE, C.L. Jr 1955. The planing characteristics of a v-shaped prismatic surface with 50 degree deadrise. DTMB, Report 920.

TAKEMOTO, H., OKA, M. and SAKUMA, M. 2000. Experiments of threshold velocity of water impact of wedges. Transactions of West Japan Society of Naval Architects, 100.

TAYLOR, J.L. 1930. Hydrodynamical inertia coefficients. Philosophical Magazine 9.

- VON KARMAN, T. 1929. The impact of seaplane floats during landing. NACA TN 321.
- VORUS, V.S. 1996. A flat cylinder theory for vessel impact and steady planing resistance. *Journal of Ship Research*, 40.
- VUGTS, J.H. 1968. The hydrodynamic coefficients for swaying, heaving and rolling cylinders in a free surface. *International Shipbuilding Progress*, 15.
- WAGNER, H. 1931. Landing of seaplanes. NACA TM 622.
- WAGNER, H. 1932. Über stoss- und gleitvorgänge an der oberfläche von flüssigkeiten. *Zeitschrift für Angewandte Mathematik und Mechanik* 12.
- WEINSTEIN, I and KAPRYAN, W.J. 1953. The high-speed planing characteristics of a rectangular flat plate over a wide range of trim. NACA TN 2981.
- ZHAO, R. and FALTINSEN, O. 1993. Water entry of two-dimensional bodies. *J. Fluid Mech.* 246.
- ZHAO, R., FALTINSEN, O. and AARSNES, J. 1997a. Water entry of arbitrary two-dimensional sections with and without flow separation. *Twenty-First Symposium on Naval Hydrodynamics*.
- ZHAO, R. and FALTINSEN, O. 1997b. A simplified nonlinear analysis of a high-speed planing craft in calm water. 4<sup>th</sup> Int. Conf. Fast Sea Transportation, Sydney.